# BULGARIAN CHEMICAL COMMUNICATIONS

**2016** Volume 48 / Special Issue E1

Selected papers presented on the XV International Scientific Conference
Renewable Energy & Innovative Technologies,
Smolyan, Bulgaria, June 10 -11, 2016

*Journal of the Chemical Institutes*
*of the Bulgarian Academy of Sciences*
*and of the Union of Chemists in Bulgaria*

*Bulgarian Chemical Communications, Volume 48, Special Issue E (pp. 3–3) 2016*

# PREFACE

The XV International Scientific Conference "Renewable Energy & Innovative Technologies" was held between 10th and 11th June 2016 at the Technical College of Smolyan, Bulgaria. Representatives of 21 countries (Bulgaria, Turkey, Russia, Cyprus, Spain, Lithuania, Kazakhstan, India, United Kingdom, Italy, Serbia, Austria, Romania, France, China, Latvia, Greece, Brazil, India, Iran and Ukraine) sent their works to the conference. Some of the reports (69 works) have been selected and are published after international peer-review in the present Special Issue of the journal "Bulgarian Chemical Communications".

It is our pleasure to be guest editors of the presented articles, which focus on new international scientific results in the field of Renewable Energy and Innovative Technologies (Solar and Hybrid Thermal Systems, Solar Photovoltaic Systems, Storages with Phase Change Materials, Energy Efficiency, Materials Science, Food Engineering and Technologies, and Biotechnologies).

Prof. Aleksandar Georgiev, PhD (European Polytechnic University, Pernik, Bulgaria)

Assoc. Prof. Daniela Dzhonova-Atanasova (Bulgarian Academy of Sciences, Sofia, Bulgaria)

**Guest editors** of the present Special Issue

# SOLAR AND HYBRID THERMAL SYSTEMS

*Bulgarian Chemical Communications, Volume 48, Special Issue E (pp. 7 - 18) 2016*

# Long term experience and research on hybrid thermal systems

A. G. Georgiev

*Technical University of Sofia, Plovdiv Branch, Dept. of Mechanics, 25 Tsanko Diustabanov Str, 4000 Plovdiv, Bulgaria*
*European Polytechnic University, Dept. of "Green Energy", 23 Kiril and Metodiy str., 2300 Pernik, Bulgaria*

There are different types of hybrid thermal systems. The term "Hybrid system" usually refers to at least two types of installations. They possess elements such as a Phase Change Material (PCM) storage, a heat pump, solar collectors, heat rejecters, a seasonal water storage and an underground thermal energy storage, which can be combined with an electrical apparatus (e.g. Photovoltaic/ Thermal.(PV/T) collectors) and a second heat pump. The aim of the hybrid thermal installation is to improve the system's energy efficiency. The article discusses different configurations of hybrid thermal systems. At the same time the article presents the long experience of the members of the scientific team at the Plovdiv Branch of the Technical University of Sofia and the research they have done on hybrid thermal systems. The prospects for future developments are also mentioned.

**Keywords:** hybrid thermal systems, renewable energy sources, underground thermal energy storages

## INTRODUCTION

A thermal system is a unit that consists of several components. There are not only thermal elements inside the aggregate - electrical and mechanical parts are available, too. What a hybrid system is, still remains without a concrete answer. Usually the term "Hybrid system" refers to at least two types of installations.

There is a great variety of hybrid thermal systems. Three types are presented in this article, namely the solar hot water supply system with a phase change material (PCM) and water hybrid storage system [1], the renewable energy sourced hybrid heating system combined with a latent heat storage and a heat pump [2] and the hybrid photovoltaic/ thermal (PV/T) system [3].

Other very popular type of hybrid thermal systems in the last decades is the Ground Source Heat Pump (GSHP) system. It contains underground thermal energy storages and one or more heat pumps of different possible types. If we combine them with another kind of equipment with the aim of improving the system's performance, we get the so-called hybrid GSHP (HGSHP) systems. A number of these HGSHPs are an object of discussion in this paper: HGSHP systems with solar collectors [4], HGSHP systems with hot water supply [5], HGSHP systems with supplemental heat rejecters [5], Hybrid storage systems for seasonal thermal energy storage in solar district heating [6], Cool thermal energy storage (BTES-PCM) for peak shaving [7] and Hybrid ground-coupled heat pump systems for air conditioning [8].

* To whom all correspondence should be sent:
ageorgiev@gmx.de

Some of the members of the scientific team at the Technical University of Sofia, Plovdiv Branch, participated in the design, construction and study of several hybrid thermal installations. The charging and discharging of a hybrid installation with solar collectors and Borehole Thermal Energy Storage Systems (BTES) [9], a novel ground heat exchanger coupled with phase change materials [10], a hybrid PV/T system at TU-Sofia, Plovdiv Branch [11], and a hybrid GSHP installation in Plovdiv [12] are presented in the current work.

## HYBRID THERMAL SYSTEMS

Although there is a big variety of hybrid thermal systems, only three of them are discussed below. They do not include any underground device, but the installations contain components such as PCM storage, heat pump, high temperature solar collectors and even a combination with electrical facility (for example PV/T solar collector) - system elements which have not been used much in the past, but are becoming more and more popular during the last three decades.

### *Solar hot water supply system with a PCM/ water hybrid storage system*

Nagano et al. [1] propose an installation with evacuated solar collectors and a PCM storage for domestic hot water (DHW) production [1]. It has three heat-pipe type vacuum tube solar collectors (VSC), which contain 70 vacuum tubes with a total collector area of 7 m². The storage system consists of a water storage (250 l) and a PCM storage (76 l). The PCM used is a mixture of $Mg(NO_3)_2 \cdot 6H_2O$ and $MgCl_2 \cdot 6H_2O$, which has a melting temperature of 59,7 °C and a heat of fusion of 161,2 kJ/kg (Fig.1).

The charging mode includes the operation of circulation pump (4) during the day. The pump moves a brine mixture through the PCM and the water storages. The pump is switched ON when the temperature difference between the collector inlet temperature of the brine and the outlet water tank temperature of the brine is higher than 3°C. After leaving the solar collectors (1) the brine heats first the PCM device (3) and then is delivered to the water storage (2). A by-pass pipeline is used to directly charge the water storage tank, if the collector outlet brine temperature is lower than the PCM temperature (the corresponding magnetic valves (6) are switched ON or OFF after receiving temperature regulator signals).

The discharging mode occurs during the night. About 500 l tap water is delivered to the bottom of the hot water tank. The water is heated initially in the water tank and after that it enters the PCM storage for additional heating to a higher temperature. The final needed temperature is about 42°C. If the outlet water temperature is higher than 42°C, a mixing with tap water takes place - the temperature sensor sends a signal to the magnetic valve (8). If the described system cannot produce water with a temperature of 42°C, an auxiliary heating source is used for additional heating.

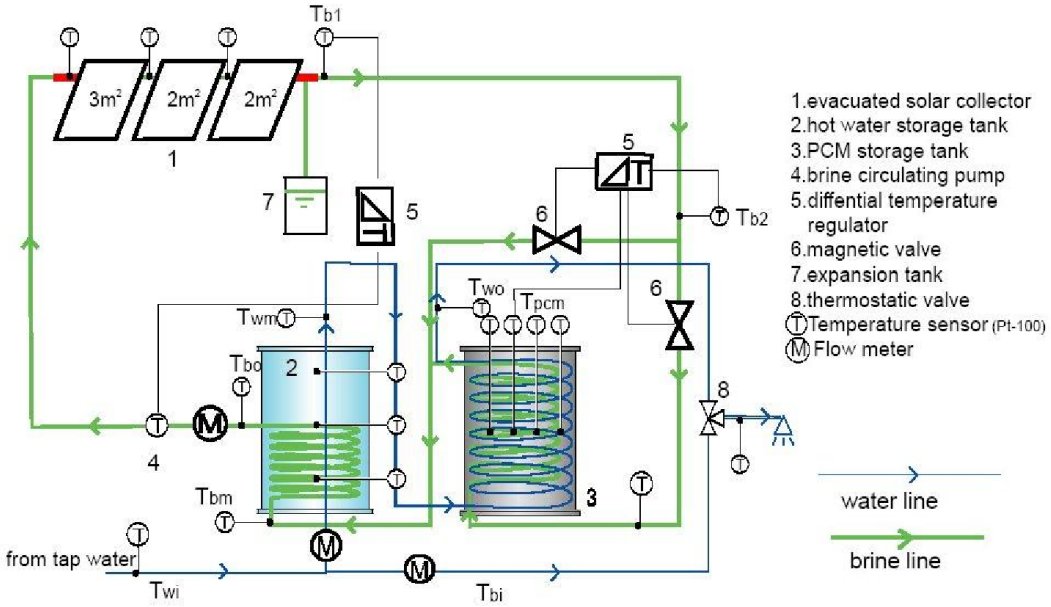


**Fig.1.** Solar hot water supply system with a PCM/ water hybrid thermal energy storage system [1]

*Renewable energy sourced hybrid heating system combined with latent heat storage*

A hybrid thermal system is set up at the Davutpasha Campus in Turkey. The installation contains three main components - solar collectors (SC), a heat pump (HP) and a latent heat storage (LHS) [2]. It is used for heating the Yildiz Renewable Energy Building (YREB).

Fig.2 shows the installation setup. In addition to the SC, HP and the LHT accumulation tank (AT), a wall heating system is available. The two installed flat plate solar collectors have a total surface area of 3,24 m². The collectors, with a theoretical efficiency of 85%, are connected to the latent storage serially. The on-off controlled circulating cycle pump has an electrical power of 100W. The latent heat storage has a steel construction and is painted black. Its external size is 0,22 m³. The paraffin is enclosed in a case with a volume of 0,063 m³. The PCM used is paraffin with a melting point between 42 and 44 °C. The working fluid delivered by the solar collectors circulates around the paraffin case within the latent heat storage. Additionally, there is a water gap in the middle of the storage with a diameter of 0,1m.

The latent storage is charged by the heat delivered from the solar collectors during the daytime. A circulating pump is switched ON if the water temperature in the latent storage is higher than 45 °C. In this way it delivers the water to the well-insulated water storage (AT). The temperature in the AT must be 45°C because the temperature regime of the wall heating is 45–35 °C. If the outlet water LHT temperature is lower than 45°C, the water is delivered to the heat pump with the aim of raising its temperature. The heat pump does not work if the water temperature in the water tank is higher than 45°C. This leads to relatively big

energy savings. The computer software DALI (Data Acquisition and Logging Interface) and TELECONTROL are used to show the temperatures at the different measuring points. A comprehensive experimental energy and exergy analysis of the system components, as well as of the system as a whole, has been performed.

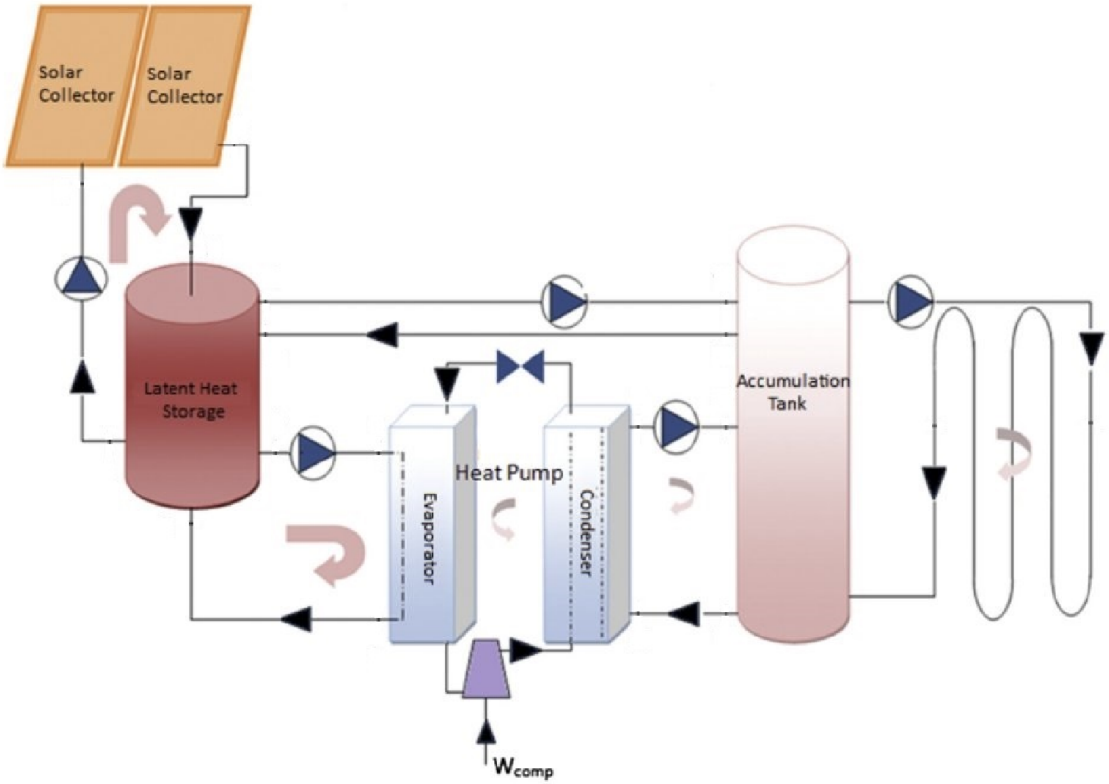


**Fig.2.** Renewable energy sourced hybrid heating system combined with latent heat storage [2]

*Hybrid PV/ T systems*

A combination of collectors which produce both heat and electricity is not uncommon. These solar collectors are called photovoltaic - thermal (PV/T) collectors. Such a collector construction has the following advantages [3]:

- the electrical efficiency of the combined PV/T collector is higher than that of the plain photovoltaic panel;
- the uniformity on the roof typical for the PV/T collectors is better compared to a separate thermal collector and a PV panel;
- the mounting of one instead of two installations is a precondition for reducing the capital expenses.

There are nine design concepts available. They can be divided in four different groups [3]. Their sketches are presented in Fig.3:

**1. Sheet-and-tube PV/T-collectors** (Fig.3A). A metal serpentine pipe of any kind is placed on the back side of the standard simplest photovoltaic panel. When this pipe is covered with an insulation, a Sheet-and-tube construction of a PV/T-collector is produced.

**2. Channel PV/T-collectors** (Fig.3B). There is a channel with a liquid which has direct contact with the PV area. The use of water can diminish the electrical efficiency with up to 4%. An additional disadvantage is the level of liquid transparency which leads to a further decrease in efficiency.

**3. Free flow PV/T-collectors** (Fig.3C). In this construction the additional glass layer between the gas and the liquid, which is available in the Channel PV/T-collector construction, is missing. Thus the two different fluids are mixed. However, one disadvantage is the higher evaporation leading to additional decrease in efficiency. The losses due to fluid transparency are similar to the channel PV/T-collectors.

**4. Two-absorber PV/T-collectors** (Fig.3D). There are two PV panels. The upper one must be transparent. There are also two water channels. Thus the liquid (eventually water) passes through the upper channel and exits through the lower one.

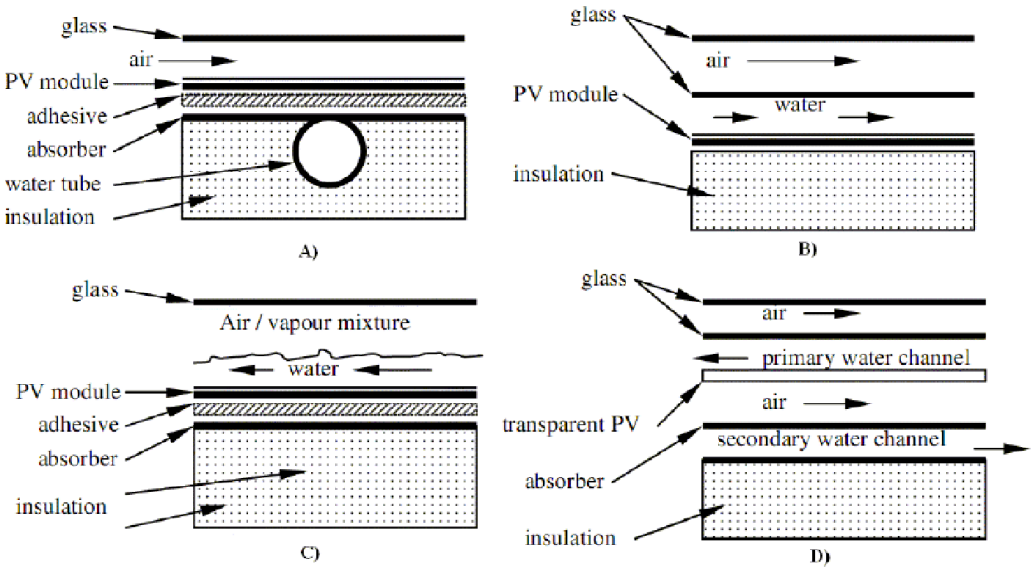


**Fig.3.** Different types of water cooled flat PV/T collectors [3]

## HYBRID GSHP SYSTEMS

The Ground source heat pump (GSHP) systems consist of an underground thermal energy storage and any type of heat pump. These systems can be used for heating and/or for cooling. Their efficiency is very good if the building's heating and cooling loads are well balanced on an annual basis. Unfortunately, in warm-climate or cold-climate areas there is always an imbalance and consequently there is a domination of either cooling or heating loads (Fig.4). In both cases a larger area of borehole heat exchangers (BHEs) is needed, which reduces the system's efficiency [13]. A good solution to the problem is to diminish the capital costs by means of a heat rejecter or a heat absorber, thus obtaining the so-called hybrid GSHP (HGSHP) systems.

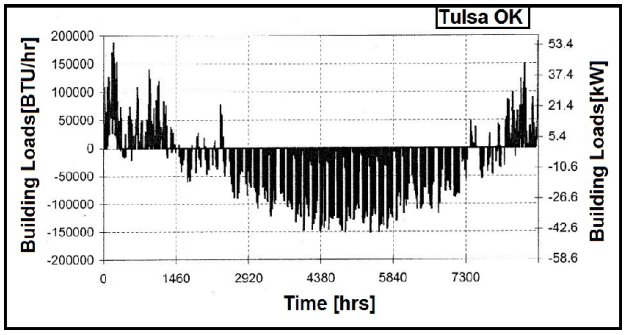


**Fig.4.** The region of Tulsa, Oklahoma with a relatively moderate climate (cooling loads are negative and heating loads are positive) [13]

Seven different constructions of HGSHP systems are discussed below. They possess additional components such as solar collectors, heat rejecters, a seasonal water storage, a PCM storage or an additional heat pump.

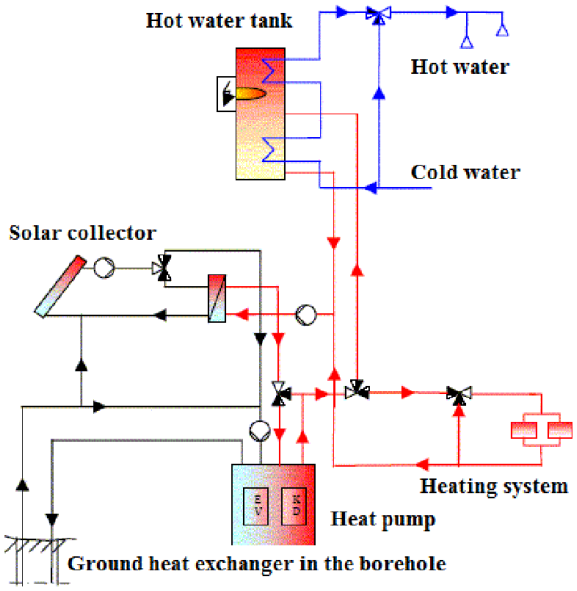


**Fig.5.** Example of a system with solar collectors in combination with a ground-source heat pump [4]

### *HGSHP systems with solar collectors*

About 40 years ago the ground was used only as a heat source. The practice shows that there is a heat depletion at the place of use. That means that in regions where more heating is needed the inlet fluid temperature in the heat pump evaporator is going to decrease in the course of a long period of time. The use of solar collectors for example is a good opportunity to raise the temperature of the used ground area. So the capital costs (in this case the number of the BHEs) will decrease

significantly. An example of a system with solar collectors which are combined with a heat pump and borehole heat exchangers is presented in Fig.5.

*HGSHP systems with hot water supply*

The production of domestic hot water (DHW) requires higher temperature. Heat is normally produced by burning fossil fuels or using electrical heaters. One interesting opportunity is the DHW production by means of HGSHP systems during a cooling season. A device called desuperheater (a small additional heat exchanger) can be installed near the heat pump compressor [5]. In this way the excess heat obtained by condensation is used to heat a certain amount of DHW (Fig.6).

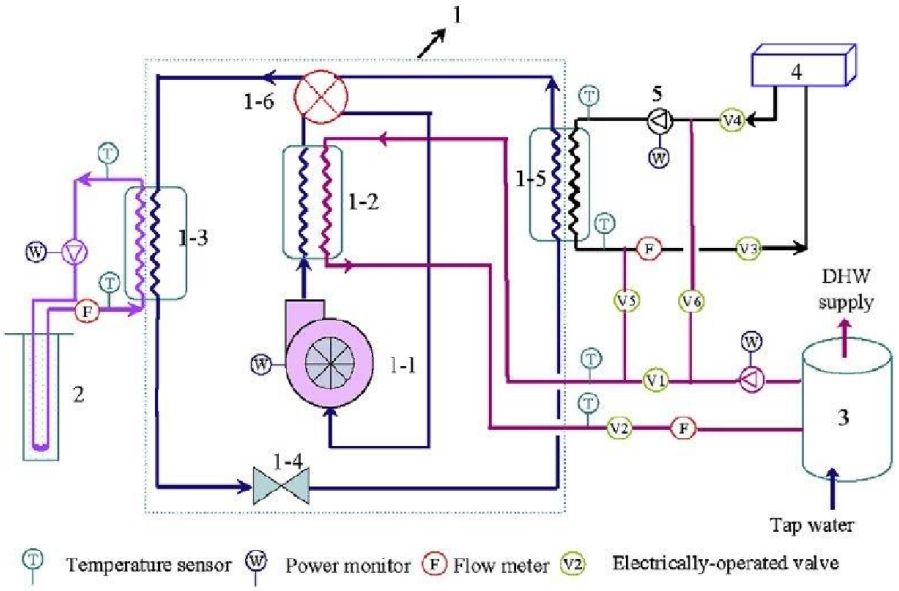


**Fig.6.** Schematic diagram of the HGSHP with a DHW heating system [5]

*HGSHP systems with supplemental heat rejecters*

Assuming that the building is in a region with dominating cooling regime such as Tulsa, Oklahoma (Fig.4). HGSHP systems can be used in this case. However, it is better to have an additional cooler during the cooling season (in order to avoid the capital cost for more BHEs). A good solution in this case is to include a cooling tower with the aim of cooling the BHEs which are connected to the condenser of the GSHP [5]. An example of this type of system is shown in Fig.7. The HGSHP system has a cooling tower which is connected in series with the ground loop (there is a heat exchanger between the boreholes and the cooling tower).

*Hybrid storage system for seasonal thermal energy storage in solar district heating*

There are different types of seasonal thermal storages that are constructed under the ground. The convective storage with water as a medium is called pit storage. The conductive storage type with the soil as a medium is called duct storage (or borehole thermal energy storage, BTES). There is also a mixed type of underground storage - it is called aquifer thermal energy storage [14].

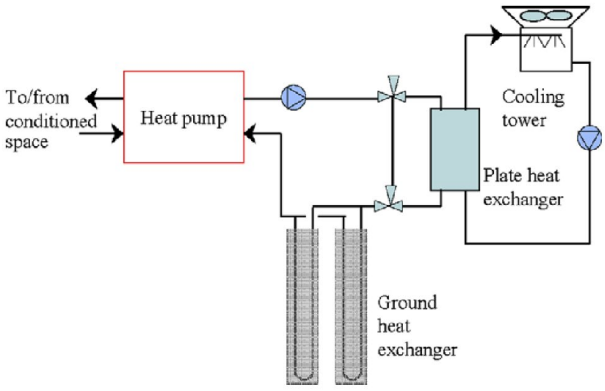


**Fig.7.** Schematic diagram of a HGSHP with cooling tower [5]

The convective storage can be heated up to 90°C (this is the requirement for implementing solar district heating). In addition, its medium can be used as a working fluid. Unfortunately the construction of a storage of this type is relatively expensive. The BTES is, to the contrary, relatively less flexible than the convective storage (there is an additional exchange process from soil to fluid and vice versa), but its construction costs are lower than the costs of building a convective storage.

A combination of the above-mentioned storages is suggested in Müller and Reuss [6]. It consists of a pit storage which is surrounded by a number of boreholes (BTES). There is no need for expensive insulation for the pit storage - the thermal losses reduce drastically due to the heat that is directed to the surrounding boreholes (Fig.8). On the other hand, the low potential heat coming from the solar collector is delivered to the BTES (if its outlet temperature is not high enough and thus not appropriate for the pit storage). The described storage combines the economical and operational advantages of both the convective and the conductive storage types.

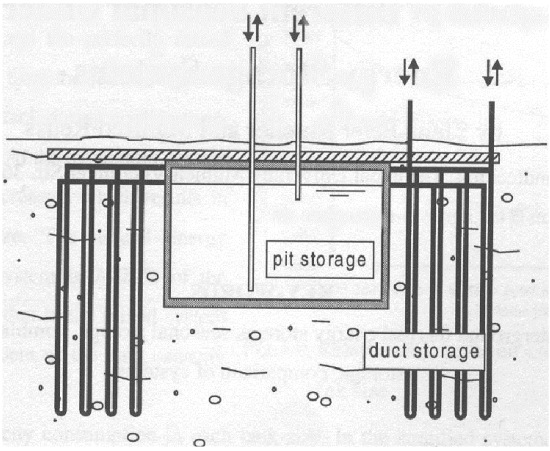


**Fig.8.** Hybrid pit/ duct store [6]

*Cool thermal energy storage (BTES-PCM) for peak shaving*

Underground thermal energy storages (UTESs) are used in Sweden in cooling mode during the summer. The BTES systems are usually connected to mechanical chillers with the aim of covering the cooling peak load in the afternoon. The use of a PCM storage can replace the chillers and avoid the relatively high electrical energy consumption. The set-up of such a system is presented in Fig.9. The BTES is presented in the diagram as a seasonal storage which is charged by using heat pumps for cooling in winter. After that, in the summer, the stored cooling is used to cool the buildings. Unfortunately there are peak loads in the afternoon. The installation that includes a PCM storage is designed for peak shaving. That means that the PCM storage is charged for about 6 hours at night using the BHEs at an approximate rate of 50 kW. This cooling is used in the afternoon (for about 3 hours) when the PCM storage is discharged with a rate of 100 kW.

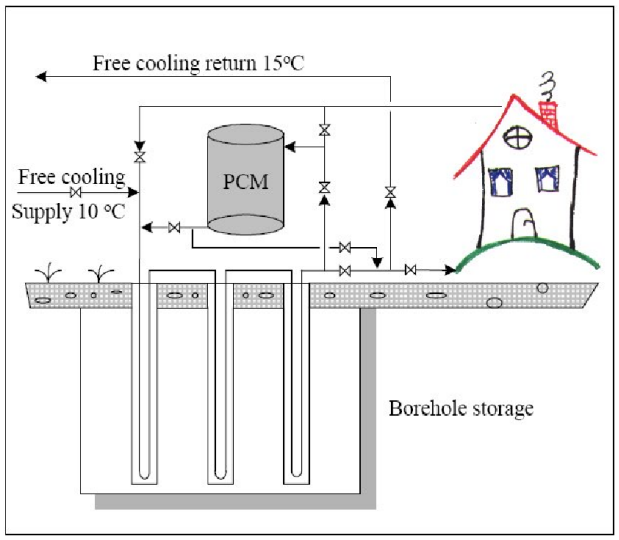


**Fig.9.** A combined BTES-PCM cool storage air conditioning system [7]

*Hybrid ground coupled heat pump system for air conditioning*

Several layouts of hybrid ground coupled heat pump systems for air conditioning are presented in Pardo et al. [8]. The main installation elements are a water to water heat pump (WWHP), an air to water heat pump (AWHP), a thermal storage device (TSD), an air fan (AF), a ground heat exchanger (GHE), an internal as well as an external water pump (IWP, EWP) and a storage water pump (SWP).

Fig.10 shows one of the proposed hybrid systems (configuration A). The aim of the installation is to cool the buildings in regions where the cooling season is longer than the heating season (e.g. Valencia, Spain). Two types of heat pumps are used because they are connected to cold sources which have different temperatures during the day and during the night.

The presented configuration has an AWHP which is switched on during the night because the air temperature then is lower than the ground temperature. This is how the TSD is loaded. The IWP is switched on during the day with the aim of cooling the building. If its capacity is not enough, the WWHP is switched on. The by-pass connection

near the storage is used when the outlet fluid storage temperature is higher than the inlet fluid storage temperature.

The proposed configuration is expected to improve the system energy efficiency during the cooling season in regions with dominating cooling loads.

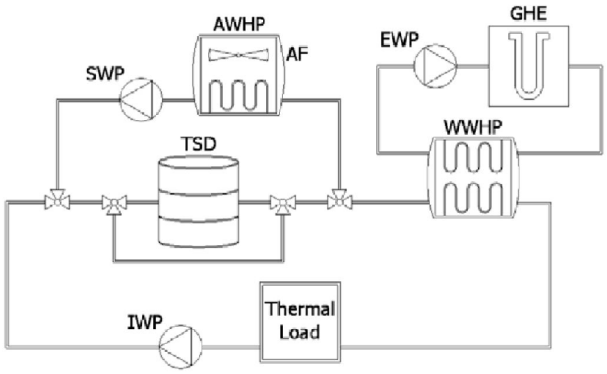


**Fig.10.** Hybrid configuration type A [8]

## BULGARIAN TEAM EXPERIENCE ON HYBRID THERMAL SYSTEMS

A scientific team was created at the Technical University of Sofia, Plovdiv Branch, in 2005. Its long experience includes work in the field of Renewable Energy Sources. The main subject of investigation was hybrid thermal systems and their components. Several of the team members had previous or parallel work in the same research area with other research groups abroad. Several hybrid systems in different types of studies are presented below.

### *Charging and discharging of hybrid installation with solar collectors and BTES*

A hybrid installation with solar collectors and Borehole Thermal Energy Storage (BTES) was set up in 2003 at the "Solar Energy Laboratory" of the Technical University Federico Santa Maria (UTFSM) in Valparaiso, Chile with the participation of Prof. A. Georgiev [9]. The shallow Borehole Heat exchanger (BHE) was used to carry out an in situ determination of ground thermal conductivity $\lambda$, borehole thermal resistance $R_b$ and undisturbed soil temperature. This technique is commonly known as Thermal Response Test (TRT). The first stage of the setup preparation included three perforations along a line to a depth of about 22 m followed by the implementation of the TRT.

At the second stage of the setup preparation, just after completing the TRT, the installation was remodelled. Three solar collectors with a total active area of about 4,4 m² were connected to the BTES. This configuration of the installation was used to charge the ground by means of solar energy (natural experiment). This charging took place in the course of 29 days (from 18th of August to 16th of September 2003).

After the charging cycle a new modification was introduced to the hydraulic system. One loop of a cross-flow water-water heat exchanger was connected to the BHE circuit instead of the solar collectors, while the other loop fed the heat exchanger with tap water (Fig.11). An old automobile radiator was adapted to work as the cross-flow water-water heat exchanger. The discharging mode started on the 17th of September and ended on the 30th of September 2003. The corresponding temperatures and flow rates as well as the solar insolation were measured and recorded during the second and third stages of the study.

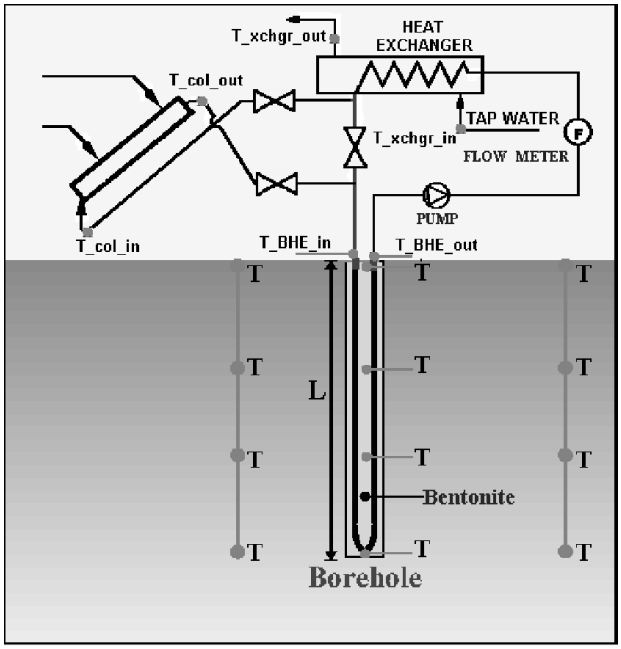


**Fig.11.** Diagram of the test installation during charging and discharging [9]

### *Novel ground heat exchanger coupled with phase change materials*

Employing Phase Change Materials (PCMs) is an effective measure to store thermal energy and it may also be used as an effective method to smooth the thermal wave generated from the operation of a GSHP. The approach is known when the PCMs are introduced directly in a tank within a closed loop, especially for vertical closed loop. However, using a tank containing PCMs could be an expensive solution for the horizontal closed loop ground heat

exchanger (GHE) system, due to the low energy performance of the PCMs. Moreover, the heat transfer may not be effective for the bulky PCM tank.

The international scientific team proposed to mix the micro-encapsulated PCMs directly with the backfill material which is close to the GHE or to install them in a surrounding shell [10]. Use of the PCMs incorporated with GHEs may meet some instantaneous heating demand by a GSHP, thus reducing the sudden heating or cooling wave upon the ground. Therefore, the peak temperature would be lower with the same GHE length, or the GHE length could be shorter with the same peak temperature. The performance of the novel GHE design with PCMs is currently being analysed by means of an experimental setup and a numerical approach.

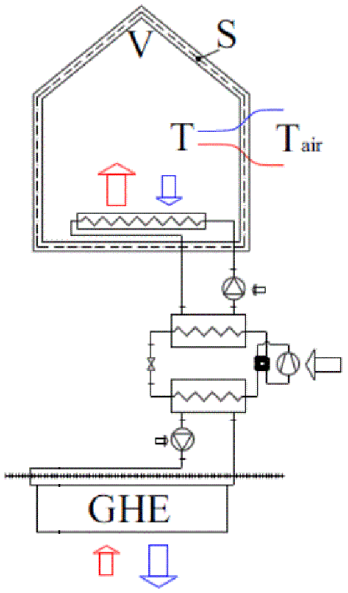


**Fig.12.** Coupling sketch of one-half symmetric model domain of a GHE with a heat pump [10]

The model domain considers a cross-section which consists of a PCM layer and a large part of the surrounding soil. The PCM layer is a mix of micro-encapsulated paraffin, water and soil with specified mass ratios. The coupling sketch of one-half symmetric model domain of a GHE with a heat pump is shown in Fig.12.

The application has been evaluated through numerical modelling to solve transient heat transfer using effective heat capacity method. Annual performance has been simulated by taking into account the estimated energy requirement for an assumed residential building located in Northern Italy. According to hourly time series boundary conditions and annual performance, the simulation results show that the use of PCMs is able to smooth the thermal wave in the ground, to improve the coefficient of performance of the heat pump (COP) and, if suitably sized, to prevent thermal depletion in winter by charging the PCMs naturally in summer with a shallow GHE.

*Hybrid PV/ T system at TU-Sofia, Plovdiv Branch*

An installation for testing of photovoltaic (PV) solar panels was set up in 2010 at the Technical University of Sofia, Plovdiv Branch (Fig.13). The main parts of the installation are a combined PV/T solar panel 1 and an ordinary photovoltaic solar panel 12. A circulation pump 2 is used to move the cooling fluid through the combined panel and the thermostat tank 3 - it is used to maintain a constant temperature through the PV/T panels. A PT100 Signal Conditioner 5 is used to measure the temperature. The signal is then sent to a data logger 6 and processed using a Laptop or a personal computer 7. An integrated solarimeter/ anemometer 8 is used to measure the global solar radiation and the wind velocity. The pyrheliometer 9 measures the direct solar radiation by means of the sun-following system (sun tracker) 10 and the direct solar radiation measurement unit 11. The current/ voltage signal conditioners 13 are utilized to measure the electrical power obtained from the sun [11].

The experiment was carried out during 2 days – 26 and 27 of May 2010. 7 tests were done. Each test had a duration of about 15 min. The following parameters were measured: intensity of the global solar radiation (using the integrated solarimeter), ambient temperature, flow rate, inlet and outlet fluid temperature trough the PV/T panel, thermal power produced by the PV panel and electrical power produced by the PV/T panel. The produced thermal power from the PV/T panel, the ratio of electrical power produced by PV/T panel to PV panel and the ratio of thermal to electrical power produced by PV/T panel were calculated.

The test results show that:

- the gained thermal power in the PV/T panel is about 9 times higher than the gained electrical power in the temperature interval (20 till 50°C);
- the effect of the increased electrical production in the PV/T panel is relatively stable over a long temperature interval;
- the cooled PV/T panel produces about 3% more electricity than the PV panel in the whole temperature interval.

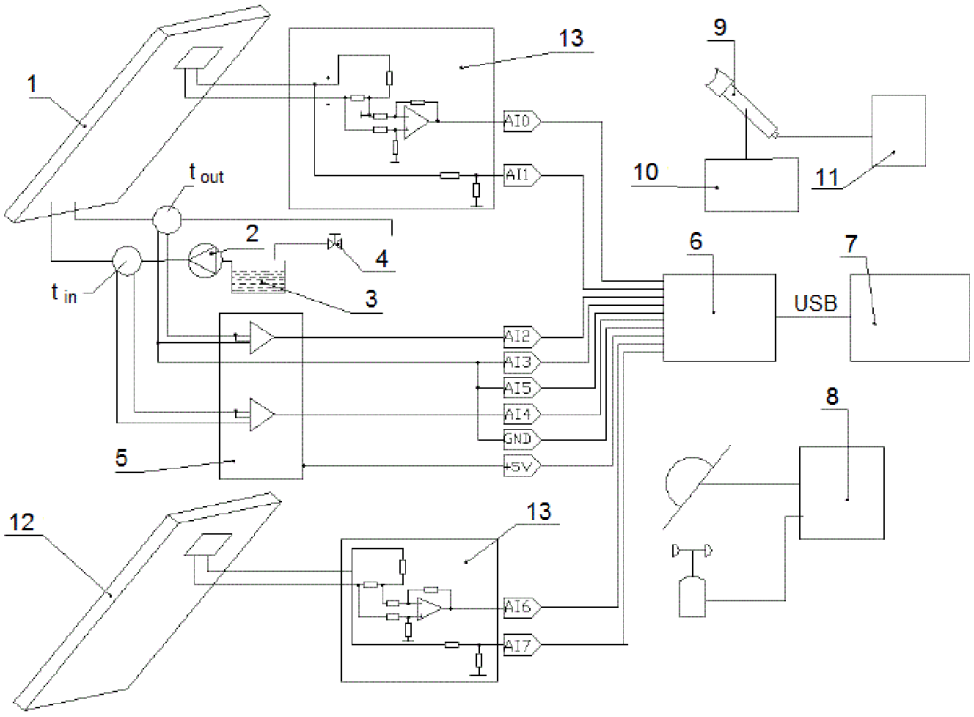


**Fig.13.** Installation setup of PV/T system in Plovdiv [11]

*Hybrid GSHP installation in Plovdiv*

In 2013 a test installation with solar collectors charging a phase change material (PCM) storage, a borehole storage and a heat pump was developed at the Technical University of Sofia, Plovdiv Branch. The main aim of the scientific team was to evaluate different types of phase change materials that could potentially be used in domestic heating, cooling and hot-water systems for daily accumulation storage. A ground borehole heat exchanger loop was also added. A photograph of the interior section of the hybrid installation is shown in Fig.14.

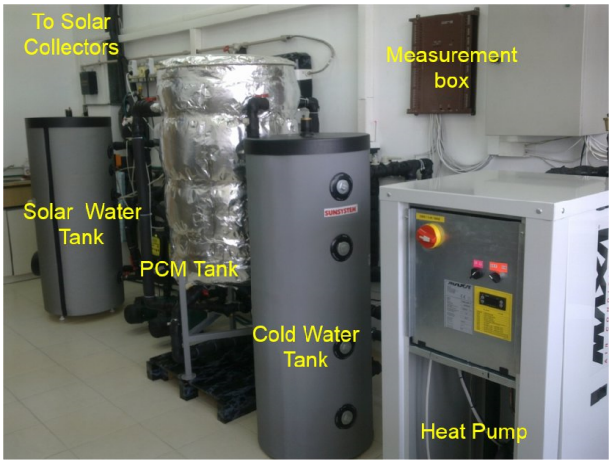


**Fig.14.** Interior laboratory view of the hybrid installation

In the experiments a large number of parameters (temperatures, flow rates, solar radiation values, electrical consumption etc.) have to be logged and monitored for a long period of time. Sophisticated methods for analysing an obtained data set have been used by implementing a Supervisory Control and Data Acquisition (SCADA) system, which also allowed remote control and supervision via Internet. The National Instruments LabView package was used in this study to develop user-friendly virtual instrumentation for the research.

**1. Construction of the system**

The installation is located in Plovdiv, Bulgaria, at the campus of the Technical university of Sofia, on the 4-th floor. Its test setup is presented in Fig.15. The main components of the installation are: solar collectors (SC), a hot-water storage (200 l), a latent heat storage (300 l), a water-water heat pump (inverter type), a cold-water storage (150 l), two borehole heat exchangers (BHEs), two expansion tanks, a flat panel heat exchanger and a fan-coil convector [12]. The installation is designed to ensure that there is no pressure in the PCM storage tank, which allows the sensors to be easily placed inside.

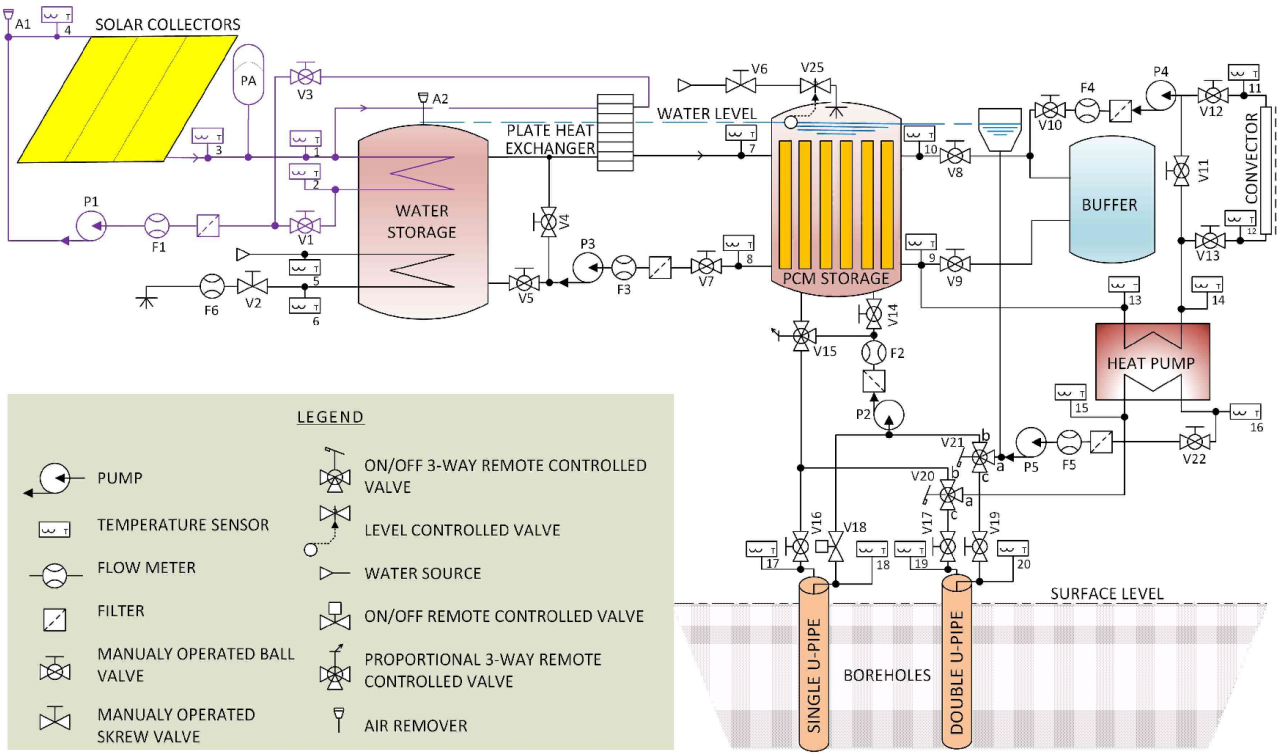


**Fig.15.** Diagram of the hybrid installation (GSHP with SC and PCM storage) [12]

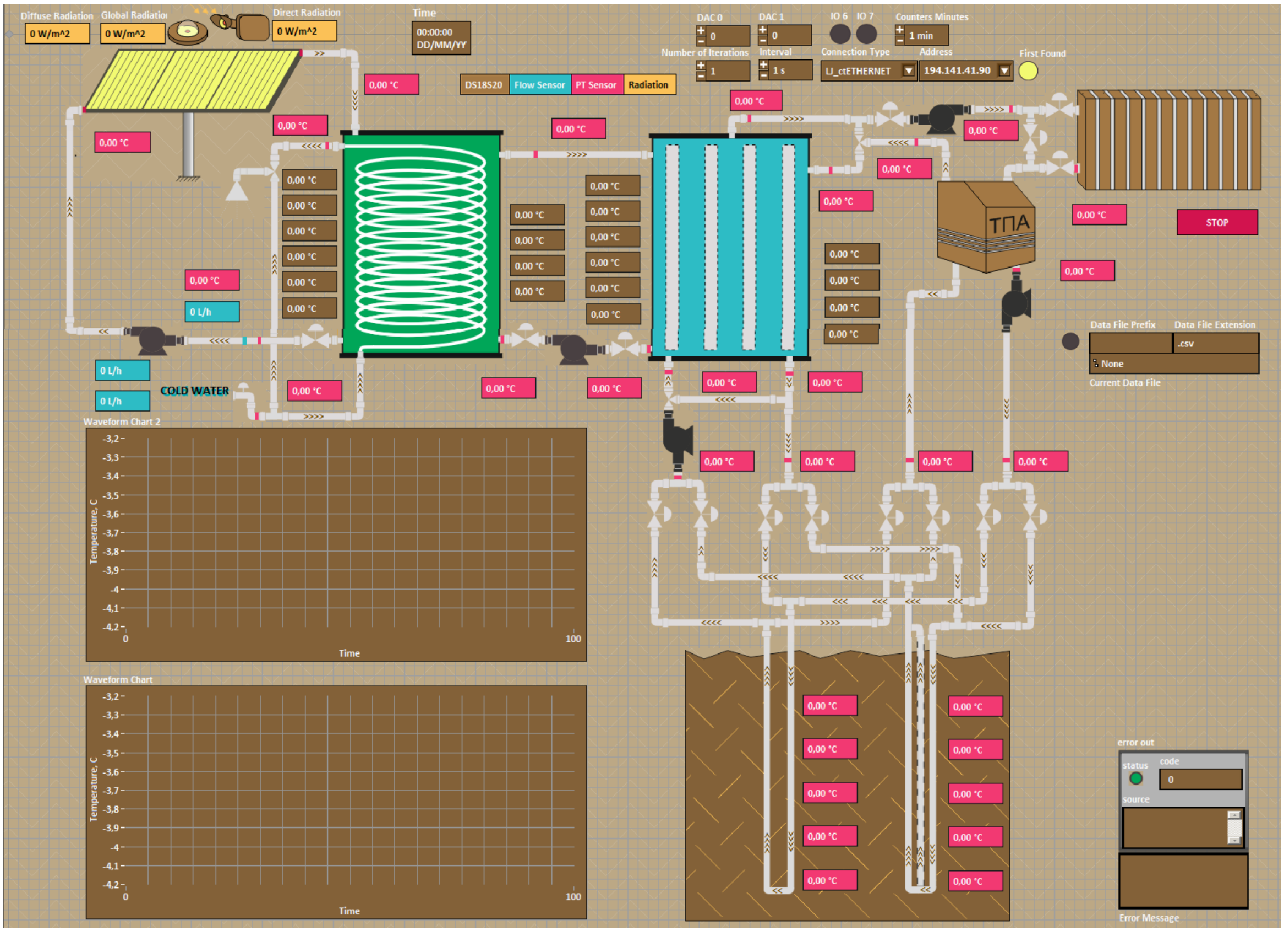


**Fig.16.** The LabVIEW Supervisory Control Screen for the hybrid system installation [12]

The indoor heating and cooling area is about 25 m² (one room). The borehole drilling was performed near the building in October 2011. Two boreholes were perforated - the first one has a single U-pipe and the second one has a double U-pipe design. The depth of the boreholes is 50 m each. Their diameter is 165 mm. Six Pt100 sensors were put in each borehole at different depths (50, 40, 30, 20, 10 and 1,5 m). The solar collectors which are mounted on the roof are filled with propylene glycol.

The storage tanks are thermally insulated (insulation with a thickness of 100 mm is used). The PCM (paraffin) is set into 39 rectangular metal boxes, which sink in the water inside the PCM storage tank. Paraffin is chosen because of its high number of recharging cycles and excellent chemical and thermal stability.

**2. Measurement and control requirements**

The system complexity demands a lot of measurement points for a long period of time in order to obtain a suitable data set that allows correct thermal and energy process analyses. The number of measurement points can be approximated depending on which specific sensor or instrument type was used.

An interactive human machine interface (HMI) gives researchers the opportunity to monitor all the process and control parameters. This system is well adapted to analyse processes in the fields of solar assisted BHE and PCM storage systems.

The operator console is designed as a PC-based station linked via USB or wireless Internet connection to a DAQ board. Depending on the type of experiment conducted, a different virtual instrument screen was prepared. The instrument screen which allowed the study of PCM storage and BTES is shown in Fig.16. It ensures that the experiment is being remotely monitored and controlled in real time [12].

The solar pyrheliometer Kipp & Zonen CH 1 (mounted on the sun tracker system) and the pyranometer Kipp & Zonen CMP 6 are used for measuring of the beam and global solar radiation correspondingly. The diffuse radiation component is calculated by a virtual instrument and all three component values are displayed in the upper left corner of the screen.

All measurement data are logged and permanently stored on the hard disk drive for future analysis. The system allows to remotely monitor and control the process through the Internet.

**3. Different regimes for system operation**

Seven different regimes are possible for system operation:

- Mode 1 (charging of the water storages);
- Mode 2 (charging of the borehole storage);
- Mode 3 (direct solar heating);
- Mode 4 (ground-source heat pump heating);
- Mode 5 (solar-assisted heat pump heating);
- Mode 6 (production of domestic hot water, DHW);
- Mode 7 (ground-source heat pump cooling).

Modes 1 to 5 have been implemented during a time period of about three months in 2014.

## CONCLUSIONS

Here are the most important conclusions regarding hybrid thermal systems:

1. If any component is to be added to an existing installation, it has to improve the system's energy efficiency.

2. The scientific team of the Technical University Sofia, Plovdiv Branch, has long experience in the research and development of hybrid thermal installations and some of their components. Their future activity can be directed as follows:

- well-designed hybrid thermal system (correct choice of the installation components);
- creation and validation of mathematical models allowing simulation of different hybrid installations and operation modes;
- regime optimisation of the already known hybrid systems with regard to different climate conditions;
- use of new and more effective materials in the system elements.

## ACKNOWLEDGEMENTS

This work has been supported financially by the research project 152ПД0045-24/ 26.03.2015 and the research project 152ПД0046-24/ 27.03.2015 of the Technical University of Sofia, which is gratefully acknowledged by the author.

## REFERENCES

1 K Nagano, K Ogawa, T Hashimoto, K Shimakura, T Mochida, A Okamoto, K Hayashi. High efficient solar hot water supply system using evacuated solar collectors with a PCM/water hybrid thermal energy storage. Proc. of Futurestock'2003, 9th Int. Conf. on Thermal Energy Storage, Warsaw, Poland, pp. 167-172.

2 Zafer Utlu, Devrim Aydin, Olcay Kincay. Comprehensive thermodynamic analysis of a renewable energy sourced hybrid heating system combined with latent heat storage. Energy Conversion and Management, 84, 2014, pp. 311–325.
3 H.A. Zondag, D.W. Vries, W.G.J. Van Hendel, R.J.C. Van Zolingen, A.A. Van Steenhoven (2003) The yield of different combined PV–thermal collector designs, Solar Energy 74 (3) pp. 253–269.
4 Kjellsson E., Hellström G., Perers B., Analyses of ground-source heat pumps combined with solar collectors in dwellings, Proc. EFFSTOCK 09, 11th Int. Conference on Thermal Energy Storage, Stockholm, Sweden, June 14 - 17, (2009), p. 83.
5 H. Yang , P. Cui, Z. Fang. Vertical-borehole ground-coupled heat pumps: A review of models and systems. Applied Energy, Vol. 87, 2010, pp. 16–27.
6 JP Müller, M. Reuss. Technical assessment of different seasonal underground thermal energy systems. Proc. of Terrastock 2000, 8th Int. Conf. on Thermal Energy Storage, Stuttgart, August 28-Sept. 1, Vol. 2, pp. 485-490, 2000.
7 B He, V Martin, O Andersson, F Setterwall. Borehole Thermal Energy Storage Coupled to Peak Load PCM Storage for Efficient Free Cooling System. Proc. of Futurestock'2003, 9th Int. Conf. on Thermal Energy Storage, Warsaw, Poland, pp. 389-397.
8 N. Pardo, Á. Montero, J.F. Urchueguía, J. Martos. Energy efficiency study of a hybrid ground coupled heat pump system in several layout combinations. 11th International Conference on Thermal Energy Storage for Efficiency and Sustainability, EFFSTOCK 2009, ISSN 978-91-976271-3-9, 66.pdf.
9 A. Georgiev, A. Busso, P. Roth. Shallow Borehole Heat Exchanger: Response test and Charging - Discharging test with solar collectors. Renewable Energy, 2006, V. 31 (7) p. 971-985.
10 M. Bottarelli, M. Bortoloni, , Y. Su, C. Yousif, A. A. Aydin, A. Georgiev. Numerical Analysis of a Novel Ground Heat Exchanger Coupled with Phase Change Materials. Applied Thermal Engineering, Vol. 88, 2015, pp. 369-375.
11 A. Georgiev, R. Popov, I. Valkov, N. Kaloferov. Utilization of the thermal energy potential in photo voltaic solar panels. Proceedings of the World Renewable Energy Congress-XI, 2010, Abu Dhabi, United Arab Emirates, 25-30 September 2010, 199.pdf.
12 R. Popov, A. Georgiev. SCADA system for study of installation consisting of solar collectors, phase change materials and borehole storages. Proc. of the 2nd Int. Conf. on Sustainable Energy Storage, June 19-21, 2013, Trinity College Dublin, Ireland, pp. 206-211.
13 M Ramamoorthy, H Jin, AD Chiasson, JD Spitler. Optimal Sizing of Hybrid Ground-Source Heat Pump Systems That Use a Cooling Pond as a Supplemental Heat Rejecter- A System Simulation Approach. ASHRAE Transactions 2001, Vol. 107, Part 1, pp. 26-38.
14 H.A. Zondag. Seasonal heat storage for heating of buildings. TU/e Energyday 8, 11 Feb. 2010, pp. 1-38.

*Bulgarian Chemical Communications, Volume 48, Special Issue E (pp. 19 - 26) 2016*

# In-situ measurements of ground thermal properties around borehole heat exchangers in Plovdiv, Bulgaria

A. G. Georgiev[1,3], R. K. Popov[2*], E. T. Toshkov[1]

[1]*Technical University of Sofia, Plovdiv Branch, Dept. of Mechanics,25 Tsanko Diustabanov Str, 4000 Plovdiv, Bulgaria*
[2]*Plovdiv University "Paisii Hilendarski", Department of Electronics, Telecommunications and Information Technologies (ETIT), 24 Tsar Assen Str, 4000 Plovdiv, Bulgaria*
[3]*European Polytechnic University, Dept. of "Green Energy", 23 Kiril and Metodiy str., 2300 Pernik, Bulgaria*

The knowledge of the geodata (subsurface characteristics) is important for the design and construction of the Underground Thermal Energy Storage (UTES) and to design an installation using Borehole Thermal Energy Storage (BTES) - it is a big advantage during the project calculations and the construction of the geothermal systems. In situ determination of ground thermal conductivity, borehole thermal resistance and undisturbed soil temperature can be done by installing a vertical borehole heat exchanger (BHE) and performing the so-called Thermal Response Test (TRT). This paper describes the determination of ground thermal properties by a research group of the Technical University of Sofia, Plovdiv Branch. A mobile system for conducting Thermal Response Test has been created recently in Plovdiv, Bulgaria. The first Bulgarian TRT was carried out in January 2009 using a 41 m deep BHE, constructed in November 2008. Later tests are carried out on other two constructed BHEs in Plovdiv (single and double, 50 m depth and 32 mm diameters of the U-tubes). The tests were realized while the ambient temperature, the inlet and outlet fluid borehole temperatures and the temperatures of the BHEs at different depths were measured every minute. A large quantity of experimental data was gathered and analyzed by two parameters curve fitting based on the analytical formula of the Line Source Model for temperature distribution in the borehole (determining the ground thermal conductivity and the borehole thermal resistance). The detailed study of ground properties in different regions of Bulgaria is a good precondition for future application of the geothermal technology in the region.

**Keywords:** Thermal Response Test, ground thermal properties, borehole heat exchangers

## INTRODUCTION

The Underground Thermal Energy Storage (UTES) is a good solution for saving energy. Laboratory methods have been used to study the ground properties - unfortunately their results are usually not precise. A very effective method used for the determination of the ground thermal conductivity is the Thermal Response Test (TRT). It is an internationally approved technique to identify geothermal underground parameters like effective ground thermal conductivity and borehole thermal resistance $R_b$. It has been in use since 1995 in International Energy Agency: Energy Conservation through Energy Storage (IEA ECES) countries but the method, equipment and evaluation procedure are still under development. Generally, these tests are performed with heat injection, using the same assumed power level as the one planned by the BHE system.

The TRT was first presented in 1983 [1] - the installation is designed as a stationary system. After that, a mobile conductivity measurement system appeared. In principle two different methods have been developed: one using electrical heater elements [2-4] and another one using a reversible heat pump in Netherlands [5]. With the latter heat can be injected and extracted from the ground. The theoretical basis of the thermal response test is presented in [6-8]. Today about 10 countries in the world undertake this type of research - e.g. in Germany [9], Sweden [2], Canada, USA [4], Norway, Netherlands [5], England, Turkey [10], Chile [11, 12] and Cyprus [13].

Several TRTs are done in Bulgaria, too. Some activities in Bulgaria have preceded the first official TRT [14]. Several Thermal Response Tests had already been employed in Bulgaria [15-17]. This paper describes the results of three TRT tests, conducted by the mobile unit constructed at the Technical University of Sofia, Plovdiv Branch. One test was performed in the campus 3, and the other two tests in the campus 2.

## MOBILE SYSTEM FOR EXAMINING GROUND THERMAL PROPERTIES

The basic quality requirements for the experimental apparatus are an uninterruptible supply of constant heat power to the borehole and the capability to take highly accurate temperature and flow rate measurements. Fig.1 shows the unit design.

* To whom all correspondence should be sent:
rum_pop@yahoo.com

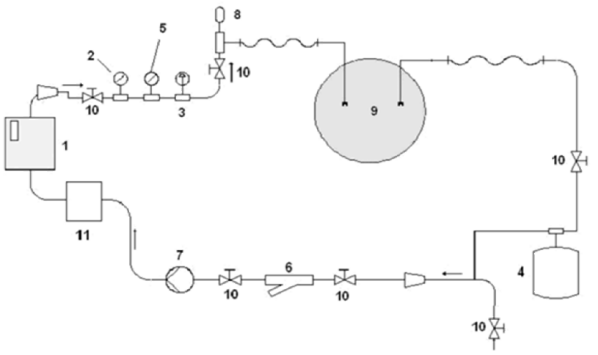


**Fig.1.** System set-up

The following elements are presented here: electrical boiler 1, calorimeter 2, pressure relief valve 3, expansion tank 4, thermomanometer 5, filter 6, circulation pump 7, de-aeration pipe 8, quick couplings 9, valves 10 and electrical unit 11. The laboratory is installed on a mobile trailer, which contains the equipment for conducting the TRT (Fig.2). The constructed trailer combines the characteristics of both an experimental unit and a place for temporary lodging. The lodging part is foreseen as a complete outfit delivering the corresponding comfortable living conditions to the researchers during the tests (the tests are normally carried out on locations outside populated areas). The experimental unit has two different parts - a mechanical one and a measuring and control part (Fig.3).

**Fig.2**. Test mobile system with the borehole (top end)

The Electrical boiler 1 consists of a body and a control unit. Three tubular electrical heaters are situated in the well-insulated steel body of the boiler. The heaters are capable of producing different heating temperatures. A three phase circulation pump 7 ensures the movement of the heating medium through the boiler. This pump possesses the function of flow rate regulation on frequency.

The calorimeter MEGATRON2 2 produced by SIEMENS is built in the system. It is an independent electronic apparatus for tracking and reporting the consumed heat in automatic heating and cooling installations. The calorimeter has a memory and a display which reports the measured values of energy consumed on a chosen day.

**Fig.3.** Measuring device

"AEROFLEX" insulation is used in the mobile unit to avoid errors heat losses during the measurement.

A pressure relief valve 3 protects the pump and the unit from high pressure or from overheating of the fluid in the boiler. The protection is fulfilled through the automatic current switching of the pump motor and the boiler heaters. The used pressure watch is produced by the "WATTS", Italy - PM/5 model.

The expansion tank 4 of the system is needed to balance the small variations of the heating medium. The used expansion tank is of the membrane type and has a capacity of 8 litres.

A thermo-manometer 5 is needed in the setup to monitor the pressure and the temperature of the heating medium after it leaves the electrical boiler and before it enters the borehole.

A system filter 6 is used to eliminate all impurities which enter the system while the heating medium fills it up. The filter is of the net type and allows movement only in the direction of the working fluid flow.

The pipes used in the unit are produced by the German company "AQUATHERM". The main advantages of the pipes are the following: absolute corrosion stability, chemical stability, high impact

stability, low tube roughness, very good welding characteristics and high thermal stability.

Some measuring elements and sensors are mounted on the mobile station. The flow rate through the borehole is measured on the basis of the calorimeter sensor and on the basis of the electronic transformer of frequency to voltage. An inductive sensor with a code disc is used for measuring the rotation frequency of the electricity generator. The data-logging system (SIGMATECH) is used for measuring and archiving the installation parameter values. A computer (supplied with processing software) analyzes the collected information. There are 8 temperature elements with PT100 which are used to measure the fluid temperature difference of the borehole (input and output), the temperature in the borehole at different depth and the ambient temperature. All elements have an accuracy of about ±0.15K in the temperature range 0°C - 120°C (Class A PT100). An additional calibration was done of the temperature elements on the borehole input and output (they have an accuracy of ±0.05K).

A fully automated system for data archiving of the company "SIGMATECH" LTD (logger for collecting of the temperature data) Plovdiv has been selected. The multiprocessor system SH700 automates the measurement process of the ground thermal conductivity and analyses the obtained data. It collects the data of the measured inlet and outlet borehole temperatures, the five temperatures in the borehole depth and the ambient temperature. The maximum number of measured temperatures is 20. The controller has a memory, where the measuring data are recorded. If a computer is used, it is possible to show the measurement in real time and to analyse the collected data.

A power regulator is situated in the electrical unit 11. It is used to control the power of the electrical heater. Thus a precise regulation of the measurement process is ensured.

The induction motor of the circulation pump is regulated with the help of a frequency regulator (MOELLER" DF51-322 company production), which is built in the electrical unit. The frequency regulator can be used to manage the speed, torque, direction, start and stop of the pump motor.

Later some improvements have been made - a mains voltage stabilizer SVC-5000WS was added to the installation with the aim to keep constant the heat transfer rate to borehole despite diurnal variations of the power line voltage.

## PREPARATION OF THE BOREHOLE HEAT EXCHANGERS (BHES)

A number of different BHEs were constructed in the territory of TU – Sofia, Plovdiv Branch. Electrocarotage measurements were made with the carotage station KFE-2-12 on the campus 3 of the Technical University – Sofia, Plovdiv branch. They were compared to the lithological data of the soil. The station consists of three electrodes, which are directed down into the drilling hole and a fourth one is grounded. A 40 Hz electricity current is fed in and the potential difference between the electrodes in the hole is measured. The data received are recorded by means of the electrocarotage equipment. A general lithological structure is worked out on its base (Fig.4).

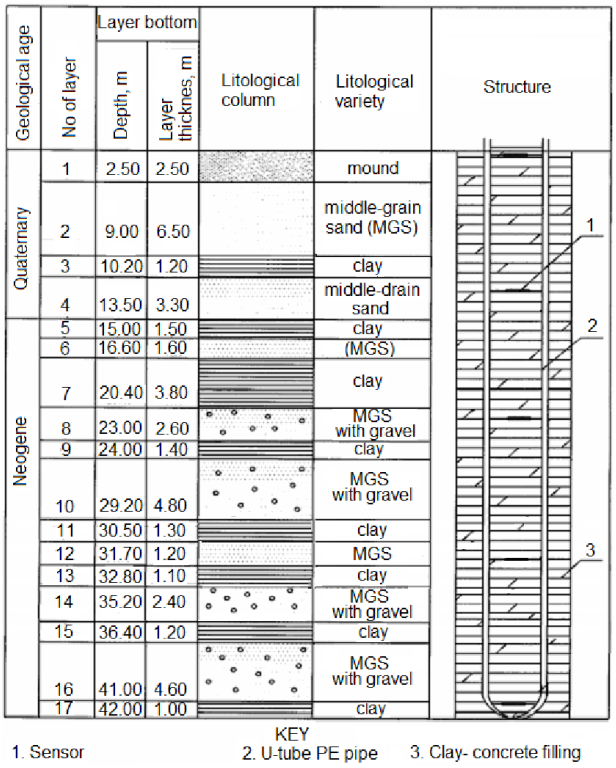


**Fig.4.** Geological section

The lithological structure of the ground at campus 2 is very similar. It consists mainly of clay, sands with different size of grains and some gravel (the distance between the both campuses is about 2 km).

A single U-tube heat exchanger of PN10 HDPE pipe, 25 mm diameter, was installed in the borehole with a depth of 41 m at the campus 3. The borehole has a diameter of 0,18 m and was backfilled with 11% bentonite and 2% cement mixture. Cement was added because of the specific soil type: sand soil with high water content. The U-shape was inserted in hole by connecting two separate pipes

(42m long each) - a welding process and two joints were used (Fig.5).

**Fig.5.** Mounted temperature sensor in the lower part of the U-tube

Polyethylene (PE) pipes are used in the geothermal drills. The chosen polyethylene pipes are of the PE 100 type and their technical specifications are given in Table 1.

**Table 1.** Specifications of PE 100 pipes

| **Marking** | **PE 100** |
|---|---|
| Material | Polyethylene |
| Pipe roughness | 0.04 mm |
| Mean thermal coefficient of linear extension | 0.20 mm/mk |
| Minimal temperature of laying | -10° C |
| Flow limit | 26 MPa |
| Strength | >10 MPa |
| Melting index | 0.2 – 0.5 g/10 min |

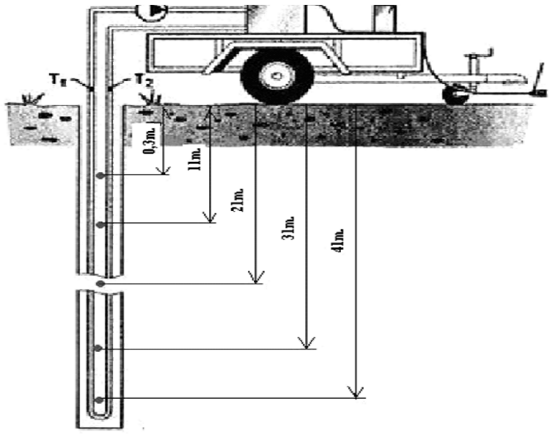


**Fig.6.** Placement of temperature sensors in the borehole

Five detectors RD Pt100 type are attached between the two pipes at regular intervals (Fig.6). They are used to collect data from the temperature field inside the BHE. Cement mixtures with low permeability rate are used to fill the hole after the pipes have been mounted.

The pipes stand out about 0,5m above the ground level and are insulated with porous insulation of the Aeroflex type to minimize thermal losses. The BHE has to be insulated from the surrounding environment with any available type of insulation material. We covered an area of 4 m² over the borehole pipes with insulation of the type XPS (extruded polyester) known under its commercial name “fibran” - two layers of 0.05m thickness each (Fig.2).

**Fig.7.** Drilling of boreholes with MDT Mc 200 B

Two vertical perforations were drilled in the laboratory vicinity of campus 2 with depth of 50 m, diameter of 165 mm and distance of 13 m between the holes. It was done by the help of a modern Italian hydraulic drilling machine MDT Mc 200 B (Fig.7).

**Fig.8.** Inserting the HDPE tubes in the perforations

Two different loop types were inserted in the boreholes (single and double loop of high density polythene, HDPE PE 100) with external diameter 32 mm. They have been backfilled with cement-bentonite grout (mixture of cement and bentonite with factor 0.5) to enhance thermal transfer between tubes and ground (Fig.8). Before backfilling in the two boreholes were inserted 6

three-wire thermoresistors Pt100 along the tubes on every 10 meters to measure the temperature distribution underground. So two different types of BHEs were designed. Fig.9 shows the upper part of the double U-tube borehole.

**Fig.9.** Upper part of the double U-tube borehole

## THERMAL RESPONSE TESTS

### *First Thermal response test in campus 3*

The first TRT, 10 days long, was carried out from the 11th to the 21st of January. The measured parameters were the ambient temperature, the inlet and outlet fluid temperatures of the borehole and the temperatures of the BHE at different depths. The flow rate was measured and controlled at the constant value of 6.45 l/min. The electrical power was regulated and maintained constant at about 1500 W. The electrical power of the circulating pump was about 100 W. The water pressure in the installation was maintained at about $2.2.10^5$ Pa. The measuring time step was 60 s. The mean undisturbed ground temperature $T_{0,m}$ was determined by pumping the heat carrier fluid out of the borehole pipes and measuring its outlet temperature over a time of 10s [18]. $T_{0,m}$ is then calculated as the mean of the measurement data. In the presented experiments $T_{0,m}$ has been established to be 16.3°C.

All data are automatically controlled by a specially designed system for the laboratory trailer that is installed on the control board. The system is fully automatic and stores all measured data in text files. In the experiments the aim of a constant heat flow was realized by a constant frequency control of the circulation pump and boiler.

### *Thermal response tests in campus 2*

Tests with duration about 7 days were implemented to evaluate soil thermal conductivity around the two boreholes and temperature distribution in depth. The experiments were carried out in December 2011 (with double loop) and in August 2012 (with single loop).

The test conditions were as follows:

- Test from 3rd till 10th December 2011: pump flow rate of 550 l/h, electric heater power - 2820W, electric power of circulating pump - 100W, measured intervals – 10s for the undisturbed temperature and 60s for the rest parameters; the mean undisturbed ground temperature $T_{0,m}$ was 16,5°C;
- Test from 7th till 14th August 2012: pump flow rate of 540l/h, electric heater power - 2630W, electric power of circulating pump - 100W, measured intervals – 10s for the undisturbed temperature and 60s for the rest parameters; the mean undisturbed ground temperature $T_{0,m}$ was respectively 16.7°C.

A turbulent regime for circulating water like heat carrier with Reynolds number more than 8000 was available during the two tests.

## RESPONSE ANALYSIS

### *Basic equation*

The Kelvin's line source theory [19] is normally used as a base for mathematical evaluation of the Thermal Response Test. The temperature of the surrounding ground is raised as a result of the circulating heating fluid through the borehole heat exchanger. The following formula gives the distribution of the temperature field as a function of the borehole radius and time:

$$\Delta T(r_b,t) = \frac{q}{4\pi\lambda} \int_{r/2\sqrt{at}}^{\infty} \frac{e^{-\beta^2}}{\beta} d\beta \qquad (1)$$

where:

$\Delta T(r_b,t)$ - temperature rise, K;

$q$ - heat injection power per unit borehole length, W/m;

$\lambda$ - ground thermal conductivity, W/mK;

$t$ – time, s;

$a$ - thermal diffusivity, m²/s;

$r$ - radius from the borehole, m;

$\beta$ - integration variable, -;

$r_b$ - radius of the borehole, m.

### *Slope determination technique*

With this approximation, the delivered heat is considered as coming from a line source, the borehole [2]. The heating process is presented by the equation:

$$T_{f,m} = \frac{Q}{4\pi\lambda H}\ln(t) + \left[\frac{Q}{H}\left(\frac{1}{4\pi\lambda}\left(\ln\left(\frac{4a}{r_b^2}\right) - \gamma\right) + R_b\right) + T_o\right]$$

$$\text{for} \quad t \geq \frac{5r_b^2}{a}. \qquad (2)$$

where:

$T_{f,m} = (T_{f,in} + T_{f,out})/2$ - mean fluid temperature, K;

$Q$ - delivered heat power, W;

$\lambda$ - ground thermal conductivity, W/mK;

$H$ - borehole depth, m;

$t$ - time from start, s;

$a$ - thermal diffusivity, m²/s;

$r_b$ - radius of the borehole, m;

$\gamma = 0{,}5772$ – Euler's constant;

$R_b$ – borehole thermal resistance, mK/W;

$T_0$ – undisturbed ground temperature, K.

Equation (2) is simplified with

$$T_{f,m} = c.\ln(t) + d \qquad (3)$$

where $c$ and $d$ are constants.

The value of c is to be determined from the inclination of the line in the plot of the mean fluid temperature versus ln(t). The conductivity λ is computed then from the graph slope:

$$\lambda = \frac{Q}{4\pi c H} \qquad (4)$$

Respectively to calculate $R_b$ we are applying the following formula:

$$R_b = \frac{H}{Q}(T_{f,m} - T_o) - \frac{1}{4\pi\lambda}\left(\ln(t) + \ln\left(\frac{4a}{r_b^2}\right) - \gamma\right) \qquad (5)$$

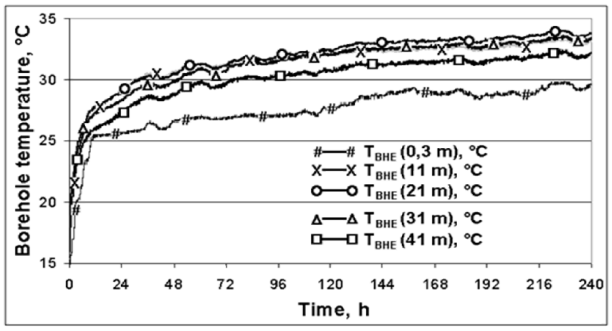


**Fig.10.** Temperature profile in the borehole heat exchanger (January 2009).

*Experimental data*

The measured temperatures in the borehole heat exchanger are presented in Fig.10 (campus 3). They show the temperature field inside the BHE at depth of 0.3m, 11m, 21 m, 31 m and 41 m. The ambient temperatures and the mean inlet and outlet fluid borehole temperatures for the month of January are also indicated in Fig.11 (campus 3).

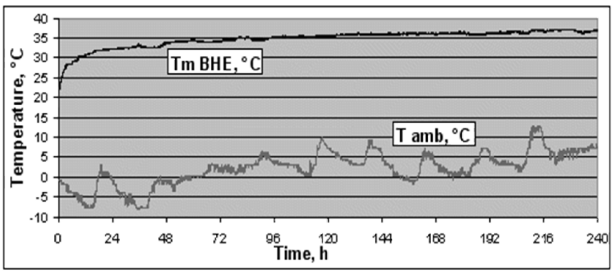


**Fig.11.** Test temperature profile (mean fluid borehole and ambient temperatures) in January 2009

Fig.12 and Fig.13 show the temperature profiles of mean fluid borehole and ambient temperatures concerning experiments in campus 2.

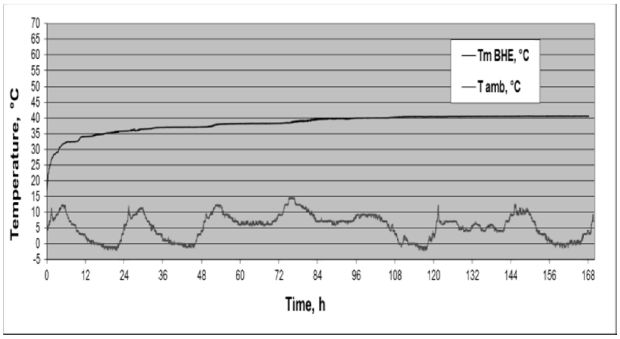


**Fig.12.** Test temperature profile (mean fluid borehole and ambient temperatures) in December 2011

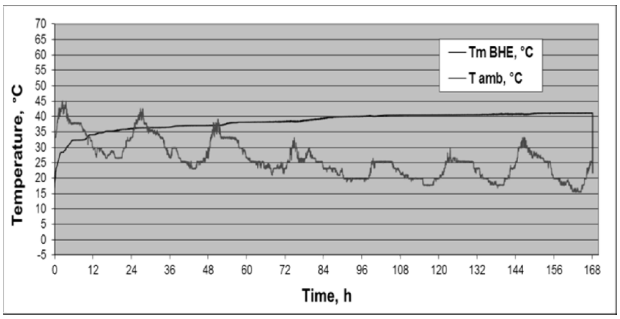


**Fig.13.** Test temperature profile (mean fluid borehole and ambient temperatures) in August 2012

*Hours-off and duration of the test analysis*

The Line Source Model was used for determination of the ground thermal conductivity and the borehole thermal resistance. Normally, the data corresponding to the first 7 to 24 hours of experiment are not taken into account in the analysis. The reason for discarding initial data points from the original set is based on the fact that

the solution used for data evaluation is an approximation applicable for times satisfying the criterion $t \geq \frac{5r_b^2}{a}$.

To assess how the starting point (hours-off) of the evaluation data interval affects the values of the thermal conductivity and the borehole thermal resistance, a series of evaluations were performed on intervals with the same end point but different hours-off at the beginning. Table 2 shows that the dispersion from the average value is no more than 1.4 % for the thermal conductivity and 0.57 % for the borehole thermal resistance (campus 3).

**Table 2.** Results of the hours-off analysis for sets of data intervals beginning at the hour-off point (January 2009)

| Hours-off, h | Slope | λ, W/m K | $R_b$, m K/W |
|---|---|---|---|
| 7 | 2.0515 | 1.37 | 0.310 |
| 10 | 2.0437 | 1.38 | 0.312 |
| 15 | 2.0465 | 1.38 | 0.314 |
| 20 | 2.0682 | 1.36 | 0.312 |
| 24 | 2.0831 | 1.35 | 0.311 |
| Average | | 1.37 | 0.312 |

Fig.14 (campus 3) shows the logarithmic time dependence of the temperature and the slope of the associated regression line (the accepted hours-off period is 15 hours).

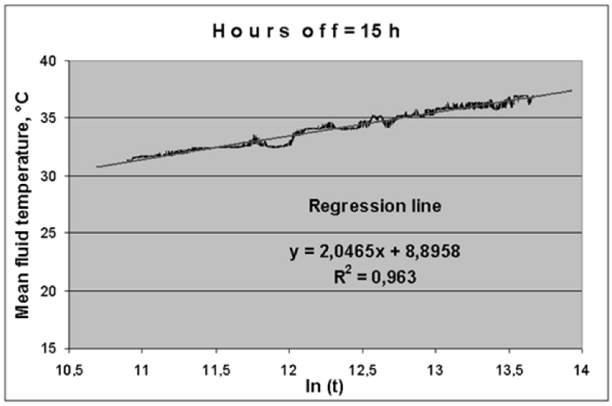


**Fig.14.** Logarithmic time plot of the mean temperature for the entire test length in January 2009 (excluding the first 15 hours)

The thermal conductivity λ is related to the slope of the resulting line, given by Eq. (2). The resulting values received during the tests for λ vary between 1.35 and 1.38 W/mK and for $R_b$ vary between 0.310 and 0.314 mK/W (campus 3).

The results of the experiments done in campus 2 are presented in Fig.15 and Fig.16. They are as follows - thermal conductivity λ is 1.58 W/mK and thermal resistance is $R_b$ – 0.187mK/W (December 2011, Fig.15). Respectively for August 2012 - thermal conductivity λ is 1.65 W/mK and for thermal resistance $R_b$ – 0.179mK/W (Fig.16). Both results are closed to those for campus 3 in 2009.

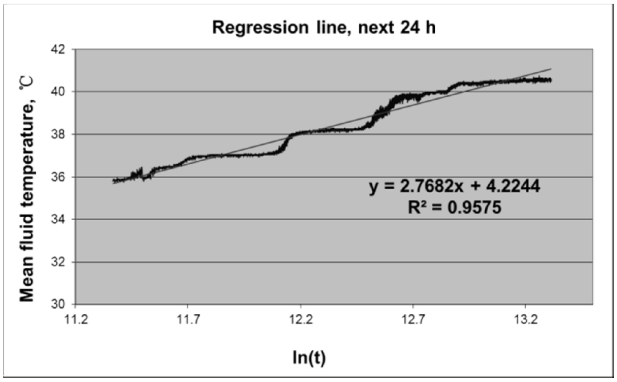


**Fig.15.** Logarithmic time plot of the mean temperature for the entire test length in December 2011 (excluding the first 24 hours)

A comparison with the results of different experiments [9, 11, 20] performed elsewhere in the world was done. It shows that the values of thermal conductivity and thermal resistance of the borehole obtained by our tests (in Plovdiv) are comparable with the values obtained by other tests.

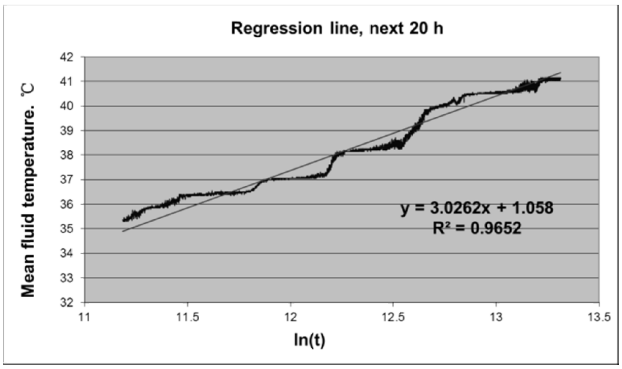


**Fig.16.** Logarithmic time plot of the mean temperature for the entire test length in August 2012 (excluding the first 20 hours)

## CONCLUSIONS

Some TRTs have been conducted in 2009, 2011 and 2012 at the Technical University of Sofia, Plovdiv Branch, with the created mobile installation. Here are the main conclusions:

- The working installation, which is incorporated in the mobile laboratory, works fully automatically;
- The Line Source Model is used as a method for estimation of the experimental results. Several additional estimation methods have to be used in the future with the purpose to determine more

exactly the values of the thermal conductivity and the borehole thermal resistance;

- The resulting values received during the tests in campus 3 for λ were between 1.35 and 1.38 W/mK and for $R_b$ - between 0.310 and 0.314 mK/W;

- The obtained results for campus 2 are as follows: thermal conductivity λ=1,58 W/mK, thermal resistance $R_b$=0.187 mK/W (December 2011); λ=1.65 W/mK and thermal resistance $R_b$=0.179 mK/W (August 2012) respectively;

- The values of thermal conductivity and borehole resistance are similar in both campuses (2 and 3) of the University situated in a distance of only 2 km, but the differences are explained by differences on the soil characteristics (density water content) and on the geological structure;

- The values of the conductivity λ and of the borehole thermal resistance $R_b$ for the experiment values are comparable with the values obtained by other tests in the world [9,11,20].

## REFERENCES


1 P. Mogensen, P., 1983. Fluid to duct wall heat transfer in duct system heat storages. *Proc. of the int. conf. on subsurface heat storage in theory and practice, Stockholm, Sweden*, pp. 652–657 (1983).

2 C. Eklöf, S. Gehlin. TED - a mobile equipment for thermal response test. *Master's Thesis 1996:198E. Sweden: Luleå University of Technology* (1996).

3 S. Gehlin, B. Nordell. Thermal response test - a mobile equipment for determining thermal resistance of borehole. *Proc. of Megastock 1997, 7th int. conf. on thermal energy storage, Sapporo,* pp. 103–108 (1997).

4 W.A. Austin. Development of an in-situ system for measuring ground thermal properties. *Master's Thesis. Oklahoma State University, Stillwater, Oklahoma* (1998).

5 H. Witte, S. Kalma, A.J. van Gelder. In-situ thermal conductivity testing: The Dutch perspective (part 1 and 2). The Source 13 (3) and The Source 13 (4), (2000).

6 G. Hellström. Ground heat storage. Thermal analysis of duct storage systems. *Part I theory. Lund, Sweden: Department of Mathematical Physics, University of Lund*, pp. 148–154 (1991).

7 S. Gehlin. Thermal Response Test. Method Development and Evaluation. *Ph.D. Dissertation. Luleå University of Technology,* 2002:39, Sweden (2002).

8 S. P. Kavanaugh, R. Rafferty. Ground-source heat pumps: design of geothermal systems for commercial and institutional buildings. *Atlanta: ASHRAE, Inc;* pp. 22–31 (1997).

9 B. Sanner, M. Reuss, E. Mands, J. Müller. Thermal response test - experiences in Germany. *Proc. of Terrastock 2000, 8th Int. conf. on thermal energy storage, Stuttgart, Germany*, pp. 177-182 (2000).

10 H. Paksoy, Z. Gurbuz, B. Turgut, D. Dikici, H. Evliya. Aquifer thermal storage (ATES) for air-conditioning of a supermarket in Turkey. *Proc. of world renewable energy congress-VII 2002, Cologne, Germany,* 10_n66.pdf (2002).

11 P. Roth, A. Georgiev, A. Busso, E. Barraza. First In-situ Determination of Ground and Borehole Thermal Properties in Latin America. *Renewable Energy 29,* pp. 1947-1963 (2004).

12 A. Georgiev, A. Busso, P. Roth. Shallow Borehole Heat Exchanger: Response test and Charging - Discharging test with solar collectors. *Renewable Energy 31*, pp. 971-985 (2006).

13 G. Florides, S. Kalogirou. First in situ determination of the thermal performance of a U-pipe borehole heat exchanger, in Cyprus. *Applied Thermal Engineering 28*, 157-163 (2008).

14 A. Georgiev, O. Pekov, A. Angelov, R. Popov, J. Urchueguia, H. Witte. First steps of the ground accumulation in Bulgaria. *Proc. of the World Renewable Energy Congress-IX, Italy, Florence, Italy,* Bulgaria.pdf (2006).

15 A. Georgiev, S. Tabakova, R. Popov, Y. Todorov. Bulgarian Variant of a Mobile Installation for Ground Thermal Properties Determination. *Yang SS, Sayigh AAM, Lai CM, Chen S. Progress in Development and Applications of Renewable Energy, National Taiwan University, Taipei, Taiwan, first Edition,* pp. 197-208 (2009).

16 A. Georgiev, R. Popov, S. Tabakova. First Thermal Response Test in Bulgaria. *Proc. of Effstock 2009, 11th int. conf. on thermal energy storage, Stockholm*, 24.pdf (2009).

17 A. Georgiev, R. Popov, S. Tabakova. Computer Simulation of Ground Thermal Properties. In: *Proc. of the 11th nat. congress on theoretical and applied mechanics, Borovets, Bulgaria*, Georgiev_128.pdf (2009).

18 I. Zervantonakis, M. Reuss. Quality requirements of a Thermal Response Test. Proc. of Ecostock 2006, 10th Int. conf. on thermal energy storage, Stockton, USA, pp. 435-441 (2006).

19 S. Gehlin. Thermal response test—in-situ measurements of thermal properties in hard rock. Licentiate Thesis. Luleå University of Technology, Department of Environmental Engineering, Division of Water Resources Engineering, 1998:37, Sweden (1998).

20 G. Hellström. Duct ground heat storage model, Manual for Computer Code. Sweden: Department of Mathematical Physics, University of Lund (1989).

*Bulgarian Chemical Communications, Volume 48, Special Issue E (pp. 27 - 30) 2016*

# Iller bank-Atasehir-building ground source heat pump system and thermal response test - case study

Aysegul Cetin[1,*], Orhan Isık[1], Suheyla Cetin[1] Yusuf K. Kadioglu[2] Halime Paksoy[3]

[1] *Iller Bank. Inc. Com. Superstructure Application Department Diskapi/Ankara*
[2] *Ankara University Geol. Dept., Ankara – Turkey*

Turkey has a great geothermal energy capacity due to Alpin Orogenesis. There are a lot of young magmatic intrusions and geothermal areas that is waiting be exploited in terms of shallow geothermal energy. Turkey's implementation of renewable energy is increasing in recent years due to the new energy policy targets. Shallow geothermal energy systems in Turkey have been increasing since 2007. Installed capacity of these systems is approximately 42,3 MW. Iller Bank Inc. Com. is a Development and Investment Bank servicing financial and technical support to municipalities in Turkey. With the purpose of setting an example of shallow geothermal application in official buildings for municipalities, a ground source heat pump system has been implemented at Iller Bank headquarters building in Istanbul-Atasehir in 2015. The building is located on metasandstone belonging to Paleozoic aged Kocatongel Formation. Heating and cooling demands of the building are approximately 1160 and 1817 kWh respectively. The ground source heat pump system was designed to supply some portion of this demand. 24 borehole heat exchangers with depths varying between 60 and 153 meters were installed. Thermal Response Test (TRT) was carried at two different borehole heat exchangers and effective ground thermal conductivity, undisturbed ground temperature, and resistivity were obtained. Thermal conductivity data from the TRT test showed significant differences due to ground water flow effect in one of the boreholes. In this paper, an overview of shallow geothermal systems in Turkey with a special focus on geological parameters will be given. As a case study, Iller Bank Atasehir Ground Source Heat Pump System will be analyzed.

**Keywords:** shallow geothermal systems, thermal response test, Iller Bank Atasehir Building ground source heat pump system case study

## INTRODUCTION

In Turkey, we see an increase in renewable energy implementations in recent years due to the concerns over increasing energy demand, energy security and global climate change. There are 16 million buildings in Turkey, which is the second largest energy consumer with a share of 35% following the industry (1). About 80% of this share is used to meet heating demand. Fossil fuels are mostly used for heating leading to increased greenhouse emissions.

Shallow geothermal systems increase energy efficiency and provide a beneficial alternative as a renewable energy source for heating and cooling demands. Shallow geothermal systems have two main groups of applications: "Ground Source Heat Pump (GSHP)" and "Underground Thermal Heat Storage". Although Heat Pump Systems are well known in Turkey, there are few applications of shallow geothermal systems reaching to an installed capacity of 42,3 MW (2).

Iller Bank. Inc. Comp. is a development and investment bank in Turkey that supports municipalities technically and financially. Recently, more focus on activities to supply renewable heating and electricity municipalities was given.

In order to set an example of shallow geothermal application in official buildings for municipalities, a ground source heat pump system has been implemented at Iller Bank headquarters building in Istanbul-Atasehir in 2015 (Fig.1 and Fig.2). In addition, photovoltaic and gray water systems are employed in this building. Project and installation was made between 2012 and 2015. The system was commissioned and started operation in 2015. In this paper, experiences from this project are given.


**Fig.1.** General view of Atasehir Building

* To whom all correspondence should be sent:
aysegulcetin32@gmail.com


**Fig.2.** General view of BHE's area

## GEOLOGY

Iller Bank Atasehir Building is located on a geological unit called Istanbul sequence (Fig.3). The rock formations in this area listed from older to younger are:

- Kocatongel Formation (QPkc) consisting of metasandstone and claystone, Paleozoic aged;
- Kurtkoy Formation (QPk) consisting of sandstone and conglomerate rocks, Paleozoic aged;
- Pelitli Formation (SDp) consisting of limestone, Devonien aged;
- Kartal member of Pendik (Dpkz) Formation consisting of shale, Devonien aged.

The building is located mainly on metasandstone, which is very fractured and covered with solid waste filling material of 10-15 meters in depth. Metasandstone has groundwater at three different layers.

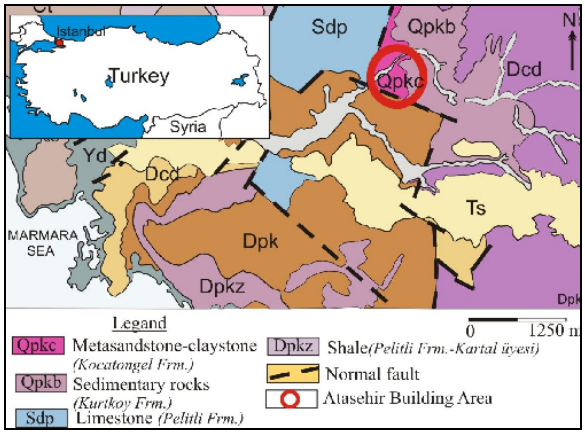


**Fig.3.** Simplified geological setting map of Atasehir Building [3]

## GROUND SOURCE HEAT PUMP SYSTEM

150 kW of the building heating and cooling load was planned to be met with GSHP system with 24 boreholes each at 150 m. Two different drilling methods - rotary and pneumatic - were used depending on rock properties (Fig.4).

**Fig.4.** General view of drilling stage

Thickness of solid waste filling material on the top varied between 5 to 15 m. Greenish-gray Metasandstone units were seen throughout the depth after the top layer. Metasandstone had fractured levels at 40, 80 and 120 m depths. Secondary limestone was seen in fractured levels, which are related to the existence of groundwater (Fig.5). Thermal conductivity of solid waste filling material was measured at Ankara University Geological Department as 0,65 to 1,65 W/mK.

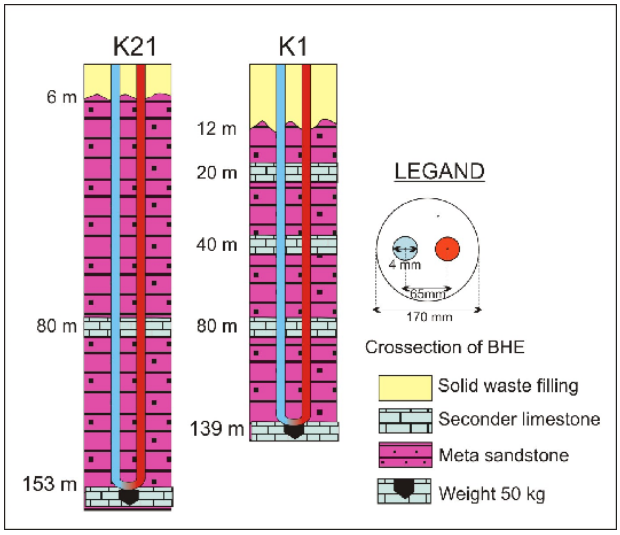


**Fig.5.** BHE's cross-section and geological layers

Fig.6 shows the location of the 24 boreholes used in the GSHP system. The depths vary from 60 to 153 m. Due to the difficulties of the sloped

drilling area, it was not possible to have all the wells at the same depth. The distance between the boreholes was 6 m. BHE consisted of a single U pipe (HDPE) of 16 bar (PN16) and 0,04 m outer diameter, grouting material having 2,35 W/mK thermal conductivity and spacers were used at every 3 meters. Injection pipe having ¾" was used and grouting material mix was prepared on site. Grouting mix composition was 52% sand, 24% Portland cement and 24% water. Pressure test (2 hours at 6 bar) was carried out before and after inserting U pipes. While preparing vertical piping of BHE, horizontal piping was implemented at the same time in the construction area. For installation of horizontal pipes, pits were excavated at 1,5 meter depth and sand layer having 15 cm thick was placed both under and top of pipes for protecting from any damages. Heat transfer fluid used in U-Pipes was water.

Three collectors were used for linking to the mechanical room and each collector was linked to 8 BHEs.

Two heat pumps (one of them as backup) having 500 kW capacity were installed. The heat pump's COP is 4,82 for heating and EER is 4,67 for cooling.

First monitoring results show that 207 kW of the load was met with the installed GSHP system. This was higher than the expected design value of 150 kW.

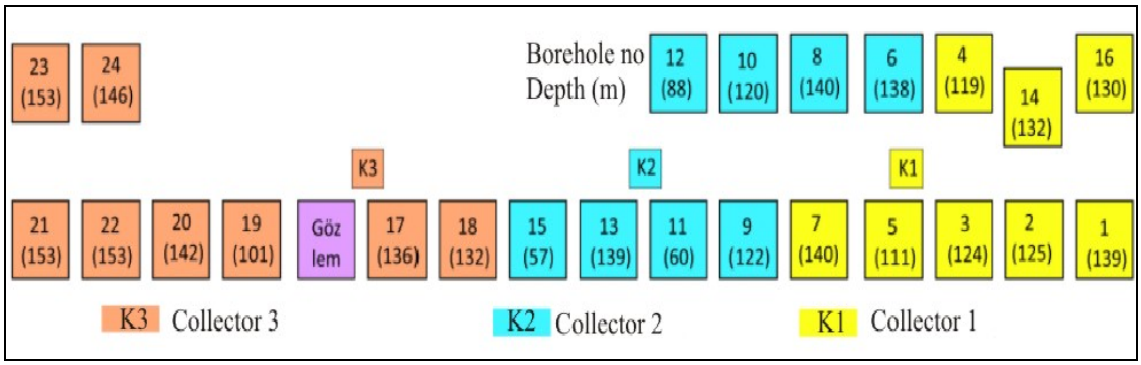


**Fig.6.** Schematic view of Borehole heat exchangers

## THERMAL RESPONSE TEST

Thermal response test (TRT) is carried out to determine thermal properties of borehole heat exchanger such as undisturbed ground temperature, effective thermal conductivity (λeff) and borehole resistance (Rb). TRT was carried out at K1 and K21 boreholes shown in Fig.3 by Center for Environmental Research of Cukurova University (Fig.7) in a total duration of 6 days.

**Fig.7.** TRT test device of Center for Environmental Research of Cukurova University

For determining undisturbed ground temperature, temperature measurements without heat injection during the first hour were used. Heat injection rate has been selected as 9 kW based on the depth of the boreholes.

Undisturbed ground temperature was calculated as 17,6 $^0$C (Fig.8). This value shows a 0,6 $^0$C deviation from annual average air temperature which is expected to be 15 ±1-2 $^0$C. It is estimated that this increase of soil temperature is caused by the intense building developments in the vicinity as shown in Fig.2.

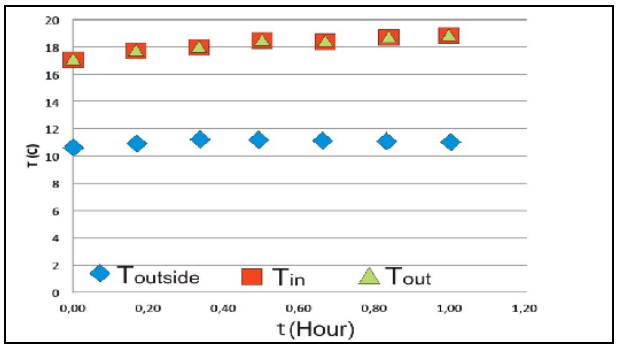


**Fig.8.** Temperature distribution during first hour of TRT without heat injection

Fig.9 and Fig.10 show temperature distributions of ambient, inlet and outlet fluid temperatures during TRT tests for K1 and K21 borehole heat exchangers, respectively. Measured data was evaluated using line source approximation method to determine $\lambda_{eff}$ and $R_b$. For K1, $R_b$ was 0,12 K/(W/m) and $\lambda_{eff}$ was 4,5 W/mK and for K21 $R_b$ was 0,04 K/(W/m) and $\lambda_{eff}$ was 2,8 W/mK [4].

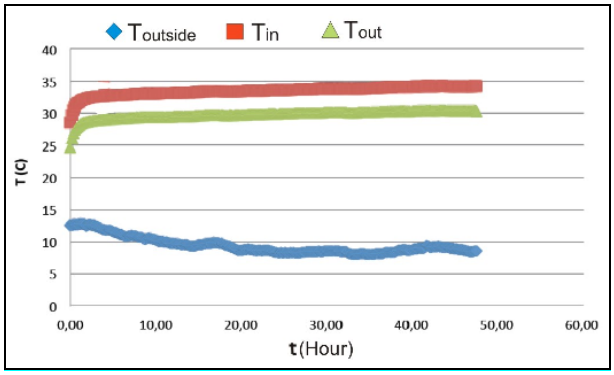


**Fig.9.** Temperatures distributions during TRT at K1 borehole [4]

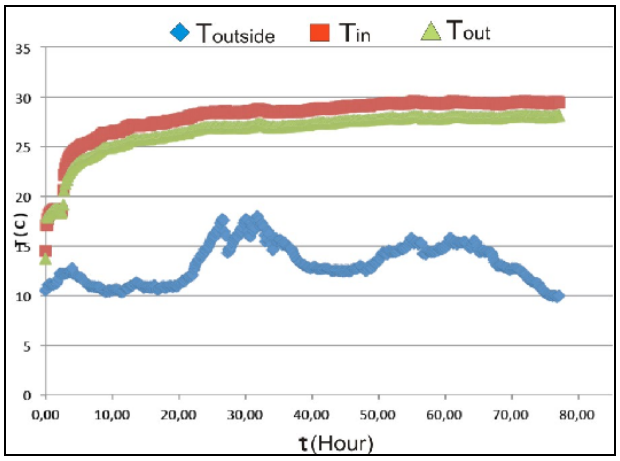


**Fig.10.** Temperature distributions during TRT at K21 borehole [4]

The differences of thermal conductivity and borehole resistance between K1 and K21 boreholes are caused by increased amount of groundwater due to the fractured zones in K1 (Fig.11).

## CONCLUSION

Iller Bank In. Com. constructed its headquarters in Ataşehir as an energy efficient building with GSHP, solar photovoltaic and waste water systems in order to set an example to the municipalities. This building is also considered to be a pioneer among the official buildings in Turkey.

GSHP system with a capacity of 207 kW has 24 BHEs, at various depths from 60 to 153 m. Total length of single U-pipe installed in the BHEs was 3000 m. Geological layers consisted of solid waste filling material (10-15 meter) and metasandstone onwards. Thermal conductivity values of solid waste filling material varied between 0,65 W/mK and 1,15 W/mK.

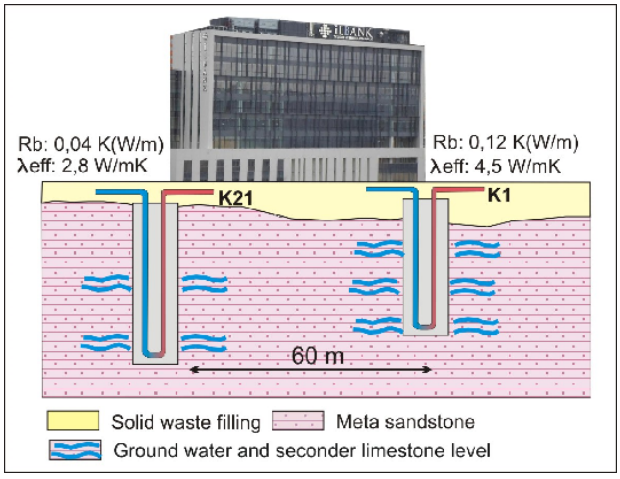


**Fig.11.** Schematic view of thermal properties BHE's

TRT results from two different BHEs show that effective thermal conductivity values were 2,5 W/mK and 4,5 W/mK and borehole resistance values were 0,04 and 0,12 K/(W/m). The undisturbed ground temperature was determined 17,6 $^0$C. Differences between effective thermal conductivity values can be explained by increased amount of groundwater due to the fractured zones around K1 borehole.

## REFERENCES

1 http://www.eie.gov.tr/duyurular_haberler/document/UEVEP_TASLAK.pdf (2016).
2 Cetin, A., Paksoy, H. O., 2013, Shallow Geothermal Application in Turkey, EGEC, Italy.
3 Ozgul, N., Geological properties of Istanbul area, Istanbul Municipality, Department of soil and earthquake, (2011).
4 H.O. Paksoy Thermal Response Test Report of Atasehir Building GSHP System, (2014).

*Bulgarian Chemical Communications, Volume 48, Special Issue E (pp. 31 - 40) 2016*

# Thermal energy storage systems – review

B. Akhmetov[1*], A. G. Georgiev[2,5], A. Kaltayev[1] A. A. Dzhomartov[4], R. Popov[3] M. S. Tungatarova[1]

[1]*Al-Farabi Kazakh National University, Almaty, 050000, Kazakhstan*
[2]*Technical University of Sofia, Plovdiv Branch, Dept. of Mechanics,25 Tsanko Diustabanov Str, 4000 Plovdiv, Bulgaria*
[3]*Faculty of Physics, Plovdiv University "Paisii Hilendarski", 24 Tzar Assen Str., 4000 Plovdiv, Bulgaria*
[4]*Institute of Mechanics and Machine Science n.a. U.A. Dzholdasbekov, Almaty, 050000, Kazakhstan*
[5]*European Polytechnic University, Dept. of "Green Energy", 23 Kiril and Metodiy str., 2300 Pernik, Bulgaria*

There are several thermal energy-consuming appliances in buildings such as heating, ventilation, air conditioning and hot water systems, which are generally responsible for significant proportion of total building energy consumption. One of the effective ways to decrease the amount energy consumption of these appliances from traditional grids, is the application of renewable energy sources, especially solar energy, as the main thermal energy provider. But, because of intermittent and unpredictable nature of solar energy, it is difficult to supply necessary thermal energy to aforementioned appliances without help of effective storage. Therefore, development of a storage that can store thermal energy harvested from renewable energy sources has high importance and one of the active research areas among scientists. Aim of the current work is to review different types of thermal energy storage systems, their technical characteristics, advantages and disadvantages, and compare them with each other. Particularly, this paper is concentrated in two energy storage technologies. One of the technologies, which allows storing thermal energy in a large-scale, is underground thermal energy storage (UTES) and another one is based on phase change materials named as latent heat storage (LHS).

**Keywords:** renewable energy, thermal energy storage, borehole, latent heat storage, phase change material

## INTRODUCTION

Among built environment, buildings are major energy intensive consumers of energy and main contributors of greenhouse gas emissions [1]. Most demanded energy for buildings is thermal energy because of its thermal energy-consuming appliances such as heating, ventilation, air conditioning (HVAC) and domestic hot water (DHW) systems [2, 3]. In order to supply the necessary amount of energy to these appliances, most of the time conventional energy sources are used which are not eco-friendly and hazardous. On the other hand, it would be possible to use renewable energy sources, especially, solar energy as the main source of thermal energy for the above mentioned energy intensive appliances because technologies for harvesting thermal energy from solar energy are becoming efficient, and cost effective. But solar energy value is periodic and unpredictable [4]. For instance, it is not possible to use abundant summer solar energy during winter for space heating purposes unless a large-scale thermal energy storage is considered. Therefore, development of effective energy storage techniques is becoming one of the main research topics for scientists along with improvement of performance of energy harvesting technologies [5].

* To whom all correspondence should be sent:
eng.akhmetov@gmail.com

There are a number of thermal energy storage technologies which are being studied and developed during the last decades. Some of them for storing thermal energy at small and medium scales, while others for storing thermal energy in a large amount [6].

The aim of the study in the current paper is to review different types of thermal energy storage technologies since such review studies help to choose appropriate storage types for developing a pilot plant of a hybrid thermal energy storage system at Al-Farabi Kazakh National University based on the experience of the research team of Prof. A. Georgiev from Technical University of Sofia, Plovdiv Branch [7]. The hybrid storage system is going to be developed in a way that it will be able to store thermal energy for short term as well as for long term purposes. Therefore, main concentration of this review paper is underground thermal energy storage system (UTES) which is also named as long term storage and latent heat storage (LHS) based on phase change materials (PCM) – short term storage.

## UNDERGROUND THERMAL ENERGY STORAGE

### *General*

Thermal energy is abundant and available during warm seasons, but heating demand increases

during cold days of the year. Similarly, cold thermal energy is necessary during summer, which is available in the nature during winter. Therefore, the development of large-scale seasonal thermal energy storage is useful in terms of using heat or cold at necessary time [6].

One of the technologies, which allows storing thermal energy in a large-scale, is Underground Thermal Energy Storage (UTES). Such technology gives opportunity to store heat into the ground and groundwater in the summer, and extract it during winter. In a similar way, cold can be stored during winter and extracted in the summer for cooling purposes. The examples of UTES systems can be found in the papers [8, 9].

According to the measurements the ground temperature at a certain depth remains relatively constant and higher than the surrounding air temperature during the winter and lower during the summer. The temperature fluctuations of the surrounding air influence shallow ground and groundwater temperatures up to a depth of approximately 10 m. With increasing depth the underground temperature increases by an average progression of 3 ºC per 100 meter because of the geothermal gradient [10]. Hence, the ground and groundwater are suitable media for heat extraction during winter and heat rejection during summer. This type of thermal energy extraction method can be applied for heating during winter and cooling during summer. If extracted thermal energy recharged during summer or winter back to the ground, the ground is considered as a thermal energy storage system.

Several types of large-scale or seasonal thermal energy storages are well established worldwide [11, 12]. The most common systems are Borehole Thermal Energy Storage (BTES), Aquifer Thermal Energy Storage (ATES), Tank Thermal Energy Storage (TTES) and Pit Thermal Energy Storage (PTES).

UTES systems are divided into two types:

- Systems where working fluid is circulated through heat exchangers in the ground which are also named as “closed loop” systems (BTES).
- Systems where groundwater is pumped out of the ground and after extracting thermal energy from the water, it charged back into the groundwater layer by means of wells. Such systems are known as open loop systems (ATES).

*ATES - Aquifer Thermal Energy Storage*

ATES is one of the geothermal technologies which is considered as innovative open-loop seasonal storage based on cold/warm groundwater in an aquifer. Main storage media is underground water together with sand, gravel, sandstone or limestone layers which have high hydraulic conductivities. This technology was developed over 20 years and it is now mostly used in Europe, especially, in the Netherlands and Scandinavia. However, ATES is not popular in the United States, with the exception of ATES project at Richard Stockton College in Pomona [14, 15].

Application of ATES system for space heating and cooling is efficient and very green, but it can’t be considered as renewable technology. Although, it is usually used together with renewables, for instance, with solar collectors or wind powered devise with the purpose of providing electrical power to drive the mechanical components of ATES [16].

The main components of ATES system are its wells installed into a ground where the ends of the wells reach an aquifer (Fig.1). The number of wells must be at least two, one of them for water discharging from the aquifer and another one for pumping water back to the aquifer. For instance, if cooling is demanded by the user, cold water is discharged from the cold well, and applied for cooling purposes. Water is then charged back to the aquifer by the warm well at an elevated temperature. In large scale ATES systems, it requires several cold and warm wells. Besides wells, there are other main components of ATES such as heat exchangers, conveyance piping, and mechanical and control systems for integrating it with heating or cooling systems of buildings.

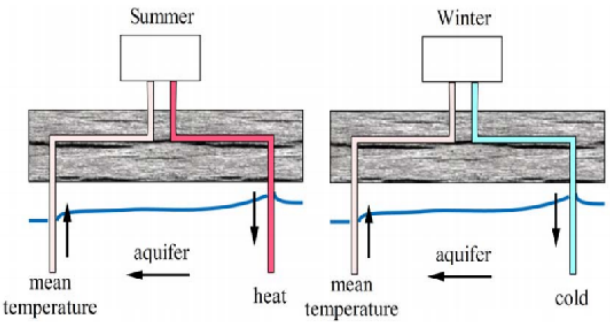


**Fig.1.** Aquifer Thermal Energy Storage [16]

**Table 1.** Major criteria for unconsolidated aquifer [15]

| Aspect | Lower limit | Typical | Upper limit |
|---|---|---|---|
| Aquifer thickness (m) | 2–5 | 25 | None (partial use) |
| Aquifer depth (mbgs) | 5 (injection pressure) | 50 | 150 (economic) |
| Aquifer permeability (m/s) | $3 \times 10^{-5}$ | $3 \times 10^{-4}$ | $1 \times 10^{-3}$ |
| Groundwater flow (m/d) | 0 | 0.1 | 0.3 |
| Static head (mbgs) | 50 | 10 | –5 |

Unfortunately ATES technology is not applicable to every location because it is geologically dependent. There are a number of limitations such as water chemistry, permeability of the underground formations, depth and thinness of aquifer, natural groundwater flow and static head (Table 1). In case of large ATES system, much attention is paid to distribution and location of warm and cold wells. If warm and cold wells are located separately, it leads to large changes in hydraulic head which might cause, for instance, land subsidence. Therefore, the careful design of the field layout must be set up in a number of pairs where each pair consists of one warm and one cold well. Moreover, the distance between warm and cold wells is also very important. In order to avoid short-circuiting between wells located on both sides of natural temperature, minimum distance between warm and cold wells should be three times the thermal radius of the stored heat or cold. Thermal radius can be estimated using the following formula [15]:

$$r_{th} = \sqrt{\frac{c_w Q}{c_a H \pi}} \qquad (1)$$

where $r_{th}$ is thermal radius of the stored thermal energy ($m$), $c_w$ and $c_a$ are heat capacities of water and aquifer material respectively ($J/m^3K$), $Q$ is the amount of pumped water during the season ($m^3$) and $H$ is the screen length (m).

On the other hand, if warm and cold wells are located on one side of the natural groundwater temperature, short-circuiting helps to increase the thermal efficiency. Consequently, distance between wells should be 1-2 times the thermal radius.

The extracted energy during cooling or heating period is determined using formula (2) [16]:

$$E_{extracted} = \int_{extraction} c_w \cdot Q \cdot \left| T_{extraction} - T_{injection} \right| \cdot dt \qquad (2)$$

Here, $Q$ is the total pumping rate ($m^3$/min), $T_{extraction}$ temperature of the water extracted from production well ($K$), $T_{injection}$ temperature of the water entering injection well ($K$).

### *BTES - Borehole Thermal Energy Storage*

Borehole thermal energy storage (BTES) is more practical and can be installed anywhere except in places where high pressure geysers or large empty caverns exist in underground rocks. BTES uses the underground itself as the storage material which may range from unconsolidated material to rock with or without groundwater. Depending on the water content of the underground, subsurface layers can be saturated or unsaturated [18].

The main component of BTES is a vertical heat exchanger (BHE) or also named as borehole heat exchanger. By circulating heat carrier fluid through BHE, thermal energy can be transferred between BHE and subsurface layers which are usually solid state materials where the main heat transport mechanism is by conduction. There are different types of BHE due to geological conditions. Open water-filled boreholes became popular in hard rock areas of Scandinavia, because of their excellent heat exchange performance. This technique is not efficient in the areas of unconsolidated rock. Common ones are single and double U-type BHE and coaxial BHE (Fig.2.). While double U-tubes are common in central Europe, most BTES systems today use single U-tubes. In case of single and double U-type BHE, polyethylene or polypropylene pipes are used as BHE. More information about typical BHE can be found in article [9]. These days,

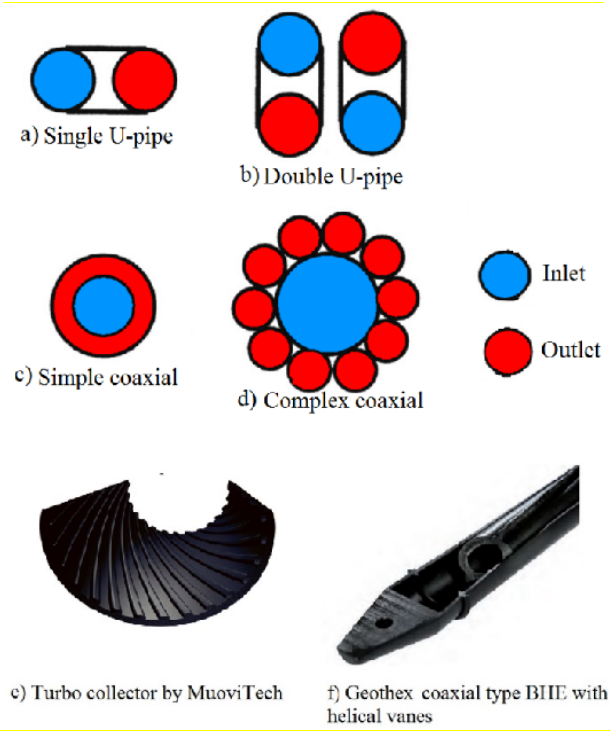


**Fig.2.** BTES types: a) singe and b) double U-type, c) simple and d) complex coaxial [9]; e) Turbo collector by Muovitech f) coaxial type BHE by Geothex (pictures are from muovitech and geothex websites)

there are other advanced BHE exist in the market. They are: turbo collector developed by Muovitech company. The main advantage of the collector is its fins located inside, which creates turbulent flow thus assists in increasing the heat transfer process.

The collector can be used instead of conventional pipes of single or double U-type BHE. Another recently developed high efficiency ground heat exchanger is the one by Geothex. It has insulated inner pipe and helical vanes between outer and inner pipes. These vanes are designed to increase the heat transfer between heat carrier fluid and the surrounding media.

BTES may consist of one or several borehole heat exchangers installed into boreholes. BTES construction is relatively simple. Firstly, a borehole is drilled up to the required depth. In a standard borehole, depth of a borehole is usually 20-300 m. After drilling of the borehole, the BHE is mounted into the borehole and the space between the pipe and the hole is filled with grouting material to ensure good contact between the BHE and surrounding soil (Fig.3). Moreover, the arrangement of flow channels of the GHE (i.e. distance between inlet and outlet pipes of U-type BHE) and types of grouting material are another important aspect of developing effective BTES system. It was found that when shank spacing was increased, borehole thermal resistance $R_b$ was decreased [20]. Moreover, choice of appropriate grouting material helps to effectively transfer the necessary thermal energy between rocks and BHE. Detailed study of backfilling materials and their thermal properties can be found in the articles [21].

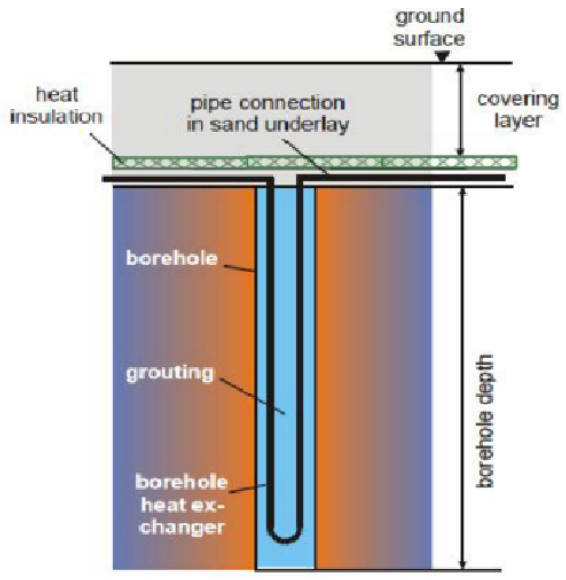


**Fig.3.** Side and top view of single U-type BHE installed into the borehole [16]

BTES is considered as sensible heat storage, therefore, high heat capacity of storage medium is important. All types of underground material have volumetric thermal capacity which is about half that of water (4,15 MJ/m$^3$ K). This value depends on the material itself, the bulk density and the water content. Thermal properties of underground materials are discussed in the article by Reuss [22].

High groundwater content of underground porous materials increase the heat capacity, but groundwater flow may reduce the efficiency of BTES because of increasing losses due to convective heat transport. Therefore, the local geology and hydrology are important in selection of storage type (BTES or other types) [23].

The first project of BTES system for storing solar or waste heat from summer to winter for space heating was carried out in Sweden in 1980s. In the following decades, this technology became popular in other countries too. The majority of BTES systems were integrated with heat pumps for extraction of heat from the storage to provide the required supply temperatures for users. Although, in early days the BTES system was applied to satisfy heating demands, today it is also used for cooling purposes, and in most cases for combined heating and cooling.

In order to develop proper BTES design good knowledge of the heat demand and the heat sources are required. Not only is the amount of charged and discharged energy has importance, but also the dynamics of the heat flux due to the limited thermal conductivity of the underground plays an important role. Knowledge of heat flux dynamics in subsurface layers may be estimated from geological maps of a location. But, still the accuracy of these data usually is poor and can't give enough information about the thermal behaviour of the underground. Therefore, site investigation by test drillings is essential to obtain detailed geological profile and evaluate the thermophysical properties of subsurface layers.

A well-known method used to determine subsurface and borehole thermal properties is Thermal Response Test (TRT) which was developed at Oklahoma State University (USA) and Technical University Luleå (Sweden) [23]. Based on this methods, it is possible to evaluate effective thermal conductivity over the whole length of the BHE and the borehole resistance [24, 25]. To carry out the test procedure, a test installation must be constructed first (Fig.4).

As mentioned above, the size of BTES system depends on the energy demand and type of building. The first BTES systems for seasonal storage were developed in Sweden and Netherlands in 1980s for solar district heating systems and effective use of waste heat from industrial systems

[26]. Moreover, several solar district heating systems were built with different types of seasonal storage under the R&D program 'Solarthermie 2000' and three of them were based on BTES.

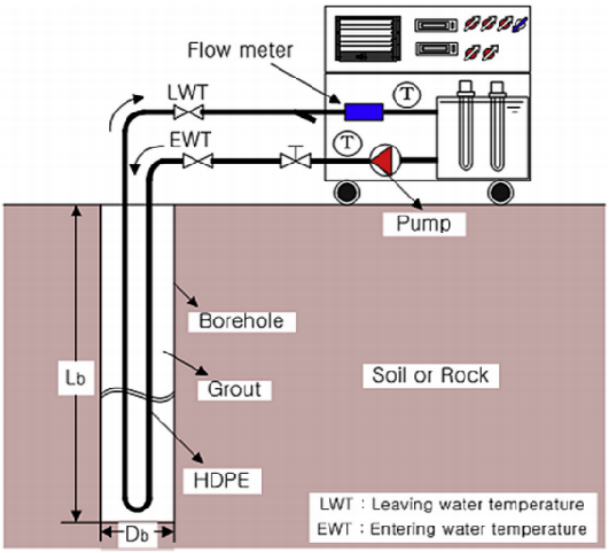


**Fig.4.** BHE and description of TRT installation [24]

Solar district heating in Neckarsulm, Germany, is significant and has the first large project where BTES technology was used for space heating and domestic hot water of 700 apartments of different sizes and residential buildings [22]. Around 5000 $m^2$ of solar flat-plate collectors installed on buildings and two buffer storages of 100 $m^3$ each were used to deliver thermal energy to district heating directly or to the seasonal storage. The number of boreholes in the first operational stage (1997) was 36 and this was extended in two stages in 2001 to 528 boreholes. Because of the local geological formation where highly permeable dolomite layer with groundwater flow starts below 30-35 meters, the depth of the boreholes was chosen to be 30 meters to avoid high bottom losses. Borehole heat exchangers were double-U pipes made of polybutene which has high life expectancy at temperatures up to 85 °C and pressure up to 10 bars.

Other large-scale BTES systems are: Solar district heating at Okotoks, Canada, solar district heating with hybrid storage in Attenkirchen, Germany and so on (Table 2).

*TTES - Tank Thermal Energy Storages*

Most of the small tank storages are connected to solar collectors as a buffer storage for single-family houses. Although, there are some examples of tank storages being used as seasonal storage. Seasonal tank storage is made of reinforced concrete and partially buried in the ground. This type of storage can be built almost independently of geological conditions. It is thermally insulated on the top and on the vertical walls (Fig.5). One of the first tank storages were developed in Germany in 1995. The pilot heat store of 600 $m^3$ used water as the storage material. The shape of the store was cylindrical and half of it was buried into the ground. Stainless steel liners and insulation were used on the top and on the sides. Moreover, 4500 $m^3$ store in Hamburg and the 12000 $m^3$ store in Friedrichshafen are other examples of large scale tank storage. Inside of these storages, stainless-steel liners are used to ensure water tightness and to reduce heat losses caused by steam diffusion via the concrete wall. In addition, polyethylene or polyvinylchloride film was applied as the thermal insulation to the storage. Inner steel liner can be avoided if high-density concrete (HDC) material with lower vapour permeability is used. One of such storages was developed in Hannover [28].

Large-scale solar-heated tank seasonal heat storage systems were developed in Sweden. But, some of them were not successful. For instance, the solar heating plant at Ingelstad designed to cover 50% of the annual energy demand of 52 houses and volume of the storage was 5000 $m^3$. But, because of the low efficiency of the solar collectors and thermal losses from the storage the system covered only 14% of the annual energy. Tank storages in Hoerby and Herlev in Denmark with storage capacity of 500 $m^3$ and 3000 $m^3$ respectively showed leakage problems at the beginning and were not competitive for large storage volumes [11].

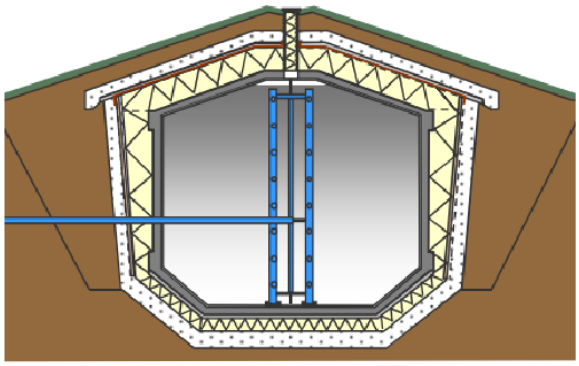

**Fig.5.** Tank thermal energy storage [33]

Numerical simulations were used to predict performance of central solar heating plants with seasonal storage (CSHPSS) and later validated with

**Table 2.** Examples of BTES projects over the world [27]

| N°= | Location | Country | Type of building | Heated floor area (m²) | Heating power (kW) | Refrigerating power (kW) | Number of BHE | Active length of the BHE (m) |
|---|---|---|---|---|---|---|---|---|
| 1 | Langen | Germany | Office | 44500 | 330 | 340 | 154 | 70 |
| 2 | Lucerne | Switzerland | Office | 20000 | 450 | 700 | 49 | 160 |
| 3 | Neckarsulm | Germany | District heating | 25000 | 500 | | 528 | 30 |
| 4 | Crailsheim | Germany | District heating | 40000 | 530 | | 80 | 49 |
| 5 | Truro | Canada | Prison | 3837 | 211 | | 24 | 63 |
| 6 | Lugano | Switzerland | Single family house | 250 | 14 | no cooling | 3 | 80 |
| 7 | Sopot | Poland | Hospital | 4223 | 200 (300 with the boiler) | | 80 | 50 |
| 8 | Münster | Germany | Office | 14000 | 529 | 379 | 95 | 100 |
| 9 | Ulm | Germany | Office | 6911 | 120 | | 40 | 99 |
| 10 | Athens | Greece | Office | 6000 | 526 | 461 | 13 | 90 |
| 11 | Lincoln | USA | School | 6410 | 694 (1081 with the boiler) | | 120 | 73 |
| 12 | Melle | Belgium | Office | 20700 | 500 (200 with the boiler) | 378 (1200 with the refrigerating machine) | 90 | 120 |
| 13 | Attenkirchen | Germany | District heating | 6075 | | | 90 | 30 |
| 14 | Aachen | Germany | Office | 2072 | 56 | | 28 | 45 |
| 15 | Donaueschingen | Germany | Office | 3500 | 90 | 452 | 56 | 95 |
| 16 | Schöffengrund | Germany | Office | 385 | 22 | no cooling | 8 | 50 |
| 17 | Stuttgart | Germany | Office | 2400 | 67 | | 18 | 55 |
| 18 | Markham | Canada | School | 16822 | 1442 | | 360 | 61 |
| 19 | Pylaia | Greece | Town Hall | 2500 | 265 | 168 | 21 | 80 |
| 20 | Wollerau | Switzerland | Office | 3000 | 190 | 210 | 32 | 135 |
| 21 | Stadl Paura | Austria | Office | 1540 | 43 | | 8 | 100 |
| 22 | Onamia | USA | School | 7246 | 679 | | 560 | 15,2 |
| 23 | Vestal | USA | Office | 743 | 84,4 | | 16 | 76,2 |
| 24 | York County | USA | Office | 2480 | 351,7 | | 96 | 50 |
| 25 | Oslo | Norway | Office, hotel | 180000 | 6000 | 9500 | 180 | 200 |
| 26 | Setubal | Portugal | University | 220 | 15 | 12 | 5 | 80 |
| 27 | Sabadell | Spain | Office | 1546 | 165 | 165 | 14 | |
| 28 | Montreal | Canada | Store | 4180 | | | 12 | 175 |
| 29 | Lancaster | USA | Restaurant | 1394 | 90 | | 6 | 153 |
| 30 | Wysox | USA | Hotel | 3623 | 341,1 | | 30 | 91,4 |

the experimental data obtained [29]. For instance, TRNSYS and OmSim were used to simulate the performance of CSHPSS developed at Saro, Sweden. Argiriou compared the results of MINSUN and SOLCHIPS used to simulate the performance of Lukovrissi Solar Village, in Greece. Zhang at al. developed a model to study tank storage performance which included a surface water pond with polystyrene foam as insulating cover, which works as a heat source in winter and heat sink in summer [30].

### *PTES - Pit Thermal Energy Storages*

Pit thermal energy storages (PTES) are constructed without static constructions installing a liner and insulation in a pit. The type of lid depends on a geometry of the PTES as well as on the storage medium. But there are examples where the pit is filled both with gravel along with water. In that case, the lid may be constructed similar to the walls (Fig.6.). Indeed, construction of a lid of a PTES requires most of the effort and expensive part of the storage. Usually, then lid is not supported by the walls of PTES, instead, it floats on top of the water [11].

Typically, PTES is entirely buried into the ground and can be installed almost anywhere regardless of the type of geological location. The gravel water PTES has lower specific heat capacity compared to water alone PTES. Therefore, the size of gravel water PTES systems is bigger than water alone PTES systems, for the same heat storage capacity.

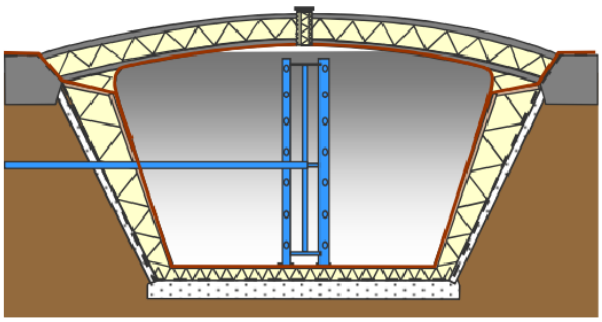

**Fig.6.** Pit thermal energy storage [33]

First large scale PTES was developed at the Institute for Thermodynamics and Thermal Engineering of Stuttgart University in 1984 [31]. The shape of the pit was similar to truncated cone and storage was filled with pebbles and water. High-density polyethylene liner was used and thermally insulated only on top with porous lava

**Table 3.** Comparison of hot water and gravel water PTES [33]

| Hot water pit thermal energy storage | Gravel / sand / soil water pit thermal energy storage |
|---|---|
| + thermal capacity<br>+ operation characteristic<br>+ thermal stratification<br>+ maintenance / repair | + low static requirements<br>+ simple cover |
| - sophisticated and expensive cover<br>- low static cover load<br>- costs for landfill of excavated soil (if applicable) | - thermal capacity<br>- charging system<br>- additional buffer storage (if applicable)<br>- maintenance / repair<br>- gravel costs |

and earth layers. One of the largest PTES constructed in Denmark has a storage volume of 75000 $m^3$. It was sealed with a HDPE liner and covered by a floating lid made of coated elements of PUR. Other examples of PTES are: 8000 $m^3$ heat storage at Chemnitz (Germany); 1500 $m^3$ storage at Steinfurt–Borghorst (Germany); and gravel–water storage with the capacity of 500 $m^3$ developed at the Technical University of Denmark, Lyngby [32].

Compared to TTES, PTES requires less construction cost and the upper part of the storage can be used as a part of a residential area, but needs bigger size to achieve the capacity of TTES. Moreover, it is easy to have maintenance or repair for TTES than PTES, although the former has higher construction costs for the cover (lid). Table 3 summarizes the advantages and disadvantages of both tank and pit thermal energy storages [33].

The above mentioned storages are usually used as large scale thermal energy storage systems. They can be used separately or can be coupled together to achieve better performance depending on the energy demand. One of the combined storage which used BTES and TTES is the solar district heating system in Attenkirchen, Germany. The concrete TTES with a height of 8.5 m and a diameter of 9 m (total volume is 500 $m^3$) is installed in the centre of the BTES field. The number of BTES is 90 with a depth of 30 m. The top of the tank storage was covered with 20 cm thick layer of polystyrene. Heat losses of the tank storages from the side walls and the bottom is the partial heat gains of BTES. Around 765 $m^2$ of solar collectors serve as thermal energy deliverers [34].

It is possible to combine two or more large-scale thermal energy storage systems to achieve better performance in thermal energy storage techniques, but combination of the storage systems depends on things such as properties of large-scale storages (Table 4), geological formations of the location, thermal energy demand, cost recovery and construction risks that might influence on the performance of the system.

## LATENT HEAT STORAGE WITH PHASE CHANGE MATERIAL

Among the methods for heat accumulation, thermal storage in the form of latent heat is very attractive and considered as promising candidates for effective heat storage technique [35]. Latent heat storage (LHS) relies on storage materials which absorbs/ releases heat while undergoes phase transition. Such phase change materials (PCMs) have higher energy storage density with the range of 150-200 kJ/kg and narrower temperature range between storing and releasing heat compared to sensible heat storage. However, LHS systems suffer from the low thermal conductivity of the phase change materials. In turn, this leads to low charging and discharging rates [36].

There are different types of phase change materials and they have various built-in thermal properties. PCMs are divided into three main groups: organic, inorganic and eutectic. For instance, paraffinic and non-paraffinic materials are considered as organic PCMs, while salt hydrated are inorganic materials. About PCMs, their types and thermal characteristics can be found in the papers [36, 37].

As mentioned above, one of the problems related to PCMs is their low thermal conductivity feature. To enhance heat transfer process during charging or discharging of LHS filled with PCMs, different methods are applied based on thermal conductivity improvement techniques. One of the methods is the application of metal foams as a heat transfer intensifier. For instance, Xiao at al. [38] studied paraffin/ nickel foam and paraffin/ copper foam composite phase change materials. According to the experimental results, it was found that compared with pure paraffin, the thermal conductivities of the composite PCMs were drastically enhanced, especially, the thermal conductivity of the paraffin/ nickel foam composite was about three times higher than that of pure paraffin.

**Table 4.** Comparison of large-scale storage systems [33]

| TTES | PTES | | BTES | ATES |
|---|---|---|---|---|
| *storage medium* | | | | |
| water | water* | gravel-water* | soil / rock | sand-water |
| *heat capacity in kWh/m³* | | | | |
| 60 - 80 | 60 - 80 | 30 - 50 | 15 - 30 | 30 - 40 |
| *storage volume for 1 m³ water equivalent* | | | | |
| 1 m³ | 1 m³ | 1.3 - 2 m³ | 3 - 5 m³ | 2 - 3 m³ |
| *geological requirements* | | | | |
| - stable ground conditions<br>- preferably no groundwater<br>- 5 – 15 m deep | - stable ground conditions<br>- preferably no groundwater<br>- 5 – 15 m deep | | - drillable ground<br>- groundwater favourable<br>- high heat capacity<br>- high thermal conductivity<br>- low hydraulic conductivity ($k_f < 10^{-10}$ m/s)<br>- natural ground-water flow < 1 m/a<br>- 30 - 100 m deep | - natural aquifer layer with high hydraulic conductivity ($k_f > 10^{-5}$ m/s)<br>- confining layers on top and below<br>- no or low natural groundwater flow<br>- suitable water chemistry at high temperatures<br>- aquifer thickness of 20 - 50 m |

There were other experimental and numerical studies, which have been conducted and reported in papers [39, 40]. Another method which was applied to improve thermal efficiency of PCMs is based on extended surfaces. In other words, fins are attached to the surfaces between hear carrier fluid and PCM with the purpose of improving heat transfer between them. Wang at al. [41] studied PCM melting in enclosures with vertically-finned internal surfaces end concluded that fins help to enhance phase change process during charging/ discharging of LHS. Heat exchangers mounted into PCM storage were also equipped with extended surfaces and results showed that process of phase transition was improved [42]. Scientists also studied PCMs which included particles with high thermal conductivity [43, 44]. As a result, particles also have some assessment in enhancement of phase transition process. Encapsulation of phase change material within a heat carrier fluid is another effective method which helps to improve heat transfer process [45, 46]. Usually, encapsulated PCM are placed in a latent heat storage and during charging process upper layer of encapsulated PCM gains thermal energy of heat transfer fluid. Layers below cannot gain same amount of thermal energy as the upper layers. Therefore, a series of PCMs with a decreasing melting temperature along the heat carrier fluid flow direction are used. Moreover, different designs of LHS are proposed by researchers. Most considered ones are shell and tube heat exchanger mounted storages, storages which equipped with vertical or horizontal PCM filled containers [4], and LHS with finned tubes designed to intensify heat transfer between heat transfer fluid and PCM.

## CONCLUSION

This review paper is focused on thermal energy storage technologies, especially, large-scale thermal storages such as aquifer and borehole thermal storages, tank and pit thermal energy storages. As it can be concluded from the studies presented in this paper, each storage has its own advantages and disadvantages as well. ATES systems are highly dependent on the geological structure of the subsurface layers, especially on an aquifer type, while BTES systems do not need special geological conditions, except there should not be emptied caverns or high pressure geysers in the subsurface. Moreover, TTES system can be built independently of geological conditions and it is reliable and efficient if it was constructed properly, otherwise leakage problems might arise. Special liners are

used in TTES system to hinder thermal energy loses from the storage. Another large scale storage is PTES system. Some PTES systems include gravel with water as the storage media. TTES storage is usually covered by a lid and construction of a lid requires most of the effort and is the most expensive part of the storage. In addition, small and medium scale thermal energy storages based on phase change materials (PCMs) are considered as well. Particularly, thermal properties of PCMs, methods for improving thermal conductivities of PCMs and latent heat storage types are discussed. Is can be concluded that usually PCMs have low conductivity problems, therefore, methods used to increase conduction heat transfer in the PCMs are developed. Some of them are adding high conductive micro or nanoparticles, encapsulation of PCMs in small sizes, application finned heat exchangers or metal foams in PCMs. Moreover, design of the storage tank plays important role in developing efficient storage with PCM.

Additional aim of the review was to gather necessary knowledge from last year scientific papers in the area of thermal energy storage and apply the knowledge to develop hybrid thermal energy storage, which is able to store thermal energy for short term as well as long term purposes. The hybrid storage will be developed in Al-Farabi Kazakh National University with the help of Bulgarian research team under the guidance of Professor Georgiev from Technical University of Sofia, Branch Plovdiv.

## ACKNOWLEDGEMENT

The authors acknowledge the support provided by the Institute of Mathematics and Mechanics at Al-Farabi Kazakh National University under the grant funding named “Development of charging and discharging regimes for hybrid thermal energy storage system consisting of latent heat storage and borehole thermal energy storage, designed to accumulate solar thermal energy”.

## REFERENCES

1 E. G. Dascalaki, K. Droutsa, A. G. Gaglia, S. Kontoyiannidis, C. A. Balaras, Data collection and analysis of the building stock and its energy performance—An example for Hellenic buildings, Energy and Buildings, 42, 1231-1237 (2010).
2 L. Perez-Lombard, J. Ortiz, C. Pout, A review on buildings energy consumption information, 40, 394-398, (2008).
3 A. Allouhi, Y. El Fouih, T. Kousksou, A. Jamil, Y. Zeraouli, Y. Mourad, Energy consumption and efficiency in buildings: current status and future trends, *Jour. of Cleaner Production*, 109, 118-130, (2015).
4 R. Popov, A. Georgiev, SCADA system for study of installation consisting of solar collectors, phase change materials and borehole storages, *2nd Int. Conf. Sust .En. Storage*, Dublin, Ireland, (2013).
5 B. Nordell, G. Hellstrom, High temperature solar heated seasonal storage system for low temperature heating of buildings, *Solar Energy*, 69, No. 6, 511-523 (2000).
6 E. Michaelides, Alternative Energy Sources, 459 (2012).
7 M. Bottarelli, M. Bortoloni, Y. Su, C. Yousif, A. Aydin, A. Georgiev, Numerical analysis of a novel ground heat exchanger coupled with phase change materials, *Applied Thermal Engineering*, 88, 1-7 (2014).
8 M. Lundh, J.-O. Dalenback, Swedish solar heated residential area with seasonal storage in rock: Initial evaluation, *Renewable Energy*, 33, 703-711 (2008).
9 T. Schmidt, D. Mangold, H. Müller-Steinhagen, Central solar heating plants with seasonal storage in Germany, *Solar Energy*, 76, 165-174 (2004).
10 G. Florides, S. Kalogirou, Ground heat exchangers - A review of systems, models and applications, *Renewable Energy*, 32, 2461-2478 (2007).
11 V. Novo, J. R. Bayon, D. Castro-Fresno, J. Rodriguez-Hernandez, Review of seasonal heat storage in large basins: Water tanks and gravel–water pits, *Applied Energy*, 87, 390-397 (2010).
12 B. Sibbitt, D. McClenahan, R. Djebbar, J. Thornton, B. Wong, J. Carriere, J. Kokko, The Performance of a High Solar Fraction Seasonal Storage District Heating System – Five Years of Operation, *Energy Procedia*, 30, 856-865 (2012).
13 A. Reverberi, A. Del Borghi, V. Dovм, Optimal Design of Cogeneration Systems in Industrial Plants Combined with District Heating/Cooling and Underground Thermal Energy Storage, *Energies*, 4, 2151-2165 (2011).
14 C.-F. Tsang, Aquifer thermal energy storage, *Lawrence Berkeley National Laboratory*, 28 (2011).
15 B. Nordell, A. Snijders, L. Stiles, The use of aquifers as thermal energy storage (TES) systems, *Advances in Thermal Energy Storage*, Part 5, 87-115 (2014).
16 L. G. Socaciu, Seasonal sensible thermal energy storage solutions, *Leonardo Electronic Journal of Practices and Technologies,* 19, 49-68 (2011).
17 W. Sommer, J. Valstar, I. Leusbrock, T. Grotenhuis, H. Rijnaarts, Optimization and spatial pattern of large-scale aquifer thermal energy storage, *Applied Energy*, 137, 322-337 (2015).
18 K. S. Lee, Underground Thermal Energy Storage, *Springer*, 95-122 (2013).
19 H. Zeng, N. Diao, Zh. Fang, Heat transfer analysis of boreholes in vertical ground heat exchangers, *Int. Jour. of Heat and Mass Tr.*, 46, 4467–4481 (2003).

20 R. Al-Chalabi, Thermal Resistance of U-tube Borehole Heat Exchanger System: Numerical Study, (2013), master thesis, 2013.
21 S. Erol, B. Francois, Efficiency of various grouting materials for borehole heat exchangers, *Applied Thermal Engineering*, 70, 788-799 (2014).
22 M. Reuss, The use of borehole thermal energy storage (BTES) systems, *Advances in Thermal Energy Storage Systems,* 117-147, (2015).
23 J. Acuna, Distributed thermal response tests – new insights on U-pipe and coaxial heat exchangers in groundwater-filled boreholes, *Doctoral Thesis in Energy Technology*, Stockholm, Sweden, 2013.
24 K. S. Chang, Thermal performance evaluation of vertical U-loop ground heat exchanger using in-situ thermal response test, *Renewable Energy*, 87, 585-591 (2016).
25 A.-M.Gustafsson, L. Westerlund., Heat extraction thermal response test in groundwater-filled borehole heat exchanger - Investigation of the borehole thermal resistance, *Renewable Energy*, 36, 2388-2394 (2011).
26 S. Gehlin, Thermal Response Test, Method Development and Evaluation, Doctoral Thesis, 2002.
27 M. Philippe, D. Marchio, S. Hagspiel, P. Riederer, V. Partenay, Analysis of 30 underground thermal energy storage systems for building heating and cooling and district heating, Conference Proceedings, Effstock 2009, Stockholm, Schweden, 2009.
28 M. Chung, J.U. Park, H.K. Yoon, Simulation of a central solar heating system with seasonal storage in Korea, *Solar Energy*, Pergamon, 64, 163-178, (1998).
29 A. A. Argiriou, CSHPSS systems in Greece: test of simulation software and analysis of typical systems. Sol Energy; 60(3-4):159-70 (1997).
30 H-F. Zhang, X-S. Ge, H. Ye, Modeling of space heating and cooling system with seasonal energy storage. *Energy*, 32, 51-58, (2007).
31 E. Hahne, The ITW solar heating system: an oldtimer fully in action. *Sol Energy*, 69(6), 469-493 (2000).
32 A. Heller, 15 years of R&D in central solar heating in Denmark. Sol Energy, 69 (6), 437-447 (2000).
33 Solar district heating guidelines, Fact sheet 7.2.
34 VDI Guideline VDI 4640, Thermal Use of the Underground, Part 1-3, Fundamentals, Approvals, Environmental Aspects. Beuth-Verlag Berlin (2010).
35 H. Mehling, L.F. Cabeza, Heat and Cold Storage with PCM: An Up to Date Introduction into Basics and Applications, Springer (2008).
36 N. Soares, J.J. Costa, A.R. Gaspar, P. Santos, Review of passive PCM latent heat thermal energy storage systems towards buildings' energy efficiency, *Energy and Buildings*, 59, 82–103 (2013).
37 B. Zalba, J.M. Marín, L.F. Cabeza, H. Mehling, Review on thermal energy storage with phase change: materials, heat transfer analysis and applications, *Applied Thermal Engineering* 23(3), 51–83 (2003).
38 X. Xiao, P. Zhang and M. Li, Preparation and thermal characterization of paraffin/ metal foam composite phase change material, *Applied Energy*, 112, 1357-1366 (2013).
39 P. Chen, X. Gao, Y. Wang, T. Yu, Y. Fang, Zh. Zhang., Metal foam embedded in SEBS/ paraffin/ HDPE form-stable PCMs for thermal energy storage, *Solar Energy Materials & Solar Cells*, 149, 60–65 (2016).
40 S. A. Nada, W. G. Alshaer, Comprehensive parametric study of using carbon foam structures saturated with PCMs in thermal management of electronic systems, *Energy Conversion and Management*, 105, 93–102 (2015).
41 P. Wang, H. Yao, Zh. Lan, Zh. Peng, Y. Huang, Y. Ding, Numerical investigation of PCM melting process in sleeve tube with internal fins, *Energy Conversion and Management*, 110, 428–435 (2016).
42 A. J. Parry, P. C. Eames, F. B. Agyenim, Modeling of Thermal Energy Storage Shell-and-Tube Heat Exchanger, *Heat Transfer Engineering*, 35 (1) 1-14, (2014).
43 A. A. Altohamy, M.F. Abd Rabbo, R.Y. Sakr, A.A. Attia, Effect of water based Al2O3 nanoparticle PCM on cool storage performance, *Applied Thermal Engineering*, 84, 331-338 (2015).
44 S. Park, Y. Lee, Y. S. Kim, H. M. Lee, J. H. Kim, I. W. Cheong, W.-G. Koh, Magnetic nanoparticle-embedded PCM nanocapsules based on paraffin core and polyurea shell, *Colloids and Surfaces A: Physicochem. Eng. Aspects*, 450, 46–51 (2014).
45 V.V. Tyagi, A.K. Pandey, D. Buddhi, R. Kothari, Thermal performance assessment of encapsulated PCM based thermal management system to reduce peak energy demand in buildings, *Energy and Buildings*, 117, 44–52 (2016).
46 A. R. Archibold, D. Y. Goswami, M. M. Rahman, E. K. Stefanakos, Multi-mode heat transfer analysis during freezing of an encapsulated storage medium, *International Journal of Heat and Mass Transfer*, 84, 600–609 (2015).

*Bulgarian Chemical Communications, Volume 48, Special Issue E (pp. 41 - 54) 2016*

# Thermo-mechanical behavior of a thermo-active precast pile

C. de Santiago[1*], F. Pardo de Santayana[1], M. de Groot[1], J. Urchueguía[2], B. Badenes[2], T. Magraner[2], J.L. Arcos[3], Francisco Martín[3]

[1] *Laboratorio de Geotecnia (CEDEX) C/ Alfonso XII, 3 y 5. 28014, Madrid (Spain)*
[2] *Departamento de Física Aplicada. Universitat Politecnica de Valencia. Valencia (Spain)*
[3] *Grupo Rodio Kronsa. C/ Velazquez, 50-5ª 28001 Madrid (Spain)*

A new research and development project has been launched in Spain to undertake some studies on the geothermal use of pile foundations (PITERM PROJECT). The experiment, consists of a specifically designed, constructed and fully monitored geothermal precast pile driven at Polytechnic University of Valencia. The pile is under two types of loads: mechanical and thermal. The mechanical load was applied by means of a mechanical frame anchored to the ground, as element of reaction, and three anchors used to induce an active compressive force. The thermal load was provided by a thermal installation, with a data logger to record the outflow and return temperatures. The testing set is fully instrumented in order to register the thermo-mechanical behaviour of the system in terms of thermally induced movements, thermal axial strain profiles and shaft resistance mobilized as a result of cooling and heating. The results obtained permitted the quantification of three significant effects brought about by the temperature increase: pile uplift, additional load generated in the pile by constrain of the thermal stains, and mobilization of side friction due to the relative displacement of the pile with respect to the ground. The pile strain is of the thermo-elastic type and is strongly affected by the type of surrounding soil.

**Keywords:** geothermal energy, thermo-active pile, thermo-mechanical behaviour, thermal loads

## INTRODUCTION

Energy piles (thermo-active piles or geothermal piles) are foundations with double usefulness: to support the loads of the building and to serve as a heat exchanger with the ground. The geothermal use of pile foundations is a useful, efficient and cost effective method of installing ground heat exchangers for cooling and heating buildings. The key factor in the sustainability of thermo-active foundations systems is utilizing geo-structures that are already needed for structural purposes. This way, coupling piles with ground source heat pumps only requires a low extra over cost for geothermal installation, and it supposes a minimal impact on the piling program. They constitute a growing energy technology that improve the energy efficiency of heating and cooling systems in building and have been widely developed and researched in recent years [1, 2, 3, 4, 5, 6, 7] but it is still necessary to understand how the thermal and mechanical loads affect the mechanical behaviour of the pile. On the other hand, as this is a relatively new technology, robust standards and guidelines have not yet been developed for the design of these systems.

Although it is widely accepted that energy piles foundations are an efficient solution for long-term carbon emission reduction and sustainable construction, they have received only partial acceptance, because of concerns regarding the impact of cyclic thermal changes on their serviceability. In this sense, specific research is still needed to better understand how the thermal loads affect the pile behaviour: changes in vertical strains, stresses and axial loads along the pile, changes in shear stresses between pile shaft and soil, movements at head and toe of pile, changes in soil strength parameters, influence of ground lithological profile and water table position, effects of constrictions at head and toe of pile, possible associated phenomena regarding soil consolidation or negative skin friction, etc.

A research and development project in energy piles was performed in Spain from 2011 to 2015 (PITERM PROJECT). The purpose of this experiment was to improve the knowledge and understanding the effects of cooling and heating on precast piles subjected to mechanical loads in terms of mechanical, geotechnical and thermal actions.

## BACKGROUND: PILE-SOIL INTERACTION UNDER MECHANICAL AND THERMAL LOADS

Since the beginning of 1980s, geothermal energy has been increasingly extracted through structural elements in direct contact with the soil [3]. Energy geo-structures have been constructed particularly in Switzerland, Austria, Germany, England and Japan. Two well-documented

* To whom all correspondence should be sent:
cristina.desantiagobuey@gmail.com

thermomechanical tests on full-scale foundations can be pointed out: in Switzerland [1,2], and in the UK [5,6].

The mechanisms of thermo-mechanical effects on energy foundations can be evaluated by assessing data presented by Bourne-Webb et al. [5], who performed a series of thermal and mechanical loading tests on a full-scale foundation at Lambeth College in England, Laloui et al. [2], who performed a series of thermal and mechanical loading tests on a full-scale foundation at the Swiss Federal Institute of Technology in Lausanne, in Switzerland, and Loveridge and Powrie [8], who identified the key factors which influence the heat transfer and thermal–mechanical interactions of such structures and highlighted that the pile aspect ratio is an important parameter controlling the overall thermal performance.

Murphy, K.D. and McCartney [9], focused on the response of two full-scale energy foundations beneath an 8-story building during operation of a heat pump over a 658-day period. During circulation of fluid having temperatures ranging from 7 to 35 °C through the closed-loop heat exchangers within the foundations, the temperature of the reinforced concrete ranged from 9 to 30 °C and was relatively uniform with depth. The thermal axial strains during the first year of heating and cooling were elastic and recoverable, but a change in mobilized coefficient of thermal expansion occurred in the second year, potentially due to changes in interface shear stresses

The coupled thermo-mechanical loads in energy foundation produce unique stress and strain profiles, shown schematically by Bourne-Webb et al. [5]. Under loading alone, the pile is in compression and moves into the supporting soil, and resistance at the pile/soil interface opposes the loading. When a heating cycle is applied, the pile tends to expand, but the surrounding soil will offer restraint to the pile shaft, which will cause compressive axial load developing; at the pile/soil interface, shear induced by heat on the pile/soil interface will oppose that induced by compressive pile loading in the upper part of the pile, but will be additive in the lower. The reverse will happen when the pile is cooled. In both cases the sign of the change in pile/soil interface shear will be opposite in the upper and in the lower part of the pile [5]. Heating a pile subjected to a mechanical load will result in an increase in compression axial load [2, 5] being the pile/soil interface shear stresses modified. Cyclic temperature variations affect in terms of alteration of the mobilized shaft friction and bearing capacity at the soil-pile interface [10].

All the concepts and information offered by these authors are considered in the analysis of the thermo-mechanical behaviour of the energy pile in this work.

## PILE DESIGN AND CONSTRUCTION

A geothermal precast concrete pile was specifically designed and constructed at the Rodio-Kronsa factory (Fig.1).

**Fig.1.** Precast pile at the factory Rodio-Kronsa

This test pile, made of reinforced concrete with characteristic resistance ($f_{ck}$) of 50 N/mm$^2$ and a Young modulus of 31314 N/mm$^2$ ($E=8500\cdot(f_{ck})^{1/3}$[11] ), with a square cross section of 35 cm side and a total length of 17.4 m, was made of two pieces 8.70 m long each, connected by a joint. To activate it thermally, two polyethylene tubes were installed vertically within a steel pipe, 11.3 cm nominal diameter, located in the centre of the pile with a double U-shaped configuration to allow the passage of the heat carrier fluid.

Ground conditions of the testing site in Valencia and mechanical ground properties (Table 1) were taken into account for the foundation design: A superficial fill layer of sandy gravel (1m thick); a second layer of stiff clay (1 m thick); a 6 m thick layer of soft and black organic clays; and below depth 8 m, layers of sandy gravels extended up to a depth of at least 27 m, interlayered with some stiff clays levels. The ground water table is located at a depth of 2.0 m. Under these lithological conditions, the pile should work transferring loads to the soil levels located at more than 11 m of depth.

**Table1. Material parameters**

| Depth (m) | Lithology | Geotechnical Parameters |
|---|---|---|
| 0 – 1.00 | Sandy gravel | $\rho_{ap}$ = 18 kNt/m$^3$<br>c' = 0 kPa<br>φ = 28º |
| 1.00 – 2.00<br>F.L ∇ | Stiff clay | $\rho_{ap}$ = 20 kN/m$^3$<br>c' = 1 kPa<br>φ = 26º<br>$c_u$ = 30 kPa |
| 2.00 – 7.80 | Soft and black organic clays | $\rho_{ap}$ = 19 kN/m$^3$<br>c' = 5 kPa<br>φ = 26º<br>$c_u$ = 20 kPa |
| 7.80 – 26.0 | Sandy gravels | $\rho_{ap}$ = 22 kN/m$^3$<br>c'= 0-20 kPa<br>φ = 35º<br>$c_u$ = 30 - 50 kPa |

The ultimate compressive resistance of the pile, calculated from ground test results by the method established in the Spanish Building Code [12], was 2568 kN. Subsequently, a service compression load of 1000 kN was decided at the pile head.

The pile was fully instrumented before being cast in the factory. The aim of the instrumentation was to monitor the distributions of temperature and axial strain with depth, as well as the supply and return temperatures of the heat exchanger fluid. Pairs of vibrating wire concrete-embedment strain gauges (VWSG) (GS2100 Geosense) with a gauge factor of 3.51 and a coefficient of linear thermal expansion of the steel wire in the gauges of 12.2 με/°C ,were oriented longitudinally and attached to the lateral reinforcing bars at seven different depths along the pile, then cast in concrete during construction (Fig.2). Each VWSG contained a thermistor to monitor temperature in the concrete at each sensor location.

**Fig.2.** VWSG attached to the reinforcement bar

With the aim of comparing with the conventional instrumentation, Optical Fibre Sensors (OFS) (Micron Optics, OS3600), based on fiber Bragg grating (FBG) technology providing integrated temperature compensation, were installed to measure temperature and vertical strain each 2 m along the length of the pile. Schematics of the foundation, the embedded sensors and the geological profile are shown in Fig.3 and Fig.4.

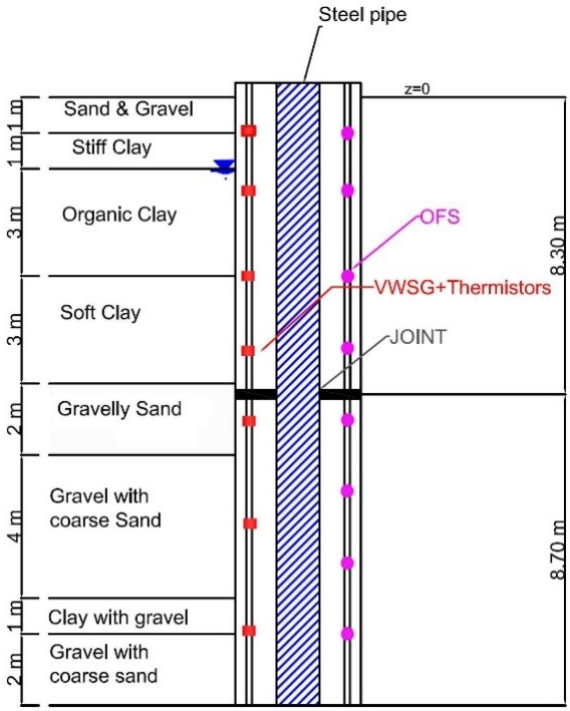


**Fig.3.** Soil profile and instrumentation

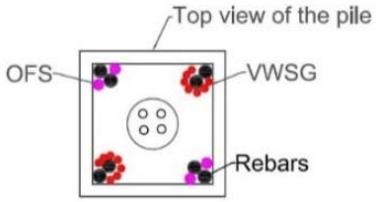


**Fig.4.** Top view of the pile

## EXPERIMENTAL SET UP

The pile was driven in the ground the 27$^{th}$ of June, 2012 in Valencia. Using CAPWAP® (Case Pile Wave Analysis Program) software the total bearing capacity of the pile, as well as the resistance distribution along the shaft and at the toe were calculated during the driving, by means of the Pile Driving Analyzer (PDA) system . The program takes as input the force and velocity data obtained with dynamic load tests. These tests were carried out to assess the ultimate vertical compressive resistance, resulting in a base resistance of 1800 kN and a shaft resistance of 711 kN.

The pile was then subjected first to two static load tests (test A and test B), and secondly to thermal tests by maintaining the mechanical service load of 1000 kN(test C). Therefore, two types of load application systems were needed: mechanical and thermal.

The mechanical load was applied by means of a metallic frame, as element of reaction, fixed to the ground by means of three 25 m long anchors, with an inclination of 5º. The compressive force was applied to the pile head by a hydraulic jack. A calibrated load cell measured the real load throughout the test (Fig.5).

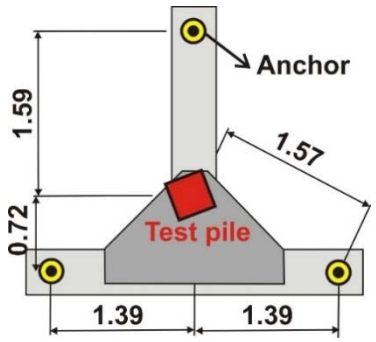


**Fig.5.** Scheme of the mechanical loading system

The thermal load was provided by a thermal installation (Fig.6), including a reversible air-source heat pump, a tank, a three-way valve for temperature regulation of the water entering into the EP, a flowmeter and a number of temperature probes with a data logger system to record the inflow and outflow temperatures during the test.

Once the pile was driven into the soil and thermally activated, the steel pipe located in the centre of the pile was filled with high thermal conductivity mortar ($\lambda$ = 2.1 W/mK) made up of quartz sand and sulphate resistant cement. The characteristic resistance of this grout material is almost equal to that of the concrete used in the pile.

The initial temperatures recorded by all the sensors prior to start the initial load test were between 17ºC and 21ºC. Below 10.40 m depth the ground temperature remains constant at 19ºC.

Finally, additional displacement sensors were located outside the pile, in strategic points of the loading frame and anchors, in order to monitor the pile behaviour during the thermal and mechanical loads (Fig.6 and Table 2).

The Fiber Optics Sensors, based on fiber Bragg grating (FBG) technology, are intended exclusively for embedding in concrete structures. Although the technical sheet of these sensors offer nominal wavelength for 22ºC ($\lambda_{22}$) and a temperature sensitivity constant value ($S_t$) of 23.8 pm/ºC, a lab-calibration was performed prior to their installation within the energy pile. In this manner, all the individual real $\lambda_{22}$ and $S_t$ values were determined to allow the later conversion of the raw signals into temperature and strain values.

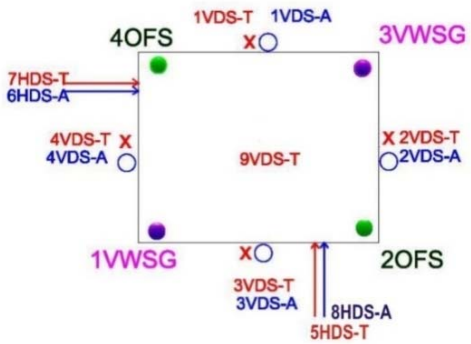


VDS-$_T$: Vertical displacement transducer: LVDT
VDS-$_A$: Vertical displacement analog dial gauge
HDS-$_T$: Horizontal displacement transducer: LVDT
HDS-$_A$: Horizontal displacement analog dial gauge
OFS: Optical fibre sensors
VWSG: Vibrating wire strain gages

**Fig.6.** External sensors on the pile head

**Table 2.** Total monitoring during the study

| Test element | Monitoring |
|---|---|
| **Test pile** (external) | 4 analog dial gauges for vertical pile head displacements<br>4 electronic transducers (LVDT) for vertical pile head displacements<br>2 analog dial gauges for horizontal pile head displacements<br>2 electronic transducers (LVDT) for horizontal pile head displacements<br>1 LVDT to loading frame<br>Load cell |
| **Test pile** (internal) | VWSG at seven levels in rebars diametrically opposed over 17 m length of pile<br>OFS cables, 2 loops for strain and temperature measurement at the same time placed each loop diametrically opposed |
| **Anchors** | VWSG in each anchor to measure strain and temperature |

As for the VWSG sensors, the ideal methodology to measure the global thermal correction factor would have involved measuring the axial heave of the energy pile during heating before applying the mechanical load of 1000 kN and comparing this with the measured thermal axial strains using a soil-structure interaction analysis such as that of Knellwolf et al. [13]. In the absence of this type of test, the calibration factor given by the factory (11 με/ ºC) was used in calculations.

## FIELD ASESSMENT OF THERMAL PERFORMANCE

Energy pile (EP) design needs to integrate geotechnical, structural and thermal considerations. The geothermal heat exchange capacity of an

energy pile is a key design parameter to dimension the geothermal loops and the heat pump system. Thermal characteristics of the ground as well as the heating and cooling loads from the structure need to be considered for the number of EPs that will be utilized as heat exchangers. Therefore, the thermal properties of the site need to be evaluated in addition to the geotechnical characterization for foundation design. In this project, the first test performed to evaluate the thermal behaviour of the experimental EP has been a thermal response test (TRT).

TRT is a widely used field method for estimating soil thermal conductivity and the thermal resistance of traditional borehole heat exchangers (BHE). However, there is a lack of scientifically supported guidelines for analysing TRT data from energy piles [14]. Recently, the Ground Source Heat Pump Association (GSHPA) published a manual on the design and construction of energy piles [15], including TRT guidelines for EP. Testing methods for BHE systems assume a high length to diameter ratio so that the shape of the borehole approaches a line source. The diameter of an energy pile is significantly larger and the depth is typically much less. The difference in geometry means that the testing practices of BHEs do not necessarily apply to EPs, for this reason, the GSHPA association has made some recommendations in regards to conducting TRTs for EP systems:

1. When the potential use of EP systems is identified early in the design process a BHE can be constructed with a single loop and tested to find the local thermal properties.

2. If the designed piles are no larger than 30cm in diameter, a TRT can be carried out using the recommendations made for a BHE system.

3. If the EP system design consists of piles larger than 30 cm in diameter, the TRT should be extended to ensure that the thermal resistance of the pile is overcome. Furthermore, more sophisticated interpretation techniques can be applied.

4. Once the EP is fully instrumented with strain gauges and temperature gauges, it is possible to conduct a complete stress-strain analysis as well as a thermal analysis in order to better understand the structural and thermal behaviour of the pile under the superimposed action of coupled mechanical and thermal loads.

Since the experimental energy pile has a 0.35 m side square section, and bearing in mind the recommendations of GSHPA, the field assessment of thermal performance in this project consists of two different tests: firstly, two bespoke TRT of longer duration (5 + 6 days) were performed to ensure that the thermal resistance of the pile is overcome. Then, as the EP is fully instrumented with VWSG extensometers, thermistors and Fiber Optics Sensors, a complete stress-strain analysis was undertaken in order to better understand the structural and thermal behaviour of the pile under the superimposed action of coupled mechanical and thermal loads.

### *Thermal loads generating facility*

The main objective of the facility is to produce the thermal heat injection and to monitor the associated variables that allow to perform the thermal response test analysis.

In order to produce thermal loads, the appliance uses a reversible heat pump (cooling) or a thermal resistance (heating) and a hydraulic circuit. Several measurement elements and electronic circuits are necessary for the required data-logging and measurement control. The facility is shown in figure 8 schematically.

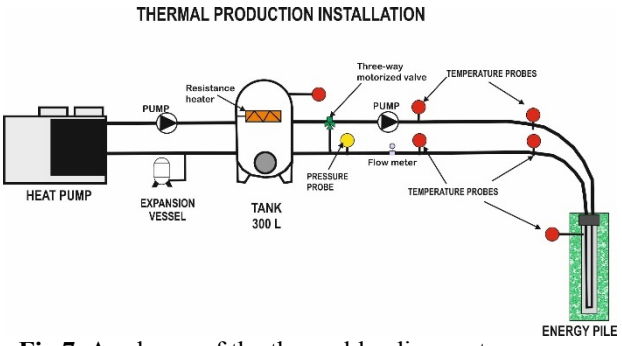


**Fig.7.** A scheme of the thermal loading system

The air-water-heat pump (AWHP) allows to heat or cool down the water entering into the pile, whereby the control system fixes the temperature difference between entering and outflow water temperature, thus allowing to keep a constant heat flux within the EP.

Throughout the test, water is circulated into the EP and heat is exchanged with the surrounding soil through the pipes located inside, in a thermo-hydraulic configuration alike any conventional BHE. For that purpose, the system comprises two water loops:

- The primary loop, which contains the heat exchanger pipes, installed in the pile, the primary circulation pump, a three-way valve for regulating the temperature of the injected water, a flow meter and various temperatures probes;
- The secondary loop, comprising the heat pump, a storage tank equipped with a thermal

resistance, an expansion vessel and the secondary circulation pump.

The primary loop is responsible for maintaining a constant heat flux to the EP, by keeping a constant temperature difference between inlet and outlet flow. The secondary circuit supplies heated or chilled water either by the thermal resistance or the AWHP.

The temperatures of the heat exchange fluid entering and exiting the pile during heat pump operation were monitored using pipe-plug thermocouples installed in the inlet and outlet ports of the manifold. The facility is able to extract or inject heat at constant rates into the ground depending on the relationship between the temperatures of the heat carrier fluid and the ground around the pile. Summarizing the main characteristics of the facility:

- Cold generation (heat pump) and heat generation (electric resistance).
- Regulation of the injected power by means of pulse width modulation.
- Monitoring of the flow, inlet and outlet temperature and pressure.
- Remote control of the process.
- Data logging.

### *Thermal characterization of the pile*

The thermal characterization of the experimental pile was done by a heat injection test, simulating the thermal pile behaviour working in cooling mode. Once the working load was applied (1000 kN), two heat injection tests were performed to characterize the installation. Taking into account the EP geometry (Table 3) and the GSHPA recommendations [11], the tests duration was longer than usual. The extended testing time ensures that the pile thermal resistance has reached a near steady state behaviour.

**Table 3.** Geometry of the tested energy pile

| | |
|---|---|
| Pile length (m) | 17.4 |
| Square cross section side (m) | 0.35 |
| Active pipe length (m) | 17 |
| Heat exchanger type | Double U |
| Number of pipes | 4 |
| PE Pipe Outer Diameter (m) | 25.0 |
| PE Pipe Inner Diameter (m) | 20.6 |

The EP characterization was carried out during 11 (5+6) days by introducing different heat injection levels to the experimental pile (700 and 1400W). The temperatures of the heat exchange fluid entering and exiting the EP during heat pump operation were monitored using pipe-plug thermocouples installed in the inlet and outlet ports of the manifold. In this way, checking the temperature variations of the inlet and outlet pipes allowed to obtain the evolution of temperature over time. The main test parameters are shown in Table 4.

**Table 4.** Thermal response test parameters

| | Test 1 | Test 2 |
|---|---|---|
| **Inflow-outflow temperature increase** | 1ºC | 2ºC |
| **Flow rate** | 0.6 $m^3/h$ (10 l/min). | 0.6 $m^3/h$ (10 l/min). |
| **Heat carrier fluid** | Tap water | Tap water |
| **Nominal heat injection rate** | 700 W | 1.400 W |
| **Nominal specific heat injection rate** | 40 W/m | 80 W/m |
| **Test duration** | 5 days | 6 days |

For the thermal analysis as conventionally used to analyse TRT tests, the EP is approximated by a line source in an homogeneous semi-infinite medium. In this so called *infinite line source approximation (ILS)*, the evolution of the mean fluid temperature $T_f$ (t) would follow the trend described by the following equation (1) [16]:

$$T_f(t) - T_0 = \frac{q_c}{4\pi\lambda}\left(\ln\left(\frac{4\alpha t}{r_b^2}\right) - \gamma\right) + q_c \cdot R_b = \\ = \frac{q_c}{4\pi\lambda}\ln(t) + q_c\left[R_b + \frac{1}{4\pi\lambda}\left(\ln\left(\frac{4\alpha}{r_b^2}\right) - \gamma\right)\right] \quad (1)$$

Where $q_c$ represents the constant heat injection rate used for the response test (W/m), $T_0$ the undisturbed ground temperature (ºC), t denotes time after start of the heat injection (s), $r_b$ the borehole (pile) radius and γ is Euler's constant (0.5772). The so-called borehole resistance, $R_b$, is an important design parameter and represents the short-term thermal response of the system.

A maximum error of a 10% for $t \geq 5r^2/\alpha$ is generally accepted in thermal response test applications [17].

For a proper analysis, the previous equation is adapted to the equation for the line (2):

$$T_f(t) = k \cdot x(t) + m \quad (2)$$

- where k is the slope of the line and it is related with the ground thermal conductivity according to the following expression:

$$k = \frac{1}{4\pi\lambda} \quad (3)$$

- and m is the coordinate in the origin, which represents the value when the time is equal to 0.

Considering the thermal resistance of the borehole a constant value over time:

$$m = T_0 + R_b q_c \quad (4)$$

- and finally, the time-dependent term:

$$x(t) = q_c \left( \ln\left(\frac{t}{t_0}\right) - \gamma \right) \quad (5)$$

Being $t_0 = \frac{r_0^2}{4\alpha}$

It is clearly evident that the equation (1) corresponds to equation (2) using the values in (3), (4) and (5).

The measurements recorded during the tests allow to infer the ground thermal conductivity and the pile thermal resistance by means of a heat transfer model such as has been described above. Fig.8 shows the evolution of the average fluid temperature against time recorded during testing.

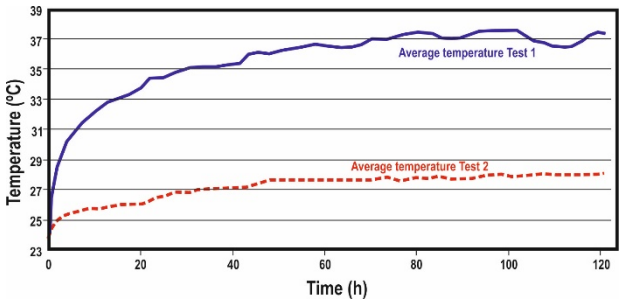


**Fig.8.** Average fluid temperature throughout TRT

As the evolution of the fluid temperature is logarithmic (Fig. 9), the ground thermal conductivity (λ) can be evaluated by plotting the fluid temperature against ln (t) and determining the slope of the line k:

$$\lambda = \frac{q_c}{4\pi k} \quad (6)$$

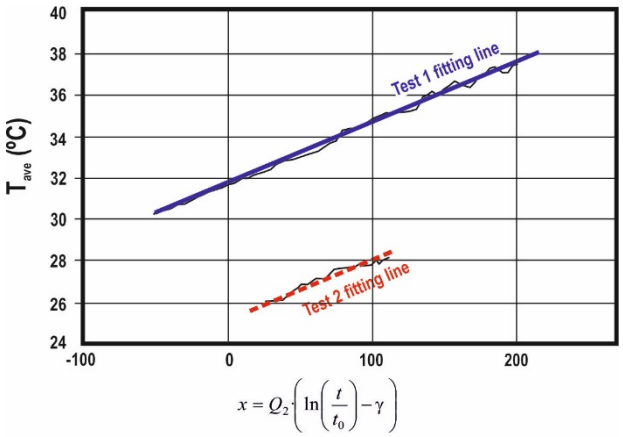


**Fig.9.** Semi logarithmic graph of average fluid temperature versus ln (t)

The equations obtained for the two test performed were:

$$\text{Test 1: } 0.029x + 31{,}7$$

$$\text{Test 2: } 0.029x + 25{,}3$$

The slope of the line is the same in both tests, as it only depends on the ground thermal conductivity:

$$k = \frac{1}{4\pi\lambda} = 0.029$$

resulting in:

$$\lambda = 2.7 \pm 11.7\% \text{ W/mK}$$

Once the ground thermal conductivity is known, the pile thermal resistance can be assessed on the basis of equation 3. This requires knowledge of the undisturbed ground temperature. In this case, assuming that $T_0$ is the same in both tests, the energy pile thermal resistance ($R_b$) can be determined independently of the undisturbed ground temperature giving rise to:

$$R_b = 0.16 \pm 11.7\% \, mK/\text{W}$$

Compared to other works [18, 19, 20] the EP thermal resistance value calculated is in line with existing data, as shown in the following table (Table 5).

**Table 5.** Energy pile thermal resistance values

| **EP characteristics** | **Rb (mK/W)** |
|---|---|
| Concrete driven<br>Square cross section 0.27x0.27 m$^2$<br>Simple U pipe | 0.17 |
| Continuous auger pile<br>0.3 m<br>Simple U pipe | 0.22 |
| Precast high strength concrete<br>0.4 outer and 0.12 inner hollow<br>W shape pipe | 0.131 |
| Precast high strength concrete<br>0.4 outer and 0.12 inner hollow<br>3U shape pipe | 0.098 |

## THERMO-MECHANICAL BEHAVIOUR OF THE PILE

Geotechnical design requires consideration of the complex interaction between temperature change and induced stresses and strains in the foundation, which may affect building performance. Specifically, contraction or expansion of the foundation during cooling or heating may lead to mechanical distress movements of the structural foundation elements or the building itself, as well as changes in pile shaft shear stresses and

base loads and, therefore, in the factors of safety for bearing resistance of the foundation. An important aspect of this study was to evaluate thermally induced axial strains and stresses in the energy foundations caused by temperature changes.

The parameters measured and registered by VWSG and FOS were quite similar, both in relative values and in trends with depth and temperature.

The first step to define the thermal axial strain is to isolate the effect of the mechanical loading. To achieve this, an initial measurement was performed under a mechanical load of 1000 kN, without any temperature action upon the pile. From this initial measurement onwards, the value of mechanical component of the strain after this point is considered constant, assuming that there is negligible variation in the mechanical load applied to the pile head over time. Accordingly, the measured strain values $\varepsilon_m$ were zeroed by subtracting the mechanical axial strain. Next, the zeroed strain values were corrected for the differential thermal deformation between the gauge (steel) and the concrete, in which it is embedded, by means of: $(\alpha_{gauge} - \alpha_{concrete})\Delta T$, where $\alpha_{gauge}$ is the coefficient of linear thermal expansion of the steel wire in the gauges (-12.2 με/ºC); $\alpha_{concrete}$ is the coefficient of linear thermal expansion of the concrete(11με/ºC) and $\Delta T$ is the temperature change of the pile.

"Test C" is meant to show the thermo-mechanical behaviour of the pile under a constant and stable mechanical load of 1000 kN and a wide range of thermal loads, simulating its use within a geothermal installation working on summer mode (cooling the building and heating up the foundation). This test was performed between 26$^{th}$ of June and 10$^{th}$ of July of 2013, following the procedure and stages shown in Fig. 11. These three stages correspond to different heat injection rates by applying different heating rate values (Table 6).

**Table 6.** Stages of the test C

| | Stages | | |
|---|---|---|---|
| | **1** | **2** | **3** |
| Initial date | 26/6/2013 | 01/7/2013 | 05/7/2013 |
| Initial hour | 11:09 | 12:33 | 12:03 |
| Final date | 01/7/2013 | 05/7/2013 | 10/7/2013 |
| Final hour | 11:06 | 11:12 | 13:30 |
| Fluid | Tap water | | |
| ΔTºC | 1ºC | 3ºC | 1.5ºC |
| Heating power (W) | 700 | 2100 | 1050 |
| Heat injection rate (W/m) | 40 | 120 | 60 |

In order to define profiles of thermal axial strain representative of the pile performance, some specific moments in time were identified. All of them were chosen at the end of each thermal stage, after a time enough to reach thermal equilibrium in the system (Table 7 and Fig.10).

**Table 7.** Strategic moments identified during test C

| ***Moment*** | ***Date and hour*** | ***Observations*** | ***Surface temperature(º C)*** |
|---|---|---|---|
| **Static load test B** | 29/05/2013 | To compare and validate both types of sensors before test C. After test B the pile head load was kept constant at 1000 kN until completion of all the experimental study. | |
| **C0** | 26/06/2013 10:57 | Prior to test C | 22.9 |
| **Ca** | 01/07/2013 12:27 | After thermal equilibrium at stage 1 | 30.4 |
| **Cb** | 05/07/2013 12:27 | After thermal equilibrium at stage 2 | 32.3 |
| **Cc** | 10/07/2013 14:30 | After thermal equilibrium at stage 3 | 26.2 |
| **Cd** | 11/07/2013 11:54 | End of test C | 23.1 |
| **Ce** | 30/07/2013 10:07 | 19 days after end of test C | 29.8 |

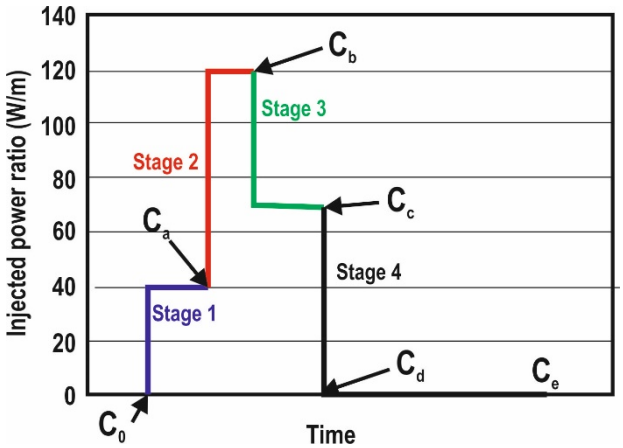


**Fig.10.** Schematic of the test C and identification of strategic moments: $C_0$, $C_a$, $C_b$, $C_c$, $C_d$ and $C_e$.

Throughout test C, strains and temperatures, power and flow were registered, to be able to analyse any possible out of phase results regarding the thermal and the geotechnical behaviour of the pile.

### *Temperatures*

Firstly, all the profiles obtained during the test show a temperature decreasing with depth (Fig.11).

Near the surface the pile temperature is affected by both the injected thermal power and the atmospheric temperature variations. This phenomenon, well explained by McCartney & Murphy [21] and Bourne-Webb [5], is less significant when larger depths are considered, less affected by atmospheric temperature changes.

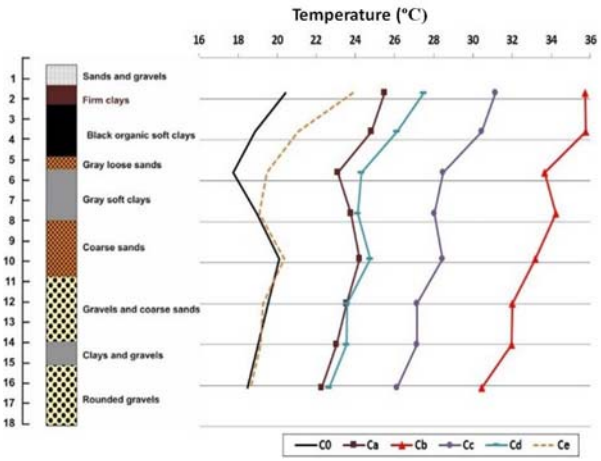


**Fig.11.** Temperature profile evolution during test C

Prior to starting the test C (C0), the ground temperature is more or less homogeneous around 19-20ºC. Once the test begins, the effect of heat injection in the temperature profile of the pile is clear: in Cb (after 120 W/m heat injection rate equilibrium is achieved) the temperature is 35-36ºC in the upper meters and 30-31ºC in the lower zone. In terms of temperature changes, comparing these values to the moment C0, the first meters of pile show a temperature increment of 17ºC, while 12ºC change is registered in the lower part of the pile. In Ca (after 40 W/m heat injection rate thermal equilibrium is achieved) the temperature profile is close to the one corresponding to Cd, after finishing the test. This highlights the fact that the pile needs some time to dissipate the heat generated during heat injection. In Ce, after 19 days of thermal stabilization, the temperature profile comes back to the initial state (C0) in the deeper part of the pile. The 6 most superficial meters the Ce profile shows higher temperature values than the C0 profile. This is due to the different climatological conditions and ambient temperatures. While in C0 (26$^{th}$ of June) the ambient temperature was 22.9ºC, in Ce (30$^{th}$ of July) it was 29.8ºC.

Fig.12 shows the thermal evolution of the pile in terms of temperature change with respect to C0. The close shape of the response at different depths along the pile shows a strong dependence of the thermal temperature changes on the heat injection rate at the different stages of the test.

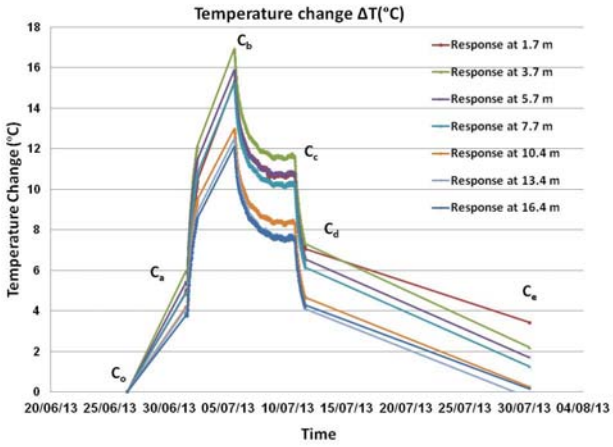


**Fig.12.** Temperature change detected at different depths throughout the test stages

### *Pile head movements*

The sensors installed at the pile head allowed to measure in real time the vertical and horizontal movements generated due to thermal changes during the test C (Fig.13 and Fig.14).

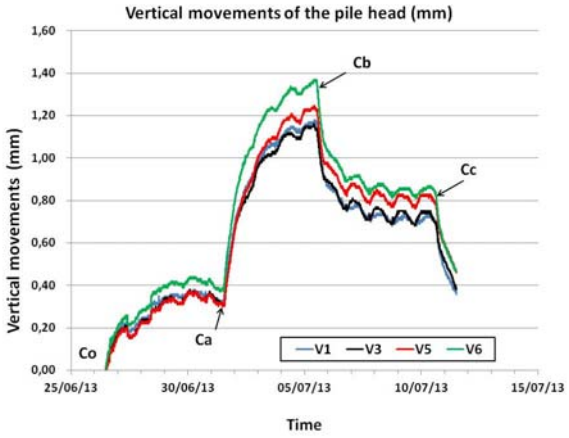


**Fig.13.** Vertical movements of the pile head during test C

The maximum vertical movements measured at the pile head were 0.4 mm in Ca (40 W/m injected), 1.4 mm in Cb (120 W/m injected), and 0.8 mm in Cc (70 W/m injected). After this moment, all the sensors showed a trend to diminish towards zero as the pile thermally recovered. Furthermore, a clear cyclic oscillation due to thermal daily variations can be detected. The pile head did not return to its original elevation upon cooling (Cd), but maintained an upward displacement of approximately 0.4 mm.

The horizontal movements of the pile head (Fig. 14) do not show the same clear correlation to the sequence of different stages throughout test C as vertical movements do.

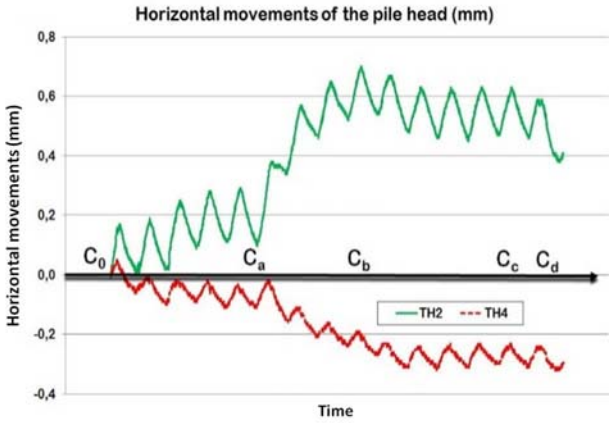


**Fig.14.** Horizontal movements of the pile head during test C

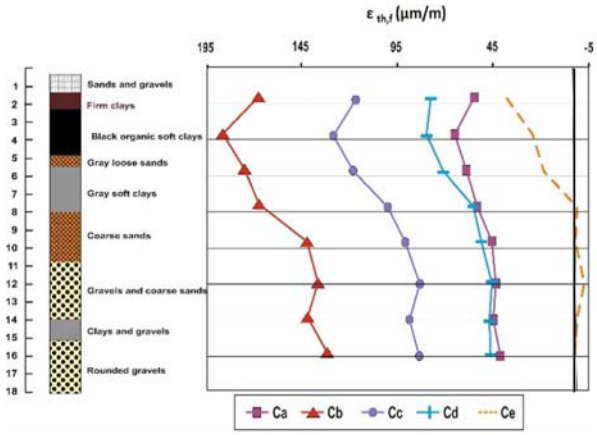


**Fig.15.** Theoretical thermal unrestrained strains in a completely free of movements pile ($\varepsilon_{th,f}$)

TH2 sensor measured a movement towards a maximum value of +0.6 mm, while TH4 sensor moved towards -0.3 mm. These two components give a resulting movement of 0.65 mm towards South-Southeast. Daily oscillation are quite evident.

*Strains*

When a pile under working load is heated or cooled, a complex behaviour is imposed upon the pile that varies with ground conditions and different degrees of end restraints. Heating induces expansion while cooling induces contraction leading to pile vertical strains, displacements of the pile head and changes in shaft friction and base stresses. The total strain due to mechanical and thermal loads ($\varepsilon_T$) is:

$$\varepsilon_T = \varepsilon_m + \varepsilon_{th} \qquad (7)$$

where $\varepsilon_m$ is the strain due to a mechanical load and $\varepsilon_{th}$ is the strain due to the thermal loads.

**1. Thermal free strains**

Thermal deformations (Fig.15) may occur in energy foundations due to thermo-elastic expansion, in which thermal strain $\varepsilon_{th}$ occurs during a change in temperature proportionally to this change, by means of a coefficient of thermal expansion. Considering a theoretical unrestrained pile, the change in temperature induces a uniform free strain [22]:

$$\varepsilon_{th,f} = \alpha_{pile} \cdot \Delta T \qquad (8)$$

α is the coefficient of thermal expansion of the pile (11 με/°C) and ΔT the variation of temperature between the initial moment (CO) and the different stages during test C (Fig.13).

**2. Observed strains**

Actually, the energy pile is far from unrestrained. The surrounding soil provides a confining effect on the pile, constraining the possible deformations. For this reason, depending on soil-structure interaction conditions, the real expansion or contraction observed and measured ($\varepsilon_{obs}$) by the VWSG extensometers within the energy pile due to the applied thermal loads results much lower than the theoretical free thermal unrestrained strains calculated previously from the temperature change measured in the pile.

$$\varepsilon_{obs} = \varepsilon_{final} - \varepsilon_{initial} + \alpha_{\,gauge} \cdot \Delta T \qquad (9)$$

where α is the coefficient of thermal expansion of the gauge (12.2 με/°C) and ΔT the variation of temperature between the initial moment (CO) and the different stages during test C (Fig.13).

The profiles of observed axial strain induced by the thermal loads corresponding to the specific moments defined above are shown in Fig. 16. In these figures, negative strains indicate compression in the pile, while positive strains indicate expansion.

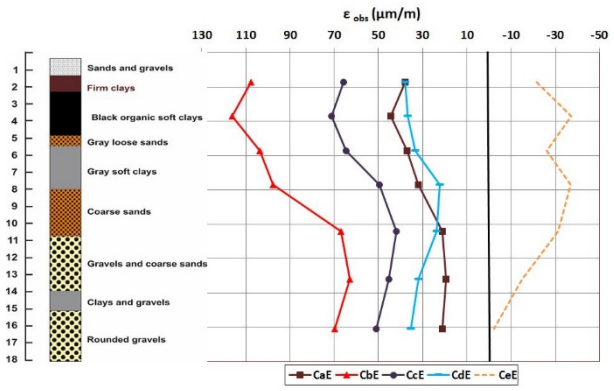


**Fig.16.** Observed deformation, measured by the VWSG extensometers

Regardless of the shapes of the mechanical strain profiles, it is clear that the heating operation led to a shift in the observed strain profiles to the left, towards positive values (expansion). Cooling after the test leads to a recovering and shift of the profile to the right, towards negative values (compression).

All the curves show positive values, corresponding to tensile strains, with the exception of the Ce profile, corresponding to 19 days after finishing the test C, where a 38 μm/m maximum compression strain was registered. The maximum tensile deformation is measured in Cb, when the heat injection is maximum, as well as the temperature measured in the pile. In Cd, just after the interruption of heat release, a 40 μm/m tensile strain was measured. The shape of the strain profiles depends not only on the temperature changes, but also on the resistance the ground around the pile offers to its deformation. With this view, larger deformation values are measured in the upper part of the pile, at all the heat injection curves, while the deeper part of the pile tends to show lower strain values. This can be explained partially by the different geological strata surrounding the pile. The upper meters of ground are composed of soft clayey materials, which offer less resistance to the dilation of the pile than the gravels existing in the lower meters of the pile.

From the strain data obtained at different depths, the whole elongation of the pile can be calculated. At moment Cb, under the action of a heat injection rate of 120W/m, the pile exhibits a maximum elongation of +1.6 mm. Meanwhile, the maximum pile head vertical movement measured by the LVDT's is +1.23 mm. By comparing these two values (Fig.17), a settlement of the pile toe of 0.37 mm is deduced.

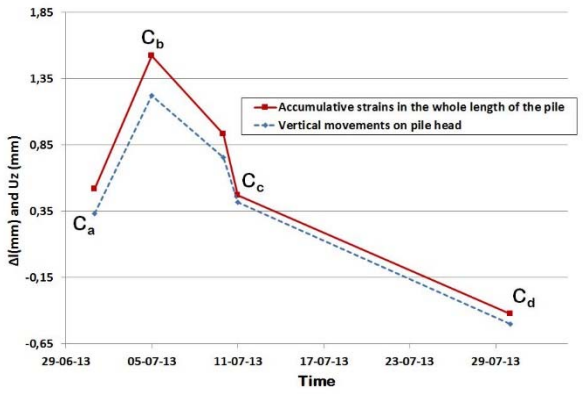


**Fig.17.** Comparison between the accumulative strains along the pile and the vertical movements measured on pile head

Since part of the pile deformation is constrained by the surrounding soil, a blocked, non-manifested, strain has to be considered:

$$\varepsilon_{th,c} = \varepsilon_{th,f} - \varepsilon_{obs} \quad (10)$$

Part of the free strain is effectively observed while the remaining part is converted into the internal thermal stress.

*Stresses*

**1. Thermal stresses**

The average thermal axial stresses induced in the foundation by the temperature changes (kN) can be calculated from the measured thermal axial strains at the location of each gauge as follows:

$$\sigma_{th} = -E \cdot \varepsilon_{th,c} \quad (11)$$

where the minus sign represents the convention of negative compression; $\varepsilon_{th,c}$ is the non-produced thermal axial strain (μm/m) and E is the Young's modulus of the pile (31314 MN/m$^2$).

The calculated thermal ($\sigma_{th}$) and total ($\sigma_{th+mec} = \sigma_{mec} + \sigma_{th}$) axial stress profiles are shown in Fig. 18 and 20. In these figures, negative stresses indicate compression while positive values indicate extension.

Comparison of this figure with the evolution of strains allows seeing that the locations of the smallest observed strains in the energy pile (where the pile is surrounded by stiff sands and gravels) correspond to the locations of the maximum thermal axial stresses, possibly due to the resistance to thermal axial expansion by mobilization of shaft shear stresses. In other words, compressive (negative) thermal axial stresses occur during heating of the pile (cooling of the building) when the axial expansion of the foundation is restrained by the ground at the pile/soil interface and at the pile base. Though not clearly visible in Fig. 19, a trend to zero thermal stresses at the head pile exists, due to the lack of restriction to expansion at this point of the pile, since the mechanical load is maintained constant at 1000 kN. (Actually, this trend is much clearer with the OFV results). In Ce, 19 days after end of test C, the stress profile tends to the initial state in the deeper part of the pile, while the first meters show that more time is needed to recover the initial state prior to test C.

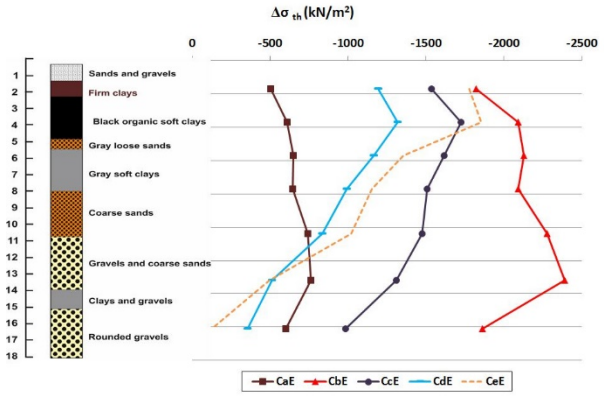


**Fig.18.** Thermal axial stress due to heating and cooling during test C

## 2. Total stresses

The thermal axial stress profiles observed during heating and cooling of the pile were superimposed upon the stress profile due to mechanical loading (1000 kN) to define the total thermo-mechanical axial stresses (Fig.19).

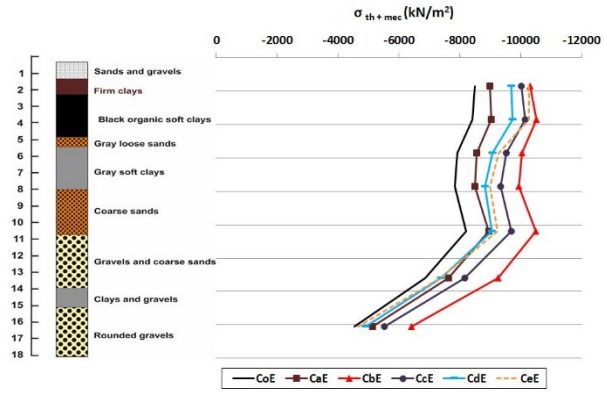


**Fig.19.** Total axial stress evolution throughout the test C

Two main different zones can be distinguished in the pile: an upper part, between 2m and 10 m of depth, where the surrounding ground consists of soft soils (soft clays, organic clays and loose sands), that shows an almost vertical profile; a lower part of the pile, from about depth -10m, showing a diminishing stress towards the pile toe, as a consequence of the presence of stiff gravels and sands with a higher frictional resistance. Comparing Figs. 19 and 20, it can be seen that the thermal axial stresses are clearly lower than the mechanical axial stresses; nevertheless, they are not at all insignificant (about 2500 kN/m$^2$ of maximum thermal stress, relatively to 8163 kN/m$^2$ of maximum mechanical stress).

### *Loads*

The thermal and total stresses profiles can be converted into thermal and total load profiles respectively (Fig. 20 and 21), by simply using the following equation:

$$N = \sigma \cdot S \qquad (12)$$

Where N is the axial load (kN), σ is the average stress in the corresponding section (kN/m$^2$) and S is the area of the pile section (S = 0.35·0.35 = 0.12 m$^2$).

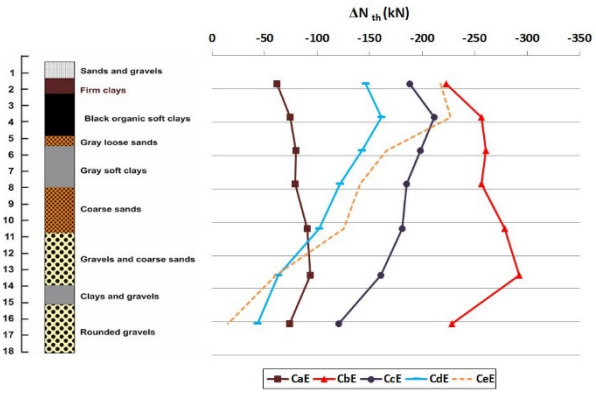


**Fig.20.** Thermal axial load profiles during test C

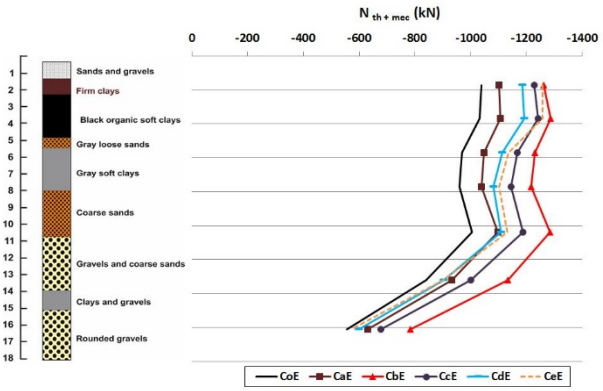


**Fig.21.** Total axial load profiles during test C

### *Pile/ soil interface shear stress*

It is worthwhile to remark how the thermal and total shear stresses originated along the pile shaft (Fig. 22 and 23) are related to the heat injection in the pile.

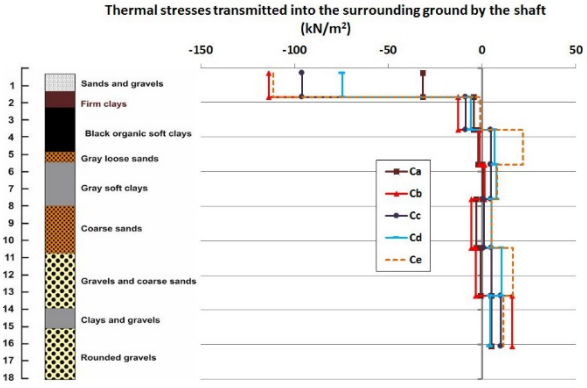


**Fig.22.** Thermal shear stresses along pile shaft during test C (kN/m$^2$)

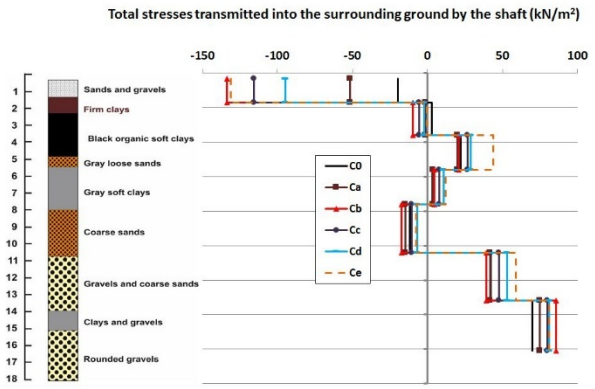


**Fig.23.** Total shear stresses along pile shaft during test C (kN/m$^2$)

Heating the pile results in dilatation deformations. As a result of the tendency of the surrounding soil to constrain the pile dilation, the mobilized shaft friction during heating shows an opposite response at the upper part, where the friction is negative (the soil is exerting a downwards force on the pile shaft), and the lower part of the pile, where the friction is positive (the soil is exerting an upwards load on the pile shaft). The resistance to pile stretching is not uniformly distributed along the pile depth, but depends on the ground profile, specifically on the existence of soft or stiff soil levels. Only those layers of stiff or very frictional materials will be able to oppose the pile dilation or contraction. At the depths where the pile is surrounded by soft soils, the opposition to thermal dilation or contraction of the pile will be negligible. In our experiment, it appears that the resistance to pile dilation is concentrated at both ends of the pile, the upper 2 metres, where the soil consists in artificial fills and stiff clays, and at the toe area, where the soil is composed of coarse sands and gravels. This evidences the importance of the stratigraphic column in the thermo-mechanical behaviour of the system.

The described trend towards stretching reverses at Cc and Cd, when the pile cools down with respect to Cb. During this process, the soil tends also to show a stronger opposition to pile contraction at both ends.

In summary, pile/soil interface shear stresses generated due to heat injection into the pile during the test C, are coherent with the theoretical considerations and previous observations, [5], with some specific peculiarities derived from the local geological profile, showing two main zones of stiff lithologies that can constrain the potential pile deformation: the upper 2 metres and the toe zone. During the cooling part of the test C (Cc, Cd moments) the thermal inertia of the soils surrounding the pile are also determinant in the evolution of the profiles.

## CONCLUSIONS

This work presents the results from a thermo-mechanical evaluation of a full-scale precast energy pile, under a constant and stable mechanical load of 1000 kN and a wide range of thermal loads, simulating its use within a geothermal installation working on summer mode (cooling the building and heating the foundation).

Data collected from both types of sensors allowed to assess the thermo-mechanical behaviour of the pile in terms of axial strains, stresses and loads, as well as pile/soil interface shear stress values. Thermal and total axial strains measured are consistent with a pile predominantly working at its toe. It is important to notice that the thermal loads applied during the test C, described in this paper, are probably higher than those that would be needed in a real case of geothermal exploration of a normal office or residential building founded on piles like the one used in this study. Nevertheless, the thermal impacts on the mechanical response of the pile would not likely lead to significant structural problems. Anyhow, an analysis of the effects of both the mechanical loads and the thermal loads is considered necessary for a proper design of thermo-active piles.

Further research is still needed to improve the understanding of the thermo-mechanical behaviour of geothermal piles and to formalize design guidelines and safety factors for assuring the ultimate and serviceability limit states of the energy foundations.

## ACKNOWLEDGEMENTS

We thank the Spanish Ministry of Economy and Competitiveness for its financial support, through the program INNPACTO 2011, for the design, installation and instrumentation of the geothermal pile in Valencia.

## REFERENCES

1 L. Laloui, M. Moreni & L. Vulliet, Can. Geotech. J. 40, 388-402 (2003).
2 L. Laloui, M. Nuth & L. Vulliet, International Journal for Numerical & Analytical Methods in Geomechanics, 30, No 8, 401, (2006).
3 H. Brandl, Geotechnique, 56, No 2, 81, (2006).
4 A. Amis, P. Bourne-Webb, B. Amatya, K. Soga, & C. Davidson, 3rd Ann. and 11th Int. DFI Conf., New York, 10 pp (2008).

5 P. Bourne□Webb, B. Amatya, K. Soga, A. Amis, C. Davidson & P. Payne, Géotechnique, 59, 237 (2009).
6 L. Laloui & A. di Donna, Civil Engineering, 164, 184, (2011).
7 B.L. Amatya, K. Soga, P. Bourne-Webb, T. Amis & L. Laloui, Géotechnique, 62, 1, (2012).
8 F.A.Loveridge & W. Powrie (2013) Pile heat exchangers: thermal behaviour and interactions. Proceedings of the Institute of Civil Engineers: Geotechnical Engineering, 166, (2), 178-196.
9 K.D. Murphy & J.S. McCartney (2014). "Seasonal Response of Energy Foundations during Building Operation." Geotechnical and Geological Engineering. 1-14.
10 M.E. Suryatriyastuti, H. Mroueh,S. Burlon & J. Habert. Energy Geostructures (2013) Chapter seven
11 Instrucción Española del Hormigón Estructural (EHE-08).
12 Código Técnico de la Edificación – Documento Básico de Seguridad Estructural (DB-SE C, 2006).
13 C. Knellwolf, H. Peron & L. Laloui, Journal of Geotechnical and Geoenvironmental Engineering, 137, No 10, 890 (2011).
14 F. Loveridge, Ground Source Seminar, Homerton College, Cambridge University, (2011).
15 GSHPA Association. Thermal pile design, installation and material standards. Issue 1.0, 1st October 2012.
16 Eskilson, P., (1987). Thermal Analyses of Heat Extraction Boreholes. Ph.D. Thesis. Department of Mathematical Physics, Lund Institute of Technology, Box~118, S-221~00 Lund, Sweden.
17 Gehlin S. 2002. Thermal Response Teast, Meathod Development and Evaluation. Doctoral Thesis 2002:39. Luleå University of Technology. Sweden.
18 D.J. Lennon, E. Watt & T.P. Suckling, Proceedings of the Fifth International Conference on Deep Foundations on Bored and Auger Piles (Eds: Taylor & Fran-cis Group, ed), 15 May 2009 Frankfurt., London.
19 C.J. Wood, H. Liu & S.B. Riffat, International Journal of Low-Carbon Technologies, 5, 137, 2010.
20 H. Park, S.R. Lee, S. Yoon & J.C. Choi, Applied Energy, 103, 12, (2013).
21 J.S. McCartney & K. Murphy, DFI Journal, 6 No 2, 26, 2012.
22 H. Peron, C. Knellwolf & L. Laloui, L, GeoFrontiers, ASCE, 470, 2011.

*Bulgarian Chemical Communications, Volume 48, Special Issue E (pp. 55 - 63) 2016*

# Computational modelling of a ground heat exchanger with groundwater flow

Lazaros Aresti[1], Paul Christodoulides[2], Georgios A. Florides[2*]

[1]*Department of Electrical Engineering, Computer Engineering and Informatics, Cyprus University of Technology, Limassol, Cyprus*
[2]*Faculty of Engineering and Technology, Cyprus University of Technology, Limassol, Cyprus*

Multiple layers of ground and the flow of groundwater in some layers have a significant effect on the cooling of vertical heat columns and heat exchangers. This paper investigates the important implication on the design of the Ground Heat Exchanger with regard to their heating effect. For this reason, a thermal model is constructed in COMSOL Multiphysics software and the effect of various parameters such as thermal conductivity of the ground and the groundwater flow velocity is considered. The model parameters were adjusted to present actual (known) parameters of an installed column and were validated against experimental values. The key for an overall capital cost reduction is the borehole length, where the results indicate that by using the groundwater available, construction of shallower Ground Source Heat Pump systems can be achieved with an increase of the coefficient of performance (COP).

**Keywords:** groundwater flow, Ground Heat Exchanger, multilayer ground

## INTRODUCTION

Ground Source Heat Pump (GSHP) systems constitute an evolving technology that has been given significant attention in recent years. GSHP systems have higher energy efficiency and lower environmental impact than regular heat pumps [1]. Geothermal energy, although developed for many years, has not reached a stable and popular state to be widely used. This is due to the high manufacturing and installation cost of Ground Heat Exchangers (GHE) compared to similar, albeit not so effective systems. The capital cost of an air-to-air heat exchanger is lower than that of a GSHP system, although the operation cost is lower for the GSHP system. Only recently the GSHP systems have gained more recognition due to their high efficiency. It is noted that GSHP installations have increased dramatically in recent years (after 2010) with a rate of 10–30% annually [2].

A reliable GSHP system depends on the proper design of the GHE, where the depth reduction is the key to reduce the overall capital cost of a vertical GSHP system. Now, the two most important parameters for designing a GHE are the soil thermal conductivity and the borehole thermal resistance. In its turn, the borehole thermal resistance depends upon the borehole diameter, the pipe size and configuration, the pipe material and the backfill material [3]. In particular, for high soil thermal conductivity and a low borehole thermal resistance, the heat exchange rate will be higher for a given borehole [3]. It is therefore of high importance to determine the thermal characteristics of the ground prior to the system design. For larger installations borehole tests are carried out in a test borehole.

There are several methods available in the literature for the determination of ground thermal characteristics [3], such as soil and rock identification [4], experimental testing of drill cuttings [5], in situ probes [6], and inverse heat conduction models. However, the most commonly used is the Thermal Response Test. The TRT is a method to determine the ground thermal characteristics and it was first introduced by Mogensen in 1983 [7]. TRT is based on heat injection in the borehole at constant power, while the mean borehole temperature is recorded continuously during the test. The recorded fluid temperature response is the temperature developed over time, which is evaluated to obtain the thermal characteristics of the borehole such as the thermal resistance, the volumetric specific heat capacity, and the soil conductivity by using inverse heat transfer analysis [8].

Throughout the years, several analytical and numerical models have been developed to implement fast and reliable predictions of a GHE, where all the models are based on the Fourier's law of heat conduction [9]. The models can be categorized with regard to the type of the 'source' heat (infinite or finite, linear or not) [25]. The most commonly used models are based on: (a) the "infinite line source method," developed by Lord Kelvin [10] and later on applied to the radial heat transfer model by Ingersoll et al. [11], [12]; (b) the "cylindrical heat source method," firstly described

* To whom all correspondence should be sent:
georgios.florides@cut.ac.cy

by Carslaw and Jaeger [13]; (c) the "finite line source method," developed by Eskilson [14] and Claesson and Eskilson [15], which consists of an analytical g-function expression where the solution is determined using a line source with finite length.

Another important aspect to consider when designing a GSHP system is the groundwater flow in the case where an aquifer is present. It must be emphasized that the implementation of the groundwater flow is not adequately supported by current model approaches where overestimates of the thermal conductivities occur as only heat conduction is considered. An indicative case of groundwater flow effect is the in-situ experiment performed in Minnesota [16], where unusually high thermal conductivity values were observed.

The aim of this paper is to study the effect of the groundwater flow on a GHE using a computational modeling approach. The geometry used in this paper (Fig.1) is similar to the one in Florides *et al.* [17] and has been reconstructed by COMSOL Multiphysics v.5.1, which is a computational modelling software allowing the user to use general equations. The user can also add and edit equations manually. It also allows the user to create a CAD model, construct the mesh, apply the physical parameters and post process the results under the same user interface.

## MATHEMATICAL MODEL

The heat distribution over time is described by the general heat transfer equation based on the energy balance. For the current application the rate of energy accumulated in the system is equal to the rate of energy entering the system plus the rate of energy generated within the system minus the rate of energy leaving the system [17].

Thus the three dimensional conservation of the transient heat equation for an incompressible fluid is used (and applied in COMSOL Multiphysics) as follows:

$$\rho c_p \frac{\partial T}{\partial t} + \rho_w c_{pw} u \nabla T + \nabla \cdot q = Q \qquad (1)$$

where T is the temperature [K], t is time [s], $\rho$ is the density of the borehole/soil material [kg m$^{-3}$], $c_p$ is the specific heat capacity of the borehole/soil material at constant pressure [J kg$^{-1}$ K$^{-1}$], $\rho_w$ is the density of the ground water, $c_{pw}$ is the specific heat capacity of the ground water at constant pressure, $u$ is the velocity of the groundwater [m s$^{-1}$], $Q$ is the heat source [W m$^{-3}$] and q is given by the Fourier's law of heat conduction that describes the relationship between the heat flux vector field and the temperature gradient:

$$q = -k\nabla T \qquad (2)$$

where k is the thermal conductivity of the borehole/soil material [W m$^{-1}$ K$^{-1}$].

In Eq.1, the first term represents the internal energy, the second term is the part of the heat carried away by the flow of water and the third term represents the net heat conducted (as described in Eq.2).

Since the problem will be solved in a transient mode and is time-dependent, the first term is not ruled out as in the case of the steady-state solution. It is worthy to note that in the case where the groundwater is absent, parameter u (velocity) is zero and the second term disappears.

The heat source term describes heat generation within the domain and is set as the heat transfer rate

$$Q = \frac{P_0}{V} \qquad (3)$$

where V is the domain (borehole) volume [m$^3$] and $P_0$ is the power [W]. In the case of a single U-tube pipe it is described as

$$P_0 = \dot{m}_w c_{p\,w} dT \qquad (4)$$

where dT is the temperature difference between the inlet and the outlet tubes and $\dot{m}_w$ is the mass flow rate of the water in the tube [kg s$^{-1}$], defined as

$$\dot{m}_w = \rho_w A_p u_p \qquad (5)$$

where $A_p$ is the area of the tube [m$^2$] and $u_p$ is the flow velocity in the tubes.

Boundary conditions were set by COMSOL Multiphysics default as "thermal insulation," where there is no heat flux across the boundaries. This setting does not affect the heat distribution along the examined area of the borehole as the domain is set to be significantly larger than the borehole itself.

When water is present in the ground layer, the heat transfer equation in porous media is applied [18] (similar to Eq.1):

$$\rho_{eff} c_{p.eff} \frac{\partial T}{\partial t} + \rho_w c_{pw} u \nabla T + \nabla \cdot q = Q \qquad (6)$$

where $\rho_{eff} c_{p.eff}$ is the volumetric heat capacity of the porous media at constant pressure ($\rho_{eff}$ is the density and $c_{p.eff}$ the specific heat capacity) given by:

$$\rho_{eff} c_{p.eff} = \theta_s \rho_s c_{ps} + (1 - \theta_s) \rho_w c_{pw} \qquad (7)$$

where $\theta_s$ is the soil material volume fraction given, ranging from 0 to 1, $\rho_s c_{ps}$ is the volumetric heat capacity of the porous soil material ($\rho_s$ is the density and $c_{ps}$ the specific heat capacity), and, $\rho_w c_{pw}$ is the volumetric heat capacity of the fluid material (water) (being $\rho_w$ the density and $c_{pw}$ the specific heat capacity). The velocity u in the second term of Eq. 6 represents the *Darcy's* velocity as specified in the next section.

The heat conduction q in Eq. 6 can be expressed as:

$$q = -k_{eff}\nabla T \tag{8}$$

where $k_{eff}$ is the effective thermal conductivity that can be calculated by three different methods [19]. The first method, named volume average, assumes that the heat conduction occurs in parallel through the solid material and the fluid (water) and the effective thermal conductivity is expressed as

$$k_{eff} = \theta_s k_s + (1-\theta_s)k_w \tag{9}$$

where $k_s$ is the thermal conductivity of the solid material and $k_w$ is the thermal conductivity of water. The second method considers the heat conduction to occur in series. In this case, the effective thermal conductivity is obtained from the reciprocal average law:

$$\frac{1}{k_{eff}} = \frac{\theta_s}{k_s} + \frac{1-\theta_s}{k_w} \tag{10}$$

The third method calculates the effective thermal conductivity from the weighted geometric mean of the thermal conductivity of both, solid and fluid, materials:

$$k_{eff} = k_s^{\theta_s} k_w^{1-\theta_s} \tag{11}$$

In the current model set-up, the first method of determining the effective thermal conductivity (Eq. 9) was chosen, as it was closer to the requirements of the specific application.

## DARCY'S VELOCITY

In order to describe the flow through a porous medium, Darcy's law needs to be applied. The theory was firstly established by Henry Darcy based on experimental results [20] and allows the estimation of the velocity or flow rate within an aquifer. In the investigation of the groundwater effect on the GHE Darcy's velocity is used in the porous media heat transfer equation as stated in Eq. 6.

Darcy's velocity (also called *Specific Discharge*) assumes that flow occurs across the entire cross-section of the soil [21] and is determined as:

$$V_D = -Ki = -K\frac{dh}{L} \tag{12}$$

where K is the hydraulic conductivity [m $s^{-1}$] that measures the ability for the flow though porous media, i is the hydraulic gradient with dh being the head difference from a datum point [m] and L the distance between the two heads (or boreholes). The minus sign indicates that the flow is moving away from the head. Darcy's velocity is accurately represented though experiments when laminar flow is observed with low Reynolds number [22].

To determine where the Darcy's velocity is applicable the Reynolds number, described below, should be examined:

$$Re = \frac{\rho D V_D}{\mu} \tag{13}$$

where $V_D$ is the discharge velocity or Darcy velocity [m $s^{-1}$], D is the average soil particle diameter [m], $\rho$ is the density of the fluid [kg $m^{-3}$] and $\mu$ is the dynamic viscosity [kg $m^{-1}$ $s^{-1}$]. Experiments have shown that the transition from laminar to turbulent conditions occurs approximately at $Re \approx 10$, which is lower than the free flow conditions. The validity of Darcy's law is acceptable at $Re \leq 1$ [22].

As stated in [22], the specific discharge does not predict accurately the flow through a porous media but through a pipe. In order to overcome this issue, the *seepage velocity* was introduced representing the average fluid velocity within the pores and includes a porosity term as described below:

$$v_S = -K\frac{dh}{Ln} = \frac{V_D}{n} \tag{14}$$

where n is the porosity term ($n = A_v/A$) defined as the area of the void space ($A_v$) through which fluid can flow over the total area (A) of the ground.

## COORDINATE SCALING

When modeling a system, as in the present case, it is commonly observed that one of the dimensions may have an enormous difference in relation with the others, and by meshing the model with equilateral cells, high computational memory and time will be required. The way to overcome this difficulty is to scale the large dimension and

balance the coordinate sizes. Consider a coordinate transformation:

$$z = sw \quad (15)$$

where w is the physical coordinate, s is the scaling factor, z is the model coordinate. The general heat equation (Eq. 1 combined with Eq. 2) reads in expanded form (upon substitution of Eq. 15):

$$\rho c_p \frac{\partial T}{\partial t} + \rho c_p u \nabla T + \frac{\partial}{\partial x}\left(k \frac{\partial T}{\partial x}\right) + \frac{\partial}{\partial y}\left(k \frac{\partial T}{\partial y}\right) + s \frac{\partial}{\partial z}\left(s\, k \frac{\partial T}{\partial z}\right) = Q \quad (16)$$

The required physical model has a very large height, 100 m, in contrast with the length and width of the model, which are 10 m and 5 m respectively. Therefore, the model was scaled down on the vertical axis (height). In order to achieve this reduction, the geometry in the COMSOL Multiphysics was built with a scale factor of 0.1 using the thermal conductivity in the materials section. Since multilayer ground is considered, the z-direction thermal conductivity in each layer is scaled as follows:

$$k_z = k(s^2) \quad (17)$$

For the flux conservation and how to un-scale fluxes in scaled models one can refer to [23].

## COMPUTATIONAL MODELING

As already mentioned, following the required parameters the model was constructed by COMSOL Multiphysics software. The geometry as seen in Fig.1 was set with two cylinders representing the boreholes. The multilayer ground was constructed with different material properties in order to achieve the required results and the general model, as described in the Coordinate scaling section, was scaled down on the z-axis.

The material properties of each ground layer and the boreholes are described in Table 1 and were taken from the experimental results provided by Florides *et al.* [17]. A simple COMSOL Multiphysics model was validated against the already experimentally validated results of Florides *et al.* [17], giving a good agreement.

**Table 1.** Material properties

| Layer | Height (m) | k (W m$^{-1}$ K$^{-1}$) | $C_p$ (W kg$^{-1}$ K$^{-1}$) | ρ (kg m$^{-3}$) |
|---|---|---|---|---|
| Top (top) | 9×zscale | 1.64 | 2353 | 731 |
| Region 1 | 41×zscale | 1.73 | 2290 | 780 |
| Region 2 | 30×zscale | 1.94 | 2330 | 840 |
| Region 3 | 20×zscale | 1.94 | 2330 | 840 |
| Bottom | 5×zscale | 1.94 | 2330 | 840 |
| Boreholes | 95×zscale | 1 | 800 | 1500 |

Subsequently, the groundwater velocity was set using the seepage velocity as described in the previous section, where the hydraulic conductivity is considered for the minimum and maximum values from typical data presented in Domenico and Schwartz [24].

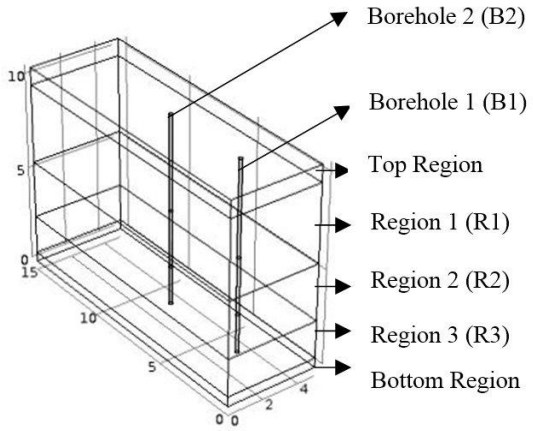


**Fig.1.** Model Geometry

The value of power used was 2780 W, the same as in Florides *et al.* [17], and the boreholes were set as a heat source with a general source applied of 1275 W m$^{-3}$. The heat source was not constantly (24 hours) applied as this is not a realistic situation. It was chosen to emit heat for 12 hours, and remain idle for the next 12 hours. To achieve this in COMSOL Multiphysics a rectangle function and an analytic function were selected. Moreover, a heat source applied time function was set (with lower limit 0 and upper limit 12 hours) within the rectangle function. Following on, an argument *t* (time) was introduced in the analytic function (expression of: comp1.rect1(t[1/s]), where rect1 is the rectangle function and comp1 (component) is the location of the function), defining the overall length of 7 days (upper limit) and setting a period of 1 day (periodic extension). For presenting a nearly realistic model, a pulse function was applied, by equating the heat source term to 1 for 12 hours

and to 0 for the next 12 hours, throughout the 7 consecutive days as shown in Fig.2. The analytic function is described graphically in Fig.2. It must be noted that *smoothing* is added by default in COMSOL Multiphysics in order to prevent the equations from shocking, and hence, from producing invalid results.

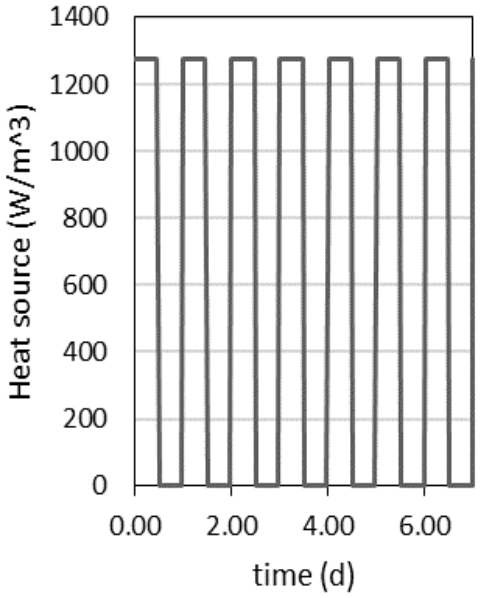


**Fig.2.** Heat Source analytic function

## RESULTS AND DISCUSSION

After the computational model set-up, a set of runs were performed in order to confirm that the scale factor produced reasonable results within acceptable error. The scale comparison was run for the factors of 0.1, 0.2, 0.3 and 0.4. The average temperature on the outer surface of both boreholes in region 3 ground layer (seen in Fig.1) were recorded and analyzed.

The results for all scale factors' values demonstrate a good agreement with less than 0.5 K in temperature difference (Fig.3). These results compare well with professional equipment accuracy, where the tolerance exhibited is usually ±0.2 K. It should be noted that all the parameter values are the same for all 4 cases considered, except the mesh density that had to be changed. The mesh density on the boreholes was maintained at a minimum of 10 to 12 points on the boreholes diameter with a growth rate of 1.2–1.4.

As a consequence, the selected scale factor to proceed with the computational models was 0.1 as it required the least computational time and memory.

The values presented in all the figures are the average surface temperature on the outer wall on region 3 as shown in Fig.1.

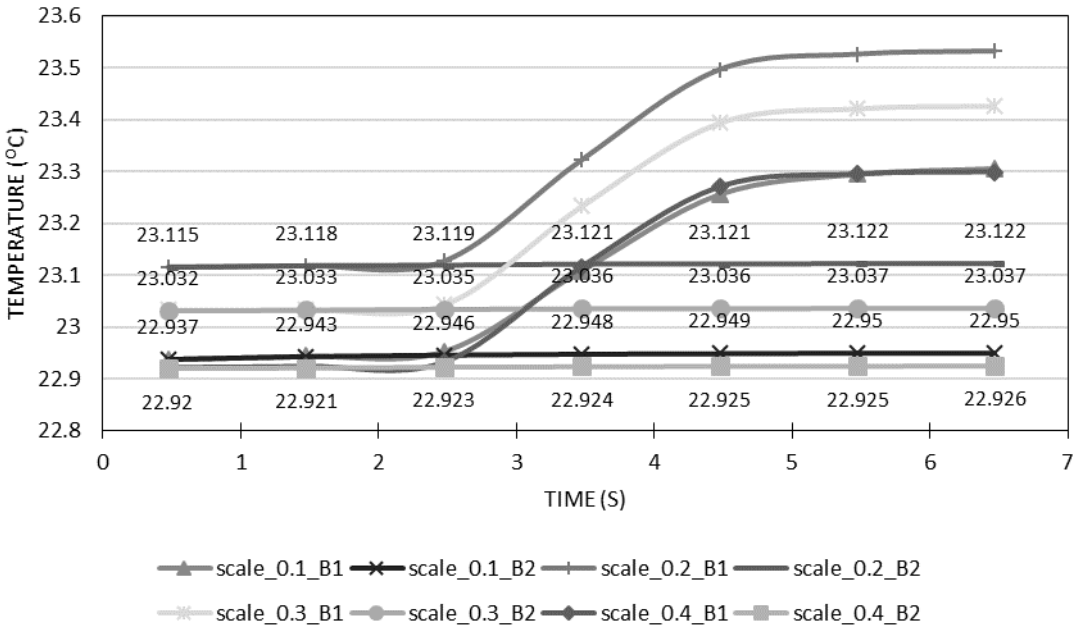


**Fig.3.** Scale comparison of the region 3 borehole surface showing average temperature over time

Analysis of individual boreholes at different regions allows to observe that the temperature increases with time except in the region of the groundwater (Fig.4). This is due to the fact that groundwater, where is present, dissipates heat away from the borehole. On the contrary, at depths where there is no groundwater, heat is generated and maintained nearby the borehole. In addition, 7 peak points are noticeable due to the pulse function applied. The temperature reaches its peak point each day in the middle of the day after the 12 hours of continuous heat injection.

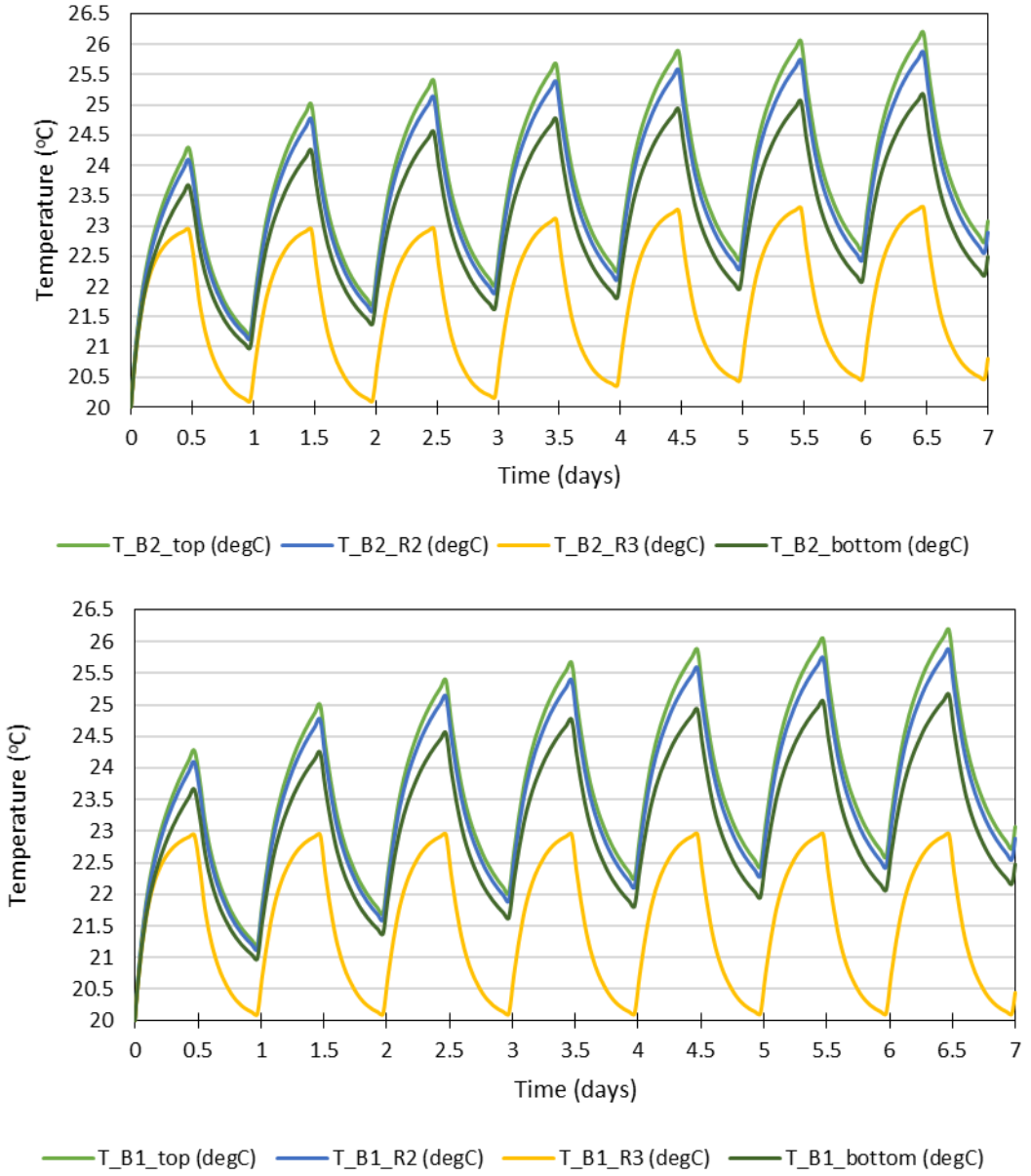


**Fig.4.** Temperature profiles versus time for a seepage velocity vS = $10^{-5}$ m $s^{-1}$ for Borehole 1 (B1-upstream) and Borehole 2 (B2-downstream)

It is easier to examine the rise of the heat by plotting only the maximum points in each borehole (Fig.5 and Fig.6). In Fig.5 it can be observed that by increasing the groundwater velocity (seepage velocity as applied in the model) the average surface temperature on the groundwater region decreases. It is noteworthy that when low seepage velocity values are applied ($v_S$=1.6667×$10^{-9}$ and $v_S$=$10^{-9}$), the model generates the same temperature peak points (see plots).

Thus, it can be concluded that when seepage velocity is smaller than $10^{-9}$, it is not enough to cool down the boreholes, whereas under maximum seepage velocity regime, the boreholes show a lower average temperature and reach steady state in a shorter time. It is also noticeable that in the first borehole, the average temperature reaches a steady state the first day, whereas in the second borehole (downstream) there is an increase in temperature before it reaches steady state again the fourth day.

In order to further examine the temperature increasing in the second borehole, a direct comparison between the two boreholes, under the same conditions, is shown in Fig.7. The heat carried away from the first borehole interferes with the second borehole when the groundwater velocity is high enough – like in the case of the maximum seepage velocity ($v_S$ = $10^{-5}$ m $s^{-1}$) – as can be observed in 2D y-z and x-y plots (Fig.8 and Fig.9).

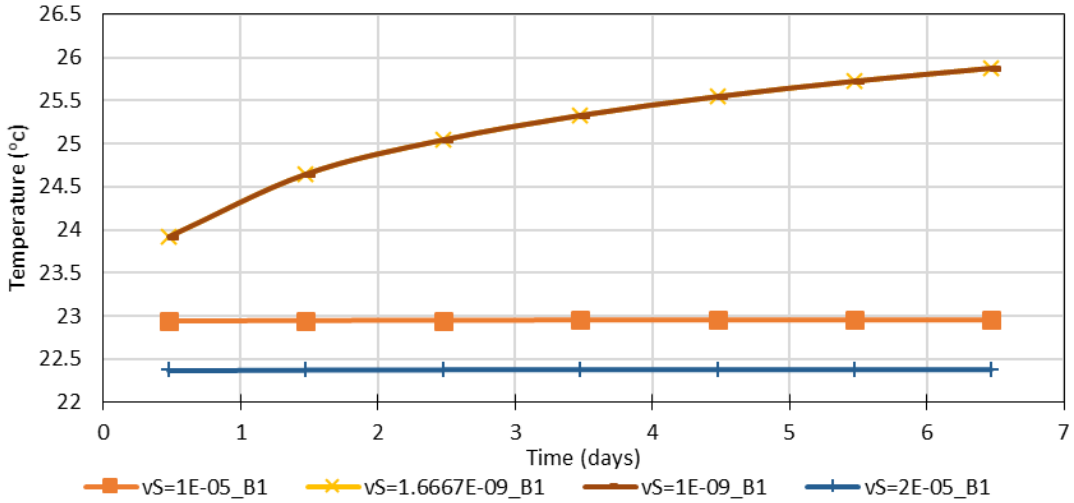


**Fig.5.** Temperature peak points versus time for borehole 1 (B1) in region 3 for various values of seepage velocity ($v_S$)

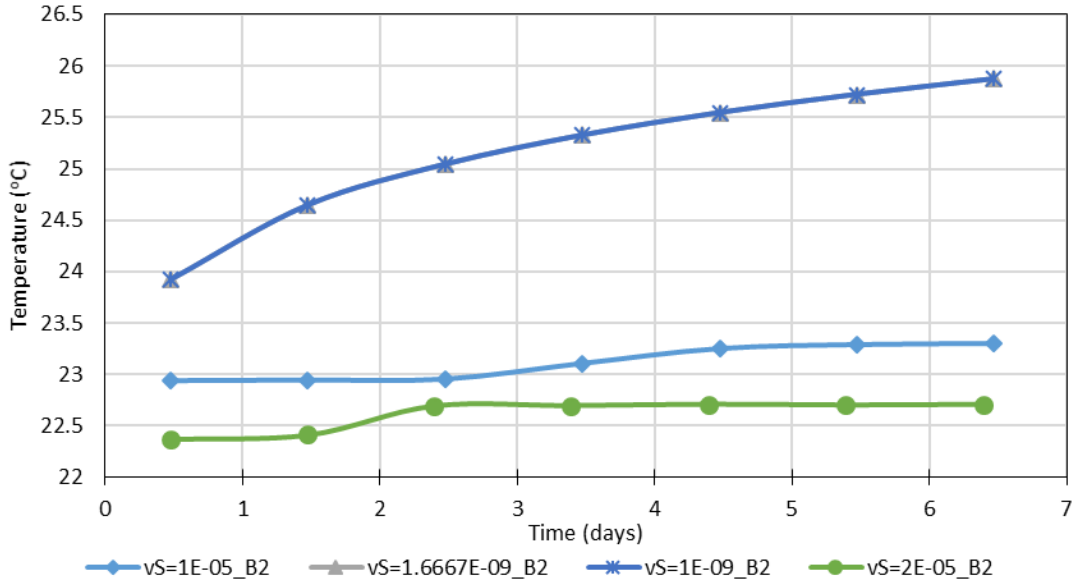


**Fig.6.** Temperature peak points versus time for borehole 2 (B2) in region 3 for various values of seepage velocity ($v_S$)

This interference occurs after 60 hours and continues for another 3 days until the heat flow is steady and the average surface temperature on the second borehole reaches steady state.

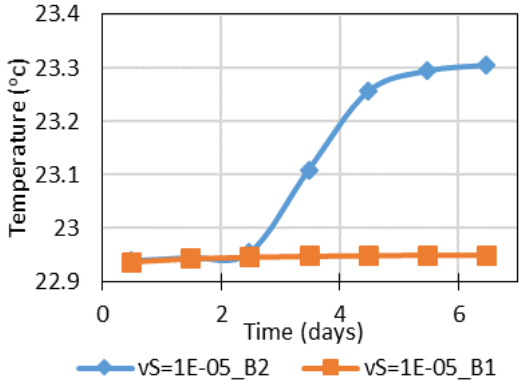


**Fig.7.** Temperature peak points at vS = $10^{-5}$ms$^{-1}$ versus time for both boreholes in region 3

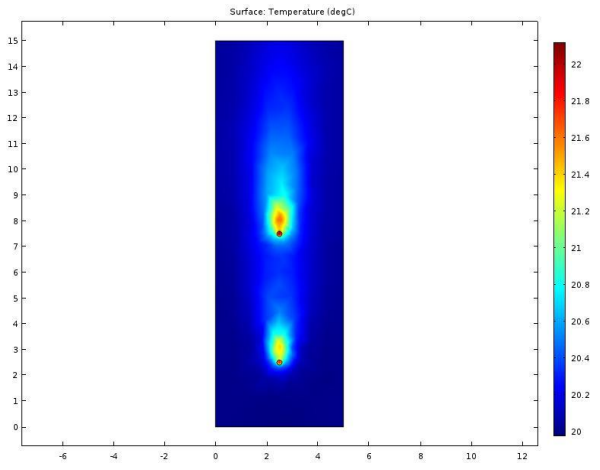


**Fig.8.** 2D cut-plane on the x-y plane, vS = $10^{-5}$ m s$^{-1}$, t = 7 days, center of region 3

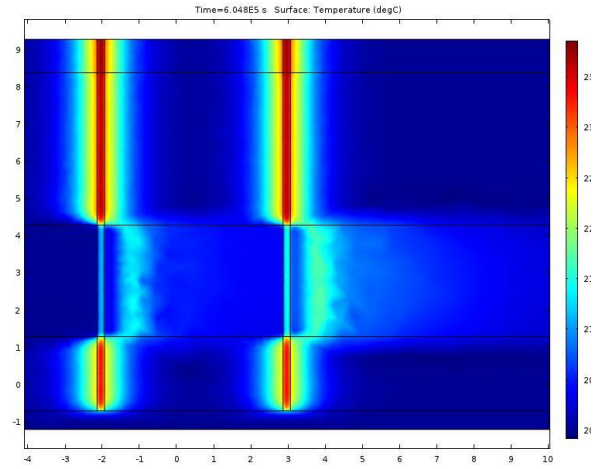


**Fig.9.** 2D cut-plane on the y-z plane, vS = $10^{-5}$ m $s^{-1}$, t = 7 days, center of boreholes

The effect of the interference, when the maximum hydraulic conductivity is applied, can also be noticed by plotting the isothermal contours. After a 2 days run the isothermal contours of the first borehole have not reached the second borehole (Fig.10). After a 5 days run (Fig.11), the first borehole interferes with the second borehole, whence the increased temperature detected.

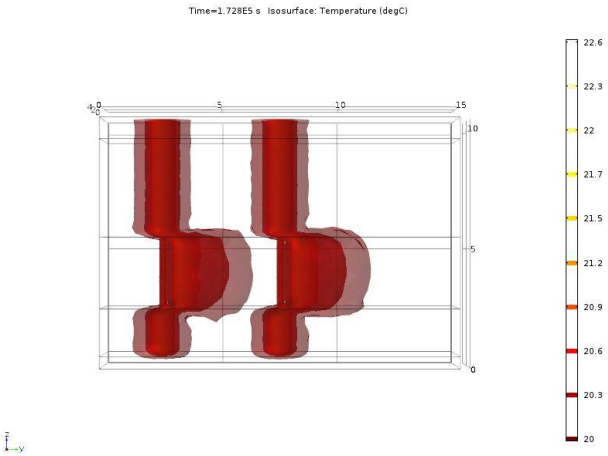


**Fig.10.** Isothermal contours, vS = $10^{-5}$ m $s^{-1}$, t = 2 days

As can be clearly seen in Fig.12, the interference does not occur at lower velocities (e.g. vS = 1.6667×10–9 m s–1 for minimum hydraulic conductivity applied) as expected due to the low velocity in the groundwater region. Of course, even this very low seepage velocity can still produce lower average surface temperature in region 3 that in the other regions (as seen in Fig.4). Note that steady state has not been reached after 7 days of computational run (Fig.5 and Fig.6), as in the case of the higher seepage velocity applied (vS = 10–5 m s–1 for maximum hydraulic conductivity).

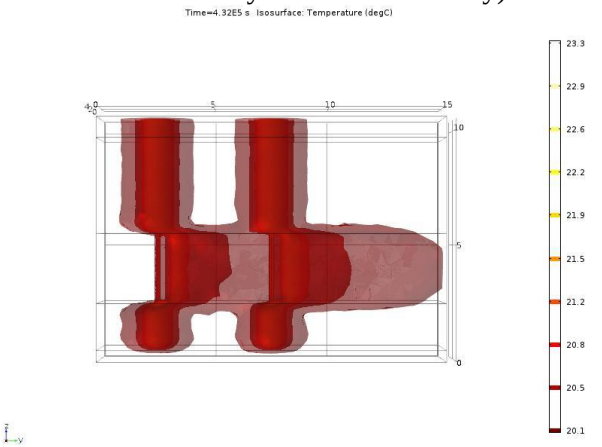


**Fig.11.** Isothermal contours, $v_S$ = $10^{-5}$ m $s^{-1}$, t=5 days

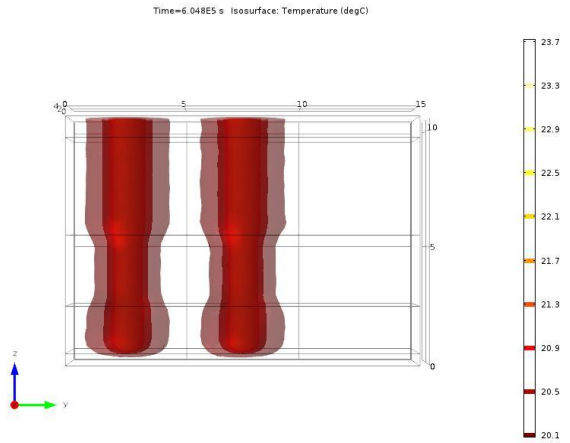


**Fig.12.** Isothermal contours, vS = 1.6667×$10^{-9}$ m $s^{-1}$, t = 7 days

## CONCLUSIONS

In this paper the effect of the groundwater flow on a GHE in cooling mode has been examined through computational modeling using COMSOL Multiphysics software. Heat transfer in porous media, Darcy's velocity and seepage velocity were introduced by taking typical values of hydraulic conductivity and were adapted in COMSOL Multiphysics. The coordinate scaling technique was employed in order to save valuable computational time and memory. The heat source was added to the model as a pulse function and it was activated 12 hours a day.

Moreover, the average borehole surface temperatures on every ground layer were presented for low and high seepage velocities. The results indicate that groundwater flow has an effect on the average surface temperature, and in the water-bearing layer the average temperature decreases as

opposed to the dry regions. It is also noticeable that the temperature of the affected ground layer reaches a steady-state much sooner than in other regions. Additionally, when the groundwater flow velocity is high, the two boreholes are observed to interfere with each other. This interference has an effect on the downstream borehole that can reach a lower steady-state temperature.

Further examination of cooling and heating mode must be considered in the future and in addition, in-situ experiments could be conducted in order to validate directly the model using a groundwater flow GHE.

## REFERENCES


1 Y. Xiaohui, Z. Yufeng, D. Na, W. Jianshuan, Z. Dongwen and W. Jilin, "Thermal response test and numerical analysis based on two models for ground-source heat pump system," *Energy and Buildings*, vol. 66, pp. 657-666, 2013.

2 H. Yang, P. Cui, Z. Fang, "Vertical-borehole ground-coupled heat pumps: A review of models and systems," *Applied Energy*, vol. 87, no. 1, pp. 16-27, 2010.

3 Z. Changxing, G. Zhanjun, L. Yufeng, C. Xiaochun and P. Donggen, "A review on thermal response test of ground-coupled heat pump systems," *Renewable and Sustainable Energy Reviews*, vol. 40, no. 851-867, 2014.

4 J. Bose, "Soil and rock classification for design of ground coupled heat pump systems-field manual," Electric Power Research Institute, 1989.

5 J. Sass, A. Lachenbruch and R. Munroe, "Thermal conductivity of rockes from measurments on fragments and its application to heat flow determinations," *J Geophys Res*, vol. 76, pp. 3391-401, 1971.

6 A. Choudhary, "An approach to determine the termal conductivity and diffusivity of a rock in situ.," Oklahoma State University, 1976.

7 P. Mogensen, "Fluid to Duct Wall Heat Transfer in Duct System Heat Storage," Stockholm. Sweden, 1983.

8 S. Gehlin, "Thermal response test: method development and evaluation.," Sweden, 2002.

9 G. Florides and S. Kalogirou, "Ground heat exchanges - A review on systems, models and applications," *Reneable energy*, vol. 32, no. 15, p. 2461–2478, 2007.

10 T. Kelvin, Mathematical and physical papers. London: Cambridge University Press, 1882.

11 L. Ingersoll, O. J. Zobel and A. C. Ingersoll, Heat conduction with engineering, geological and other applications., New York: McGraw-Hill, 1954.

12 L. Ingersoll, F. Adler, H. Plass and A. Ingersoll, "Theory of earth heat exchangers for the heat pump," *ASHVE Trans*, vol. 56, pp. 167-88, 1950.

13 H. Carslaw and J. Jaeger, Conduction of heat in solids, 2nd ed., Oxford, UK: Oxford University Press, 1959.

14 P. Eskilson, "Thermal analysis of heat extraction boreholes," University of Lund, Lund, Sweden, 1987.

15 J. Claesson and P. Eskilson, "Conductive heat extraction by a deep borehole," Sweden, 1988.

16 C. Remund, Personal communication., Northern Geo- thermal Support Center: South Dakota State University, Brookings, South Dakota, 1998.

17 G. Florides, E. Theofanous, I. Iosif-Stylianou, S. Tassou, P. Christodoulides, Z. Zomeni, E. Tsiolakis, S. Kalogirou, V. Messaritis, P. Pouloupatis and G. Panayiotou, "Modeling and assessment of the efficiency of horizontal and vertical ground heat exchangers," *Energy*, vol. 58, pp. 655-663, 2013.

18 J. Bear and Y. Bachmat, Introduction to Modeling of Transport Phenomena in Porous Media, vol. 4, Springer Science & Business Media, 1990.

19 D. Nield and A. Bejan, Convection in Porous Media, in Convection Heat Transfer, Fourth Edition, Hoboken, NJ, USA: John Wiley & Sons, Inc., 2013.

20 H. Darcy, Les Fontaines Publiques de la Ville de Dijon, Paris: Dalmont, 1856.

21 A. D. Chiasson, S. J. Rees and J. D. Spitler, "Preliminary assessment of the effects of groundwater flow on closed-loop ground-source heat pump systems," *ASHRAE Transactions*, vol. 106, no. 1, pp. 380-393, 2000.

22 M. E. Harr, Groundwater and Seepage, New York: Dover Publication Inc, 1990.

23 P. S. Inc, "FlexPDE user guide," 2010. [Online]. Available: http://www.pdesolutions.com/help/index.html?coordinatescaling.html. [Accessed Nov 2015].

24 P. Domenico and F. Schwartz, Physical and chemical hydrogeology, New York: John Wiley & Sons, 1990.

25 S. Javed, P. Fahlén and J. Claesson, "Vertical ground heat exchangers: A review of heat flow models.," in *Proceedings vol. CD-proceedings*, Stockholm, Sweden, 2009.

*Bulgarian Chemical Communications, Volume 48, Special Issue E (pp. 64 - 70) 2016*

# Energy performance of a dual air and ground-source heat pump coupled with a Flat-Panel ground heat exchanger

Michele Bottarelli [1, *], Li Zhang [2], Marco Bortoloni[1], Yuehong Su [2]

[1]*Department of Architecture, University of Ferrara, Via Quartieri 8, Ferrara 44121, Italy*
[2]*Department of Architecture and Built Environment, University of Nottingham, University Park, NG7 2RD, UK*

Integrating air and ground source can be an effective solution to improve the performance of a heat pump by reducing the drawbacks of each individual technology. In fact, a dual source system not only greatly reduce the size of the ground heat exchanger, but also can achieve a higher efficiency by selecting the more thermally favourable source. Hence, the frosting/defrosting process, which regularly occurs in a common air source heat pump (ASHP) could be avoided. In the present contribution, the performance of a dual source heat pump (DSHP) has been numerically analysed. The energy demand for both heating and cooling of building has been estimated by means of the software EnergyPlus. Then, the resulting time series values are used as the boundary heat fluxes to model a ground heat exchanger. The commercial Finite Element Method (FEM) simulation package COMSOL Multiphysics is implemented to simulate the heat transfer in the ground which is produced by a horizontal Flat-Panel ground heat exchanger. A function has been properly implemented in COMSOL to control the switching between air and ground sources, according to their temperatures. Compared with an ASHP, the DSHP shows much higher efficiency because of the more favourable working conditions and the protection against frosting. Consequently, a DSHP should be a viable solution to combine the respective advantages of air source and ground source heat pumps.

**Keywords:** dual-source heat pumps, horizontal ground heat exchanger, finite element model (FEM)

## INTRODUCTION

Nowadays, the reduction of greenhouse gas emissions and the rational use of energy have become a major issue. In view of this, the recent environmental policies have been promoting the renewable technologies expanded worldwide. Among them, air-source heat pumps (ASHPs) and ground-coupled heat pumps (GCHPs) are regarded as viable and efficient technologies for applications of heating and cooling in residential and commercial buildings [1]. These systems are gradually being applied with significant savings in terms of primary energy, due to their universal applicability and versatility. Due to their universal applicability and versatility, these systems have been gradually applied with significant saving of primary energy use in the recent years. The performance of a heat pump is significantly affected by the operating conditions, which depend on the heating/cooling demand and the heat source feature. In order to achieve higher efficiency than the widespread ASHPs, the GCHP systems use the ground as a heat source/sink, which often provides more favourable and stable temperature than outdoor air temperature. As the depth increases, the ground temperature fluctuations are reduced. The annual average temperature of the shallow ground depends on the location and it is approximately equal to the annual average air temperature [2]. In addition, the ground temperature can be significantly different between rural and urban areas, where the soil is usually warmer due to the urban heat island effect [3].

Besides the high efficiency, GCHPs have also higher purchase and installation cost than air-source systems due to the initial cost of the ground heat exchanger [4], which is recognized as the least efficient component of these systems. In addition, the performance of a GCHP is strongly affected by the ground heat exchanger, which can be installed in vertical boreholes or in shallow horizontal trenches (also referred as VGHE and HGHE, respectively). The HGHEs hold some advantages in terms of costs and installation but as well have drawbacks in terms of land area requirements and efficiency of soil heat transfer. In order to overcome the drawbacks of current available technology, recent studies have attempted to develop more efficient arrangements for the widespread HGHE configurations [5] or novel shapes such as the Flat-Panel, which has been developed at the University of Ferrara in 2012 [6].

In contrast, ASHPs have a low initial installation cost and are almost easily applied. However, during winter operations as well as under cold and humid weather condition, these systems are subjected to frosting on the evaporator. This phenomenon

* To whom all correspondence should be sent:
michele.bottarelli@unife.it

produces both reduction in the efficiency and the heating capacity of an ASHP [7], thus defrost cycles are required to remove the frost and improve the performance. If defrosting is obtained by inverting the refrigeration cycle, the coefficient of performance (COP) for the whole heating season can be reduced up to 12.6%, under certain conditions of relative humidity and outdoor air temperature [8]. Many techniques have been investigated to efficiently reduce defrosting cycles or completely prevent frosting on the outdoor unit of an ASHP [9].

In view of the disadvantages of a single source heat pump, the opportunity to couple the air-source with the ground-source in a dual air and ground source heat pump system can produce a significant efficiency improvement [10]. An optimised DSHP can achieve high efficiency by switching between air and ground sources/sinks according to the source temperature, thus preventing the frosting during winter. Moreover, the size of the ground heat exchanger can be considerably reduced with DSHPs, according the lower thermal energy exchanged with the ground in comparison with conventional GCHPs [11-12]. Therefore, the DSHP solution could offer a right balance between the individual ASHP and GCHP, thus enhancing the performance of heat pumps.

This study aims to evaluate the opportunity to realise a DSHP, and its potential benefits over conventional ASHP and GSHP. The analysis is carried out numerically, as the first step of future studies.

## METHODS

This study has simulated the performance of a dual-source heat pump (DSHP) by using numerical analysis method. The ground coupling is intended to be used for supplemental heat extraction or rejection and as an alternative of a conventional outdoor air unit. The DSHP is assumed to be coupled with the ground by means of an innovative HGHE, named Flat-Panel (FP), which has been recently developed at the University of Ferrara.

The Flat-Panel is a rectangular module, 3m long and 1m high, consisting of two polypropylene (PP) sheets with the thickness of 4mm. They are welded by leaving 0.02m space between them in order to form a cavity to allow the working fluid flows. Within the cavity, a labyrinth has been designed as a series of rectangular channels with a high width-height ratio. The fluid flows for most of the length in a vertical direction, in order to avoid thermal stratification caused by buoyancy forces. The performance of Flat-Panel has been tested with an experimental setup at the Department of Architecture, the University of Ferrara (Italy) since 2011. The experimental setup covers a land area of about 320 $m^2$, and it is equipped with a 2 Flat-Panel which are installed 1.85 m deep in the soil to serve as the HGHE. Tests were conducted in different operating conditions (heating and cooling) and for different operating modes (continuous, discontinuous and pulsed). Tests were performed for different flow rates, in the range of 80l/h and 260l/h, thus the flow regime is always laminar. Overall, the HGHE showed very good performance in terms of heat transfer rate both in cooling and heating operations. A detailed description of the experimental setup and testing activity is reported in [13].

The TekneHub laboratory of the University of Ferrara, located in the northern Italy, has been taken as the reference case. The building has been simulated by means of the EnergyPlus (E+) software, in order to estimate the heating and cooling demand.

The resulting time series at hourly scale is used as the heat load in a 2D model of the HGHE, which is implemented in the commercial FEM numerical code COMSOL Multiphysics. The model is used to simulate the heat transfer in the ground with Flat-Panels, in order to evaluate the temperature trend of the ground source in comparison with that of the air. A user defined function has been used in the model to control the switching between air and ground sources, according to their temperatures. Finally, by analysing the system operation, the frosting prevention offered by the DSHP is calculated. Details are presented in the next paragraphs.

### *Building energy demand*

In this study, the reference target for heating and cooling demand is the TekneHub laboratory of the University of Ferrara, shown in Fig.1, which belongs to the High Technology Network of Emilia-Romagna region of Italy. The Network is intended to promote the technology transfer between the university and industry sectors. In order to estimate the heating and cooling loads, the well-known building energy simulation software, EnergyPlus, is employed to simulate the TekneHub laboratory. EnergyPlus can predict the dynamic values of heating, cooling, lighting, ventilation, renewable energy generation as well as water use in buildings [14]. The accuracy of EnergyPlus simulation has been verified by many researchers, so it has been well accepted worldwide.

The TekneHub is in the city of Ferrara (N44.831, E11.599), which is located in the northern Italy, in the valley of the Po river. The local climate is usually referred to as a humid continental climate. The winter is harsh and humid, and the temperature often decreases below 0°C (2326 heating degree days). The summer is hot and muggy, with high temperature (higher than 35°C) during the day.

The building has only one floor with a gross floor area of 880m$^2$ and a gross volume of 3488m$^3$, subdivided in twenty rooms, laboratories and technical spaces. The building envelope is compliant with recent Italian regulations on the energy performance of building: the external walls are made of cavity brick walls with a polystyrene thermal insulation layer (calculated U-value of 0.21 W/m$^2$K); the roof is made of predalles precast roof slabs with 160mm of polystyrene thermal insulation layer (calculated U-value of 0.20W/m$^2$K); the floor consists of an insulated light concrete layer supported by a structural concrete aired slab and a concrete sub-foundation (calculated U-value of 0.24W/m$^2$K).

**Fig.1.** TekneHub laboratory

Further details of the buildings components are not included in the present manuscript, for sake of brevity. An experimental analysis was carried to calculate the effective U-value of the external walls [15]. In view of this, the walls U-value in the model has been corrected to 0.38W/m$^2$K, according the experimental data we monitored. The building envelope has been modelled in 3D, as shown in Fig.2, by means of OpenStudio, which is a plug-in to the software Sketch-up, offering a graphic interface for EnergyPlus. The geometry model was first built up in OpenStudio with the default settings for EnergyPlus simulation, and some modifications were made through the IDF Editor of EnergyPlus.

Finally, the heating and cooling system of TekneHub is equipped with two air-to-air rooftop heat pumps with a capacity of 40kW each. In the EnergyPlus model, the air-conditioning plant is assumed to be a variable refrigerant flow (VRF) type, according to the two ASHPs installed. The details about the model of VRF and its settings can be found in the documentation of EnergyPlus [16]. The building is divided in two separate thermal zones, each one is assigned to a heat pump; the heating/cooling distribution system is modelled according to that installed and consists of several fan coil units which are set to operate continuously during the heating season whereas during cooling season from Monday to Friday, 12h a day; during public holidays the system is assumed to be turned off.

A comprehensive weather dataset (e.g. outdoor air temperature, solar radiation, humidity, soil temperature at different depths) were imported in EnergyPlus in order to run simulations. The dataset was collected in 2015 by means of a weather station (Davis Vantage Pro 2) installed in the garden of the TekneHub laboratory.

The EnergyPlus simulation has run for a whole year (2015), as shown in Fig.3, where the cooling peak load is obviously higher than the heating.

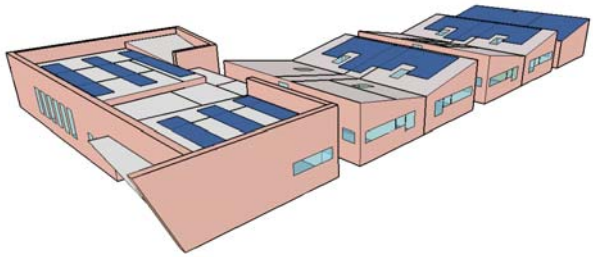

**Fig.2.** 3D model of the building envelope

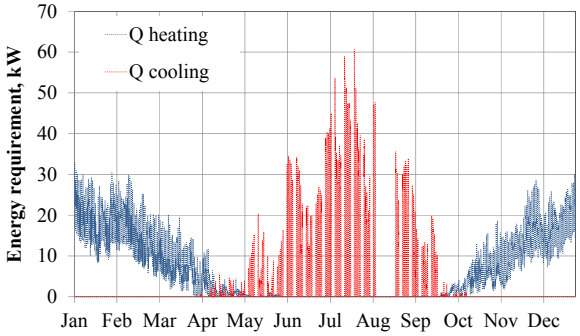


**Fig.3.** Building heating and cooling demand

The time series at hourly scale of the energy requirement for space heating and cooling were used to define the heat flux at the HGHE in the FEM model, as detailed in Section 2.2.

### *Numerical modelling*

The numerical analysis is conducted by means of a commercial finite element numerical code COMSOL Multiphysics, solving the heat transfer problem in solids, thus, only conductive heat

transport is considered. This study is focused on the evolution of the temperature distribution of the ground source, due to heat extraction/rejection by the ground coupling of the DSHP. The efficiency of the heat pump in fact depends on the temperature of the ground as a heat source or sink. Solving the 3D thermo-fluid dynamic problem within the HGHE is beyond the scope of this work. Therefore, the soil heat transfer has been simulated in a 2D domain. Here, the HGHE is assumed to be a Flat-panel (FP) [6, 13].

The 2D computational domain is modelled as a cross-section of an HGHE and a large surrounding soil part (6 m wide and 10 m deep), as shown in Fig.4 together with the full mesh and the boundary conditions.

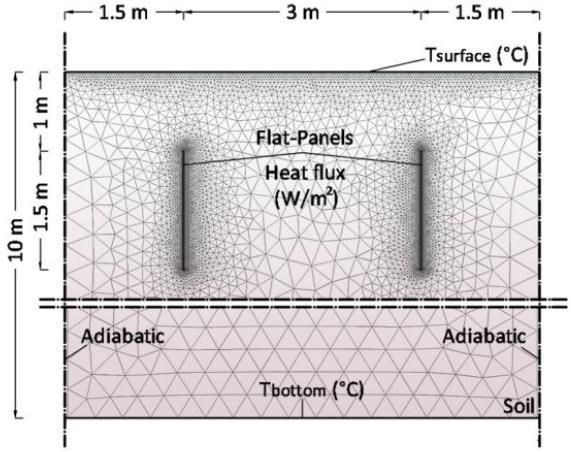


**Fig.4.** Sketch of the 2D model domain, boundary conditions and mesh

Two parallel lines equipped with Flat-Panels (1.5m high) are assumed to be placed at an average depth of 1.75m with a distance of 3m, in order to take into account of the thermal interference between each line. In the model domain, the FPs were simplified as boundary condition. According to a 2D approach, the Flat-Panel shape may be simplified as a cold/hot plate, to and from which heat flows from the surrounding soil mainly by heat conduction. From this point of view, a 2D model can be considered as representative of a three-dimensional geometry in the hypothesis that the temperature variations are small along the exchanger (between inlet and outlet sections) and that no thermal stratification occurs within the working fluid (for FPs this is not expected due to the labyrinth). In view of this, the results are compared in terms of the average temperature at the interface between HGHE and the ground, which is representative of the average temperature of the working fluid.

The soil is considered to be homogeneous with constant thermal properties (thermal conductivity, density, heat capacity), as reported in Table.1.

**Table 1**. Physical properties of soil

| Thermal conductivity | Density | Specific heat |
|---|---|---|
| (W/mK) | (kg/m$^3$) | (J/kgK) |
| 0.8 | 1600 | 1500 |

In the model, the hourly scale time series of the measured temperature at the soil surface in 2015 is set as the boundary condition at the top, whereas a constant temperature at the bottom, is equal to the yearly average ground temperature at shallow depth (16.7°C). An adiabatic condition is assigned to the side boundaries of the domain.

In the model, the Flat-Panels were treated as boundary heat sources at the interface between the ground and the Flat-Panels, thus the heat flux $q_g$ (W/m$^2$) is calculated at hourly scale by means of Eq. 1:

$$q_g(t) = \frac{r \cdot q_t}{S_{FP}} \quad (1)$$

Where: $q_t$ (W/m$^3$) is the building heating/cooling demand, as calculated at hourly scale by means of the EnergyPlus model according to the building gross volume (3488m$^3$); $S_{FP}$ (3 m$^2$/m) is the heat transfer surface of a single Flat-Panel for unit length of the HGHE (1m) and $r$ (m$^3$/m) is a parameter which is used to assign a portion of the building gross volume to the unit length of HGHE (1m). Therefore, the product of $r$ and $q_t$ is the rate of heat transfer for unit length of HGHE, expressed in W/m, which commonly used to identify the performance of HGHEs and VGHEs.

In the model, the resulting $q_g$ time series was assigned as a 2$^{nd}$ kind boundary condition at each line composing the flat-panel HGHE.

In setting the heating/cooling load at the HGHE we assumed a simplification by neglecting the electricity share as defined by the heat pumps coefficient of performance, since the analysis is focused on the ground heat transfer due to HGHEs.

To control the switching between air and ground sources thus simulating the operation of a DSHP, a user-defined function has been programmed in COMSOL. On one hand, the temperature of the air source is defined by means of the outdoor air temperature time series (year 2015) implemented in the model. On the other hand, the temperature of the ground source is the calculated average temperature at the Flat-Panel boundary condition at each time step (1h).

The function is set to activate the boundary heat source at the Flat-Panel, according to the ground heating/cooling load, when the ground source temperature is more favourable than that of the air source, and meantime the outdoor air temperature is lower than 5°C (thus avoiding most of frosting conditions). The ground allows better working conditions when its temperature is higher than that of the outdoor air in winter, or lower in summer. Otherwise, in all other conditions, the boundary heat source term is set to zero, thus simulating the operation of the ASHP using the air source only.

The finite element grid resolution is higher at the FP boundary where higher temperature gradients are expected and coarse in the outer domain. The full mesh consists of 11,200 elements. In order to check the grid independence, a preliminary analysis has been carried out by increasing the number of the elements.

The initial temperature profile of the soil for simulations is obtained from the measured temperature of the ground at different depth.

A parametric study of the heat load at the flat-panel HGHE has been performed, thus simulating different sizing of HGHE. In a DSHP in fact, the HGHE is intended to be used as an alternative of a conventional outdoor air unit for heat extraction or rejection, thus the size of the HGHE can be significantly reduced with DSHPs, because the ground source is not always operating. In view of this, five different values of the parameter *r* have been assumed (5, 7.5, 10, 15, 20), i.e., for example, when $r$ = 5, 5m$^3$ of building volume is supplied for each meter of FP.

## RESULTS AND DISCUSSION

The numerical simulations were run for the different values of the parameter *r* under the same boundary conditions. Each simulation was carried out for two consecutive years. The present paper is focused on the temperature variation in the ground source occurring due to the heat extraction/rejection by the HGHE.

The daily average temperature of the ground source is shown in Fig.5 for each test case, throughout a whole year.

The temperature is calculated as the average temperature at the FP boundaries, where the heat flux was applied as shown in the previous Fig.4. The ground source temperature is compared with the outdoor air temperature $T_{air}$, which represents the air temperature at the outdoor unit of an ASHP.

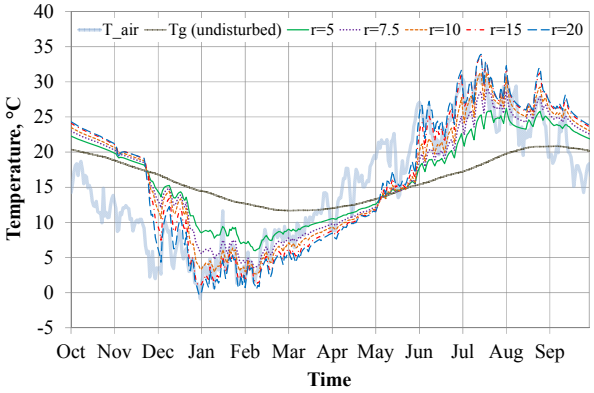


**Fig.5.** Daily average temperature of the ground

The undisturbed ground temperature at the average depth of the HGHE (-1.75m) is also included in Fig.5. Up to the middle of November, the outdoor air temperature allows more favourable working condition (>5°C) therefore the air source is selected by the DSHP instead of ground source. After the 20$^{th}$ of November the ground temperature is profitable during the night-time and when $T_{air}$ decreases below 5°C, the DSHP switches to the HGHE. On the contrary, the ground is used as a heat sink for the whole summer period, when its temperature is more favourable than that of the air. Summertime, the discontinuous operating mode of the air-conditioning system produces a quick temperature increase at each start-up, due to the higher ground load. Overall, the higher the value of *r*, the higher the ground load is for heating and cooling at the HGHE. Therefore a significant variation is observed in the ground temperature. As a consequence, for *r* equal to 15 and 20m$^3$/m, the ground source is no longer convenient in late heating and cooling season.

The maximum and minimum temperatures of the ground source (in the heating and cooling season, respectively) are summarized in Table.2 for each case, together with maximum value of the heat transfer rate at the Flat-Panel. In addition, we calculated the overall length of the HGHE which is required to cover the peak energy demand of the building (60.57kW), according to the values of parameter *r*. The size of the HGHE can be reduced

**Table 2**. Temperature of the ground source, HGHE size

| *r* | $HGHE_L$ | $q_{max}$ | $T_{max}$ | $T_{min}$ |
|---|---|---|---|---|
| (m$^3$/m) | (m) | (W/m) | (°C) | (°C) |
| 5 | 698 | 86.8 | 27.4 | 5.5 |
| 7.5 | 465 | 130.2 | 31.1 | 2.7 |
| 10 | 349 | 173.7 | 34.4 | 1.4 |
| 15 | 233 | 260.5 | 37.7 | -1 |
| 20 | 174 | 347.3 | 38.4 | -3.2 |

significantly with a DSHP: for $r$=10m$^3$/m the overall length of the HGHE can be almost halved, while maintaining acceptable operating conditions. Although a further reduction can be achievable for $r$=15m$^3$/m and $r$=20m$^3$/m, the temperatures of the ground source are not favourable and would require the use of a mixture water/glycol as working fluid, in order to prevent freezing wintertime.

A DSHP use the ground as the heat source/sink only partially, according to the adopted criteria and the environmental conditions. Fig.6 shows the ratio between the operating time (h) of the flat-panel HGHE and the overall operating time of the DSHP for heating and cooling. Similarly, we calculated the ratio of the energy exchanged with the ground (Wh/m) and the overall energy requirements. According to the adopted operating criteria and for $r$=5 m$^3$/m, the geothermal heat exchanger is operating the 23.4% and 88.5% of the time in winter and summer, respectively; the energy exchanged is the 41.7% and 95%. As the value of $r$ increases (therefore the HGHE size decreases) a negative trend was observed. The reduction is significant for $r$=15 m$^3$/m and 20 m$^3$/m, due to the progressive thermal degradation of the ground source.

In addition, a DSHP can prevent the frosting at the outdoor unit by switching between air and ground sources that is always occurring when the average air temperature at the evaporator is below the frosting point temperature, In view of this, we calculated the amount of days in 2015 during which the frosting can be avoided. The frosting is assumed to occur when the leaving air temperature at the outdoor unit is below 0°C and below the dew-point. Moreover, we assumed that the air-source exchanger cools the air flowing across the fins by 4K.

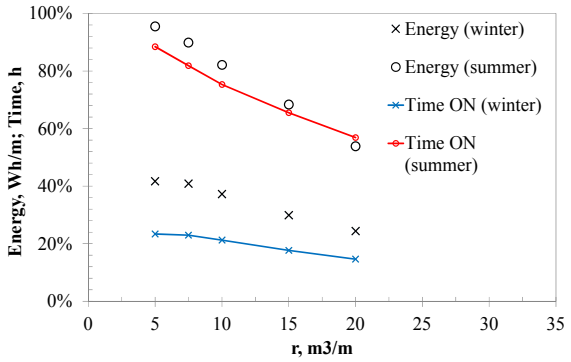


**Fig.6.** Annual percentage operation time of the flat-panel HGHE

The frosting prevention occurs only when the HGHE is operating. The resulting days of frosting prevention are reported in Fig.7, for each test case, together with the outdoor air and the dew point temperature.

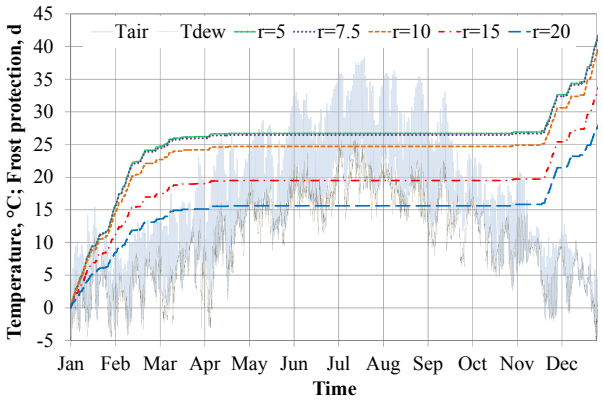


**Fig.7.** Frosting prevention as indicated by the accumulative days, owing to use of the DSHP

## CONCLUSIONS

This study has evaluated a dual source heat pump (DSHP), in order to demonstrate its potential benefits over conventional individual air-source heat pump (ASHP) or ground-source heat pump (GSHP). A combined use of two software, COMSOL and EnergyPlus, has been used to evaluate a dual air and ground source heat pump. The model has been put forward as a modification to an existing air source air conditioning plant, in order to find out the potential benefit of coupling a novel flat-panel horizontal ground heat exchanger (HGHE).

The simulation results show that an HGHE can be suitable for supplemental heat extraction or rejection and as an alternative of a conventional outdoor air unit, allowing more favourable working conditions. The installation of the innovative Flat-Panel HGHE offers an efficient and cost effective solution to the generally expensive ground heat exchanger. Use of a DSHP can reduce the required size of a ground heat exchanger, so the presented dual source heat pump may be fairly profitable. In addition, the switch between the air source and ground source can effectively alleviate the frosting issue which is a common issue for operation of a heat pump in the cold winter. The preliminary results by this study have provided a valuable information for further investigation.

## REFERENCES

1 M. Bottarelli, M. Bortoloni, Y. Su, Heat transfer analysis of underground thermal energy storage in shallow trenches filled with encapsulated phase change materials, *Applied Thermal Engineering*, 90, 1044–1051, (2015).

2 Hart, D. P., Couvillion, R., Earth-coupled Heat Transfer. National Water Well Association, (1986).
3 Z. Luo, C. Asproudi, Subsurface urban heat island and its effect on horizontal ground-source heat pump potential under climate change. *Applied Thermal Engineering*, 90, 530-537, (2015).
4 H. Yang, P. Cui, Z. H. Fang, Vertical borehole ground source heat pumps: a review of models and systems. *Applied Energy*, 87, 16–27 (2010).
5 H. Fujii, S. Yamasaki, T. Maehara, T. Ishikami, N. Chou, Numerical Simulation and Sensitivity Study of Double-Layer Slinky-Coil Horizontal Ground Heat Exchangers. *Geothermics*, 47, 61-68, (2013).
6 M. Bottarelli, A preliminary testing of a flat panel ground heat exchanger. *International Journal of Low-Carbon Technologies*, 8(2), 80-87, (2013).
7 F. Wang, G. Wang, Y. Zheng, Z. Lin, P. Hao, C. Huan, T. Wang, Performance investigation of a novel frost-free air-source heat pump water heater combined with energy storage and dehumidification. *Applied Ene*rgy, 139, 212-219, (2015).
8 P. Vocale, G. L. Morini, M. Spiga, Influence of outdoor air conditions on the air source heat pumps performance. *Energy Procedia*, 45, 653-662, (2014).
9 Y. J. Jang, H. B. Bae, J. S. Lee, Y. M. Ha, Continuous heating of an air-source heat pump during defrosting and improvement of energy efficiency. *Applied Energy*, 110, 9-16, (2013).
10 H. Wang, X. Liu, G. Feng, Z. Kang, Y. Luo, B. Bai, L. Chi, Simulation Analysis of Air-Ground Dual source Heat Pump operating efficiency. *Procedia Engineering*, 121, 1413-1419, (2015).
11 U.S. Department of Energy (DOE), Energy Savings from Dual-Source Heat Pump Technology. DOE/EE-0220, (2000). http://www.eren.doe.gov/femp
12 A. Chiasson, A feasibility study of a multi-source hybrid district geothermal heat pump system. *GHC Bullettin*, 9-14, (2011).
13 M. Bortoloni, Experimental analysis and numerical simulation of a Flat-Panel ground heat exchanger. Ph.D. Thesis, Ferrara: University of Ferrara, (2016).
14 D.B. Crawley, L. K. Lawrie, F. C. Winkelmann, W. F. Buhl et al., EnergyPlus: creating a new-generation building energy simulation program. *Energy and Buildings*, 33, 319-331 (2001).
15 M. Valarin, Applicazione del modello EnergyPlus per la valutazione delle prestazioni termiche di un edificio. Master's thesis, (2016).
16 EnergyPlus Documentation http://nrel.github.io/EnergyPlus

*Bulgarian Chemical Communications, Volume 48, Special Issue E (pp. 71 - 76) 2016*

# Simulation study of hybrid ground-source heat pump system with solar collectors

N. Vassileva[1], A. Georgiev[1,3], R. Popov[2*]

[1]*Technical University of Sofia, Plovdiv Branch, Department of Mechanics, 25 Tsanko Diustabanov Str, 4000 Plovdiv, Bulgaria*
[2]*Plovdiv University, Department of Electronics Telecommunications & Information Technologies 24 Tzsar Asen Str, 4000 Plovdiv, Bulgaria*
[3]*European Polytechnic University, Dept. of "Green Energy", 23 Kiril and Metodiy str., 2300 Pernik, Bulgaria*

A simulation model of a hybrid thermal heating and cooling system consisting of solar collectors, vertical borehole heat exchangers and heat pump is presented in this article. The system model is built in the "TRNSYS studio" simulation environment and allows to explore different modes of operation and to analyze an influence of system parameters on performance characteristics. The model describes the behavior of a real laboratory installation and will be used for the optimization of its operation and costs. TRNBuild application was used to design the building model and allowed sample way to change model properties. The developed model could be a useful tool in hybrid heating and cooling system design process. Simple procedure needed to adopt model to any different system size and components parameters.

**Keywords:** hybrid thermal systems, solar collectors, borehole heat exchangers, heat pump, TRNSYS model

## INTRODUCTION

By applying in geothermal heat pump installation solar thermal collectors a long term sustainable system is achieving. The operation of the Ground Source Heat Pump (GSHP) system with solar thermal collectors includes multiple physical processes. They are: building load dynamics, heat transfer in the soil, heat pump dynamics, and solar thermal processes. For each process a different timescale is required ranging from a decade to minutes. Energy efficient heating and cooling of the building is a system that includes in itself heat pumps coupled to vertical, closed-loop borehole heat exchangers (BHEs). This system is not economically advantageous. If the main operational mode is heating, then heat pump takes heat from the ground, which reduces the temperature near the borehole. By reducing the temperature of the soil the coefficient of performance (COP) of the heat pump is reduced, too. This requires the injection of solar energy into the borehole array to raise the soil temperature. The costs are reduced by incorporating a solar collector system to the BHE [1]. The hybrid GSHP systems with solar thermal collectors have the following advantages:

- they can potentially expand the residential Ground Source Heat Pump market by allowing reduced BHE footprint in both heating and cooling dominated climates;
- solar thermal collectors can be used to balance the ground loads over the annual cycle, thus making the BHE fully sustainable;
- in cooling dominated buildings, use of unglazed solar collectors as a heat rejecter allows for passive heat rejection, in contrast to a cooling tower that consumes a significant amount of energy to operate with stringent maintenance needs;
- in heating dominated buildings, the hybrid energy source (i.e., solar) is renewable, in contrast to a typical fossil fuel boiler or electric resistance heater as the hybrid component.

Fig.1 shows an example structure of a family house with a hybrid geothermal heat pump system and solar collectors [2].

The design of the hybrid thermal systems depends on time-variated functions driven by weather conditions, ground loop temperature history, and solar radiation availability [3]. Such systems are too complex and their design requires prior modeling in order to obtain optimum configuration and performance. For this purpose the simulation system has been developed by using commercial software TRNSYS. It is flexible software designed to simulate the properties of transition processes in hybrid systems [4].

In this article a simulation model of a hybrid thermal heating and cooling system consisting of solar collectors, vertical BHE and heat pump is developed. The model may be easy modified and adopted to any system components size, parameter values and specific climate conditions.

* To whom all correspondence should be sent:
rum_pop@yahoo.com

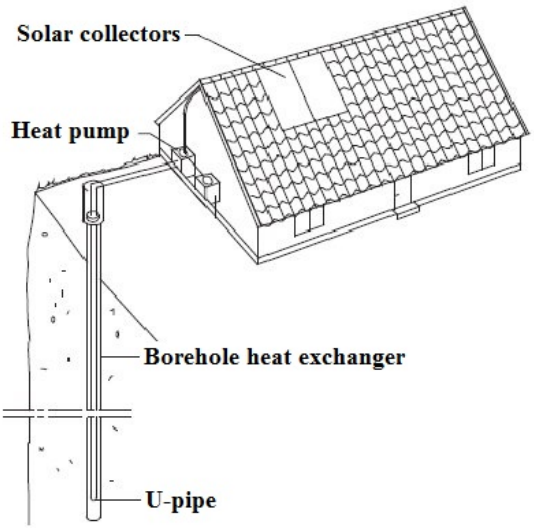


**Fig.1.** Example of a family house with hybrid Ground Source Heat Pump system and solar collectors [2]

## SYSTEM COMPONENTS

A hybrid GSHP system with solar thermal collectors was constructed in the Technical University of Sofia, Plovdiv Branch. The principal scheme of the hybrid system is presented in Fig.2. The main system components are listed below.

*Solar collectors:*

- manufactured by PK Select-CL "Sun system" Ltd Bulgaria; flat glazed type;
- 3 pieces, each with 2,15m$^2$ cooper absorption surface;
- transparent coating of prismatic tempered glass with a thickness of 4,2 mm;
- 8 pieces heat-absorbing pipes;
- coefficient of absorption – 95%;
- coefficient of reflection – 5%;
- heat carrier – 10/90% water/propylene-glycol solution;
- the volume of heat transfer medium in the collector is 1,6 l with maximum flow rate of 50 l/m$^2$h;
- mineral wool with a thickness of d = 40mm is used for the insulation.

*Borehole heat exchangers (BHEs):*

- two borehole heat exchangers;
- the distance between the boreholes is 13m;
- borehole diameter is 165 mm;
- the boreholes depth is 50m;
- piping of high density polythene (HDPE) PE100 type with outside diameter of 32mm were inserted in the boreholes;
- single (first borehole) and double (second borehole) U-pipe construction;
- backfilled with grout material; piping of HDPE PE100 type with outside diameter of 32 mm were inserted in the boreholes;

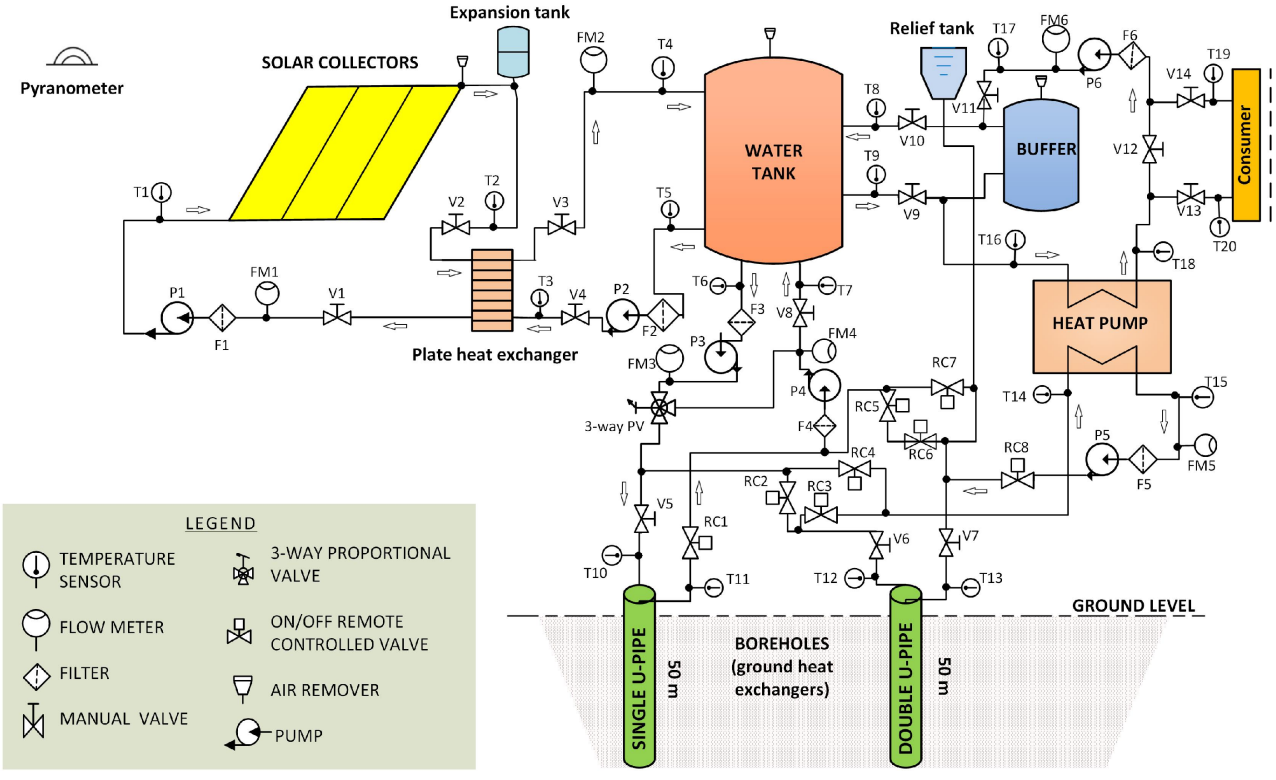


**Fig.2.** Schematic diagram of the hybrid Ground Source Heat Pump installation [5]

- single (first borehole) and double (second borehole) U-pipe construction;
- backfilled with grout material;
- the structure of the ground layers consists mainly of sands with different site of grains, clay and some gravel;
- the borehole thermal resistance and the ground thermal conductivity have been evaluated by a thermal response test (TRT); a device for it was developed at the TU-Sofia, Plovdiv Branch [6].

*Heat pump:*

- "Maxa" (Italy) heat pump model HWW-A/WP15 is used;
- heat pump type: water-water;
- maximum absorbed power– 1,2 kW (electrical);
- nominal cooling capacity – 4,6 kW;
- nominal heating capacity – 5,9 kW;
- compressor type – one rotary Scroll;
- oil charge – 0,4 kg;
- weight – 77 kg;
- power supply – 230 V, 50 Hz, single phase;
- refrigerant – 0,5 kg of R410A;
- input/ output connection diameter - 1 inch.

*Heating conditions of the heat pump*:

- temp. in/ out on condenser +40/45 °C;
- temp. in/ out on evaporator +15/10 °C.

*Cooling conditions of the heat pump*:

- temp. in/ out on condenser + 15/ 35 °C;
- temp. in/ out on evaporator +12/7 °C.

## SYSTEM SIMULATION

For the system simulation commercial software TRNSYS [7] was used. In examining the various systems the following parameters are to be determined [2]:

- the net heat extraction from the ground;
- the use of electricity;
- the lowest and mean temperatures to the evaporator;
- the savings of electricity;
- the seasonal performance factor (SPF) of the system and coefficient of performance (COP) of the heat pump.

The structural components used in the system are listed below.

*House Model*

In creating building model component weather data reader and radiation processor Type 109, have been selected. Weather data for Plovdiv, BG (BG-Plovdiv-156250.tm2) are used. Type 109 is reading weather data from a data file at a regular time intervals, and converting it to a desired system of units. Then the processing of solar radiation data to obtain the tilted surface radiation and angle of surfaces incidence is performed for an arbitrary number of surfaces. This component is using a typical meteorological year format TMY2 [8].

The model of the house was designed in TRNBuild. Main house properties are listed in Table 1. To create files using the component type 56 generated with TRNBuild, the parameters are determined for the input variables. To create the model still additional components are necessary. They serve to process the data from the house:

Type 33 (Psychometrics) – calculates the corresponding wet bulb temperature and percent relative humidity and obtains the dry bulb temperature and relative humidity from weather data;

Type 69 – calculates the effective sky temperature for long-wave radiation exchange;

Type 667b – in this module, the fresh air temperature and relative humidity is fed by weather data component;

Type 24 – the Quantity Integrator was used to calculate the accumulated energy demand of different zones as well as the total accumulated energy demand of the house.

**Table 1.** Main house properties

| Zone | Main properties |
|---|---|
| Basement | area of 67 $m^2$; volume of 201 $m^3$ |
| 1-st floor | area of 155 $m^2$; volume of 464 $m^3$ |
| 2-nd floor | area of 117 $m^2$; volume of 350 $m^3$ |
| Attic | area of 120 $m^2$; volume of 240 $m^3$ |

*Heat Pump Model*

The water source heat pump model uses component of type 505. A single-stage liquid source heat pump, which works in two modes heating and cooling, is modeled through it. The heat pump model is designed for residential GSHP application [9]. This model is based on user delivered data files having catalogue data for the capacity and power, based on heat pump, the air flow rate, and the speed of flow rate setting up [10].

*Borehole Heat Exchanger Model*

To make the model of BHE thermally connected to the ground the component type 557 have been used. This component describes both: the vertical U-tube and vertical tube-in-tube heat exchangers. The soil temperature around BHE is calculated from the three parts: a local solution, a global temperature, and a steady-flux solution. The steady-flux solution is derived analytically, to solve local

and global problems using finite-difference method. The superposition method is used to calculate the resulting temperature. This component was created by Department of Mathematical Physics at the University of Lund, Sweden [10, 11]. In this model four layers of ground are described. To calculate storage volume equation (1) is used [12].

$$Storage\ Volume = \pi \times Number\ of\ Boreholes \times Borehole\ Depth \times (0{,}525 \times Borehole\ Spacing)^2 \quad (1)$$

$$Storage\ Volume = 14633\ m^3$$

A backfilled borehole with grout material (mixture of cement and bentonite with factor 0,5) was used to enhance the thermal transfer between the tubes and ground.

*Solar Collector Model*

Type 1 is used for modeling the thermal characteristics of system which consists of three connected flat-plate solar collectors. The incidence angle modifier is calculated by quadratic function Eqn. (2). From ASHRAE or an equivalent test the coefficients of the function (2) are presented [12]. Standard test for efficiency of the collector is compiled by a ratio of fluid temperature minus the ambient temperature to solar radiation. The temperature of the fluid is obtained by averaging the temperature of the inlet and outlet temperatures. The Hottel-Whillier equation [13] is used as a general equation of solar collector efficiency.

$$Modifier = a_0 - a_1 \frac{\Delta T}{L_T} - a_2 \frac{(\Delta T)^2}{L_T}, \quad (2)$$

where:

$\Delta T$ is the difference between the inlet and ambient temperatures, °C;

$L_T$ radiation is trapped on the solar collector, kJ/h.m$^2$;

$a_0$, $a_1$, $a_2$ are thermal efficiency coefficients [14].

*Water Tank Model*

Component Type 4 is selected for this model. It is intended to stratified storage tank with variable inlets and uniform losses. A water tank which comprises N (N = 6) fully-mixed equal volume segments is selected. The degree of stratification determined N. The storage tank can operate in one of three modes. The heat source for the water tank is water from the heat pump.

*Ventilation Model*

For the modeling of ventilation in the house component Type 667b is used. It is of air-to-air heat recovery type. As an input parameters a relative humidity, ambient temperature, flow rate and the second floor temperature are used in this model. Relative humidity and temperature of the HRV are outputs of the module.

Fig.3 shows the complete model of the hybrid system composed in TRNSYS studio.

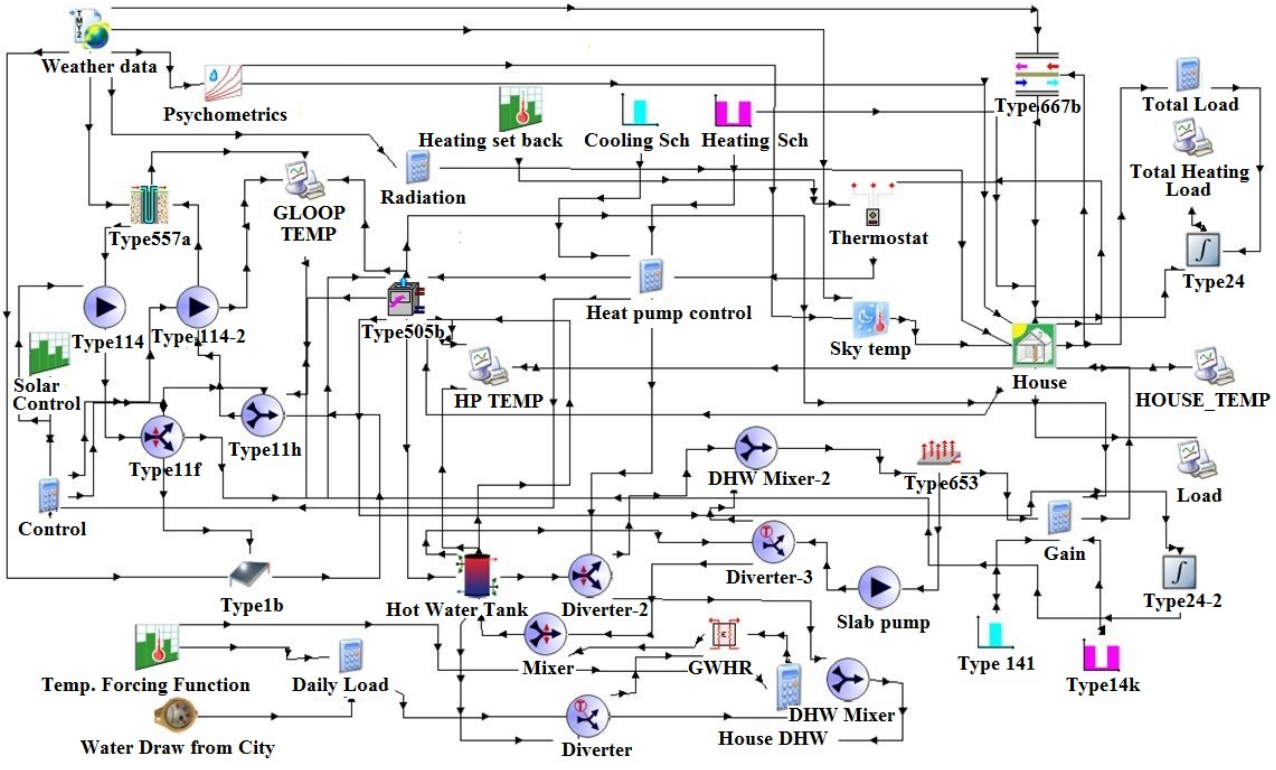


**Fig.3.** The structure of the model in TRNSYS Simulation Studio

## SIMULATION RESULTS

In this study, the energy simulations run in the case with fixed solar collectors and GSHP. The house model describes four zones: basement (zone volume of 201 $m^3$), 1-st floor (zone volume of 464 $m^3$), 2-nd floor (zone volume of 350 $m^3$) and attic (zone volume of 240 $m^3$). The simulated heating load values for different zones as well as the total energy heating demand are presented on Fig.4. It may be mentioned that the main part of the heating power is spent for two zones: 1-st floor and 2-nd floor. The attic is not heated. The basement is heated, but at a lower temperature settings in a temperature controller.

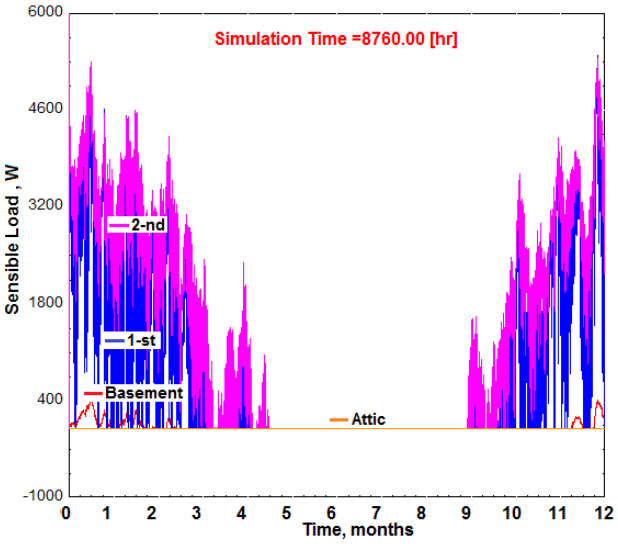


**Fig.4.** Simulated heating load for one typical year

Total heating energy demand of the house has been calculated by the integration of power in different zones and then by summing. Estimated annual values are shown in Fig.5. Yearly a quantity of 19,5 MJ required for the house heating.

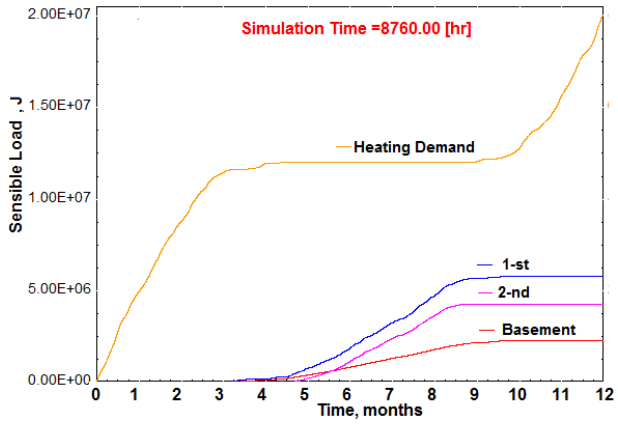


**Fig.5.** Simulated annual total heating and cooling demands

The annual cooling demand of the first, second floors and the basement has been calculated. The reported values are 5,8 MJ, 3,6 MJ and 2,2 MJ accordingly. The yearly simulation results for temperature values at different zones are shown in Fig.6. High quality of regulation may be observed. The temperature values in regulated areas vary in 1 degree region.

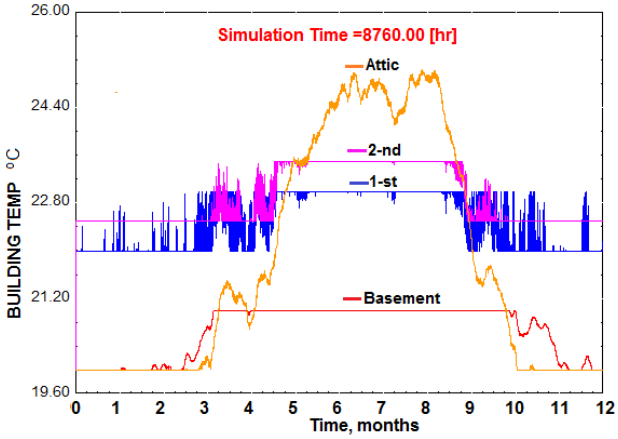


**Fig.6.** Yearly simulation of temperature values at different zones

## CONCLUSIONS

A hybrid geothermal heat pump system with solar thermal collectors was constructed in the Technical University of Sofia, Plovdiv Branch. Simulation model of such systems have been developed in TRNSYS Simulation Studio. Running simulations showed that ground source heat pump systems with solar collectors are very perspective solution in a high efficiency building heating and cooling installations. The following conclusions have been made:

1. The developed model could be a useful tool in hybrid heating and cooling system design process. Simple procedure needed to adopt model to any different system size and components parameters. The designer has only to change: the building plane and requirements; the type, size and parameters of the solar collectors, boreholes; heat pump; and the weather data;

2. A thermal response test (TRT) has to be previously performed for the purpose of validation of the borehole model parameters;

3. Additional experimental works in each design case are needed to validate model parameters;

4. System energy simulations carried out by the model allow the designer to optimise system components size and to reduce the costs;

5. The developed model may be used to optimize modes of system operation and to build and approve new control algorithms that lead to higher energy efficiency.

## ACKNOWLEDGEMENTS

This work has been supported financially by the research project 152ПД0045-24/ 26.03.2015 and the research project 152ПД0046-24/ 27.03.2015 of the Technical University of Sofia, which is gratefully acknowledged by the authors.

## REFERENCES

1 Chiasson, A.D., C. Yavuzturk, Simulation of Hybrid Solar-Geothermal Heat Pump Systems. PROCEEDINGS, Thirty-Ninth Workshop on Geothermal Reservoir Engineering Stanford University, Stanford, California, February 24-26, 2014 SGP-TR-202.

2 Kjellsson E., Hellström G., Perers B., Optimization of systems with the combination of ground-source heat pump and solar collectors in dwellings. Energy 35 (2010) 2667–2673.

3 ASHRAE. 2008: Technical Research Project 1384, Development of Design Guidelines for Hybrid Ground-Coupled Heat Pump Systems. American Society of Heating, Refrigerating, and Air-Conditioning Engineers, Atlanta, GA.

4 Klein S.A. et al., TRNSYS manual, a transient simulation program, Madison: Solar Engineering Laboratory, University of Wisconsin-Madison; (1996).

5 TOSHKOV E., Build-up of hybrid installation with ground source heat pump and solar collectors. Technical university Varna Edition, Thermo techniques, year 4, book 2, 2013, ISSN 1314-2550, pp. 24-27

6 Georgiev A., Tabakova S., Popov R. The Bulgarian Experience in the Thermal Response Tests, Proc. of World Geothermal Congress 2010, Bali, Indonesia, 25-29 April 2010, Nusa Dua - Bali, Indonesia, 2924.pdf.

7 Klein SA, Beckman WA, Mitchell JW, Duffie JA, Duffie NA, Freeman TL, et al. TRNSYS 16 – a transient system simulation program. Madison, USA: Solar Energy Laboratory, University of Wisconsin; June 2006.

8 NREL, National Renewable Energy Laboratory, US Department of Energy. http://www.nrel.gov/

9 TRNSYS 16 Manual, TESS library Ver.2, 2004

10 Essential Innovation Technology Corp., EI Geo-Exchange system, Surrey, BC, Canada, 2005, http://www.eitechcorp.com

11 Hellstrom, G., “Duct Ground Heat Storage Model, Manual for Computer Code,” Department of Mathematical Physics, University of Lund, Sweden.

12 TRNSYS Manual, a Transient Simulation Program, Version 15 and 16. Solar Engineering laboratory, University of Wisconsin-Madison, 2000 and 2004.

13 Duffie, JA, and Beckman, W.A., “Solar Engineering of Thermal Processes”, Wiley Publication, 1991.

14 ASHRAE Standard 93-2003 “Methods of testing to determine the performance of solar collectors”, ASHRAE, Atlanta, 2003.

*Bulgarian Chemical Communications, Volume 48, Special Issue E (pp. 77 - 87) 2016*

# Performance study of a parabolic trough solar collector with an inner radiation shield

Qiliang Wang[1], Gang Pei[*,1], Yang Honglun[1], Anjum Munir[2], Hu Mingke[1]

[1] *Department of Thermal Science and Energy Engineering, University of Science and Technology of China, Hefei 230027, China*

[2] *Department of Energy Systems Engineering, University of Agriculture, Faisalabad-Pakistan*

Parabolic trough collectors (PTCs) have become the most popular technology to harvest solar energy in high-temperature solar thermal utilization areas. The evacuated tube used as the receiver of PTC is the key part and has the highest temperature in the entire system. Heat loss occurs in the evacuated tube at high temperature mainly through thermal radiation, when heat convection and heat conduction are ignored under vacuum condition. This study is a preliminary investigation of a new idea to decrease heat loss by introducing an inner radiation shield at the upper annular vacuum gap, which does not receive concentrated radiation from the parabolic mirrors but receives sunlight directly from the sun. The study presents numerical performance evaluation and comparative analyses based on numerical simulation with and without radiation shields under different environmental conditions, involving the factors of ambient temperature, wind speed, solar irradiance, and so on. The numerical simulation relies on the spectrum parameter model of radiation heat transfer, which has been rarely applied in previous PTC analyses. Results show that, when the working temperature is higher than the critical temperature, the evacuated tube with a radiation shield leads to less radiation heat loss than that without a shield. The converse result is obtained when the working temperature is lower than the critical temperature. The critical temperature is 285 °C in this study when the ambient temperature, wind speed, and solar irradiance are 15 °C, 2.5 m/s, and 800 W/m$^2$, respectively. When the working temperatures of the tube are 300, 400, 500, and 600 °C, the heat losses from the evacuated collector with a shield are 6.1%, 18.0%, 23.4%, and 25.8% less than the heat losses from that without a shield, respectively.

**Keywords:** solar energy, parabolic trough collector, radiation shield, heat loss

## INTRODUCTION

Parabolic trough collectors (PTCs) represent an advanced technology to harvest solar energy to generate high heat flux, and are applied popularly to areas of solar thermal utilization with high temperature, such as solar thermal power generation system, solar cooling, and solar desalination [1–4].

The evacuated receiver as the key part of PTC is mainly composed of a metal absorber tube with a solar selective absorbing coating on its outer surface, a glass envelope, glass-metal sealing, and a metal bellow [5–6]. To reduce the heat loss by conduction and convection, the annular gap between the metal absorber and the glass envelope is pumped up to vacuum state. In particular, the heat loss that the energy transfers from the receiver to the environment is the sum of heat transfer from the glass envelope, metal bellow, and absorber tube to environment. Moreover, the heat loss of the evacuated receiver is one of the most important parameters to indicate the performance of the receiver, and is a large part of the total heat loss of PTC [5, 7–8]. In reality, the operating temperature can be as high as 400 °C in the system of solar thermal power generation [9]; accordingly, the selective sunlight-absorbing surface coating on the outer surface of the absorber tube is diminished with the increase of temperature because of its higher average emittance in the entire band [10]. This phenomenon leads to excessive radiation losses including that from the absorber tube to the glass envelope and that from the absorber tube through the glass envelope directly to the sky. Specifically, the heat loss of the evacuated receiver deteriorates considerably, thereby resulting in low system operating efficiency. Thus, investigating the heat loss of evacuated receivers is important.

Researchers in relevant fields have attempted to reduce the heat loss of evacuated receivers by improving the performance of selective coating on the absorber tube that possesses low emittance and evacuating the annular of the receiver [11–13]. Another easy and effective way proposed by researchers is introducing a radiation shield to a certain position of vacuum annular, wherein the radiant heat loss intercepted by the radiation shield is larger than the solar irradiation intercepted by the radiation shield. Hany Al-Ansary et al. [14–15] introduced a new PTC with gas-filled annuli. The main idea is to fill the outward-facing half of the gas-filled annulus with a heat-resistant insulating material (fiberglass). They simulated the conduction and convection heat losses from a new PTC receiver and compared them with a conventional receiver with an air-filled annulus. The comparison showed that the heat loss from a

* To whom all correspondence should be sent:
peigang@ustc.edu.cn

receiver using this technique was reduced by a maximum of approximately 25%. Zhang et al. [16] investigated direct-flow coaxial evacuated-tube solar collectors with and without heat shields by experimental performance evaluation and comparative analyses. The test showed that the evacuated tube collector with heat shield had higher optical efficiency, lower heat loss, and better thermal performance compared with that without heat shield.

The PTC receiver intercepts and absorbs the majority of concentrated sunlight at its lower portion, as well as sunlight directly from the sun with low energy density at its upper portion. This fact can be considered to design a new evacuated receiver by introducing a radiation shield to the upper portion of the receiver.

The study investigates the heat loss of two kinds of new evacuated receivers with radiation shields. The study creates a spectrum parameter model of radiation heat transfer, associating the spectral emittance of selective sunlight-absorbing coating and spectral transmittance of the glass envelope. The heat loss by radiation from the absorber tube through the glass envelope to the sky, which is rarely mentioned in previous studies, is also simulated. The simulation is conducted by employing the measurement of the radiation resistance network. The study also presents the numerical evaluation of the heat loss of evacuated tubes with and without radiation shields under different environment conditions and conducted a comparison analysis on both.

## SIMULATION MODELS

As stated previously, a radiation shield is introduced to a receiver at the upper outward-facing portion of the vacuum annular space. In this space, the absorber only absorbs the direct solar irradiance. The angle at which the radiation shield surrounds the absorber is set as 120°, the reason for this angle is that the sunlight reflected from the parabolic mirror is ensured to be not intercepted by the radiation shield, as shown in Fig.1. The evacuated receiver without a radiation shield and the two kinds of evacuated receivers with radiation shields are named original evacuated receiver, evacuated receiver I, and evacuated receiver II, for ease of investigation. Evacuated receivers I and II differ in terms of the outer surface material of their radiation shields, selective sunlight-absorbing coating, and polished metal surface. Their inner surfaces are polished metal.

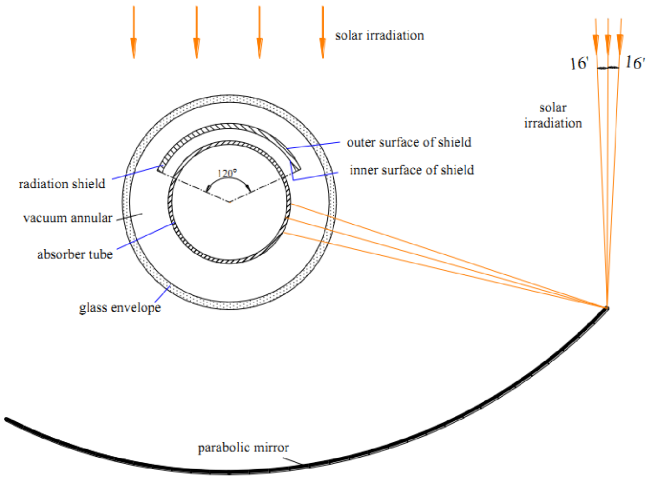


**Fig.1.** Shcematic cross-section diagram of the PTC system with a new evacuated receiver

The following assumptions are made to simplify the model: ① The heat loss of two ends of the receiver and metal bellow is disregarded, that is, the radiation heat transfer of the evacuated receiver is a 1D heat transfer model. ② The temperature gradient of the glass envelope is ignored because of its thinness. ③ All the involved surfaces in this study are diffusing surfaces. ④ The little natural convection and air conduction in the vacuum annular gap can be satisfied when high vacuum is guaranteed. ⑤ The parabolic trough mirror and concentrated sunlight from the mirror need not reflect in the model because no mutual influence exists between them and the radiation shields. Another reason is that the model is performed under simulated condition in the laboratory. The simplified 1D heat transfer models of the original and new-type receivers are shown in Fig.2.

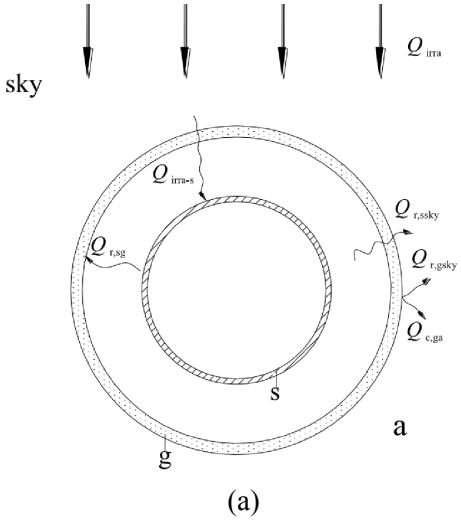


(a)

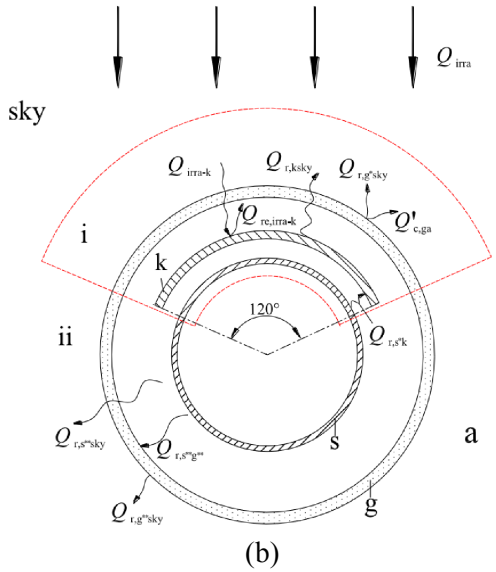


**Fig.2.** 1D heat transfer model. (a) heat transfer radial cross-section of original receiver, and (b) heat transfer radial cross-section of new-type receiver

### *Radiation heat transfer model and total heat loss computation model*

Simulating the total heat losses of the original and new-type evacuated receivers numerically is the key component to compare and analyze the performance between the two. Radiation heat transfer between the absorber and the sky should also be considered. A large amount of radiation heat losses from the absorber are obtained through the glass envelope directly to the sky, when the PTC receiver operates with a high temperature. This phenomenon occurs because of the increase of radiation power in the solar spectrum wavelength band on the absorber surface. A radiation heat transfer model that employs spectral parameters is established to accurately calculate total heat loss and radiation heat loss between the absorber and the sky. The model is based on a formula derivation of radiation heat transfer by Holman J P [17]. Fig.3 shows the radiation resistance network of the original receiver. The thermal resistances of this receiver are presented in Table 1.

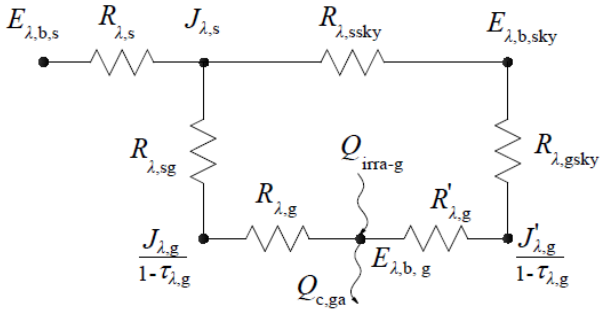


**Fig.3.** Radiation resistance network of original evacuated receiver

**Table 1.** Values of equivalent resistances of original evacuated receiver

| | |
|---|---|
| $R_{\lambda,s}$ | $(1-\varepsilon_{\lambda,s})/(\varepsilon_{\lambda,s}A_s)$ |
| $R_{\lambda,sg}$ | $1/[A_sF_{sg}(1-\tau_{\lambda,g})]$ |
| $R_{\lambda,gsky}$ | $1/[A_gF_{gsky}(1-\tau_{\lambda,g})]$ |
| $R_{\lambda,ssky}$ | $1/(A_sF_{ssky}\tau_{\lambda,g})$ |
| $R_{\lambda,g}$ | $\rho_{\lambda,g}/[\varepsilon_{\lambda,g}A_g(1-\tau_{\lambda,g})]$ |
| $R'_{\lambda,g}$ | $\rho_{\lambda,g}/[\varepsilon_{\lambda,g}A_g(1-\tau_{\lambda,g})]$ |

To effectively describe and interpret the model mechanism with and without radiation shield, the new-type evacuated receiver is divided into two parts, as shown in Fig.2b. The part surrounded by a red dotted line is called i-zone, and the other part is called ii-zone. The radiation shield in the i-zone of the new-type evacuated receiver corresponds to a new thermal resistance added to the radiation heat resistance network of the original evacuated receiver, as shown in Fig.4. Table 2 presents the corresponding thermal resistances of the new-type evacuated receiver.

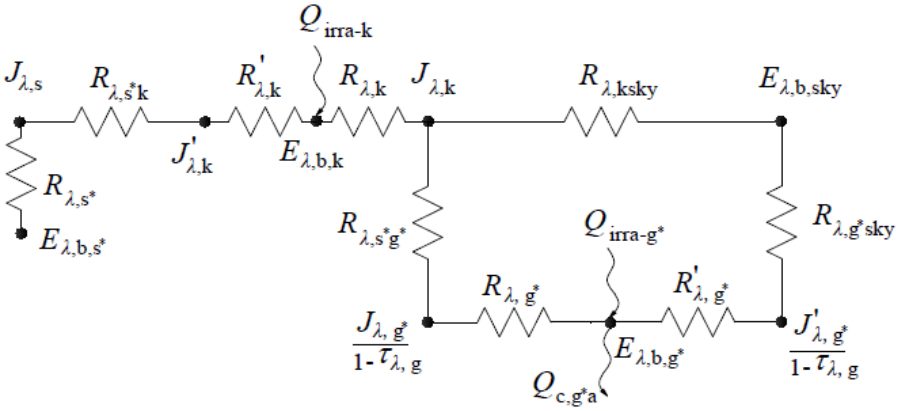


**Fig.4.** Radiation resistance network in i-zone of new-type evacuated receiver

**Table 2.** Values of equivalent resistances in i-zone of new-type evacuated receiver

| | |
|---|---|
| $R_{\lambda,s^*}$ | $(1-\varepsilon_{\lambda,s})/(\varepsilon_{\lambda,s}A_{s^*})$ |
| $R_{\lambda,s^*k}$ | $1/(A_{s^*}F_{s^*k})$ |
| $R_{\lambda,k}$ | $(1-\varepsilon_{\lambda,ko})/(\varepsilon_{\lambda,ko}A_k)$ |
| $R'_{\lambda,k}$ | $(1-\varepsilon_{\lambda,ki})/(\varepsilon_{\lambda,ki}A_k)$ |
| $R_{\lambda,kg^*}$ | $1/[A_kF_{kg^*}(1-\tau_{\lambda,g})]$ |
| $R_{\lambda,g^*sky}$ | $1/[A_gF_{g^*sky}(1-\tau_{\lambda,g})]$ |
| $R_{\lambda,ksky}$ | $1/(A_kF_{ksky}\tau_{\lambda,g})$ |
| $R_{\lambda,g^*}$ | $\rho_g/[\varepsilon_{\lambda,g}A_{g^*}(1-\tau_{\lambda,g})]$ |
| $R'_{\lambda,g^*}$ | $\rho_{\lambda,g}/[\varepsilon_{\lambda,g}A_{g^*}(1-\tau_{\lambda,g})]$ |

All property parameters of materials including $\varepsilon_{\lambda,g}$, $\tau_{\lambda,g}$, $\rho_{\lambda,g}$, $\varepsilon_{\lambda,ki}$, $\varepsilon_{\lambda,ko}$, and $\varepsilon_{\lambda,s}$, are the functions of wavelength $\lambda$, as well as the equivalent thermal resistances and emissive power of blackbody related to the parameters. The values of all property parameters, continuously assigned from 0.36 μm to 100.20 μm per fraction of 0.1 μm, are substituted in networks shown in Fig.2 and Fig.3. The relevant temperatures, including $T_a$, $T_{sky}$, $T_s$, $T_g$, and $T_k$, are also essential in solving the models. The emissive power of the blackbody at each node can be obtained from the results of the models. Accordingly, radiation heat flux per unit wavelength at each line of network can be achieved. Table 3 lists the radiation heat flux of each part of the system, that is, the accumulation of radiation heat flux from 0.36 μm to 100.20 μm per fraction of 0.1 μm.

Similarly, the radiation heat transfers in the ii-zone of new-type evacuated receiver, including that between the absorber and the sky, that between the absorber and the glass envelope, and that between the glass envelope and the sky, can be determined by computing the aforementioned heat loss model of the original receiver. Then, the three radiation heat fluxes by integrating both radiation heat fluxes of the i-zone and ii-zone of the new-type evacuated tube can be expressed as

$$Q'_{r,gsky} = Q_{r,g^*sky} + Q_{r,g^{**}sky} \quad (1)$$

$$Q'_{r,(sk)g} = Q_{r,s^{**}g^{**}} + Q_{r,kg^*} \quad (2)$$

$$Q'_{r,(sk)sky} = Q_{r,s^{**}sky} + Q_{r,ksky} \quad (3)$$

The total heat losses of the original and new-type evacuated receivers are as follows:

$$Q_{loss} = Q_{r,gsky} + Q_{c,ga} + Q_{r,ssky} \quad (4)$$

$$Q'_{loss} = Q'_{r,gsky} + Q'_{c,ga} + Q'_{r,(sk)sky} + Q_{re,irra-k} \quad (5)$$

**Table 3.** Radiation heat fluxes of all parts of system

| Types of evacuated receiver | Radiation heat flux |
|---|---|
| Original evacuated receiver | $Q_{r,ssky} = \sum_{\lambda=0.36}^{100.20} \frac{J_{\lambda,s} - E_{\lambda,b,sky}}{R_{\lambda,ssky}} \times 0.1$ |
| | $Q_{r,sg} = \sum_{\lambda=0.36}^{100.20} \frac{J_{\lambda,s} - E_{\lambda,b,g}}{R_{\lambda,sg} + R_{\lambda,g}} \times 0.1$ |
| | $Q_{r,gsky} = \sum_{\lambda=0.36}^{100.20} \frac{E_{\lambda,b,g} - E_{\lambda,b,sky}}{R_{\lambda,gsky} + R'_{\lambda,g}} \times 0.1$ |
| | $Q_{irra-s} = A_s\alpha_{\lambda,s}\tau_{\lambda,g} \times Q_{irra}$ |
| i-zone of new-type evacuated receiver | $Q_{r,ksky} = \sum_{\lambda=0.36}^{100.20} \frac{J_{\lambda,k} - E_{\lambda,b,sky}}{R_{\lambda,ksky}} \times 0.1$ |
| | $Q_{r,kg^*} = \sum_{\lambda=0.36}^{100.20} \frac{J_{\lambda,k} - E_{\lambda,b,g^*}}{R_{\lambda,kg^*} + R_{\lambda,g^*}} \times 0.1$ |
| | $Q_{r,g^*sky} = \sum_{\lambda=0.36}^{100.20} \frac{E_{\lambda,b,g^*} - E_{\lambda,b,sky}}{R_{\lambda,g^*sky} + R'_{\lambda,g}} \times 0.1$ |
| | $Q_{r,s^*k} = \sum_{\lambda=0.36}^{100.20} \frac{J_{\lambda,s^*} - E_{\lambda,b,sky}}{R_{\lambda,s^*k} + R'_{\lambda,k}} \times 0.1$ |
| | $Q_{irra-k} = A_k\varepsilon_{\lambda,ko}\tau_{\lambda,g} \times Q_{irra}$ |
| | $Q_{re,irra-k} = A_k(1-\varepsilon_{\lambda,ko})\tau_{\lambda,g} \times Q_{irra}$ |

Iterative computation is applied to calculate the heat loss model based on the thermal equilibrium state of the evacuated receiver. For the new-type receiver, two quantitative expressions are used to model calculation with the given variables $T_s$, $T_g$, and $T_k$. The two expressions incorporate the thermal equilibrium equations of the glass envelope and the radiation shield, as shown in (6) and (7). However, for the original receiver, using one quantitative expression, that is, thermal equilibrium of glass envelope, is enough. This expression is related to the given variables $T_s$ and $T_g$, and is presented as (8).

$$Q_{r,ksky} + Q_{r,kg^*} = Q_{r,s^*k} + Q_{irra-k} \quad (6)$$

$$Q'_{r,gsky} + Q'_{c,ga} = Q'_{r,(sk)g} + Q_{re,irra-k-g^*} + Q_{irra-g} \quad (7)$$

$$Q_{r,gsky} + Q_{c,ga} = Q_{r,sg} + Q_{irra-g} \quad (8)$$

where $Q_{re,irra-k-g^*}$ refers to solar energy reflected from the radiation shield absorbed by the glass

envelope, that is, it is the product of absorptivity of the glass envelope and $Q_{\text{re,irra-k}}$.

*Spectral emissive power*

The spectral emissive power of each part of the system, which plays an important linkage role in the calculation of models, is solved by the algorithm of blackbody spectral emissive power [18], as shown in Equation (9).

$$E_{\lambda,\text{b}}(\lambda,T)=\pi I_{\lambda,\text{b}}(\lambda,T)=\frac{C_1}{\lambda^5\{\exp[C_2/(\lambda T)]-1\}} \quad (9)$$

where $T$ is the absolute temperature of the blackbody (K). The first and second radiation constants are $C_1$=3.742 × $10^8$ W·μm$^4$/m$^2$ and $C_2$=1.439 × $10^4$ μm·K. $I_{\lambda,\text{b}}(\lambda,T)$ is the blackbody spectral intensity and is expressed as

$$I_{\lambda,\text{b}}(\lambda,T)=\frac{2hc_0^2}{\lambda^5\{\exp[hc_0/(\lambda kT)]-1\}} \quad (10)$$

where $h$=6.626 × $10^{-34}$ $J$·s and $k$=1.381 × $10^{-34}$ $J$/K are the universal Planck and Boltzmann constants, respectively; $c_o$ =2.998 × $10^8$ m/s is the speed of light in a vacuum.

Then, the different spectral emissive powers restricted to a certain wavelength, including $E_{\lambda,\text{b,s}}$, $E_{\lambda,\text{b,g}}$, $E_{\lambda,\text{b,k}}$, and $E_{\lambda,\text{b,sky}}$, can be obtained with several related temperatures.

*Convection heat transfer*

Apart from radiation heat transfer between the glass envelope and ambient, convection heat transfer between the outer surface of the glass envelope and ambient is also an important mode of heat loss in the glass envelope, and is expressed as follows:

$$Q_{\text{c,ga}}=h_c(T_\text{g}-T_\text{a})A_\text{g} \quad (11)$$

For an isothermal cylinder, $h_{\text{c,}}$ the convection heat transfer coefficient of air around the horizontal glass envelope is expressed in the following form:

$$h_c=\frac{K}{D_\text{g}}Nu_D \quad (12)$$

When wind velocity is less than 0.1 m/s, wind flow around the PTC receiver can be regarded as natural convection. Nusselt number $N_{\text{uD}}$ can be expressed as

$$Nu_D=\{0.60+\frac{0.387Ra_\text{D}^{1/6}}{[1+(0.559/Pr)^{9/16}]^{8/27}}\}^2 \quad (13)$$

By contrast, wind flow around the PTC receiver can be regarded as forced convection when wind velocity is higher than or equal to 0.1 m/s. The corresponding expression of Nusselt number is

$$Nu_\text{D}=CRe_\text{D}^m Pr^n(\frac{Pr}{Pr_\text{s}})^{1/4} \quad (14)$$

where values of $C$ and $m$ are listed in Table 4. If $Pr\leq 10$, then n=0.37; if $Pr>10$, then n=0.36.

**Table 4.** Values of $C$ and $m$ with changes of $Re_\text{D}$

| $Re_\text{D}$ | $C$ | $m$ |
|---|---|---|
| 0.4–40 | 0.75 | 0.4 |
| 40–1000 | 0.51 | 0.5 |
| 1000–2×$10^5$ | 0.26 | 0.6 |
| 2×$10^5$–$10^8$ | 0.076 | 0.7 |

## INVESTIGATION ON Φ102 EVACUATED RECEIVERS AND RESULT ANALYSIS

The Φ102 evacuated receiver provided by Beijing Jindu Solar Energy Tech. Co. Ltd. is used in this study.

*Basic parameters of φ102 evacuated receiver*

**Table 5.** Materials of Φ102 evacuated receiver

| Name | Material | Dimension |
|---|---|---|
| Outer tube | High borosilicate glass | External diameter: 102 mm<br>Internal diameter: 97 mm |
| Absorber | SUS304 stainless steel | External diameter: 51 mm<br>Internal diameter: 48 mm |
| Radiation shield | Aluminum sheet | Diameter: 66 mm<br>Angle: 120° |

The length of the Φ102 evacuated receiver is 1.98 m and its basic parameters are presented in Table 5. Fig.5a shows the curve of spectral absorptivity of selective sunlight-absorbing coating on the outer surface of the absorber and radiation shield. Fig.5b shows the curve of spectral transmittance of the glass envelope. The emittance of polished aluminum surface is reported in the literature [18].

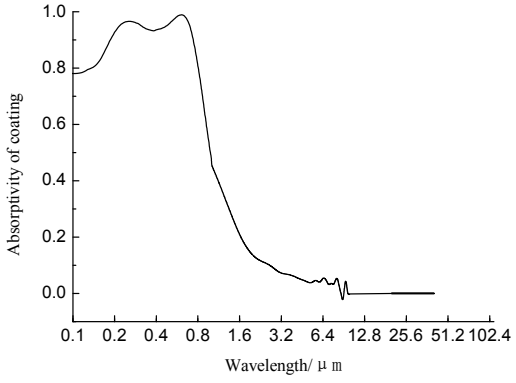


(a)

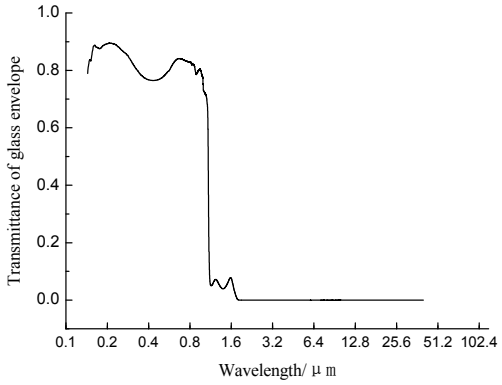


(b)

**Fig.5.** Spectral properties of physical parameters. (a) spectral absorptivity of selective sunlight-absorbing coating, and (b) spectral transmittance of glass envelope

*Analysis of results of heat loss model*

The heat loss model in this study is applicable to the test platform under laboratory conditions. The model is based on the investigation of the performance of Schott 2008 PTR70 PTC receiver conducted by NREL [19]. Thus, $T_a$ is equal to $T_{sky}$ under laboratory.

When the ambient temperature, wind speed, and solar irradiance are set as 15 °C, 2.5 m/s, and 800 W/m$^2$, the heat loss simulations of the original and new-type receivers are conducted at different absorber temperatures varying from 160 °C to 600 °C at 20 °C intervals. The simulation results (40 °C intervals) are presented in Table 6 and Fig.6.

**Table 6.** Results of heat loss model

| $T_s$/°C | Original receiver | | Receiver I | | | | Receiver II | | | |
|---|---|---|---|---|---|---|---|---|---|---|
| | $Q_{loss}$ / W·m$^{-1}$ | $T_g$/°C | $Q'_{loss}$ /W·m$^{-1}$ | $T_g$ /°C | Increments of heat gain / W·m$^{-1}$ | Heat loss reduction /% | $Q'_{loss}$ / W·m$^{-1}$ | $T_g$ /°C | Increments of heat gain /W·m$^{-1}$ | Heat loss reduction /% |
| 160 | 23.1 | 17.9 | 41.7 | 20.8 | –18.6 | –80.5 | 53.3 | 17.9 | –30.2 | –130.7 |
| 200 | 39.1 | 20.0 | 57.9 | 23.1 | –18.8 | –48.1 | 69.4 | 18.6 | –30.3 | –77.5 |
| 240 | 63.8 | 22.3 | 75.1 | 24.9 | –11.3 | –17.7 | 85.8 | 20.7 | –22.0 | –34.5 |
| 280 | 90.8 | 25.6 | 93.0 | 26.8 | –2.2 | –2.4 | 107.2 | 23.9 | –16.4 | –18.1 |
| 320 | 136.5 | 30.5 | 121.0 | 30.0 | 15.5 | 11.4 | 135.2 | 26.8 | 1.3 | 1.0 |
| 360 | 195.6 | 36.8 | 168.8 | 34.9 | 26.8 | 13.7 | 180.3 | 30.8 | 15.3 | 7.8 |
| 400 | 271.1 | 43.4 | 222.2 | 40.2 | 48.9 | 18.0 | 232.6 | 36.1 | 38.5 | 14.2 |
| 440 | 374.9 | 52.5 | 300.0 | 46.8 | 74.9 | 20.0 | 305.9 | 42.6 | 69.0 | 18.4 |
| 480 | 512.6 | 63.9 | 397.4 | 54.9 | 115.2 | 22.4 | 410.5 | 50.8 | 102.1 | 19.9 |
| 520 | 681.9 | 75.5 | 518.8 | 63.9 | 163.1 | 23.9 | 522.0 | 60.1 | 159.9 | 23.4 |
| 560 | 899.3 | 89.7 | 677.5 | 74.1 | 221.8 | 24.7 | 676.3 | 71.9 | 223.0 | 24.8 |
| 600 | 1174.0 | 105.7 | 871.2 | 86.5 | 302.8 | 25.8 | 868.3 | 83.5 | 305.7 | 26.0 |

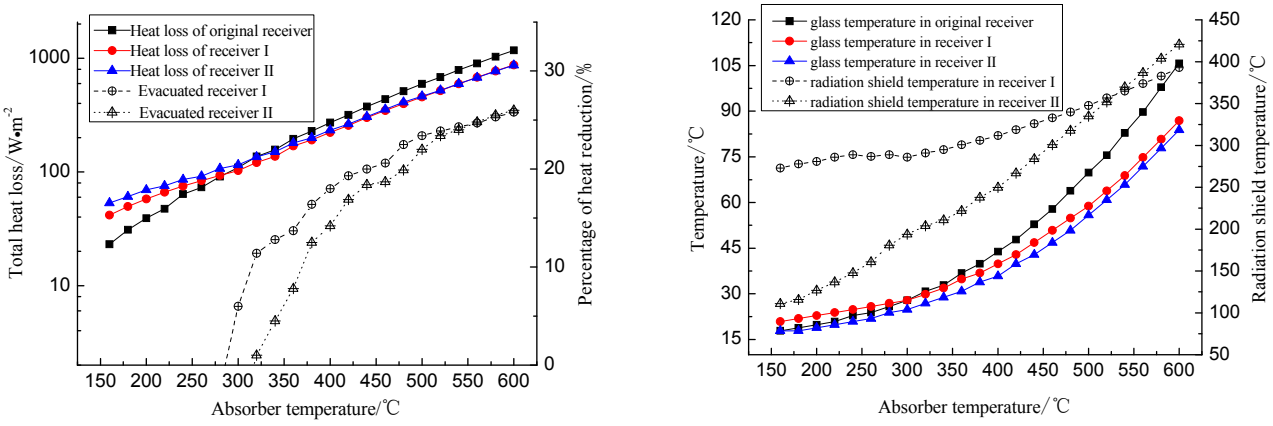


(a) (b)

**Fig.6.** Simulation results of all kinds of evacuated receivers. (a) values of heat loss varied with absorber temperature, and (b) glass envelope temperature varied with absorber temperature

Table 6 shows that the total heat losses of the original and new-type receivers grow rapidly with the increase of absorber temperature. However, the increments of the two kinds of new-type receivers are larger than that of the original receiver. The four columns of data indicating the heat gain increments and heat reduction percentages of PTC receivers I and II compared with the original PTC receiver increase from negative to positive. This increase shows that the new-type PTC receivers are advantageous to reduce the heat loss of the original PTC receiver at a higher temperature. As the absorber temperature reaches 600 °C, the percentages of heat reduction of the PTC receivers I

and II are 25.8% and 26.0%, respectively. Their increments of heat gain are 302.8 W/m and 305.7 W/m. The increment of heat gain is different between the total heat loss of an original PTC receiver and that of a new-type PTC receiver.

When the absorber is at a lower temperature, the total heat loss of new-type receivers with radiation shield is higher than that of the original receiver. The reason is that radiant energy intercepted and reflected back to the absorber by radiation shield is lower than the incident solar irradiance that should have been absorbed by the absorber if the radiation shield does not exist. However, the increase of absorber temperature gradually increased the intercepted radiant energy, such that the new-type evacuated receiver has less total heat loss than the original receiver. Therefore, the radiation shield starts to come into play. As shown in Fig.6a, the percentage of heat reduction of PTC receiver I is zero when the critical absorber temperature is approximately 285 °C. This finding illustrates that the total heat loss of PTC receiver I is equivalent to that of the original PTC receiver at this critical temperature point. Moreover, the percentage of heat reduction increases dramatically when absorber temperature exceeds 285 °C, given the growing radiant energy intercepted by the radiation shield. Similarly, the critical temperature of the PTC receiver II is approximately 320 °C, which is higher than that of PTC receiver I. Furthermore, the corresponding absorber temperature is nearly 540 °C at the intersection point of the two curves of the total heat loss of PTC receivers I and II. This temperature corresponds to the intersection point of the two curves of heat reduction percentage of receivers I and II. Therefore, two amounts of total heat loss of receivers I and II are equivalent when the absorber temperature is 540 °C. The former is more than the latter because the temperature is lower than 540 °C. However, the converse result is obtained when the temperature is higher than 540 °C.

The aforementioned phenomenon is due to the temperature of the radiation shield in PTC receiver I being higher than that in PTC receiver II at a lower working temperature, as shown in Fig.6b. The reason for this difference is that the coating on the outer surface of the radiation shield in PTC receiver I can absorb most of the incident solar irradiances, but that for the radiation shield of PTC receiver II cannot. In the case of lower working temperature, the transfer direction of the net radiation flux between the absorber and the radiation shield is from the radiation shield with a higher temperature to the absorber. The radiation flux can be regarded as thermal compensation of the intercepted incident solar irradiance for the absorber. In other words, the heat gain of PTC receiver I with higher radiation shield temperature is larger than that of PTC receiver II. This phenomenon explains why the absorber temperature of PTC receiver I compared with PTC receiver II is lower, at which the radiation shield starts to play a role. However, in the case of a higher temperature that exceeds the radiation shield temperature, the role of coating on the surface of the radiation shield decreases. The result from the transfer direction of the net radiation flux is reverse. Thus, the absorber temperature becomes the major factor that affects the temperature of the radiation shield. In addition, the radiative heat loss on the outer surface of the radiation shield in the PTC receiver II appears to increase, but is below that for PTC receiver II. The reason is that the sharply growing coating mean emittance in the entire wavelength is above the increasing mean emittance of polished aluminum outer surface of radiation shield in PTC receiver II. As a result, the shield temperature in PTC receiver II approaches and even exceeds that in PTC receiver I. The absorber temperature is 540 °C, at which the radiation shield temperatures of two kinds of new-type PTC receiver are the same. This phenomenon explains why the difference in the total heat losses of PTC receivers I and II changes before and after 540 °C.

Fig.6b also presents three curves of the relationship between the temperature of glass envelope and absorber temperature. The glass envelope temperature of PTC II is always the lowest by comparing the three curves. The reason lies in the lower radiation heat transfer between the polished outer surface of the radiation shield and the glass envelope.

## DISCUSSIONS

All variable parameters used in the models, influencing the performance of PTC receiver, are discussed in this section. These parameters are the transmittance of the glass envelope, ambient temperature, wind velocity, and solar irradiance. Accordingly, we determine whether these parameters have significant influences on the performance of the PTC receiver.

### *Transmittance of glass envelope*

The spectral region in which the radiation is concentrated depends on temperature, with

increased radiation appearing at shorter wavelengths as the temperature rises. Therefore, the value of cumulative emissive power of the absorber at shorter wavelengths is considerable at a higher operating temperature. The majority of value is able to pass through the glass envelope because of high transmittance in the visible region of the solar spectrum maintained by ordinary borosilicate glass. In particular, the $Q_{r,ssky}$ becomes larger with the increase of operating temperature.

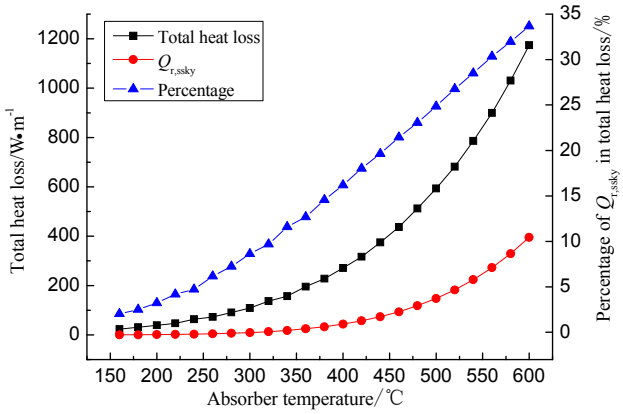


**Fig.7.** Total heat loss and heat loss transferring through outside glass tube with the changes of absorber temperature

Fig.7 shows the curves of $Q_{r,ssky}$ and total heat loss with varying absorber temperatures, as the ambient temperature, wind speed, and solar irradiance are 15 °C, 2.5 m/s, and 800 W/m$^2$, respectively. As observed from the curves, the value of $Q_{r,ssky}$ is nearly 0 when the absorber temperature is lower than 400 °C. Then, the value increases significantly as the temperature increases, and the corresponding percentage of $Q_{r,ssky}$ from the total heat loss rises linearly. The percentage reaches 33.7% when the working temperature is 600 °C. Therefore, the radiation heat loss between the absorber and the sky is an important part of total heat loss and cannot be ignored when the operating temperature is higher.

*Ambient temperature and wind velocity*

In the case where the absorber temperature and solar irradiance are determined, lower ambient temperature and higher wind speed lead to increased heat loss and reduced glass envelope temperature. In fact, the variation of heat loss in an evacuated receiver is insignificantly large with the different ambient temperatures and wind speeds. Heat loss in the glass envelope ($Q_{r,gsky}$+$Q_{c,ga}$) and that between the absorber and the sky ($Q_{r,ssky}$) are two main aspects included in the total heat loss of an original evacuated receiver, according to Formula (4). Moreover, the ($Q_{r,gsky}$+$Q_{c,ga}$) depends on the radiation heat transfer between the absorber and the glass envelope ($Q_{r,sg}$), which is proportional to ($T_s^4 - T_g^4$) as well as $Q_{r,ssky}$ and ($T_s^4 - T_{sky}^4$). $T_s^4 \gg T_g^4$ and $T_s^4 \gg T_{sky}^4$; thus, the decreases of $T_g$ and $T_{sky}$ have a slight influence on the thermal performance of the PTC receiver.

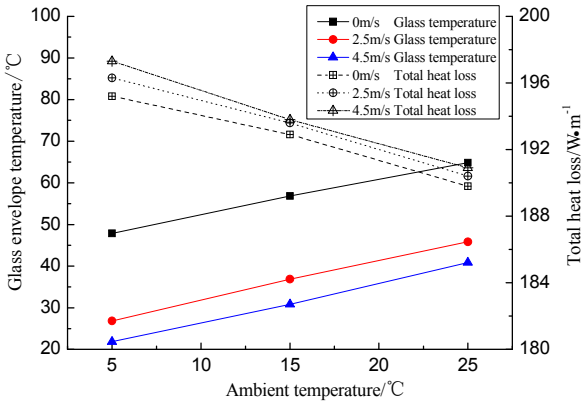


**Fig.8.** Heat loss of original collector and outside tube temperature with changes of ambient temperature and wind speed (absorber temperature is 360 °C and solar irradiance is 800 W/m$^2$)

The absorber temperature and solar irradiance are assumed to be 360 °C and 800 W/m$^2$, respectively; the heat loss and glass temperature are determined for varying laboratory ambient and sky temperatures (5–30 °C) and wind speeds (0–4.5 m/s), as shown in Fig.8. The figure shows that the ambient temperatures and wind speeds can affect the glass temperature by ±25 °C from its average value. However, the heat loss varies slightly with changes in these parameters by ±5 W/m. The difference of respective total heat loss is only 8.5 W/m in the case where ambient temperature is 25 °C and wind speed is 0 m/s, and in the case where ambient temperature is 5 °C and wind speed is 4.5 m/s. Therefore, the heat loss in the PTC receivers is insensitive to the ambient temperature and the wind speed.

*Solar irradiance*

The radiation shield temperature of PTC receiver I, which affects the heat gain in the absorber associated with the radiant heat loss in the absorber, exhibits a larger variation with the changes in solar irradiance because of the surface coating on it. For PTC receiver I, radiation heat flux $Q_{r,s*k}$ and ($Q_{r,s**g}$+$Q_{r,s**sky}$) are two main parts of heat loss in the absorber according to the simulation model. Smaller net radiation heat flux is obtained in the case where the absorber temperature, ambient temperature, and wind speed are determined. The

reason is that a higher radiation shield temperature is obtained with the increase of solar irradiance. Specifically, the total heat loss in the PTC receiver decreases.

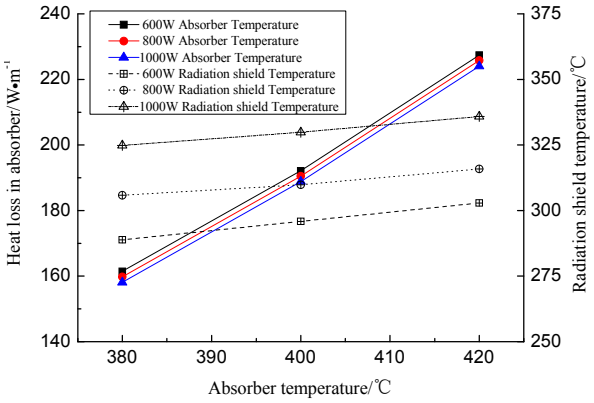


**Fig.9.** Heat loss in absorber and the radiation shield temperature with varying absorber temperatures (360–420 °C) and solar irradiances (600–1000 W/m$^2$)

As shown in Fig.9, the heat loss in the absorber and the radiation shield temperature are determined for varying absorber temperatures (360–420 °C) and solar irradiances (600–1000 W/m$^2$). The figure shows that the solar irradiance can markedly affect the radiation shield temperature by ±15 °C and the heat loss in the absorber by ±2.5 W/m, from their average values at different absorber temperatures. In the case of 400 °C radiation shield temperature, the heat loss in the absorber with solar irradiance 1000 W/m$^2$ is only 4 W/m, more than that with 600 W/m$^2$. This phenomenon illustrates that the radiation heat loss in the absorber is insensitive particularly to the radiation shield temperature because of the reduced surface emittances of both the radiation shield inner surface and the absorber outer surface.

## CONCLUSIONS

Two kinds of new-type evacuated receivers with inner radiation shield are proposed to improve the performance of the PTC receiver. The study calculates and compares the heat loss of the new-type and original PTC receivers by establishing simulation models based on laboratory conditions. Several important parameters are also analyzed to verify their influence on the performance of the PTC receiver. The obtained conclusions are as follows:

1) The two kinds of new-type PTC receivers can decrease the heat loss in the evacuated receiver. When the working temperature is lower than 540 °C, the receiver with selective sunlight-absorbing coating on the outer surface of the radiation shield is superior to that with polished aluminum outer surface of the radiation shield. However, the latter is superior to the former if the working temperature surpasses 540 °C. In the case where the absorber temperature reaches 600 °C, the heat reduction percentages of both compared with that of the original receiver are 25.8% and 26.0%. Therefore, the two kinds of new-type receiver have remarkable performances.

2) The percentage of radiant heat loss through the glass envelope between the absorber and the sky from the total heat loss increases gradually with the increase of operating temperature. In particular, at a medium-high temperature such as 600 °C, the percentage increases to 33.7%, which should be considered.

3) The lower temperature of the glass envelope is obtained with lower ambient temperature and faster wind speed, but the total heat loss varies slightly if a good vacuum is guaranteed. The difference of respective total heat loss is only 8.5 W/m in the case where ambient temperature is 25 °C and wind speed is 0 m/s, and in the case where ambient temperature is 5 °C and wind speed is 4.5 m/s.

## ACKNOWLEDGMENT

This study was sponsored by (1) the National Science Foundation of China (NSFC 51476159 and 51206154), (2) the Dongguan Innovative Research Team Program (No. 2014607101008), and (3) the National Science and Technology Support Program (No. 2015BAD19B02).

The authors are grateful for the support provided by Beijing Jindu Solar Energy Tech. Co. Ltd. and Mr. Ge Hongchuan.

## NOMENCLATURE

$s$ Outer surface of inner absorber tube
$g$ Outer (inner) surface of glass envelope
$k$ Radiation shield
$s^*$ Outer surface of inner absorber tube in i-zone
$g^*$ Outer (inner) surface of glass envelope in i-zone
$s^{**}$ Outer surface of inner absorber tube in ii-zone
$g^{**}$ Outer (inner) surface of glass envelope in ii-zone
$\varepsilon_{\lambda,s}$ Spectral emittance on outer surface of inner absorber tube
$\varepsilon_{\lambda,g}$ Spectral emittance on outer (inner) surface of glass envelope
$\alpha_{\lambda,g}$ Spectral absorptivity on outer (inner) surface of glass envelope

$\rho_{\lambda,g}$ Spectral reflectivity on outer (inner) surface of glass envelope

$\tau_{\lambda,g}$ Spectral transmittance of glass envelope

$\varepsilon_{\lambda,ki}$ Spectral emittance on inter surface of radiation shield

$\varepsilon_{\lambda,ko}$ Spectral emittance on outer surface of radiation shield

$A_s$ Area of surface s ($m^2$)

$A_g$ Area of surface g ($m^2$)

$A_k$ Area of inner (outer) surface of radiation shield ($m^2$)

$A_{s*}$ Area of surface $s^*$ ($m^2$)

$A_{g*}$ Area of surface $g^*$ ($m^2$)

$T_a$ Ambient temperature (°C)

$T_{sky}$ Sky temperature (°C)

$T_s$ Absorber temperature (°C)

$T_g$ Glass envelope temperature (°C)

$T_k$ Radiation shield temperature (°C)

$R_{\lambda,s}$ Surface radiative resistance of surface s

$R_{\lambda,g}$ Surface radiative resistance of outer surface of glass envelope

$R'_{\lambda,g}$ Surface radiative resistance of inner surface of glass envelope

$R_{\lambda,gsky}$ Space resistance between glass envelope and sky

$R_{\lambda,ssky}$ Space resistance between absorber and sky

$R_{\lambda,sg}$ Space resistance between absorber and glass envelope

$R_{\lambda,s^*}$ Surface radiative resistance of surface $s^*$ in i-zone of new-type evacuated receiver

$R_{\lambda,k}$ Surface radiative resistance of outer surface of radiation shield in i-zone

$R'_{\lambda,k}$ Surface radiative resistance of inner surface of radiation shield in i-zone

$R_{\lambda,g^*}$ Surface radiative resistance of outer surface of glass envelope in i-zone

$R'_{\lambda,g^*}$ Surface radiative resistance of inner surface of glass envelope in i-zone

$R_{\lambda,s^*k}$ Space resistance between $s^*$ and inner surface of radiation shield in i-zone

$R_{\lambda,ksky}$ Space resistance between outer surface of radiation shield and sky in i-zone

$R_{\lambda,kg^*}$ Space resistance between outer surface of radiation shield and inner surface of glass envelope in i-zone

$R_{\lambda,g^*sky}$ Space resistance between outer surface of glass envelope and sky in i-zone

$F_{sg}$ View factor of surface s with respect to inner surface of glass envelope

$F_{ssky}$ View factor of surface s with respect to sky

$F_{s*k}$ View factor of surface $s^*$ with respect to sky

$F_{ksky}$ View factor of outer surface of radiation shield with respect to sky

$F_{kg*}$ View factor of outer surface of radiation shield with respect to inner surface of glass envelope

$F_{gsky}$ View factor of outer surface of glass envelope with respect to sky

$E_{\lambda,b,s}$ Blackbody spectral emissive power of surface s ($W/(m^2 \cdot \mu m)$)

$E_{\lambda,b,g}$ Blackbody spectral emissive power of surface g ($W/(m^2 \cdot \mu m)$)

$E_{\lambda,b,sky}$ Blackbody spectral emissive power of sky ($W/(m^2 \cdot \mu m)$)

$E_{\lambda,b,s^*}$ Blackbody spectral emissive power of surface $s^*$ ($W/(m^2 \cdot \mu m)$)

$E_{\lambda,b,k}$ Blackbody spectral emissive power of inner (outer) surface of radiation shield ($W/(m^2 \cdot \mu m)$)

$E_{\lambda,b,g^*}$ Blackbody spectral emissive power of inner (outer) surface of glass envelope ($W/(m^2 \cdot \mu m)$)

$Q_{r,ssky}$ Net radiation heat flux between absorber and sky in original evacuated receiver (W/m)

$Q_{r,sg}$ Net radiation heat flux between absorber and glass envelope in original evacuated receiver (W/m)

$Q_{r,gsky}$ Net radiation heat flux between glass envelope and sky in original evacuated receiver (W/m)

$Q_{irra}$ Solar irradiance ($W/m^2$)

$Q_{irra-s}$ Solar energy absorbed by absorber tube (W/m)

$Q_{r,ksky}$ Net radiation heat flux between radiation shield and sky (W/m)

$Q_{r,kg*}$ Net radiation heat flux between radiation shield and the part of glass envelope in i-zone (W/m)

$Q_{r,g*sky}$ Net radiation heat flux between the part of glass envelope in i-zone and sky (W/m)

$Q_{r,s^*k}$ Net radiation heat flux between surface $s^*$ and radiation shield in i-zone (W/m)

$Q_{irra\text{-}k}$ Solar energy absorbed by radiation shield (W/m)

$Q_{re,irra\text{-}k}$ Solar energy reflected by radiation shield (W/m)

$Q_{r,s^{**}sky}$ Net radiation heat flux between surface $s^{**}$ and sky (W/m)

$Q_{r,s^{**}g^{**}}$ Net radiation heat flux between surface $s^{**}$ and glass envelope in ii-zone (W/m)

$Q_{r,g^{**}sky}$ Net radiation heat flux between part of glass envelope in ii-zone and sky (W/m)

$Q'_{r,gsky}$ Net radiation heat flux between glass envelope and sky in new-type evacuated receiver (W/m)

$Q'_{r,(sk)g}$ Total net radiation heat flux between surface $s^{**}$, radiation shield, and glass envelope in new-type evacuated receiver (W/m)

$Q'_{r,(sk)sky}$ Total net radiation heat flux between surface $s^{**}$, radiation shield, and sky in new-type evacuated receiver (W/m)

$Q_{irra\text{-}g}$ Solar energy absorbed by glass envelope (W/m)

$Q_{re,irra\text{-}k\text{-}g^*}$ Solar energy reflected from radiation shield absorbed by glass envelope (W/m)

$Q_{loss}$ Total heat loss of original evacuated receiver (W/m)

$Q'_{loss}$ Total heat loss of new-type evacuated receiver (W/m)

$Q_{c,ga}$ Convection between glass envelope and environment (W/m)

## REFERENCES


1 He Xinnian, Solar thermal application, Hefei: Publishing House of University of Science and Technology of China, 444-466 (2009).

2 Liu Jianmin, Solar energy application, Beijing: Publishing House of Electronics Industry, 303-374 (2010).

3 Behar Omar, Khellaf Abdallah, Mohammedi, Kamal, A review of studies on central receiver solar thermal power plants, Renewable & Sustainable Energy Reviews, Elsevier, 23, (2013).

4 Fernandez-Garcia A., Zarza E., Valenzuela L., Perez M., Parabolic-trough solar collectors and their applications, Renewable & Sustainable Energy Reviews, Elsevier, 14, (2010).

5 Xiong YaXuan, Wu YuTing, Ma ChongFang, et al., Numerical investigation of thermal performance of heat loss of parabolic trough receiver. Science China-Technological Sciences, Elsevier, 53, (2010).

6 Kalogirou, SA., Solar thermal collectors and applications. Progress in Energy and Combustion Science, Elsevier, 30, (2004).

7 Luepfert Eckhard, Riffelmann Klaus-J., Price Henry, et al., Experimental analysis of overall thermal properties of parabolic trough receivers, Journal of Solar Energy Engineering-Transactions of the ASME, Elsevier, 130, (2008).

8 Mills D., Advances in solar thermal electricity technology, Solar Energy, Elsevier, 76, (2004).

9 Nishith B. Desai, Santanu Bandyopadhyay, Optimization of concentrating solar thermal power plant based on parabolic trough collector, Journal of Cleaner Production, Elsevier, 89, (2015).

10 Xie Guangning, et al., A summary on middle-high temperature solar selective absorbing surface, Proc of ICEA2001[C], Wuhan, China, (2001).

11 Caron S., Roeger M., Pernpeintner J., Transient infrared thermography heat loss measurements on parabolic trough receivers under laboratory conditions, International Conference on Concentrating Solar Power and Chemical Energy Systems, Beijing, Peoples R China, (2014).

12 Pigozzo Filho, Victor C., de Sa, Alexandre B., Passos, Julio C., et al., Experimental and numerical analysis of thermal losses of a parabolic trough solar collector, ISES Solar World Congress (SWC), Cancun, MEXICO, (2013).

13 Daniel Premjit, Joshi Yashavant, Das Abhik K., Numerical investigation of parabolic trough receiver performance with outer vacuum shell, Solar Energy., Elsevier, 85, (2013).

14 Hany Al-Ansary, Obida Zeitoun, Heat Loss Experiments on a Non-Evacuated Parabolic Trough Receiver Employing a Thermally Insulating Layer in the Annular Gap, ASME 2013 7th International Conference on Energy Sustainability collocated with the ASME 2013 Heat Transfer Summer Conference and the ASME 2013 11th International Conference on Fuel Cell Science, Engineering and Technology, Minneapolis, Minnesota, USA, (2013).

15 Hany Al-Ansary, Obida Zeitoun, Numerical study of conduction and convection heat losses from a half-insulated air-filled annulus of the receiver of a parabolic trough collector. Solar energy, Elsevier, 85, (2011).

16 Xin Zhang, Shijun You, Hongchuan Ge, et al., Thermal performance of direct-flow coaxial evacuated-tube solar collectors with and without a heat shield, Energy Conversion and Management, Elsevier, 84, (2014).

17 Holman J P. Heat transfer, New York: McGraw-Hill Inc, 420-460, (1997).

18 Incropera F P, DeWitt D P, Fundamentals of heat and mass transfer, 6th edition, New York: John Wiley and Sons, (1990).

19 Burkholder F, Kutscher C, Heat loss testing of Sehott's 2008 PrR70 parabolic trough receiver [EB／OL], http://www.rtrel.gov/esp/troughnet/pdfs/45633.pdf,2009-05/2009-07.

*Bulgarian Chemical Communications, Volume 48, Special Issue E (pp. 88 - 95) 2016*

# Parameter estimation of borehole thermal properties using artificial intelligence methods

R. K. Popov[1*], A. G. Georgiev[2,4], D. B. Dzhonova-Atanasova[3]

[1]*Faculty of Physics, Plovdiv University "Paisii Hilendarski", 24 Tzar Assen Str., 4000 Plovdiv, Bulgaria*
[2]*Faculty of Mechanical Engineering, Technical University - Sofia, Plovdiv Branch, 25 Tsanko Diustabanov Str., 4000 Plovdiv, Bulgaria*
[3] *Institute of Chemical Engineering, Bulgarian Academy of Sciences, Acad. G. Bonchev Str., Bl. 103, 1113, Sofia, Bulgaria*
[4]*European Polytechnic University, Dept. of "Green Energy", 23 Kiril and Metodiy str., 2300 Pernik, Bulgaria*

There are many estimation techniques, which are used in Thermal Response Test (TRT) data analysis. The commonly used models, Line Source Model, Cylindrical Source Model, numerical models do not take into account the nonlinear system effects like for example the phase change. The present work suggests the use of the input/output black box identification technique for TRT data analysis. A nonlinear autoregressive exogenous (ARX) model structure and stochastic search algorithms are used to estimate model parameters. Artificial intelligence techniques, Genetic Algorithm and Particle Swarm Optimization Algorithm are employed to avoid local maxima problems. The study is based on data sets obtained during real TRT tests without phase change effects. All analyses are performed in MATLAB environment. The purpose of this paper is to verify that the proposed algorithms are suitable for processing of TRT data with the aim of future identification of thermal parameters of boreholes with phase change effects. The given solution is also useful when common techniques fail in search for the global optimum if the search space is not differentiable or linear in the parameters.

**Keywords:** artificial intelligence methods, parameter estimation, thermal response test, thermal properties, MATLAB

## INTRODUCTION

Thermal Response Test (TRT) is an internationally approved technique to identify geothermal underground parameters like effective ground thermal conductivity and borehole thermal resistance. It is considered to be the method which gives the highest accuracy of evaluation. Generally, these tests are performed with heat injection, using the same assumed power level as the one planned by the Borehole Heat Exchanger (BHE) system. For first time TRT was presented by Mogensen – his installation was designed as an immobile system [1]. Later, TRT was developed as a mobile measurement installation at the Oklahoma State University (USA) by Austin [2] and at the Technical University Lulea, Sweden [3]. Now, this type of measurement is used also in Germany [4], Canada, Norway, Netherlands, England, Turkey [5] and Chile [6]. Several TRTs are done in Bulgaria, too. Some activities in Bulgaria preceded the first official TRT [7].

### *Algorithm Overview*

The genetic algorithm (GA), first proposed in [8], is a method for solving optimization problems which are not easy manageable by standard optimization methods, e.g. when the objective function is discontinuous, non-differentiable, stochastic, or highly nonlinear. It is used for both constrained and unconstrained optimization problems.

GA concept is taken from the principles of the evolution of the species by survival of the fittest. Like in a population of organisms [9] the solutions are created by reproduction of solutions and compete for survival in the next iteration. At each step the randomly selected individuals of the current population become parents and produce the children of the next generation. Over successive generations, the population improves to the optimal solution.

In the initial population *P(0)*, encoded randomly by strings [10], the more fit elements of each generation *(t)* are selected and processed by the basic genetic operators, crossover, and mutation, to create the next generation. On the basis of the evolution principles the best chromosome of a candidate solution is preserved. Thus the GA uses three main types of rules at each step towards the next generation of the current population: *Selection rules* select the individuals, called *parents*, which contribute to the population at the next generation; *Crossover rules* combine two parents to form children for the next generation; *Mutation rules* apply random changes to individual parents to form children.

* To whom all correspondence should be sent:
rum_pop@yahoo.com

The computational procedure is illustrated by the following GA pseudo code [11]:

```
Procedure GA
begin
   t=0
   initialize P(t)
   evaluate P(t)
   while not satisfy stopping rule do
      begin
        t= t+1
        select P(t) from P(t1)
        alter P(t)
        evaluate P(t)
      end
   end
```

In the present work, the GA is employed for model identification in Autoregressive integrated moving average (ARIMA) models because of the following very powerful characteristic: simultaneous searching of a population of points, not a single one, which results in finding the approximate optimum quickly and without falling into a local optimum. Moreover GA is free from the limitation of differentiability, unlike other mathematical techniques.

### *Concepts of the Particle Swarm Optimization Approach*

As the neural network is a simplified model of a human brain and the genetic algorithm is inspired by the biological evolution, an optimization approach known as swamp intelligence is inspired by the collective behavior of the individuals in a social system when interacting with the environment and each other. Two of the popular swamp inspired methods of computational intelligence area are Ant Colony Optimization (ACO) and Particle Swarm Optimization (PSO).

The first is inspired by the behavior of ants and has many successful applications in discrete optimization problems [12].

The PSO concept was originally developed for graphical simulation of the choreography in a bird flock or a fish school and employed afterwards as an optimizer. It was proposed in [13] as a population based stochastic optimization technique, inspired by social behavior of bird flocking or fish schooling. PSO simulates the bird flocking according to the following scenario: a group of birds are randomly searching only one piece of food in an area. They do not know where the food is, but do know how far it is in each iteration. The best searching strategy is to follow the bird nearest to the food.

In solving optimization problems by using this scenario, each solution in the search space is “bird”, called “particle”. All the particles have fitness values, which are evaluated by the fitness function to be optimized. The particles have flying velocities and fly through the problem space by following the current optimum particles.

PSO shares many similarities with evolutionary computation techniques. Like in the GA, the system is initialized with a population of random solutions and searches for optima over successive generations. However, unlike the GA, the PSO has no evolution operators such as crossover and mutation. The potential solutions, called particles, fly through the problem space by following the current optimum particles.

At the first step in PSO the position and velocity of the particles are randomly initialized. In every iteration, each particle is updated by following two "best" values. The first one is the best position (fitness) it has achieved so far denoted by $p_{best}$. (The fitness value is also stored). The second one is the best position, obtained so far by any particle in the population, called global best value and denoted by $g_{best}$. Each particle communicates with its topological neighbors and knows the best position found so far by any of them. If a particle takes part of the population as its neighbors, the best value is a local best and is called $l_{best}$.

After finding the two best values, the particle updates its velocity and position by the following equations (1) and (2)

$$v[\,] = v[\,] + c1 * rand(\,)*(pbest[\,] - present[\,]) + + c2*rand(\,)*(gbest[\,] - present[\,]) \quad (1)$$

$$present[\,] = present[\,] + v[\,], \quad (2)$$

where $v[\,]$ is the particle velocity, $present[\,]$ is the current particle (solution). $pbest[\,]$ and $gbest[\,]$ are defined as stated before. $rand(\,)$ is a random number between (0,1). $c1$, $c2$ are learning factors. Usually $c1 = c2 = 2$.

The pseudo code of the procedure is as follows:

```
for each particle
  Initialize particle
end
do
    for each particle
        Calculate fitness value
        if the fitness value is better than the best
           fitness value (pbest) in history
        set current value as the new pbest
```

end
Choose the particle with the best fitness value of all the particles as the gbest
for each particle
Calculate particle velocity according equation (1)
Update particle position according equation (2)
end
while maximum iterations or minimum error criteria is not attained

On each dimension a maximum velocity $V_{max}$ is specified by the user as a limit of the particles' velocities.

## INSTALLATION FOR IMPLEMENTING OF THERMAL RESPONSE TEST

An original construction of a Thermal Response Test rig has been built recently at the Technical University of Sofia, branch Plovdiv. The equipment for implementing of TRT is situated on a mobile trailer consisting of two parts. The first one contains the working installation. The second part is formed as a living room for the investigators, who will implement the in-situ tests. The scheme of the installation is shown in Fig.1. It consists of the following parts: electrical boiler 1, calorimeter 2, pressure watch 3, expansion tank 4, thermo – manometer 5, filter 6, circulation pump 7, de-aeration pipe 8, quick couplings 9, valves 10 and electrical unit 11. A 41,10m deep hole was drilled on the territory of the Technical University – Sofia, branch Plovdiv. The borehole has a diameter of 0.18 m and has been backfilled with 11% bentonite and 2% cement solution. There are two temperature sensors Pt 100 for measuring the inlet and outlet borehole temperatures. There are five other temperature sensors placed at different depths inside the borehole.

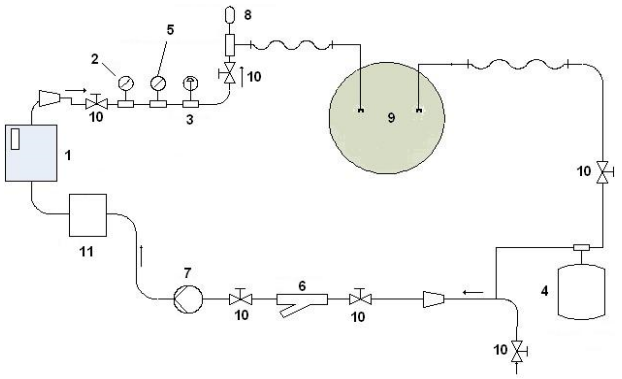


**Fig.1**. Installation setup

## THERMAL RESPONSE TEST - EXPERIMENT AND EVALUATION

The tests were implemented in January, March and April 2009. The following parameters were measured: the inlet and outlet fluid temperatures of the borehole, the ambient air temperature and five temperatures in the borehole body. The electrical power (about 1500 W) was controlled and maintained constant during the whole test. The flow rate of water was 4.06 l/min.

There are different methods to evaluate the experimental data and to calculate the unknown thermal conductivity $\lambda$ and borehole thermal resistance. The Line Source Model (LSM) is the widely used and simplest method [3]. The delivered heat is considered as coming from an infinite line source (the borehole). The following equation represents the heating process:

$$T_{f,m} = \frac{Q}{4\pi\lambda H}\ln(t) + \left[\frac{Q}{H}\left(\frac{1}{4\pi\lambda}\left(\ln\left(\frac{4a}{r_b^2}\right) - \gamma\right) + R_b\right) + T_s\right] \quad (3)$$

for $t \geq \frac{5r_b^2}{a}$

*where* $T_{f,m} = (T_{f,i} + T_{f,o})/2$ - mean fluid inlet/ outlet temperature*, K;*

$Q$ – delivered heat power, W;
$\lambda$ – thermal conductivity, W/mK;
$H$ – borehole depth, m;
$t$ – time from start, s;
$a$ – thermal diffusivity, $m^2/s$;
$r_b$ – radius of the borehole, m;
$\gamma = 0.5772$ – Euler's constant;
$R_b$ – borehole thermal resistance, mK/W;
$T_s$ – initial soil temperature, K.

### *Test Evaluation*

The average undisturbed ground temperature $T_s$ is a key parameter in Eq. (3) and should be measured prior to the test start before switching on the electrical heaters, when the borehole is at thermal equilibrium with its surroundings. $T_s$ was determined by pumping the heat carrier fluid out of the borehole pipes and measuring its outlet temperature over a time of 10s. $T_s$ was then calculated as the average of the measurement data. In the presented experiments, $T_s$ was found to be about 16.3°C. As soon as $T_s$ is measured the electric heaters are switched on and a constant heat starts to be injected in the BHE.

The flow rate was fixed at a constant value during the tests. The electrical heater power and the electrical power of the circulating pump were maintained constant automatically. For the

experiment purpose the installation was filled with water and a pressure of 2.2 bars was established. Most of the main characteristics of the performed Bulgarian TRTs in 2009 are shown in Table 1.

**Table 1.** Main characteristics of the Bulgarian TRTs carried out in 2009

| Properties | January | March | April |
|---|---|---|---|
| Date | 11-21 | 16-24 | 13-17 |
| Duration, days | 10 | 8 | 4.3 |
| Flow rate, l/ min | 4.06 | 3.83 | 4.6 |
| Electrical heater power, W | 1500 | 2000 | 1500 |
| Circulating pump power, W | 100 | 100 | 100 |
| Water pressure, bar | 2.2 | 2.2 | 2.2 |
| Undisturbed soil temperature, °C | 16.3 | 16.3 | 16.35 |
| Measuring interval step, s | 60 | 60 | 60 |

The control of the test rig is the most challenging part of the system. All data are automatically controlled by a specially designed system for the laboratory trailer needs, installed on the control board. The system is fully automatic and writes down all measured data in text files. If appropriate software is available, the data collecting process could be visualized in real time or after finishing the experiment. In the experiments the aim of a constant heat flow was realized by a constant frequency control of the circulation pump and boiler.

The application of equation (3) to the real problem is connected with a systematic error, which diminishes with time and increases with borehole radius. Eq. (3) can be rewritten for evaluation purposes in the form of:

$$T_{f,m}(t) = k_1 \ln(t) + k_2 \qquad (4)$$

Further on the test evaluation is based on Eq. (4), which is fitted to the experimental data, and the curve constants $k_1$ and $k_2$ are determined. Usually a Least Squares Method (LSM) is used to calculate $k_1$ and $k_2$. The thermal ground conductivity $\lambda$ and the borehole resistance $R_b$ can be adequately calculated, by comparing Eqs. (3) and (4) when the curve parameters $k_1$ and $k_2$ are known. In this article instead of LMS method, the GA and PSO search approaches are employed to fit the data and to compare the agreement.

## *Test Results*

The mean fluid temperature in the borehole (average temperature of the inlet and outlet fluid temperature of the borehole) and the ambient temperature are shown for the test done in January in Fig.2. The figure shows that the experimental fluid temperature rises slow and with small deviations.

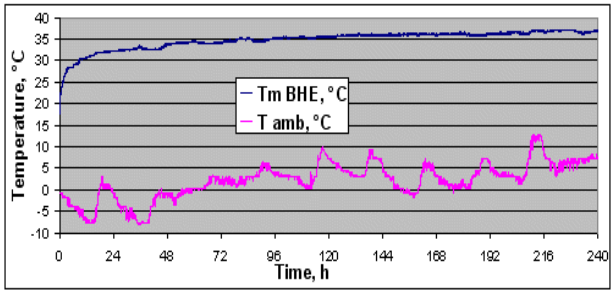


**Fig.2.** Profile of the mean fluid temperature in the borehole and the ambient temperature in January 2009

The number of the data points is very large (about 14400). In order to decrease the processing time of the GA and PSO stochastic search algorithms the number of the points was reduced by a factor of 30, using averaged values. The averaged trends of the same temperatures are showed in Fig.3.

## *Test Data Evaluation, Using Standard LSM Regression Method*

The Line Source Model gives more exact temperature estimations for longer terms of time. It takes some hours to the real BHE to behave as an ideal line source. Therefore, usually the data correspondent to the first 7 to 30 hours of experiment is not taken into account in the analysis.

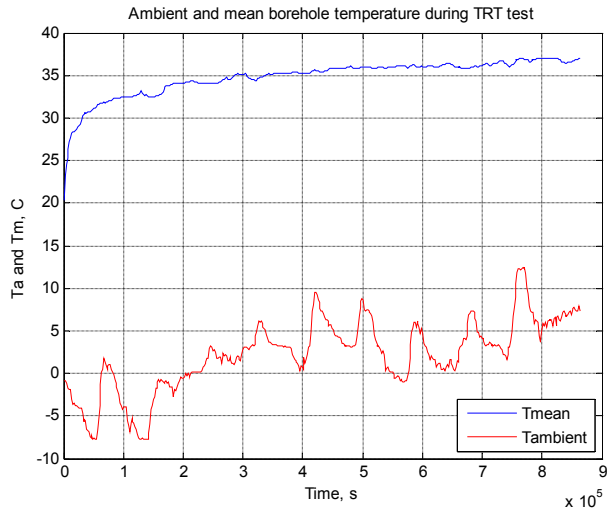


**Fig.3.** The reduced number of values of fluid mean temperature in the borehole and the ambient temperature in January 2009

In the present work, this period is accepted to be 20 hours, as it depends on the estimated data. Fig.4 shows the logarithmic time dependence of the temperature and the slope of the associated regression line. As stated previously, the thermal conductivity $\lambda$ is related to the slope of the resulting line by Eq. (4). The resulting value calculated

during the test for $\lambda$ is *0.83* W/mK and for $R_b$ – *0.532* mK/W.

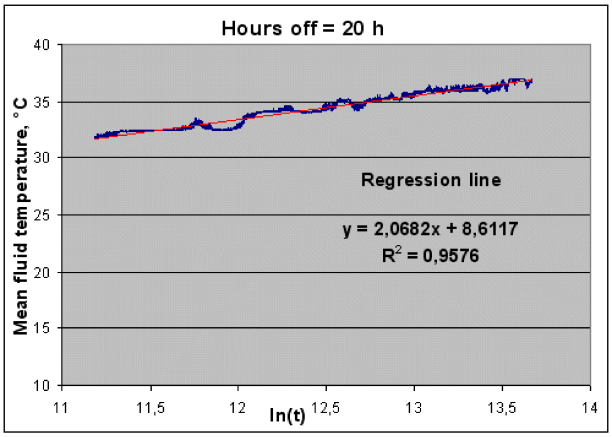


**Fig.4.** Logarithmic time plot of the mean temperature for the entire test length in January 2009 (excluding the first 20 hours)

*Test data evaluation, using artificial intelligence methods*

First we have to choose the input factors, which are to be varied. In GA algorithm they are:

- Crossover_p – Crossover probability parameter;
- Mutation_r – Mutation rate.

Output parameter is AvSAE variable (error) end value. It is the average value of the sum of absolute errors between data and model outputs at the end of the estimation process. If 50 generations are performed in GA search, then last column in variable AvSAE (50) is used. In the next step central composite experiment design is performed. Only one central point is used in case of obtaining uniform value distribution in the parameter space. The Matlab function "ccdesign" have been used for this purpose. After that factor variance bounds are chosen:

- Crossover_p = 0 … 1;
- Mutation_r = 0.05 … 0.5

Then matrix table is multiplied by factor n=10 in case of running not only 9 but 90 tests, because output value AvSAE ( ) is statistically dependent on the run. Now parameters are bounded to parameter space, using Matlab function "coded2real". Next step is to randomize runs' order in the test matrix. The positions of the input variables in the parameter space are shown in Fig.5.

The varied factors in the PSO algorithm are chosen to be:

- correction_factor;
- inertia.

The bonds chosen in this task are 1.6 to 2.4 for the Correction factor and 0.4 to 0.8 for the Inertia parameter. The central composite design for the PSO – test and the factors' variation in a Monte Carlo simulation are presented respectively in Fig.6.

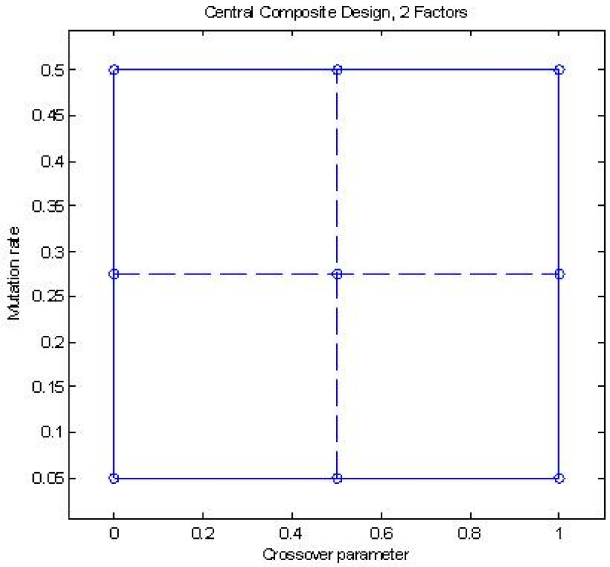


**Fig.5.** Positions of the input variables in the parameter space in GA tests

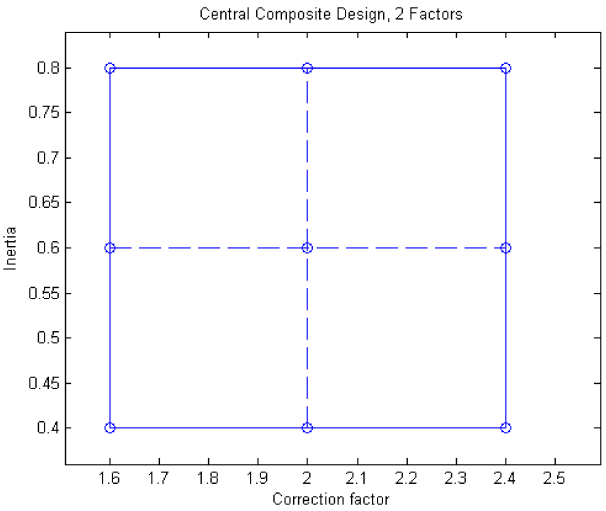


**Fig.6.** Positions of the input variables in the parameter space in PSO tests

*Genetic algorithm-based search function developed in Matlab*

The Genetic Algorithm-based search procedure is coded as a Matlab – function with the next syntax:

*[A B AvSAE] = ga_proc(err, popsize, crossover_p, mutation_r, n_generations),*

where:

*A* is a vector, containing evaluated 'a' parameters;
*B* is a vector, containing evaluated 'b' parameters;
*AvSAE* is a vector of average sum of absolute error of the model for all passed generations;
*err* is an error tolerance;
*popsize* is the size of population;
*crossover_p* is the crossover probability parameter;
*mutation_r* is the mutation rate;
*n_generations* is the number of generations.

### *Particle Swarm Optimization algorithm function developed in MATLAB*

The Particle Swarm Optimization -based search algorithm is written as a MATLAB – function with the following syntax:

*[A B AvSAE] = pso_proc (swarm_size, correction_factor, inertia, iterations, err);, where:*

*A* is a vector, containing evaluated 'a' parameters;
*B* is a vector, containing evaluated 'b' parameters;
*AvSAE* is a vector of average sum of absolute error of the model for all passed generations;
*err* is an error tolerance;
*swarm_size* is the size of the swarm;
*correction_factor* is the particle velocity correction factor;
*inertia* is the inertia factor
*iterations* is the number of iterations. number of generations.

### *Data evaluation using statistical search approaches: GA and PSO*

The 90 data fitting experiments were performed using GA and the same number of tests was carried out for the PSO approach. The results for the first 10 tests in each case are listed in the Table 2 (GA) and Table 3 (PSO).

**Table 2.** Monte Carlo simulation test results using GA

| Run Number | Cross-over_p | Mutation _r | AvSAE_ fin_value | Rb | Lambda |
|---|---|---|---|---|---|
| 1 | 1 | 0.050 | 0.91366 | 0.19607 | 0.88152 |
| 2 | 0.2 | 0.050 | 1.03060 | 0.10000 | 0.50000 |
| 3 | 1 | 0.275 | 0.22162 | 0.47185 | 0.87500 |
| 4 | 1 | 0.275 | 0.43971 | 0.10000 | 0.67388 |
| 5 | 0.6 | 0.275 | 0.94431 | 0.68193 | 2.44960 |
| 6 | 0.6 | 0.500 | 0.82120 | 0.60871 | 1.46410 |
| 7 | 0.2 | 0.050 | 1.22590 | 0.78088 | 5.48230 |
| 8 | 1 | 0.275 | 0.28684 | 0.10000 | 0.74713 |
| 9 | 0.2 | 0.500 | 0.40257 | 0.27394 | 0.68405 |
| 10 | 0.2 | 0.050 | 1.04250 | 0.10000 | 0.50000 |

**Table 3.** Monte Carlo simulation test results using PSO

| Run Number | Correction factor | Inertia | AvSAE_ fin_value | Rb | Lambda |
|---|---|---|---|---|---|
| 1 | 2 | 0.4 | 0.21792 | 0.46962 | 0.90854 |
| 2 | 2.4 | 0.4 | 0.21815 | 0.65663 | 1.80560 |
| 3 | 1.6 | 0.4 | 0.63708 | 0.60304 | 1.49490 |
| 4 | 2 | 0.6 | 0.21785 | 0.46567 | 0.86166 |
| 5 | 2 | 0.8 | 0.21785 | 0.46085 | 0.85269 |
| 6 | 1.6 | 0.6 | 0.21785 | 0.45883 | 0.84906 |
| 7 | 2.4 | 0.6 | 0.21790 | 0.46255 | 0.80732 |
| 8 | 2.4 | 0.6 | 0.21790 | 0.59181 | 1.25950 |
| 9 | 2.4 | 0.4 | 0.21786 | 0.45730 | 0.84441 |
| 10 | 1.6 | 0.6 | 0.21785 | 0.45608 | 0.84335 |

The GA tests duration was measured to be 24:52,256 min and the duration of the PSO tests was 21:05,385 min.

3D combined scatter plot of AvSAe versus GA parameters (factors) during the tests is showed in Fig.7 and Fig.8. Best values for the crossover parameter and the mutation rate are 1 and 0,5. For the correction factor and the inertia (in PSO) the combination of the values 2.4 and 0.6 reports lower error rate. The scatter plots show that all the factors are significant.

In the next step all test results, reporting AvSAe values higher than 0.3, were rejected. The calculated average values of the remaining estimated parameters are:

- in GA - tests:

$R_b = 0.4181513$ *mK/W*; $\lambda = 0.874063$ *W/mK;*

- in PSO - tests:

$R_b = 0.49098$ *mK/W*; $\lambda = 0.92624$ *W/ mK.*

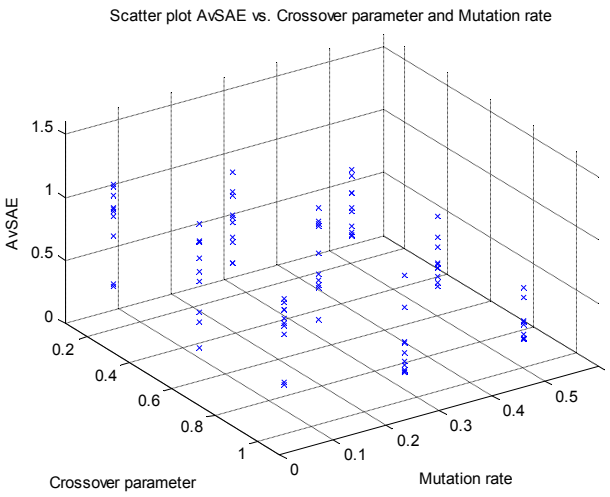


**Fig.7.** Positions scatter plot of AvSAE vs. crossover parameter and mutation rate in GA tests

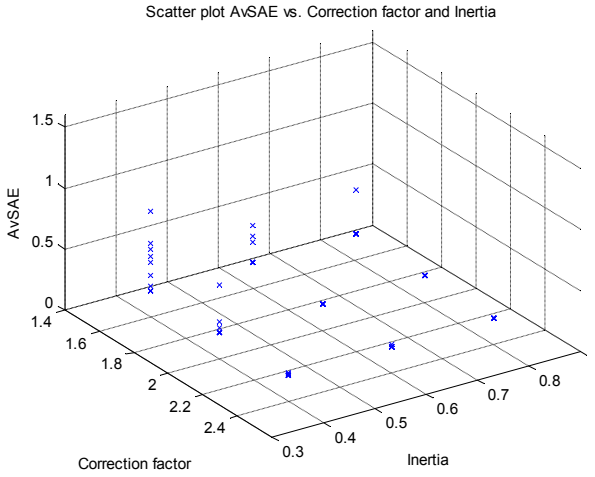


**Fig.8.** Scatter plot of AvSAE versus correction factor and inertia in PSO tests

The values of AvSAE (error) for both algorithms PSO and GA for the tests with the same number are compared in the Fig.9.

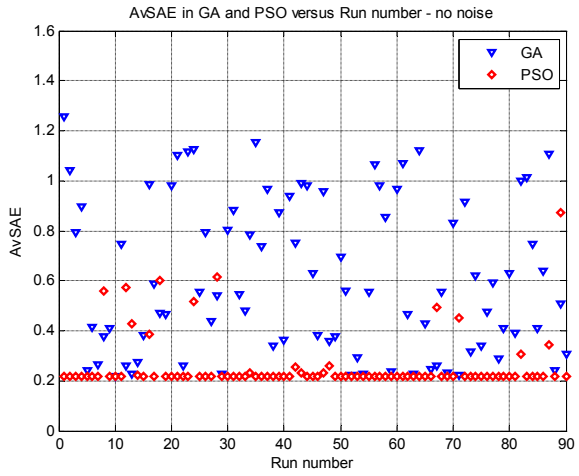


**Fig.9.** Value of AvSAE for both algorithms PSO (diamonds) and GA (triangles)

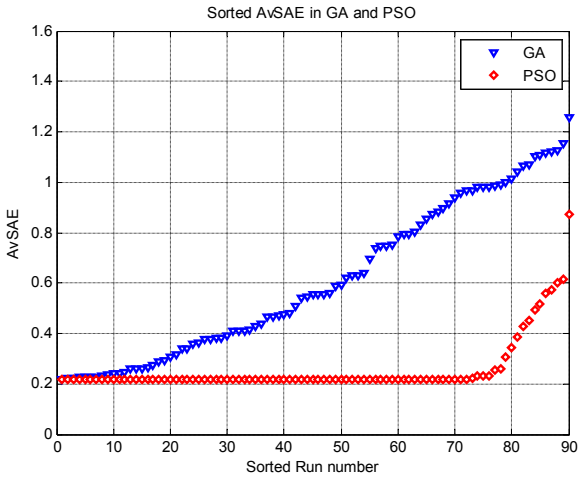


**Fig.10.** Sorted by values of AvSAE for both algorithms PSO (diamonds) and GA (triangles)

The next Fig.10 shows sorted values of AvSAE for both algorithms PSO (in red) and GA (in blue). It can be mentioned, that PSO procedure reports more accurate estimation of the system parameters.

## CONCLUSIONS

The estimated values of the thermal properties, using different algorithms are presented in Table 4.

**Table 4.** Estimated values of the thermal properties, using different algorithms

| **Algorithm** | $R_b$ **, mK/W** | $\lambda$ **, W/ mK** |
|---|---|---|
| LSM linear regression | 0.5320000 | 0.830000 |
| GA | 0.4181513 | 0.874063 |
| PSO | 0.4909800 | 0.926240 |

The results demonstrate a good accordance in estimates and possibility to apply GA and PSO – based approaches in TRT data evaluation procedure. In the reported case no phase change process occurs in the BHE and the main advantages of these two artificial intelligence techniques are not demonstrated in their full range. So an additional experimental investigation should be performed to obtain data from the BHE, working with $CO_2$, especially in a freezing/melting process. That will give the possibility to identify thermal parameters of Phase Change Materials (PCM) and Slurries, used in thermal storages.

Based on the results of the parameter estimation experiments additionally the next conclusions are to be drawn:

1. PSO algorithm reports better performance than GA. The calculation time for the two procedures is similar because the time for model evaluation is determining, equal in both cases.
2. ARX Model structure (linear or nonlinear) is well suited to parameter estimation procedure, using usual or Evolutionary algorithms;
3. Population size of 30 citizens is well enough for low order linear ARX model parameter estimation procedure, using GA and PSO – based approaches;
4. When using GA and PSO – based approaches a number of 30 iterations gives in the linear case a good estimation accuracy AvSAE = 0.2 in our experiments;
5. When using GA and PSO – based approaches accuracy and efficiency become statistical parameters, which depends on the initial population generation and mutation variance;
6. For low order linear ARX model parameter estimation procedure the GA – based approach

gives a little bit higher performance than PSO – based approach;
7. For low order linear ARX model parameter estimation procedure the PSO – based approach gives much more higher accuracy than GA – based approach;
8. Significance analysis in all cases has shown that all varied parameters are significant;
9. The best values for the Crossover parameter and the Mutation rate in GA algorithm are: 1.0 and 0.5;
10. The best values for the Correction factor and the Inertia rate in PSO algorithm are: 2.4 and 0.6.

## ACKNOWLEDGEMENTS

This work has been supported financially by the research project 152ПД0045-24/ 26.03.2015 and the research project 152ПД0046-24/ 27.03.2015 of the Technical University of Sofia, which is gratefully acknowledged by the author.

## REFERENCES

1 Mogensen P. (1983). Fluid to Duct Wall Heat Transfer in Duct System Heat Storages. Proc. of Int. Conf. on Subsurface Heat Storage in Theory and Practice, Stockholm, Sweden, June 6-8, 1983, p. 652-657.
2 Austin, W. A. (1998), Development of an In-Situ System for Measuring Ground Thermal Properties. Master's thesis. Oklahoma State University. Stillwater, Oklahoma.
3 Eklöf, C., and S. Gehlin, S.: TED – A Mobile Equipment for Thermal Response Test, Master's Thesis 1996:198E. Luleå University of Technology, Sweden, (1996).
4 Sanner, B.; Reuss, M.; Mands, E. and Müller, J. (2000). Thermal Response Test - Experiences in Germany. Proc. of Terrastock 2000, 8th Int. Conf. on Thermal Energy Storage, Stuttgart, August 28-September 1, 2000, Vol. 1, p. 177-182.
5 Paksoy, H., Gurbuz, Z., Turgut, B., Dikici, D. and Evliya, H.: Aquifer thermal storage (ATES) for airconditioningof a supermarket in Turkey. Proc. of World Renewable Energy Congress-VII 2002, Cologne, Germany, (2002), 10_n66.pdf.
6 Roth, P., Georgiev, A., Busso, A., Barraza, E. First In-situ Determination of Ground and Borehole Thermal Properties in Latin America, Renewable Energy, 29, (2004), 1947-1963.
7 Georgiev, A., Pekov, O., Angelov, A., Popov, R., Urchueguía, J. F., and Witte, H.: First steps of ground accumulation in Bulgaria. Proc. of the World Renewable Energy Congress-IX, Italy, Florence, (2006).
8 Holland J.H., Adaptation in natural and artificial system, Ann Arbor, The University of Michigan Press, 1975.
9 Kargupta, H., Smith, R. E., System identification with evolving polynomial networks, Proceeding of the 4th International Conference on Genetic Algorithm, University of California, San Diego, USA, 1991, pp. 370-376.
10 Kristinsson, K., Dumont, G., System identification and control using Genetic Algorithms, IEEE Trans. on Systems, Man and Cybernetics, 1992 22 (5), pp. 1033–46.
11 Kent Allen, James G. Williams: Encyclopedia of Computer Science and Technology: Volume 21 - Supplement 6: ADA and Distributed Systems to Visual Languages, CRC Press, 1989.
12 Dorigo, M. (1992). Optimization, Learning and Natural Algorithms, PhD thesis, Politecnico di Milano, Italy.
13 Kennedy, J.; Eberhart, R. (1995). "Particle Swarm Optimization". Proc. of IEEE Int. Conf. on Neural Networks IV. pp. 1942–1948.

*Bulgarian Chemical Communications, Volume 48, Special Issue E (pp. 96 - 101) 2016*

# Specialized measuring system for analysing thermal fields in hybrid systems

S. N. Lishev[1], R. K. Popov[2*], A. G. Georgiev[3,4]

[1]*Department of Optoelectronics and Laser Engineering, Technical University of Sofia - Plovdiv Branch, 25 Tsanko Diustabanov St., 4000 Plovdiv, Bulgaria*
[2] *Department of Electronics, Communications and Information Technologies, Plovdiv University "Paisii Hilendarski", 24 Tzar Assen St., 4000 Plovdiv, Bulgaria*
[3]*Dept. of Mechanics, Technical University of Sofia, Plovdiv Branch, 25 Tsanko Diustabanov St, 4000 Plovdiv, Bulgaria*
[4]*European Polytechnic University, Dept. of "Green Energy", 23 Kiril and Metodiy str., 2300 Pernik, Bulgaria*

The analysis of thermal fields requires the collection and processing of information about the temperature in many points in the zone that is under investigation. A specialized autonomous measurement system, developed by Bulgarian scientific team from Plovdiv is presented in the article. It enables long-term recording of temperature data in more than 100 points. The system is designed for analysing thermal fields in Phase change materials storages in hybrid systems. It is also suitable for related applications like chemical and biochemical reactors, and columns, if the temperature is in the range of -20 ° to +125 °C. Data is stored in SD-card and can be transferred via USB interface to the PC by specialized software, where the thermal fields could be visualized.

**Keywords:** hybrid thermal systems, thermal field measurement, chemical and biochemical reactors

## INTRODUCTION

There is a growing use of renewable energy sources to reduce the greenhouse gasses released into the atmosphere. The efficient use of solar and wind energy is among the main tasks in solving the energy problem of humanity. Its disadvantage is the uneven distribution, frequent changes over time and their difficult prediction. This has led to the development of a number of technologies for flexible usage, one of which is energy storage [1].

One of the ways for energy storage is the use of phase change materials (PCM). PCMs are used to balance temporary temperature alternations. They have a number of advantages compared to other heat storage methods - high specific heat capacity, relatively constant temperature during charging/ discharging. However, there are still some problems in the use of materials with change of phase state:

- Phase separation leads to inhomogeneous distribution of the material and thus alter the characteristics of the storage of heat;
- Overcooling leads to a change of phase at a lower temperature, resulting in the release of energy at a lower temperature;

Low thermal conductivity is problematic because it requires more time to reach the desired temperature throughout the material over time, which leads to change in temperature with distance from the heat source [2].

The solving of these problems can be accomplished by better study of their technical characteristics like thermal and hydrodynamic behaviour during operation, which makes possible to improve the structure of the latent heat storages. During the design phase in a particular PCM application tasks numerical modelling and analysis becomes an essential tool [3]. Common approach in modelling is the finite-element analysis. Gong et al. [4] use this method to develop a model in order to simulate cyclic thermal process occurring in shell-and-tube latent heat thermal storage exchanger. Another type of analysis is done by Amin et al. [5] to calculate the phase change effectiveness using the ε-NTU method. Although there are many models developed, there are still many aspects that are not studied completely like heat transfer characteristics inside packed bed and thermal gradients inside the capsules at high temperatures in packed bed thermal storage systems [6]. In order to validate simulation and numerical models more experiments are needed with real thermal systems.

To satisfy this requirement a specific demand exists in measurement systems:

- multiple point measurement;
- long-time autonomous data acquisition;
- adequate accuracy and precision;
- automation of the measurement process etc.

On the market today there are no available such devices. Some portable, battery powered data loggers ensure up to 2-8 measurement channels [7].

Another approach is using PC based data acquisition systems [8]. In this case [9] a 1-Wire to

* To whom all correspondence should be sent:
rum_pop@yahoo.com

USB gateway unit performs interface connection to the sensor network. Several hours of autonomous operation is provided by the laptop battery. The number of the measurement and control points is more than 100. Instead of temperature sensors, humidity sensors, memories and output control devices can be connected to the 1-Wire network.

In this article the development of a specialized, portable, multichannel system for study of thermal fields in hybrid thermal installations with latent heat accumulators is proposed by the scientific team from Plovdiv. The system can provide stand-alone operation for at least a month.

## TEST SYSTEM OVERVIEW

Experimental hybrid installation for heating, ventilation and air conditioning (HVAC), developed by scientific team from "Technical University of Sofia", Plovdiv Branch is used [10]. Its purpose is to study the system parameters in the process of testing the latent heat accumulator that is charged by solar energy. On Fig.1 is shown the schematic of the system. Three solar collectors with a total area of 5.82 $m^2$ are used. They are connected to a water tank, which acts as a heat exchanger.

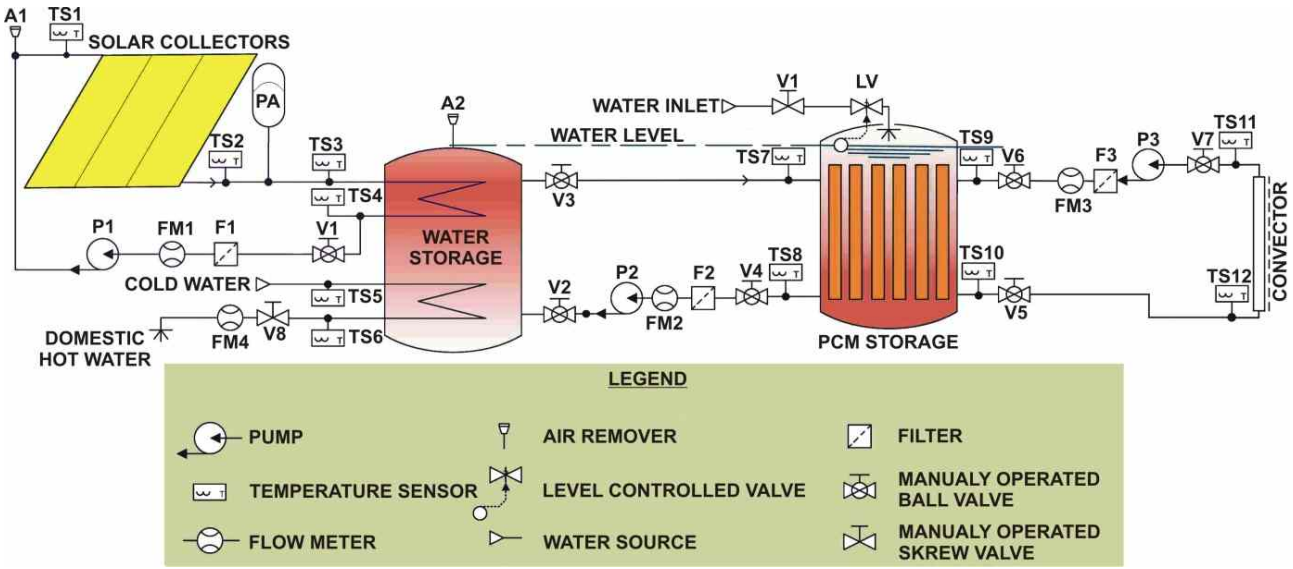


**Fig.1.** Block scheme of the test system [10]

The solar collectors are divided by a heat exchanger from the rest of the system, thus enabling its use in the winter season, by the use of a liquid having a low freezing point.

The water storage tank is equipped with a heater, which is used in case, that the solar radiation is not sufficient. Through the heat exchanger the hot water passes into the heat storage based on phase change materials (different types of paraffin wax are used). The construction of the heat storage tank is shown in Fig.2.

In the water tank there are 39 containers filled with paraffin wax. The containers are made of stainless steel square pipes with dimensions of 80 x 50 x 1,5 mm. The tank has three inlet pipes, located in the centre of the bottom side and three outlet pipes, situated at the periphery of the top side. The angle between pipes is 120 °.

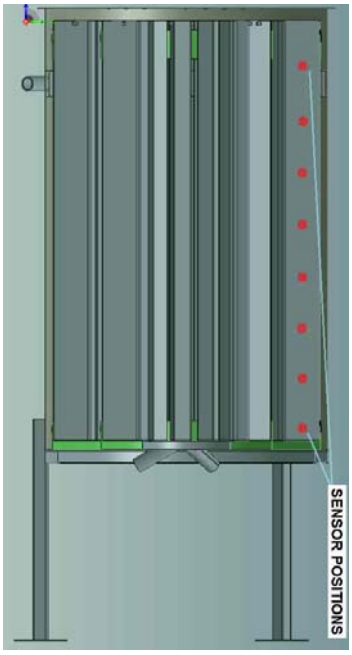


**Fig.2.** Vertical positioning of sensors

The temperature sensors are placed inside and outside the containers at the shape of 5 vertical lines. The vertical plane of the sensor's positions is shown on Fig.2. The location of the vertical sensor lines in a horizontal plane is shown on Fig.3.

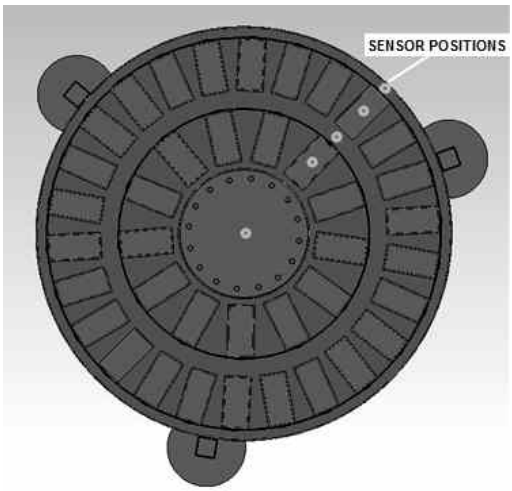


**Fig.3.** Horizontal positioning of sensors

To study the properties of paraffin wax and thermal behaviour of the heat storage, the temperature has to be measured in multiple points. Using this data an accurate temperature profile of the system may be done. For this purpose it has been developed specialized measurement system that simplifies and automates the measurement of thermal fields in hybrid systems. The unit can be easily adapted for other types of applications.

## MEASUREMENT SYSTEM HARDWARE

The measurement system is capable to carry out periodic measurements in up to 128 points by temperature sensors of DS18S20/ DS18B20 type. The sensors have precision of ± 0.5 °C in the range of -20 °C to +125 °C which is adequate for the application.

The measurement system consists of:

- Measurement module;
- Specialized software for visualizing data;
- Temperature sensors DS18S20/DS18B20.

Measuring module was developed using 8-bit PIC18F47J53 microcontroller [11]. The microcontroller is with RISC architecture (Reduced Instruction Set Computer), which has the following key features [12]:

- A small number of instructions;
- Simple instructions are executed in one machine cycle - it makes possible the precise times for real-time tasks in embedded systems;
- A smaller number of transistors compared to the CISC (Complex Instruction Set Computer) architecture, which leads to lower consumption.

One of the main objectives of this development is the low power consumption that provides long-term operation of autonomous battery. The chosen microcontroller meets these requirements with the "nanoWatt XLP" mode, having the following characteristics:

- Deep sleep mode with minimum consumption of 13 nA, real-time clock of 850 nA, inactive processor and other peripheral modules;
- Sleep mode inactive processor and peripheral modules, and active operating memory;
- Idle mode with inactive processor and active peripheral modules.

Different modes allow flexible organization of resources used to achieve low power consumption. The disadvantage of the selected microcontroller is the insufficient amount of RAM and the lack of convenient Flash Memory for storing the system settings. For this purpose external SRAM and EEPROM memory of size respectively 512Kbit and 2Kbit are added, and together with the SD card operates with a common bus interface SPI/$I^2C$. The external RAM is mainly used for:

- Input and output buffers for SD card recording and reading;
- 1-Wire temperature sensors DS18S20/ DS18B20 addresses storage;
- USB to PC transition buffer.

The general scheme of the measurement module is presented on Fig.4. The microcontroller communicates with the temperature sensors network and saves the accumulated data periodically in a SD card. There is a PC to USB interface connection mode. The device is registered as a serial terminal in text mode and can receive commands and send messages. In this mode, the measured temperatures are displayed at the moment. The measurements are carried out periodically, and the time can be set in a range, starting from 5s and up to one week in an interval of 1s. The minimum required time depends on the number of connected sensors. Each sensor has analog-to-digital converter and digital 1-Wire interface [13], formerly known as MicroLAN™. It is designed to perform communication between computer or microcontroller and multiple 1-Wire devices such as sensors, memories etc. via twisted pair cable. This protocol uses only one line for transmitting and receiving and can say that it is a "half-duplex" transmission. There are (in our case) 40 temperature sensors, arranged in 5 rows at 120

mm distance. Taking into account the number of sensors and the physical characteristics of transmission media, the system can be considered as a transmission line. In such cases, the decision is to use termination resistors at both ends, but in this case it is not applicable. So an alternative measures are taken to increase the length of the rising and falling edge, which limits upper bandwidth of the signal. For this purpose a specialized interface chip (DS2482-100) is used. It communicates with the sensor network and connects to the microcontroller through a digital $I^2C$ interface.

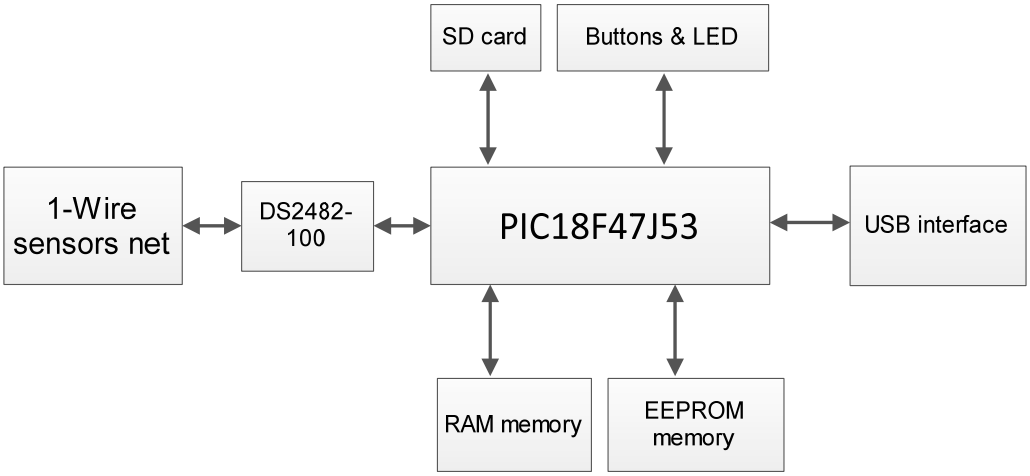


**Fig.4.** Block scheme of the measurement module

Fig.5 shows the view of the prototype board, developed in the Technical University of Sofia, Plovdiv Branch.

**Fig.5.** The prototype of the measurement module

Measurement module is powered by two AA size batteries that allow long term autonomous operation – up to 1 month. That is obtained by the special design of the electronic part, the software algorithm and modes of the microcontroller operation. The most of the time the microcontroller is put into a "deep sleep" mode and turns off the "1-Wire" interface and SD-card power supply. That operation saves the battery life.

## USER INTERFACE

The measuring module has a simple user interface of two buttons and one LED lamp. Their functions are to start and stop the measurement, as well as for any system indications. The operating mode parameters are set via USB connection to a PC. It uses serial terminal interface in text mode. The terminal commands are presented in Table 1.

**Table 1.** Terminal command set

| Type | Name | Description |
|---|---|---|
| get | mperiod | Prints the time between measurements. The value is returned in seconds. |
| get | search | Performs search procedure of connected sensors and prints a list of ROM addresses. |
| get | time | Prints the system time of the device. |
| get | flist | Prints list of files that are on the SD card with extension "*.txt". |
| get | file | Prints the contents of the file with the given name. Example: *get file dat_0020.txt* |
| get | snum | Prints the number of sensors. |
| set | mperiod | Sets the time period between measurements in seconds. Example: *set mperiod 10* |
| set | time | Sets the system time of the device. Example for 10:00:00 1 March 2016: *set time 10 0 0 1 3 16* |
| set | start | Starts measurement |
| set | stop | Ends measurement |
| set | delete | Deletes the given file by its name. Example: *set delete dat_0025.txt* |

The user can obtain information on current operating parameters and/or to reassign a new one

through the serial terminal interface. The command format is:

*<command type> <command name> <parameter 1> <parameter 2> ... <parameter n>,*

where the string "*command type*" can be both: "*set*" - recording the settings or "*get*" - reading the settings.

The system is able to measure the gradient of the wax temperature along the containers. To achieve the necessary precision the sensors must be located in a fixed positions inside the wax. The proposed solution to this problem is through the use of bamboo sticks as a carrier for the sensors (Fig.6).

Special attention is paid to minimizing the impact of the thermal conductivity of electrical wires connecting the sensors. Thin enamelled, high temperature (180 °C) wires are used in the sensor network connections.

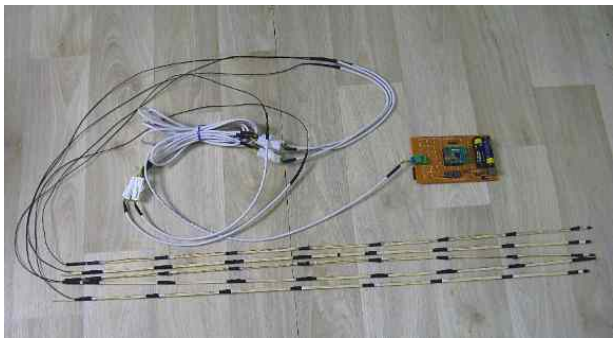

**Fig.6.** General view of the measurement system

## EXPERIMENTAL RESULTS

Experimental measurement with 8 connected sensors of DS18S20 type was carried out for testing and validation of the system. The experimental setup, shown on Fig.7 has been arranged by using:

1. Electrical oven;
2. Container filled with cold water. At the start of the experiment the water temperature was about 20 °C;
3. 8 sensors put into the water at different depth. The sensor spacing was 120 mm;
4. Measuring module;
5. PC, equipped with terminal software.

The number of acquisitions was 71 with time interval of 20 s. The test system simulates the charging mode of the thermal water storage. The heat flux, delivered by the oven passed from bottom part of the container to the top. The collected data was transferred via USB/serial terminal interface and saved as a plain text file. The visualized data is presented on Fig.8 and shows clear picture of the thermal field inside the storage container.

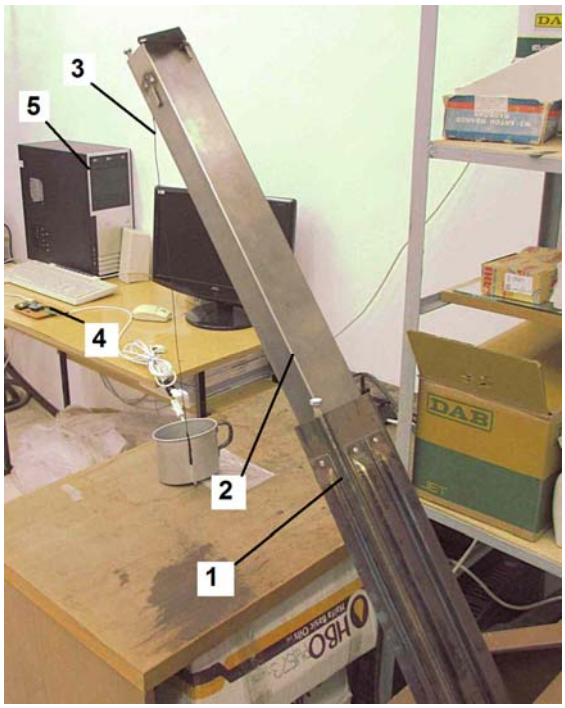


**Fig.7.** Test measurement setup

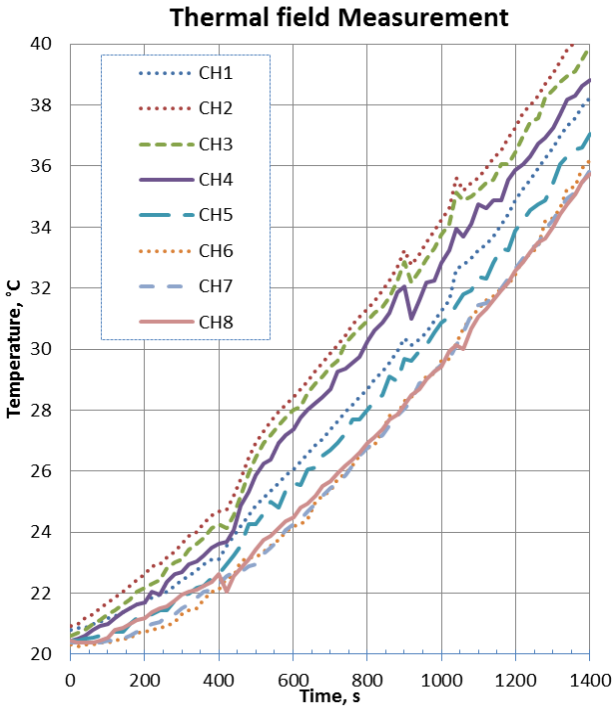


**Fig.8.** Test measurement results

There can be noticed a marked stratification in temperature along the depth. The sensor accuracy reports the value of ± 0.5 °C in the full temperature

range of -20 °C to +125 °C and ± 0.2 °C in the temperature range of 0 °C to +80 °C.

## CONCLUSIONS

The specialized measurement system, that enables long-term (up to one month) recording of temperature data in more than 100 points has been developed in the Technical University of Sofia, Plovdiv Branch. The system's functionality has been approved by real experiments and the following conclusions are made:

1. The system is compatible for analyzing thermal fields in the hybrid systems equipped with thermal energy storages with PCM;
2. Large amount of data may be stored in the SD-card and by specialized software it can be transferred via USB interface to the PC, where the thermal fields could be visualized;
4. The small size sensors are placed into tested area by the way not influencing its thermal field;
5. The measurement system is also suitable to investigate the thermal fields in related applications like chemical and biochemical reactors and columns, if the temperature is in the range of -20 °C to +125 °C.

## ACKNOWLEDGEMENTS

This work has been supported financially by the research project 152ПД0045-24/ 26.03.2015 and the research project 152ПД0046-24/ 27.03.2015 of the Technical University of Sofia, which is gratefully acknowledged by the authors.

## LIST OF ABBREVIATIONS

CISC – complex instruction set computer;
EPROM – electrically programmed read only memory;
HVAC – heating, ventilation and air conditioning;
$I^2C$ – (IIC) inter-integrated circuit (interface);
LED – light emitted diode;
NTU – number of transfer units;
PC – personal computer;
PCM – phase change material;
RAM – random access memory;
RISC – reduced instruction set computer;
ROM – read only memory;
SD – secure digital;
SPI – serial peripheral interface;
SRAM – static random access memory;
USB – universal serial bus.

## REFERENCES

1 T. Bocklisch, Hybrid energy storage systems for renewable energy applications, 9th International Renewable Energy Storage Conference, IRES (2015).
2 E. Milisic, Modelling of energy storage using phase-change materials (PCM), Master's Thesis, Norwegian University of Science and Technology, July 2013.
3 A. V. Waghmarea, A. T. Piseb, Numerical investigation of concentric cylinder latent heat storage with/without gravity and buoyancy, The 7th International Conference on Applied Energy – ICAE2015.
4 Z. Gong, A. Mujumdar, Finite-element analysis of cyclic heat transfer in a shell-and-tube latent heat energy storage exchanger, Applies Thermal Engineering Vol. 17, No 6, pp. 583-591, 1997.
5 N. A. M. Amin, M. A. Said, A. Mohamad, M. S. Majid, M. Afendi, R. Daud, F. Bruno, M. Belusko, Mathematical modeling on thermal energy storage systems, Applied Mechanics and Materials Vol. 695 (2015) pp 553-557.
6 S. Bellana, J. Gonzalez-Aguilara, M. Romeroa, M. M. Rahmanb, D. Y. Goswami, E. K. Stefanakos, Numerical investigation of PCM-based thermal energy storage system, International Conference on Concentrating Solar Power and Chemical Energy Systems, SolarPACES 2014, pp 758 – 768.
7 http://www.omega.co.uk/pptst/AQM-101.html.
8 http://www.pcsensor.com/software-d6.html.
9 CAS2500-26-UL- 1-Wire Data Client. Chipkin Automation Systems: www.chipkin.com.
10 A. Stoyanov, A. Georgiev, R. Popov, Experimental installation for investigation of latent heat accumulator as a part of hybrid system for air-conditioning
11 PIC18F47J53 Family Data Sheet.
12 A. Parmar , D. Kumar, I. Bala, Comparison between RISC and CISC, International journal of innovative research in technology, Volume 1, Issue 12 ISSN: 2349-6002, 2015.
13 Springbok Digitronics, 1-Wire Design Guide v1.0, 2004.

*Bulgarian Chemical Communications, Volume 48, Special Issue E (pp. 102 - 108) 2016*

# Building integrated solar thermal systems – a new era of renewables in buildings

Soteris A. Kalogirou

*Cyprus University of Technology, Department of Mechanical Engineering and Materials Sciences and Engineering, P.O. Box 50320, 3603 Limassol, Cyprus*

Buildings' in EU consume 40% of the primary energy requirements. This is the main reason the Energy Performance of Buildings Directive was implemented whereas the recast of the Directive, specifies that the buildings erected after 2020 should be of nearly zero energy consumption, a requirement that assumes extensive use of renewables. This new role of renewables implies that in addition to photovoltaics, solar thermal systems (STS) will also have a main role to play. The primary use of STS is to meet the building thermal loads, after the traditional standard building energy saving measures are applied, like thermal insulation, double glazing, etc. STS are typically mounted on building roofs as add-on components with no attempt to incorporate them into the building envelope. In this way aesthetic challenges, space availability issues and envelope integrity problems need to be considered. The purpose of this paper is to give a survey of possible applications of STS integration on the building roofs and façades. Details of some projects already under development are also presented.

**Keywords:** building integration, building performance, solar thermal systems, flat-plate collectors

## INTRODUCTION

Buildings energy consumption, account for 40% of the total primary energy requirements in the EU [1]. For this reason, the Renewable Energy Framework Directive, known as the 20-20-20 Directive, is developed which sets a 20% target for renewables by 2020. It is therefore imperative to develop effective energy alternatives suitable to be applied in buildings. An effective and environmental friendly way to reduce fossil fuel dependence in buildings is the use of renewable energy systems (RES). These can be used mainly for heating, cooling and the provision of sanitary hot water. For example, in Cyprus RES, and more specifically solar water heating, are used extensively for the sanitary hot water preparation to more than 93% of the dwellings. Usually these are mounted on building roofs not in a very aesthetic way and sometimes are seen as a foreign element on the roof. For this fact alone and irrespective of the significant economic benefits obtained, some architects do not like this use of solar water heaters or tried to hide them, which usually creates operational problem mainly due to shading. There is therefore a need to find ways to integrate solar systems on the building envelope (walls and roof), which should be done in an aesthetic pleasing way. This is usually done in a win-win situation, i.e., by replacing a part of the building construction the solar system becomes more economically viable and at the same time the building structure provides thermal energy for use in the building.

* To whom all correspondence should be sent:
soteris.kalogirou@cut.ac.cy

Energy Performance of Buildings Directive (EPBD) from its inception, and especially its recast published a few years ago, requires that RES are actively employed to offset conventional fossil fuel consumption in buildings. Such a use of RES reduces the overall building energy consumption and thus a better building category is achieved. Solar thermal systems (STS) integration will directly support this Directive, leading to an increased use of renewables in buildings, which is expected to rise drastically in the coming years. Moreover, the recast of EPBD, specifies that by the year 2020 the buildings in EU should be of nearly zero energy consumption, meaning that after applying various measures to reduce building consumption the rest of the load is covered by RES to achieve nearly zero consumption on a yearly estimation basis. This mean that the building thermal loads will be primarily covered through an extensive use of renewables, which is done after standard building energy saving measures, such as the use of good thermal insulation, advanced glazing systems, etc. are applied. Therefore, STS are expected to take a leading role in covering the building energy needs, and they can contribute directly to the building heating and cooling loads and the provision of domestic hot water for the needs of the occupants.

## BUILDING INTEGRATION OF SOLAR THERMAL SYSTEMS

Among the various renewable energy resources, solar energy is considered as the most effective that

can be applied to buildings to achieve sustainable development mainly because of its abundance and the relatively easy way that this can be used. In particular, solar thermal systems can supply thermal energy for space heating/cooling and the provision of hot water for the needs of a building. An effective building integration of STS, can also create aesthetic improvement, and there would be more space on the building for the installation of the required area of collectors. This is also cost beneficial as the traditional building component is replaced by the STS one, which increases the economic viability of the systems, both of the building and the solar system.

The adoption of building integrated solar collectors, in addition to the architectural and aesthetic benefits that this integration will bring, it creates also some practical issues which need to be addressed; such as rainwater sealing and protection from overheating (avoiding increased cooling loads during summer). As façade installed STS are latitude dependent with respect to solar incidence angle effects, this needs to be considered in detail as countries close to the equator have high solar incidence angles, especially during summer, but more energy is available year round, compared to the high-latitude countries where the sun is much lower, thus smaller incidence angles are evident but the sky is usually cloud covered.

The adoption of building integration of STS, abbreviated to BISTS, can fundamentally change the accepted way solar installations are implemented. These could affect residential and commercial buildings throughout the world. This will surely create a new era of the use of renewables in buildings.

A solar energy system is considered to be building integrated, if for a building component this is a prerequisite for the integrity of the building's functionality. If the building integrated STS is dismounted, dismounting includes or affects the adjacent building component, which will have to be replaced partly or totally by a conventional building component.

The scope of this paper is to present a review of current building integrated STS state of the art technological developments and the most suitable options to achieve this objective. This will enable an understanding of how this integration is applied so far in various buildings worldwide, which will help to identify new ways to achieve better integration. For architects, the application of STS on buildings must form part of a holistic approach. A high-quality solar system can provide a substantial part of the building's energy needs if the building has been designed in the right way. Through a holistic approach, integrating these systems does not only mean replacing a conventional building material, but also aesthetically integrating it into the building design. The integration then takes over other functions of the building's skin. For example, mounted on a sloped roof, profiled systems mean that the STS modules can be part of the watertight skin. A distinction can be made between integration of these systems in the building skin as cladding elements or integrated into the roof or as building components like awnings, shading devices etc. The aim of architectural and building integration of these systems into buildings is to reduce the requirement for land and additional costs, in addition to aesthetics that is generated by the process. This could be the cost of a support structure and the cost of building elements, such as tiles and cladding elements. It is evident that STS integrated into buildings give a more elegant look, and it is more efficient to integrate these systems when constructing the building, rather than mounting them afterwards. Additionally, the integration can bring other added benefits, as for example they may provide a high degree of solar shading for the building itself, which is particularly important in warm climates.

Usually there are three zones for integrating the systems into buildings. These are the roofs, façades and building components like balcony railings, sunshades and sunscreens [2]. STS can be incorporated into buildings by either superimposition - where the system is attached over the existing building envelope, or integration where the system forms a part of the building envelope [3].

## COLLECTOR SYSTEMS THAT CAN BE BUILDING INTEGRATED

The solar collecting methodologies that can be applied in buildings are the simple thermosiphonic units, forced circulation systems employing flat plate collectors, integrated collector storage units, evacuated tube collector systems and various low concentration compound parabolic units [4].

In some countries, such as Cyprus, renewable energy systems and in particular solar water heating are used extensively, with 93% of all domestic dwellings currently equipped with such a system [5]. Most solar collecting components are mounted on building roofs with no attempt to incorporate them into the building envelope. In many instances,

these are actually seen as a foreign element on the building roof. Many architects, irrespective of the substantial benefits that these systems offer, object to this use of renewable energy due to this fact alone. The problem will be even more serious, when solar space heating and cooling systems are used, as they required much more solar collector area. It is therefore necessary to find ways to better integrate solar collectors within the building envelope and/or structures, which should be done in a way that blends into the aesthetic appearance and form of the building architecture in the most cost effective way.

*Classification*

BISTS have been classified across a range of operating characteristics, system features and mounting configurations. The main classification criteria of any solar thermal system is based on the method of transferring collected solar energy to the application (active or passive), the energy carrier (air, water, water-glycol, oil, electricity etc.) and the final application for the energy collected (hot water and/or space heating, cooling, process heat or mixed applications). Additionally, for BISTS the architectural integration quality based on structural, functional and aesthetical variations have to be classified. The collector as a central element of integration has to fulfil in some cases many more specifications than ordinary, add-on collectors. Fig.1 illustrates a simple BISTS classification.

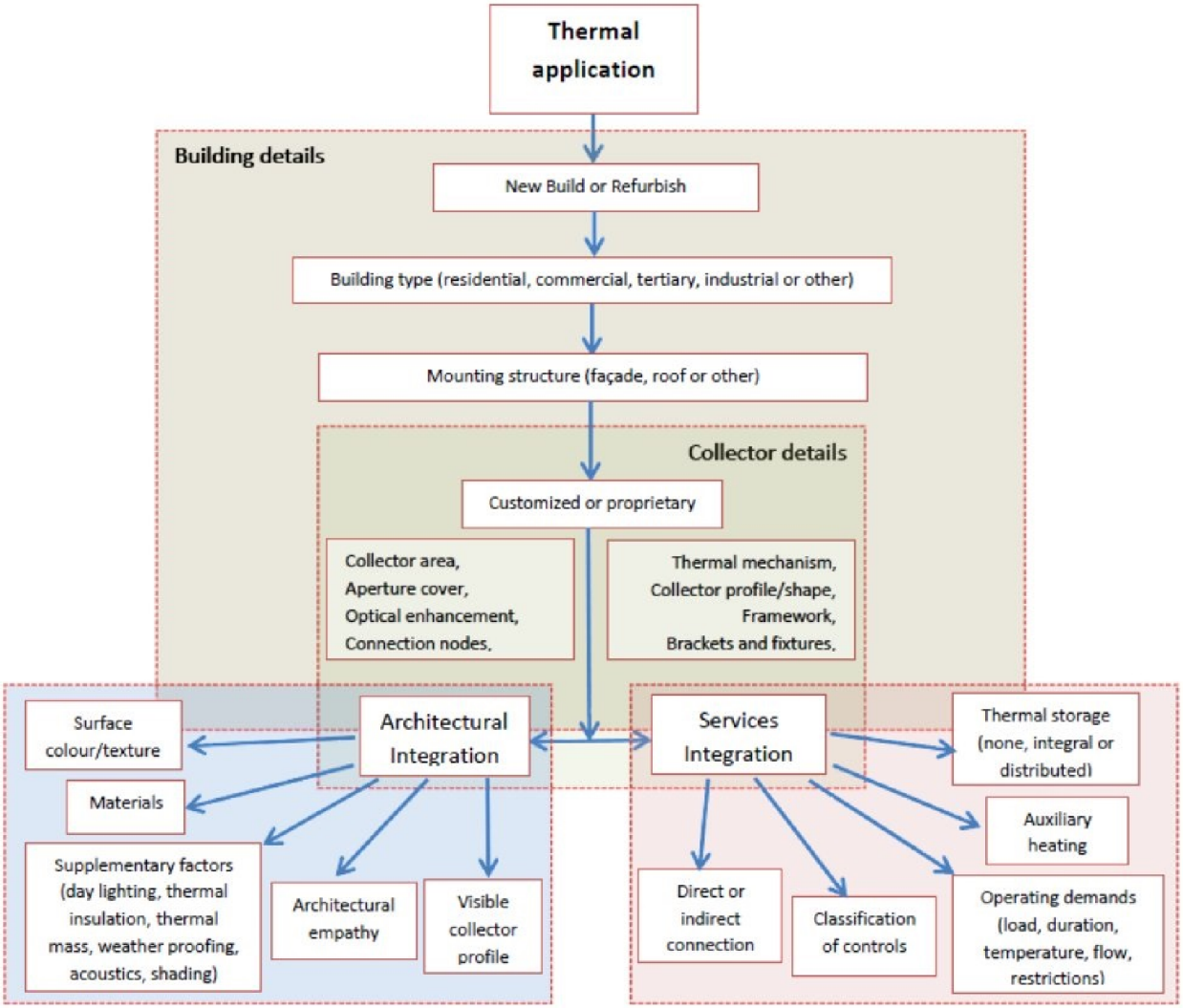


**Fig.1.** BISTS classification

The majority of BISTS can be classified as being either passive or active, e.g. in the former case using thermal buoyancy for fluid transport (natural convection or circulation) or no transport at all, and in the latter case utilizing pumps or fans to circulate the thermal transfer fluid to a point of demand or storage (forced convection or circulation). A number of systems are hybrids, i.e.,

operating in part through a combination of natural and forced transport methods. Many façade solar air heaters use thermal buoyancy to induce an air flow through the vertical cavities that can be further augmented with in-line fans (and auxiliary heating) as necessary.

BISTS deliver thermal energy to the building but other forms of energy may contribute additionally to the buildings energy balance. For instance, daylight comes through a transparent window or façade collector. Heated air or water can be stored or delivered directly to the point of use. Although the range of applications for thermal energy is extensive, all of the evaluated studies demonstrate that the energy is used to provide one or a combination of the following [6]:

**1. Space heating:** Thermal energy produced by a BISTS may reduce the space heating load of a building by adding solar gains directly (e.g. by a passive window) or indirectly (e.g. by transferring heat from the collector via a storage to a heating element) into the building. An example is shown in Fig.2.


**Fig.2.** An indirect solar construction BISTS

**2. Air heating and ventilation:** Thermal heat can be used to preheat fresh air supply to the building. Air is heated directly or indirectly (in a secondary circuit), using forced flow or thermosiphonic flow (natural circulation) to provide space air heating and/or ventilation to the building as shown in Fig.3. In some instances, an auxiliary heating system is used to augment the heat input because of comfort reasons. A variation of this system is the transpired collector in which the sheet metal in front of the building has thousands of small holes to draw the air which gets warm by flowing over the hot sheet.

**3. Water heating:** Hot water demand in the building is the most popular application. In the majority of water heating BISTS, a customized heat exchanger is used to transfer collected heat to a (forced) heat transfer fluid circuit and on to an intermediate thermal store and/or directly to a domestic hot water application. Usually, an auxiliary heating system is used to augment the heat input. An example is shown in Fig.4.

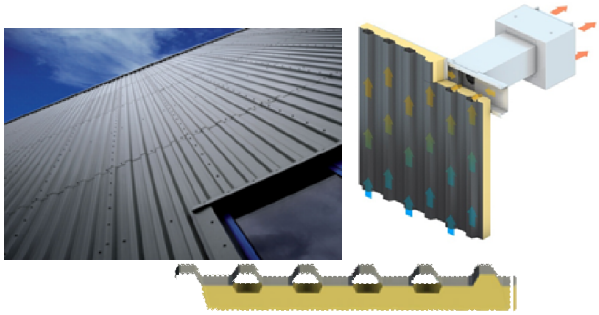

**Fig.3.** Solar air heating façade BISTS with auxiliary heating system

**Fig.4.** Roof integrated flat plate BISTS for Solar Water Heating

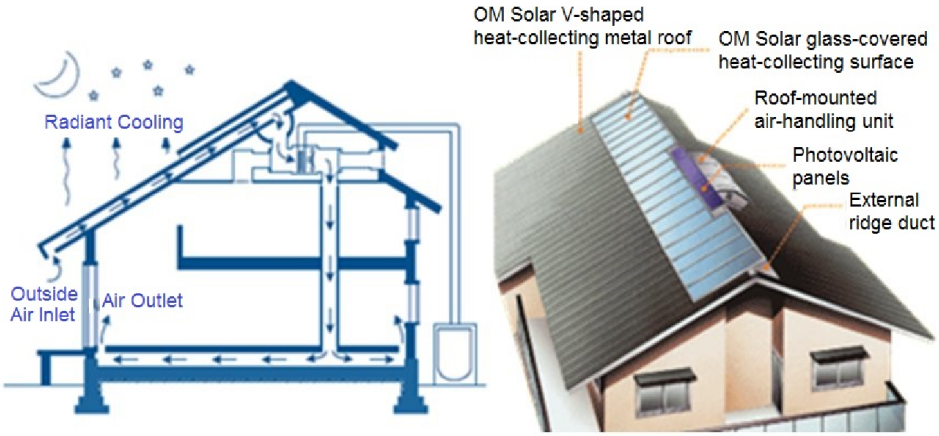


**Fig.5.** Radiant cooling via a reversed BISTS [7]

**4. Cooling and ventilation:** In cooling-dominated climates, buildings most of the time have an excess of thermal energy, and therefore there is a requirement to remove this heat in order to create a comfortable environment. In this view BISTS can also be a technology to extract heat from a building. A number of methods can be used to provide cooling (and/or ventilation) like; shading vital building elements, desiccant linings, supplying heat directly to 'sorption' equipment, or induced ventilation through a stack effect and reverse operation of solar collecting elements for night-time radiation cooling as illustrated in Fig.5 [7].

With reference to Fig.5, during the solar heating mode, fresh outdoor air enters a channel under the roof and flows upward. The air is heated on contact with the metal roof sheet, passing through an upper glazed section (to reduce heat losses) so the heated air enters roof top duct and is mechanically forced through the air-regulating unit. The temperature controlled air is directed down into the space to be heated via underfloor channels between the floor and the concrete slab before finally being diffused into the room through floor diffusers. In cooling mode during summer, outdoor air is drawn through the roof channels at night-time, sub-cooled using radiant cooling, and as with the heating mode, directed into the space to be cooled via the underfloor channels [7].

**5. Other applications:** The majority of BISTS presented so far are mounted on the façade or roofing structures, but a significant number can be classified as being other applications. This includes a number of mounting options, from shading devices or protective barriers to balcony balustrades such as those shown in Fig.6.

**Fig.6.** BISTS balustrade/railing feature

*Taxonomy*

A different classification can relate systems to the mode of installation, i.e., new build, refurbishment or retrofit which is often related to the form of the design or components utilized such as proprietary/pre-fabricated or customized. Further sub-section classification can be related to features such as optical enhancements or indirect benefits associated with the BISTS, such as weatherproofing, acoustic attenuation or thermal insulation. A pictorial taxonomy of the wider BISTS family is shown in Fig.7 [6].

| | | | | Installed element | | | | | |
|---|---|---|---|---|---|---|---|---|---|
| | | | | Façade | | Roof | | Other | |
| | | | | New | Retrofit | New | Retrofit | New | Retrofit |
| OUTPUT | AIR | Air heating & ventilation | Active | 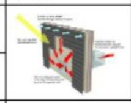 |  |  |  | |  |
| | | | Passive | | | | | | |
| | | Space heating | Active | 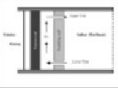 |  | 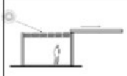 | |  |  |
| | | | Passive | | | | | | |
| | | Combined air and water heating | Active | 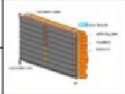 | | 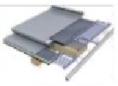 | |  | |
| | | | Passive | | | | | | |
| | WATER | Water heating | Active |  |  |  |  |  |  |
| | | | Passive | | | | | | |
| | | Cooling & ventilation | Active |  | |  |  |  | |
| | | | Passive | | | | | | |
| | ELECTRICITY | PVT | Active |  | |  |  | |  |
| | | | Passive | | | | | | |

**Fig.7.** Taxonomy of BISTS

## NEW SOLUTIONS

A COST Action is currently investigating the building integration of solar thermal systems (BISTS). The COST identification number of the Action is TU1205 and the Action belongs to the Transport and Urban Development (TUD) Domain. More details can be obtained from COST web page (www.cost.eu/domains_actions/tud/Actions/TU1205) or the project web page (http://www.tu1205-bists.eu/).

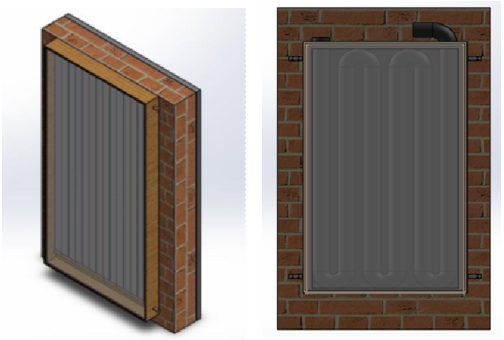

(a) Flat-plate collector water system (left) and air system (right)

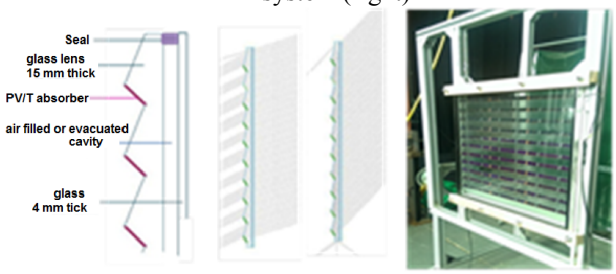


(b) Concentrating PV/Thermal Double Glazing

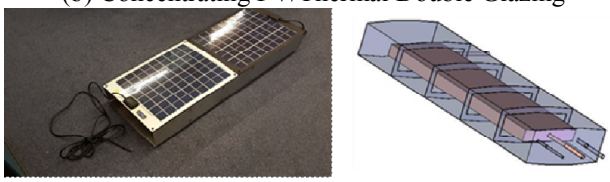

(c) Hybrid Photovoltaic/Solar Thermal (HyPV/T) Façade Module

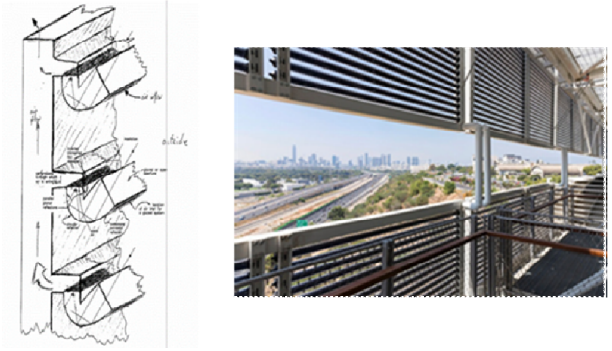

(d) Solar plenum (e) Façade mounded evacuated tube collectors

**Fig.8.** New solutions of façade building integrated solar collectors

As part of this Action, a number of new solutions of building integrated solar thermal systems are currently under development as shown in Fig.8. The first one is a flat-plate collector, which consists of the usual parts found in stand-alone systems without the casing and the whole construction is set up in front of the brick of the normal brick-wall. The system can use water or air as heat transfer medium.

The concentrating PV/Thermal Double Glazing, shown in Fig.8(b) is a façade technology that integrates glazing based solar concentrating elements, coupled with PV/Thermal absorbers [8]. As a multifunctional building component based on conventional double glazing, the system is compatible with traditional façade structures and fenestration, facilitating direct integration into new and retrofit building applications. It can provide solar electricity and heat while insulating the building thermally by using inert gases to suppress convective heat loss inside the glazing cavity. Further thermal insulation levels can be achieved by evacuation of the glazing cavity [8].

The innovative modular HyPV/T façade concept shown in Fig.8(c) integrates a novel cascade thermal diode solar water heater technology with PV cells into a single multi-functional facade element [9]. Two flattened structural vessels (outer absorbing vessel and inner storage vessel) are arranged to create a cavity between the walls of respective vessels. The cavity (maintained at a sub-atmospheric pressure) contains a liquid/vapour phase change material which is the working Heat Transfer Fluid (HTF). The HTF using an absorption/evaporation/condensation processes, the diode concept promotes solar collection and thus thermal storage during collection periods but reduces thermal losses at non-collection periods. The system can produce useful amounts of hot water and electricity [9].

The "solar plenum" shown in Fig.8(d) is an air heating solar collector in which the inclusion of an asymmetric compound parabolic concentrator with a tertiary reflector sector that reflects solar radiation into a downward facing absorber surface. Being downward-facing convection heat loss from the absorber surface is inhibited. The concentration of insolation to an absorber leads to it being at a much higher temperature than ambient. Air enters the solar plenum via a grille beneath its glazed aperture. Heat is removed by the air passing through pin holes in the transpired absorber. The flow rate is maintained at a rate that allows air plumes to pass through the thermally stratified air

layers beneath the absorber without significantly diminishing the thermal insulation of the absorber provided by the stratification.

Finally, the evacuated tube collector integration shown in Fig.8(e) is already tried in Porter school of environmental studies in Israel. A number of facade and roof applications are demonstrated and the idea is to find additional ways to incorporate this type of collector of the building envelope.

Additionally, many readymade products already appear on the market, like roof singles, façade coverings etc. Some typical examples are shown in Fig.9.

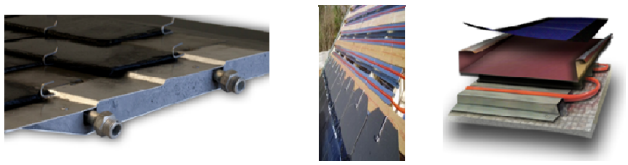

(a) Thermoslate (b) Englert Solar Sandwich

**Fig.9.** Commercial BISTS products

## CONCLUSION

A number of building integrated solar thermal systems are presented in this paper. The implementation of EPBD and its recast which demands nearly zero energy consumption, requires that RES are actively promoted in offsetting conventional fossil fuel use in buildings. Therefore, this uptake in RES in buildings is expected to rise dramatically in the next few years. Meeting building thermal loads will be primarily achieved through an extensive use of renewables, following standard building energy saving measures. STS are expected to take a leading role in providing the thermal energy needs, as they can contribute to the building heating, cooling and domestic hot water requirements. Most of the solutions presented can be applied both to domestic and commercial buildings.

The various systems that can be integrated are classified as presented in this paper. Additionally, the taxonomy is presented according to the working fluid, application component and new or retrofit application. A number of new systems that are currently under development are also presented. As can be seen from the solutions presented in this paper a number of ideas have been tried and others are just at the concept stage and generally more R&D effort is needed. It is believed that in the coming years more and more of these solutions/ideas will find their way in the market in view of the implementation of the directives imposed by the EU.

## ACKNOWLEDGEMENT

The author is grateful to the EU COST Action TU1205: ‘‘Building integration of solar thermal systems (BISTS)” for its sponsorship.

## REFERENCES

1 European Commission, Doing more with less, Green Paper on energy efficiency, 22.06.2005 COM, 2005.
2 T. H. Reijenga, H. F. Kaan, PV in Architecture. In Antonio Luque, Steven Hegedus (Eds.): Handbook of Photovoltaic Science and Engineering: John Wiley & Sons, 2011.
3 M. Fuentes,: Integration of PV into the built environment. Available online at http://www.brita-in-pubs.eu/bit/uk/03viewer/ retrofit_measures/pdf/FINAL_12_Integration_of_PV _red_kth_rev1.pdf, (2007).
4 S.A. Kalogirou, *Solar Energy Engineering: Processes and Systems*, Academic Press, Elsevier, New York, (2009).
5 C.N. Maxoulis, S.A. Kalogirou, Cyprus energy policy: the road to the 2006 World Renewable Energy Congress Trophy, *Renewable Energy*, 33, 355, (2008).
6 COST TU1205: Overview of BISTS state of the art, models and applications, ISBN: 978-9963-697-16-8, (2015).
7 OM Solar Association. http://www.omsolar.net/ en/omsolar2/roof.html.
8 A. Zacharopoulos, C. McAnearney, T.J. Hyde, J.D. Mondol, M. Smyth, I. Lytvyn, Experimental evaluation of a Concentrating PV/Thermal Glazing Façade Technology, Proceedings of COST Action TU1205 Symposium, Guimaraes, Portugal, pp 128-137, ISBN: 978-9963-697-17-5, (2015).
9 M. Smyth, A Besheer, A. Zacharopoulos, J.D. Mondol, A Pugsley, M Novaes. Experimental evaluation of a Hybrid PV/Solar Thermal (HyPVT) Façade Module Technology, Proceedings of COST Action TU1205 Symposium, Guimaraes, Portugal, pp 68-77, ISBN: 978-9963-697-17-5, (2015).

*Bulgarian Chemical Communications, Volume 48, Special Issue E (pp. 109 - 114) 2016*

# Numerical modelling as a supplementary tool for Thermal Response Test

T. Amanzholov[1], B. Akhmetov[2*], A. Georgiev[3,6], A. Kaltayev[1], R. Popov[4], D. Dzhonova-Atanasova[5], M. Tungatarova[1]

[1]*Al-Farabi Kazakh National University, Almaty, 050000, Kazakhstan*
[2]*Research Institute of Mathematics and Mechanics, Almaty, 050000, Kazakhstan*
[3]*Faculty of Mechanical Engineering, Technical University - Sofia, Plovdiv Branch, 25 Tsanko Diustabanov Str., 4000 Plovdiv, Bulgaria*
[4]*Faculty of Physics, Plovdiv University "Paisii Hilendarski", 24 Tzar Assen Str., 4000 Plovdiv, Bulgaria*
[5] *Institute of Chemical Engineering, Bulgarian Academy of Sciences, Acad. G. Bonchev Str., Bl. 103, 1113, Sofia, Bulgaria*
[6]*European Polytechnic University, Dept. of "Green Energy", 23 Kiril and Metodiy str., 2300 Pernik, Bulgaria*

Nowadays, development of efficient thermal energy storage systems is becoming very important since they assist in storing gained heat from renewable energy sources at medium or large scales in an effective way with the purpose of balancing the demand and supply of energy. One of the technologies which allow thermal energy accumulation in a large-scale is Borehole Thermal Energy Storage (BTES). Such technology gives opportunity to store heat into the ground and/or groundwater in summer, and extract it during winter. To evaluate the BTES performance, the ground thermal properties must be known. One of the in situ methods for this purpose is the thermal response test (TRT). But, TRT gives an overall evaluation of the thermal properties of the ground. Therefore, for more precise evaluation, mathematical modelling is used as a supplementary tool for TRT technique. The current paper focuses on experimental TRT technique and mathematical modelling of a TRT process.

**Keywords:** Borehole Heat Exchanger, Thermal Response Test, numerical modelling

## INTRODUCTION

Technologies for harnessing thermal energy from renewable energy sources are being developed and improved at a good pace worldwide. Consequently, the improved efficiency of such technologies gives opportunity to gain thermal energy at a large amount in a short time. But, in order to effectively use the harnessed energy, heat storages are needed.

There are several types of thermal energy storage techniques and storage types vary with storage capacities. Typical storages for accumulation of thermal energy in a large amount are the underground thermal energy storage (UTES) systems. One of the most common systems among UTES is the borehole thermal energy storage (BTES). BTES is attractive since: it can be installed almost everywhere except in locations with underground caverns or high pressure geysers; and it is a long-term system if borehole heat exchanger is installed by carefully following the installation rules [1, 2].

An accurate estimation of the borehole heat exchanger thermal performance can be obtained when the thermal properties of the ground and the borehole are properly evaluated.

A team from the partner universities, Al-Farabi Kazakh National University and Technical University of Sofia, Plovdiv Branch, installed a 50m BTES with a single U-pipe borehole heat exchanger (BHE) in order to test the performance of the BTES and to evaluate the thermal properties of the ground. A vertical U-tube ground heat exchanger, shown in Fig.1, is a key component in any geothermal energy utilization system [3]. The BTES system developed by the authors consists of a high-density-polyethylene (HDPE) U-tube with inner diameter of 25 mm and outer diameter of 32 mm. The U-tube was inserted into 50 m deep borehole and grouted with the mixture of betonite and cement.

Knowledge about thermal properties of the surrounding soil of BTES is very important for estimating the efficiency of the system. One of the well-known experimental methods for evaluation of the ground thermal properties is the thermal response test (TRT). During the TRT, a constant amount of thermal energy is transferred into the ground by using a TRT installation connected to the BHE and the temperatures of the circulating heat carrier fluid are recorded at the inlet and outlet sections of the BHE [4].

After the temperature measurements, which usually last about 7 to 10 days, analysing the

* To whom all correspondence should be sent:
eng.akhmetov@gmail.com

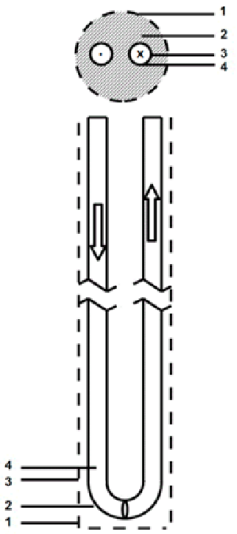


1 - borehole wall; 2 - grout; 3 - interior of U-tube; 4 - U-tube wall.

**Fig.1.** Single U-type borehole heat exchanger [3]

recorded data by means of the line source theory, the effective thermal conductivity of the ground $\lambda_{eff}$, and the borehole resistance $R_b$, are evaluated. Thus, the equation obtained on the base of the line source theory is [5]:

$$T_f = \frac{Q}{4\pi\lambda H}\ln(t) + \left[\frac{Q}{H}\left(\frac{1}{4\pi\lambda}\left(\ln\left(\frac{4a}{r_b^2}\right) - \gamma\right) + R_b\right) + T_g\right]$$

for $t \geq \frac{5r_b^2}{a}$ (1)

$$T_f(t) = k \cdot \ln(t) + m, \qquad (2)$$

where $$\lambda = \frac{Q}{H \cdot 4\pi \cdot k} \qquad (3)$$

where $T_f$- is average temperature, °C; $\lambda$ - is thermal conductivity of the ground, W/mK; $H$ - is depth of borehole, m; $Q$ - is heat flux, W; $t$ – is time from start, s; $R_b$- is borehole thermal resistance, mk/W; $r_b$ - is radius of the borehole, m; $a$ - is thermal diffusivity, m²/s; $T_g$ - is initial temperature before the charging of borehole, °C; $\gamma$=0.5772 - is Eulerian constant.

But, Eqn. (1) gives an overall evaluation of the effective thermal conductivity $\lambda_{eff}$ and the borehole thermal resistance $R_b$. In other words, the Line Source Model (LSM) [5] does not take into account subsurface layers of the ground around the borehole, but only assumes that the surrounding medium is homogenous and non-porous, without any groundwater flows. Therefore, the heat transfer process is only conductive. Moreover, the line source model includes the borehole thermal resistance between the fluid and the surrounding formation. Other limitations of the LSM were discussed by Wagner at al. [6].

In the current paper we apply numerical modelling techniques, which consider geological heterogeneity, groundwater flows, and heat transfer in porous media, the properties of the material of the BHE pipe, the grouting material and the subsurface layers.

## NUMERICAL SIMULATION

On the contrary to the Line Source Model, the numerical approach allows for the simulation of subsurface physical as well as hydrodynamic processes during a TRT [7, 8]. The numerical

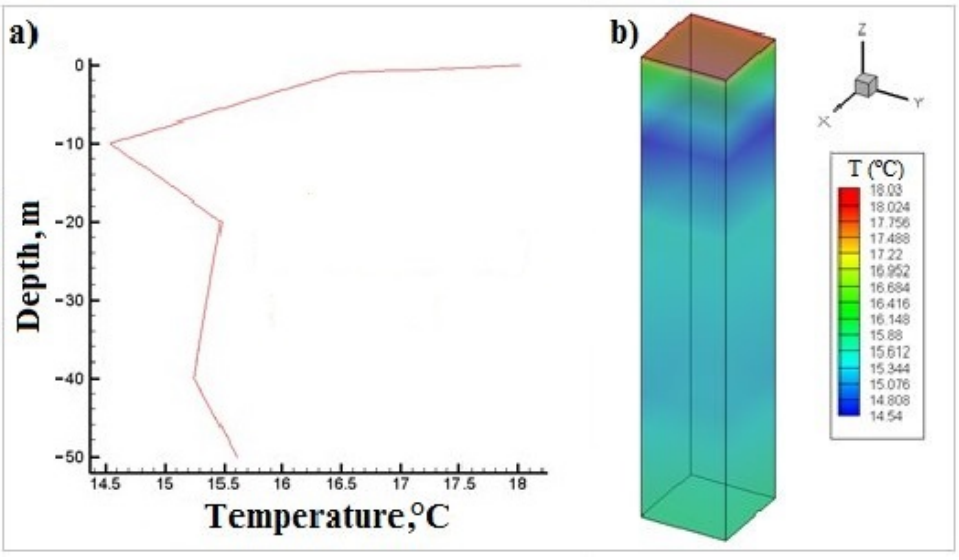


**Fig.2.** Initial temperature distribution in the soil: a) testing data; b) simulation data

model, coupled with the results of the experimental studies, can be used to simulate the TRT and the working modes of BHE under realistic conditions.

Experimental data of a TRT, carried out in August 2015 at the Technical University of Sofia, Plovdiv Branch, was taken as input data for the numerical modelling purposes. The initial temperature distribution around the BHE was obtained by circulating the working fluid through the BHE and the TRT installation without providing any thermal energy to the loop about 1 hour.

Fig.2a presents the temperature distribution along the borehole obtained from the temperature measurements of the buried Pt 100 sensors. Applying these results in the modelling by linear interpolation of the temperatures between two adjacent sensors, initial temperature distribution in the soil can be introduced to the numerical approach (Fig.2b).

Moreover, ground heterogeneity was also included in the modelling. In fact, types of the soils were determined while drilling the borehole, and thermal properties of these materials were taken from paper [9]. Thus, the properties of the soil layers surrounding the BHE are given in Table 1. In addition, when drilling the borehole, the presence of the aquifer was noticed around 10 m depth. This is also confirmed by the significant decrease of the temperature gradient at 10th meter, which is due to the groundwater (Fig.2a). In the modelling, the thickness of the groundwater layer was taken as 10 m, starting from 5 meter depth. And velocity of the groundwater flow was taken as 0.1 mm/s which is quite reasonable for most of the time.

**Table 1.** Properties of the underground materials [9]

| Material | Thermal conductivity (W/m K) | Volumetric heat capacity (MJ/m³) | Density (kg/m³) | Depth (m) |
|---|---|---|---|---|
| Sandy soil | 0.3 | 800 | 1600 | 0-0.4 |
| Technical ground | 0.83 | 1970 | 800 | 0.4-2.0 |
| Clay | 1.58 | 2000 | 1550 | 2.0-9.4 |
| Saturated sand | 2.2 | 2000 | 1480 | 9.4-50.0 |

The temperature at the inlet section of the BHE, measured during the TRT, is also taken as input data to the modelling. Measurement results of the ambient temperature variation during the test, and temperature development at the inlet and the outlet of the BHE are presented in Fig.3. The numerical modelling was carried out in three dimensional space with a size of $10\times10\times60$m (length $\times$width $\times$depth).

The dimensions of the BHE are listed in Table 2. The diameter of the borehole is taken as 165 mm, and the inlet and outlet pipes are considered to be evenly located in the borehole. Therefore, shank spacing between the pipes is about 28 mm.

Mesh resolution is not regular, but increases towards the borehole where the temperature gradients are steepest. Groundwater was determined during the drilling of the borehole at a depth of about 12 m. Therefore, in the modelling meshing is finer at the groundwater flow level and

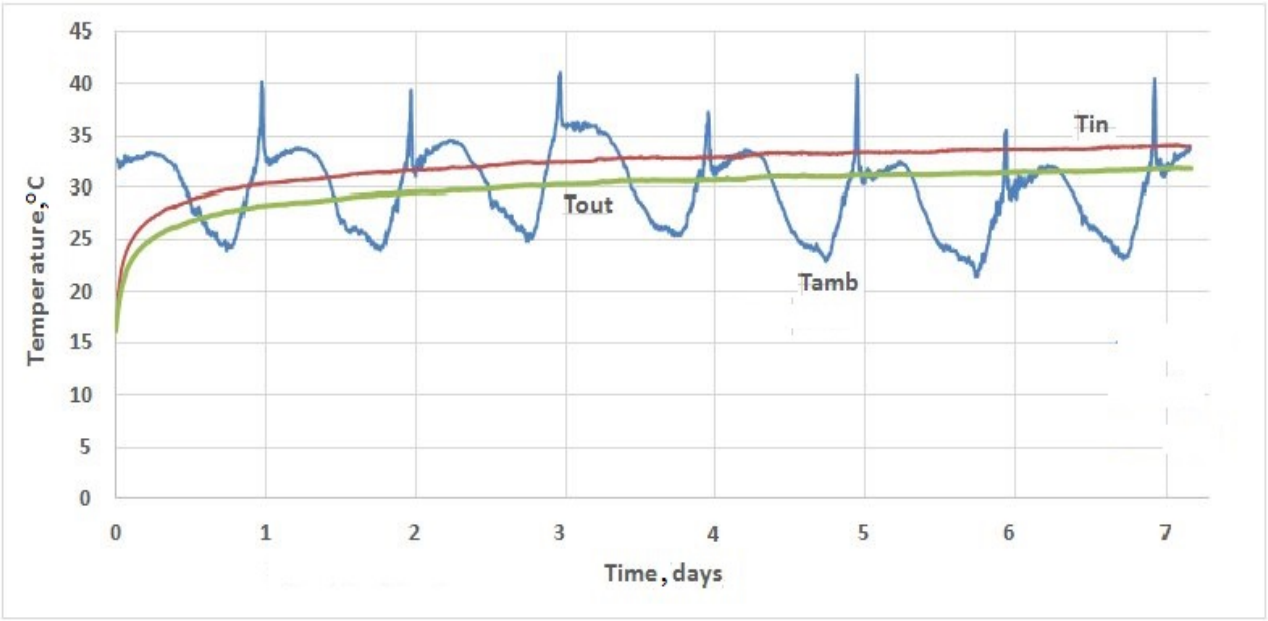


**Fig.3.** Ambient temperature variation and development of the temperature at the inlet and outlet sections of the BHE during experimental TRT

at the bottom of the borehole because of significant temperature gradient (Fig.4).

**Table 2.** Dimensions of the borehole heat exchanger

| Name | Value (meter) |
|---|---|
| Inner radius of the BHE pipe $r_{in}$ | 0.0125 |
| Outer radius of the BHE pipe $r_{out}$ | 0.016 |
| Radius of the borehole $r_b$ | 0.0825 |
| Depth of the BHE $d_{BHE}$ | 50 |

### *Equations*

Inside the BHE, fluid flow is modelled by the pipe flow equations together with conservation law [10]. This approach uses "edge elements, solving for the tangential cross-section averaged velocity along the edges, to avoid meshing the cross section of the pipe with a full 3D mesh. This means that the modelled variables are averaged in the pipe's cross sections and vary only along the length of the pipe" [10]:

$$\rho\frac{\partial u}{\partial t}+\rho u\cdot\nabla u=-\nabla p-f_D\frac{\rho}{2d_h}u|u|+F \quad (4)$$

$$\frac{\partial A\rho}{\partial t}+\nabla\cdot(A\rho u)=0\ , \quad (5)$$

where $u$ is the cross section average velocity, m/s; $\rho$ is the fluid density, kg/m$^3$; $p$ is the pressure, Pa; $f_D$ (dimensionless) the Darcy friction factor; $F$ is a volume force term, N/m$^3$ and $d_h$ is hydraulic diameter, m. Moreover, the energy equation for an incompressible fluid flowing in a pipe is [10]:

$$\rho AC_p\frac{\partial T}{\partial t}+\rho AC_p u\cdot\nabla T=\nabla\cdot A\lambda\nabla T+f_D\frac{\rho A}{2d_h}|u|^3+\dot{Q}\ , \quad (6)$$

where $A$ is the pipe cross section area, m$^2$; $C_p$ is the specific heat capacity at constant pressure, J/kg $K$; $T$ is the temperature, $K$; $\lambda$ is the thermal conductivity of the water, W/mK.

For heat transfer in porous media, the following equation is solved [11]:

$$(\rho C_p)_{eff}\frac{\partial T}{\partial t}+\rho C_p u\cdot\nabla T+\nabla(\lambda_{eff}\nabla T)=\dot{Q} \quad (7)$$

where $(\rho C_p)_{eff}$ is the effective volumetric heat capacity at constant pressure, J/m³.K; $u$ is the fluid velocity m/s; $\lambda_{eff}$ is the effective thermal conductivity of the ground, W/mK, and $\dot{Q}$ - heat source term for equations (6) and (7) measured in W/m$^3$. For Eqn. (6) it is zero since there is no any heat source in the pipe.

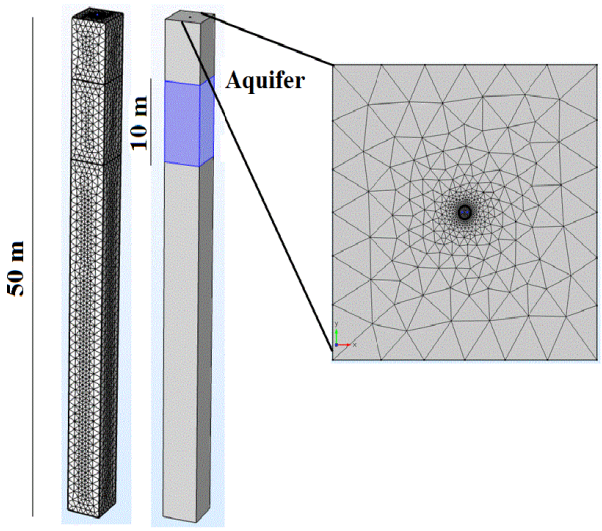


**Fig.4.** Overview of the modelling domain and numerical discretization

In order to model the TRT process, both hydrodynamic and energy equations need to be solved with appropriate initial and boundary conditions. As mentioned above, initial temperature distribution inside the borehole as well as in the subsurface layers was set up as given in Fig.2. At the edges (i.e. boundaries) of the geometry outflow thermal boundary was set up, although the dimensions of the computational domain are large enough to minimize boundary effects for the time of the TRT (7 days in our case). The experimental inlet temperature was applied as an inlet boundary condition for the numerical simulation of the TRT process. Once the inlet temperature and velocity is given, fluid flow and heat transfer in the BHE pipe is calculated based on Eqns. (4)-(6). The resulting temperature distribution in the BHE obtained by numerically solving these equations is used as a heat source in Eqn. (7) to model the heat transfer in subsurface layers in three dimensional space.

## RESULTS AND DISCUSSION

To analyze the correctness of the numerical modelling results, they were compared with the experimental data. During the experimental TRT heat was injected using electrical heater in the installation with a constant power of 2 kW to the ground, with water flow rate of 600 l/h through the BHE while measuring the inlet and outlet temperatures. The results of the comparative

analysis in respect to the inlet and outlet temperature developments are presented in Fig.5, which illustrates a good agreement between the experimental and the numerical data. Although, the inlet temperature for the modeling was taken from experimental studies, the data was interpolated first and its approximate equation was obtained and then used in the modelling. The interpolation was necessary because recording time interval during the test and time step in the modelling were different. That is the reason of some deviations occurred when inlet temperature of experimental and numerical studies are compared. But, the most significant results is the outlet temperatures agreement. Therefore, it can be concluded that the modelling approach is correctly set up and its results describe the TRT process taking into account heterogeneities of the soil, groundwater flows, and heat transfer in porous media which are not considered in the LSM.

Based on the results of the numerical simulation, which is more reliable tool compared to the analytical methods, it is possible to evaluate the temperature field around the borehole (Fig.6). Moreover, the numerical model easily accounts for different heat injection rates by specifying the water temperature at the inlet of the BHE to simulate the process, for instance charging or discharging of the BTES system for a desired time duration. Moreover, the number of the boreholes can be increased up to the desired number of BHE depending on the thermal demand for the users, thus, creating a large scale borehole thermal energy storage, and the performance of the system and its working modes can be modelled together with the temperature field in subsurface layers.

## CONCLUSIONS

As commented above, the Line Source Model, typically used to analyse a TRT, assumes that the surrounding soil is homogeneous, heat transfer is in the form of conduction only, and no aquifer flows are present. In the current paper, on the contrary to the analytical approach, we developed numerical technique, using a 3-D finite-element numerical model, which takes into account major and necessary physical process and parameters such as heterogeneities of the subsurface layers, ground water flows and conductive and convective heat transfer in porous media. In other words, the numerical simulation helps to reduce the errors in estimating the thermal properties, which originate from the analytical methods such as the Line Source Model, especially when the real test conditions do not satisfy the assumption of the analytical approach.

The experimental verification of the numerical technique shows a good agreement with experimental data form the TRT studies carried out at the Technical University of Sofia, Plovdiv Branch. With the help of the developed numerical tool, it is possible to simulate the underground temperature field during TRT, and to understand the thermal energy transfer across the subsurface layers of the ground.

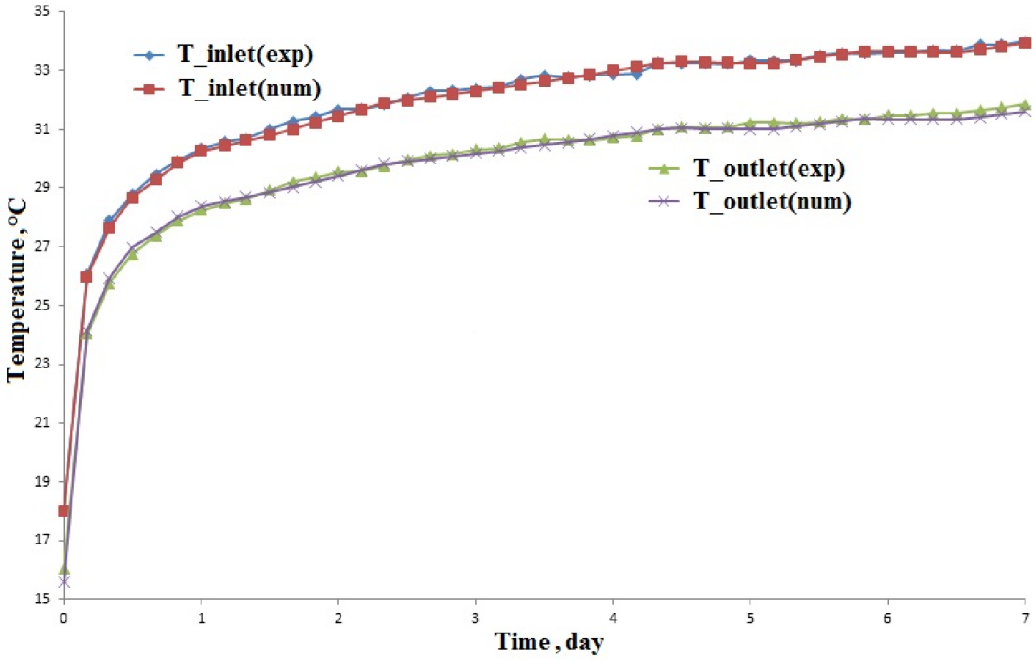


**Fig.5.** Comparison of inlet and outlet temperatures of experimental and numerical studies

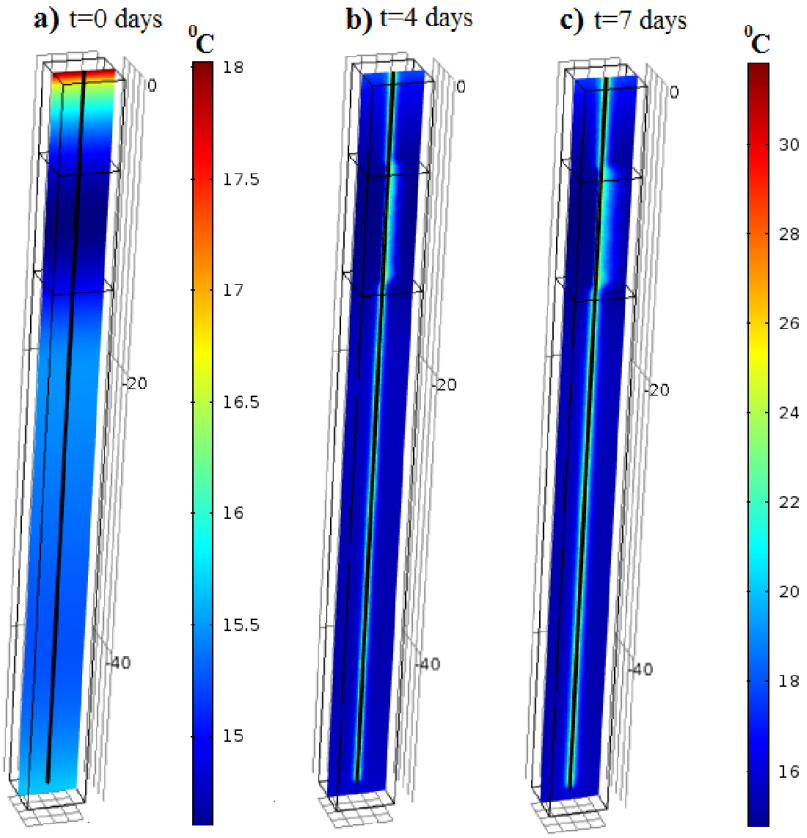


**Fig.6.** Temperature distribution at a) the beginning, b) after 4 days and c) after 7 days for the TRT simulation

## ACKNOWLEDGMENTS

The authors acknowledge the support provided by the Institute of Mathematics and Mechanics of Al-Farabi Kazakh National University, under the grant funding (GF-3289) named "Development of charging and discharging regimes for hybrid thermal energy storage system consisting of latent heat storage and borehole thermal energy storage, designed to accumulate solar thermal energy".

## REFERENCES

1 I. Dincer, M. Rosen, Thermal energy storage systems and applications, Wiley, 2002.
2 P. Pinel, C. A. Cruickshank, I. Beausoleil-Morrison, A. Wills, A review of available methods for seasonal storage of solar thermal energy in residential applications, *Renewable and Sustainable Energy Reviews*, 15, 3341-3359, (2011).
3 T. Sliwa and M.A. Rosen, Natural and Artificial Methods for Regeneration of Heat Resources for Borehole Heat Exchangers to Enhance the Sustainability of Underground Thermal Storages: A Review, Sustainability, 7(10), 13104-13125 (2015).
4 S. Gehlin, G. Hellstrom, Influence on thermal response test by groundwater flow in vertical fractures in hard rock, *Renewable Energy*, 28 (14), 2221-2238 (2003).
5 P. Eskilson, Thermal Analysis of Heat Extraction Boreholes. Doctoral Thesis. Department of Mathematical Physics, University of Lund, Lund, Sweden (1987).
6 V. Wagner, P Bayer, M Kubert, P. Blum, Numerical sensitivity study of thermal response tests, *Renewable Energy* 41, 245-253, (2012).
7 J. Raymond, R. Therrien, L. Gosselin, R. Lefebvre Numerical analysis of thermal response tests with a groundwater flow and heat transfer model, *Renewable Energy* 36, 315-324, (2011).
8 S. Signorelli, S. Bassetti, D. Pahud, T. Kohl, Numerical evaluation of thermal response tests. *Geothermics*, 36(2), 141-166 (2007).
9 Toshkov, E.T. Investigation of a Hybrid System with a Ground Source Heat Pump and Solar Collectors. *Technical university of Sofia, Plovdiv Branch, PhD Thesis*, 2015 (in Bulgarian).
10 Comsol user guide, The Heat Transfer Module, version 5.2.
11 F. P. Incropera, D. P. Dewitt, Bergman, T.L., Lavine, A.S., 2006. Fundamentals of Heat and Mass Transfer, 6th ed. John Wiley & Sons Inc., New York, NY, USA.

*Bulgarian Chemical Communications, Volume 48, Special Issue E (pp. 115 - 119) 2016*

# Energy pile and ground temperature response to heating test: a case study in Brazil

T. S. O. Morais, C. H C. Tsuha*

*Geotechnical Engineering Department, University of Sao Paulo at Sao Carlos, Av. Trabalhador Saocarlense, 400, Sao Carlos, Brazil.*

Geothermal energy piles have been used as space heating and cooling in residential and commercial buildings, as well as a sustainable and environmentally friendly alternative energy system. Brazil is currently the fifth largest buyer of air conditioner in the world, mainly due its tropical and subtropical climate. Seeing the need of studies about the use of energy piles in Brazil as a new solution for space conditioning and water heating, this paper presents some results of a preliminary investigation carried out in Brazil on the effect of the pile heating process on the ground temperatures, and the ground thermal recovery. For this study, a bored energy pile of 12 m length and 500 mm diameter was installed at the Geotechnical Experimental field of the University of São Paulo at São Carlos (Brazil). The experimental area is composed of an unsaturated tropical soil, including a lateritic superficial layer composed of colluvial clayey sand overlaying a residual sandstone soil, with average temperature of around 24°C. Temperature sensors were installed inside the pile and in the surrounding soil in order to provide the results of temperature variations during the heating loading-unloading. This paper presents the response of energy pile and ground temperatures to heating test at different depths.

**Keywords:** energy piles, unsaturated tropical soil, tropical and subtropical climate

## INTRODUCTION

Ground-Coupled Heat Exchanger Systems have been used as acclimatization system for residential and commercial buildings [1]. This system was adapted to pile foundations in order to exchange thermal energy with the ground [2]. Energy pile systems have been implemented in many countries to replace an important part of electrical and other sources of energy.

Shallow geothermal resources have revealed a great potential of usable energy, especially in connection with pile foundations and by means of borehole heat exchangers [1]. Energy foundations are used for the environmental-friendly heating and cooling of the building. For this, the piles are installed with heat exchanger tubes [3].

The object of the design process of energy piles is to determine how much energy can be extracted or stored within the ground, or how many energy piles are required to achieve a certain energy demand. The energy attainable from the piles depends on the ground conditions and thermal properties [4]. Additionally, during heating and cooling cycles the energy pile expands and contracts, and this fact influences the pile-soil interactions [5] therefore, the thermal-mechanical response of energy piles should be evaluated in the design stage.

Brazil is the ninth largest consumer of electrical energy in the world [6], and much of this energy is used for air conditioning. Therefore, the present paper is part of an overall study proposed to investigate the use of energy piles in order to reduce the consumption of electricity in Brazil.

This paper explores: (i) the ground temperature response to heating (thermal loading condition that simulates operation of a geothermal pile during summer) by a pile heat exchanger; (ii) the radial heat transfer; and (iii) the ground recovery at a site in São Carlos, São Paulo state (Southeast Region of Brazil).

## GROUND CONDITION AND PROPRIETIES

The key factor that motivates this study is that unsaturated tropical soils cover a significant part of the Brazilian territory, and the performance of heat exchanger piles in typical Brazilian soil and climate was not investigated before.

The pile heating test was conducted on a bored pile (12 m depth) installed in the Geotechnical Experimental field of the University of São Paulo at São Carlos (Brazil), consisted of unsaturated tropical lateritic soil, including a superficial layer composed of colluvial clayey sand (lateritic) overlaying a residual sandstone soil.

Fig.1 and Fig.2 shows the characterization of the soil at the site investigated and the results of the SPTs and CPTs. The mineralogical composition of the soil of this test site indicates that the fraction of quartz along the pile depth varies from 50 to 60%, and around 30% of the soil consists of aluminium and iron oxides, formed by lateralization process.

* To whom all correspondence should be sent:
chctsuha@sc.usp.br

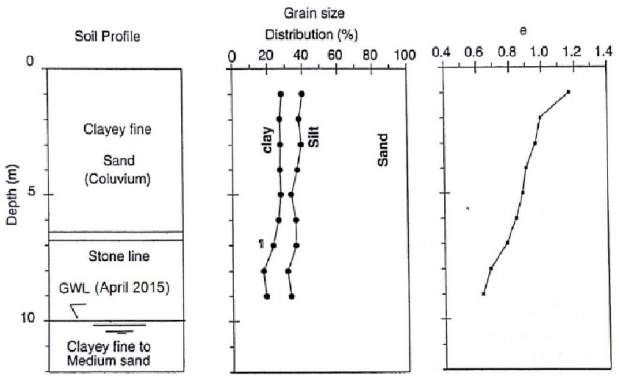


**Fig.1.** Grain size distribution and average void ratio of soil at the test site [7]

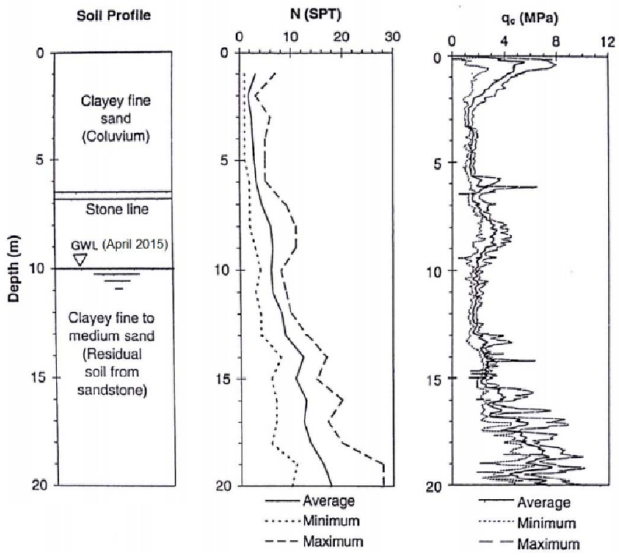


**Fig.2.** Results of SPT and CPT tests in the test site [7]

## EXPERIMENTAL SYSTEM

The pile heating test was carried out using a thermal response test unit (Fig.3) built in Brazil for the current research. The unit consists of a 100-L water heater reservoir tank and a pump, two heating elements (two 1000 W independent resistances), a data logger, a turbine flowmeter and one inlet and one outlet for the heating fluid. The data logger monitored and recorded inflow and outflow heat-exchange fluid (pure water in the current case) temperatures, and the flow rate.

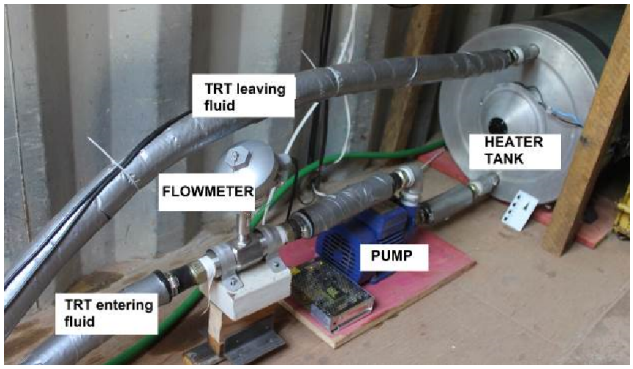


**Fig.3.** Thermal response test unit (water heater reservoir tank, water pump, and the turbine flowmeter)

For this investigation, a bored pile with 0.50 m diameter and 12 m depth was used as heat exchanger pile. As illustrated in Fig.4 and Fig.5, a polyethylene piping system (32 x 3,0 mm) was fixed to the reinforcement cage of the energy pile. Before the concrete filling, the cage with a double "U" loop was installed inside the pile in the borehole (Fig.5a).

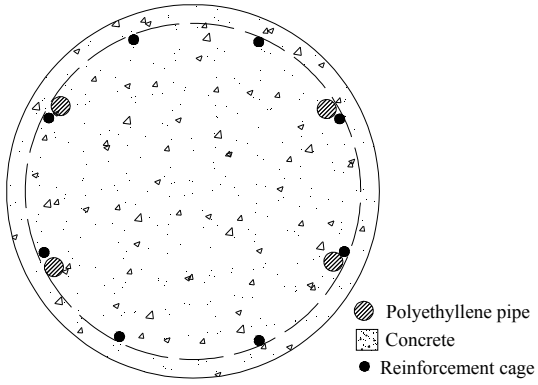


**Fig.4.** Cross-cutting section of energy pile

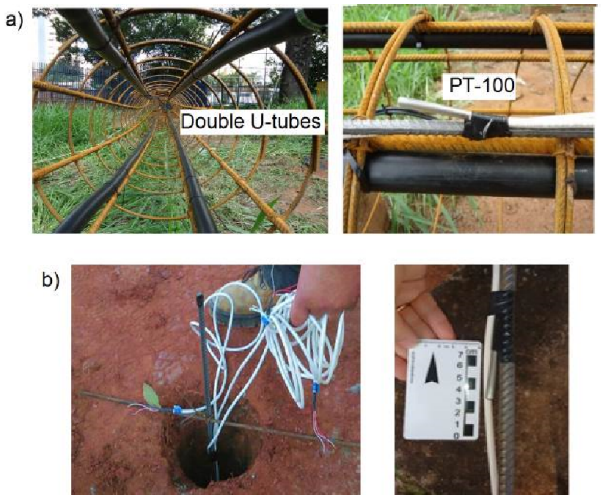


**Fig.5.** Installation of Pt100 temperature sensors (a) in the pile cage and (b) in the ground

The energy pile was instrumented with strain and temperature sensors placed at different depths. The thermistors (PT 100) were installed inside the pile and into the ground in two boreholes close to the pile (BH1 and BH2) at different depths: 3.5, 7.5, and 11.5 m, as described in Fig.6.

The boreholes were installed at distances of 1.0 m (BH1) and 2.0 m (BH2) from the pile center axis (Fig.6). These temperature sensors were attached to steel bars (Fig.5b), and after that the boreholes were filled with grout.

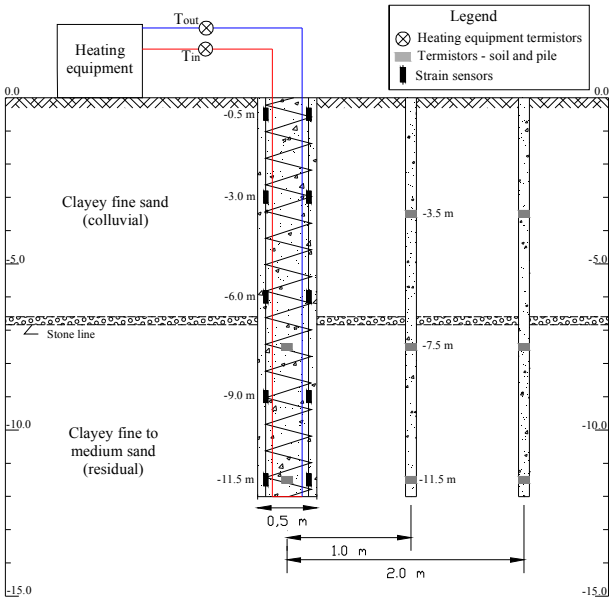


**Fig.6.** Scheme of the energy pile and instrumented soil boreholes (BH1 and BH2)

Fig.7 shows the temperature distribution of the underground soil at different depths (in BH2) and at the soil surface in a period started after 30 days after the heating test is completed. This figure illustrates that the soil surface temperature oscillates periodically, and at the depth of 3.5m the temperature is reduced compared to the results measured at 7.5 and 11.5mm depth. Probably the temperature of the soil at 3.5m is more affected by ambient air temperature.

## HEATING TEST

The pipes of the heating test equipment were connected to the pipes inside the energy pile, and the system was filled with fluid (water in this case).

The heating test consists in circulating fluid thought an energy pile while supplying a constant amount of power to the fluid. The current heating test was conducted during a period of 8.5 days. Inflow and outflow temperature of the heat-exchange fluid, and the temperatures of the pile, the ground and the atmosphere were recorded continuously during and after the heating period.

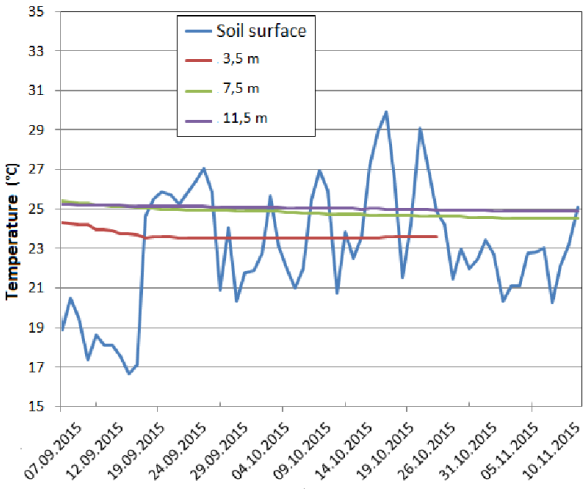


**Fig.7.** Ground temperature fluctuations measured at the borehole BH2 30 days after the end of heating test

After the end of the heating test, the pile and the ground were cooled by stopping the fluid circulation and letting the induced heat dissipate into the surrounding soil. Further details on the heating tests and the ground thermal properties are presented in Morais et al. [8].

The heating fluid temperatures measured within the pipes entering and leaving the pile during the heating period are presented in Fig.8.

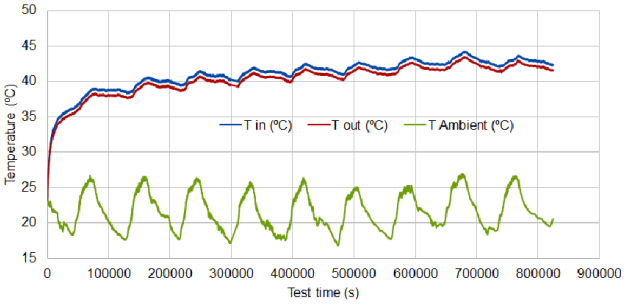


**Fig.8.** Fluid temperatures registered during the heating period

During the heating test, the temperatures inside the pile and in the two boreholes around the pile (1m and 2m distance from pile axis) were registered. The temperature sensor installed at 3.5m depth inside the pile was damaged; therefore, the measurements of temperature at 3.5m depth were obtained only inside the boreholes around the pile.

Fig.9 presents the pile transient temperature in response to the heat test. The temperature was found to increase within the pile during the heating test and decrease progressively after the test was

stopped. This figure shows that the temperature inside the pile increased during the test, mainly at -7.5m depth (compared to the bottom part of the pile at -11.5m). During the heating test the temperatures kept rising as the days passed, however the rate of increase tended to stabilize. The temperature decreases rapidly and uniformly in the first 5 days after the heating test is completed.

Fig.9 shows an almost full thermal recovery after around 30 days. The pile takes around three times the amount of time used for the heating test to have full thermal recovery. After around 60 days cooling the pile returned fully to the temperature levels recorded before the heating test.

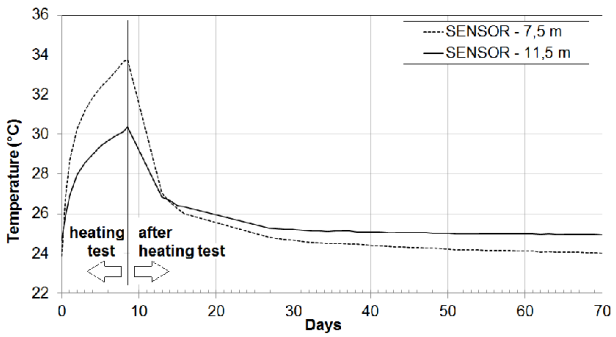


**Fig.9.** Energy pile temperature response to heating test

Fig.10 shows the ground temperature variation of BH1 (at a distance of 1.0 m from the pile axis) during the heating test. The maximum temperature of 27.5ºC was observed at 7.5 m depth at the end of the heating test. The minimum temperature was observed at 3.5 m depth, however, the amount of temperature increase during the test are similar at these both depths, and smaller at the pile base (-11.5 m depth). This figure also illustrates that, as observed inside the pile, the ground temperatures started to decrease as soon as the heating test was stopped. This shows the immediate ground thermal response during and after the heating test. The shape of thermal profiles is similar at all the selected time periods; therefore the ground thermal response to the heat test is uniform at all tested depths.

The heat test has increased 3.2ºC of the ground temperature, in distance of 1.0 m from the pile axis, at 3.5 m and 7.5 m. Therefore, it could be concluded from this observation that the heat moved in radial direction. Lower temperature increase was observed at 11.5 m depth, probably because in the vicinity of pile head and base the radial heat transfer are reduced.

Fig.10 indicates that the temperature drop is higher in the first 20 days after the end of the heating test. Heat dissipated faster in the beginning after the heating is stopped. The ground recovery took around three times of the heating test duration as observed earlier within the pile. Full thermal recovery took around 60 days to complete, however, at 3.5 m depth the recovery time is smaller (around 30 days) due to the influence of the ambient air temperature.

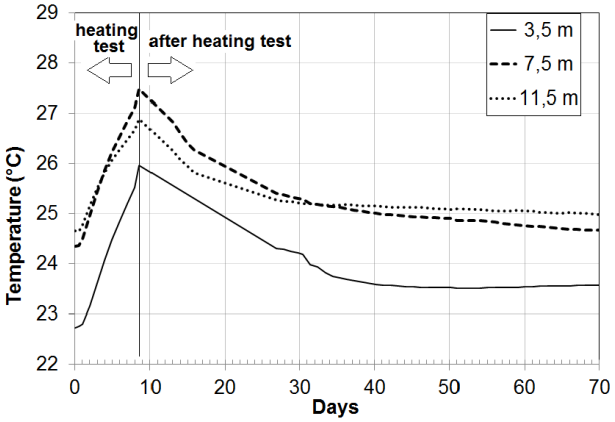


**Fig.10.** Ground temperature response of BH1 (at a distance of 1.0 m from the pile axis) to heating test

The ground temperature response in BH2 (at a distance of 2.0 m from the pile axis) is shown in Fig.11. This figure shows that the temperature increase immediately following the start of the heating test, and continues to increase after the end of the heating test.

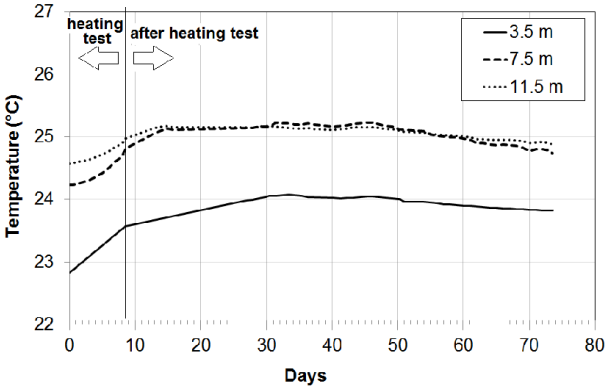


**Fig.11.** Ground temperature response of BH2 (at a distance of 2.0 m from the pile axis) to heating test

Fig.11 shows that at the horizontal distance of 2.0 m from the pile axis, there is little increase in ground temperature during the heating test. The maximum increase in temperature at 7.5 m and 11.5 m occurred 6 days after the completion of the heating test, and at 3.5 m depth occurred after 25

days (due to the influence of the ambient air temperature). The ground temperature started to decrease around 40 days after the heating test was stopped. The ground thermal recovery in BH2 is slower compared to the pile and in BH1.

Similar response of pile and ground temperatures of the current investigation was observed in the experimental work of Singh et al. [9].

Fig.12 shows the temperature distribution in a horizontal section at 7.5 m depth around the pile. The pile temperature increases from 23.9°C to 33.7°C during the heating test. The temperature 2 m from the pile center increased approximately 0.8°C compared the original soil temperature (24.2°C). Therefore, the temperature influence radius of the single pile after 8.5 days of heating should be slightly greater than 2 m (8 times the pile radius).

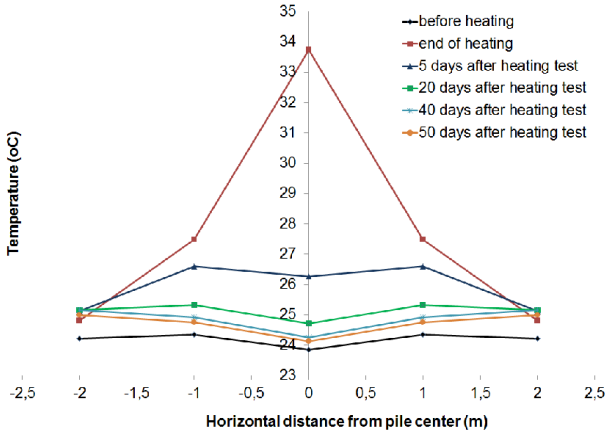


**Fig.12.** Temperature distribution around the pile in the horizontal direction at 7.5 m depth

A superposition effect may occur due to the thermal interaction of the close spacing residential energy piles [10]. The temperature influence zones for the grouped piles under the test conditions overlap. Therefore, the suggested spacing for the current case of energy pile should be larger than 2 m (8 times the pile radius).

Ghasemi-Fare & Basu [11] showed that the thermal influence zone around the heat exchanger pile extends approximately up to a radius of 11 times the pile radius after 60 days of heat rejection from the pile to the ground. These authors commented that the thermal influence zone continuously grows with time after heat rejection starts.

## CONCLUSION

This paper describes the temperature response of a bored geothermal energy pile installed in an unsaturated tropical soil in Brazil with two observation boreholes.

The preliminary results obtained for a short heating period of 8.5 days showed that: (a) the energy pile subjected to a heating test was allowed to recover through natural heat dissipation; (b) the heat moved in radial direction; (c) the measurements of the temperature distribution around the pile in the horizontal direction indicate that the temperature influence radius of a single pile exceeds 2 m. The thermal interaction effects due to cooling of more than one pile should be evaluated in a latter study.

## ACKNOWLEDGEMENTS

The authors are thankful to the Fundação de Amparo à Pesquisa do Estado de São Paulo (FAPESP), for financial support by project Nº. 2014/14496-0.

## REFERENCES

1 M. H. Sharqawy, E. M. Mokheimer, & H. M. Badr. *Geothermics*, 38(2), 271 (2009).
2 H. Brandl. *Géotechnique*, 56(2), 81 (2006).
3 H. Quick, S. Meissner, J. Michael & U. Arslan. In The 1st Intelligent Building Middle East Conference (2005).
4 F. Loveridge. The thermal performance of foundation piles used as heat exchangers in ground energy systems, Doctoral Thesis, University of Southampton (2012).
5 B. L. Amatya, K. Soga, P. J. Bourne-Webb, T. Amis & L. Laloui. *Géotechnique*, 62(6), 503 (2012).
6 C. D. Pereira, R. Lamberts, E. Ghisi. Technical note. CB3E – Centro Brasileiro de Eficiência Energética em Edificações (in Portuguese), Brazil (2013).
7 S. L. Machado, O. M. Vilar. *Characterisation and Engineering Properties of Natural Soils*, 2, 1305 (2013).
8 T. S. O. Morais, L. A. Bandeira Neto, C. H. C. Tsuha (to be submitted for publication). Thermal performance and ground temperature of an energy pile in an unsaturated tropical soil in Brazil, (2016).
9 R. M. Singh, A. Bouazza, B. Wang, C. H. Haberfield, S. Baycan, & Y. Carden. Proc. World Geothermal Congress, Australia (2015).
10 C. J. Wood, H. Liu & S. B. Riffat. *Géotechnique*, 59(3), 287 (2009).
11 O. Ghasemi-Fare & P. Basu. *Energy and Buildings*, 66, 470 (2013).

*Bulgarian Chemical Communications, Volume 48 Special Issue E (pp. 120 - 125) 2016*

# Performance characteristics of solar drying system for agricultural products

Xu Ji*, Ming Li, Yunfeng Wang, Deli Ling, Xi Luo

*Key Laboratory of Advanced Technique and Preparation for Renewable Energy Materials, Ministry of Education, School of Energy and Environmental Science, Yunnan Normal University, Kunming 650500, China*

Drying has important influences on agricultural products' quality and storage. Drying characteristics of different agricultural products vary. Temperature and velocity of drying airflow affect greatly drying quality and drying efficiency of agricultural products. Two types of solar drying systems for different drying temperature requirement were designed and characterized in this paper: solar air drying system with plate air collector and solar parabolic trough concentrating drying system. In solar air drying system with plate air collector, the drying oven has two ventilation modes. With top inlet and bottom outlet ventilation mode, the overall temperature in drying oven is relatively high, however large vertical temperature difference exists in drying oven. With bottom inlet and top outlet ventilation mode, the temperature in drying oven is uniformity, however relatively low. In notoginseng drying experiment, the drying time is shortened to half of that in nature drying. The average thermal efficiency is 66.5%. The solar trough concentrating drying system utilizes a low cost and reliable V-type metal cavity to collect solar irradiation. In the system, the heat conducting oil can be heated to 230℃, and the air flow from heat exchanger reaches above 200℃. The tobacco shred drying experiments verifies that the drying temperature of the system meets the tobacco shred drying requirement. Solar trough concentrating drying system matchts the drying temperature scope of 80℃~200℃.

**Keywords**: solar drying, drying system for agricultural products, parabolic trough concentrating, drying temperature

## INTRODUCTION

Drying is an essential processing technology for agricultural products, and affects directly their quality, appearance, taste and production cost [1,2]. Solar drying saves traditional energy, and improves the dried products' quality [3-5].

In 2001, Liu [6] employed solar collectors to dry corn. In 2005, Fadhel [7] performed solar grape drying by three different processes. In 2006, Turhan Koyuncu [8] designed six types of solar air collectors, and test their performances for crop drying. Md Azharul Karim [9] conducted performance evaluation on a V-groove solar air collector for drying applications. In 2008, Smitabhindu [10] conducted numerical simulation and experimental researches on economy and efficiency of a drying system with collector area of 26m$^2$ for bananas drying. Augustus Leon and Kumar [11] designed a solar-assisted biomass drying system with thermal storage. Utilizing the system, the moisture content of red hot chili peppers was decreased from 76.7% to 8.4% within 32.5 hours. In 2009, Sethi [12] improved solar greenhouse drying technology by using inclined northwall reflection. Zhao [13] investigated sewage sludge drying characteristics in solar greenhouse. In 2011, Romdhane [14] studied the orange peels dryings kinetics and developed a solar dryer by forced convection. Afriyie [15] simulated and optimised the ventilation in a chimney-dependent solar crop dryer. Peng [16] discussed the energy saving ways of heat pump and solar energy bulk curing barn. With solar-assisted heat pump drying system, the energy cost was USD 0.15 for 1kg tobacco shred drying, and was cut by 32.86% comparing with heat pump alone. In 2012, Shobhana [17] studied test method for thermal performance based rating of various solar dryer. In 2013, Esakkimuthu [18] conducted experimental investigation on phase change material based thermal storage system for solar air heating applications. In 2014, Ahmad Fudholi [19] studied performance of a solar drying system for red chilli. The red chili was dried to final moisture content of 10% w.b from 80% w.b in 33 hours. Some drying applications for agriculture products require higher temperature. Solar trough concentrator can provide heat source to meet such temperature requirements. Tan [20] employed solar trough concentration system to produce electricity and thermal energy with higher temperature.

Generally, solar drying should meet the following conditions: There is abundant solar resource, and the drying system matches with the local climate.

## SOLAR DRYING SYSTEM WITH PLATE AIR COLLECTOR

The solar drying system with plate air collector mainly consists of solar plate air collector, drying

* To whom all correspondence should be sent:
jixu@ynnu.edu.cn

oven, vent-pipe, and draught fan, as shown in Fig.1. Two 2m$^2$ double-channel plate air collectors are connected in parallel in the system. The diameter of the vent-pipe is 15cm. The air flow direction in drying oven can be adjusted by regulating valve 1-4. The size of the drying oven is 1350mm×1070mm×960mm. In our experiments, the material to be dried is 8kg fresh notoginseng.

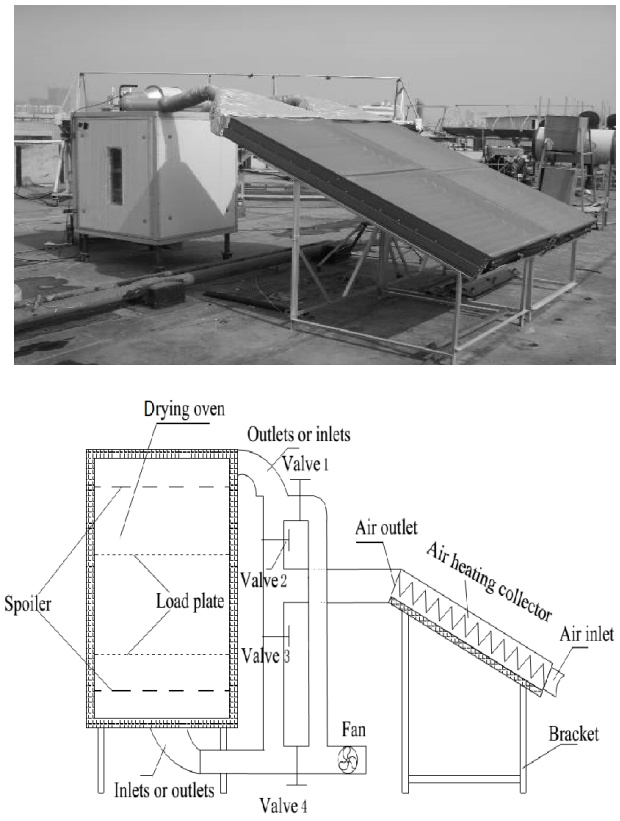


**Fig.1.** Schematic diagram of solar drying system with plate air collector

Three temperature sensors are separately fixed at the top, middle and bottom of the drying oven to record the temperature distribution in the drying oven. Three humidity sensors HD100S (KIMO instruments, France, measuring range 0~99%, accuracy ±1.8%RH) are respectively fixed at the inlet of the air heating collector, inside the oven and at the air outlet of the drying oven to measure relative humidity. The hot air flow rate in the vent-pipes is measured by the anemometer AR816 (Smarsensor, Hongkong, measuring range 0.3～30m/s, accuracy ±5%). The total radiation is measured by a pyranometer of TBQ-2 (Jinzhou sunshine technology Co. Ltd, China) with an accuracy of ±0.2%. Ambient temperature is also measured by a temperature sensor. All climatic data and temperature readings are recorded by a computerized data logger (TRM-2) every 5 minutes during experiment.

Fig.2 shows the efficiency and the outlet temperature of solar air collector under different solar irradiation. In figure, the thermal efficiency is always beyond 50%. With sunny weather, the daily average thermal efficiency is above 60%. The outlet temperature of the air collector stays above 54℃.

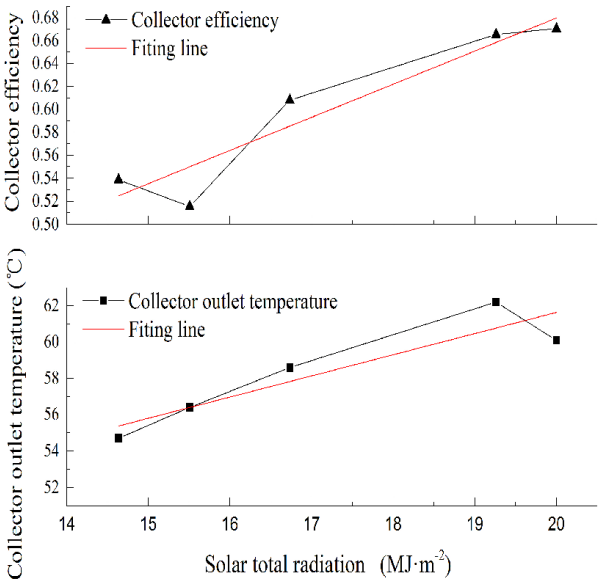


**Fig.2.** Efficiency and outlet temperature of solar air collector with different solar irradiation

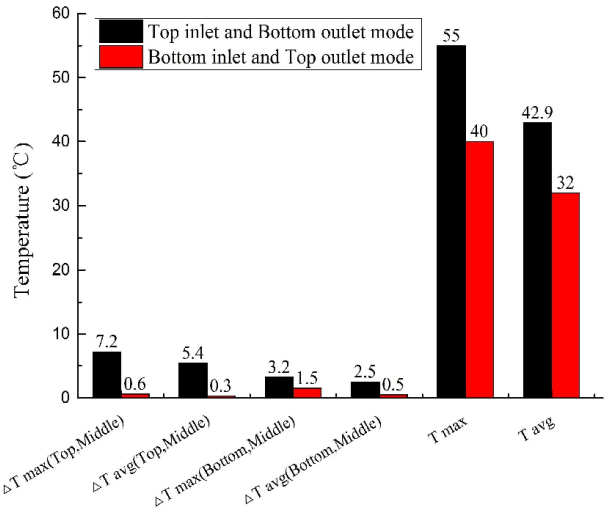


**Fig.3.** Temperature difference in drying oven with different ventilation modes

For the solar plate air-collector drying system, there are two ventilation modes for drying oven: the bottom outlet top inlet and the top inlet bottom outlet. Fig.3 shows the vertical temperature

differences in drying oven under two modes with the same inlet air flow rate.

With the top inlet and bottom outlet mode, there is large temperature difference between the top, middle and bottom sections of the drying oven. The highest temperature is at the top, and the lowest is at the bottom. The temperature difference between the bottom section and the air flow at the exit is also large. The maximum is up to 17℃, and the average is above 10 ℃. However, the overall temperature in drying oven increases quickly with the ventilation mode. After the system operates for 1 hour, the temperature at the top of the drying oven reaches 40℃, and the overall temperature in the drying oven exceeds 40 ℃ after 2 hours. Afterwards, with the increase of solar irradiance, the temperature in drying oven increases slowly and become gradually stable. The maximum temperature at the top section is 55℃. After 14:00 pm, with the decrease of solar irradiance, the temperature difference in drying oven gradually decreases due to the decrease of the inlet air flow temperature. At 16:00 pm, the temperature of each section in the drying oven approaches to 42℃, with a solar irradiation of 401W/m$^2$.

With the bottom inlet and top outlet mode, due to the relative high temperature and the relative low density of the air flow at the inlet, the hot air rises from the bottom of the drying oven. The air convection in the drying oven is strong, thus the temperature in the drying oven is relatively uniformity. The temperature difference in drying oven is approximately 1℃. The temperature at the bottom is a little higher and a little lower at the top. The temperature at the top and the temperature of the air flow at the exit is almost the same, and their maximum temperature difference is 2.3 ℃. However, the overall temperature in drying oven is relatively low. At 14:00 pm, with a solar irradiation of 990W·m$^{-2}$, the maximum temperature 40℃ is reached. It results from that the air flow temperature at the outlet is high, which causes a large heat loss. At the later period of drying process, the drying decelerates, and the required drying temperature need be guaranteed. The bottom inlet and top outlet ventilation mode adverse to energy saving and drying temperature guarantee.

Fig.4 compares notoginseng moisture content changes in solar drying process with the system and in nature drying process. After 450 minutes from drying initiating, the notoginseng moisture content decrease from the initial moisture content of 66.53% to the final moisture content of 17.15% by utilizing the solar drying system, however, decreases to only 34.11% in nature drying process. With a more 450-minitues drying, the notoginseng moisture content reaches finally 18.36% in nature drying process. In figure, the notoginseng moisture content change rates have little difference within 100 minutes from drying initiating between solar drying process and nature drying process. It results from that the stripped moisture is the unbound moisture and the adhesive moisture in notoginseng in the stage. The bounding strength of these type of moisture is relatively weak, thus easy to dehydrate, and the dehydrating speeds depend mainly on the ambient temperature and the airflow velocity. Thereafter, the notoginseng moisture content change speeds with nature drying are lower than that with solar drying. In this stage, the moisture loss is mainly the bound moisture. This type of moisture is relatively hard to dehydrate, and the dehydrating speeds are mainly dependent on the relative humidity of the ambient air. The temperature in solar drying oven is higher than that in the ambient, thus the relative humidity is low. The moisture partial pressure in notogingseng is higher than that in the ambient air, which will push the moisture to move from the inner to the surface of the notogingseng. It results into the quicker drying with solar drying system.

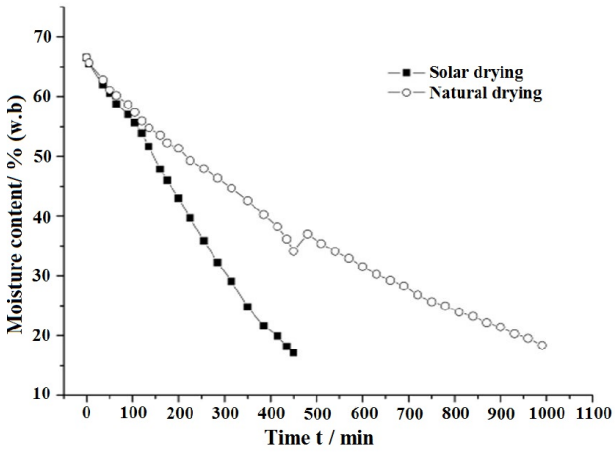


**Fig.4.** Notoginseng moisture content changes in solar drying process and nature drying process

## SOLAR PARABOLIC TROUGH CONCENTRATING DRYING SYSTEM

The solar parabolic trough concentrating drying system mainly consists of solar parabolic trough concentrator, V-type heat-collecting metal cavity, heat insulated oil tank, liquid-gas heat exchanger, vent-pipe and air drying tube, as shown in Fig.5.

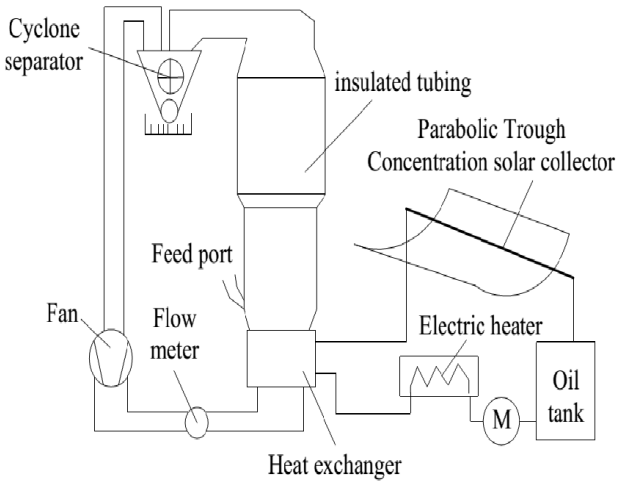


Schematic diagram of solar parabolic trough concentrating drying system

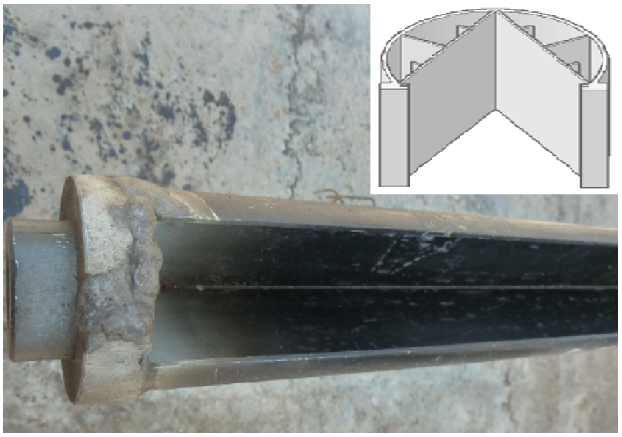

V-type heat-collecting metal cavity

**Fig.5.** Solar parabolic trough concentrating air drying system

The solar parabolic trough concentrator collects and concentrates solar irradiation on the V-type heat-collecting metal cavity. A layer of anodic alumina film is electroplated on the heat-collecting surface of the V-type metal cavity to absorb solar irradiation. Some flat fins are arranged in the working medium channel between the heat-collecting surface and the outer surface of the V-type metal cavity to enhance heat transfer. Such V-type heat-collecting metal cavity has high heat collecting efficiency, and is reliable and low cost. The working medium-heat conducting oil flows through the channel and is heated, then is stored in the heat insulated oil tank. In liquid-gas heat exchanger, the heat is exchanged from the heat conducting oil to the air flow.

The material to be dried is tobacco shred, which is dried by hot air from heat exchanger. In order to obtain tobacco shred with high expansion rate and low tar content, a long straight drying tube is usually employed. The height of such straight drying tube reaches 12m, which results in high cost and strict requirement for plants. An adjustable air flow drying tube is designed to decrease the height of the drying tube, and matches with the solar parabolic trough concentrator. The adjustable drying tube consists of two straight tubes with different diameters, which are connected by employing a reducer tube. The length and diameter of the accelerating drying tube are 1.2m and 200mm, respectively. The length and diameter of the constant drying tube are 2m and 300mm, respectively. The taper angle of the reducer is 60°. All climatic data and temperatures are recorded in experiments.

The mass of heat conduction oil in the system is 42.65 kg. In sunny weather, after the system operates for 2 hours, the heat conducting oil temperature in the tank reached 230℃. Fig.6 shows the relationship between solar irradiation and the heat conduction oil temperature. Under solar irradiance around 1000W·m$^{-2}$, the heat conduction oil is heated from 20℃ to above 220℃ within 2 hours with a heat collection efficiency of 30%.

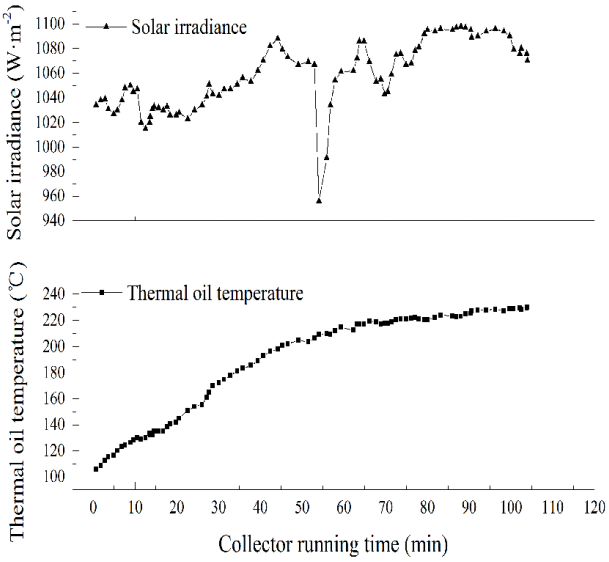


**Fig.6.** Heating performance of the parabolic trough concentrating system

The heat utilization degree of the drying system is described by heat efficiency η, the ratio of the temperature difference between inlet air temperature of drying tube $T_i$ and outlet air temperature of drying tube $T_o$ and the temperature difference between the inlet air temperature of

drying tube $T_i$ and the inlet air temperature of the heat exchanger T, namely:

$$\eta = (T_i - T_o)/(T_i - T) \quad (1)$$

**Table 1.** Drying performances of drying system for different tobacco shred

| Type | $T_i$ /℃ | $T_o$ /℃ | $\Phi_{tobacco}$ /% | η/% |
|---|---|---|---|---|
| A | 190.3 | 148.5 | 14.33 | 52.57 |
| B | 199.5 | 163.4 | 12.37 | 47.12 |
| C | 199.8 | 156.9 | 14.15 | 52.31 |
| D | 200.4 | 157.7 | 13.39 | 51.94 |

The drying performances of the drying system for four types of tobacco shred are given in Table 1. The initial moisture contents of four types of tobacco shred A, B, C, D are 24% ~ 26%. With the air flow rate of 15m/s, and the heat conduction oil flow rate of 0.4kg/s, the moisture contents are 12.3%~14.3% at the end of drying and meet the drying requirements. When the air temperature in drying tube increases, the outlet temperature of tobacco shred increase. However the moisture content of tobacco shred maintains at about 13%, and there is no obvious change. The drying efficiency maintains at around 50%. It is due to the fact when the tobacco shred moisture content reduce to below 14%, the moisture in tobacco shred mainly exists in the form of bound water, and the moisture content of tobacco shred has few changes.

In the parabolic trough concentrating system, according to the initial moisture content of the dried material, by regulating the air flow temperature and flow rate at the inlet of drying tube, the final moisture content requirement could be reached. The thermal efficiency of the drying system could be improved by better thermal insulation, sealing measures and preheating air and dried materials.

## CONCLUSIONS

Two types of drying systems for different drying temperature requirements are designed and characterized. Solar plate air heat-collector drying system is for drying temperature within 80℃ and solar parabolic trough concentrating drying system is for drying temperature within 80℃~240℃.

In solar plate air heat-collector drying system, the air flow direction in drying oven is adjustable by regulating valves. The temperature and humidity uniformity in drying oven are improved by adopting suitable ventilation mode. In notoginseng drying experiment, the drying temperature reaches 62.2 ℃, and the average thermal efficiency is 66.5%. Even with cloudy weather, the heat efficiency of the system maintains over 50%.

By employing solar parabolic trough concentrator drying system, the tobacco shred drying experiments shows that the conductive oil temperature of 230℃ is reached, and the hot air temperature of 200℃ from the heat exchanger is obtained. The drying temperature meets the temperature requirement for tobacco shred drying.

## ACKNOWLEDGEMENTS

The present study was supported by National Natural Science Foundation, China (Grant Nos. 51366014).

## REFERENCES

1 Belessiotis.V, E. Delyannis, Solar drying, Solar Energy, 85, No. 8, 1665–1691, (2011).
2 Pirasteh.G, R. Saidur, S.M.A. Rahman, N.A. Rahim. A review on development of solar drying applications, Renewable and Sustainable Energy Reviews, 31, 133–148, (2014).
3 Öztekin.S, A. Başçetinçelik, Y. Soysal. Crop drying programme in Turkey, Renewable Energy. 16, No. 1-4, 789–794, (1999).
4 Jairaj.K.S, S.P. Singh, K. Srikant, A review of solar dryers developed for grape drying, Solar Energy, 83, No. 9, 1698–1712, (2009).
5 Erick Cesar Lopez-Vidan, Lilia L. Mendez-Lagunas, Juan Rodrıguez-Ramırez, Efficiency of a hybrid solar–gas dryer, Solar Energy, 93, 23–31, (2013).
6 Shengyong Liu, Bailiang Zhang, Chao Yuan. et al. Experimental Study on Drying Corn Using Solar Collectors, Transactions of Chinese society of Agricultural Engineering, 17, No. 6, 93-96, (2001).
7 Fadhel.A, Kooli.S, Farhat.A et al. Study of the solar drying of grapes by three different processes, Desalination, 85, No. 1-3, 535-541, (2005).
8 Turhan Koyuncu. Performance of various design of solar air heaters for crop drying applications, Renewable Energy, 31, No. 7, 1073-1088, (2006).
9 Md Azharul Karim, M.N.A, Hawlader. Performance evaluation of a V-groove solar air collector for drying applications, Applied Thermal Engineering, 26, No. 1, 121-130, (2006).
10 Smitabhindu.R, Janjai.S, Chankong.V. Optimization of a solar-assisted drying system for drying bananas, Renewable Energy, 33, No. 7, 1523-1531, (2008).
11 Augustus Leon. M, Kumar. S. Design and performance evaluation of a solar-assisted biomass drying system with thermal storage, Drying Technology, 26, No. 7, 936-947, (2008).
12 Sethi.V.P, Sadhna.A. Improvement in greenhouse solar drying using inclined northwall reflection, Solar Energy, 83, No. 9, 1472–1484, (2009).

13 Lei Zhao, Dezhen Chen, Zhonghui Wang. Changing of sewage sludge characteristics during its solar drying in greenhouses. Acta energiae solaris sinica, 30, No. 9, 1264-1270, (2009).
14 Romdhane Ben Slama, Michel Combarnous, Study of orange peels dryings kinetics and development of a solar dryer by forced convection, Solar Energy, 85, No. 3, 570–578, (2011).
15 Afriyie.J.K, Rajakaruna.H, M.A.A. Nazha, F.K. Forson. Simulation and optimisation of the ventilation in a chimney-dependent solar crop dryer, Solar Energy, 85, No. 7, 1560–1573, (2011).
16 Yu Peng, Gang Wang, Ying Ma. Discussions on Energy Saving Ways of Heat Pump and Solar Energy Bulk Curing Barn, Journal of Henan Agricultural Sciences, 40, No. 8, 215-218, (2011).
17 Shobhana Singh, Subodh Kumar, Testing method for thermal performance based rating of various solar dryer designs, Solar Energy, 86, No. 1, 87–98, (2012).
18 Esakkimuthu.S, Abdel Hakim Hassabou, C. Palaniappan, Markus Spinnler, Jurgen Blumenberg, R. Velra, Experimental investigation on phase change material based thermal storage system for solar air heating applications, Solar Energy, 88, 144–153, (2013).
19 Ahmad Fudholi, Kamaruzzaman Sopian, Mohammad H. Yazdi, Mohd Hafidz Ruslana, Mohamed Gabbasa, Hussein A. Kazem. Performance analysis of solar drying system for red chilli, Solar Energy, 99, 47–54, (2014).
20 Lijun Tan, Xu Ji, Ming Li, Congbin Leng, Xi Luo, Haili Li, The experimental study of a two-stage photovoltaic thermal system based on solar trough concentration, Energy Conversion and Management, 86, 410-417, (2014).

*Bulgarian Chemical Communications, Volume 48, Special Issue E (pp. 126 - 132) 2016*

# Numerical simulation of a heat pump assisted regenerative solar still for cold climates of Kazakhstan

Ye. Shakir[1], M. Mohanraj[2], Ye. Belyayev[1*], S. Jayaraj[3], A. Kaltayev[1]

[1]*Department of Mechanics, Al-Farabi Kazakh National University, Almaty, Kazakhstan*
[2]*Department of Mechanical Engineering, Hindusthan College of Engineering and Technology, Coimbatore, India*
*3Department of Mechanical Engineering, National Institute of Technology, Calicut, India*

A numerical model has been proposed in this work for predicting the performances of the heat pump assisted regenerative solar still under meteorological conditions of Kazakhstan. The numerical model is based on energy and mass balance. A new regenerative heat pump configuration is proposed to improve the performance of a simple solar still. A comparison of results has been made between the conventional solar still and heat pump assisted regenerative solar still. The numerical simulation was performed for wide range of ambient temperatures between -30°C and 30°C with wide range of solar intensities between 100 W/m$^2$ and 900 W/m$^2$. The numerical simulation results showed that heat pump assisted regenerative solar still is more efficient and produce better yield when compared to the conventional simple solar still. The influences of solar intensity, ambient temperature, heat pump operating temperatures are also discussed. The predicted values were found to be in good agreement with experimental results reported in literature.

**Keywords:** solar stills, heat pumps, cold climates, Kazakhstan

## INTRODUCTION

Water is the main element and it is essential for all forms of life; for the existence of natural ecosystems, social and economic development of any country. Fresh water on Earth is just 3%. In addition, water resources are distributed according to the land surface is extremely uneven. By 2025, according to UN forecasts, the acute shortage of water will be experienced by more than 2.8 billion people. Increasing water scarcity is caused by the growing world population and the development of the global economy and climate change.

To date, as a result of combination of anthropogenic and natural factors the desertification processes in varying degrees subject to more than 70% of the territory of Kazakhstan. For example, the Aral Sea dried up almost 90%. Kazakhstan is experiencing an acute shortage of water resources for the needs of industry and agriculture and for drinking water.

This problem can be partially solved by the introduction of desalination systems, particularly solar desalination. The solar still integrated with external condenser increases the productivity of distillate by 2-3 times. In this paper the common use of heat pump with a solar distiller is proposed. In addition to cold climates use the heat pump for pre-heating of water is justified. Comprehensive discussion of using heat pump as the source of heat energy for desalination of seawater is presented in paper [1]. In paper [2] the technology of desalination based on freezing using a heat pump is discussed. According to ref. [2] COP of the heat pump is in the range of 8 to 12, which results in specific energy consumption in the range of 9 to 11 kWh/m$^3$ of produced water. In the following works [3-9] combination of desalination system with absorption heat pump is considered, whereas in other studies [10-13] integration with a compression heat pump is performed. LiBr–$H_2O$ absorption heat pump desalination system thermal performance is studied in [3-4, 7]. For example, in [3] thermal and economic performance comparison between absorption heat pump and ejector heat pump water desalination system has been conducted. The results show that the absorption heat pump has a more favorable thermal performance than the ejector heat pump only in certain parameters ranges. In [7] it is shown that thermal performance ratios of the absorption heat pump desalination system of 2.4–2.8, which are higher by 50–70% than those for the single-effect thermal vapor compression system. The superior performance of high temperature operation for the absorption heat pump single-effect system makes it extremely suitable for adoption by remote and small communities [7]. Solar assisted heat pump desalination system performance character-ristics under meteorological conditions of Singapore have been investigated in [11]. The performance

* To whom all correspondence should be sent:
yerzhan.belyayev@gmail.com

ratio (PR) obtained from the experiments ranges from 0.77 to 1.15 and COP of the system was found to vary between 5.0 and 7.0 [11]. The simulation results of the paper [12] showed that the efficiency of the solar still with compression heat pump is 75% higher than that of the conventional solar still. In this paper we investigate numerically the thermal performance of the solar desalination in coupled with a heat pump under meteorological conditions of Kazakhstan.

## SYSTEM DESCRIPTION

The schematic diagram of the proposed heat pump assisted regenerative solar still is depicted in Fig.1. The system used consists of a 500 W hermetically sealed reciprocating compressor, a shell and coil type condenser, plate type evaporator with basin area 1 $m^2$ that accommodates brackish water. The heat release from condenser during the condensation of R134a preheat the water before entering to the basin, moreover, the solar intensity transmitted through the glazing surface is also used to heat the water and makes the brackish water to evaporate. The evaporated water will start condensate on the back side of glazing surface, which will be collected separately as glass yield. The evaporator placed inside the still will also dehumidify vapor mixture and collected separately as an evaporator yield. The heat rejection in the condenser has maintained constant water temperature inside the basin even there is fluctuating in solar intensity and daily off sunshine hours.

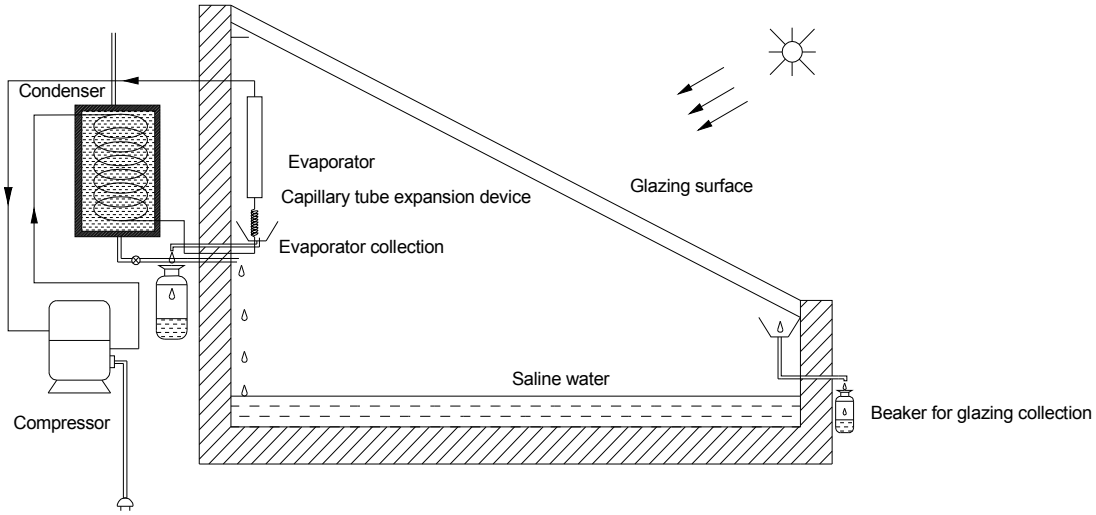


**Fig.1.** Schematic view of the heat pump assisted regenerative solar still

## MATHEMATICAL MODEL

To simulate the performance of heat pump assisted regenerative solar still the following mathematical model according to [12] was formulated. Basic assumptions of mathematical model:

1) all the process are steady state;
2) pressure drop, potential, kinetic and chemical effects are assumed to be negligible in heat pump circuit;
3) compression of the refrigerant vapor is assumed to follow a polytrophic process;
4) expansion of refrigerant liquid is considered to be isenthalpic;
5) the water temperature gradient is negligible;
6) vapor losses through the side, as well as other losses are negligible;
7) the heat conduction within the still is negligible.

According to [12] energy balance equations for different part of heat pump assisted regenerative solar still are as follow:

Energy balance for glass cover:

$$m_g \cdot C_g \cdot \frac{dT_g}{dt} = (1-\rho_g) \cdot \alpha_g \cdot G_H + (q_{ev,w-g} + q_{r,w-g} + q_{c,w-g}) - q_{r,g-a} + q_{c,g-a} \quad (1)$$

Energy balance for the evaporator

$$m_e \cdot C_e \cdot \frac{dT_e}{dt} = q_{c,w-e} + q_{ev,w-e} - q_{ev,f} \quad (2)$$

Energy balance for the water

$$m_w \cdot C_w \cdot \frac{dT_w}{dt} = (1-\rho_g) \cdot (1-\alpha_g) \cdot \alpha_w \cdot G_H - (q_{ev,w-g} + q_{r,w-g} + q_{c,w-g}) \cdot \frac{A_g}{A_w} + q_{c,b-w} + \frac{W}{A_w} \quad (3)$$

Energy balance for the absorber

$$m_b \cdot C_b \cdot \frac{dT_b}{dt} = (1-\rho_g)\cdot(1-\alpha_g)\cdot(1-\alpha_w)\cdot\alpha_b \cdot G_H - \\ - q_{c,b-w} - q_{loss} \quad (4)$$

The rate of condensation is estimated:

$$\frac{dm_c}{dt} = \frac{q_{ev,w}}{H_w} = \frac{A_w \cdot q_{ev,w-g} + A_e \cdot q_{ev,w-e}}{A_w \cdot H_w} \quad (5)$$

In the right hand side of expressions (1)-(5) unknown terms mainly describe convective and radiative heat transfer between different parts of the heat pump assisted solar still according to [12].

## METHOD OF SOLUTION

Numerical algorithm for solution of (1)-(5) based on the fourth order Runge-Kutta method [12]. Computer program for implementation of numerical algorithm developed by means of C++ programming language. As the initial conditions for temperature at the different part of the heat pump assisted solar still ambient temperature were assumed. At the first time step this temperature value was used to calculate convective and radiative heat transfer coefficients. Based on this values and physical properties temperatures at the different positions of the system were calculated. In Table 1 the basic system parameters are performed.

**Table 1.** Basic parameters of the heat pump assisted solar still

| Parameter | Symbol | Value | Unit |
|---|---|---|---|
| Mass of the glass cover | $m_g$ | 10.12 | $kg\ m^{-2}$ |
| Specific heat of glass | $C_g$ | 800 | $J \cdot kg^{-1} \cdot °C^{-1}$ |
| Absorptivity of glass | $\sigma_g$ | 0.0475 | - |
| Reflectivity of glass | $\rho_g$ | 0.0735 | - |
| Mass of water | $w_g$ | 20.60 | $kg\ m^{-2}$ |
| Specific heat of water | $C_w$ | 4178 | $J \cdot kg^{-1} \cdot °C^{-1}$ |
| Absorptivity of water | $\sigma_w$ | 0.05 | - |
| Mass of plate absorber | $m_b$ | 15.60 | $kg\ m^{-2}$ |
| Specific heat of plate absorber | $C_b$ | 480 | $J \cdot kg^{-1} \cdot °C^{-1}$ |
| Absorptivity of plate absorber | $\sigma_b$ | 0.95 | - |
| Thermal conductivity of plate absorber | $k_b$ | 16.30 | $W \cdot m^{-1} \cdot K^{-1}$ |
| Thermal conductivity of insulation | $k_i$ | 0.039 | $W \cdot m^{-1} \cdot K^{-1}$ |
| Mass of evaporator | $m_e$ | 7.35 | $kg\ m^{-2}$ |
| Specific heat of evaporator | $C_e$ | 385 | $J \cdot kg^{-1} \cdot °C^{-1}$ |

## RESULTS AND DISCUSSION

Temperature variation of different parts of the distiller was numerically estimated for cold climate conditions of Kazakhstan. In the present paper three small cities of Kazakhstan were considered: Aralsk, Balkhash and Fort-Shevchenko, which are corresponding to Aral sea, Balkhash lake and Caspian sea. As the ambient temperature the coldest day of the winter months of 2014-2015 was taken. Fig.2 shows the temperature variation of the coldest day of December (2014), January (2015) and February (2015).

Fig.3 shows the average daily direct and diffuse solar radiation on a horizontal surface with actual conditions of cloudiness, W/m$^2$. Kazakhstan is one of the leading countries in the Central Asian region with the average annual solar radiation potential. Annual duration of sunshine is 2200-3000 hours, and the estimated capacity of 1300-1700 kW per 1 m$^2$ per year, which exceeds that of Northern and Central Europe. According to Fig.3 the average daily intensity of solar radiation in the summer season is about 600 W/m$^2$. Similarly, for the winter season in the above cities is about 180-200 W/m$^2$.

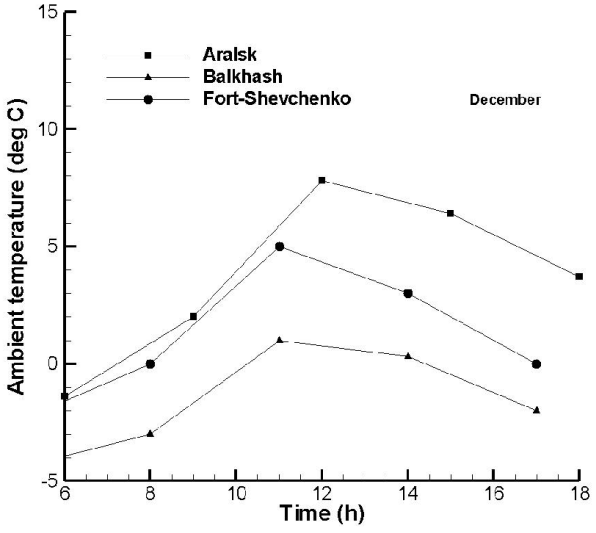


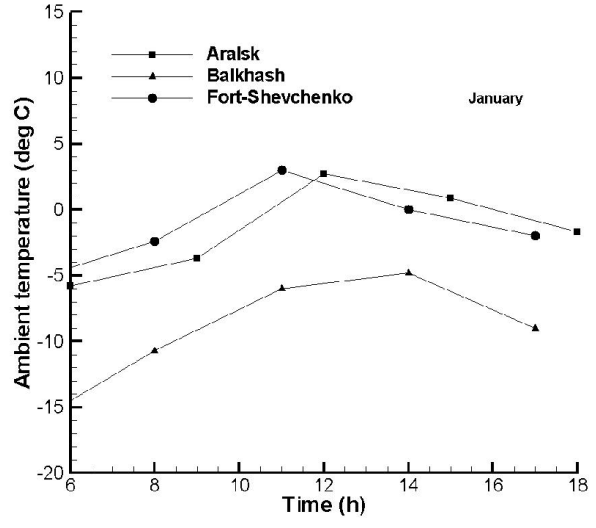

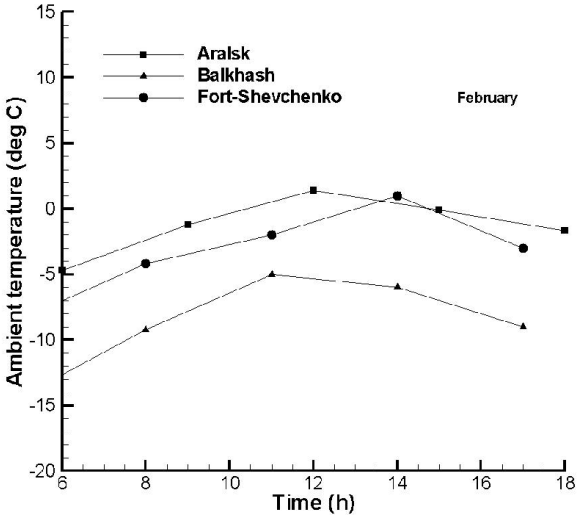


**Fig.2.** The temperature variation of the winter coldest day of 2014-2015

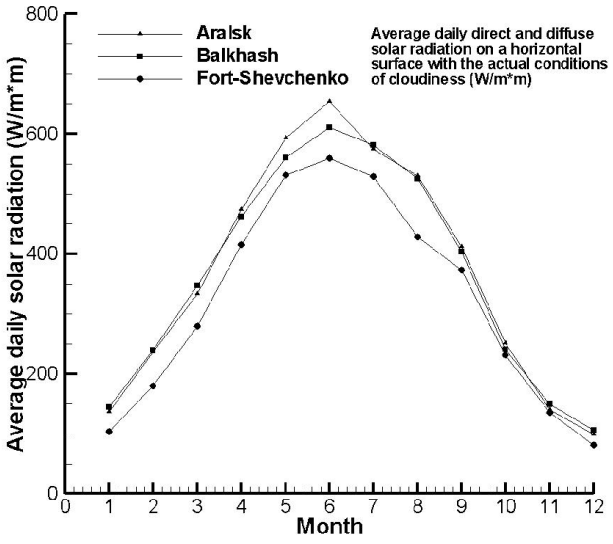


**Fig.3.** Average daily direct and diffuse solar radiation, W/m$^2$

The temperature variation of different parts of the distiller in function of time for the coldest winter days is presented in Fig.4 for Aralsk near Aral sea. It is known that the Aral Sea dries up and is now divided into two parts Large and Small Aral. Today, the Small Aral restored by constructing Kokaral dam by Kazakhstan. On the part of the Small Aral Sea the Aralsk city is located, where there is the prospect of using solar desalination for domestic purpose.

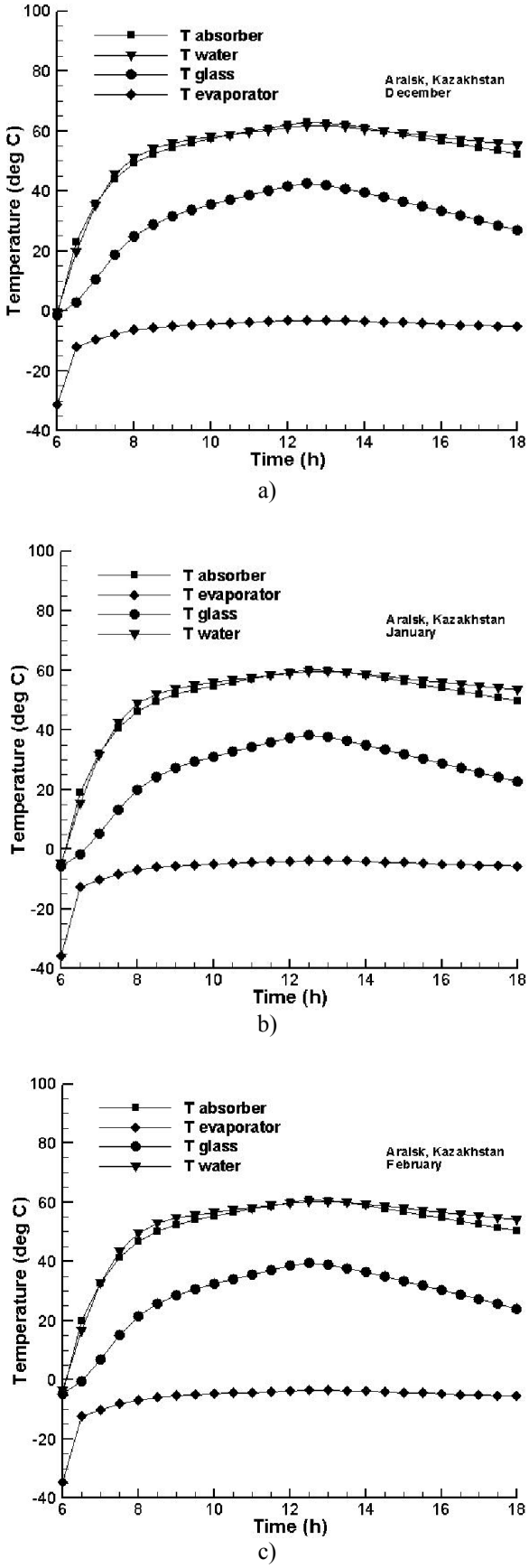


**Fig.4.** The temperature variation of the different solar still parts (Aralsk)

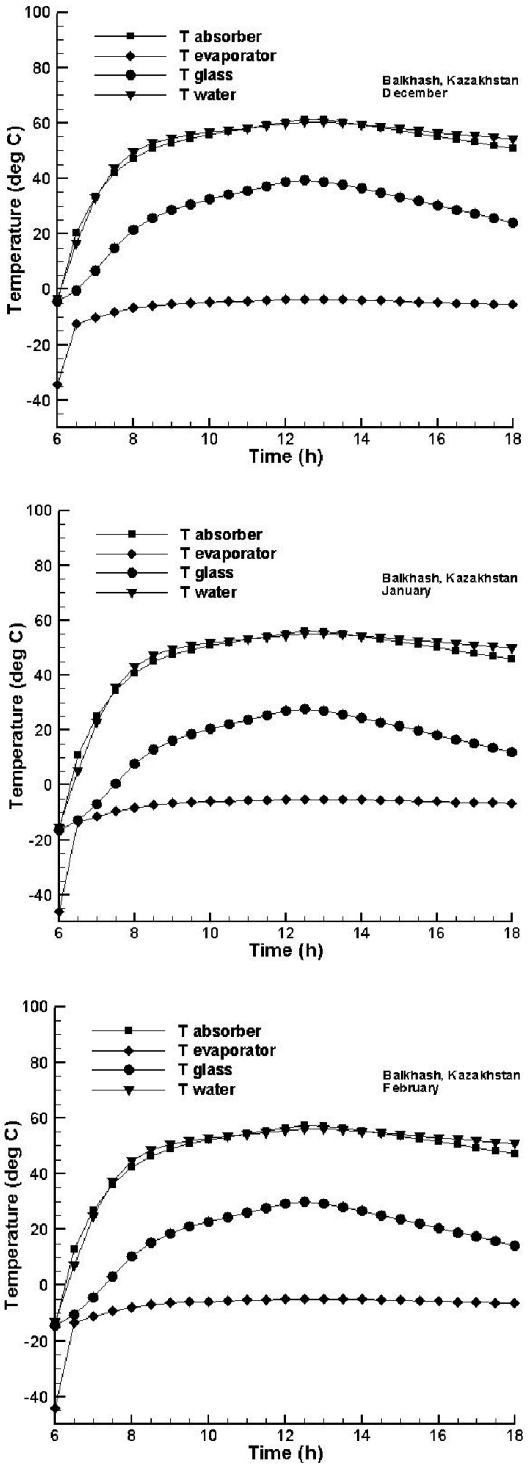


**Fig.5.** The temperature variation of the different solar still parts (Balkhash)

According to the Fig.4 at the beginning of the day the curves gradually increase, reaching maximum at 12 h and 14 h, then gradually decreased. Due to the high absorption coefficient of the absorption plate with black paint it's temperature reaches a maximum value of 63 $^{o}$C in December, 61 $^{o}$C in January and February. Accordingly the temperature of the glass is 43 $^{o}$C, 39 $^{o}$C and 40 $^{o}$C, respectively. Almost 20 $^{o}$C difference between absorber and glass temperatures is due to convective heat exchange with ambient air and water vapor condensation at the evaporator. Water temperature is practically same as absorber temperature for all three winter months.

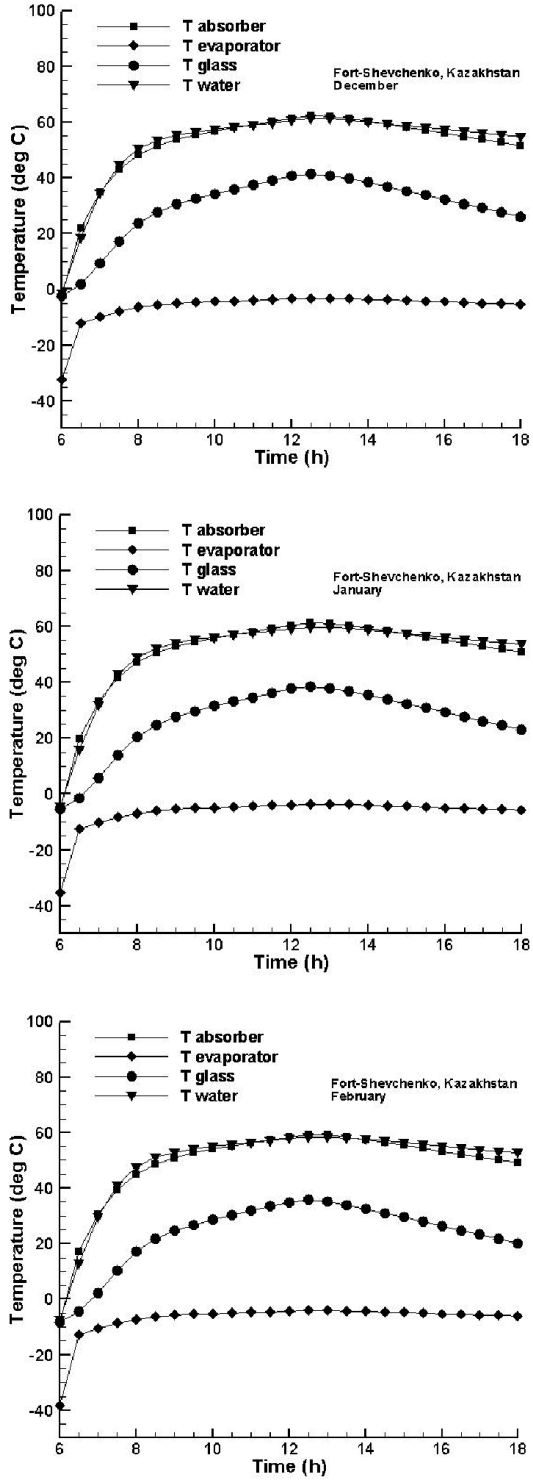


**Fig.6.** The temperature variation of the different solar still parts (Fort-Shevchenko)

Analogically, temperature variation for Balkhash and Fort-Shevchenko cities are illustrated in Fig.5 and Fig.6.

From Fig.5 it is obvious, that for Balkhash maximum absorber temperature is 62 $^{o}$C in December, 56 $^{o}$C in January and 58 $^{o}$C in February. While in Fort-Shevchenko, these figures are 63 $^{o}$C, 62 $^{o}$C and 60 $^{o}$C, respectively.

Fig.7 shows the temperature variation for the month July in Fort-Shevchenko.

Comparing to the winter conditions maximum absorber temperature reaches a value 91 $^{o}$C for July (Fig.7).

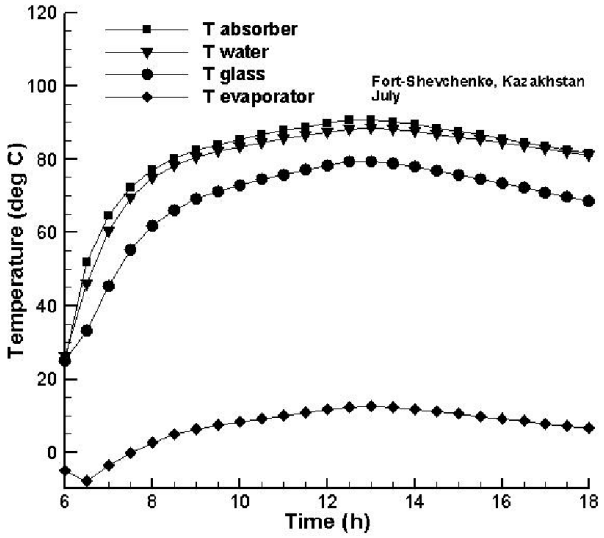


**Fig.7.** The temperature variation of the different solar still parts (Fort-Shevchenko)

Comparison of productivity at the evaporator and the glass cover is presented in Fig.8.

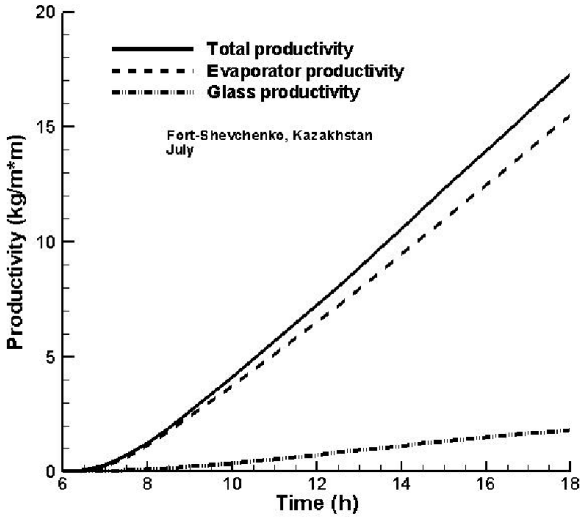


**Fig.8.** Productivity of the distiller for July in Fort-Shevchenko

More than 75% of condensed water is produced by evaporator comparing to glass cover (Fig.8). A large amount of water vapor is condensate very quickly due to the low temperature of the refrigerant.

The average daily fresh water production for each month is plotted in Fig.9 for each city.

According to the Fig.9 the maximum daily production of fresh water reaches in summer, when the solar radiation reaches the maximum value. The average daily solar distiller production for Aralsk is 9.91 kg/m$^2$/day in July, for Balkhash is 10.16 kg/m$^2$/day in July and for Fort-Shevchenko is 9.72 kg/m$^2$/day in July.

## CONCLUSION

Numerical simulation of a heat pump assisted regenerative solar still under meteorological conditions of Kazakhstan has been carried out and following conclusions are drawn:

- Numerical results are found to be closed to the experimental results found in literature;
- The heat pump assisted regenerative solar still produced 75% improved productivity when compared to simple solar still;
- Numerical simulation results for three different locations: Aralsk, Balkhash and Fort-Shevchenko confirm that heat pump assisted regenerative solar still is suitable for producing good drinking water in remote locations of Kazakhstan.

Further, the authors are developing a commercial regenerative solar still for producing good drinking water in water scarcity locations of Kazakhstan.

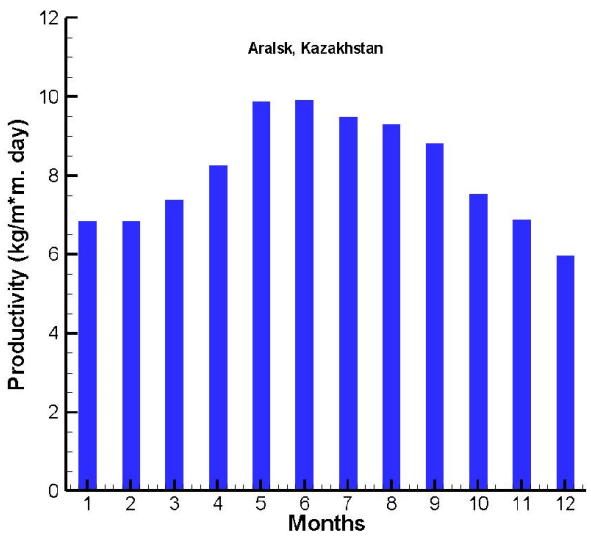


a)

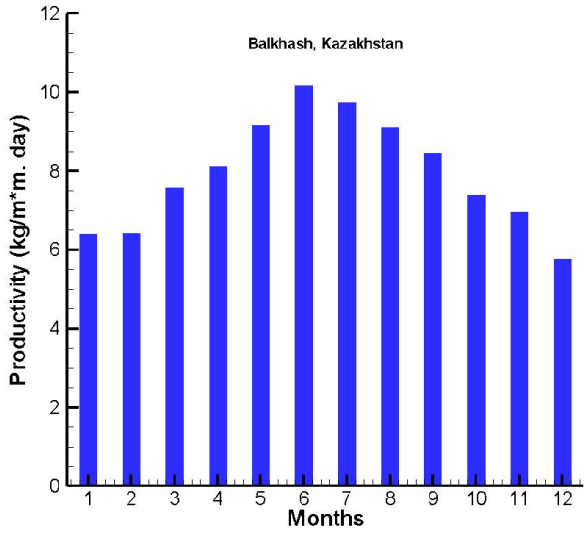


b)

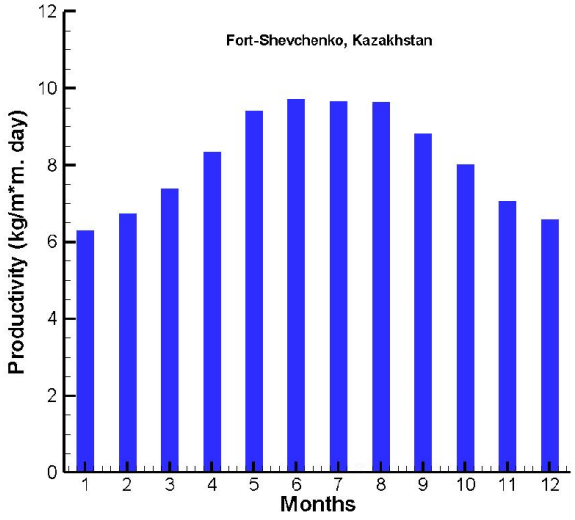


c)

**Fig.9.** The average daily production for different months

## REFERENCES


1 Jinzeng Chen, Suyi Huang, A discussion of "Heat pumps as a source of heat energy for desalination of seawater", Desalination, 169 (2004), 161–165.

2 M.V. Rane, Y.S. Padiya, Heat pump operated freeze concentration system with tubular heat exchanger for seawater desalination, Energy for Sustainable Development, 15 (2011), 184-191.

3 Yongqing Wang, Noam Lior, Thermoeconomic analysis of a low-temperature multi-effect thermal desalination system coupled with an absorption heat pump, Energy 36 (2011), 3878–3887.

4 Diego C. Alarcón-Padilla , Lourdes García-Rodríguez, Julián Blanco-Gálveza, Design recommendations for a multi-effect distillation plant connected to a double-effect absorption heat pump: A solar desalination case study, Desalination, 262 (2010), 11-14.

5 Diego-César Alarcón-Padilla, Lourdes García-Rodríguez, Application of absorption heat pumps to multi-effect distillation: a case study of solar desalination, Desalination , 212 (2007), 294-302.

6 V.V. Slesarenko, Desalination plant with absorption heat pump for power station, Desalination, 126 (1999), 281-285.

7 Faisal Mandani, Hisham Ettouney, Hisham El-Dessouky, LiB - $H_2O$ absorption heat pump for single-effect evaporation desalination process, Desalination , 128 (200), 161-176.

8 Ahmad Al-Ansari, Hisham Ettouney , Hisham El-Dessouky, Water–zeolite adsorption heat pump combined with single effect evaporation desalination process, Renewable Energy 24 (2001), 91-111.

9 Iman Janghorban Esfahani, Seung Chul Lee, Chang Kyoo Yoo, Evaluation and optimization of a multi-effect evaporation–absorption heat pump desalination based conventional and advanced exergy and exergoeconomic analyses, Desalination, 359, (2015), 92-107.

10 Ahmed A.A. Attia, New proposed system for freeze water desalination using auto reversed R-22 vapor compression heat pump, Desalination, 254, (2010), 179-184.

11 M.N.A. Hawlader , Prasant K. Dey, Sufyan Dia, Chan Ying Chung, Solar assisted heat pump desalination system, Desalination, 168 (2004), 49-54.

12 Hanen Ben Halima , Nader Frikha, Romdhane Ben Slama, Numerical investigation of a simple solar still coupled to a compression heat pump, Desalination, 337, (2014), 60-66.

13 Zakaria Mohd Amin, M.N.A. Hawlader, Analysis of solar desalination system using heat pump, Renewable Energy, 74, (2015), 116-123.

# SOLAR PHOTOVOLTAIC SYSTEMS

*Bulgarian Chemical Communications, Volume 48, Special Issue E (pp. 135 - 139) 2016*

# Numerical modelling of photovoltaic thermal evaporator for heat pumps

A. Aliuly[1], M. Mohanraj[2], Ye. Belyayev[1,*], S. Jayaraj[3], A. Kaltayev[1]

[1]*Department of Mechanics, Al-Farabi Kazakh National University, Almaty, Kazakhstan*
[2]*Department of Mechanical Engineering, Hindusthan College of Engineering and Technology, Coimbatore, India*
[3]*Department of Mechanical Engineering, National Institute of Technology, Calicut, India*

A numerical model is proposed in this paper to evaluate the energy performance parameters of photovoltaic-thermal hybrid evaporators. The energy performance parameters such as photovoltaic electrical efficiency, thermal efficiency of the evaporator, overall efficiency of photovoltaic-thermal evaporators, solar energy absorption ratio and evaporator heat gain were predicted for the meteorological conditions of Almaty city in Republic of Kazakhstan. R134a is selected as a working fluid in this work. The ambient temperature was simulated in the range between -20 $^{o}$C and 30 $^{o}$C with solar intensity in the range from 100 W/m$^2$ to 900 W/m$^2$. The wind velocity variations in the range between 0 and 10 m/s was also considered. The energy performance parameters under the influence of above three ambient parameters are discussed. The modelling results were also compared with experimental results reported in literature and found to be in good agreement with acceptable deviations.

**Keywords*:*** photovoltaic-thermal hybrid system, heat pumps, cold climates, Kazakhstan

## INTRODUCTION

Probably the most important source of renewable energy is sun. Solar energy can be used as a low-grade heat source for heat pumps. Today direct expansion solar assisted heat pump (DXSAHP) system has been actively studied by many scientists of Western and East Asian countries to use in seawater desalination, domestic hot water, cottages heating and air conditioning, heating greenhouses, etc. However, in the CIS countries, including Kazakhstan, this system has not been paid any attention. With proper operation of DXSAHP system, it can achieve a high coefficient of performance as compared with heat pumps that power by geothermal, water and air. DXSAHP installation is inexpensive, it uses solar collectors, which regardless of weather conditions is able to accumulate sufficient energy and convert the solar radiation into heat.

The main objective of this paper is to increase the conversion efficiency of solar and ambient energy into heat, i.e. to increase coefficient of performance (COP). One of the ways to solve this problem is to integrate photovoltaic and thermal evaporator systems into one solar collector for generating electricity and heat simultaneously. The combination of photovoltaic and thermal evaporator (PV/T) systems in one module has the potential to reduce the use of materials and the required space [1]. Also, the hybrid system allows saving the aesthetic appearance of the building. In references [1-4] presented literature review of a photovoltaic-thermal hybrid system. The use of PV/T hybrid technology in conjunction with a solar assisted heat pump is presented in [5-7]. For example, in [5] a novel solar polygeneration system, which combines solar cooling, solar-assisted heat pump and photovoltaic/thermal collector technologies, is presented. The results showed a total energy efficiency of the PV/T is 0.49, a heat pump yearly COP is more than 4 and the adsorption chiller COP is 0.55. While in the paper [7] an experimental study on operation performance of PV/T solar heat pump air-conditioning system was conducted and its corresponding COP is 2.88. Experimental and numerical investigations of other type of hybrid PV/T solar collector were considered in [8-13]. In [8] a novel flat heat pipe design has been developed, where solar thermal collector with and without PV bonded directly to its surface. Performance study of solar water and space heating is discussed in papers [10-13]. In the present paper preliminary numerical results of thermal performance of hybrid PV/T solar collector used for DXSAHP under meteorological conditions of Kazakhstan is presented.

## DESCRIPTION OF DIRECT EXPANSION SOLAR ASSISTED HEAT PUMP CYCLE

The detailed configuration of a direct expansion solar assisted heat pump and pressure-enthalpy diagram are shown in the Fig.1 and Fig.2, respectively. The DXSAHP consists of a R134 based hermetically sealed reciprocating

* To whom all correspondence should be sent:
yerzhan.belyayev@gmail.com

compressor, a water cooled condenser, a liquid receiver, a sealed type refrigerant drier, a sight glass, a thermostatic expansion device and a glazed solar collector integrated with PV modules, which acts as an evaporator. The geometric characteristics of the hybrid PV/T system have been taken in accordance with the [14]. Dimensions of PV/T collector-evaporator is 1.01 m x 0.73 m. The PV/T collector-evaporator is a hybrid solar collector with solar cell encapsulation laminated on to the front surface of a thermal absorber plate [14]. Evaporator's copper tube has 6 m length with 7 mm outer diameter and 6 mm inner diameter. A glass cover and a thermal insulation layer are provided. The solar PV/T collector (evaporator) was tilted to an angle of about 45° with respect to horizontal [14]. The system is oriented to face south to maximize the solar radiation incident on the collector (evaporator). Experiments will be conducted in Almaty (latitude of 43.25 °N, longitude of 76.91 °E). During the experiment the following parameters will be taken into account: solar radiation, ambient temperature and wind velocity. Kazakhstan is one of the leading countries in the Central Asian region with the average annual solar radiation potential. Annual duration of sunshine is 2200-3000 hours, and the estimated capacity of 1300-1700 kW per 1 m$^2$ per year, which exceeds that of Europe.

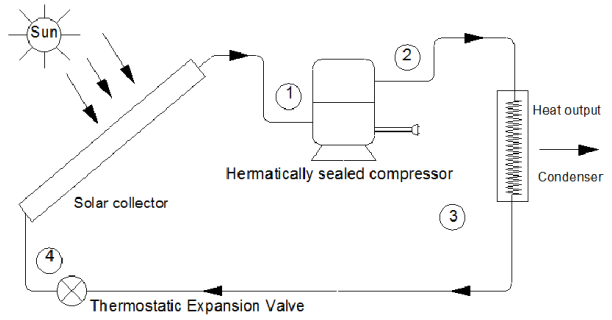


**Fig.1.** Schematic diagram of a direct expansion solar assisted heat pump

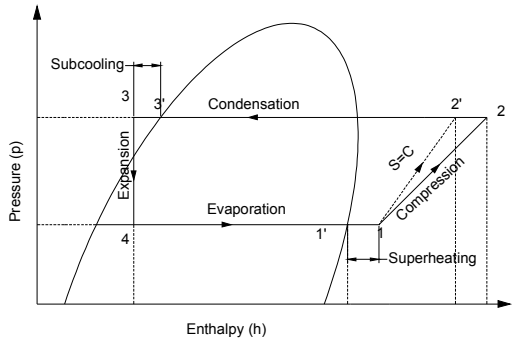


**Fig.2.** Pressure enthalpy representation of a direct expansion solar assisted heat pump

## MATHEMATICAL MODEL

The thermal performance of the system was numerically evaluated according to a mathematical model [15]. Heat balance equation of the PV module is:

$$l_{pv}\rho_{pv}C_{pv}\frac{\partial T_{pv}}{\partial t}=G(\tau\beta)_{pv}-E+\alpha_{a-pv}(T_a-T_{pv})+\alpha_{r,a-pv}(T_{sky}-T_{pv})+\frac{T_c-T_{pv}}{R_{pv-c}} \quad (1)$$

where $l_{pv}$, $\rho_{pv}$ and $C_{pv}$ are the effective thickness, density and specific heat of PV cells, respectively. Other terms in the right hand side of the equation (1) are described in detail in ref. [15]. Two-dimensional heat conduction equation of the thermal collector is given by the following formula:

$$m_cC_c\frac{\partial T_c}{\partial t}=G(\tau\beta)_c(1-\xi)A_c+\alpha_{a-c}(1-\xi)A_c(T_a-T_c)+\alpha_{r,a-c}(1-\xi)A_c(T_{sky}-T_c)+\xi A_c\frac{T_{pv}-T_c}{R_{pv-c}}+A_c\frac{T_a-T_c}{R_b}+\lambda_{c,y}l_{c,y}A_c\frac{\partial^2T_c}{\partial y^2}+\lambda_{c,z}l_{c,z}A_c\frac{\partial^2T_c}{\partial z^2} \quad (2)$$

where $R_b$ is the thermal resistance between the back of the thermal collector and the ambient; $l_{c,y}$ and $l_{c,z}$ are the effective thicknesses along the $Y$ direction and $Z$ direction, respectively; and $\xi$ is the PV cell coverage ratio [15].

## METHOD OF SOLUTION

Finite-difference form of the equations (1)-(2) is based on the implicit scheme according to the [15].

$$l_{pv}\rho_{pv}C_{pv}\frac{T_{pv,j,k}^{n+1}-T_{pv,j,k}^{n}}{\Delta t}=G(\tau\beta)_{pv}-E+\alpha_{a-pv}(T_a-T_{pv,j,k}^{n+1})+\alpha_{r,a-pv}(T_{sky}-T_{pv,j,k}^{n+1})+\frac{T_{c,j,k}^{n+1}-T_{pv,j,k}^{n+1}}{R_{pv-c}} \quad (3)$$

$$m_cC_c\frac{T_{c,j,k}^{n+1}-T_{c,j,k}^{n}}{\Delta t}=G(\tau\beta)_c(1-\xi)A_c+\alpha_{a-c}(1-\xi)A_c(T_a-T_{c,j,k}^{n+1})+\alpha_{r,a-c}(1-\xi)A_c(T_{sky}-T_{c,j,k}^{n+1})+\xi A_c\frac{T_{pv}-T_{c,j,k}^{n+1}}{R_{pv-c}}+A_c\frac{T_a-T_{c,j,k}^{n+1}}{R_b}+\lambda_{c,y}l_{c,y}A_c\frac{T_{c,j,k+1}^{n+1}+T_{c,j,k-1}^{n+1}-2T_{c,j,k}^{n+1}}{\Delta y^2}+\lambda_{c,z}l_{c,z}A_c\frac{T_{c,j+1,k}^{n+1}+T_{c,j+1,k}^{n+1}-2T_{c,j,k}^{n+1}}{\Delta z^2} \quad (4)$$

where $l_{pv}$, $\rho_{pv}$ and $C_{pv}$ the effective thickness, density and specific heat of PV cells, respectively. As an input data solar irradiance, ambient temperature and physical constants were taken. For the hybrid PV/T absorber plate as the temperature boundary conditions during numerical implementation of the equation (4) zero first derivatives were adopted.

## RESULTS AND DISCUSSION

Temperature variation of PV cells and solar collector were numerically estimated for climate conditions of Kazakhstan. In the present paper three cities of Kazakhstan were considered: Astana, Almaty and Oral. The corresponding ambient temperature and solar radiation were taken into account during the calculation.

The available solar radiation data for Astana, Almaty and Oral are presented in Fig.3.

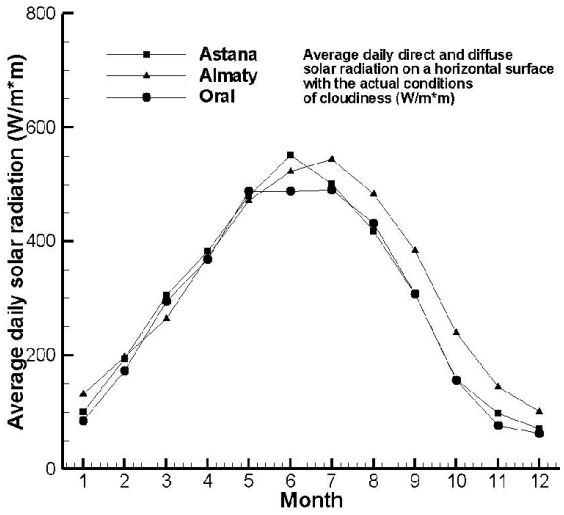


**Fig.3.** Solar radiation data

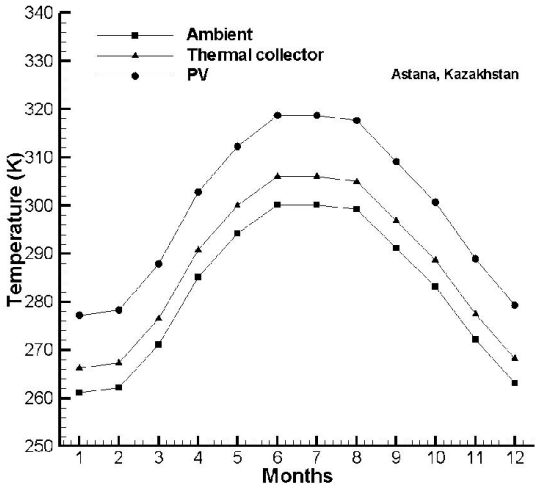


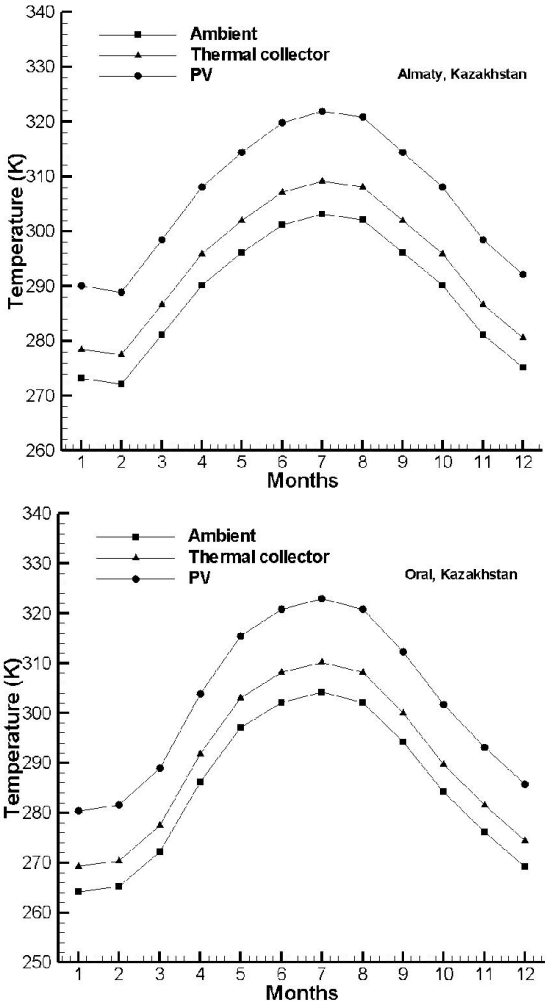


**Fig.4.** PV cell and thermal collector temperature variation by months

Fig.4 shows temperature variation of PV cells and solar collector depending of months. It can be seen from simulation results that the temperature of PV and thermal collector reach their maximum in the summer season. The trend is the same as the solar irradiation. Temperature difference of 3-20 K between PV cell and the thermal collector also can be observed.

Fig.5 and Fig.6 shows prediction of the heat gain by absorber plate and the output electricity by PV, respectively.

Both parameters generally increase with the solar irradiation. According to Fig.5 and Fig.6, the maximum value for Almaty city is achieved in the July months with heat indices of 5.55 kW and output electricity of around 1.0 kWh.

Thermal and PV efficiencies were assessed according to the solar energy input ratio (SEIR) parameter. In the calculations it was assumed that a solar collector area of 2 $m^2$, whereas the area of the photo elements covering the absorber plate is 1.7$m^2$. Solar energy input ratio for PV evaporator

is presented in Fig.7 and Fig.8. The maximum value of SEIR thermal for Almaty city reaches 0.22 in May, whereas SEIR electrical is equal to 0.13 in August.

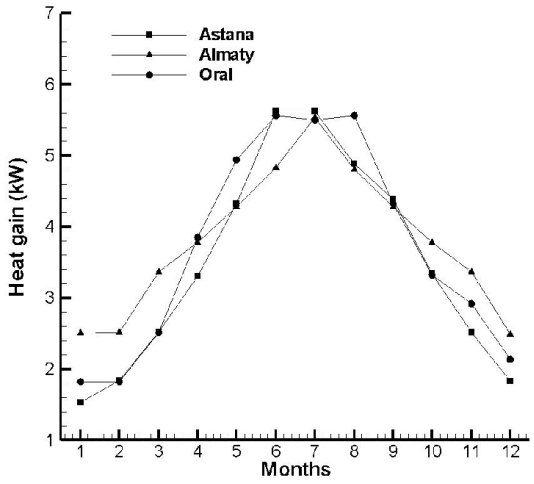


**Fig.5.** The heat gain of the evaporator

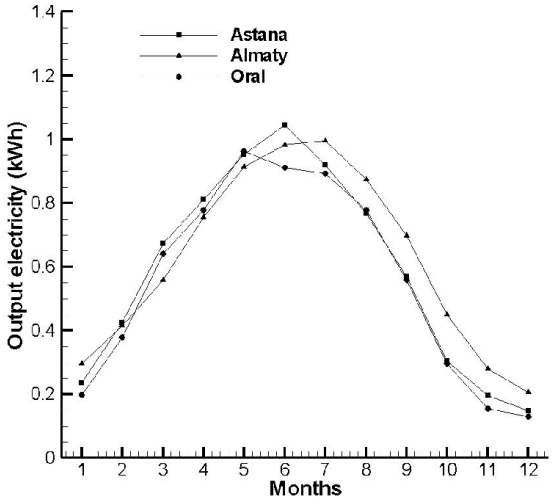


**Fig.6.** The output electricity of the PV evaporator

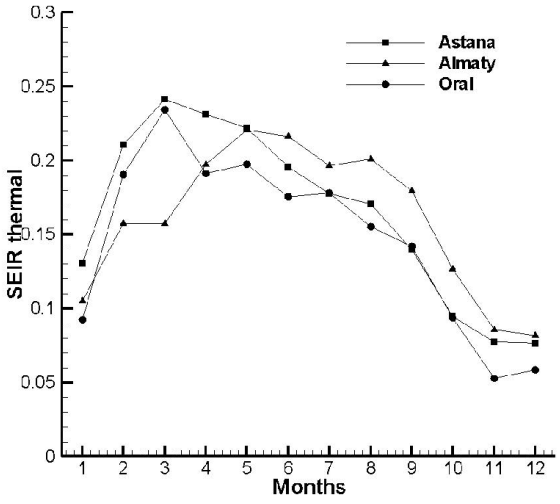


**Fig.7.** The SEIR thermal of the PV evaporator

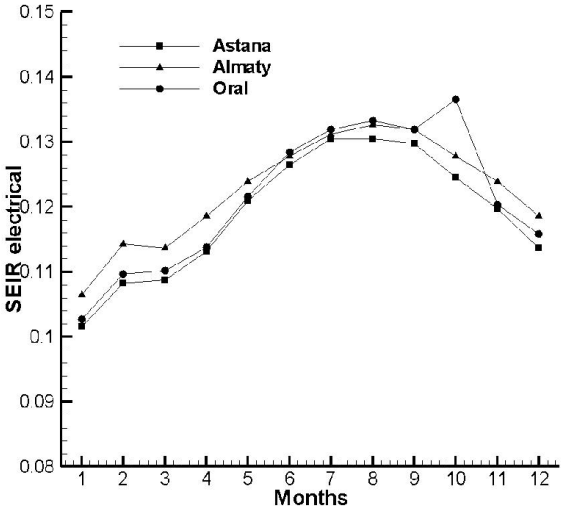


**Fig.8.** The SEIR electrical of the PV evaporator

## CONCLUSION

Numerical modeling of photovoltaic thermal evaporator for heat pumps under meteorological conditions of Kazakhstan has been conducted. The predicted results are closer to the measured results reported in literature with acceptable deviations. Results are shown for currently available data for the total solar radiation on a horizontal surface with the actual conditions of cloudiness. In the future work it is planned to build an experimental setup of PV evaporator to integrate with direct expansion solar assisted heat pump system. Mathematical model and numerical algorithm accurately characterizes the thermal performance of the PV evaporator. In the future, the hydrodynamic calculation of the refrigerant flow in the tube of PV evaporator will be taken into account. Also daily solar radiation distribution for daily performance calculation will be considered.

## REFERENCES

1 Clara Good, Environmental impact assessments of hybrid photovoltaic–thermal (PV/T) systems – A review, Renewable and Sustainable Energy Reviews, 55, March (2016), 234–239.
2 Jee Joe Michael, Iniyan S, Ranko Goic, Flat plate solar photovoltaic–thermal (PV/T) systems: A reference guide, Renewable and Sustainable Energy Reviews, 51, November (2015), 62–88.
3 P.G. Charalambous, G.G. Maidment, S.A. Kalogirou, K. Yiakoumetti, Photovoltaic thermal (PV/T) collectors: A review, Applied Thermal Engineering, 27, Issues 2–3, February (2007), 275–286.

4 Suhaila Abdul Hamid, Mohd Yusof Othman, Kamaruzzaman Sopian, Saleem H. Zaidi, An overview of photovoltaic thermal combination (PV/T combi) technology, Renewable and Sustainable Energy Reviews, V 38, October (2014), 212–222.
5 Francesco Calise, Massimo Dentice d'Accadia, Rafal Damian Figaj, Laura Vanoli, A novel solar-assisted heat pump driven by photovoltaic/thermal collectors: Dynamic simulation and thermoeconomic optimization, Energy, 95, 15 January (2016), 346–366.
6 N. Gunasekar, M. Mohanraj, V. Velmurugan, Artificial neural network modeling of a photovoltaic-thermal evaporator of solar assisted heat pumps, Energy, 93, Part 1, 15 December (2015), 908–922.
7 Guiyin Fang, Hainan Hu, Xu Liu, Experimental investigation on the photovoltaic–thermal solar heat pump air-conditioning system on water-heating mode, Experimental Thermal and Fluid Science, 34, Issue 6, September (2010), 736–743.
8 H. Jouhara, J. Milko, J. Danielewicz, M.A. Sayegh, M. Szulgowska-Zgrzywa, J.B. Ramos, S.P. Lester, The performance of a novel flat heat pipe based thermal and PV/T (photovoltaic and thermal systems) solar collector that can be used as an energy-active building envelope material, Energy, Available online, 3 August (2015).
9 Hasila Jarimi, Mohd Nazari Abu Bakar, Mahmod Othman, Mahadzir Hj Din, Bi-fluid photovoltaic/thermal (PV/T) solar collector: Experimental validation of a 2-D theoretical model, Renewable Energy, 85, January (2016), 1052–1067.
10 Ruobing Liang, Jili Zhang, Chao Zhou, Dynamic Simulation of a Novel Solar Heating System Based on Hybrid Photovoltaic/Thermal Collectors (PVT), Procedia Engineering, 121, 2015, 675–683.
11 Pierrick Haurant, Christophe Ménézo, Leon Gaillard, Patrick Dupeyrat, A Numerical Model of a Solar Domestic Hot Water System Integrating Hybrid Photovoltaic/Thermal Collectors, Energy Procedia, 78, November (2015), 1991–1997.
12 N. Amrizal, D. Chemisana, J.I. Rosell, Hybrid photovoltaic–thermal solar collectors dynamic modeling, Applied Energy, 101, January (2013), 797–807.
13 Swapnil Dubey, G.N. Tiwari, Thermal modeling of a combined system of photovoltaic thermal (PV/T) solar water heater, Solar Energy, 82, Issue 7, July (2008), 602–612.
14 M. Mohanraj, S. Jayaraj, S. Muraleedharan, Exergy assessment of a direct expansion solar-assisted heat pump working with R22 and R407LC/LPG mixture, International Journal of Green Energy, 7, Issue 1, (2010).
15 Jie Ji, Hanfeng He, Tintai Chow, Gang Pei, Wei He, Keliang Liu. Distributed dynamic modeling and experimental study of PV evaporator in a PV/T solar-assisted heat pump. International Journal of Heat and Mass Transfer, 52, (2009) 1365-1373.

*Bulgarian Chemical Communications, Volume 48, Special Issue E (pp. 140 - 146) 2016*

# Evaluation of primary energy factor values of photovoltaics: The case of Lithuania

R. Tamašauskas[1*], E. Monstvilas[1], K. Miškinis[1], A. Burlingis[1], P. Bruzgevičius[2]

[1] *Institute of Architecture and Construction of Kaunas University of Technology, Tunelio str. 60, LT-4440 Kaunas Lithuania*

[2] *JSC "Įrąža" Tunelio str. 60, LT-4440 Kaunas, Lithuania*

It is necessary to evaluate primary energy consumption from renewable energy resources in energy efficient buildings in accordance with the requirements of the European Parliament and Council Directive 2010/31/EC "Energy performance of buildings". The problem is that in different EU countries, there are no unified methods that evaluate primary energy factor values of photovoltaics. Another problem is that there are various calculation methods, which are lack of clear description, and the results of these methods are inaccurate. In this paper a comparison of different methods for the evaluation of primary energy factor values of photovoltaics are given and as a case study the case of Lithuania was chosen. The comparison showed that empirical value of primary energy factor for photovoltaics is much smaller than that currently used in the EU standard.

**Keywords:** primary energy, photovoltaics, evaluation methods, Lithuania

## INTRODUCTION

Energy balance takes into account of various energy streams entering the national energy network, their transformation and losses in supply is up to the final consumer. To avoid repetitive evaluation of these streams, it is important to distinguish between primary and secondary energy.

Thus, the need for primary energy necessary to generate one unit of secondary energy is based on primary energy factors (PEF), which are also referred to as conversion factors describing the total amount of energy in the energy generation chain up to the final usage (Fig.1) [1].

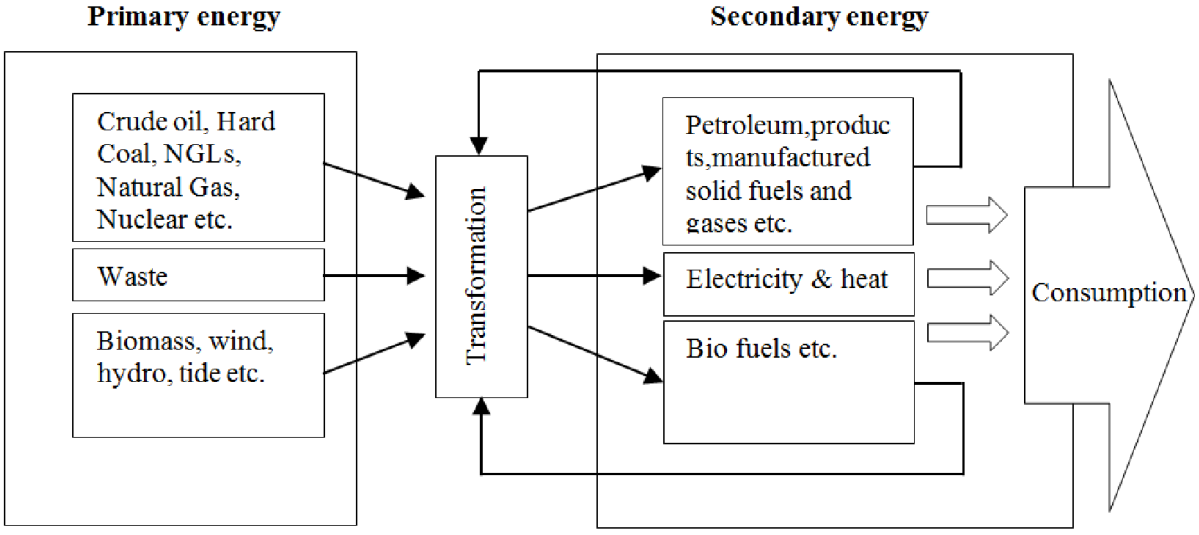


**Fig.1.** Interdependence of primary and secondary energy [1]

Every country has a different energy generation and supply chain, so the PEF values also differ accordingly.

However, only a few countries make these values publicly available (Table 1).

According to the information presented in Table 1, national building standards of the EU countries are either missing some data or give unspecified renewable energy values, which make it unclear whether these values are, in fact, applied for photovoltaic energy or are only politically justified having no direct relation to engineering or science.

Various methods may be applied to calculate primary energy factor (PEF) for the production of electrical energy (Table 2) [23].

* To whom all correspondence should be sent:
rokas.tamasauskas@gmail.com

**Table 1.** Photovoltaic electrical energy values in EU building standards

| Country | Primary Energy Factor | Total Primary Energy Factor | Non-Renewable Primary Energy Factor | Renewable Primary Energy Factor | References and remarks |
|---|---|---|---|---|---|
| Ireland | 2.45 | - | - | - | [2] |
| Austria | - | - | - | - | [3] |
| Belgium | - | - | - | - | [4] |
| Czech Republic | - | 1.0 | 0 | - | [5] |
| Denmark | 2.5 | - | - | - | [6] |
| Denmark | 1.8 | - | - | - | [6 since year 2020] |
| United Kingdom | - | - | - | - | [7] |
| Estonia | - | - | - | - | [8] |
| Greece | - | - | - | - | [9] |
| Spain | - | - | - | - | [10] |
| Italy | - | 2.174 | 2.174 | - | [11] |
| Cyprus | 1 | - | - | - | [12] |
| Poland | - | 1 | 0 | 1 | [13] |
| Netherlands | - | - | - | - | [14] |
| France | 1 | - | - | - | [15] |
| Slovakia | - | - | - | - | [16] |
| Slovenia | 0 | - | - | - | [17] |
| Finland | - | - | - | - | [18] |
| Sweden | - | 0.17 | - | - | [19] |
| Germany | - | 1 | 0 | - | [20] |
| *amorphous (DE)* | - | 1.29 | 0.27 | 1.03 | [21] |
| *mono crystal (DE)* | - | 1.53 | 0.47 | 1.05 | [21] |
| *poly crystal (DE)* | - | 1.25 | 0.23 | 1.02 | [21] |
| Hungary | 0 | - | - | - | [22] |

**Table 2.** Parameters of different methods for the estimation of primary solar energy (photovoltaics)

| | $MJ_{primary\ energy}/MJ_{electricity}$ | Primary energy evaluation description | PEF | PEF value | References |
|---|---|---|---|---|---|
| 1. | Zero equivalent | Electricity and thermal energy production from renewable energy sources are not estimated | (Total) primary energy | 0 | [24] |
| 2. | 2a -Direct equivalent | Electricity and thermal energy production from non-combustible renewable energy sources and nuclear energy are estimated | (Total) primary energy | 1.0 | [25-27] |
| | 2b-Physical energy content | Primary energy form appeared during generation process is estimated | (Total) primary energy | 1.0 | [28] |
| | 2c-Substitution | It is seen as a form of energy, which first is included in the statistical energy balance before transforming into the secondary or tertiary form of energy | (Total) primary energy | 2.5 | [29-33] |
| 3. | Only non-renewable primary energy | - | Non-renewable primary energy | 0.15 | [34] |
| 4. | 4a-Technical conversion efficiencies | Is evaluated all energy production chain, seperating renewable and non-renewable energy. | Non-renewable primary energy | 0.15 | [29,30,34] |
| | | | Renewable primary energy | 7.5 | |
| | 4b-Physical energy content | Is treated as the first form of energy appeared during the generation process. | Non-renewable primary energy | 0.15 | [28,34] |
| | | | Renewable primary energy | 1.0 | |

The data given in Table 2 demonstrates that PEF values for photovoltaic energy estimation differ throughout the methods. Depending on the type of primary energy and the evaluation method applied, primary energy factor of the same renewable energy source may significantly vary [35-37].

The analysed literary sources were lack of data on PEF evaluation: the established PEF values differ considerably regarding the same type of energy due to a great number of methods to estimate PEF. So far no systematic research on the topic has been done and for this reason the aim of the paper is to determine the most suitable method to establish PEF for photovoltaic power stations. The calculation method is based on the statistical data obtained from the Lithuanian photovoltaic power stations. The values determined for photovoltaic power stations are going to be applied for building energy certification to ensure the implementation of the goals and regulations determined by Directive 2010/31/EU.

## METHODOLOGY

Energy performance of buildings is the balance between the amount of energy generated and consumed in a building. The type and amount of energy consumed depend on various factors, for instance architectural solutions and engineering systems of a building, climate of the country and its level of economic development. Compared to the underdeveloped countries, in the economically developed ones, buildings consume more energy due to the use of various domestic appliances [38]. The key purpose in constructing energy efficient buildings is to increase the amount of renewable energy supply and reduce the use of primary non-renewable energy sources. Here two principal opportunities emerge: the first one is to increase the amount of renewable energy in electrical energy networks [39], and the second one – to use electrical energy generated from renewable energy sources, i.e. photovoltaic power stations in or nearby the building [40].

Following the requirements of Directive 2010/31/EU, more than a half of energy consumed in nearly zero-energy buildings is required to derive from renewable sources. However, all renewable energy sources include a certain amount of non-renewable energy that is not evaluated, which is why the methods provided in Table 2 are not accurate enough for calculating PEF of photovoltaic power stations. Taking the mentioned (methods) into consideration, the method provided in the standard EN 15603:2014 is applied to determine PEF of photovoltaic power stations. Therefore, the total demand for primary energy in a building is calculated as follows (Eq.1) [41]:

$$E_p = \sum (E_{del,i} f_{P,del,i}) - \sum (E_{\exp,i} f_{P,\exp,i}) \quad (1)$$

where: $E_p$ – primary energy demand; $E_{del,i}$ – final energy demand by the energy carrier; $f_{P,del,i}$ – primary energy factor depending on the energy carrier; $E_{exp,i}$ – final energy exported by the energy carrier; $f_{P,exp,i}$ – primary energy factor of the exported energy carrier.

The total primary energy may be calculated by Eq.2:

$$f_{P,tot} = f_{P,nren} + f_{P,ren} \quad (2)$$

where: $f_{P,\,tot}$ – total primary energy; $f_{P,nren}$ – non-renewable primary energy; $f_{P,ren}$ – renewable primary energy.

### *Evaluation method of electrical energy generated from photovoltaic energy sources*

Energy generated in photovoltaic systems can be evaluated by different methods varying in their degree of simplicity and accuracy. Among all, three principal methods may be distinguished: empirical correlation, analytical accounting and detailed modelling [42]. Analytical accounting method was chosen to calculate the parameters of the photovoltaic power stations analysed herein. Following the method, electrical energy generated in a photovoltaic power station can be estimated by Eq.3:

$$E_{PV} = PR \cdot P_n \cdot \frac{H_T}{G_{STC}} \quad (3)$$

where: $E_{PV}$ – amount of electrical energy generated in a photovoltaic power station during the analysed period of time, kWh; $PR$ – efficiency coefficient of the station, $P_n$ – nominal capacity of the station determined under standard testing conditions, kW; $H_T$ – total amount of solar radiation onto the surface of a photovoltaic module, kWh/m$^2$; $G_{STC}$ – solar radiation under standard testing conditions, kW/m$^2$.

$PR$ coefficient is estimated following formula 4 [43]:

$$PR = k_\theta \cdot k_Q \cdot k_{BI} \cdot k_\gamma \cdot k_w \cdot k_s \cdot \eta_{inv} \cdot k_{\deg} \quad (4)$$

where: $k_\theta$ – optical reflection reduction coefficient; $k_Q$ – spectral reduction coefficient; $k_{BI}$ – minor exposure reduction coefficient; $k_\gamma$ – module temperature reduction coefficient; $k_w$ – installation loss reduction coefficient; $k_s$ – dirt reduction coefficient; $\eta_{inv}$ – inverter conversion efficiency; $k_{deg}$ – module ageing reduction coefficient.

### *Potential of solar energy in Lithuania*

According to Alisov's climate classification, the territory of Lithuania is in temperate climate zone and so can be ascribed to the south-western sub-area of the Atlantic continental zone [44] (Fig.2).

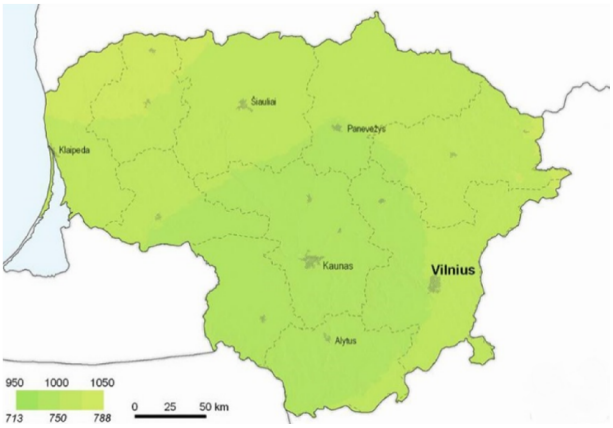


**Fig.2.** Potential of solar electrical energy in the Lithuanian territory [45]

Multiannual observation data suggests that the average annual solar radiation impinging onto the horizontal surface of Lithuania reaches approximately 1000 kWh/m$^2$. Sunlight lasts the longest in the western part and shortens while moving towards the eastern, i.e. 1840-1900 h/year and 1700 h/year accordingly [46].

Generative efficiency of photovoltaic power stations is directly dependent on solar radiation [44]. In order to use solar radiation to its maximum under the Lithuanian climate conditions photovoltaic modules are directed towards south with 25°-45° lean angle from the horizontal plane. Such orientation of one square metre of the area of a photovoltaic power station generates 130-160 kWh electrical energy annually under the Lithuanian climate conditions [47].

### *The analysed photovoltaic power stations*

The total capacity of photovoltaic power stations operating in Lithuania sums up to 60.60 MW. Lithuanian electricity transmission system encompasses 1969 unique photovoltaic power stations or station groups: 1953 small power stations (from 1 to 199.68 kW), 12 medium (from 225 to 999.6 kW), and 4 large ones (from 1488.81 to 2559.84 kW) [48].

Since the level of solar radiation is similar in the whole territory of Lithuania, the most suitable places to install photovoltaic power stations are selected on the basis of other parameters, such as the development of transmission network infrastructure as well as the synthesis of local climate conditions and relief [49].

The research has been carried out on the basis of statistical data obtained from 30 photovoltaic power stations (Table 3-5) and their analyses are presented in Section 3. PEF values were estimated by applying Eq.2, while technical parameters of photovoltaic power stations were analysed based on Eq.3.

**Table 3.** Main characteristics of the analysed photovoltaic power stations (0.02< >0.03 MW)

| Studied photovoltaic power plants No | Installed capacity MW | Power plant location |
|---|---|---|
| 1A | 0.028 | Kaunas region |
| 2A | 0.028 | Akmenės region |
| 3A | 0.029 | Kaunas region |
| 4A | 0.030 | Molėtai region |
| 5A | 0.030 | Šiauliai region |
| 6A | 0.030 | Kaunas city |
| 7A | 0.030 | Kaunas region |
| 8A | 0.030 | Elektrėnai region |
| 9A | 0.030 | Raseiniai region |
| 10A | 0.030 | Telšiai region |

**Table 4.** Main characteristics of the analysed photovoltaic power stations (0.01< >0.02 MW)

| Studied photovoltaic power plants No | Installed capacity MW | Power plant location |
|---|---|---|
| 1B | 0.010 | Vilkaviškis region |
| 2B | 0.012 | Marijampolė region |
| 3B | 0.012 | Vilnius region |
| 4B | 0.014 | Kaunas city |
| 5B | 0.014 | Mažeikiai region |
| 6B | 0.015 | Kaunas region |
| 7B | 0.017 | Palanga city |
| 8B | 0.018 | Kaunas city |
| 9B | 0.018 | Visaginas city |
| 10B | 0.020 | Mažeikiai region |

**Table 5.** Main characteristics of the analysed photovoltaic power stations (<0.01MW)

| Studied photovoltaic power plants No | Installed capacity MW | Power plant location |
|---|---|---|
| 1C | 0.001 | Rokiškis region |
| 2C | 0.002 | Ukmergė region |
| 3C | 0.003 | Kaunas city |
| 4C | 0.003 | Kaunas city |
| 5C | 0.004 | Varėna region |
| 6C | 0.005 | Vilnius region |
| 7C | 0.006 | Mažeikiai region |
| 8C | 0.008 | Vilnius city |
| 9C | 0.010 | Vilnius city |
| 10C | 0.010 | Alytus region |

## RESULTS AND DISCUSSION OF LITHUANIAN PHOTOVOLTAIC POWER STATION ANALYSIS

The primary value of the non-renewable energy factor depends on the ratio of the amount of primary energy to renewable energy generated in a photovoltaic power station and non-renewable electrical energy consumed. If the amount of the consumed non-renewable electrical energy increases or the amount of the generated renewable electrical energy drops, the primary value of the non-renewable energy factor rises.

The methodology in EN 15603:2014 provides a single PEF value for photovoltaic power stations regardless of the different capacity they have, thus the influence of electrical capacity on the PEF value is not known. Therefore, it is reasonable to group the analysed photovoltaic power stations depending on their capacity and establish their PEF values, which then in turn could be compared to the values presented in EN 15603:2014 methodology.

Fig.3 provides *the calculated* factors $f_{Pnren}$ of the analysed photovoltaic power stations of (0.02< >0.03) MW capacity.

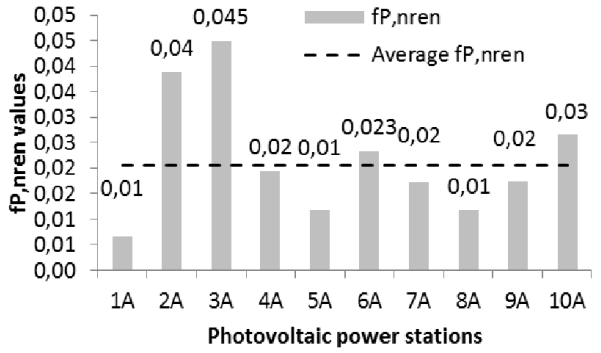


**Fig.3.** $f_{Pnren}$ factors of photovoltaic power stations of (0.02< >0.03) MW capacity

Fig.4 gives $f_{Pnren}$ factors of the analysed photovoltaic power stations of (0.01< >0.02) MW capacity.

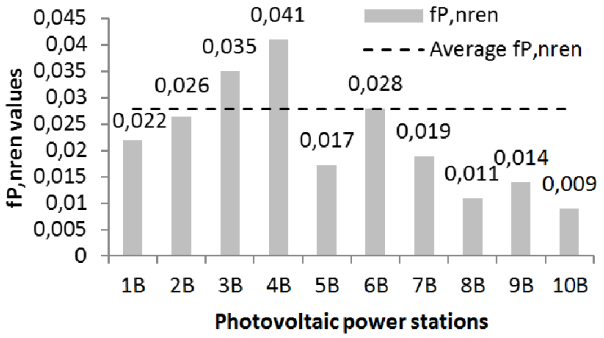


**Fig.4**. $f_{Pnren}$ factors of photovoltaic power stations of (0.01< >0.02) MW capacity

Similarly, Fig.5 demonstrates $f_{Pnren}$ factors of photovoltaic power stations of (< 0.01) MW capacity.

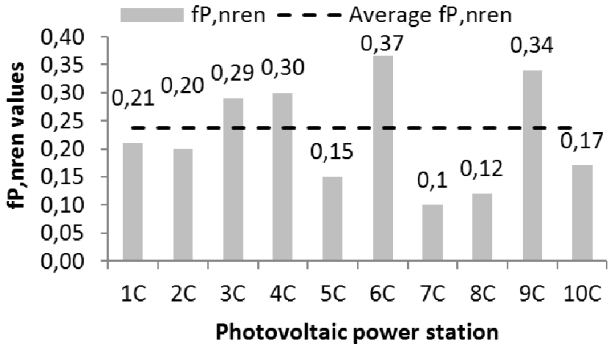


**Fig.5.** $f_{Pnren}$ factors of photovoltaic power stations of (< 0.01) MW capacity

The average numerical value of $f_{Pnren}$ factor for photovoltaic power stations of (0.02< >0.03) MW capacity equals to 0.021 (dotted line). The lowest $f_{Pnren}$ factor – 0.01 was estimated for 1A, 5A, 8A power stations, while the highest – 0.45 for 3A station. In the case of photovoltaic power stations of (0.01< >0.02) MW capacity, the average numerical value of $f_{Pnren}$ factor amounts to 0.028 (dotted line). Here, the lowest $f_{Pnren}$ factor is 0.009 for 10B station and the highest – 0.041 for 4B station. Finally, the average numerical value of $f_{Pnren}$ factor for stations of (< 0.01) MW capacity reaches 0.238 (dotted line). In this case, 7C power station received the lowest $f_{Pnren}$ factor – 0.1, whereas the highest – 0.37 was for 6C station. Thus, the obtained results suggest that the capacity of photovoltaic power stations has influence on $f_{Pnren}$ factor.

Analyzing produced and consumed electrical energy impact of photovoltaic fPnren index value, the following research was made, which results are presented in Fig.6 to Fig.8.

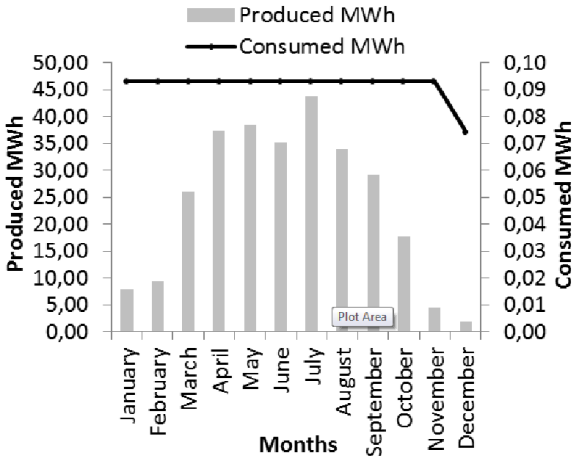


**Fig.6**. Average activity factors of photovoltaic power stations of (0.02< >0.03) MW capacity

Fig.6 provides average electricity production and consumption quantities by months of the analysed photovoltaic power stations of (0.02< >0.03) MW capacity.

Fig.7 provides average electricity production and consumption quantities by months of the analysed photovoltaic power stations of (0.01< >0.02) MW capacity.

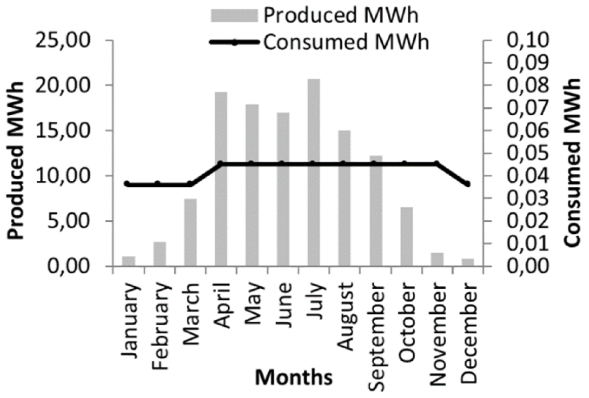


**Fig.7.** Average activity factors of photovoltaic power stations of (0.01< >0.02) MW capacity

Fig.8 provides average electricity production and consumption quantities by months of the analysed photovoltaic power stations of (<0.01) MW capacity.

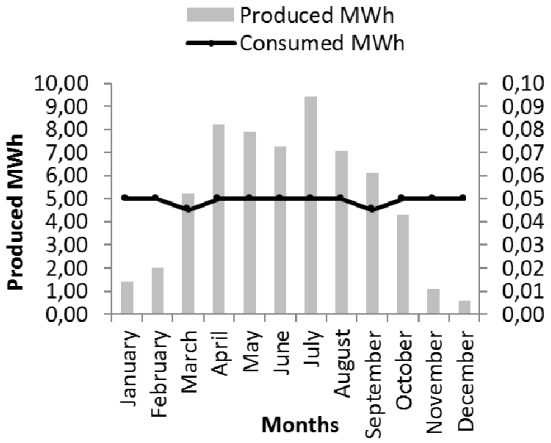


**Fig.8.** Average activity factors of photovoltaic power stations of (<0.01) MW capacity

The average annual of photovoltaic power stations of (0.02< >0.03) MW capacity from the total produced electricity amount equals to 0.9 %.

In the case of photovoltaic power stations of (0.01< >0.02) MW capacity, the average annual consumption from the total produced electricity amount equals to 1.24 %.

Finally, the average annual consumption value in percent for stations of (< 0.01) MW capacity reaches 2.1 %. Thus, the obtained results suggest that there is no relation between the produced and consumed electrical energy in photovoltaic power plants. Electricity consumption is almost constant each month. Fluctuations are small and can be explained by hardware factors. A comparison of photovoltaic power station capacities and $f_{Pnren}$, $f_{Pren}$ and $f_{Ptot}$ factors are presented in Table 6.

**Table 6.** Comparison of power station capacity and $f_{Pnren}$, $f_{Pren}$ and $f_{Ptot}$ factors

| Index | Photovoltaic power stations that operate in Lithuania value in kW•h | | | | According EN 15603:2014 |
|---|---|---|---|---|---|
| | (0.02< >0.03) MW capacity | (0.01<>0.02) MW capacity | (<0.01) MW capacity | Average | |
| $f_{Pnren}$ | 0.021 | 0.028 | 0.238 | 0.038 | 0.7 |
| $f_{Pren}$ | 1 | 1 | 1 | 1 | 1 |
| $f_{Ptot}$ | 1.021 | 1.028 | 1.238 | 1.038 | 1.7 |

The data in Table 6 indicates that the average non-renewable primary energy factor of the Lithuanian photovoltaic power stations is 0.038, which is 20 times less (i.e. only 5,4% of the standard value from the standard) than the factor given in the standard EN 15603:2008 and currently used for the calculations. Such a difference may be explained by the lack of clarity in the conditions and criteria applied to established the mentioned standard factor. A country that relies on the standard EN 15603 has two options: to apply the factor given therein or to determine the factor by invoking the presented calculation methodology and taking into account the specificity of their own country. In the latter case, the quite rapid development of photovoltaic power station technologies that impacts the values of the factor should also be considered.

## CONCLUSION

Having applied the EN 15603:2014 methodology to estimate $f_{Pnren}$, $f_{Pren}$ $f_{Ptot}$ factors, the average numerical values of 0.038, 1 and 1.038 were determined accordingly (photovoltaic power stations of 0.02< > 0.03 MW capacity – 0.021, 1 , 1.021; those of 0.01< > 0.02 MW capacity – 0.028, 1, 1.028; and <0.01 MW capacity – 0.238, 1, 1.238). These results are going to be applied for building energy certification to ensure the implementation of the goals and regulations determined by Directive 2010/31/EU.

Since the capacity of photovoltaic power stations varies, it is reasonable to classify them accordingly for the evaluation and calculation of PEF factor because the probability of errors and inaccuracies increases if only a single general numerical value is used in the calculations.

To monitor the future implementation of the goals set in the EU directives and regulations related to energy saving and the use of renewable energy sources, it is highly advisable that all the EU members use the same or similar methodology to estimate the primary energy factor of renewable and non-renewable energy sources.

## REFERENCES


1 S. Øvergaard, Issue Paper: Definition of Primary and Secondary Energy. Prepared as input to Chapter 3: Standard International Energy Classification (SIEC) in the International recommendation on Energy Statistic (IRES) (2008).
2 DEAP, Ireland building regulations (2012).
3 OiB-Richtline 6. Energieeinsparung und Wärmeschutz. Ausgabe. Austria national regulation (2015).
4 VEA: Methodologie. Belgium national regulation (2013).
5 78/2013 Sb Vyhláška o energetické náročnosti budov. Czech national regulation (2013).
6 BR10. Danish building regulations (2010).
7 SAP. UK building regulations (2012).
8 Vabariigi Valitsuse määrus Nr. 68 (30.08.2012) Estonian building regulations (2012).
9 TOTEE 20701-1/2010 Greek building regulations (2010).
10 LIDER-CALENER Spanish building regulations (2014).
11 CTI Raccomandazione 14, Prestazioni ener-getiche degli edifici – Determinazione della prestazione energetica per la classificazione dell'edificio, Italian building regulations (2013).
12 Infogrend Innovations/BRE: Methodology for Assessing the Energy Performance of Buildings. Cyprus national regulation (2009).
13 Poz 888 Dz. U. Poland building regulations (2014).
14 NEN 2904:2004 Energieprestatie van utiliteitsgebouwen – Bepalingsmethode, Dutch building regulations (2004).
15 RT 2012. Arrêté du 26 octobre 2010 relatif aux caractéristiques thermiques et aux exigences de performance énergétique des bâtiments nouveaux et des parties nouvelles de bâtiments. French building regulations (2012).
16 364/2012 Slovakia national regulation (2012).
17 TSG-1-004:2010 Učinkovita raba energije, Slovenian building regulations (2010).
18 D3 Rakennusten energiatehokkuus. Finland building regulations (2012).
19 IVL. Sweden building regulations (2011).
20 DIN V 18599-10:2011-12. Energetische Bewertung von Gebäuden. Germany Standard (2011).
21 M. Großklos, Kumulierter Energieaufwand und $CO_2$-Emissionsfaktoren verschiedener Energieträger und –versorgungen. IWU (2014).
22 20/2014 (III.7) Hungarian building regulations (2014).
23 Primary Energy Demand of Renewable Energy Carriers, PE International (2014).
24 AGFW. Energy performance of district heating – determination of the specific primary energy factors in district heating supply, Arbeitsblatt FW 309 Part 1 (2010).
25 T. B. Johansson, A. Patwardhan, N. Nakicenovic, L.Gomez-Echeverri, *Global Energy Assessment – Towards a Sustainable Future.* International Institute for Applied Systems Analysis (2012).
26 UN, Energy Statistics (2012).
27 IPPC. Fifth Assessment Report. Intergovernmental Panel on Climate Change (2014).
28 IEA, OECD: Energy Statistics Manual (2004).
29 IEAa, Projections: Energy policies of IEA countries. Documentation for beyond 2020 files (2012).
30 IEAb Statistics-Electricity Information (2012).
31 EIA U.S. Energy Information Administration. Glossary-Primary Energy Consumption (2013).
32 S. Te Buck, B. van Keulen, L. Bosselaar, T. Gerlagh, Renewable energy monitoring protocol (2010).
33 BP Statistical Review of World Energy (2013).
34 GaBi. Database & Modelling Principles (2012).
35 IPCC, Special Report on Renewable Energy Sources and Climate Change Mitigation (2012).
36 J. Macknick, *Carbon management* **2**, 2, (2011).
37 R. Harmsen, B. Wesselink, W. Eichhammer, E. Worrell, *Energy Policy* **39**, 6, (2011).
38 P. L. Lombard, J. Ortiz, C. Pout, *Energy and Buildings*, **40**, 3, (2008).
39 E. Baake, B. Ubbenjans, The Scope for Electricity & Carbon Saving in the EU through the use of EPM Technologies (2012).
40 ECOFYS, Primary energy factors for electricity in buildings, Sustainable energy for everyone (2012).
41 FprEN 15603:2014 Energy Performance of Buildings Overarching Standard EPBD.
42 N. Aste, C. Del Pero, F. Leonforte, M. Manfren, Energy, 59, 12 (2013).
43 B. Norton, P. C. Eames, T. K. Mallick, M. J. Huang, S. J. McCormack, J. D. Mondol, Y. G. Yohanis, *Solar Energy* **85**, 8, (2011).
44 A. Galvonaitė, M. Misiūnienė, D. Valiukas, M.S. Buitkuvienė, The climate in Lithuania, (2007).
45 Photovoltaic Geographical Information System-Interactive Maps. European Communities, 2001–2008.
46 RSN 156–94 Building Climatology, (1995).
47 T. Vaškevičius, Evaluation of wind and photovoltaic power plant, (2012).
48 Lithuanian electricity transmission system operator LITGRID report, (2015).
49 S. Mekhilefa, R. Saidur, A. Kamalisarvestani, *Renewable and Sustainable Energy Reviews* ,**16**, 5 (2012).

*Bulgarian Chemical Communications, Volume 48, Special Issue E (pp. 147 - 151) 2016*

# A device for the analysis of photovoltaic panels

S. I. Sotirov*, D. K. Gospodinov , D. A. Zlatanski

*Plovdiv University "Paisii Hilendarski", 24 Tzar Assen Str., 4000 Plovdiv, Bulgaria*

In this paper we present the elaboration and functioning of an electronic unit for examining the Volt-Ampere (V-I) and the output (P-V) characteristics of a PV panel. The unit was designed by us to record the PV panel voltage at different current loads. A digitally controlled electronic load was developed to set the current values by a chosen increment. Then, the unit measures the corresponding voltage value for each current value by an analog-digital converter (ADC). All pairs of values are used as input to a microcontroller and then transferred to a PC, where they can be graphically visualized by a specialized software. Different PV panels with varying output (P-V) characteristics were used to test the performance of the elaborated electronic unit. These experiments revealed that the unit is appropriate for PV panel analysis both under laboratory and field conditions.

**Keywords:** photovoltaic panel, current vs. voltage characteristic, power output vs. voltage characteristic

## INTRODUCTION

The rapid development of technologies for energy production from renewable sources, such as the Sun, makes it necessary to introduce new algorithms and methods for increasing the efficiency of the devices for energy output, conversion and storage. To meet market needs, manufacturers are using new technologies for the production of photovoltaic cells and modules. One of the main photovoltaic modules parameters is their efficiency and tests and studies are constantly being performed to improve the modules efficiency. Basic parameters and characteristics of the photovoltaic cell are the voltage vs. current characteristic, the short-circuit current, the open circuit voltage, the maximum power output and the Fill-Factor.

The study of these parameters and characteristics is applied for the comparison of the power, produced by the cells in laboratory and in actual field conditions. Typically, devices for testing the characteristics and parameters of a photovoltaic cell are using DC loads, whose resistance changes across the operating range of the cell. These equipment solutions are expensive and complex. In recent years a number of devices for testing of photovoltaic cells and modules has been developed [1, 2, 4].

This publication presents an electronic circuit and a device, developed to study the voltage vs. current and the power output (I-V and P-V) characteristics of photovoltaic panels. Relatively inexpensive and up-to-date components and integrated circuits were used in the development of this appliance, making it suitable for conducting both laboratory tests and field studies.

* To whom all correspondence should be sent:
s.i.sotirov@abv.bg

## DESCRIPTION

When examining the characteristics of the photovoltaic panels the following basic values are usually considered; ($I_{sc}$) - short circuit current; ($V_{oc}$) - open circuit voltage; ($I_{mp}$) - rated current; ($V_{mp}$) - rated voltage; (MPP) - the point of maximum power; (FF - Fill-Factor) – a coefficient of filling; η - solar element efficiency. A voltage vs. current characteristic can be calculated to give an idea of the photocurrent generation, the panel surface being irradiated with light for this purpose [2].

Typical voltage vs. current relation, known as an I/V curve (red line) and power output vs. voltage characteristic (blue line) are revealed on Fig.1 [3]. The ratio of the dark violet rectangle area, to the area of the bright violet rectangle is defined as the FF-factor (factor of filling).

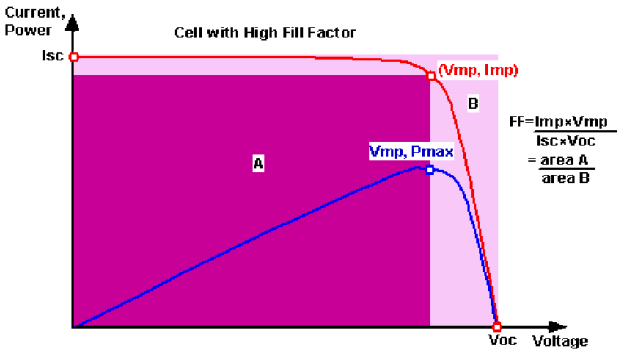


**Fig.1.** A voltage vs. current and power output characteristics of a PV cell and definition of the duty cycle (FF- Fill Factor)

The FF-factor is used to assess the quality of photovoltaic panels and it is also known as the efficiency coefficient of a panel and should be as close to 1 as possible [4]. It may be determined by formula (1):

$$FF = \frac{I_{mp}.V_{mp}}{I_{sc}.V_{oc}} \quad (1)$$

Another key parameter of a photovoltaic panel is its efficiency, which is the ratio of the electrical power output to the input radiant power (formula (2)).

$$\eta = \frac{P_{out}}{H.S}.100\% \quad (2)$$

where η is the efficiency, $P_{out}$ – the electrical power output ($I_{mp}.V_{mp}$), H – the radiant energy falling on the photoelectric cell in mW/ cm$^2$, and S - the active area of the photoelectric cell in cm$^2$ [1, 5]. The purpose of our paper was to develop an electronic device, which by performing voltage and current measurements on a PV panel, to calculate and provide its main parameters.

The full scheme of the device for testing PV panel parameters and characteristics is presented on Fig.2. The elaborated appliance allows to determine the I/V curve of photovoltaic panels with voltage up to 22V and maximum output current up to 1 A. The I/V curve and the power output curve of a PV panel can be displayed graphically on a PC monitor.

The development of the unit for testing PV panel parameters and characteristics is based on the PIC16F876A microcontroller When using a microcontroller in a device, its principle of operation can largely be changed only by introducing the necessary adjustments in the controller program [6].

The main functions, which the microcontroller performs, are to communicate with a personal computer, manage the digital to analog converter MCP4821 [7] and to convert analog data into digital form by using the integrated module in it for analog-digital conversion (ADC) [8]. The operational amplifier LM324, which is powered by stabilized unipolar constant voltage 24V, was used to measure the voltage, produced by the photovoltaic panel. For this purpose the integral stabilizer uA7824 was applied. The operational amplifier U2 acts as a voltage follower. His non-inverting input is connected directly to the positive output terminal of the panel. This solution provides the highest possible entrance impedance of the amplifier. Thus, the current consumption in the input circuit will be minimal, which is essential for the accuracy of these measurements.

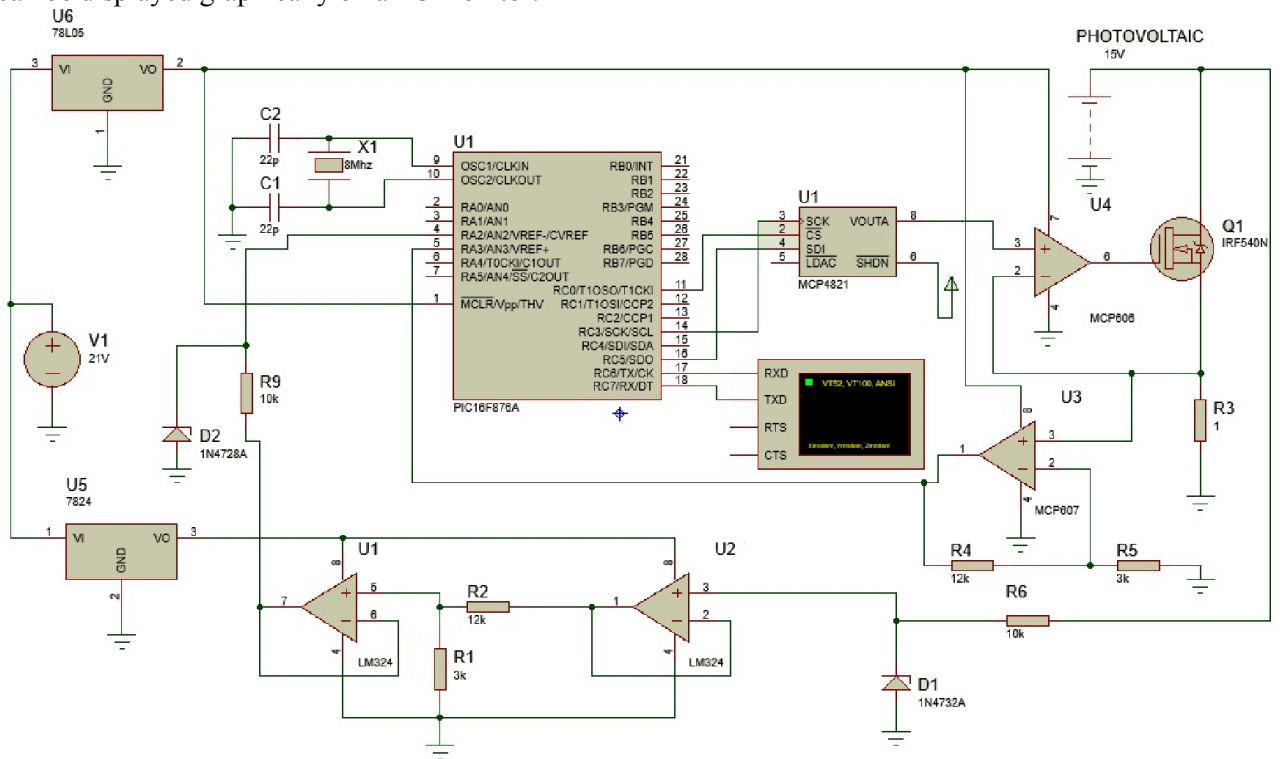


**Fig.2.** General circuit of the device for analyzing of the PV panels

At the same time the voltage follower provides a low output impedance, which in this case is a necessary condition as to the output of U2 is connected to a voltage divider, constructed of resistors R1 / R2. The divisor transmission coefficient is 1/5. Since the ADC works with the reference voltage 5V, the maximum value of the analog input voltage, that can be converted into digital code, can not exceed 5V. By using this divider we enable the possibility to submit voltages to the ADC up to 25V. The ADC resolution, which is (4.88mV), can be determined by formula (3).

$$\Delta V = \frac{V_{REF}}{2^{10}}, \quad (3)$$

where $V_{REF}$ is the reference voltage of the ADC (5V), $2^{10}$ is the ADC sparsity (10bit).
The output of the second operational amplifier U1 is connected directly to the ADC module analog input (AN2) of the PIC16F876A microcontroller.

To determine the current flowing through the photovoltaic panel, a circuit has been developed, consisting of a DAC and a current generator, and thereby we achieved a controllable electronic load. The circuit is powered by a stabilized DC voltage 5V, which is obtained from the integral stabilizer 78L05. It can be divided into two main parts. The front part is developed by DAC (MCP4821) and an operational amplifier, in which the DAC converts the digital code and turns it into analog voltage that is fed to the operational amplifier [9]. The voltage which is obtained at the output of MC4821 can be calculated by formula (4).

$$V_{out} = \frac{(2048.D_n)}{2^n}.G \quad (4)$$

The minimum step, by which the voltage can be altered at the output of the DAC, can be 1mV at G = 2 and 0,5mV at G = 1, where G is the gain of the integrated amplifier in the DAC. This voltage serves to control the transistor. The amplifier, used in this case, is MCP607. It is characterized by a very small asymmetry voltage (offset of 250 μV) and is designed to operate with unipolar power [10]. The small amplifier offset is essential for the proper operation of the scheme, as this voltage would lead to an error in the electric current control. The N-channel MOSFET transistor (IRF540) plays the role of a controllable load and serves to ensure high output current. Through negative feedback, connecting the source of transistor with the inverting input of the operational amplifier, the electric current value through the reference resistor R3 is being adjusted. The electric current in the load circuit can be determined by formula (5).

$$I_{load} = \frac{V_{in}}{R3} \quad (5)$$

where $V_{in}$ is the input voltage of the operational amplifier, which is set by the DAC. It is obvious that the value of the current in the load circuit depends on the input voltage $V_{in}$ and the value of the resistor R3. It is known that the current flow through a resistor dissipates heat. This will lead to an increase in temperature, and accordingly to a change of its resistance value. This may cause deviation between the digital set point current through the DAC and the actual value of the flowing current in the circuit. To reduce this effect, it is necessary to use a resistor with a low temperature coefficient and to shorten the measurement time. Since this temperature dependence cannot be completely avoided, the amplifier U3 is applied for monitoring and measuring of the exact current value in the load circuit. It helps to monitor the voltage drop across the reference resistor R3, which is proportional to the current, flowing into the load circuit. In this circuit U3 is connected as non-inverting amplifier with a gain of 3.

The advantage of such a circuit topology is the high input impedance of the amplifier, which is important in order to avoid its influence on the current generator. The voltage at the output of U3 is fed directly to the analog input (AN3) of the ADC module, where it is converted into digital form. Thus, information is constantly submitted to the microcontroller about the actual value of the current flowing through the photovoltaic panel.

The conversion of analog current and voltage values of the photovoltaic panel in digital form and the communication with the PC is carried out by the microcontroller. The setting of a series of values for the load current in the circuit of the photovoltaic panel, which vary by the chosen step, is performed by a PC, which communicates with the microcontroller via a serial interface (UART). The microcontroller measures the current and the voltage values after each change of the load current. The measured values are converted into digital form and transmitted to the PC where they are displayed graphically on the computer monitor by specially developed software.

## RESULTS

Fig.3 and Fig.4 expose the I-V curve and the PV characteristic, which were obtained, using the device, we developed. Analysis of two different PV panels was performed with power output of 5W and 0.7W. From the voltage vs. current characteristic, shown on Fig.3 (blue curve), it can be seen that when the voltage of the photovoltaic panel has a minimum value, the current in the load circuit is maximum. One can also get that at a minimum load current the voltage between the terminals of the panel has a maximum value, which is characterized as an open circuit voltage.

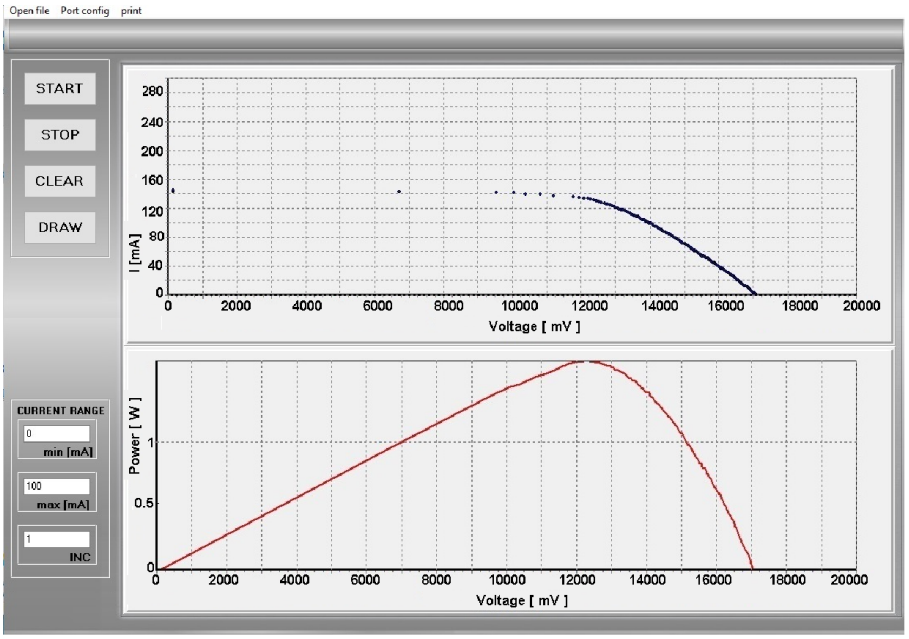


**Fig.3.** I-V curve and P-V characteristic for the PV panel of maximum 5W power output. The experiment was done at an illuminance level of 78 000 lx and surface temperature of the studied photovoltaic module of 28° C

The point of maximum curvature of the I-V graph identifies the I-V combination, for which the panel generates maximum power output. At voltages well below Vmp, the electric current, generated by the photovoltaic panel is relatively independent of the output voltage. Near the area where the curvature increases, one can see that the nature of the correlation sharply changes. As the voltage in this region increases, a greater percentage of the generated charge carriers recombine within the volume of the photovoltaic panel and a smaller portion flows through the load (low current). At the point where the voltage is maximum and hence the current through the photovoltaic panel is minimal all carriers recombine within volume.The red curve on Fig.3 exposes the power output vs. the voltage (P-V) curve. Since the photovoltaic panel is a DC source, its power output is calculated by the relationship R = U.I. If we calculate the power output of the photovoltaic panel for each point of the I-V curve, we obtain the P-V curve, its maximum identifying the maximum power output of the respective panel.

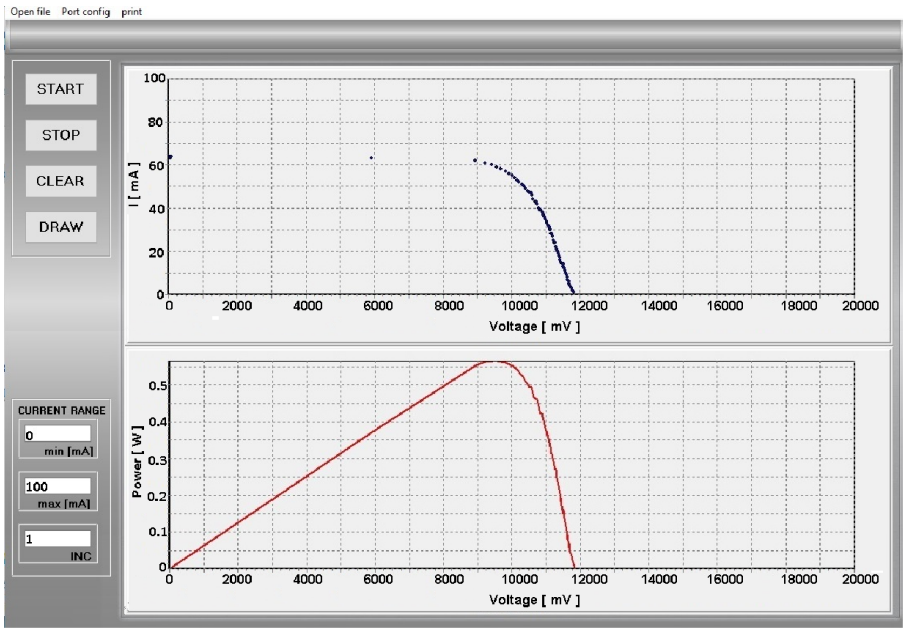


**Fig.4**. I-V curve and P-V characteristic for the PV panel of maximum 0.7W power output. The experiment was done at an illuminance level of 115 000 lx and surface temperature of the studied photovoltaic module of 28° C

The graph on Fig.4 is for a mono-silicon panel with maximum power output of 0.7W. When comparing the P-V curves for both experiments, one can clearly see that the power-voltage curve exibits a typical form, as revealed on Fig.1.

## CONCLUSIONS

In this paper we describe an electronic device, we developed for measuring output current and voltage of a PV panel, by which to study its power output characteristics. We present the appliance scheme and describe in detail how to perform the measurements. Some simulations have been performed before the unit elaboration by the application of the Proteus software. These simulations cover both the hardware and the software parts, allowing the verification in advance of the correct work of the developed schemes and the corresponding PIC microcontroller software. The obtained results demonstrate that the scheme is suitable for the planned device elaboration. The obtained results demonstrate that the scheme is suitable for the planned measurements. After the simulations we designed and developed the hardware circuit itself, based on the PIC16F876A microcontroller, which measures the output voltage and current from the studied module and thus we examined the parameters under concern. The results were visualized on a PC by specialized software.

By measuring the current and the voltage at the panel output, we can calculate the studied characteristics and thus we can test whether the measured characteristics values of a PV panel meet the factory. This was done for both PV panels (5W and 0.7W) and calculated values fit well the factory ones, considering the variation of the experiment conditions.

The device can examine PV panels of voltage up to 22V and maximum output current up to 1A. The implemented experiments demonstrate that the developed device is appropriate for testing and evaluating PV panels efficiency both in laboratory and in field conditions.

## ACKNOWLEDGMENTS

This research was financed by the University of Plovdiv ”Paisii Hilendarski”, under contract № NI15-FFIT-005/23.04.2015.

## REFERENCES

1 A. Sahbela, N. Hassanb, M. Abdelhameedb, A. Zekryb, Experimental Performance Characterization of Photovoltaic Modules Using DAQ, TerraGreen 13 International Conference 2013, Energy Procedia 36, 2013

2 V. Zhelyazova, G. Gospodinov, A. Bauazir, V. Mutkov, Q. Neykov, K. Stereva. A prototype device for testing the parameters of photovoltaic elements. Scientific papers of University of Rousse, (in Bulgarian), 52, 2013

3 http://www.pveducation.org/pvcdrom/solar-cell-operation/fill-factor

4 E. Van Dyk, A. Gxasheka, E. Meyer, Monitoring Current–Voltage Characteristics and Energy Output of Silicon Photovoltaic Modules, ELSEVIER, Renewable Energy, 30, 399–411, 2005

5 V. Leite, J. Batista, F. Chenlo, J. Afonso, Low-Cost Instrument for Tracing Current-Voltage Characteristics of Photovoltaic Modules, International Conference on Renewable Energies and Power Quality (ICREPQ’12), Santiago de Compostela (Spain), 28th to 30th March, 2012

6 N. Kenarov, PIC Microcontrollers, Part 1, Young developer Varna, ( in Bulgarian ), 24, 2006

7 http://ww1.microchip.com/downloads/en/DeviceDoc/22244B.pdf

8 E. Van Dyk, A. Gxasheka, E. Meyer, Monitoring current-voltage characteristics of photovoltaic modules, IEEE PVSC, 1516-1519, 2002

9 9http://www.tuvarna.bg/tuvarnaknt/images/tutorials/cir/ digitalschemas.pdf

10 V. Zlatarov, L. Denevska, D. Stamenov, I. Nemigenchev, Electronic analog circuits and devices, Technique Sofia, ( in Bulgarian ) ,105, 1994

*Bulgarian Chemical Communications, Volume 48, Special Issue E (pp. 152 - 157) 2016*

# Software for measuring the characteristics of photovoltaic panels

S. I. Sotirov*, D. K. Gospodinov , S. V. Stoyanova-Petrova, D. A. Zlatanski

*Plovdiv University "Paisii Hilendarski", 24 Tzar Assen Str., 4000 Plovdiv, Bulgaria*

This paper presents the design and the development of specialized software, by which the characteristics of a photovoltaic panel can be tested and analyzed. The software controls a hardware module, which implements the electrical load of a photovoltaic panel and monitors its voltage. The values, measured by the hardware module, are transmitted to a PC via a serial interface. Then, these values can be visualized in a graphic form by the software, which allows the plotting of the volt-ampere and the power-volt output characteristics of the photovoltaic panel. The elaborated software enables us to set the parameters of the study: initial current and the current increment steps. The measured parameter values are recorded as PC files, allowing subsequent visualization and examination of data.

**Keywords:** photovoltaic solar panel, microcontroller programming, photovoltaic (PV) panel characteristics

## INTRODUCTION

In recent years increased interest is observed in implementing photovoltaic systems for electrical energy production. At present renewable energy sources are becoming a larger share of the energy systems. For these two reasons the need to develop new technologies for testing and monitoring photovoltaic sources arises. Major indicators of the quality of any photovoltaic source are its I-V (Current vs. Voltage) and P-V (Power output vs. Voltage) characteristics, which often need experimental determination [1, 2]. Current vs. Voltage and power output characteristics are presented on Fig.1.

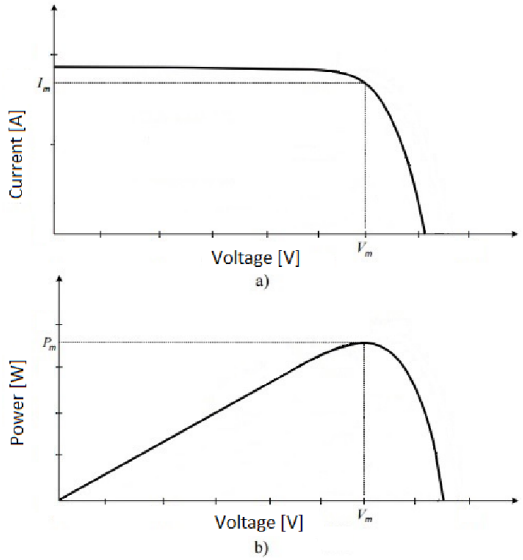


**Fig.1.** Graphs of the photovoltaic module under different temperature and illuminance: a) *Current vs. Voltage* I-V characteristic; b) *Power output vs. Voltage* P-V characteristic of the photovoltaic panel

The basic characteristic points of the I-V and P-V characteristics are: maximum current at voltage 0V of the photovoltaic source (short circuit current $I_{sc}$), maximum voltage of the photovoltaic source at current 0A (voltage at open circuit $V_{oc}$) [3]. For each point of the I-V curve, the current and the voltage give information about the power output under the corresponding conditions [4]. The point of maximum power (maximum power point MPP), which can be obtained, is achieved in those points of the characteristics, where the I-V has a maximum curvature.

The Fill-Factor is defined by formula (1):

$$FF = \frac{I_m.V_m}{I_{sc}.V_{oc}} \ , \qquad (1)$$

where $I_m$ is the rated current and $V_m$ is the rated voltage. Usually the FF is used to shows how close a PV cell or panel is to the ideal case. [5]. These parameters allow to determine the status of a photovoltaic system and to detect failures in it. The main principle for experimental determination of the I-V curve is based on controlling the current flowing through the photovoltaic module and measuring its voltage. There are a number of methods for solving this task, in which controlling the load current through the photovoltaic module is accomplished by a variable resistor, capacitive load or electronic load [1].

This paper presents the design and development of specialized software, by means of which the I-V and P-V characteristics of photovoltaic panels can be experimentally determined. The software controls a hardware module, by which electrical loading of a

* To whom all correspondence should be sent:
s.i.sotirov@abv.bg

photovoltaic panel is accomplished, continuously monitoring its voltage.

The hardware module for studying photovoltaic panels consists of a power supply block, a block for measuring the voltage of the photovoltaic module, a block for regulation and measurement of the current through the photovoltaic module, a PIC microcontroller (MCU), and a personal computer (PC). The block diagram of the hardware module is shown in Fig.2.

The microcontroller sends the values from the measurements to a personal computer, where the I-V and P-V characteristics are visualized in a graphic form by means of the especially developed for this purpose software.

The developed specialized software includes: software for a personal computer and control program for the microcontroller.

## PC SOFTWARE FOR MEASUREMENT AND VISUALIZATION OF THE I-V AND THE P-V CHARACTERISTICS OF PHOTOVOLTAIC PANELS

The developed software is aimed at configuring the computer as a monitoring system for studying the I-V and P-V characteristics of photovoltaic sources, and also as an interface system for communication with the MCU microcontroller. The connection between the two devices is realized by means of a serial interface for communication (UART). The main user interface of the developed software is shown in Fig.3.

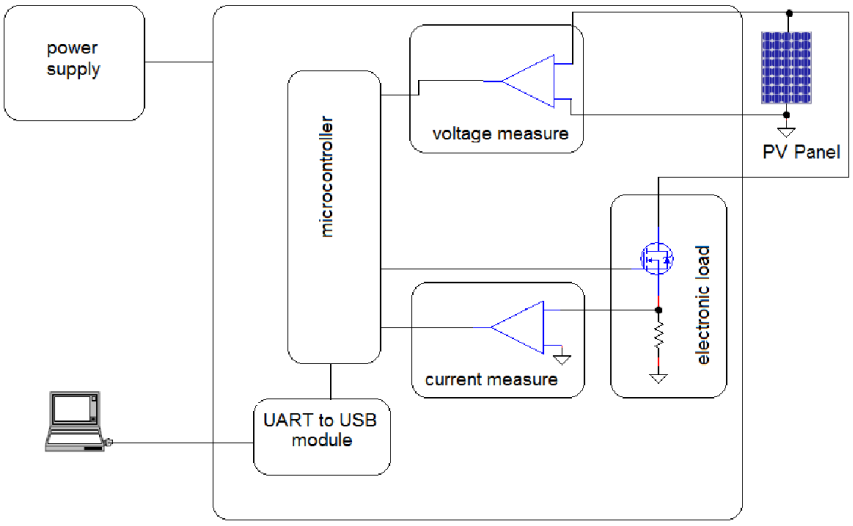


**Fig.2.** Block diagram of the hardware module

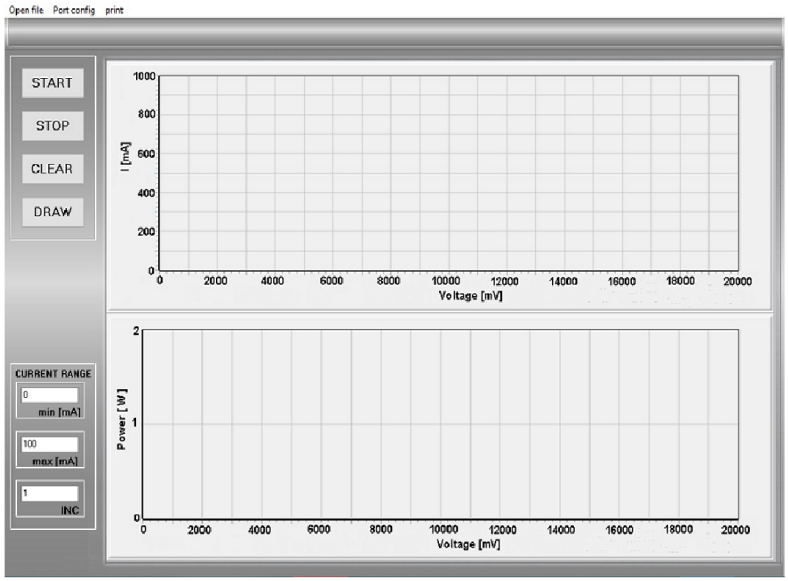


**Fig.3**. PC Software graphical user interface

The software sends commands to the microcontroller for measuring both the current and the voltage of the photovoltaic panel. The software receives the measurement data from the microcontroller, records them in a file, processes them mathematically and then displays them graphically. A possibility is envisaged to back up the measured voltage, current and power values in files of user's choice.

The developed software allows setting the basic parameters of the measurement: minimum value of the load current, maximum value of the load current, and step of increase of the current. There are fields in the main package of the user interface, where the corresponding values are introduced.The voltage of the photovoltaic panel is measured under certain conditions of illuminance. After the program has been started, the voltage at the terminals of the photovoltaic panel is first measured when there is no current flowing through the panel. Thus, the maximum voltage of the photovoltaic source is determined (voltage at open circuit $V_{oc}$). After that from the personal computer the value of the current to flow in the load circuit of the panel is sent. The microcontroller receives this value and sends it to a digital-to-analogue converter (DAC), which controls an electronic load, implemented by a MOSFET transistor. Immediately after establishing the predetermined current, the microcontroller starts measuring both the voltage of the photovoltaic panel, and the value of the current in the load circuit of the photovoltaic panel.

The accuracy in setting the value of the current in the load circuit depends on a number of parameters, including the steps of measuring and the temperature at which the device is situated. The current flow increases the temperature of the electronic components, which make up the electronic resistance. This can lead to occurrence of a difference between the digitally set value of the current by a DAC and the real value of the current, flowing in the circuit. In order to reduce this effect it is necessary to use components with a small temperature coefficient and to reduce the measuring time.

Since the temperature dependence cannot be entirely avoided, it is envisaged that the value of the current in the load circuit is continuously measured by an ADC.

After completing the measurements, the microcontroller sends the values to the personal computer. By means of the developed software, the measurements values are visualized in a graphic form and recorded in a file. This is repeated until the value of the current in the load circuit of the photovoltaic panel reaches the preliminary set value of the maximum current in the field of the main software panel.

The possibility to back up all measurements is of great significance as they can be visualized and analyzed afterwards. This is important when studying photovoltaic sources for long periods of time or when carrying out quality control of a series of copies. A possibility for printing the obtained graphs on paper is envisaged.

A generalized flow chart of the developed software is given in Fig.4.

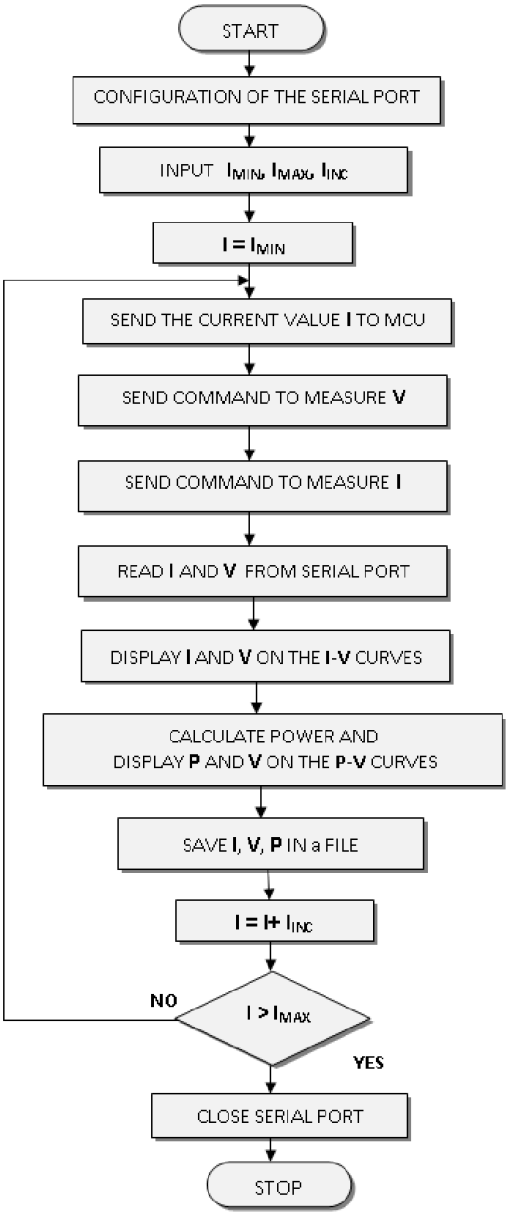


**Fig.4.** PC Software Flow chart

## MICROCONTROLLER CONTROL PROGRAM

The microcontroller, which is used in the present development, is an 8-bit CMOS microcontroller PIC16F876A. Its clock frequency is 8 MHz, which can provide 2 MIPS. The communication between the microcontroller and the personal computer is realized by means of a series interface UART and the USB port of the PC. A USB port converter FT232RL is used for the purpose. A DAC, generating an analogue signal, is connected to the SPI port of the microcontroller. Thus the current, flowing through the photovoltaic panel, is controlled. Port A of the microcontroller is programmed as an analogue input for the ADC. Channels 1 and 2 are used for measuring the voltage and the current. Fig.5 presents a generalized flow chart of the microcontroller control program.

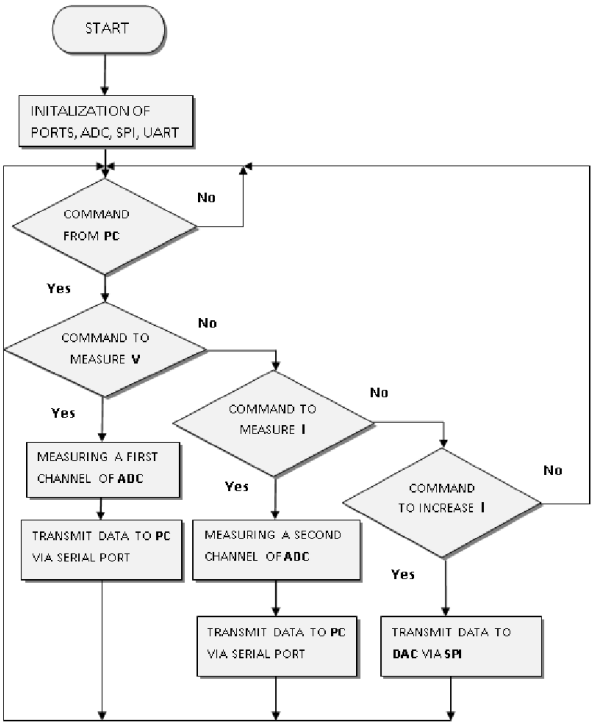


**Fig.5.** Microcontroller control program flow chart

## EXPERIMENTAL RESULTS

Fig.6 and Fig.7 present experimentally obtained I-V and P-V characteristics of a monocrystalline silicon photovoltaic panel with maximum power of 5W at different illuminance levels and different surface temperatures of the studied photovoltaic module. We performed outdoor experiments and the corresponding temperatures were measured by a MS8209 digital multimeter, while the illuminance levels were measured by a MS6612 Digital Light Meter. The obtained graphic dependences allow for a fast and easy definition of the basic parameters, summarized in Table 1.

**Table 1.** Basic parameters of a monocrystalline silicon photovoltaic panel with maximum rated power 5W

| Illuminance [lx] | Short-circuit current Isc [mA] | Open-circuit voltage U [V] | Maximum power P [W] |
|---|---|---|---|
| 78 000 | 145 | 17.1 | 1.62 |
| 115 000 | 258 | 17.5 | 2.15 |

The results show that together with increasing the light power, incident on the active area of the photovoltaic panel, the maximum electric power, which the panel can release toward the load, also increases. It is obvious that light intensity change influences the short-circuit current stronger than it influences the idle-run voltage. From Fig.6 it can be clearly seen that when increasing the temperature of the photovoltaic panel, the shape of the I-V characteristic also changes, what, in turn, leads to reduction in the Fill-Factor, compared to its value at lower temperature.

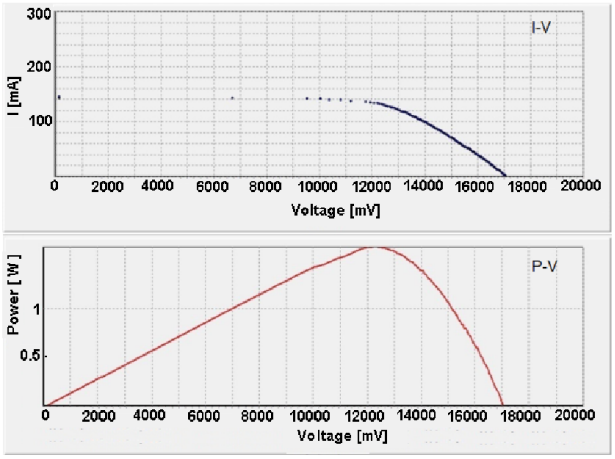


**Fig.6.** I-V and P-V characteristics of a monocrystalline silicon photovoltaic panel with maximum power 5W at illuminance levels of 115 000 lx and surface temperature of the studied photovoltaic module of 60° C

Similar experiments have been conducted for a monocrystalline silicon photovoltaic panel with rated power of 0.7W and the obtained I-V and P-V characteristics are presented in Fig.8 and Fig.9. The defined basic parameters of the photovoltaic panel are presented in Table 2. The tests show an increase in the electrical power output of the photovoltaic panel with an increase in solar radiation.

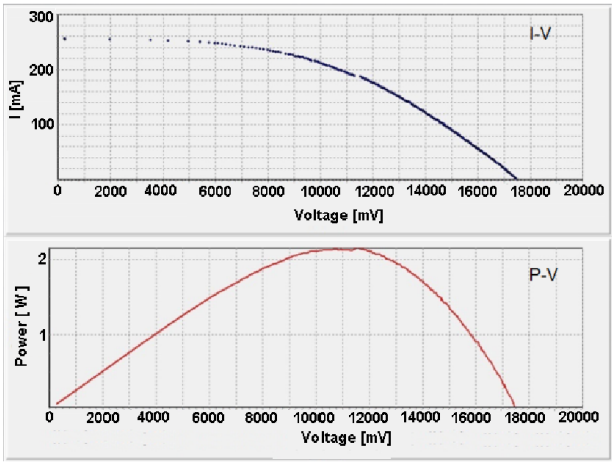


**Fig.7.** I-V and P-V characteristics of a monocrystalline silicon photovoltaic panel with maximum power of 5W at illuminance levels of 78 000 lx and surface temperature of the studied photovoltaic module of 28° C

**Table 2.** Basic parameters of a monocrystalline silicon photovoltaic panel with maximum rated power of 0.7W

| Illuminance [lx] | Short-circuit current Isc [mA] | Open-circuit voltage U [V] | Maximum power P [W] |
|---|---|---|---|
| 115 000 | 64 | 11.8 | 0.56 |
| 70 000 | 41 | 11.75 | 0.37 |

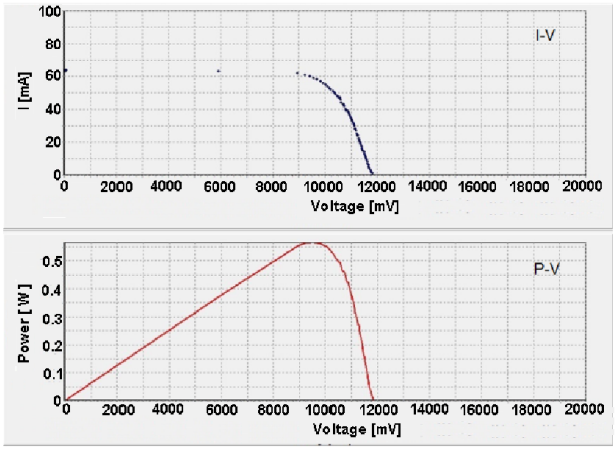


**Fig.8.** I-V and P-V characteristics of a monocrystalline silicon photovoltaic panel with maximum power of 0.7 W at illuminance levels of 115 000 lx and surface temperature of the studied photovoltaic module of 28° C

From the conducted experiments it can be concluded that the output power produced by the photovoltaic module depends mainly on solar radiation. Consequently, in order to achieve maximum efficiency of a renewable energy system, it is necessary to define the working point at which the photovoltaic system can provide maximum power of the load (maximum power point MPP). The location of this point depends on the solar radiation and the temperature of the panel.

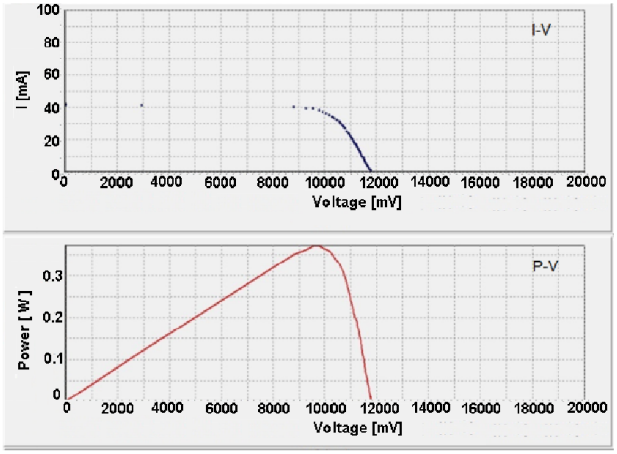


**Fig.9.** I-V and P-V characteristics of a monocrystalline silicon photovoltaic panel with maximum power of 0.7 W at illuminance levels of 70 000 lx and surface temperature of the studied photovoltaic module of 28° C

## CONCLUSION

The developed software proposes a fast and easy solution for making a device for studying the parameters and characteristics of photovoltaic panels and modules. Modern easily accessible components and circuits are used for the hardware part, controlled by the developed software. The software can be successfully used for studying both individual panels and entire modules from photovoltaic systems.

## ACKNOWLEDGEMENTS

This research was financed by the University of Plovdiv "Paisii Hilendarski", under contract № NI15-FFIT-005/23.04.2015.

## REFERENCES

1 E. Durán, M. B. Ferrera, J. M. Andújar, M. S. Mesa, I-V and P-V Curves Measuring System for PV Modules based on DC-DC Converters and Portable Graphical Environment, Industrial Electronics (ISIE), 2010 IEEE International Symposium, 3323 – 3328, (2010).

2 E. Durán, J.M. Andújar, J. Galán, M. Sidrach-de-Cardona, Methodology and Experimental System for Measuring and Displaying I-V Characteristic Curves of PV Facilities, Progress in Photovoltaics Research and Applications, 574-586, (2009).

3 Y. Hishikaw, Y. Tsuno, K. Kurokawa, Translation of the I-V curves of various solar cells by improved linear interpolation, 21st European Photovoltaic Solar Energy Conference, Dresden, Germany, (2006).
4 Y. Atia, M. Zahran, A novel system for photovoltaic solar cell test and characteristics measurements, ERJ Engineering Research Journal, Faculty of Engineering Minoufiya University, Vol. 32, No. 4, (2009).
5 A. Ndiaye, C. M. F. Kébé, P. Ndiaye, A. Charki, A. Kobi, V. Sambou, Impact of dust on the photovoltaic (PV) modules characteristics after an exposition year in Sahelian environment: The case of Senegal, International Journal of Physical Sciences, Vol. 8, 1166-1173, (2013).

*Bulgarian Chemical Communications, Volume 48, Special Issue E (pp. 158 - 164) 2016*

# An experimental study of building thermal environment in building integrated photovoltaic (BIPV) installation

Wang Yunfeng [1], Reda Hassanien Emam Hassanien [1,2], Li Ming [1], Xu Guixian [1], Ji Xu [1]

[1]*Solar Energy Research Institute, Yunnan normal University, No.798 Juxian street, Chenggong district, Kunming 650500, China*

[2]*Agricultural Engineering Department, Faculty of Agriculture, Cairo University, Cairo 12613, Egypt*

A 120kWp building integrated photovoltaic (BIPV) system was installed on the south facade of the building of Solar Energy Research Institute in Yunnan Normal University in October 2014. The area of curtain wall was 1560m$^2$(26m×60m), which consists of 720 semi-transparent monocrystalline silicon double glazing PV panels. The windows of many rooms from the fifth to the ground floors were covered by the PV curtain wall. The PV light transmittance was about 47%. Therefore, this paper studied the monthly and seasonal variations of thermal environment for building in terms of solar data and meteorological parameters. In summer and winter, the ambient temperatures and the indoor temperatures of the covered rooms by the PV curtain wall in different floors were tested and compared to the reference rooms without PV curtain wall. Results showed that the indoor temperature was 6℃ higher than the ambient temperature in winter. Therefore, it can be concluded that the integration of semi-transparent BIPV reduces the heating demand in winter.

**Keywords:** building-integrated photovoltaic system, building thermal environment, experimental study

## INTRODUCTION

In the last 20 years, the world's energy consumption has sharply increased (40%) and is expected to continue to grow by one-third in the period to 2035 [1]. Buildings can be classified among the leading energy consumers and $CO_2$ emitters [2]. Especially, building energy consumption has been continuously increased, which has been doubled during the last decades in China [3]. According to the growing trend of developed countries, the building energy consumption will account for at least 40% of all social total energy consumption in China [4]. In this situation, the development of alternative, cost effective sources of renewable energy for residential and non-residential buildings should be given the priority for further research and solutions to these challenges. Therefore, designing energy efficient and affordable solutions integrated in buildings dealing with summer and winter climate challenges represents a very ambitious goal. The integration of PV systems into buildings becomes an imperative [5]. Building integrated photovoltaics (BIPV) have a prominent position due to the availability of large building surface areas and PV's ability to transform sunlight directly to electricity [6]. The BIPV may represent an important component of a zero net energy building, which produces as much energy as it consumes [7]. Norton et al. [8] mentioned that BIPV can serve as a shading device for a window, a semi-transparent glass facade, a building exterior cladding panel, a skylight, and parapet unit or roofing system. Moreover, BIPV can be designed to generate electricity at a building's peak usage times and reduce the building's peak grid electricity demand [9]. The peak power cost for large-scale BIPV systems could drop down, which also lead to PV electricity costs comparable to large centralized power plants and then by 2025, more that 3.6% of the world's electricity could be generated by PV power [10]. Furthermore, Li et al. [11] investigated the energy performance of a semi-transparent a-Si PV facade. The simulation results revealed that the semi-transparent PV facade was able to reduce the annual building energy use and peak cooling load by 1203 MWh and 450 kW, respectively. It was reported that the embodied energy pay-back period for photovoltaic system integrated with building was within the range of 12-13 years for the southern and western facades in the United Arab of Emirates [12]. James et al. [13] conducted a critical evaluation of semi-transparent PV roof glazing elements in the UK climate. They reported that taking the electricity generated, shading provided and comfort enhanced into account could render the total system viable both economically and in regard to averted carbon dioxide emissions. On the other hand, it was found that ventilated semi-transparent photovoltaic double-skin facades could improve the daily energy output by 3% because of its lower operating temperature [14]. Most of the previous

* To whom all correspondence should be sent:
wyfdoc@mail.ustc.edu.cn

studies considered the energy harvested of the PV panels as a key performance parameter of BIPV [15-17]. However, due to the "greenhouse effect", the heat from solar radiation in air channel between the building façade and the PV panels can be helpful to decrease the heating load in winter condition. But it is also associated with problems such as over-heating of the building in summertime [18] and the increase of the air conditioning loads, lack of visual and thermal comfort. Since 33% of the average building's cooling load is relate to solar heat gain through the windows. Therefore, the PV curtain wall has been used to cover the windows as a passive cooling for buildings. The experiment was the first and largest BIPV application installed on the building facade of Solar Energy Research Institute of Yunnan Normal University, which covered many windows of different floors and rooms, although Yunnan Normal University has built many rooftop PV systems, as shown in Fig.1. With the installed PV, Yunnan Normal University can save money on one million kWh electricity bill each year. Thus, the aim of this paper is to analyse and investigate the influence the semi-transparent BIPV system in the indoor thermal environment, from the point of view of indoor thermal environment as well as to provide useful information on the operating temperatures under natural convection in different seasons for more applications of semi-transparent BIPV.

(a)

(b)

(c)

**Fig.1.** Yunnan Normal University rooftop PV systems. (a) The 256.50kWp installation capacity on the roof of the library, (b) The 90 kWp installation capacity on the roof of the indoor swimming pool, (c) The 652kWp installation capacity on the roof of the sports training centre

## SYSTEM UNDER STUDY

This experiment has been conducted in Kunming city at the southwest of China (24°23′N to 26°22′N, 102°10′E to 103°40′E, 1950m above MSL), which has a mildest climate characterized by short, cool dry winter with mild days and crisp night, and long, warm and humid summers. It is controlled by a subtropical highland climate and the average temperature is around 15℃ in winter and 24℃ in summer. It also receivers an annual total solar radiation of ~5508.87MJ/m$^2$, and the monthly total solar radiation is shown in Fig.2 based on the data of typical meteorological year (TMY). Therefore, the climate and location of Kunming are suitable for solar installations. The BIPV system in this study (Fig.3) was installed outside of the south facade of the building of Solar Energy Research Institute building in Yunnan Normal University. The system was built in June 2014 and completed the installation and test in October 2014. Totally 720 monocrystalline silicon double glazing PV modules were used on the facade of five floors, which were installed on 60m length and 26m height with south facing of the building with a total area of 1560m$^2$. The modules were installed using specially designed mounting with 85° tilt angles and 6 m apart from the building for the ventilation. The PV arrays were comprised of 30 parallel strings where each string has 24 modules, and the peak power and voltage of each string were 4080Wp and 796V, respectively. The 120kWp power generated was synchronized and supplied to the 400V campus grid through a grid export conditioner built with a Maximum Power Point Tracker (MPPT).

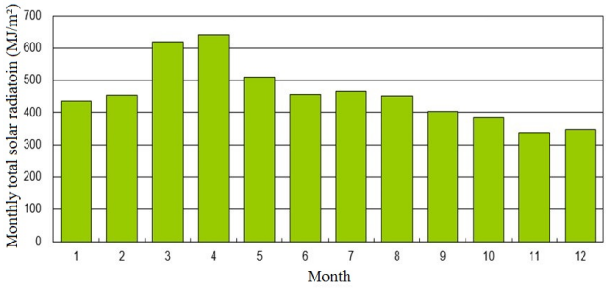


**Fig.2.** The monthly total solar radiation of TMY in Kunming

**Fig.3.** Yunnan Normal University BIPV system

**Table 1.** The PV module specifications under STC

| No. | item | parameter |
|---|---|---|
| 1 | Dimension(mm) | 1985 × 1038 × 13.52 |
| 2 | Light transmittance | 47% |
| 3 | Nominal power(Wp) | 170 |
| 4 | $I_{sc}$(A) | 5.65 |
| 5 | $U_{oc}$(V) | 39.6 |
| 6 | Efficiency | 8.25% |
| 7 | Layer structure | Toughened glass(6mm)+PVB(2.28mm)+(125 × 125mm) sc-Si cells+toughened glass(6mm) |

The specifications of the semi-transparent PV modules are given in Table 1. The PV modules have a 6mm transparent glass covers, a 6mm glass backside and a maintain space between the PV cells in order to transmit light, so that the light transmittance was 47%. And each PV module consisted of 64 pieces of solar cells, and its dimensions was 1985×1038mm. Solar cells adopted in the PV module were monocrystalline silicon wafer cells and the dimension of each cell was 125×125mm as shown in Fig.4. The efficiency of the monocrystalline silicon PV modules was 8.25%, which was lower than conventional monocrystalline silicon modules. The reason was that the areas of 64 pieces of solar cells in a module was just 48.5% of the total area of a PV module. It was based on the cost of sacrificing the efficiency of PV module to ensure partial light transmission.

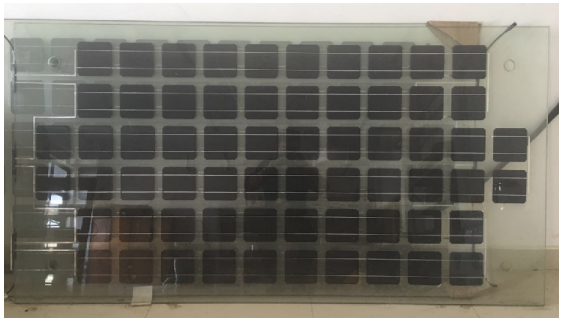

**Fig.4.** The semi-transparent double glazing PV module

**Fig.5.** The inside view of the PV curtain wall

The laminated glasses forms were installed on both west and east directions and on the rooftops of the PV curtain wall. Meanwhile, there was a space of 6 m between the building facade and PV curtain wall (Fig.5). Some ventilation blinds were placed at the top and the bottom of the PV curtain wall for a proper ventilation (Fig.6). The windows of many rooms from 5th-floor to ground floor were covered by the PV curtain wall. Therefore, the rooms' temperature would be affected around the year. However, the room temperature will be controlled or affected according to the adjustment of these ventilation blinds by opening or closing it in different seasons. As schematically shown, the BIPV system considered in the present study consisted of a PV curtain wall which was separated by air space from the building facade. Once the PV curtain wall heated by the solar radiation, the air within the space rises due to buoyancy, thus allowing ambient air to flow through the space via chimney effect. No mechanical ventilation for the air gap between the PV panels and building external envelope surface was provided. Thus only natural convective flow and heat transfer in the space were considered in the present study.

**Fig.6.** The ventilation blinds at the top and bottom of the PV curtain wall

"T" type (copper-constantan) thermocouples with accuracy of ±0.3℃ were installed to measure temperatures at different floors and rooms. Two rooms with window facing the south were chosen on each floor from the 1st floor to the 5th floor, one room with window covered by the PV curtain wall and the other room with window not covered, which was regarded as the reference room. Each room had the similar characteristics and same dimensions (10.2m long, 8.4 m wide and 3.5m high). The room temperature had not been influenced by any HVAC (Heating, Ventilating and Air Conditioning) system during the measurements. The indoor and outdoor temperature of each floor also was tested. The arrangement of test points is shown in Fig.7. Each floor had three tested rooms, the points 2B-5B were the average temperature of each floor. Each temperature test points were about 2m high of the ground and at the centre of each tested room, which has window towards to the PV curtain wall, and the air between PV curtain wall and building exterior wall can enter each tested room through window. Similarly, the point 1A-5A were the average temperature of each floor and these test points were about 2 m apart from the exterior wall of the building, each floor had three test points and each one was 15 meters apart. Two pyranometers were used to measure the solar irradiance on the surface of the PV curtain wall and through the curtain wall, respectively. These data were recorded by Agilent 34970A data acquisition instrument every 10 minutes automatically. The comparative tests were carried out from June 5th to July 11st, 2015 for summer and from October 3rd to October 29th, 2015 for winter.

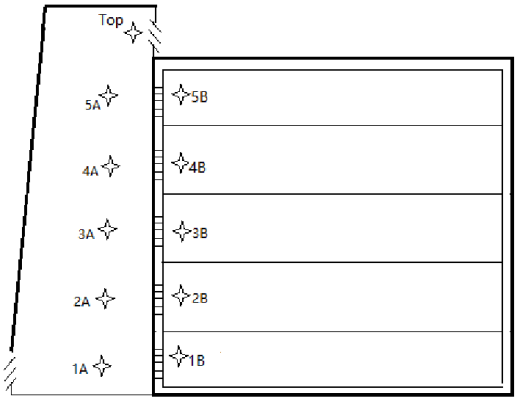


**Fig.7.** The measure spots

## RESULTS AND DISCUSSION

Results showed that the average daily sunshine duration was 10h in winter and 13h in summer during the test periods. The average daily solar radiation intensity was 0.55kW/m$^2$ and 0.19 kW/m$^2$ on the vertical surface of the PV curtain wall and through the curtain wall during October 3rd to 29th, respectively. However, during June 5th to July 11st, the average daily solar radiation intensity on the vertical surface of the PV curtain wall and through the curtain wall was 0.23kW/m$^2$ and 0.09 kW/m$^2$, respectively as shown in Fig.8. The reason why the total solar radiation on June is less than October is that the solar zenith angel is lower in winter than summer in Kunming, which means that the vertical south surface of the PV curtain wall can receive more solar radiation on October. Furthermore, the solar radiation intensity though the PV curtain wall is around 40% of what it is before though the PV curtain wall. Maybe due to closing to the curtain wall, the pyranometer which was used to measure the solar radiation intensity through the curtain wall could be shield by some solar cells or columns of curtain wall sometimes with the sun moving during the test periods. However, the solar energy received by the building through the PV curtain wall was 40%~47%, it could be considered to reduce the heat load in summer.

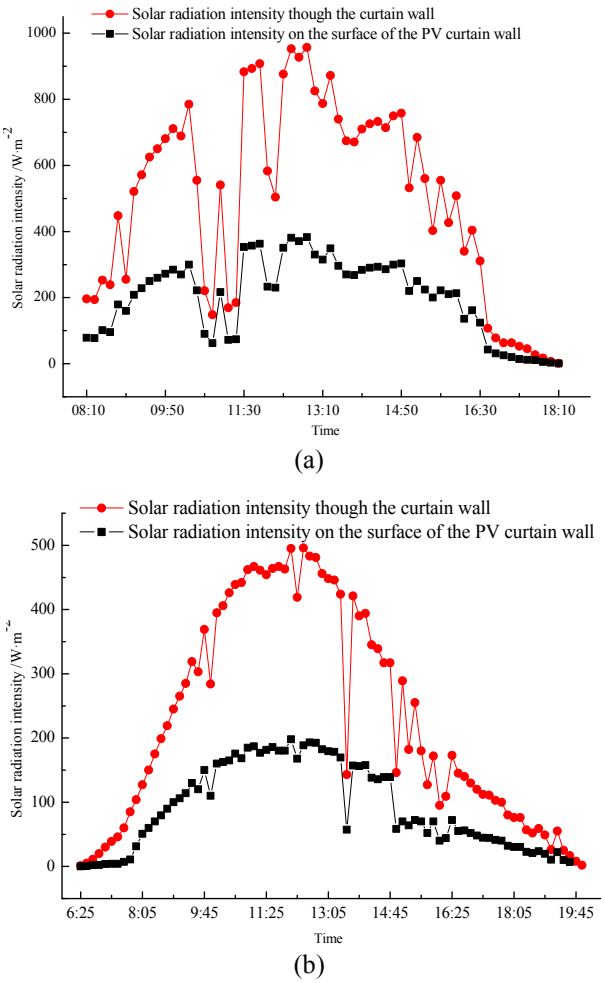


**Fig.8.** Solar radiation intensity on the vertical surface of the PV curtain wall and though the curtain wall (The (a) is a winter's data and the (b) is a summer's data)

The variation of the air average temperature in the gap (ATIG) between PV curtain wall and building exterior wall has been tested from October 3rd to October 29th, and then one day has been chosen as shown in Fig.9 to discuss the results. The trend of the ATIG was consistent with the ambient temperature that was the temperature of outside of the PV curtain wall, but the ambient temperature was the lowest. The temperature of each floor or each test spot has been clearly fluctuated, due to the ventilation blinds on top and bottom were opened during the test periods. Consequently, the internal temperatures were significantly influenced by wind speed. The air naturally moved into the gap between the PV curtain wall and building exterior wall through the bottom ventilation blinds. The wind speeds at the bottom and top ventilation blinds were 1.15m/s~1.58m/s and 0.21m/s~0.28m/s, respectively, tested by OMEGA's HHF91 digital anemometer with a velocity accuracy of 2%. However, it was clear that the ATIG increased from 1st floor to the top floor gradually. It was observed that the highest temperature of ATIG was around 32℃ on the top close to the outlet of top ventilation blinds. Meanwhile, the air temperature on the top was about 10℃ higher than on the 1st floor and the 2nd floor at noon. The 1A and 2A had a very small temperature difference all the day, because these test spots of 1st and 2nd floors in the gap were closer to the bottom ventilation blinds, thereby they became more sensitive to the environment at a better air fluidity.

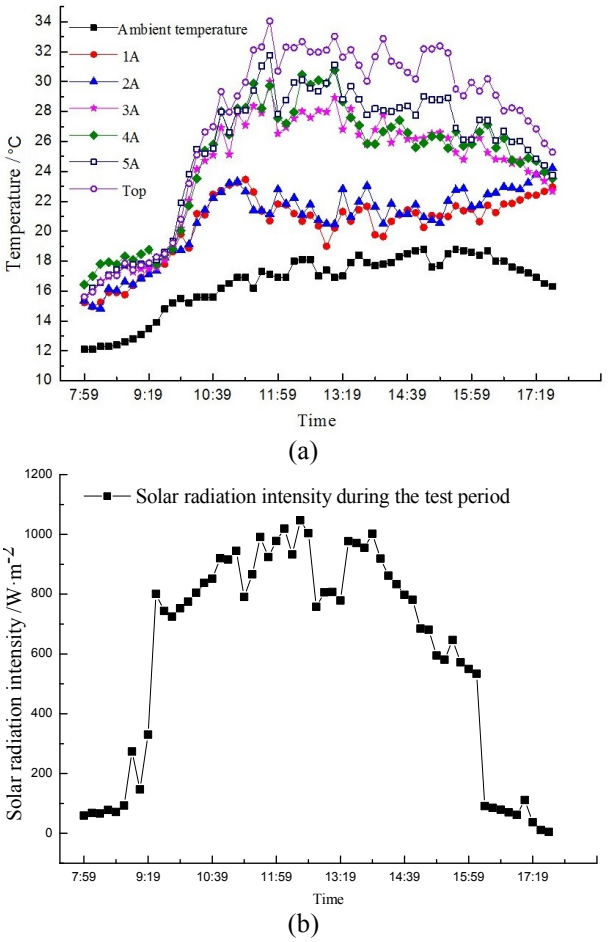


**Fig.9.** (a) The air temperature in the gap between PV curtain wall and the building exterior wall and (b) the solar radiation intensity on the surface of the PV curtain wall during the test period

Fig.9 shows the variations of internal and external air temperature on October. It was found that the ATIG at 7:59 in the morning of winter was about 4℃ higher than the ambient temperature, while in the afternoon, the ATIG was about 9℃ higher. Therefore, the ATIG increased rapidly from 9:29 then about 2 hours later, the ATIG reached the maximum temperature and no longer increased. The gradual increasing of solar radiation on the PV curtain wall from 330W/m$^2$ to 800 W/m$^2$ resulted in

a gradual increasing of air temperatures. Subsequently, the ATIG started to decrease at 15:59 and the average of 1A~Top temperature eventually reached around 22℃ which was 6℃ higher than ambient temperatures as shown in Fig.9(a).

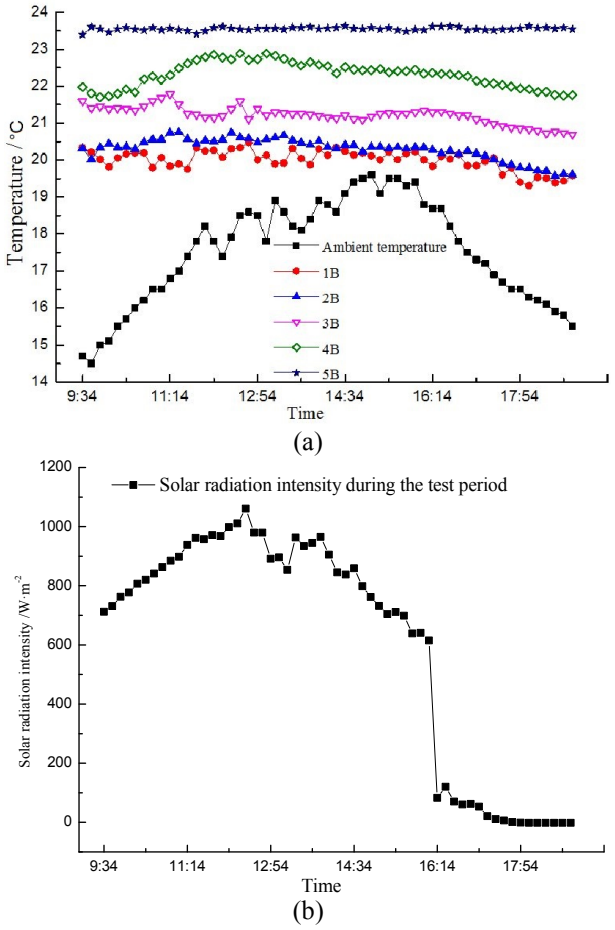


**Fig.10.** (a) The temperature of each tested room and (b) the solar radiation intensity on the surface of the PV curtain wall during the test period

Fig.10 shows the indoor temperature 1B to 5B and ambient temperature, which are the corresponding data of the same day as shown in Fig.9. It was found that the ambient temperature presented a first increases and then decreases trend while, the indoor average temperature of tested room from 1B to 5B remained stable at the beginning and then increased from 1st floor to 5th floor gradually. The test periods were during working hours and the 1B was the average temperature of the tested room, which was an office and some people worked in it, thereby the temperature was clearly fluctuated. Nevertheless, the internal air temperature at 1B (around 20℃) was the lowest indoor temperature of all the tested rooms. It was still higher than the ambient temperature all the time. In addition, there was a little difference in the average temperature at 1B and 2B comparing to the outdoor temperatures. The indoor temperature at 5B was the highest temperature (around 23.5℃) and it was higher than the 4B by 1℃. Consequently, it can be observed from Fig.10 that the indoor temperature at the upper floors was higher than the lower floors by 1℃, due to the chimney effect of the PV curtain wall, when the hot air density is lower than the cold air density so the hot air moves to the upper area and creates the temperature differences in different floors. These results will be helpful to keep the upper rooms warm without any heating facilities in winter.

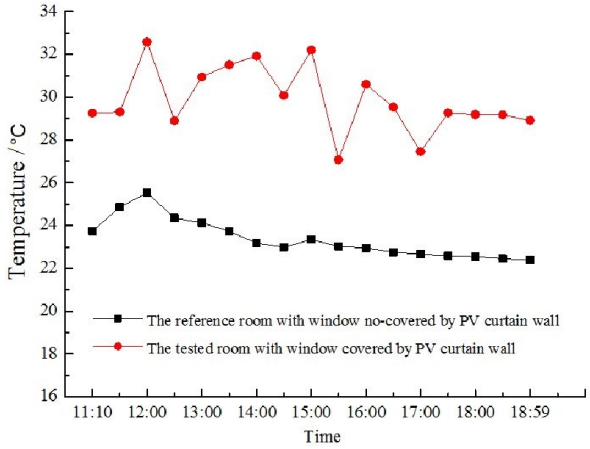


**Fig.11.** The temperature of test room and reference room

Fig.11 shows the indoor temperatures of the tested room and the reference room on the 4th floor from 11:00 to 19:00 on a sunny day, June 7th. During the comparative period, it can be clearly seen that the indoor temperature of the reference room was stable while the indoor temperature of the tested room was fluctuated and higher than the reference room by 6°C in average for most of the time. The strong fluctuations of the tested room temperature were caused by the doors opened or closed during the test periods which were the working hours. Thus, it was inevitable that there were some people working in the tested rooms and the reference rooms, admittedly, the doors were opened or closed for getting in or out of these rooms. However, the average ambient temperature was lower than the indoor temperature at 23℃. The average, maximum and minimum temperatures of the tested room was 29.8℃, 32.5℃ and 27.0℃ respectively. However, the average, the maximum and minimum temperatures of the reference room was 23.3℃, 25.7℃ and 22.2℃, respectively. Obviously, the greenhouse effect of PV curtain wall

caused overheats in summer by increasing the indoor temperatures. Therefore, the ventilation blinds on top and bottom of PV curtain wall were opened to decrease the internal air temperatures.

## CONCLUSIONS

This experiment was conducted to study the thermal environment of building and sunlight penetration in terms of the variation of air temperature in different seasons. Results revealed that the indoor thermal environment was comfortable and helpful to save energy for keeping the rooms warm in the winter season. The temperature of the tested rooms was varied from 20 ℃ to 24℃ according to different floors, and it was 6℃ higher than the ambient temperature in winter all the day. The solar radiation in the south side of the building which was shaded by the PV curtain wall has been measured and ranged from 40%~47% of the outside solar radiation on the PV curtain wall. Nevertheless, the ventilation blinds have been arranged on the top and the bottom of the PV curtain wall and were opened in summer, the phenomenon of overheat in the rooms with window covered by curtain wall was still inevitable. In conclusion, the proper design of the large PV curtain wall could be a good choice to save energy for decreasing the cooling and heating load of building.

## ACKNOWLEDGEMENTS

This work was supported by grants from Yunnan Province Science Foundation for Youths (2014FD015) and the China Postdoctoral Science Foundation (No. 2014M562349).

## REFERENCES

1 I. E. A. (IEA). World Energy Outlook 2013, http://www.worldenergyoutlook.org/publications/weo-2013/).
2 K.-S. Chen, J.-F. Salinas, H.-L. Yip, L. Huo, J. Hou and A. K. Y. Jen, *Energy & Environmental Science*, 2012, 5, 9551.
3 X. Kong, S. Lu, P. Gao, N. Zhu, W. Wu and X. Cao, *Energy and Buildings*, 2012, 48, 155-167.
4 S. Kadoshin, T. Nishiyama and T. Ito, *Applied Energy*, 2000, 67, 407-417.
5 L. Aelenei, R. Pereira, A. Ferreira, H. Gonçalves and A. Joyce, *Energy Procedia*, 2014, 58, 172-178.
6 N. Skandalos and D. Karamanis, *Renewable and Sustainable Energy Reviews*, 2015, 49, 306-322.
7 P. Hernandez and P. Kenny, *Energy and Buildings*, 2010, 42, 815-821.
8 B. Norton, P. C. Eames, T. K. Mallick, M. J. Huang, S. J. McCormack, J. D. Mondol and Y. G. Yohanis, *Sol Energy*, 2011, 85, 1629-1664.
9 G. N. Tiwari, H. Saini, A. Tiwari, A. Deo, N. Gupta and P. S. Saini, *Sol Energy*, 2016, 125, 373-380.
10 G. H. Lin and D. E. Carlson, *International Journal of Hydrogen Energy*, 2000, 25, 807-811.
11 D. H. W. Li, T. N. T. Lam, W. W. H. Chan and A. H. L. Mak, *Appl Energy*, 2009, 86, 722-729.
12 H. Radhi, *Sol Energy*, 2010, 84, 2009-2021.
13 P. A. B. James, M. F. Jentsch and A. S. Bahaj, *Sol Energy*, 2009, 83, 220-231.
14 J. Peng, L. Lu, H. Yang and T. Ma, *Appl Energy*, 2015, 138, 572-583.
15 R. Eke and A. Senturk, *Applied Energy*, 2013, 109, 154-162.
16 S. Wittkopf, S. Valliappan, L. Liu, K. S. Ang and S. C. J. Cheng, *Renewable Energy*, 2012, 47, 9-20.
17 S. Kang, T. Hwang and J. T. Kim, *Energy and Buildings*, 2012, 46, 86-91.
18 H. Manz and U.-P. Menti, *Renewable Energy*, 2012, 37, 226-232.

*Bulgarian Chemical Communications, Volume 48, Special Issue E (pp. 165 - 172) 2016*

# Performance analysis of ice storage air conditioning system driven by distributed photovoltaic energy

Y. F. Xu[1,2], M. Li[1,*], X. Luo[1], Y. F. Wang[1], Q. F. Yu[1], R. H. E. Hassaniem[1,3]

[1] *Solar Energy research Institute, Yunnan Normal University, Kunming, Yunnan 650500, China*
[2]*Zhejiang Solar Energy Product Quality Inspection Center, Haining, Zhejiang 314416, China*
[3]*Agricultural Engineering Department, Faculty of Agriculture, Cairo University, Cairo 12613, Egypt*

In this paper, an ice storage air conditioning system (ISACS) driven by distributed photovoltaic energy system (DPES) was proposed. Furthermore, the system structure optimization analysis was also investigated. The energy coupling and transferring characteristics in light-electricity-cold conversion process were analysed by the theoretical calculations and experimental tests. Results revealed that the system energy utilization efficiency and exergy efficiency were 4.64% and 43.91%, respectively. The energy losses were high in photo-electric conversion process and the ice making process of ice slide machine. Therefore, the immersed evaporator and co-integrated exchanger were adopted and the ice making efficiency and solar energy utilization ratio were improved with the increasing of the system energy efficiency.

**Keywords*:*** photovoltaic, ice storage, energy, exergy, structure optimization

## INTRODUCTION

With the dramatic climate changes, the cooling demand has been increased and led to a rapid growth of energy consumption, which causes traditional fossil fuel energy shortage and great damage to climate and environment with the emissions of $CO_2$ and harmful particles by extensive use of traditional fossil energy. Furthermore, using the electric air conditioning increases the electrical pressure in the peak time and increases the tense situation between power supply and demands. Therefore, refrigeration driven by solar energy becomes one of the promising approaches to reduce or partially replace the conventional refrigeration systems. There are two main working modes of solar refrigeration namely, solar thermal refrigeration and solar photovoltaic refrigeration [1, 2]. Several studies have been conducted about different solar refrigeration options in the last years for the improvement and development of solar thermal refrigeration system such as operation efficiency and operating stability [3-11]. Solar photovoltaic (PV) refrigeration has more advantages on refrigerating effect, stable operation and energy utilization rate compared to solar thermal refrigeration. The cost of PV module decreased by 75% from 2009 to 2014 all over the world and the cost of average electricity of large-scale photovoltaic power plant has been cut in half from 0.30 dollar/kWh in 2010 down to 0.15 dollar/ kWh in 2014; furthermore the reduction was more than 60% for distributed photovoltaic power plant. At the same time, the photoelectric conversion efficiency of PV module increased year by year and the efficiencies of poly-silicon PV module and single crystal silicon PV module were improved to 18.7% and 20.4% in 2015, respectively. Household refrigeration system, driven by distributed photovoltaic energy system (DPES), has been developed rapidly with PV investment by decreasing its operation cost and improving the conversion efficiency of PV module.

Axaopoulos et al. [12] designed a PV Ice-maker without battery and studied its performance when the compressor operating efficiency was 9.2%, they found that this prototype have a good ice-making capability and reliable operation as well as a great improvement in the start up characteristics of the compressors, which remain working even during days with low solar irradiation of 150 $W/m^2$. It was also reported that the required photovoltaic panel area of a solar electric-vapor compression refrigeration system increases as the evaporating temperature decreases and the coefficient of performance variation of the cooling system decreases with the decreasing of evaporating temperature [13]. Ekren et al. [14] studied the photovoltaic DC refrigerator system and found that PV module conversion efficiency has a greater impact on the system exergy efficiency. Aktacir [15] designed a multifunctional PV refrigerator and found that when indoor and outdoor average temperatures were 26.3 ºC and 24.9 ºC, the minimum temperature of the

* To whom all correspondence should be sent:
lmllldy@126.com

10.6 ℃. Mba et al. [16] used MATLAB software to simulate PV refrigeration system operating process and analysis system operating characteristics in different conditions. Furthermore, Tina et al.[17] designed a software for monitoring and managing stand-alone PV refrigerator system in a remote area, which had a real-time monitor running status and automatically recorded data feeding back to the terminal equipment. In addition, Kaplanis et al.[18] improved the performance of a traditional refrigerator which driven by PV. The energy conversion, management and operation performance for PV refrigerator system powered on three conditions such as, photovoltaic components, battery and outage showed that the system COP gradually decreases from morning till night [19]. The American SOLUS Refrigeration Company has developed a photovoltaic DC refrigerator substituting battery with water-propylene/ethylene glycol phase change material to store cold and reduce the system investing and running cost. Results revealed that the temperature inside the refrigerator was remaining stable at around 1.4 ℃ when the environment temperature was 32 ℃. Recently, the PV refrigeration system has been improved and developed in the aspects of product structure, operating efficiency and refrigeration performance. According to comprehensive analysis, PV refrigeration system research is currently mainly concentrated on ice maker driven by PV. Batteries are essential component to store energy and to solve the intermittent of solar energy in PV refrigeration system. However, batteries increase the investing and running costs and reduce the system energy conversion and utilization ratios. Thus, ice storage technology has attracted researcher's attention. Ice storage technology has a great role on saving building energy, transfer peak power to off-peak, improve grid load rate and others aspects. It is clear that in the tropical regions, such as Xishuang banna in China and Bangkok in Thailand, have almost 300 days for cooling demand thereby, ice storage has a good application prospect in those regions.

Thus, ice storage air conditioning system (ISACS) driven by distributed photovoltaic energy system (DPES) was established based on our previous research results [20]. A few batteries were used in order to provide the stability for system operation. At first, a theoretical model has been established and experimental work has been implemented to analyze the energy coupling and transferring characteristics in light-electricity-cold conversion process. And then, the system structure optimization analysis was also investigated for a higher energy utilization efficiency and better financial rewards.

## MATERIALS AND METHODS

### *Configuration of ISACS driven by DPES*

The ice storage air conditioning system (ISACS) of 0.2 kW driven by distributed photovoltaic energy system (DPES) was mainly configured by DPES, ice maker, cold storage system and air conditioning system. The pictures of ISACS driven by DPES are shown in Fig.1.

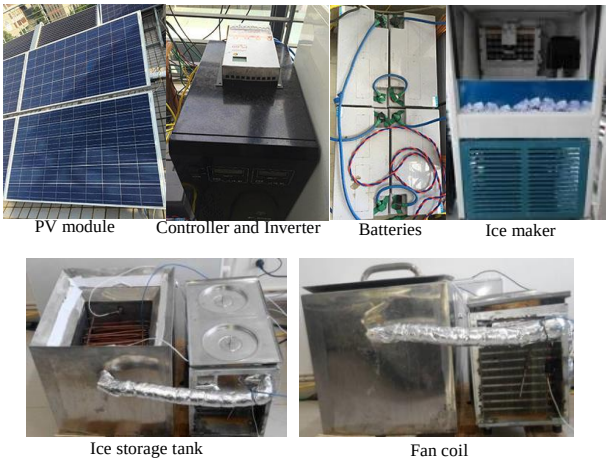


**Fig.1.** Pictures of a 0.2 kW ISACS driven by DPES

PV modules converts solar energy into electric energy which can be regulated by controller with maximum power point tracking (MPPT) to drive ice maker, ice storage system and air conditioning system. The MPPT device adopted in the controller is mainly composed of single chip microcomputer and photovoltaic power control unit and there were PWM driver, the empirical formula calculation unit, boots circuit and many other components in PV power control unit contains. The algorithm of MPPT control device, combined with the engineering mathematical model of PV modules and the two interpolation method, was employed to achieve maximum power point tracking. In daytime, DPES receives solar energy and turns it into direct-current (DC) electric power which can be converted to alternating current (AC) electric power by inverter to drive AC compressor, water pump, ethylene glycol pump and fan coil. In order to maintain the stability of electric energy supply, a few batteries were adopted and connected with controller to maintain the energy conversion and supply in the most optimized way. Ice maker and storage system was made up with AC compressor, condenser, expansion valve, disc evaporator and

ice storage tank. Circulating water can be frozen in the disc evaporator and then the ice droop into ice storage tank. Thereby, the ice maker worked as vapour compression refrigeration. In the AC compressor, the cryogenic R134a was compressed at a high temperature and high pressure gas to be filtered in gas-liquid separator and to release heat in condenser. Refrigerant was condensed to mild temperature and high pressure gas. When the gas inflows into throttle valve, it can be throttled to low temperature and low pressure liquid then feeds into plat evaporator. Subsequently, flows out of the evaporator, the refrigerant flows into the other gas-liquid separator to be sucked into the compressor. Finally, the refrigeration cycle will be completed. Air conditioning system was mainly made up of coil heat exchanger which was fixed in ice storage tank, Ethylene glycol pump, solenoid valve, proportional control valve and fan coil. Ethylene glycol was employed as a cold exchanging medium. All connecting pipes were wrapped with rubber insulation material and the ice storage tank was covered with polyurethane foam insulation.

The main components and parameters of ISACS driven by DPES are shown in Table 1.

**Table 1.** Main components and parameters of ISACS driven by DPES

| Components | Parameters |
|---|---|
| PV module | $P_m$: 245 W, $V_m$: 34.5 V, $I_m$: 7.10 A, $V_{OC}$: 43.5 V, $I_{SC}$: 8.18 A, module: length*wide: 1640 mm*990 mm, cells in series: length*wide*numbers: 155 mm*155 mm*60. |
| Controller | 12-48 V 60 A charge，30 A load |
| Inverter | $P$: 3 kW, DC input voltage: 48 V, output voltage: 220 V, output frequency: 50 Hz. |
| Batteries | Battery capacity: 12 V65 Ah, four batteries in series |
| Refrigerant | Molecular formula: $CH_2FCF_3$, boiling point: -26.1 ℃, critical temperature: 101.1 ℃. |
| Ice maker | Ice production: 2.08 kg/h, $P$: 380 W. |
| Ice storage tank | Capacity: 20 cm*20 cm*20 cm |
| Cold exchanging medium | Melting point: -12.6 ℃, viscosity: 25.66 mPa s. |
| Pump | Power: 46-93 W, life: 6 m, maximum flow rate: 3.4 $m^3$/h. |
| Fan coil | Fan type: YS 56-2, power: 180 W, voltage: 380 V, Current: 0.53 A, speed: 2800 r/min, number of fins: 95, size: 23 cm*8 cm*20 cm, coil numbers: 26, Coil inner diameter: 6 mm. |

DPES were made up of two 245 $W_p$ polycrystalline silicon PV modules in series and four valve controlled sealed maintenance free lead-acid batteries in series were used to maintain the stability of system operation. Refrigerant (R134a) temperature and pressure were measured by T-type thermocouples and pressure transducers, respectively. Voltages and currents of PV modules were measured by a digital multimeter. The wind speed was measured by the wind speed transducer. Solar irradiation was measured by pyranometer. The compressor input power was measured by a wattmeter. Electromagnetic flow meter was used to measure refrigerant flow and cold exchanging medium flow. The parameters of all instruments are shown in Table 2.

**Table 2.** The instruments parameters

| Instrument | Parameters and accuracy |
|---|---|
| Digital multimeter | FLUKE F-179, DC voltage measurement accuracy: ±0.9%+2, DC current value measurement accuracy: ±1%+3. |
| Thermocouples | Type: T, range: -200 to 350 ℃, accuracy: ±0.4% of full scale |
| Wind speed transducer | EC-9S, range: 0-70 m/s, accuracy: ±0.3 m/s, resolution ratio: 0.1 m/s |
| Electromagnetic flow meter | SIEMENS FUP 1010, range: -12 m/s~12 m/s, accuracy: <0.3 m/s (1 ft/s), ±0.5% ~ ±2.0%, |
| Electronic balance | AHW-3, range: 0-3 kg, accuracy: ±0.05 g |
| Pressure transducer | Range: 0-0.6 MPa low side and 0-1.8 MPa high side accuracy: ±0.25% of full scale at 25 ℃ |
| Pyranometer | Kipp & zonen CMP6, Range: 0-2000 W/$m^2$, accuracy: ±5% |
| Wattmeter | DELIXI DDS607, Type: 220 V 20 A 50 Hz 3200 imp/kW, accuracy: 0.01 kW ħ |
| Data acquisition | Agilent 34972A data acquisition unit |

### *The theoretical models of energy conversion and transfer characteristics of ISACS driven by DPES*

The theoretical model was established to analyze the energy conversion and transfer characteristics of ISACS driven by DPES as follow.

(1) Theoretical models of DPES

Transient energy balance equation of PV modules is expressed as:

$$Q_{pv,in} = S_P m C_P \frac{dT_P}{dt} + Q_{pv,rad} + Q_{pv,conv} + Q_{pv,elect} \quad (1)$$

The solar energy which absorbed by PV modules can be estimated as：

$$Q_{pv,in} = \alpha\tau G S_p \tag{2}$$

Radiation heat loss can be given by:

$$Q_{pv,rad} = S_p F_{ps} \sigma\left(\varepsilon_p T_p^4 - \varepsilon_s T_s^4\right) \tag{3}$$

$T_s$ is the sky temperature (K), which is 0.914 times of ambient temperature suggested by [21].

Convective heat loss can be estimated as the following:

$$Q_{pv,conv} = S_p H\left(T_p - T_a\right) \tag{4}$$

$$H = 1.2475\left[\left(T_p - T_a\right)\cos\beta\right]^{1/3} + 2.686v \tag{5}$$

Exergy used to describe energy quality and it is the energy which can be converted to usable power. Sometimes, exergy is called available energy. In the actual process, energy conversion is irreversible. Therefore, exergy loss is also inevitable.

Exergy and exergy losses of PV modules are given in Ref. [22]:

$$\begin{aligned} E_{x,out-pv} = {} & GS_p\left[1-\frac{4}{3}\frac{T_a}{T_{sun}}+\frac{1}{3}\left(\frac{T_a}{T_{sun}}\right)^4\right] - \\ & S_p\left[F_{ps}\sigma\left(\varepsilon_p T_p^4 - \varepsilon_s T_s^4\right)\right]\left(1-\frac{T_a}{T_P}\right) - \\ & S_p H\left(T_p - T_a\right)\left(1-\frac{T_a}{T_P}\right) - \left[I_{sc}V_{oc} - I_m V_m\right] \end{aligned} \tag{6}$$

$$\Delta E_{pv} = \left(Q_{pv,rad} + Q_{pv,conv}\right)\left(1-\frac{T_a}{T_P}\right) + \left[I_{sc}V_{oc} - I_m V_m\right] \tag{7}$$

The energy and exergy efficiencies of PV modules are shown:

$$\eta_{PV} = \frac{Q_{pv,elect}}{GS_p} \tag{8}$$

$$\psi_{PV} = \frac{E_{x,out-pv}}{E_{x,out-pv} + \Delta E_{pv}} \tag{9}$$

(2) Theoretical models of ISACS

(a) The compressor energy balance equation is given by:

$$\dot{m}_r h_1 + W_p = \dot{m}_r h_2 + Q_{CP,loss} \tag{10}$$

Compressor exergy model is given as:

$$\dot{m}_r\left[\left(h_1 - h_a\right) - T_a\left(s_1 - s_a\right)\right] + W_p = \dot{m}_r\left[\left(h_2 - h_a\right) - T_a\left(s_2 - s_a\right)\right] + \Delta E_{CP} \tag{11}$$

(b) The condenser energy balance equation is shown as:

$$Q_{CP,out} = \dot{m}_r h_4 + Q_a \tag{12}$$

The condenser exergy model is expressed as:

$$\dot{m}_r\left[\left(h_3 - h_a\right) - T_a\left(s_3 - s_a\right)\right] = \dot{m}_r\left[\left(h_4 - h_a\right) - T_a\left(s_4 - s_a\right)\right] + \Delta E_{CO} \tag{13}$$

(c) It is isenthalpic throttling processes to refrigerant in throttle valve, so:

$$Q_{CO,out} = Q_{TH,out} \tag{14}$$

Throttle valve exergy model is given by:

$$E_{x,out-CO} = \dot{m}_r\left[\left(h_5 - h_a\right) - T_a\left(s_5 - s_a\right)\right] + \Delta E_{TH} \tag{15}$$

(d) Evaporator energy balance equation is shown as:

$$Q_{TH,out} + Q_{AB} = Q_{CP,in} \tag{16}$$

$Q_{AB}$ is evaporator absorption heat from water (W). Evaporator exergy model is given by:

$$\dot{m}_r\left[\left(h_5 - h_a\right) - T_a\left(s_5 - s_a\right)\right] = \dot{m}_r\left[\left(h_1 - h_a\right) - T_a\left(s_1 - s_a\right)\right] + E_{x,in-IC} + \Delta E_{EV} \tag{17}$$

The energy and exergy efficiencies of ice maker can be found as:

$$\eta_{icema} = \frac{m_{ic}\Delta h}{W_P \bullet t_{CP}} \tag{18}$$

$$\psi_{icema} = \frac{E_{x,in-IC}}{E_{x,out-pv}} \tag{19}$$

(e) Energy balance equations of air conditioning are written as:

$$m_{ic}\Delta h = C_{air} m_{air} \Delta T_{indoor} + Q_{indoor,loss} \tag{20}$$

In thermal transfer process of ice storage conditioning, the exergy calculation is shown as:

$$E = -UA\left[T - T_{ID} - T_{ID}\ln\frac{T}{T_{ID}}\right] \tag{21}$$

The energy and exergy efficiencies of air conditioner can be found as:

$$\eta_{aircon} = \frac{C_{air}\dot{m}_{air}\Delta T_{indoor} \bullet t_{aircon}}{m_{ic}\Delta h} \tag{22}$$

$$\psi_{aircon} = \frac{E_{x,air}}{E_{x,in-IC}} \tag{23}$$

The system energy and exergy efficiencies are written as:

$$\eta = \eta_{PV} \bullet \eta_{icema} \bullet \eta_{aircon} \tag{24}$$

$$\psi = \psi_{PV} \bullet \psi_{icema} \bullet \psi_{aircon} \tag{25}$$

## EXPERIMENT AND CALCULATION

The ISACS of 0.2kW driven by DPES was tested on 22th of October, in Kunming city and the irradiation $q$ was 22.17 MJ/m$^2$ from 8:00 to 16:00. The time of ice maker operation cycle was 10 min and the ice production was about 0.35 kg every cycle. The ice making efficiency was 2.08 kg/h. The ice production is shown in Fig.2.

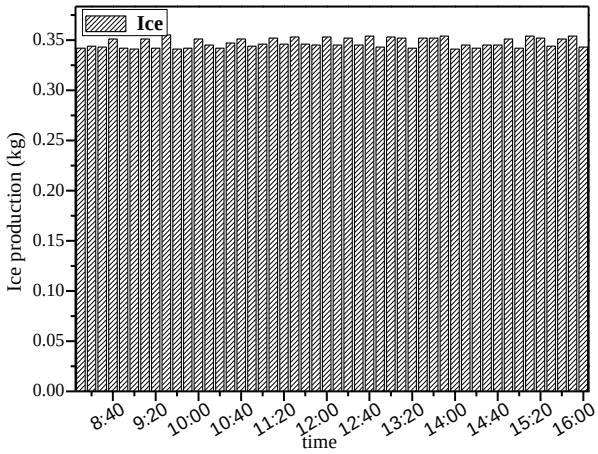


**Fig.2.** Ice production of ice maker

Results showed that the total amount of ice was 16.67 kg. The ice storage tank was a cube and the inside dimensions were 20 cm × 20 cm × 20 cm therefore, the volume was 0.008m$^3$. Results revealed that the ice storage tank can supply cold for 4 hours and the changes of temperature for exchanging cold and supplying cold processes are shown in Fig.3.

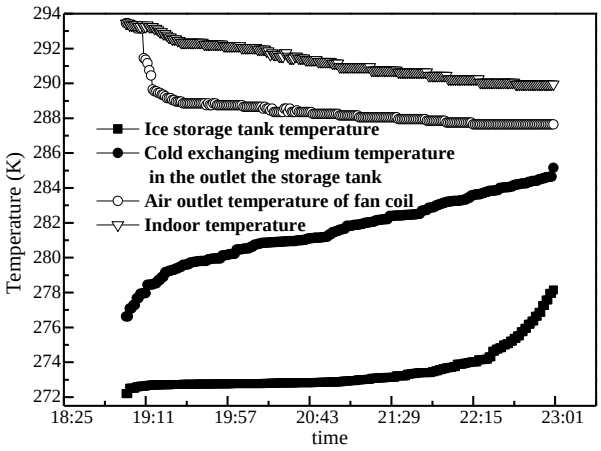


**Fig.3.** Temperatures change of exchanging cold and supplying cold process

The temperatures of ice maker with every component in thermodynamic cycle of ice making process have been tested in the experiment, as shown in Fig.4.

The average energy efficiency and exergy efficiencies of ISACS driven by DPES are shown in Table 3 and the related calculation parameters are shown in Table 4.

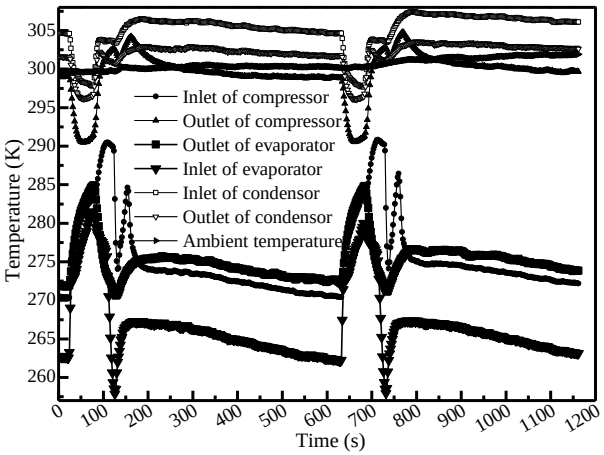


**Fig.4.** Temperature variations of ice maker components in thermodynamic cycle process

**Table 3.** Average energy and exergy efficiencies

| $\eta_{PV}$ /% | $\psi_{PV}$ /% | $\eta_{icema}$ /% | $\psi_{icema}$ /% | $\eta_{aircon}$ /% | $\psi_{aircon}$ /% | $\eta$ /% | $\Psi$ /% |
|---|---|---|---|---|---|---|---|
| 13.30 | 58.84 | 51.31 | 75.02 | 68.00 | 99.99 | 4.64 | 43.91 |

**Table 4** Related calculation parameters

| Parameters | Value | Parameters | Value |
|---|---|---|---|
| Outside (08:00-16:00) | | Condenser | |
| $T_{sun}$/K | 5778 | $P_{out}$/kPa | 700.00 |
| $T_a$/K | 293.71 -298.46 | $h_4$/(kJ kg$^{-1}$) | 241.80 |
| $v$/(m s$^{-1}$) | 0.78-2.52 | $s_3$/(kJ kg$^{-1}$ K$^{-1}$) | 1.7500 |
| $q$/(MJ m$^{-2}$) | 22.17 | $s_4$/(kJ kg$^{-1}$ K$^{-1}$) | 1.1437 |
| PV modules | | Throttle valve | |
| $Q$/(kW h) | 2.76 | $T_{in}$/K | 303.15 |
| $S_p$/m$^2$ | 2.88 | $T_{out}$/K | 263.15 |
| $S_c$/m$^2$ | 3.24 | $P_{in}$/kPa | 700.00 |
| $V_{OC}$/V | 89.35 | $P_{out}$/kPa | 200.00 |
| $I_{SC}$/A | 8.18 | $h_4$/(kJ kg$^{-1}$) | 241.80 |
| $\eta_0$/% | 17.50 | $h_5$/(kJ kg$^{-1}$) | 395.01 |
| $\alpha$ | 0.92 | $s_4$/(kJ kg$^{-1}$ K$^{-1}$) | 1.1437 |
| $\tau$ | 0.90 | $s_5$/(kJ kg$^{-1}$ K$^{-1}$) | 1.7276 |
| $m$/(kg m$^{-2}$) | 23 | Evaporator | |
| $T_P$/K | 293.71 -323.15 | $T_{in}$/K | 263.15 |
| $C_p$/(J kg$^{-1}$ K$^{-1}$) | 1179.06 | $T_{out}$/K | 268.15 |
| Compressor | | $P_{in}$/kPa | 200.00 |
| $\dot{m}$ /(kg s$^{-1}$) | 0.0127 | $P_{out}$/kPa | 243.71 |
| $W_p$/W | 380 | $h_5$/(kJ kg$^{-1}$) | 241.80 |
| $T_{in}$/K | 268.15 | $h_1$/(kJ kg$^{-1}$) | 395.01 |
| $T_{out}$/K | 313.15 | $s_5$/(kJ kg$^{-1}$ K$^{-1}$) | 1.1500 |
| $P_{in}$/kPa | 243.71 | $s_1$/(kJ kg$^{-1}$ K$^{-1}$) | 1.7276 |
| $P_{out}$/kPa | 770.21 | Air conditioning | |
| $h_1$/(kJ kg$^{-1}$) | 395.01 | $T_{EV}$/K | 263.15 |
| $h_2$/(kJ kg$^{-1}$) | 425.00 | $T_{IC}$/K | 268.15 |
| $s_1$/(kJ kg$^{-1}$ K$^{-1}$) | 1.7276 | $T_{CEC}$/K | 278.15 |
| $s_2$/(kJ kg$^{-1}$ K$^{-1}$) | 1.7500 | $T_{FC}$/K | 281.15 |
| Condenser | | $T_{ID}$/K | 293.65 |
| $T_{in}$/K | 313.15 | $\Delta T_{indoor}$/K | 0-2 |
| $T_{out}$/K | 303.15 | $UA$(W K$^{-1}$) | 22.738 |
| $P_{in}$/kPa | 700.00 | $C_{air}$/(kJ kg$^{-1}$ K$^{-1}$) | 1 |
| $h_3$/(kJ kg$^{-1}$) | 425.00 | $\dot{m}_{air}$ /( kg s$^{-1}$) | 0.12 |

## RESULTS AND DISCUSSION

From the calculation results, it was found that system energy efficiency was only 4.64% at most of energy losses in ice making process. In the ice making process, ice pasted well together with a five solid walls of grid plate evaporator and cannot be separated off by ice gravity. Thus, the compressor must be shut down and a special solenoid valve must be opened which used for adjust refrigerant flow and introduced the high temperature and high pressure refrigerant steam expelled from compressor into evaporator. And then, the evaporator plays the role of condenser to release the evaporator plays the role of condenser to release heat to ice through solid walls and ice interfaces begin melting. The ice temperature increased and was stripped off evaporator and fall into ice storage tank. Meanwhile, evaporator inlet and outlet temperatures increased sharply until the solenoid valve closed and the compressor was turned on and a new ice making process begins. The refrigerant flowed out of evaporator into throttle valve at a low temperature and low pressure liquid. And then, the refrigerant flow into condenser to absorb heat from outside and the condenser inlet and outlet temperatures decline sharply when the low temperature refrigerant flows into it. It was observed that the condenser outlet temperature was higher than the condenser inlet temperature because refrigerant can absorb heat from the outside of the condenser, as shown in Fig. 4. Then, the refrigerant flow into the compressor and the compressor inlet temperature increased compared to the ice making process. The temperature of refrigerant can be changed with the variation of inlet and outlet temperatures of the evaporator and condenser. The compressor stop running in ice melting abscission process and the refrigerant gas cannot be compressed in compressor. Therefore, the compressor outlet dropped sharply when the solenoid valve opens and it returns smoothly when ice making process started. Ice melting abscission process was extremely unfavourable for the system energy utilization for two reasons as the following:

a) The cold consumption was high and the ice temperature increased from 268.15K to 270.15K in ice melting abscission process;

b) The ice maker operation period was extended for 200s; furthermore, the ice melting abscission time was one third of the ice making cycle.

### *System optimization*

Therefore, in order to improve the performance of ISACS driven by DPES and promote the project commercial promotion, the structure optimization measurement of ice maker were proposed as the following:

a) Evaporator immersion static refrigeration mode was adopted to replace ice harvester refrigeration mode. Moreover, the optimized coil evaporator was immersed into water to absorb heat and then the water could be frozen on the evaporator. Thus, most of the energy could be utilized. The structure diagram is shown in Fig.5.

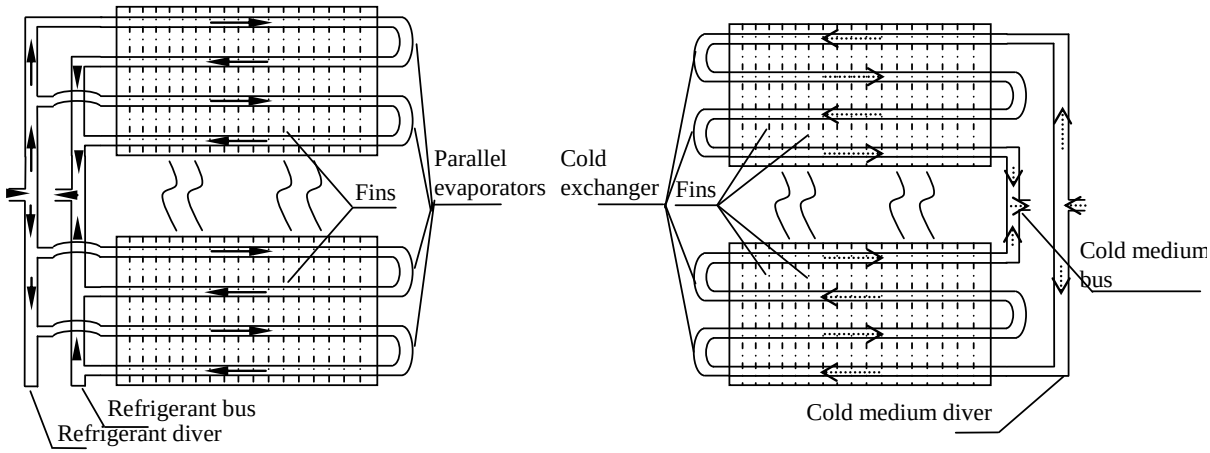


**Fig.5.** Profile of evaporators and cold exchanger immersed in the ice storage tank

b) The coil cold exchanger was co-integrated with coil evaporator. In the refrigeration process, coil cold exchanger has the priority to get cold by the transferred heat from the coil evaporator to supply cold for user and the surplus cold could be used to make ice. So, the energy could be stored in

ice. Consequently, ISACS not only has the out-of-the-box function of ordinary air conditioning, but also effectively improve the appearing phenomenon of over cooling and remedy the disadvantage of cold supply after the ice making process in the traditional submerged ice making system. The top view of co-integration evaporators and cold exchanger immersed in the ice storage tank is shown in Fig.6.

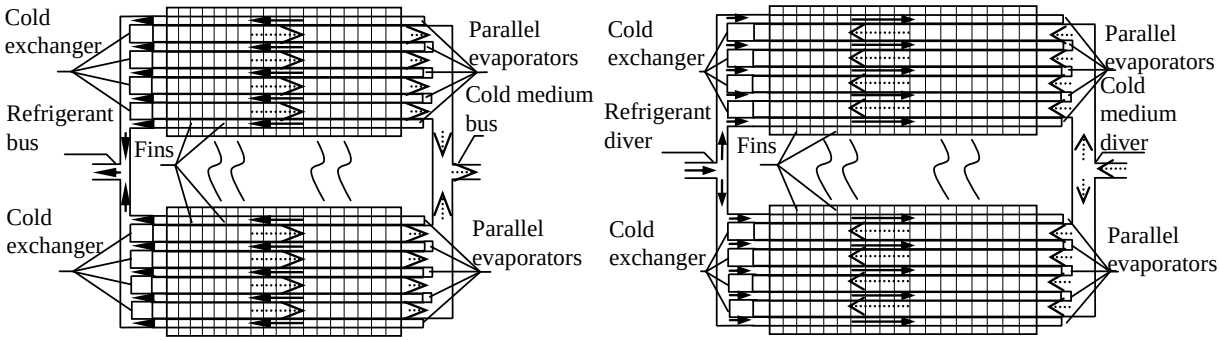


**Fig.6.** Top view of co-integration evaporators and cold exchanger immersed in the ice storage tank

The performance of optimized ISACS driven by DPES can be simulated as mentioned above. After the optimization, it was observed that the energy efficiency could be improved from 51.31% to 75.02% and the exergy efficiency could be improved from 90% to 97.45% in ice making process. The system energy efficiency increased from 4.64% to 8.14% and the system exergy efficiency increased from 43.91% to 57.33%.

## CONCLUSION

1. The energy characteristics and the simulation analysis of ISACS driven by DPES were carried out as well as the experimental platform was built to verify the theoretical model. Results showed that energy utilization ratio and exergy efficiency were 4.64% and 43.91%, respectively. The photoelectric conversion efficiency of PV modules was 13.28% at 58.83% exergy efficiency and the ice maker COP was 51.31% at 75.02% exergy efficiency. Most of the energy was consumed in the photoelectric conversing process in PV modules and refrigeration process with ice maker. It was a hard work to improve the photoelectric conversion efficiency of PV modules. So, the optimization design for the ice maker model should be carried out.

2. The evaporator immersion static refrigeration mode was adopted to replace the ice harvester refrigeration mode to achieve high efficiency refrigeration. Meanwhile, coil cold exchanger was co-integrated with coil evaporator.

3. The energy efficiency of the optimized ice maker could be increased from 51.31% to 75.02% and the exergy efficiency could be improved from 90% to 97.45%, respectively.

## ACKNOWLEDGEMENTS

The authors gratefully acknowledge the financial support provided by National International Scientific and Technological Cooperation Program (2011DFA62380). The authors are also grateful to Renewable Energy Research and Innovation Development Center in Southwest China (05300205020516009), Research and Innovation Team of Renewable Energy in Yunnan Province and Yunnan Provincial Renewable Energy Engineer Key Laboratory (2015KF05) and Yunnan Provincial Department of Education Science Research Fund Project (2015J035).

## NOMENCLATURE

| *Roman symbols* | | 1 | refrigerant in state 1 |
|---|---|---|---|
| $C$ | specific heat capacity (J kg$^{-1}$ K$^{-1}$) | 2 | refrigerant in state 2 |
| $\Delta E$ | exergy loss (W) | 3 | refrigerant in state 3 |
| $E_x$ | exergy (W) | 4 | refrigerant in state 4 |
| $F_{ps}$ | panel to sky view factor, 1 | 5 | refrigerant in state 5 |
| $G$ | solar irradiance (W m$^{-2}$) | *a* | ambient |
| $h$ | enthalpy (J kg$^{-1}$) | *air* | indoor air |
| $I$ | current (A) | *aircon* | air conditioning |
| $m$ | PV module mass per square meter (kg m$^{-2}$) | *c* | cell |
| $\dot{m}$ | mass flow (kg s$^{-1}$) | *conv* | convective |
| $Q$ | power per unit time (W) | *CP* | compressor |
| $Q_{AB}$ | evaporator absorption heat from water per unit time (W) | *CO* | condenser |
| $S$ | area(m$^2$) | *elect* | electricity |
| $s$ | entropy (J kg$^{-1}$ K$^{-1}$) | *in* | input |
| $t$ | runtime (s) | *IC* | ice |
| $T$ | temperature (K) | *ID* | indoor |
| $V$ | voltage (V) | *loss* | loss |

| | | | |
|---|---|---|---|
| $UA$ | Heat transfer resistance (W K$^{-1}$) | $m$ | maximum power point |
| $v$ | speed (m s$^{-1}$) | $oc$ | open circuit |
| $W_p$ | compressor operating power (W) | $out$ | output |
| *Greek symbols* | | $p$ | parallel |
| $\alpha$ | Solar cell absorption coefficient | $pv$ | PV modules |
| $\beta$ | PV modules tilt angle ( ) | $r$ | reference |
| $\tau$ | PV module cover glass transmittance | $rad$ | radiation |
| σ | Stephan-Boltzmann constant (5.76×10$^{-8}$ W m$^{-2}$ K$^{-4}$) | $s$ | sky |
| $\varepsilon_p$ | the average emissivity of PV modules, 0.8 | $sc$ | Short-circuit |
| $\varepsilon_s$ | average emissivity of sky, 1 | | |
| $\eta$ | average energy efficiency | $sun$ | sun |
| $\psi$ | average exergy efficiency | | |
| *Subscripts* | | $TH$ | Throttle valve |
| 0 | reverse saturation | | |

## REFERENCES


1 Allouhi A, Kousksou T, Jamil A, Bruel P, Mourad Y, Zeraouli Y, *Renew Sustain Energy Rev*, 44, 159 (2015).
2 Ghafoor A, Munir A, *Renew Sustain Energy Rev*, 43, 763, (2015).
3 Khattab NM, Sharawy H, Helmy M, *Energy Procedia*, 18, 709, (2012).
4 Attan D, Alghoul MA, Saha BB, Assadeq J, Sopian K, *Renew Sustain Energy Rev*, 15, 1708, (2011).
5 Du S, Wang RZ, Xia ZZ, *Energy*, 80, 687, (2015).
6 Pan QW, Wang RZ, Lu ZS, Wang LW, *Appl Therm Eng*, 72, 275, (2014).
7 Xu ZY, Wang RZ, *Energy*, 77, 703 (2014).
8 Du S, Wang RZ, Xia ZZ, Energy, 68, 862, (2014).
9 Jiang L, Wang LW, Wang RZ, *Int J Therm Sci*, 81, 68, (2014).
10 Ji X, Li M, Fan J, Zhang P, Luo B, Wang L, *Appl Energy*, 113, 1293, (2014).
11 Xu Ji, Xiangbo Song, Ming Li, Jiaxing Liu, Yunfeng Wang, *Energ Convers Manag*, 106, 759, (2015).
12 Axaopoulos PJ, Theodoridis MP, *Sol Energy*, 83, 1360, (2009).
13 Bilgili M, *Sol Energy*, 85, 2720, (2011).
14 Ekren O, Yilanci A, Cetin E, Ozturk HK, *IEEE Elektronika ir elektrotechnika*, 114, 7, (2011).
15 Aktacir M A, *Int J Phys Sci*, 6, 746, (2011).
16 Mba EF, Chukwuneke J L, Achebe C H, *J Info Eng App*, 2, 1, (2012).
17 Tina GM, Grasso AD, *Energ Convers Manag*, 78, 862, (2014).
18 Kaplanis S, Papanastasiou N, *Renew Energ*, 31, 771, (2006).
19 Modi A, Chaudhuri A, Vijay B, Mathur J, *Appl Energ*, 86, 2583, (2009).
20 Li Y, Zhou SH, Lin WD, Ji X, Luo X, Li M, *Acta Energ Sol Sinica*, 36, 422, (2015).
21 Rabl A, USA: *Oxford University Press* 1985.
22 Ekren O, Celik S, Noble B, Krauss R, *Int J Refig*,36,745, (2013).

*Bulgarian Chemical Communications, Volume 48, Special Issue E (pp. 173 - 177) 2016*

# The effect of non-uniform irradiation on PV cell performance in a lens-walled CPC

Yuehong Su [1, *], Hang Zhou [1], Michele Bottarelli [2], Hongbing Chen [3], Meng Tian [1], Saffa Riffat [1]

[1]*Department of Architecture and Built Environment, University of Nottingham, University Park, NG7 2RD, UK*
[2]*Department of Architecture, University of Ferrara, Via Quartieri 8, Ferrara 44121, Italy*
[3] *School of Environment and Energy Engineering, Beijing University of Civil Engineering and Architecture, Beijing 100044*

This study first describes the principle of a lens-walled CPC (compound parabolic concentrator) which compromises the advantages of common mirror CPC and solid dielectric CPC, by applying a lens shape on the surface of a common CPC. Due to the structural feature of a CPC, the irradiation on the base of a CPC is non-uniform, where a PV cell is installed for a CPC-PV application. A lens-walled CPC has a potential of producing more uniform irradiation. The profiles of irradiation are obtained with an optical simulation software Photopia for three types of CPC, i.e., mirror, solid and the proposed lens-walled CPCs. The profiles are then applied as a boundary condition in a finite element model of PV cell to evaluate the effect of non-uniform irradiation on the PV cell. The finite element model of a PV cell is validated against its specification data. The obtained IV curves and the corresponding maximum power points are compared between these three types of CPCs to check the advantage of a lens-walled CPC, for several incidence angles.

**Keywords:** lens-walled CPC, non-uniform irradiation, PV cell, finite element modelling (FEM)

## INTRODUCTION

Solar concentrators can be used to reduce the size of photovoltaics (PV) for a given area of installation. By using an inexpensive reflective sheet instead of PV cell, a low concentration PV system is promising to be about 40% cheaper than a common flat PV system [1], and fitted well with building integrated application [2]. Among the low concentration solar concentrators, the compound parabolic concentrator (CPC) is the most adopted due to its feature of stationary operation and wider acceptance angle. A lot of research efforts have been made to increase the acceptance angle of a CPC of given geometric concentration ratio, because a larger acceptance angle leads to a larger collection of solar radiation. For example, in comparison with a conventional mirror CPC, a solid dielectric CPC have larger acceptance angle for same geometric concentration ratio, but it is heavy in weight. In our previous studies [3, 4, 5], we have therefore proposed the design of a lens-walled CPC as an interesting compromise between the mirror and solid CPCs, with the aim to offer a larger acceptance angle with a lighter weight.

The incident light can be re-directed onto the base of a solar concentrator by reflection in a mirror CPC and/or refraction in a solid or lens-walled CPC. The concentrated radiation increases the energy input to a PV cell, but it can also cause certain amount of power loss due to the increased resistive loss [6]. The resistive loss is directly proportional to the non-uniformity level of light distribution profile. The non-uniform distributed light can cause a region of higher intensity and thus a higher current source farther away from the bus bar of a PV cell [7]. Vishnoi et al [8] contributed a research to investigate the combination effect of non-uniform light regarding the surface resistance of PV cell. The predication was made from theoretical and experiment evaluation shows that the non-illuminated or less illuminated regions in the PV cell are act as a load, which results a decrease in conversion efficiency and open circuit voltage. In this study, we present a numerical analysis on the optical and electrical performance of a lens-walled CPC PV cell. The non-uniformity of light distribution by a lens-walled CPC and its effect on the PV performance will be also compared with those in a mirror or solid CPCs. The light distribution will be obtained from an optical simulation, while the PV performance will be predicted using 2D numerical analysis of current continuity equation.

## NUMERICAL MODELLING OF A LENS-WALLED CPC PV CELL

### *System description*

The details about the lens-walled CPC have been presented by Su et al [3]. The shape of lens is formed by internally rotating the parabolic curves of a CPC with certain degree. The refraction of lens allows it to concentrate light from wider incident angle, as shown in Fig.1.

* To whom all correspondence should be sent:
yuehong.su@nottingham.ac.uk

The incoming light is refracted by the front surface of the lens and then reflected by its coated back surface. Due to this featuring structure, it makes a larger actual half acceptance angle $\theta_{max,\,ac}$ than its nominal half acceptance angle $\theta_{max}$. The relationship between the geometrical concentration ratio (CR) and the nominal half-acceptance angle $\theta_{max}$ is given by

$$CR = \frac{S_1}{S_2} = \left( \frac{1}{\sin \theta_{max}} \right)^{1 \text{ or } 2} \quad (1)$$

where $S_1$ is the area of the CPC aperture and $S_2$ is the area of the CPC base.

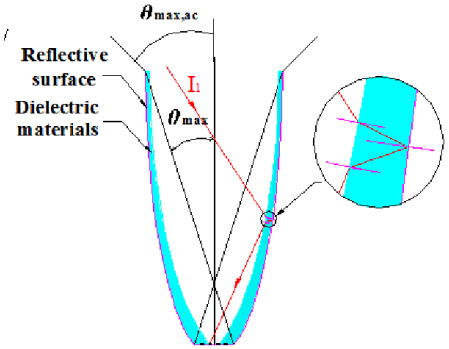


**Fig.1.** Working principle of the lens-walled CPC [4]

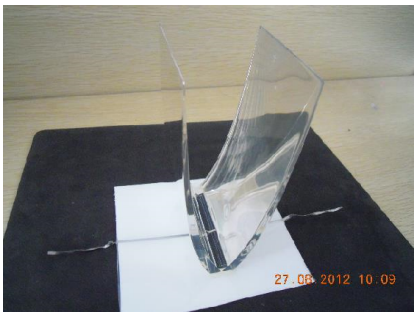

**Fig.2.** A lens-walled CPC affixed with a PV cell [10]

A sample lens-walled CPC with a geometry concentration ratio of 2.5X is shown in Fig.2. The lens-walled CPC body is made with clear acrylic material, which has a high transparency and is resistant to humidity and other solvents. A common fabrication process is using Computerized Numerical Control (CNC) machine to cut out a CPC straightaway from an acrylic block. This method can offer high accuracy in geometry sizing, but the high conducting temperature due to the cutting mechanism may decrease the material transparency. In addition, some extra machining steps increase the general costs of production. Another suggested fabrication technique is resin casting [9]. It is typically a cold forming process, which pours the acrylic resin into designed model and curing at the room temperature to form the required shape. The casting method is easier to implement in comparison with CNC cutting and allow mass production of CPC modules with lower cost.

Referring to our previous work [9], the implemented PV cell strip is from a single junction mono-crystalline silicon PV cell. It has three bus-bars (1.5 mm * 10 mm), seven fingers (0.1 mm * 156 mm), as illustrated in Fig.3.


**Fig.3.** Front grid of a PV cell strip

*Modelling theory*

In this numerical modelling study, the optical analysis of three different CPCs and electrical analysis of PV cell were conducted separately, but they were coupled by the boundary condition of irradiation on the PV cell.

**1. Optical analysis of the CPCS**

In this study, the ray-trace simulation was implemented using a commercial software Photopia for all three kinds of CPCs. Reflection, refraction and optical absorption were taken into account in simulation [3] and the detailed discussions about optical flux distribution on the base of each CPC can be found in [10]. The simulated irradiation profile would be used as a boundary condition in the numerical modelling of a PV cell.

**2. Electrical analysis of the PV cell**

In order to resolve the issue with non-uniform illuminations and determine the current density distribution, the PV cell needs to be simulated by solving the continuity equation, i.e.,

$$-\nabla \cdot (\sigma \nabla V) = Q_J \quad (2)$$

Where V is the electric potential, *Qj* represents the current source and σ is the conductivity of material [9, 11]. The current source *Qj* could be understood as the current density generated by a PV cell. This current density can be obtained by some parameter values independent of the cell dimensions, so it is possible to discuss results under different conditions for the same cell. The PV cell one diode model takes into account a photo-generated current, recombination, and shunts, so the current source in the illuminated emitter regions can be defined as:

$$Q_e = C_1 G + C_2 T^3 \exp\left(\frac{-E_g}{kT}\right)\left[\exp\left(\frac{qV_j}{nkT}\right) - 1\right] + C_3 V_j \quad (3)$$

In the finger and bus-bar regions, it can be defined as:

$$Q_d = C_2 T^3 \exp\left(\frac{-E_g}{kT}\right)\left[\exp\left(\frac{qV_j}{nkT}\right)-1\right]+C_3 V \quad (4)$$

The terms $C_1$, $C_2$ and $C_3$ are coefficients specific to a given cell, $C_1$ is the photocurrent density per unit of incident power, $C_3$ is the inverse of cell shunt resistance $R_{sh}$, and $C_2$ is related to the saturation current density Jo at the standard temperature To and can be expressed as:

$$C_2 = \frac{J_o}{T_o^3 \exp\left(\frac{-E_g}{kT_o}\right)} \quad (5)$$

This continuity equation is suggested to be solved by the finite element method (FEM) [11, 12]. In this study the finite element method was applied to obtain the solution using COMSOL Multiphysics software [9].

### 3. Boundary conditions

Three main types of boundary conditions are considered in the simulation process. The relevant interface condition at interfaces between different media and interior boundaries represents continuity;

$$n \cdot (J_1 - J_2) = 0 \quad (6)$$

The electrical insulation is applied to ensure no electrical current flows into the boundary. At the interior boundaries, this means that no current can flow through the boundary and that the electrical potential is discontinuous across the boundary.

$$n \cdot J = 0 \quad (7)$$

The ends of the bus bars are connected to the external load and have an electrical potential equal to the cell operating voltage $V_{cell}$ as an input parameter.

$$V = V_{cell} \quad (8)$$

## RESULTS

The optical analyses of three CPCs were carried out by using ray tracing technique. The light profile from each corresponding CPC was produced. Moreover, in the finite element method (FEM) analysis, a PV cell was divided into a number of small elements with relevant boundary conditions. The electrical analysis was based on the PV cell IV characteristics under different illumination distribution conditions. As the comparison was focused on the effect of illumination distribution, the average intensity values were fixed at 1000W/m$^2$ and the cell temperature was assumed at 25$^o$C.

### *Optical performance*

The different light profiles were obtained by using optical analysis tool Photopia. A comparison is made between solid CPC, mirror CPC and lens-walled CPC with light profiles under three different incident angles, as presented in Fig.4. The non-uniformity of light distribution could be defined as the difference between peak and nadir points of the irradiance. For both solid and mirror CPCs, the non-uniformity of light distribution increased with larger incident angles while the peak irradiance point also has shifted. This is due to the principle and structure of a CPC, in which light is focused onto a narrower patch when the incident angle is closer to the half acceptance angle. In the contrast, the light profile from lens-walled CPC distributes more smoothly with lower peak irradiance value. This is because the lens makes the refracted light more scattering, which is evident in ray-tracing [10].

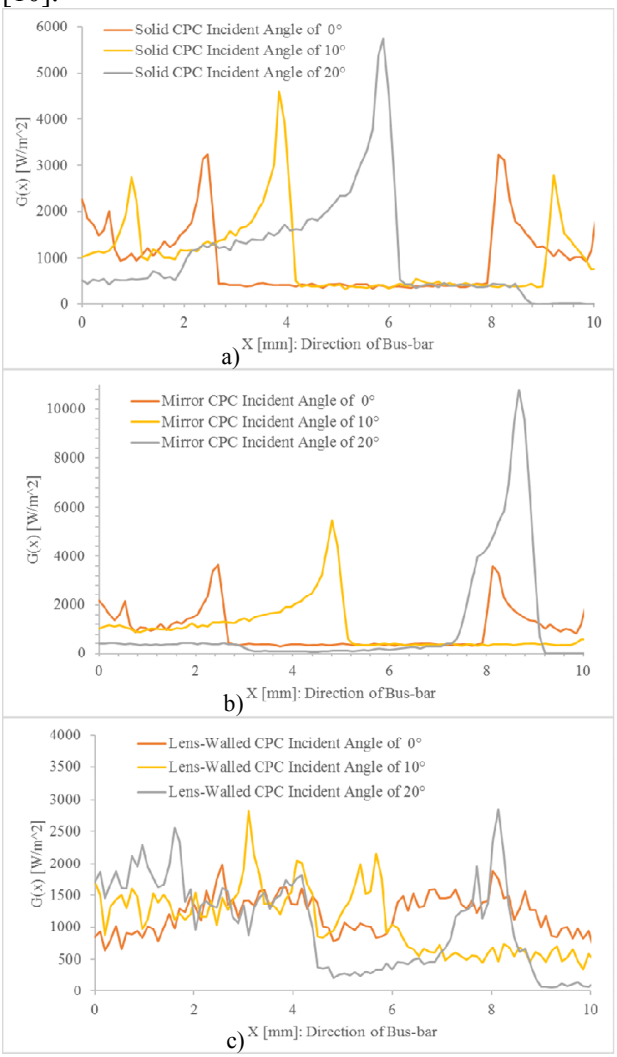


**Fig.4.** Corresponding light profiles for three different incident angles: a) Solid CPC b) Mirror CPC c) Lens-walled CPC

*Electrical performance*

The high illuminated regions produce larger resistive losses which result in the decrease in PV cell open circuit voltage [12]. Fig.5 presents the IV curve of PV cell corresponding to the light profiles of each CPC. The PV cell performances have taken varying degree of influences due to the non-uniformity of light distribution. For the cases of solid and mirror CPCs, an obvious dropping in PV cell open circuit voltage can be observed at incident angle of 20°. Table 1 lists the maximum power points (MPP) for each case of CPCs. From the results, there are no obvious variations for the case of len-walled CPC. In terms of the performance of the PV cell, the property of the light profiles makes the lens-walled CPC have less influence on the PV cell.

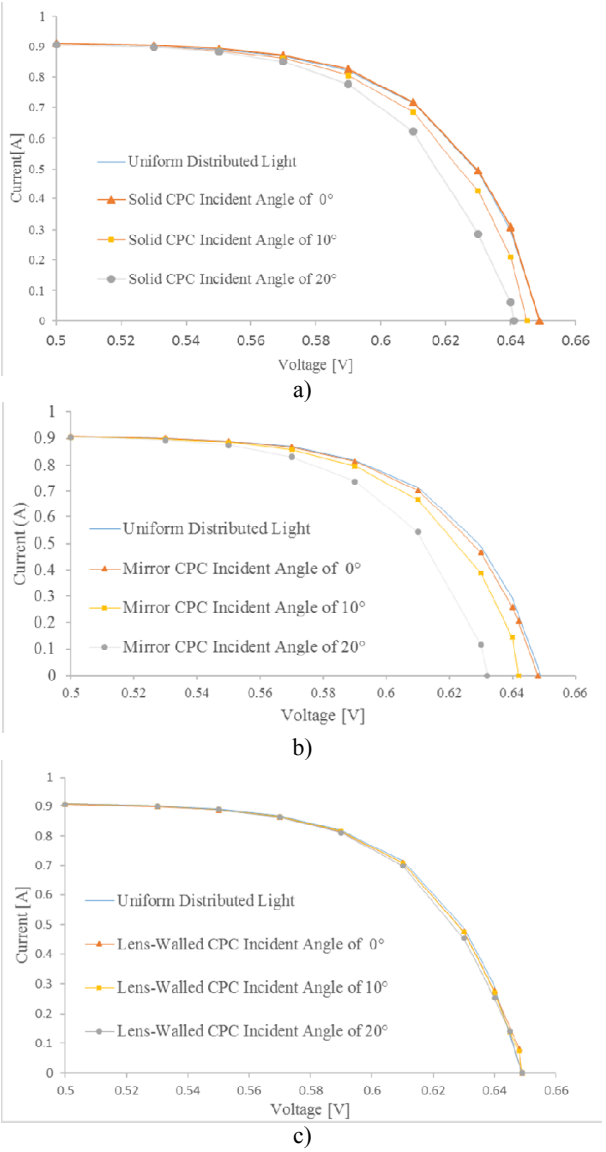


**Fig.5.** Predicted IV curves of PV cell for three kinds of CPCs (A zoom in): a) Solid CPC b) Mirror CPC c) Lens-walled CPC

**Table 1.** Maximum power points (MPP) of PV cell for three types of CPCs

| CPC | 0° incident angle | 10° incident angle | 20° incident angle |
|---|---|---|---|
| Solid | 0.493W | 0.490W | 0.485W |
| Mirror | 0.493W | 0.488W | 0.480W |
| Lens-walled | 0.493W | 0.493W | 0.492W |

According to the light distribution profiles, the resistive losses distributions for each case of CPCs are different for one to another. In Fig.6, the resistive losses distributions for all three CPCs at the 20° incident angle are illustrated. It can be observed that the lens-walled CPC has the lowest resistive loss value. It can also be seen that there are huge resistive losses for the mirror CPC, which is almost ten times greater than the lens-walled CPC.

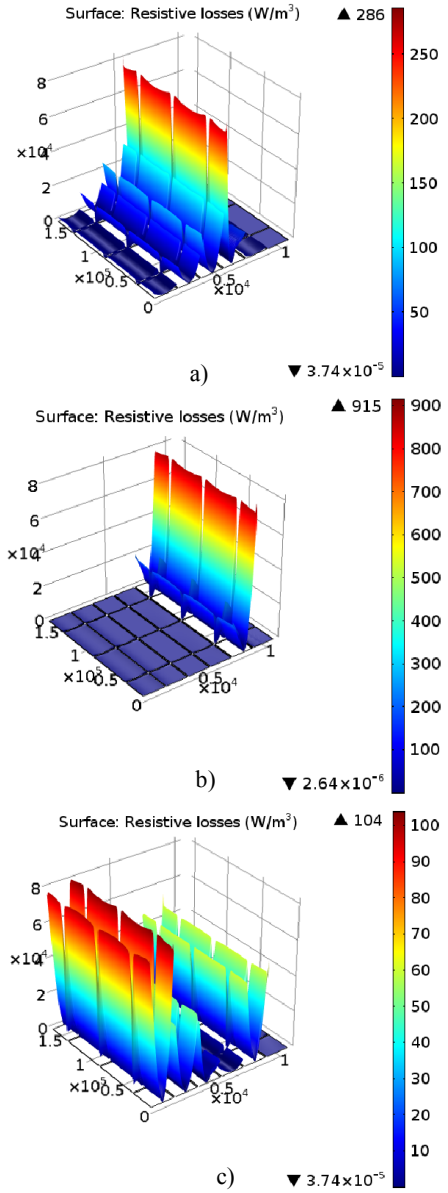


**Fig.6.** Resistive loss distribution at 20° incident angle (a) Solid CPC b) Mirror CPC c) Lens-walled CPC (not to scale ratio)

The open circuit voltage under the condition of uniform distributed light is 0.649V. Table 2 lists the percentage difference in PV cell open circuit voltages in comparison with the uniform condition for each CPC for three incident angles.

**Table 2.** Percentage difference in the open circuit voltages compared with the uniform distribution

| CPC | 0° incident angle | 10° incident angle | 20° incident angle |
|---|---|---|---|
| Solid | 0% | 0.62% | 1.23% |
| Mirror | 0.15% | 1.08% | 2.62% |
| Lens-walled | 0% | 0% | 0% |

The major effect of the non-uniform distributed light is the variation in the open circuit voltages. The high localised current density in the emitter region increases the resistive loss. Consequently, the response of the PV cell to the high resistive loss results in a reduction in the cell's open circuit voltage.

The combination effect of non-uniform light is not obvious at the 0° incident angle. The decrease in open circuit voltage is intensified as the incident angle increases. On comparison of the three CPCs, the mirror CPC has the lowest open circuit voltage at the 20° incident angle which is mainly due to the high non-uniformity of its light distribution. The light distribution profile for a lens-walled CPC is relatively uniform, which minimises the influence of resistive loss.

## CONCLUSIONS

This paper has described the optical and electrical analysis of a lens-walled CPC PV cell. The optical light distribution profiles have been obtained in order to carry out a coupled electrical analysis of PV cell in a CPC. A detailed study has been presented on the IV performance of PV cell under non-uniform distributed light. The following conclusions can be gained from this work:

a) Non-uniform light causes cell efficiency drop, reflected as the reduction of open circuit voltage. The contributor of this phenomenon is the high resistive loss under non-uniform illumination;

b) Non-uniformity of irradiation in a CPC increases with incident angle. The lens-walled CPC has smoother light distribution and bring less impact on PV cell performance among the three types of CPCs.

## ACKNOWLEDGEMENT

Thanks to European Commission for a Marie Curie Fellowship grant (PIIF-GA-2009-253945). Thanks to the University of Ferrara and Beijing University of Civil Engineering and Architecture for their support for international collaboration.

## REFERENCES

1 Mallick, T. K. and P. C. Eames (2007). "Design and fabrication of low concentrating second generation PRIDE concentrator." Solar energy materials and solar cells 91(7): 597-608

2 Zacharopoulos, A., et al. (2000). "Linear dielectric non-imaging concentrating covers for PV integrated building facades." Solar Energy 68(5): 439-452

3 Su, Y., et al. (2012). "A novel lens-walled compound parabolic concentrator for photovoltaic applications." Journal of solar energy engineering 134(2): 021010

4 G. Li, Y. Su, G. Pei, X. Yu, J. Ji & S. Riffat . Preliminary Experimental Comparison of the Performance of a Novel Lens-Walled Compound Parabolic Concentrator (CPC) with the Conventional Mirror and Solid CPCs, International Journal of Green Energy, Vol. 10, Issue 8, September 2013, pp. 848-859

5 Li, G., et al. (2014). "An Outdoor Experiment of a lens-walled Compound Parabolic Concentrator Photovoltaic Module on a Sunny Day in Nottingham." Journal of solar energy engineering 136(2): 021011

6 Vivar, M., et al. (2010). "Laser grooved buried contact cells optimised for linear concentration systems." Solar energy materials and solar cells 94(2): 187-193

7 Nasby, R. and R. Sanderson (1982). "Performance measurement techniques for concentrator photovoltaic cells." Solar Cells 6(1): 39-47

8 Vishnoi, A., et al. (1989). "Combined effect of non-uniform illumination and surface resistance on the performance of a solar cell." International Journal of Electronics 66(5): 755-774

9 Zhou, H. (2016). Modelling and experimental study of PV cells in the lens-walled CPC PV system. Department of Architecture and Built Environment, University of Nottingham. PhD thesis

10 Guiqiang, L., et al. (2013). "Experiment and simulation study on the flux distribution of lens-walled compound parabolic concentrator compared with mirror compound parabolic concentrator." Energy 58: 398-403

11 Chemisana, D. and J. I. Rosell (2013). "Electrical performance increase of concentrator solar cells under Gaussian temperature profiles." Progress in Photovoltaics: Research and Applications 21(4): 444-455

12 Mellor, A., et al. (2009). "A two-dimensional finite element model of front surface current flow in cells under non-uniform, concentrated illumination." Solar Energy 83(9): 1459-1465

13 Luque, A., et al. (1998). "Electric and thermal model for non-uniformly illuminated concentration cells." Solar energy materials and solar cells 51(3): 269-290

# STORAGES WITH PHASE CHANGE MATERIALS

*Bulgarian Chemical Communications, Volume 48, Special Issue E (pp. 181 - 188) 2016*

# Numerical simulation of thermal energy storage based on phase change materials

A. Seitov[1], B. Akhmetov[1*], A. G. Georgiev[2,5], A. Kaltayev[1], R. K. Popov[3], D. B. Dzhonova-Atanasova[4], M. S. Tungatarova[1]

[1]*Al-Farabi Kazakh National University, Almaty, 050000, Kazakhstan*
[2]*Technical University of Sofia, Plovdiv Branch, Dept. of Mechanics,25 Tsanko Diustabanov Str, 4000 Plovdiv, Bulgaria*
[3]*Faculty of Physics, Plovdiv University "Paisii Hilendarski", 24 Tzar Assen Str., 4000 Plovdiv, Bulgaria*
[4] *Institute of Chemical Engineering, Bulgarian Academy of Sciences, Acad. G. Bonchev Str., Bl. 103, 1113, Sofia, Bulgaria*
[5]*European Polytechnic University, Dept. of "Green Energy", 23 Kiril and Metodiy str., 2300 Pernik, Bulgaria*

One of the main problems related to the application of thermal energy gained from renewable energy sources is the absence of effective storage system. If we could store, for instance, solar thermal energy which is harnessed during day time, it would be possible to use it at night for space heating, ventilation, air conditioning or hot water systems. Therefore, this paper reports on the numerical analysis of heat transfer and fluid flow processes in a thermal energy storage based on phase change material designed and developed by the authors. Such study is very important in understanding of advantages and disadvantages of the design features and efficiency of the latent heat storage.

**Keywords***:* phase change materials, thermal energy storage, latent heat storage

## INTRODUCTION

Various studies indicate that built environment significantly contributes to global energy consumption and production of greenhouse gases. Within built environment, buildings consume about 40% of world's total energy and contribute to release of greenhouse gases up to 35% [1]. There are many energy consumers in buildings. But, heating ventilation and air conditioning (HVAC), and domestic hot water (DHW) systems are generally responsible for significant proportion of total building energy consumption [2].

According to the energy consumption breakdown of buildings [3], typical HVAC and DHW systems accounts for approximately 55% of total energy consumption for residential, and 35 % for non-residential buildings (Table 1). Therefore, developing carbon free heat storage that can provide thermal energy to HVAC and DHW systems of buildings is very important in terms of efficiency and environmental safety.

Renewable energy sources show significant promise in assisting to preserve many of the natural resources that we currently use as sources of energy for built environment, decrease the amount of toxins, by-products of energy use and keep the planet clean for future generation. Unlike many other renewable energy sources, solar power is by far the cleanest and it has a large potential for heating/ cooling of buildings, providing hot water, etc. Unfortunately solar energy value is periodic and unpredictable - for better use it must be accumulated into storage for further utilization [4].

**Table 1.** Breakdown of building energy use [3]

| Residential Energy Use | Commercial Energy Use |
|---|---|
| 1% – Computers | 2% – Cooking |
| 5% – Cooking | 3% – Computers |
| 5% – Wet clean | 4% – Refrigeration |
| 7% – Electronics | 6% – Officeequipment |
| 8% – Refrigeration | 6% – Ventilation |
| 11% – Lights | 26% – Lighting |
| 12% – Cooling | 13% – Cooling |
| 12% – Water heat | 7% – Water heat |
| 31% – Heating | 14% – Heating |

Thermal energy storage plays important role in effective application of gained thermal energy from renewable energy sources [5]. It permits to equalize instantaneous differences between demand and supply of thermal energy using off-peak excess energy which may be lost otherwise.

Among the methods for heat accumulation, thermal storage in the form of latent heat is very attractive one [6]. Latent heat storage relies on storage materials which absorbs/ releases heat while undergoes phase transition. Such PCMs has higher energy storage density and narrower temperature range between storing and releasing heat compared to sensible heat storage. Among PCMs which can be used for heating/ cooling and hot water systems of buildings, materials such as

* To whom all correspondence should be sent:
eng.akhmetov@gmail.com

paraffin or molten salt have been considered as the most appropriate material for heat storage due to their efficient thermal properties. Thus, using latent heat storage filled with PCM gives opportunity to develop effective daily thermal energy supplier for HVAC and DHW systems [7].

The co-author, Prof. A. Georgiev and his team from the Technical University of Sofia, Plovdiv Branch, designed and developed latent heat storage (Fig.1). Aim of the current study is concentrated on numerical analysis of heat transfer and fluid flow processes during charging and discharging regimes of the latent heat storage. Such study is very important in understanding of advantages and disadvantages of the design features of the latent heat storage and its efficiency.


**Fig.1.** Latent heat storage [8]

## DESCRIPTION OF THERMAL ENERGY STORAGE AND PHASE CHANGE MATERIALS

Detailed illustration of the latent heat storage and its design features are shown in Fig.2. PCM containers have rectangular cross section with dimensions 950 x 80 x 50 mm. They are placed into the vertical cylinder tank (storage) with 1 m height and 0,3 m radius [8]. The tank and containers are made of stainless steel grade AISI 304L. Number of PCM containers are 39 and they are located coaxially in the storage. There are two concentric circles: external circle contains 26 containers and the inner circle has 13 containers. All the containers are fixed with brackets to the lower and upper parts of the storage tank in order to make them stable during charging and discharging regimes. There are three inlet pipes in the upper side of the storage where the heat carrier fluid flows into the storage. In the base of the storage other three pipes are connected to the storage to discharge the heat carrier fluid from the storage. The storage is insulated by wrapping with glass wool from the outside.

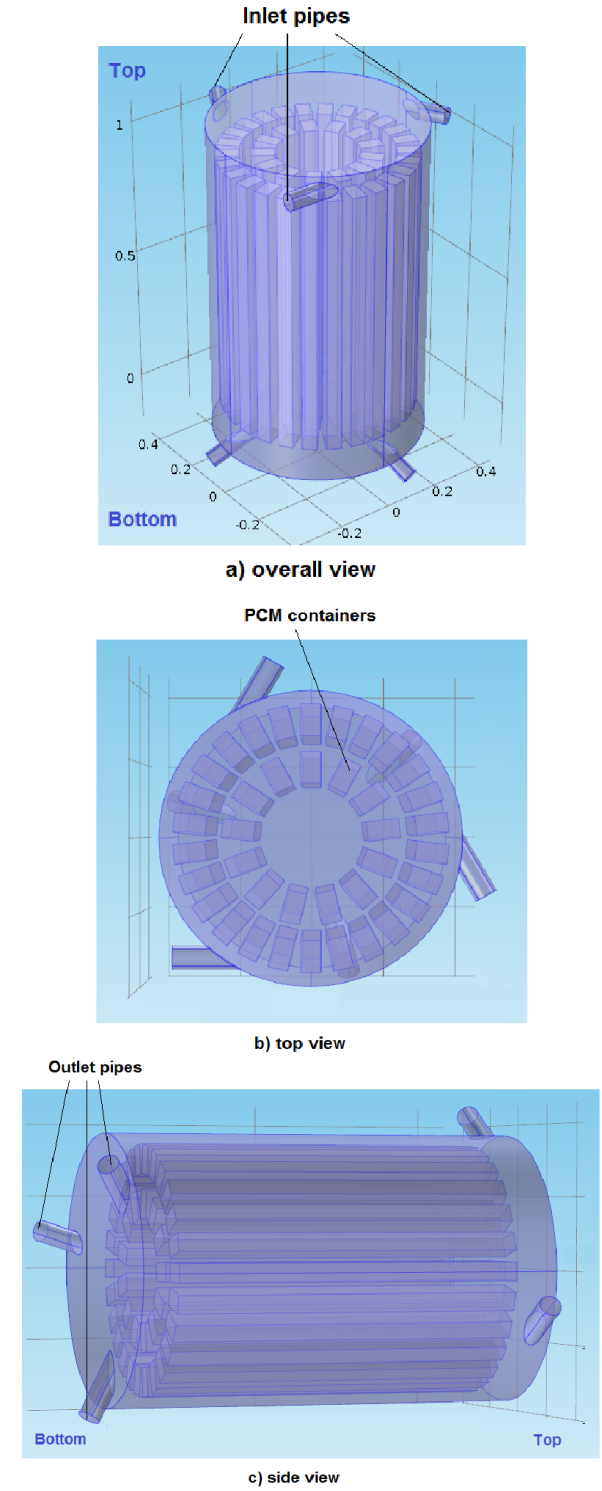


**Fig.2.** Design features of the latent heat storage

As a phase change material for the latent heat storage, we used paraffins. Paraffin is considered as effective heat storage material because of its large latent heat of melting (200 kJ/kg or 150 MJ/m³), thermal stability, negligible subcooling, non-toxic,

and low price. There are different types of paraffins. For instance, paraffin waxes, CnH2n+2, are chain polymers which crystallize in lamellar form. Consequently, properties such as phase change temperature, latent heat, density, and specific heat capacity are particular for each paraffin wax [9].

Bulgarian team and their colleagues studied thermophysical properties of three phase change paraffinic materials by means of differential scanning calorimetry (DSC). Aim of the experimental study was to thermophysically characterize two commercial paraffin waxes (E53 and E46), and a commercial paraffin-ceresine composite (ECP).

**Table 2.** Phase change temperatures and latent heat of E53, E46, and ECP paraffin samples [9]

| PCM | Cycle | $T_{on}$, °C | $T_{max}$, °C | $T_{off}$, °C | $\Delta H$, J/g |
|---|---|---|---|---|---|
| | Heating | 33.07 | 39.83 | 45.33 | 194.32 |
| *E53* | | 51.79 | 56.4 | 59.22 | |
| | Cooling | 59.41 | 57.01 | 51.93 | -194.11 |
| | | 44.36 | 39.76 | 33.02 | |
| *E46* | Heating | 46.67 | 56.57 | 61.78 | 176.77 |
| | Cooling | 59.54 | 56.99 | 47 | -165.69 |
| *ECP* | Heating | 43.85 | 54.21 | 64.00 | 143.891 |
| | Cooling | 63.39 | 55.51 | 34.03 | -142.9 |

Thermal properties obtained with DSC during heating/ cooling cycle of the three PCMs are presented in Fig.3 and Table 2. It can be seen from Fig.3 that E46 and ECP samples have single peaks while E53 sample has two peaks during heating/cooling process. Indeed, paraffins undergo multiple phase transitions. At lower temperatures phase transition occurs in the form of solid-solid while at higher temperatures solid-liquid melting process takes place. Therefore, latent heat values in Table 2 includes both solid–solid and solid–liquid phase transitions. Thus, obtained thermophysical properties of these paraffinic PCMs will be used for numerical studies.

## MATHEMATICAL FORMULATION OF PHYSICAL PROCESSES IN LATENT HEAT STORAGE

### *Equations*

Simulation is conducted in three dimensional space in a time dependent manner by means of finite element method based on Comsol multiphysics. The geometry used to perform the simulation of charging and discharging of LHS is presented in Fig.2. The containers which enclose PCM (e.g. paraffins) are thermally insulated at the top and bottom. Moreover, it is assumed that the volume of the PCM does not change during phase transition. Such assumption, allows to introduce simpler mathematical models [10], although, according to the experimental investigations, paraffins change their volume during melting or solidification [9]. Moreover, to avoid intensive numerical calculations, the containers are considered as highly conductive layers [11]. Meshing of PCM containers are shown in Fig.4.

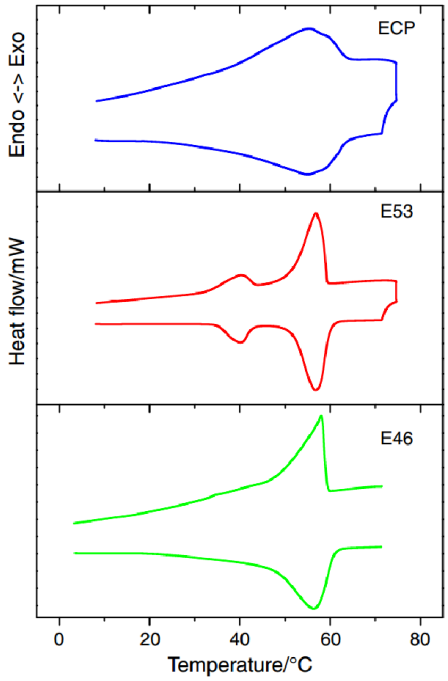


**Fig.3.** Temperature change of E53, E46, and ECP paraffin samples during heating and cooling cycles at a rate 10°C /min [9]

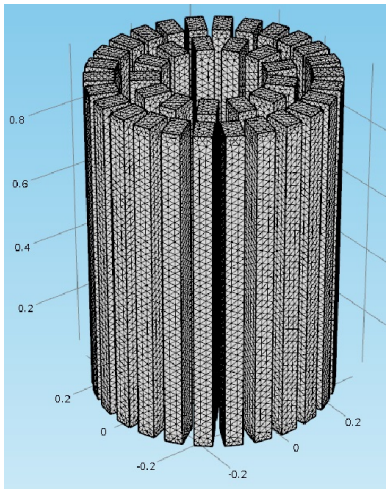

**Fig.4.** Meshing of the containers with PCM

In order to simulate the dynamic behaviour of the heat carrier fluid flowing inside the LHS, the continuity and Navier-Stokes equations must be

solved simultaneously. Continuity equation takes the form [12]:

$$\frac{\partial \rho}{\partial t} + \nabla \cdot (\rho u) = 0 \tag{1}$$

where $\rho$ - density, kg/m³ and $u$ - velocity, m/s. The Navier-Stokes equation which accounts for the conservation of the momentum is given by [12]:

$$\frac{\partial u}{\partial t} + (u \cdot \nabla)u = -\frac{1}{\rho}\nabla p + \nu \nabla^2 u + F \tag{2}$$

where $p$ - pressure in the fluid, Pa, $\nu$ - kinematic viscosity, m²/s.

Heat transfer from the water to the wall of the PCM containers takes place in the form of convection. Therefore, complete energy equation has to be solved by using the velocity field obtained from the solutions of Eqns. (1) and (2). Thus, the energy equation describing the heat transfer process is given by [13]:

$$\rho c_p \frac{\partial T}{\partial t} + \rho c_p u \cdot \nabla T = \nabla \cdot (k \nabla T) \tag{3}$$

$c_p$ - specific heat capacity, J/kgK; $k$ - thermal conductivity of the material, W/mK, $T$- temperature of the heat carrier fluid, °C. Meshing of the domain between storage vessel and PCM containers, where Eqns. (1)-(3) are solved are illustrated in Fig.5.

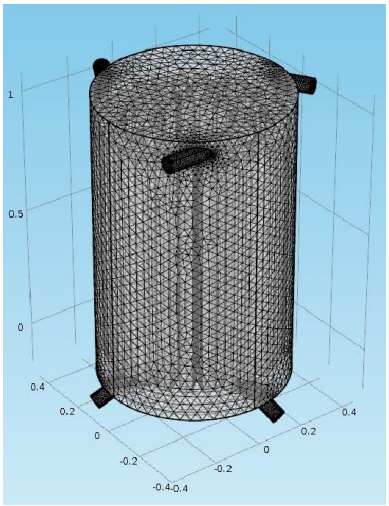

**Fig.5.** Meshing of the latent heat storage

The energy equation for the phase change material including latent heat transfer during phase change is [14]:

$$\rho c_p \frac{\partial T}{\partial t} + \rho c_p u \cdot \nabla T = \nabla \cdot (k \nabla T) \tag{4}$$

$$k = \theta_1 k_{phase1} + \theta_2 k_{phase2} \tag{5}$$

$$c_p = \theta_1 c_{p,phase1} + \theta_2 c_{p,phase2} + L\frac{d\alpha}{dT} \tag{6}$$

$$\rho = \frac{\theta_1 \rho_{phase1} c_{p,phase1} + \theta_2 \rho_{phase2} c_{p,phase2}}{\theta_1 c_{p,phase1} + \theta_2 c_{p,phase2}} \tag{7}$$

where $\theta_1 = 1 - \alpha$ and $\theta_2 = \alpha$ corresponds to phase 1 and phase 2 respectively. Moreover, $L$ is the latent heat of phase change and $\alpha$ is the liquid volume fraction in the phase change material and it is a function of temperature:

$$\begin{aligned} \alpha &= 0 && T < T_{solid} \\ \alpha &= \frac{T - T_{solid}}{T_{liquid} - T_{solid}} && T_{solid} \le T \le T_{liquid} \\ \alpha &= 1 && T > T_{liquid} \end{aligned} \tag{8}$$

In the PCM containers buoyancy flow of melted part of PCM due to temperature differences was not considered in the model, but only conduction heat transfer happens in both melted and solid part of PCM. Therefore, difference between melted and solid phases is based on their thermal conductivity coefficients $k$, specific heat capacities $c_p$ and densities $\rho$. Moreover Eqns. (4) - (7) do not consider modelling of subcooling effects during phase change processes. And, other properties of the phase change paraffinic materials for the modelling purposes were taken from experimental results [9].

*Initial and boundary conditions*

For the fluid flow, the boundary conditions (BC) at solid surfaces such as inner wall of the storage tank and on the surface of PCM containers are considered as no slip BC. Moreover, it is assumed that the storage tank was perfectly insulated which is given by:

$$-n \cdot (-k \nabla T) = 0 \tag{9}$$

where $n$ - normal vector to the heat transferring surface. Therefore, heat transfer occurs only by means of inlet and outlet pipes. The containers are considered as highly conductive layers, where heat exchange takes place between heat carrier fluid and phase change material which can be described as:

$$\begin{aligned} &-n \cdot (-k \nabla T) = \\ &d_s (Q_s - \rho_s c_s \frac{\partial T}{\partial t}) - \nabla_t \cdot (-d_s k_s \nabla_t T) \end{aligned} \tag{10}$$

where $d_s$ - layer thickness which is taken as 0,01m in our case, $Q_s$ - layer internal heat source and it is

zero in our modeling, $J$, $\rho_s$- layer density, kg/m³, $c_s$ - layer specific heat capacity, J/kgK, $k_s$ - layer thermal conductivity, W/mK - they are taken from material properties and it was mentioned above that the PCM containers are made from stainless steel.

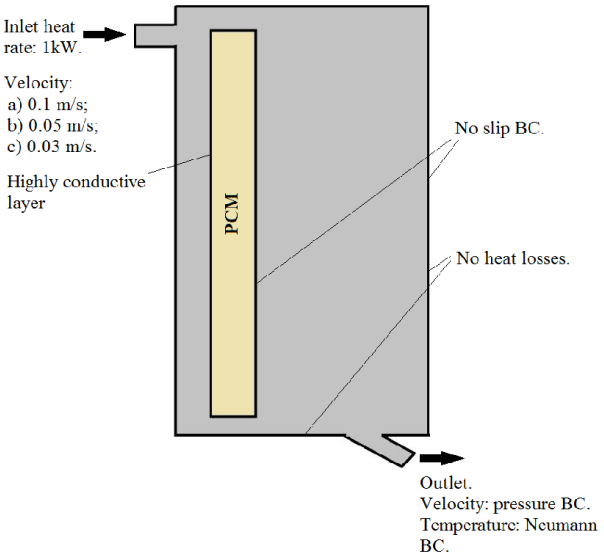


**Fig.6.** Schematic description of boundary conditions

**Table 3.** Study cases for the simulation

| Case | Number of inlet pipes used | Number of outlet pipes used | Inlet velocity |
|---|---|---|---|
| a) | 1 | 1 | 0,100 m/s |
| b) | 2 | 2 | 0,050 m/s |
| c) | 3 | 3 | 0,033 m/s |

In case of the simulation of charging process, initially it is assumed that the temperatures of the PCM and working fluid filling the storage tank are 20 $^0$C. Inlet velocities were taken as depending on the number of inlet pipes (Table 3). The storage was charged with the net heat rate of 1kW through the inlet pipes (Fig.6). For instance, in case of one inlet pipe, heat rate from the inlet is 1 kW and in case of two inlet pipes, heat rate from each pipe is 0,5 kW. Purpose of such heat rate establishment was to estimate the effectiveness of the storage depending on different number of inlet and outlet pipe working conditions, and visualize by the simulation tools, intensive heat transferring zones in the storage and PCM containers. Conversely, during discharging case, initial temperate of the storage and PCM was 80 $^0$C and 1 kW of thermal energy started to be discharged from outlet pipes. Moreover, inlet flow was maintained at 20 $^0$C during simulation of the discharging process.

Outlet BCs for the velocity was set up in terms of the pressure with suppress backflow which adjusts the outlet pressure in order to prevent fluid from entering the domain through the boundary. And, temperature BC is Neumann type:

$$-n\cdot(-k\nabla T)=0 \qquad (11)$$

## RESULTS AND DISCUSSION

Three dimensional transient heat transfer simulations with PCM phase change were performed for the cases shown in Table 3. Durations of both charging and discharging simulations were three hours long since it was enough to conduct heat transfer analysis in the storage. Note that not all the simulation results are shown in the paper but only selected simulation results are presented and discussed.

In Fig.7 simulation results are illustrated for the case-a where only one inlet and one outlet pipe was used for charging process. Moreover, paraffin E46 was considered as PCM in the simulation since it has more thermal stability than other two. Velocity of the heat carrier fluid at the inlet pipe was 0,1 m/s and thought the inlet pipe the fluid transferred into the storage 1kJ thermal energy at every second. It can be seen from Fig.7a that thermal energy came from the inlet pipe starts to charge the PCM containers which are opposite to the inlet pipe. This is true since heat carrier fluid flows to that area first but after circulation over the PCM containers most part of the fluid flows downward through the centre of the storage thus charging coaxially located PCM containers of the inner circle. Main streamlines where actively heat transfer process occurred are shown in Fig.7b. After 180 min still temperature distribution inside the storage was uneven and the PCM containers were not fully charged yet - Fig.7c.

When two inlet (inlet fluid velocity is 0,05 m/s at each inlet pipe) and two outlet pipes were used to charge the storage thermal energy still unevenly distributed in the storage (Fig.8a) but heat carrier fluid could charge more PCM containers both in outer and inner circles. Moreover, it can be noticed from heat carrier fluid flow streamlines in Fig.8b that active fluid flow process took place between inner and outer circles of PCM containers. In other words, transfer of the heat carrier fluid into the storage by two inlet pipes and two outlet pipes increased flow active areas in the storage, as a consequence, more PCM containers started to be charged during the process. When charging process reached 180 min, almost all PCM containers were fully charged (Fig.8c).

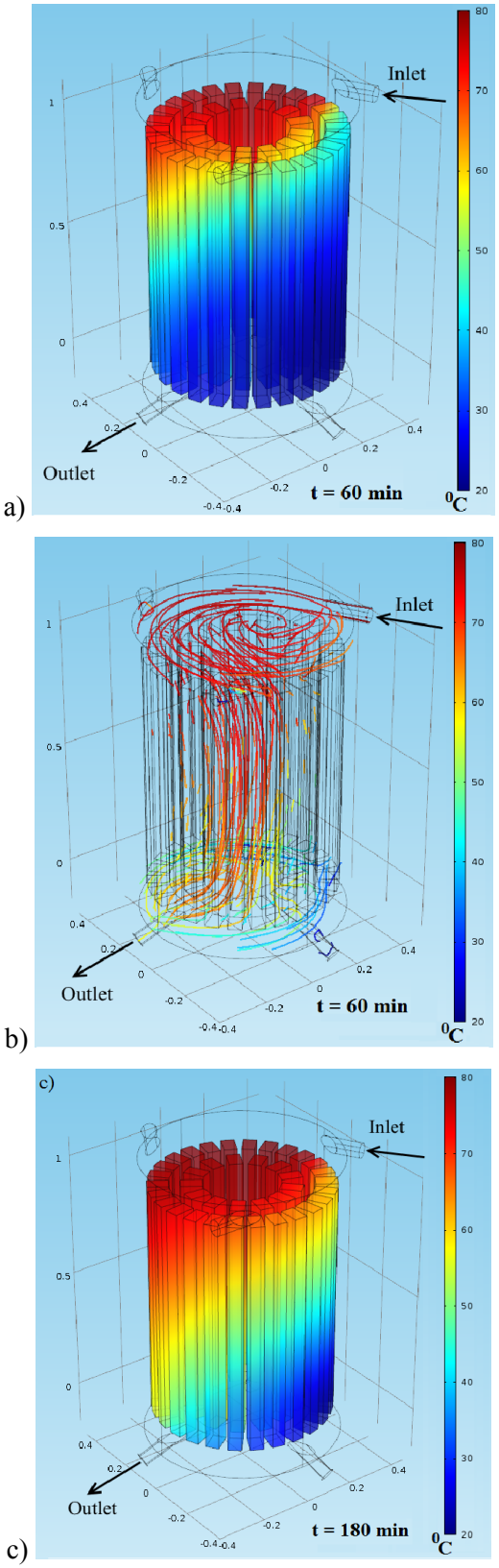


**Fig.7.** Charging process with single inlet and outlet pipes: a) Thermal energy distribution in the PCM containers after 60 min; b) Heat carrier fluid flow streamlines with thermal effect at 60 min; c) Thermal energy distribution in the PCM containers at 180 min

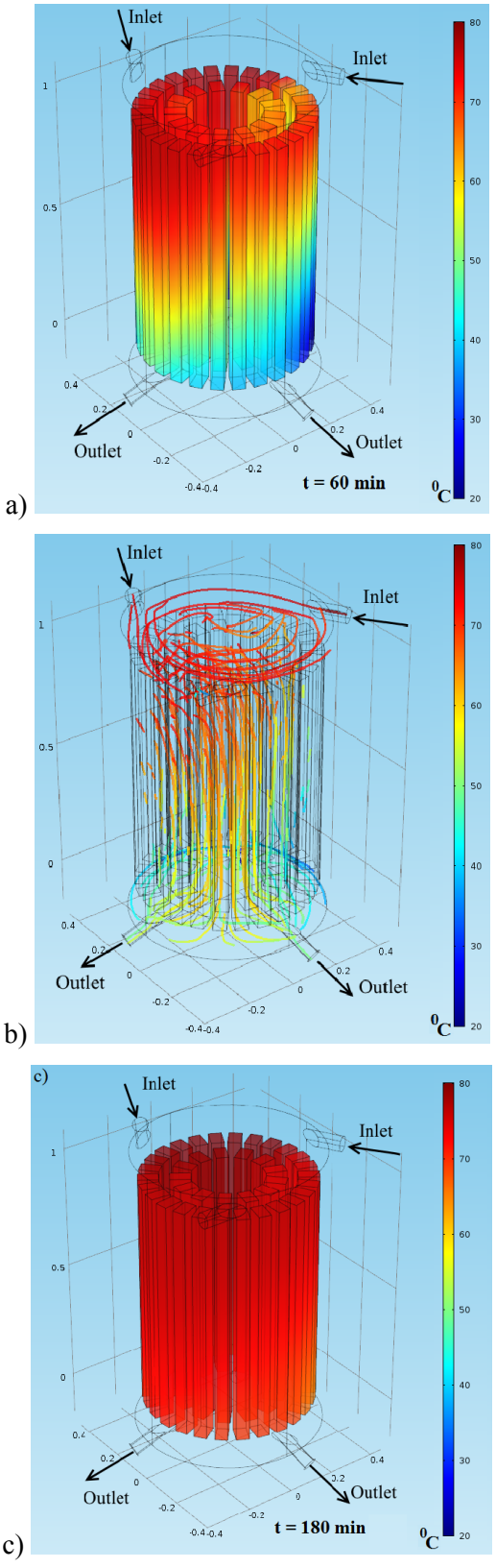


**Fig.8.** Charging process with two inlet and outlet pipes: a) Thermal energy distribution in the PCM containers at 60 min; b) Heat carrier fluid flow streamlines at 60 min; and c) Thermal energy distribution in the PCM containers at 180 min

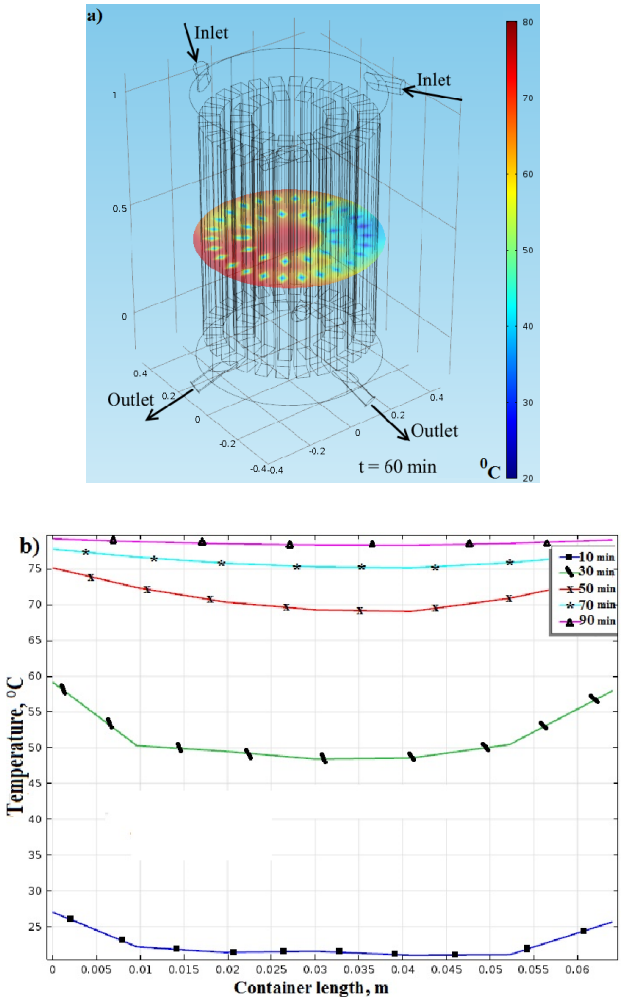


**Fig.9.** a) Temperature field at 60 min in the form of a cut plane to demonstrate the phase change process in the containers; b) Temperature change along the length of one of the containers during charging

In Fig.9a temperature field demonstrated using cut plane to see phase change processes in the PCM containers and in Fig.9b we can see temperature change over time along the length of one of the PCM containers in the inner circle at 0,5 m height.

In case of three inlet and three outlet pipes, full charging time was reduced approximately by half, that is, 80 min compared to results of case b). Simulation result in case of three outlet and three inlet pipes, shown in Fig.10 where only final temperature field is presented.

Discharging process also studied using numerical simulation in same manner as charging process. In other words, cases presented in Table 3 also were studied for discharging process. From the results of the simulation, it was noticed that in case b) where two inlet and outlet pipes were used for discharging process was more effective than other two cases. Therefore, in the Fig.11 we presented results of simulation results related to case b).

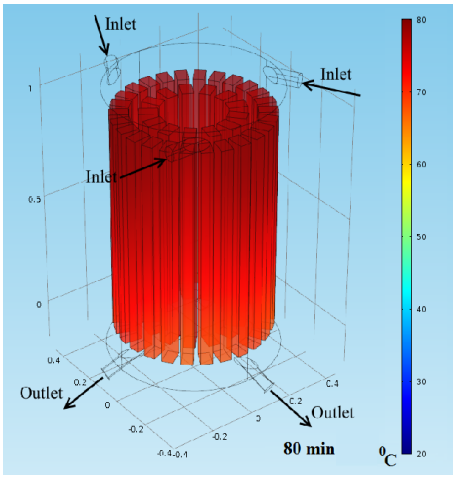


**Fig.10.** Charging process with three inlet and outlet pipes (case-c): Temperature field of PCM containers at 80 min

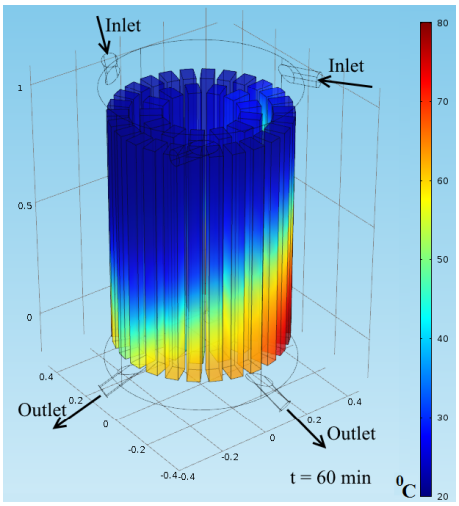


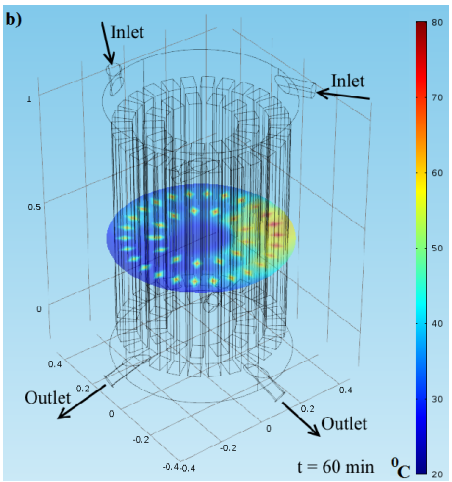


**Fig.11.** a) Thermal energy distribution during discharging case at 60 min; b) cut plane to show phase change process in the PCM containers. Note that inflow temperature is 200 °C and velocity corresponds to Table 3, case b) - two inlet and two outlet pipes

## CONCLUSIONS

In this paper, we presented charging and discharging processes of the latent heat storage in terms of simulation tools, Comsol, taking into account fluid flow and heat transfer physics in the storage tank and phase change processes in the PCM containers.

Three cases were studied in terms of numerical simulation. The results are illustrated in terms of temperature field to investigate how PCM containers were charged and velocity streamlines to understand how fluid flow process took place in the storage domain. From the results, it can be concluded that two inlet and two outlet pipes are enough to charge or discharge such LHS in enough short time, that is, three hours. Moreover, the PCM containers which are in the inner circle charged first in a short time and outer circle containers were charged after that. It can be concluded that outer circle PCM containers are very close to the storage tank walls, therefore, those areas does not allow fluid flow and heat transfer processes to be intensive.

Towards end of 2016, it is planed to build latent heat storage at Al-Farabi Kazakh National University, Almaty, Kazakhstan. Therefore, studies in this paper based on numerical simulation tools are very important in developing design features of the planned storage.

## ACKNOWLEDGMENTS

The authors acknowledge the support provided by the Institute of Mathematics and Mechanics of Al-Farabi Kazakh National University, under the grant funding (GF-3289) named “Development of charging and discharging regimes for hybrid thermal energy storage system consisting of latent heat storage and borehole thermal energy storage, designed to accumulate solar thermal energy”.

## REFERENCES

1 Perez L. Perez-Lombard, J. Ortiz, C. Pout, A review on building energy consumption information, *Energy and Building.,* 40, No 3, 394-398, (2008).

2 M. Doiron, W. O`Brien, A. Athienitis, Energy Performance, Comfort, and Lessons Learned from a Near Net Zero Energy Solar House, *ASHRAE Transactions.,* 117, No 2, 585, (2011).

3 G. Masya, Ph. Andréb, Total energy use in air conditioned buildings: Analysis of main influencing factors*, HVAC and R research*, 18, No 1-2, 21-36, (2012).

4 E. Michaelides, Alternative energy sources, *Green Energy and Technology, Springer*, (2012).

5 M.K. Hubbert, Energy sources of the earth, *Sci Am,* 224, 60-70, (1971).

6 B. Norton, Harnessing solar heat, *Lecture notes in energy, Springer,* 18, (2014).

7 L. Cabeza, M. Ibáñez, C. Soléa, J. Rocaa, M. Nogués, Experimentation with a water tank including a PCM module, *Solar Energy Materials and Solar Cells,* 90, 1273-1282, (2006).

8 R. Popov, A. Georgiev. SCADA system for study of installation consisting of solar collectors, phase change materials and borehole storages*. Proc. of the 2nd Int. Conf. on Sustainable Energy Storage, June 19-21, 2013,* Trinity College Dublin, Ireland*,* pp. 206-211.

9 E. Anghel, A. Georgiev, S. Petrescu, R. Popov, M. Constantinescu, Thermo-physical characterization of some paraffins used as phase change materials for thermal energy storage, *Journal of Thermal Analysis & Calorimetry*, 117, No 2, 557, (2014).

10 V. Alexiades, A. D. Solomon, Mathematical modeling of melting and freezing processes, *Hemisphere Pub. Corp*, 59-77 (1993).

11 F. Samara, D. Groulx, P. Biwole, Natural Convection Driven Melting of Phase Change Material: Comparison of Two Methods, Comsol Conference, Boston (2012).

12 D. A. Anderson, J. C. Tannehill, R. H. Pletcher, Computational fluid mechanics and heat transfer, *Hemisphere Publishing Corporation*, Washington (1984).

13 T. J. Chung, Computation fluid dynamics, *Cambridge university press* (2002).

14 A. J. Parry, P. C. Eames, F. B. Agyenim, Modeling of Thermal Energy Storage Shell-and-Tube Heat Exchanger, *Heat Transfer Engineering*, 35(1), 1-14 (2014).

15 V. R. Voller, C. Prakash, A fixed grid numerical modelling methodology for convection-diffusion mushy region phase-change problems, *Int. J. Heat Mass Transfer*, 30(8), 1709-1719 (1987).

*Bulgarian Chemical Communications, Volume 48, Special Issue E (pp. 189 - 194) 2016*

# Numerical study of heat transfer in macro-encapsulated phase change material for thermal energy storage

D. B. Dzhonova-Atanasova[1*], A. G. Georgiev[2,4], R. K. Popov[3]

[1]*Institute of Chemical Engineering, Bulgarian Academy of Sciences, Acad. G. Bonchev Str., Bl. 103, 1113, Sofia, Bulgaria.*
[2]*Faculty of Mechanical Engineering, Technical University - Sofia, Plovdiv Branch, 25 Tsanko Diustabanov Str., 4000 Plovdiv, Bulgaria*
[3]*Faculty of Physics, Plovdiv University "Paisii Hilendarski", 24 Tzar Assen Str., 4000 Plovdiv, Bulgaria*
[4]*European Polytechnic University, Dept. of "Green Energy", 23 Kiril and Metodiy str., 2300 Pernik, Bulgaria*

The successful development and implementation of systems using renewable energy sources, which are usually of intermittent character, require cheap and effective thermal energy storing for diurnal or seasonal heat accumulation. Thermal accumulators are also used for increasing the efficiency of conventional fuel dependent systems by storing the waste heat in low consumption periods. Much of the efforts are directed towards creation of compact solutions to replace the presently used hot water tanks requiring very large space. This is especially important for small capacity thermal systems in buildings. There are a lot of suggestions in literature using the latent heat of phase change materials (PCM), but only a few close to commercial stage of implementation. A heat accumulator with paraffin as a PCM is a cost effective innovative solution for low grade heat storage. One of the design approaches is encapsulation of the phase change material in containers with a variety of shapes and materials. The aim of the present work is a 3D numerical simulation of the phase change process in a stainless-steel container filled with commercial E53 paraffin. This is a part of a study directed towards design optimization of a hybrid solar installation with thermal storage. The focus is on development and testing of a time effective method for numerical prediction of the thermal behaviour of the container with paraffin and assessment of the factors influencing the heat transfer process prior to the physical experiment.

**Keywords*:*** latent thermal energy storage, phase change material, paraffin, macro-encapsulation, CFD modelling

## INTRODUCTION

Heat accumulation is a key problem for balancing the discrepancy between energy demand and production from renewable and conventional energy sources. The storage technology using the latent heat of paraffin phase change is under intensive investigation and development. Its main shortcomings are relatively low specific heat capacity, low heat transfer coefficient of the paraffin, and high exergy losses.

### *Advantages of encapsulation*

Paraffins are often used as a phase change material in thermal storage systems due to their availability, suitable phase change temperature range, low cost, and non-corrosiveness. Paraffin wax consists of straight-chain n-alkanes, the crystallisation of which releases a large amount of heat, the melting and solidification temperature increasing with the chain length [1]. The disadvantages of the paraffin for heat storage are low thermal conductivity, non-compatibility with plastic containers and moderate flammability. The encapsulation of the paraffin in containers fights the undesirable effects. It increases the heat transfer area, reduces the reactivity towards the outside environment and controls the volume changes during phase transition.

Over 200 potential phase change heat storage materials (including paraffins) suitable for encapsulation, melting from 10 to 90$^{o}$C, are reported by Lane [2, 3].

### *Effect of encapsulation size and geometry*

The design of the containers should ensure complete melting or solidification of the PCM in a period corresponding to the energy availability for charging mode and the energy consumption for discharging mode in diurnal or seasonal storage.

Based on size, the PCM encapsulation is classified into nano (0–1000nm), micro (0–1000 μm), and macro (above 1mm) encapsulation.

The present work focuses on the design of containers for macro-encapsulation. The cheapest containers used for that purpose are tin cans and plastic bottles. A variety of containers' shapes and materials are discussed in [1]. The container may be spherical [4, 5], tubular, cylindrical or rectangular [6, 7]. As for the container material, the metallic containers are preferred, when high heat transfer rate should be achieved, else plastic containers are widely used. In both cases the PCM should not react with the container material.

* To whom all correspondence should be sent:
dzhonova@bas.bg

The improvement of the heat transfer rate with various container geometries including sphere, cylinder, plate and tube was studied in [8] by numerical and experimental techniques. The spherical shape was reported to achieve the highest heat transfer rate. For other geometries, it decreased in the order of cylinder, plate and tube [8].

A large improvement in the heat transfer rate was obtained in a packed bed storage unit with small plastic spheres with PCM [4, 5] at the expense of high pressure drop in the packed bed and high initial cost.

The commercialization of encapsulated PCM based systems is connected with overcoming the following main challenges [9]:

(1) High cost of encapsulation connected with proper selection of the shell material, encapsulation method and size according to the application;

(2) Decreased system performance after a certain number of thermal cycles because of deterioration of the thermo-physical properties, leading to reduction in structural and thermal stability of the PCM;

(3) Precise prediction of thermal behaviour of heat storage, connected with calculating the moving solid liquid boundary during the phase change process.

Results and conclusions on the thermal behaviour of PCM enclosed in rectangular containers were reported in [10, 11]. The numerical simulation in [10] compared the effect of cylindrical and rectangular containers on the performance of air heat energy storage. It showed that at equal PCM volume and heat transfer area, the rectangular container required half of the melting time of the cylindrical container. Therefore in that case it is preferable to use rectangular containers for PCM encapsulation. The melting and solidification of PCM in rectangular containers was simulated in [11] for studying the following effects: effect of the working fluid temperature on the melting behaviour of $CaCl_2.6H_2O$ and paraffin wax C18; effect of the working fluid convection coefficient; effect of the container thickness; effect of the mass of macro-encapsulated PCM. It was found that the time for complete melting was inversely proportional to the temperature and the convective heat transfer coefficient of the heat transfer fluid (HTF); the rectangular encapsulated $CaCl_2.6H_2O$ could store much more energy than C18 paraffin with the same volume, but with longer melting time; the usage of salt hydrates could save space and cost since less volume and consequently less number of blocks were needed to provide the required storage capacity compared to paraffin wax because of the higher volumetric energy storage density of the inorganic PCMs.

The aim of the present work is to develop a fast numerical method for prediction of the thermal behaviour of PCM enclosed in a container with a specific geometry, designed as an active element in a test thermal accumulator at the Technical University Sofia, Plovdiv Branch, Fig.1 [12]. The HTF is water entering from three tangential inlet pipes at the top of the tank and leaving from three tangential outlet pipes at the bottom. This device is a part of an experimental thermal solar installation with heat storage. The typical HTF inlet temperature is 65°C (from the solar collector) in charging mode and 15°C (tap water) in discharging mode.

The purpose of the present numerical simulation is to assess prior to the physical experiment the effect on the phase change process of the following factors: external temperature, HTF convection coefficient and natural convection inside the container.

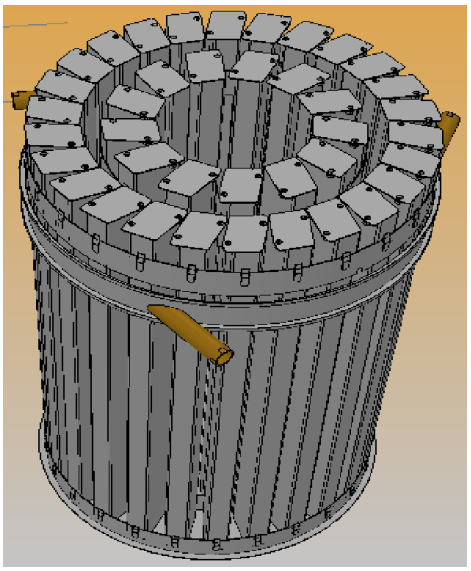

**Fig.1.** Inner construction of the latent thermal storage of the experimental thermal solar installation [12]

## NUMERICAL EXPERIMENT

### *Numerical Model*

The accepted approach for modelling the solidification/melting process is the enthalpy-porosity technique proposed in [13], employed in ANSYS Fluent [14]. This approach avoids tracking explicitly the melt interface. The fraction of the cell volume which is in liquid form, called the liquid fraction, is computed at each iteration based on the

enthalpy balance. The mushy zone, where the liquid fraction lies between 0 and 1, is modelled as a "pseudo" porous medium in which the porosity in each cell is set equal to the liquid fraction and decreases from 1 to 0 as the material solidifies, and hence the velocity drops to zero for solid state.

The transient thermal behavior of a single container with paraffin, a constituent part of the accumulator in Fig. 1, is considered. The mesh of the 3D computational domain comprises 26 000 tetrahedral elements. For the phase change process of the PCM in the container, the density difference between the solid and liquid phase is assumed negligible. The natural convection is expected to play an important role especially in a tall vertical tube like the unit under consideration, Fig. 1. The buoyant forces are modelled by the Boussinesq approximation; the reference temperature is equal to the melting temperature. The liquid phase of the PCM is assumed to be Newtonian and incompressible and the flow is laminar. In charging/discharging process, the governing equations for the liquid PCM [14] can be written as:

Continuity equation:

$$\nabla \boldsymbol{v} = 0. \quad (1)$$

Momentum equation:

$$\frac{\partial}{\partial t}(\rho \boldsymbol{v}) + \nabla(\rho \boldsymbol{v}\boldsymbol{v}) = -\nabla p + \nabla \boldsymbol{\tau} + \rho \boldsymbol{g} + \boldsymbol{F}, \quad (2)$$

where $\boldsymbol{v}$ is the velocity vector, $p$ is the static pressure, $\boldsymbol{\tau}$ is the stress tensor and $\rho \boldsymbol{g}$ and $\boldsymbol{F}$ are the vectors of gravitational and external body forces.

The momentum sink due to the reduced porosity in the mushy zone takes the following form:

$$\boldsymbol{S} = \frac{(1-\beta)^2}{(\beta^3+\varepsilon)} A_{mush} \boldsymbol{v}, \quad (3)$$

where $\beta$ is the liquid volume fraction, $\varepsilon$ is a small number (0.0001) to prevent division by zero, $A_{mush}$ $=10^5$ is the mushy zone constant.

Energy equation:

$$\frac{\partial}{\partial t}(\rho H) + \nabla(\rho \boldsymbol{v} H) = \nabla(k \nabla T). \quad (4)$$

The enthalpy $H$ consists of sensible enthalpy $h$ and latent heat $\Delta H$

$$H = h + \Delta H, \quad (5)$$

where $h = h_{ref} + \int_{T_{ref}}^{T} c_p dT$,

$\Delta H = \beta L$.

The latent heat content can vary between zero for solid and $L$ for liquid. The liquid fraction can be defined as:

$\beta = 0$ if $T < T_s$

$\beta = 1$ if $T > T_l$

$\beta = \frac{T - T_s}{T_l - T_s}$ if $T_s < T < T_l$,

where $T_s$ and $T_l$ are solidus and liquidus temperatures respectively.

Table 1 gives the values of the thermo-physical properties of the paraffin used in the calculations. The accepted constants are based on the data from [15] concerning E53 paraffin. The model does not take into account the experimental observations [15] that the paraffin properties depend on the temperature and the physical state. Moreover, according to the literature data [15], E53 paraffin undergoes two-step phase transition, the lower temperature transition is solid–solid (order-disorder) transition, while the higher temperature transition represents the solid-liquid phase change process. The present model assumes that in heating and cooling only solid–liquid transition occurs over the higher temperature range of 52-59$^o$C, yet the accepted value of the latent heat is the cumulative value of the two steps.

The container, made of stainless steel, is placed vertically, Fig.1, and its external dimensions are 40x80x950mm, the wall thickness is 1.5mm. The thermal accumulator in Fig. 1 is a part of an experimental hybrid solar system with heat storage. The equations are solved using the CFD software ANSYS FLUENT 13.0, based on finite volume technique. The following boundary conditions are assumed: no-slip conditions at the container's wall and constant temperature at all external surfaces $T=T_{wall}$. In charging mode the initial conditions are solid PCM with temperature $T_{in}$=51$^o$C, one degree lower than the solidus temperature, given in Table 1, in discharging mode $T_{in}$=60 $^o$C, one degree higher than the liquidus temperature, Table 1.

The details of the employed solution methods are as follows: (1) SIMPLE scheme of pressure-velocity coupling; (2) spatial discretization: Green-Gauss cell based for gradient, PRESTO for pressure, first order upwind for momentum and energy; (3) first order implicit transient

formulation. The under relaxation factors assumed for solution controls are: 0.3 for pressure, 1 for density and body forces, 0.2 for momentum, and 0.9 for liquid fraction update. For convergence absolute criteria, the values of the scaled residuals are: $10^{-4}$ for the continuity and velocity and $10^{-6}$ for the energy equation.

**Table 1.** Paraffin thermo-physical properties used in the calculations

| | |
|---|---|
| Solidus temperature, E53 [15], $T_s$, °C | 52 |
| Liquidus temperature, E53 [15], $T_l$, °C | 59 |
| Density(solid), E53 [15], kg/m$^3$ | 920 |
| Dynamic viscosity, kg/ms | 0.003 |
| Specific heat (solid), E53 [15], J/kgK | 1550 |
| Thermal conductivity (solid), E53 [15], W/mK | 0.34 |
| Latent heat of fusion, E53 [15], J/kg | 194110 |
| Thermal expansion coefficient, 1/K | 0.0001 |

*Model verification*

Similar set of ANSYS Fluent solution methods and settings was used in [16]. The computational model was experimentally verified by comparing the simulation results with experimental data for melting of paraffin wax n-octadecane (28.2°C melting temperature) encapsulated in a spherical container of glass with inside diameter of 101.66 mm. It was found that the prediction of the overall melting process was satisfactory, though the simulation suggested some faster melting rate than the experiment [16].

## RESULTS AND DISCUSSION

Macro-encapsulated E53 paraffin in a stainless steel container was considered as an active unit for thermal energy storage. The simulation studied the thermal behaviour of the unit at various temperatures of the external surfaces of the container, $T_{wall}$=15°C for discharging mode, $T_{wall}$= 65°C and 80°C for charging mode. All the surfaces were at constant temperature. Fig.2 shows the contour plots of the liquid fraction at 10, 15 and 20 min of the charging process in the middle-width plane parallel to the 80 mm face of the container. After 20 min charging the liquid fraction is 88%, and due to the buoyant forces the paraffin is stratified, liquid at the top, solid at the bottom. The stratification is illustrated by the contour plots of the temperature in Fig.3a. It can be seen in Fig.3b from the contour plots of the velocity y-component that, due to natural convection, there is an upward flow along the side walls of the container, and a downward flow in the central volume. Therefore, the convective heat transfer, often neglected in the simulations, affects substantially the picture of the melting process. However, as expected, it has negligible effect on the solidification in the container. This is illustrated by the identical patterns in the upper and bottom halves of the container in Fig.4, which presents solidification at 15°C of the external surfaces after 10min, 15min and 20min. This picture confirms that the natural convection in the container should be taken into consideration when organizing the fluid flows in the accumulator. Tan et al. [16] computationally and experimentally demonstrated that while conductive heat transfer was dominant in the initial stage of the phase change process, natural convection became dominant with the progress of the melting process. Ettouney et al. [17] found that natural convection was dominant during melting for upward flow of HTF and negligible for downward flow. It was observed there that the solidification process was dominated by conduction and independent of flow direction of HTF.

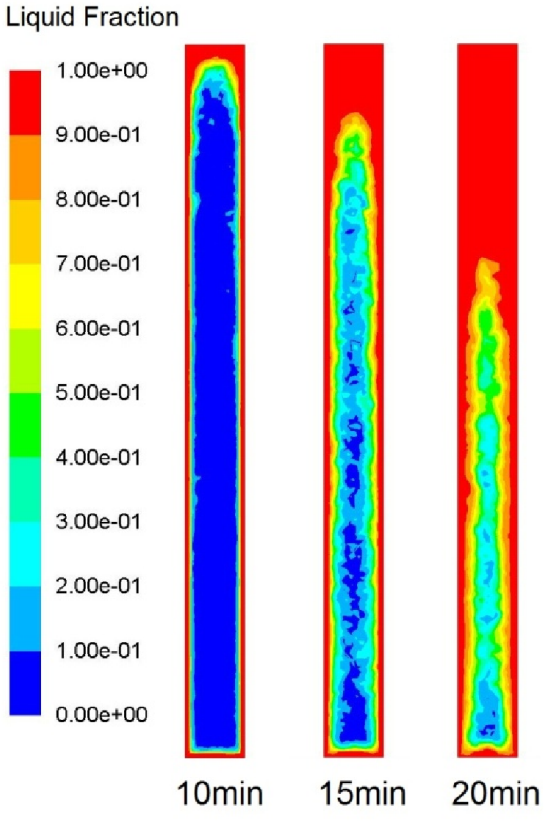


**Fig.2**. Contours of liquid fraction in the middle-width plane parallel to the 80 mm face, in charging at $T_{wall}$ = 80 °C

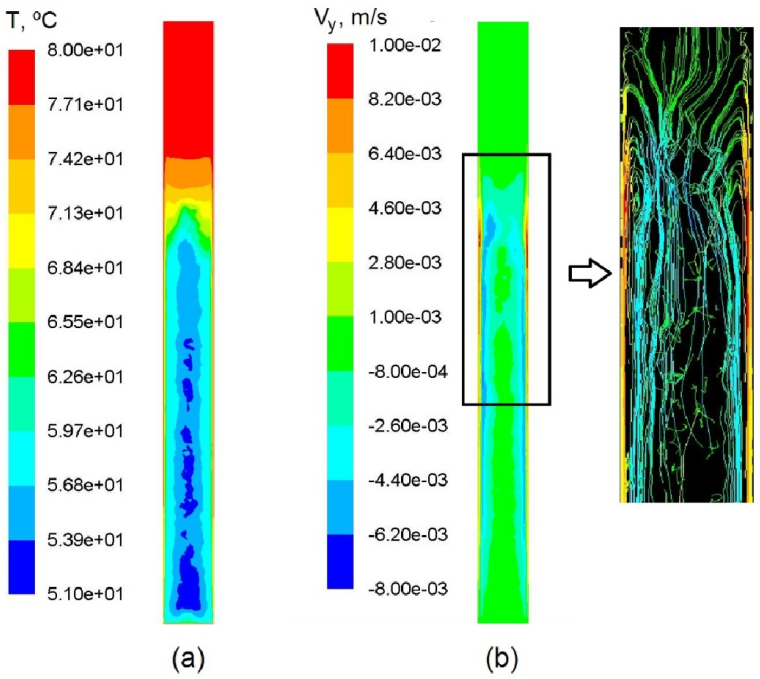


**Fig.3.** Contours of temperature $T$ (a) and y-component of velocity $v_y$ (b) in the middle-width plane parallel to the 80 mm face, in charging after 20 min at $T_{wall}$=80°C

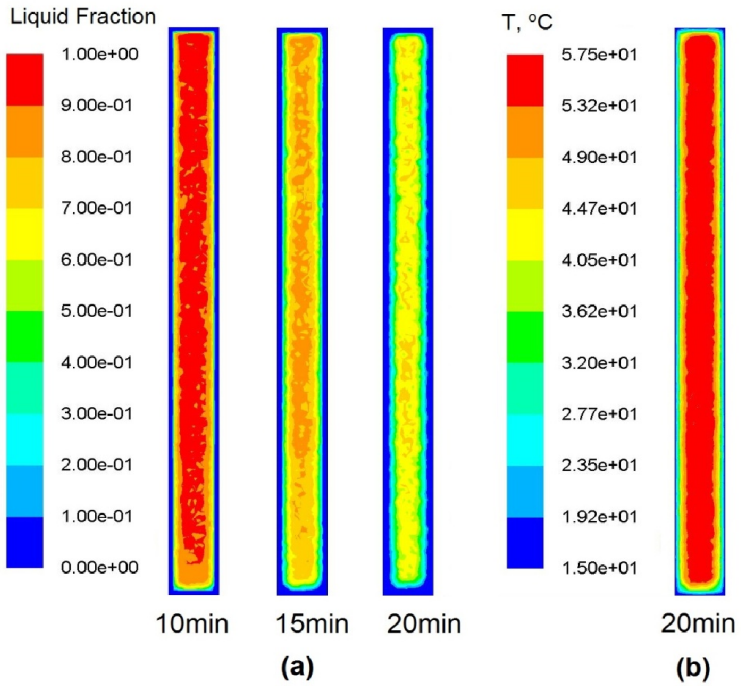


**Fig.4.** Contours of liquid fraction (a) and temperature $T$ (b) in the middle-width plane parallel to the 80 mm face, in discharging at $T_{wall}$=15°C

Fig.5 illustrates the effect of the external temperatures on the duration of the phase change process. During the phase transition, the liquid fraction in the total volume of the container lies between 0 when the total volume is in solid state and 1 when the total volume is in liquid state. A simulation was performed at a constant heat flux through the wall with a convective heat transfer coefficient α=3000 W/m$^2$K, calculated by the relation [18] for laminar boundary layer of water flow on a flat surface at a bulk fluid temperature $T_{fl}$=65°C. The results in Fig.5 in that case coincide with those calculated at a constant wall temperature $T_{wall}$=65°C. The explanation is that the thermal

resistance at the fluid-solid interface is low and the temperature difference between the fluid bulk and the solid surface of the container is negligibly small. The same was the reason for the observations in [11], where it was demonstrated that the storage material melting time was inversely proportional to the air convective heat transfer coefficient. However, it had major effect at lower values (10 and 15 W/m$^2$K, [11]) and less effect at higher convection coefficients (30 and 35 W/m$^2$K, [11]).

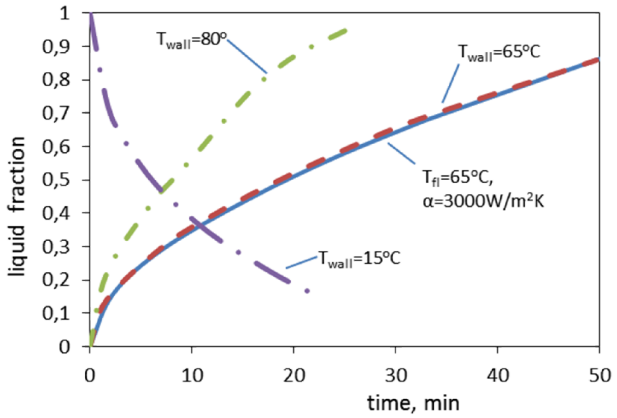


**Fig.5.** Computed liquid fraction in the total PCM volume (0 when the total volume is in solid state and 1 when the total volume is in liquid state) versus time in the phase change process

## CONCLUSIONS

The present simulation has obtained the flow pattern and temperature distribution in macro-encapsulated paraffin inside a rectangular container with specific dimensions designed as an active unit in a test heat accumulator of a thermal solar system. It demonstrates the effects on the melting/solidification process of the external temperature, the HTF conduction coefficient and the natural convection inside the PCM. A time efficient method using the ANSYS Fluent techniques for prediction of phase change processes has been tested. The calculated results correspond to the observations in the literature about the factors affecting PCM encapsulation. The simulations add information for better understanding and more precise prediction of the phase change process, which is necessary for the design of thermal energy storage systems.

## REFERENCES:


1 A. Sharma, V.V. Tyagi, C.R. Chen D. Buddhi, Review on thermal energy storage with phase change materials and applications, *Renewable and Sustainable Energy Reviews* 13, 318–345 (2009)

2 G.A. Lane, Encapsulation of heat of fusion storage materials. In: Proceedings of 2nd Southeastern *Conference on Application of Solar Energy*, 442–50 (1976).

3 G.A. Lane, Low temperature heat storage with phase change materials. *Int J Ambient Energy* 1, 155–68 (1980).

4 R.J. Wood, S.D. Gladwell, P.W.O. Callahar, S.D. Probert, Low temperature thermal energy storage using packed beds of encapsulated phase-change materials. In: *Proceedings of the International Conference on Energy Storage*, Brighton, UK, 145–58 (1981)

5 T. Saitoh, K. Hirose, High-performance of phase change thermal energy storage using spherical capsules. *Chem. Eng. Commun.* 41, 39–58 (1986)

6 /www.pcmproducts.net/

7 /www.rubitherm.com.

8 J. Wei, Y Kawaguchi, S Hirano, H. Takeuchi, Study on a PCM heat storage system for rapid heat supply, *Applied Thermal Engineering* 25, 2903–20 (2005).

9 P. B. Salunkhe, P. S. Shembekar, A review on effect of phase change material encapsulation on the thermal performance of a system, *Renewable and Sustainable Energy Reviews* 16 5603–16 (2012)

10 B. Zivkovic, I. Fuji, An analysis of isothermal phase change material within rectangular and cylindrical containers, *Solar Energy* 70, No. 1, 51–61 (2001)

11 M. Jradi, M. Gillott, S. Riffat, Simulation of the transient behaviour of encapsulated organic and inorganic phase change materials for low-temperature energy storage, *Applied Thermal Engineering* 59, 211-222 (2013)

12 A. Stoyanov, A. Georgiev, R. Popov, Experimental installation for investigation of latent heat accumulator as a part of hybrid system for air-conditioning, *Toplotehnika,* Tech. Univ. Varna 4, 2, 28 (2013)

13 V. R. Voller, C. Prakash, A fixed-grid numerical modelling methodology for convection-diffusion mushy region phase-change problems. *Int. J. Heat Mass Transfer* 30, 1709–20 (1987).

14 Theory Guide ANSYS Fluent v. 13.0.

15 E. M. Anghel, A. Georgiev, S. Petrescu, R. Popov, M. Constantinescu, Thermo-physical characterization of some paraffins used as phase change materials for thermal energy storage, *J Therm. Anal. Calorim.*, 117, 557–566 (2014)

16 F.L. Tan, S.F. Hosseinizadeh, J.M. Khodadadi, L. Fan, Experimental and computational study of constrained melting of phase change materials (PCM) inside a spherical capsule, *International Journal of Heat and Mass Transfer* 52, 3464–72 (2009)

17 H. Ettouney, H El-Dessouky, E. Al-Kandari, Heat transfer characteristics during melting and solidification of phase change energy storage process, *Industrial and Engineering Chemistry Research* 43, 5350–7 (2004)

18 J. H. Leinhard IV, J .H. Leinhard V, A heat transfer textbook, 3rd ed. Cambridge MA, Phlogiston press (2008)

*Bulgarian Chemical Communications, Volume 48, Special Issue E (pp. 195 - 198) 2016*

# Experimental analysis of a cold store integrated with phase change material: a case study

G. Alevay Kilic[1], Enver Yalcin[1], Ahmet Alper Aydın[*,2]

[1]*Department of Mechanical Engineering, Engineering Faculty of Balikesir University, 10145 Balikesir-TURKEY*
[2]*Department of Chemical Engineering, Faculty of Chemical and Metallurgical Engineering, Istanbul Technical University, 34469 Maslak, Istanbul-Turkey*

Thermal energy storage systems provide the potential to attain energy savings and reduce the environmental impact related to energy use. In this respect, phase change materials (PCMs) work as ''latent heat storage units'' which store or release large amounts of thermal energy. The aim of the presented study is to determine the function of PCM in an actively operating cold store at -18ºC during an operational failure or electricity shortage. The indoor temperature of the cold store, PCM temperature in the macrocapsules and ambient temperature are the continuously monitored parameters in this research. The results indicate that PCM macrocapsules, which cover 10% of the total heat transfer surface area, provide significant temperature maintenance under all ambient conditions and prominently extend the time to break the cold chain.

**Keywords:** cold store, phase change material (PCM), frozen storage, thermal energy storage, temperature maintenance

## INTRODUCTION

In the refrigeration and heating systems, latent heat storage is frequently used due to its high energy saving potential and high system efficiency. Since it requires a smaller volume per unit of stored energy and has a narrow temperature range for heat transfer via phase change, latent heat storage systems have attracted the interest of many researchers and many studies have been conducted on this subject [1-7]. Phase Change Materials (PCMs) are used to store energy and balance temperature changes in different fields, including electronic devices, automotive industry, buildings and heat storage systems [8-10]. In recent years, PCMs have also become a widespread solution as an alternative cooling and heating method in applications [11-13].

In frozen storage applications, aqueous salt solutions are one of the basic PCMs. However, adjusting their chemical composition to obtain desired thermal properties, subcooling, corrosion and thermal stability are some of the main difficulties [14]. Using a convenient PCM combination and encapsulation tool may lead to major benefits without the need for extra design changes in refrigeration systems or enclosures. Among these benefits, longer-term autonomy of the refrigerator, optimization of the compressor operating time, maintaining homogeneous temperature distribution in the refrigerator in case of a breakdown and coefficient of performance (COP) increase can be mentioned [15-17]. As the PCM increases the COP by 25%, PCM macrocapsule thickness of 5 and 10 mm show the same effect due to partial freezing of the material [18,19]. In this sense, determination of the PCM thickness in relation to thermal load is an important parameter. For instance, the usage of PCM plates thinner than 5 mm is recommended for household refrigerators [20].

The aim of this study is to monitor the indoor temperature changes of an actively operating cold store under frozen storage condition at -18ºC in the presence and absence of PCM load to present the useful function of PCM during an operational failure or electricity shortage. Besides, the effect of different ambient air temperatures on temperature changes insurfaces. the cold store is also discussed in detail.

## MATERIALS AND METHOD

The internal dimensions, i.e. the length, width and height (LxWxH) of the store are 212x113x218 cm, respectively. Within the cabin, the presented geometry in Fig.1a is established to circulate the air sweeping over the capsule surfaces. The side walls, ceiling and floor of the cabin contain polyurethane rigid foam blocks of 80 mm as main insulating material. Macrocapsules with PCM are mounted on the ceiling and the walls of the cabin and they cover about 10% of the total heat transfer surface area.

Fig.1b and Fig.1c show the positions of the sensors recording data and outer view of the cold store in the laboratory. The parameters measured by

* To whom all correspondence should be sent:
aydinal@itu.edu.tr

the sensors include the indoor temperature, PCM temperature in high-density polyethylene (HDPE) macrocapsules and ambient temperature. In this research, these three parameters are recorded with 10-second intervals.

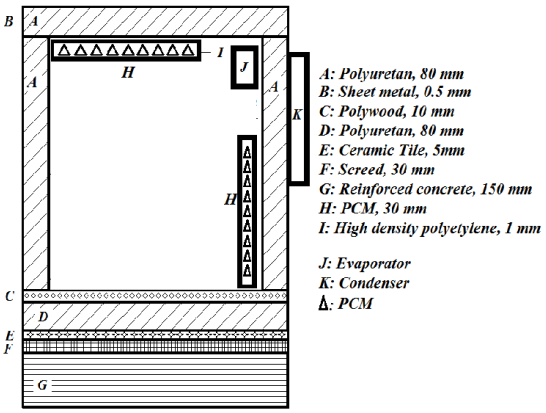


(a)

(b)

(c)

**Fig.1.** The cold store cabin: (a) Cross-sectional details, (b) inner view and (c) outer view

The PCM used in the study as heat storage medium is a commercial eutectic mixture. The thermophysical properties of the mixture are given in Table 1. In the experiments, 62 HDPE macrocapsules containing approximately 62 kg PCM were used and the the total surface area integrated with macrocapsules containing PCM was about 2.5 m2. Each experiment was repeated twice to observe the reproducibility of the data and the mean values have been reported.

Prior to monitor the indoor temperature changes under different conditions, the cold store was operated for 24 h to reach -18°C and equilibrated between -16°C and -18°C.

In data evaluation, -4°C has been taken as boundary value since it is the critical temperature for safety of some perishable goods."

**Table 1**. Thermophysical properties of the PCM used in the study

| | |
|---|---|
| Melting onset and peak temperatures, °C | -14.7/-10.7 |
| Viscosity, kg/m.s (25°C) | 0.0055 |
| Density, kg/m$^3$ (25°C) | 1.04 g/cm³ |
| Enthalpy, kJ/kg | 274.3 |

## RESULTS

In this research, the temperature changes in the PCM loaded cold store have been monitored at three different ambient air temperatures: (i) 24°C, (ii) 20°C and (iii) 13°C, whereas the thermal behavior of the cold store in the absence of PCM has been monitored at 24°C ambient air temperature as reference.

The repeated measurements indicate that the observed thermal changes are reproducible after equilibration of the cold store for 24 h between -16°C and -18°C and the observed fluctuations of the ambient temperature are ≤ ±2°C in the laboratory.

As it is given in Fig.2, the indoor temperature reaches -4°C in 5520 s (1.53 h) in the absence of PCM and breaks the frozen storage conditions when the ambient temperature is 24°C. It is relatively a short period of time in case of an operational failure.

The conducted runs with empty HDPE macrocapsules to observe the additional insulation effect of the macrocapsule material showed that the required time to reach -4oC was identical to the reference case, i.e. no significant additional insulation effect of the macrocapsule material. Therefore, it can be stated that the PCM load in the cold store cabin has a direct effect on indoor temperature maintenance. Although heat gain of the store changes with different ambient conditions, the PCM layer works both as an insulating layer and a latent heat storage volume. The resistance of PCM against heat transfer into the cold store functions in sensible heat form in solid and liquid phases and also, in latent heat form during phase change.

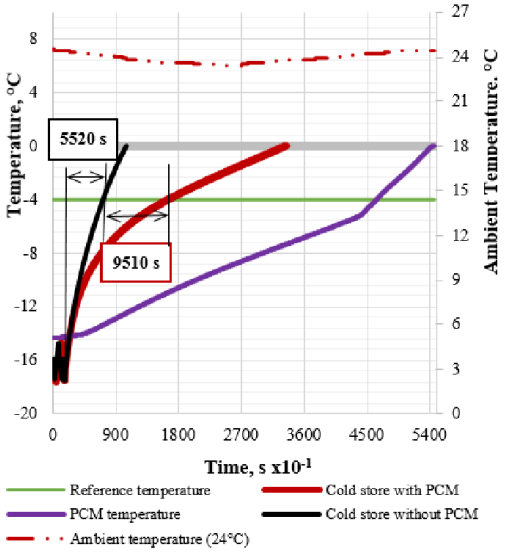


**Fig.2.** Cold store temperature changes with/ without PCM at 24°C ambient temperature

In the presence of PCM, the time period to reach -4°C shifts up to 15030 s (4.18 h), 21750 s (6.04 h) and 33210 s (9.23 h) at ambient temperatures of 24°C, 20°C and 13°C, respectively. Compared to the case without PCM load at 24°C in Fig. 2, the time period to break the cold chain is 9510 s (172%) longer in the presence of PCM macrocapsules, which cover about 10% of the total heat transfer surface area in the cold store.

The tabulated data in Table 2 indicate that in the case of lower ambient temperature levels, the PCM load provides longer temperature maintenance as a result of lower heat gain of the cold store from surrounding. Compared to the heat gain at 24°C, the time periods required to break the cold chain are 45% and 121% longer under 20°C and 13°C ambient conditions, respectively. The differences in temperature change curves in the cold store at different ambient temperatures are clearly seen in Fig.3.

**Table 2.** Changes in time to reach -4°C in cold store and PCM macrocapsules under different ambient conditions

| | 24°C | 24°C | 20°C | 13°C |
|---|---|---|---|---|
| **Cold store** | 5520 s | 15030 s | 21750 s | 33210 s |
| **% change in time** | - | 172%* | 45%** | 121%** |
| **PCM** | - | 44790 s | 45930 s | 76140 s |
| **% change in time** | - | - | 2.55% ** | 70%** |

* longer than the reference case at 24°C without PCM
** longer than the case at 24°C with PCM

As PCM layer functions as an insulating layer with its sensible heat and latent heat storage ability, the temperature changes in the PCM macrocapsules are also meaningful to monitor under different ambient temperature conditions. Although the cold chain is broken after -4°C, the PCM load continues to work as a temperature regulator and delays the time of indoor temperature to reach 0°C (Fig.3). Besides, the PCM itself reaches in 44790 s (12.44 h), 45930 s (12.75 h) and 76140 s (21.51 h) to -4°C at different ambient temperatures, which are long enough to provide sufficient thermal load for temperature maintenance in the cold store. The thermal behavior of the PCM is illustrated in Fig.4.

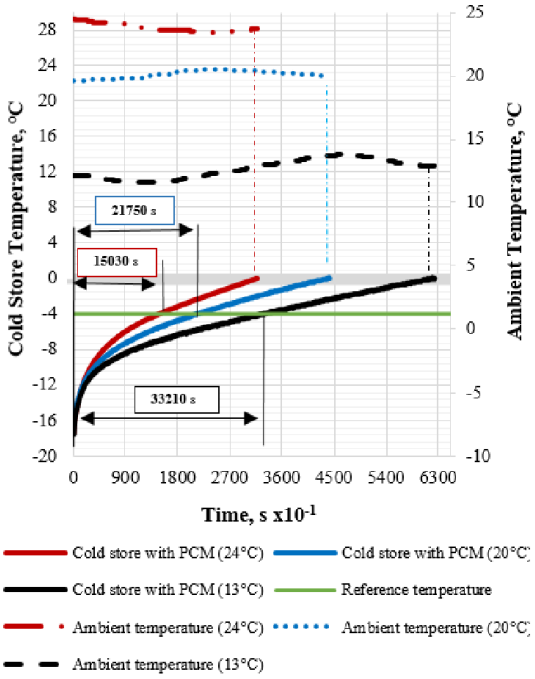


**Fig.3.** Cold store temperature changes with PCM under different ambient conditions

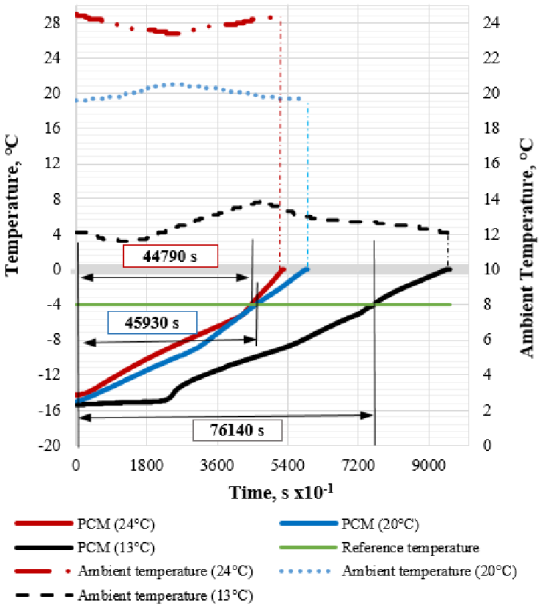


**Fig.4.** Temperature changes in PCM macrocapsules under different ambient conditions

## CONCLUSIONS

In this research, a cold store operating under frozen storage condition at -18ºC has been investigated to determine the useful function of the PCM load during an operational failure or electricity shortage. The indoor temperature change has been continuously monitored and the time required to reach -4°C, at which the frozen storage condition is broken, has been determined under different ambient conditions.

The results indicate that PCM load covering 10% of the total heat transfer surface area provides significant temperature maintenance under all ambient conditions and prominently extend the time to reach -4$^{o}$C.

In the case of highest heat gain from surrounding at 24$^{o}$C ambient temperature, the PCM load ensures 172% longer temperature maintenance period than the conventional cold store. At 13$^{o}$C ambient temperature, the thermal function of the PCM is much more effective and 9.23 h are needed to break the cold chain.

Since frozen storage conditions are very important for safety of the stored perishable goods, the presented research provides valuable data not only for cold stores, but also for refrigerated vehicles which are used for long-distance transportation. PCM macrocapsules might ensure lower fuel consumption related to continuous refrigeration, higher temperature stability with lower heat gain from surrounding and more flexible logistics planning.

## REFERENCES


1 A. Abhat, Sol. Energy, 30, 313, (1983).
2 B. Zalba, J.M. Marin, L.F. Cabeza, Appl. Therm. Eng., 23, 251, (2003).
3 M. Farid, A.M. Khudhair, S.A.K. Razack, Energy Convers. Manage., 45, 1597, (2004).
4 Y. Dutil Y., D. R. Rousse, N. B. Salah, Renewable and Sustainable Energy Rev., 15, 112, (2011).
5 C. Marques, G. Davies, G. Maidment, J. Evans, I. Wood, Proc. Inst. R., 14, 2, (2013).
6 A.A. Aydın, A. Aydın, Sol. Energy Mater. Sol. Cells, 96, 93, (2012).
7 A.A. Aydın, Sol. Energy Mater. Sol. Cells, 104, 102, (2012).
8 M. Okcu, Y. Varol, M. Fırat, Termodinamik (in Turkish), 266, (2014).
9 A.A. Aydın, Chem. Eng. J., 231, 477, (2013).
10 M. Bottarelli, M. Bortooni, Y. Su, C. Yousif, A.A. Aydın, A. Georgiev, Appl. Therm. Eng., 88, 369, (2015).
11 F. Regin, S.C. Solanki, J.S. Saini, Renewable Energy, 34, 1765, (2009).
12 M. Kenisarin, K. Mahkamov, Renewable and Sustainable Energy Rev., 11, 1913, (2007).
13 K.E. Omari, T. Kousksou, Y.L. Guer, Appl. Therm. Eng., 31, 3022, (2011).
14 E. Oró, A. De Gracia, Castell, M.M. Farid, L.F. Cabeza, Appl. Energy., 99, 513, (2012).
15 S. Yılmaz, H.O. Paksoy Subcooling in phase change materials used for cooling. In: Proceeding of Innostock. 2012, 13th International Conference on Energy Storage, Lleida, Spain.
16 S. Yılmaz, S.E. Altunbas, G. Kardas, et al. 2013. A new approach for testing corrosion behaviour of various metals in contact with phase change materials. Proceedings of 2nd International Conference on Sustainable Energy Storage, Dublin, Ireland.
17 Y. Yusufoglu, A. Apaydın, S. Yılmaz, Int. J. Refrig., 57, 173, (2015).
18 K. Azzouz, D. Leducq, D. Gobin, Int. J. Refrig., 31, 892, (2008).
19 K. Azzouz, D. Leducq, D. Gobin, Int. J. Refrig., 32, 1634, (2009).
20 C. Marques, G. Davies, G. Maidment, et al. 2010. Application of phase change materials to domestic refrigerators. In: Proceedings of IIR 9th International Conference on Phase-Change Materials and Slurries for Refrigeration and Air Conditioning, Sofia, Bulgaria.

*Bulgarian Chemical Communications, Volume 48, Special Issue E (pp. 199 - 205) 2016*

# Numerical simulation of latent heat storage with conductance enhancing fins

Nedžad R. Rudonja[1*], Mirko S. Komatina[1], Dragi Lj. Antonijević[2], Goran S. Živković[3]

*1University of Belgrade, Faculty of Mechanical Engineering, Kraljice Marije 16, Belgrade, Serbia*
*2Faculty of Applied Ecology, Singidunum University, Požeška 83a, Belgrade, Serbia*
*[3]University of Belgrade, Institute of Nuclear Sciences "Vinča", Laboratory for Thermal Engineering and Energy, P.O. Box 522, 11001 Belgrade, Serbia*

Precise understanding of heat transfer processes inside the latent thermal energy storage exposed to different initial and boundary conditions is crucial for development of optimized design and operating features of similar devices. The paper presents 3D numerical study of phase change material heat storage in the shape of vertical cylinder reservoir with axially placed heat source/sink equipped with variable number of conductance enhancing longitudinal rectangular fins. As the principally important observed is the case of vertically variable heat flux supplied to the phase change material during the melting process. The numerical modeling is based on the physical model of the process and is being carried out by Fluent software that uses finite volume method for solving continuity, momentum and energy equations. The coupling between pressure and velocity is based on the Semi-Implicit Pressure-Linked Equation (SIMPLE) algorithm. The results of numerical simulations are verified through the comparison with the own experimental results. Exemplary results for characteristic heat storage geometries and boundary conditions are presented and analyzed in the paper.

**Keywords:** thermal energy storage, phase change material, heat transfer fins, numerical simulation

## INTRODUCTION

The thermal energy storages (TES) utilizing phase change materials are used for eliminating the mismatch between energy supply and energy demand as well as for reducing energy consumption, operational costs and environmental impacts. Commonly, the phase change materials (PCM) provide high energy storage densities, by nearly constant phase change temperatures [1, 2]. Furthermore, the organic PCM (e.g. paraffin), have identical melting and solidification curve [3]. Nevertheless, most of the PCMs have low values of thermal conductivity and therefore the prolonged times of melting and solidification. A simple and reliable way for overcoming the issue of low PCM thermal conductivity is utilization of metal fins [2, 4, 5].

An accurate understanding of heat transfer processes inside TES operated with various PCMs and exposed to different initial and boundary conditions is crucial for development of optimized design and operating features of similar devices. Since the analytical methods of solving melting and solidification problem are applicable only to the limited numbers of problems [6], the approach of numerical modeling and simulation is applied. In the previous studies of similar problems [7, 8, 9] the heat transfer enhancement of PCM heat storage is analyzed based on the fins number or certain geometric feature (height, diameter, length, etc.).

* To whom all correspondence should be sent:
nrudonja@gmail.com

This study presents an improved approach where the heat transfer enhancement and the heat transfer surface variations are correlated through introduced feature named *Finned surface ratio*.

## PHYSICAL MODEL

The observed TES has the shape of vertical cylinder filled with the PCM (Fig. 1). The thermo–physical properties of the selected PCM - paraffin E53 (commercial grade wax), have been thoroughly determined and described previously [4].

Along the reservoir the heat source is placed axially. The heat source is represented by 2400 W electric heater (EH), placed inside the cylindrical steel shell with inner diameter of 54 mm and wall thickness of 3 mm. The shell is finned with longitudinal rectangular fins (160x500x3 mm) as shown in Fig.1. The height of the reservoir is 500 mm, and its inner diameter 400 mm.

The three cases were analyzed:

1. Steel shell without fins;
2. Steel shell finned with 6 longitudinal rectangular equidistant fins;
3. Steel shell finned with 12 longitudinal rectangular equidistant fins.

The tracking of heat transfer enhancement was carried out by finned surface ratio. The finned surface ratio is defined as the ratio of overall heat transfer surface area in contact with PCM in case with fins and in case of steel shell without fins, i.e. as follows:

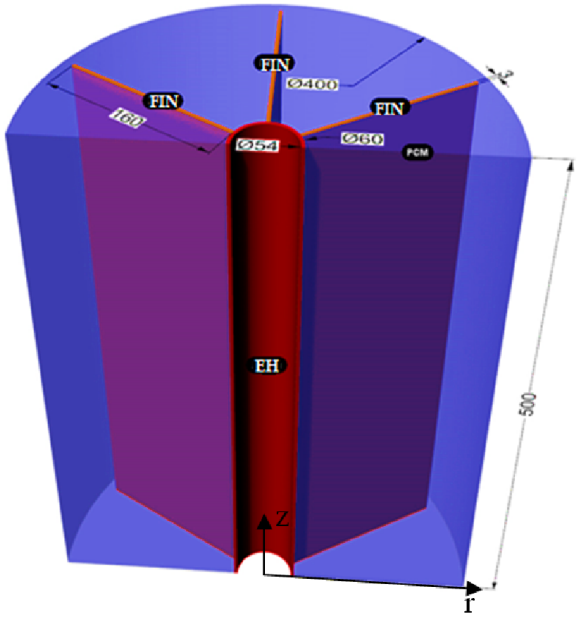


**Fig.1.** Cross section of TES physical model (case 2 - 6 longitudinal fins)

$$\gamma = \frac{n\left(2L_f Z_f + L_f \delta + 2Z_f \delta\right) + d\pi L_f - n\delta L_f}{d\pi L_f} \qquad (1)$$

where $n$ is total number of fins (0, 6 or 12), $L_f$ – fin length (500 mm), $Z_f$ – fin height (160 mm), $\delta$ – fin thickness (3 mm), $d$ – outer diameter of steel shell (60 mm). For the observed cases (1, 2 and 3), finned surface ratios calculated based on Eq.1. are: 1; 11.3 and 21.5.

## ASSUMPTIONS

The following assumptions and simplifications have been made in order to enable mathematical description of transient heating and melting processes inside the three-dimensional physical model of the observed TES.

It has been assumed that the liquid phase of PCM behaves as non-compressible Newtonian fluid and that its flow inside the TES is laminar by character.

Further, the PCM enthalpy increase due to the viscous energy dissipation (PCM fluid phase internal friction) is neglected, as well as the heat transfer by thermal radiation inside the TES.

The joints between the cylindrical heater shell and the longitudinal fins have been considered ideal, i.e. the heat transfer contact resistance at the joints has been neglected.

The natural convection heat transfer in the liquid phase has been modeled using Businesq approximation, considering that the fluid density change is minimal.

The volume change due to the insertion of supplemental fins has been neglected (e.g. relative difference of PCM volume for the heat transfer surface with 6 fins and for the case without fins, amounts approximately 1.5%).

Finally, the heat flow through the outer walls of TES reservoir has been neglected, i.e. TES has been considered adiabatically insulated during the observed PCM melting process.

## MATHEMATICAL MODEL

The physical model consists of three separate domains: domain of fin, domain of shell and domain of phase changing material. Since the domains of fin and shell remain in solid state during the observed processes, they could be well described by the energy equation in cylindrical ($r, \varphi$ and $z$) coordinates (Fig.1):

$$\frac{\partial T}{\partial t} = \frac{\lambda}{\rho c_p}\left[\frac{1}{r}\frac{\partial}{\partial r}\left(r\frac{\partial T}{\partial r}\right) + \frac{1}{r^2}\frac{\partial^2 T}{\partial \varphi^2} + \frac{\partial^2 T}{\partial z^2}\right] \qquad (2)$$

where $T, \lambda, \rho$ and $c_p$ stand for temperature, thermal conductivity, density and specific heat capacity of shell and fin.

In order to fully describe the transient heat transfer and fluid flow processes in the domain of PCM, the system of mathematical model equations should be comprised of continuity equation (3), momentum equations (4-10), energy equation (11) and enthalpy-porosity equation (12). Enthalpy-porosity equation is part of technique introduced by Voller [10] where the melt interface is not tracked explicitly. Instead, the liquid fraction of the cell volume that is in liquid form is associated with each cell in the domain.

The continuity equation for the observed PCM domain is:

$$\frac{\partial u_r}{\partial r} + \frac{1}{r}\frac{\partial u_\varphi}{\partial \varphi} + \frac{\partial u_z}{\partial z} + \frac{u_r}{r} = 0 \qquad (3)$$

where $u_r, u_\varphi$ and $u_z$ are flow velocity components for the main directions of cylindrical coordinate system.

The momentum equations of the observed PCM domain, for the main directions of the cylindrical coordinate system are:

$$\rho\left[\frac{\partial u_r}{\partial t}+u_r\frac{\partial u_r}{\partial r}+\frac{u_\varphi}{r}\frac{\partial u_r}{\partial \varphi}-\frac{u_\varphi^{\,2}}{r}+u_z\frac{\partial u_r}{\partial z}\right]$$
$$=-\frac{\partial p}{\partial r}-\left[\begin{array}{l}\frac{1}{r}\frac{\partial\left(r\tau_{rr}\right)}{\partial r}+\frac{1}{r}\frac{\partial \tau_{r\varphi}}{\partial \varphi}\\ -\frac{\tau_{\varphi\varphi}}{r}+\frac{\partial \tau_{rz}}{\partial z}\end{array}\right]+S_r, \quad (4)$$

$$\rho\left[\begin{array}{l}\frac{\partial u_\varphi}{\partial t}+u_r\frac{\partial u_\varphi}{\partial r}+\frac{u_\varphi}{r}\frac{\partial u_\varphi}{\partial \varphi}\\ +\frac{u_r u_\varphi}{r}+u_z\frac{\partial u_\varphi}{\partial z}\end{array}\right]=$$
$$-\frac{1}{r}\frac{\partial p}{\partial \varphi}-\left[\begin{array}{l}\frac{1}{r^2}\frac{\partial\left(r^2\tau_{r\varphi}\right)}{\partial r}\\ +\frac{1}{r}\frac{\partial \tau_{\varphi\varphi}}{\partial \varphi}+\frac{\partial \tau_{\varphi z}}{\partial z}\end{array}\right]+S_\varphi. \quad (5)$$

$$\rho\left[\frac{\partial u_z}{\partial t}+u_r\frac{\partial u_z}{\partial r}+\frac{u_\varphi}{r}\frac{\partial u_z}{\partial \varphi}+u_z\frac{\partial u_z}{\partial z}\right]=$$
$$-\frac{\partial p}{\partial z}-\left[\frac{1}{r}\frac{\partial\left(r\tau_{rz}\right)}{\partial r}+\frac{1}{r}\frac{\partial \tau_{\varphi z}}{\partial \varphi}+\frac{\partial \tau_{zz}}{\partial z}\right] \quad (6)$$
$$+\frac{\rho g\beta_V\left(h-h_{ref}\right)}{c_p}+S_z,$$

where $\beta v = 0.000255\ K^{-1}$ is the thermal expansion coefficient, while $h$ and $h_{ref}$ are PCM enthalpies for certain temperature $T$, and for average PCM phase change temperature ($T_{ref} = 323\ K$), respectively. On this way the density variation with temperature was only considered in the body force term using the Boussinesq approximation to take into account the buoyancy effect (Eq.6.). The components of the viscous stress tensor in equations (4-6) are calculated as (7-8):

$$\tau_{rr}=-\mu\left[2\frac{\partial u_r}{\partial r}-\frac{2}{3}\left(\nabla\cdot\vec{u}\right)\right],$$
$$\tau_{\varphi\varphi}=-\mu\left[2\left(\frac{1}{r}\frac{\partial u_\varphi}{\partial \varphi}+\frac{u_r}{r}\right)-\frac{2}{3}\left(\nabla\cdot\vec{u}\right)\right], \quad (7)$$
$$\tau_{zz}=-\mu\left[2\frac{\partial u_z}{\partial z}-\frac{2}{3}\left(\nabla\cdot\vec{u}\right)\right].$$

$$\tau_{r\varphi}=\tau_{\varphi r}=-\mu\left[r\frac{\partial}{\partial r}\left(\frac{u_\varphi}{r}\right)+\frac{1}{r}\frac{\partial u_r}{\partial \varphi}\right],$$
$$\tau_{z\varphi}=\tau_{\varphi z}=-\mu\left[\frac{\partial u_\varphi}{\partial z}+\frac{1}{r}\frac{\partial u_z}{\partial \varphi}\right], \quad (8)$$
$$\tau_{zr}=\tau_{rz}=-\mu\left[\frac{\partial u_z}{\partial r}+\frac{\partial u_r}{\partial z}\right],$$

where $\mu$ is dynamic viscosity of PCM.

The additional pressure drop due to the liquid flow through the porous media [10] can be calculated for the main directions of cylindrical coordinate system as:

$$S_r=-A_{mush}\frac{\left(1-x_m\right)^2}{x_m^{\,3}+\varepsilon}u_r,$$
$$S_\varphi=-A_{mush}\frac{\left(1-x_m\right)^2}{x_m^{\,3}+\varepsilon}u_\varphi, \quad (9)$$
$$S_z=-A_{mush}\frac{\left(1-x_m\right)^2}{x_m^{\,3}+\varepsilon}u_z,$$

where $A_{mush}$ and $\varepsilon$ are default values for porous area (*mushy zone*) constant ($10^5$) and small number (0.001) for preventing division by zero. The participation of liquid phase in total PCM mass (porosity) $x_m$ is referred to as the lever rule as a function of actual temperature in the observed location and known liquidus and solidus temperatures ($T_l$ and $T_s$) of PCM.

$$x_m=0,\ T<T_s,$$
$$x_m=\frac{T-T_s}{T_l-T_s},\ T_s<T<T_l, \quad (10)$$
$$x_m=1,\ T_l<T.$$

The energy equation for the observed PCM domain is:

$$\frac{\partial\left(\rho H\right)}{\partial t}+u_r\frac{\partial\left(\rho H\right)}{\partial r}+\frac{u_\varphi}{r}\frac{\partial\left(\rho H\right)}{\partial \varphi}$$
$$+u_z\frac{\partial\left(\rho H\right)}{\partial z}=\lambda\left[\begin{array}{l}\frac{1}{r}\frac{\partial}{\partial r}\left(r\frac{\partial T}{\partial r}\right)+\\ \frac{1}{r^2}\frac{\partial^2 T}{\partial \varphi^2}+\frac{\partial^2 T}{\partial z^2}\end{array}\right], \quad (11)$$

where $H$ stands for enthalpy of PCM.

Finally, the system of equations closes with Brent-Voller [10] enthalpy-porosity equation that

characterizes the relation between PCM enthalpy and its porosity (defined as PCM liquid phase participation in total PCM mass):

$$H = h + \Delta H = h + x_m h_{sl}. \quad (12)$$

where $h_{sl}$ is latent heat of fusion for the PCM melting at given temperature.

The boundary conditions defining the mathematical model integration domains are given for the surfaces shown in Fig.2.

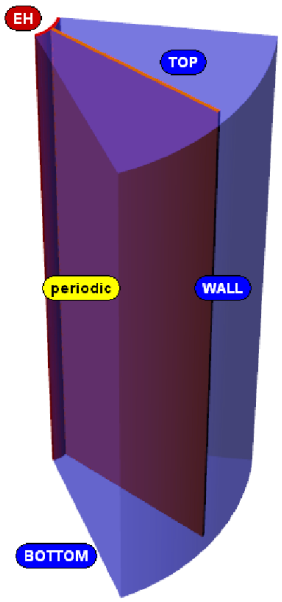


**Fig.2.** Boundary surfaces of the domains

**Table 1.** Initial and boundary conditions

| | Initial | Boundary | Conditions |
|---|---|---|---|
| HEATER | $T$ = 293 K | Top | $\dot{q} = 0$ |
| | | EH | $\dot{q}$ (Eqns.13) |
| | | Bottom | $\dot{q} = 0$ |
| PCM | $T$ = 293 K | Top | $\mu \frac{\partial u_i}{\partial x_j} \approx 0$ , $\dot{q} = 0$ |
| | $\vec{u}$ = 0 m/s | Wall | $\vec{u} = 0$ , $\dot{q} = 0$ |
| | | Bottom | $\vec{u} = 0$ $\dot{q} = 0$ |
| | | *Periodic* | Periodic b.c. |
| FINS | $T$ = 293 K | Top | $\dot{q} = 0$ |
| | | Bottom | $\dot{q} = 0$ |

The boundary condition that describes the heat transfer process from the electrical heater to the PCM, at the surface of the steel shell, has been previously experimentally determined [4] as:

$$\dot{q} = 21000 - \frac{64000 \cdot (\exp(-5.322 \cdot z) - 1)}{5.322}, \quad (13)$$

where $\dot{q}$ is specific heat flux, and $z$ axial coordinate as given in Fig.1.

The overview of the applied initial and boundary conditions for the performed calculations is given in Table1.

## NUMERICAL SIMULATION

The proposed mathematical model is solved numerically by use of *FLUENT* software. The discretization of the mathematical model equations in this CFD program is based on the division of the defined domains into the finite number of control volumes (subdomains), effectuated through the appropriate mash generation, in which the value of the observed variables are calculated. The differential equations of the mathematical model (2-12) are integrated by time and volume for each of the control volumes.

The coupling between pressure and velocity was conducted by the Semi-Implicit Method for Pressure-Linked Equations (SIMPLE) algorithm [11]. The PRESTO scheme [11] was used for discretization of the pressure correction equation, while for the momentum and energy equations the first order upwind discretization scheme was used.

The time step of the utilized numerical scheme, proven by convergence testing, has been 1s. In total 200 iterations per time step provided convergence of the solutions.

The criteria for convergence of the numerical solutions were residual values of the considered equations, namely $10^{-4}$ for the continuity equation and the momentum equation, and $10^{-6}$ for the energy equation. The residual values as well as the values of utilized under-relaxation factors were determined based on the literature recommendations [12]. The values of under-relaxation factors for pressure, body force, momentum, density, energy and porosity, were: 0.3, 1.0, 0.2, 1.0, 1.0, and 0.9, respectively.

The values of thermophysical properties of the utilized PCM material (density $\rho$, specific heat capacity $c_p$, thermal conductivity $\lambda$, dynamic viscosity $\mu$, solidus $T_s$ and liquidus $T_l$ temperatures and latent heat od fusion $h_{sl}$) as well as the properties of the other materials existing in subdomains (i.e. materials used for shell and fins), mandatory for the numerical solving of mathematical model equations, are listed in Table 2.

**Table 2.** Thermophysical characteristics of the utilized materials

| Var. | Unit | PCM | Cu | Steel | Al |
|---|---|---|---|---|---|
| $\rho$ | $\frac{kg}{m^3}$ | 842 | 8978 | 8030 | 2719 |
| $c_p$ | $\frac{J}{kgK}$ | 3000 | 381 | 502.48 | 871 |
| $\lambda$ | $\frac{W}{mK}$ | 0.36 *s*<br>0.91 *s-l*<br>0.18 *l* | 387.6 | 16.27 | 202.4 |
| $\mu$ | $Pas$ | 0.005 | – | – | – |
| $T_s$ | $K$ | 313 | – | – | – |
| $T_l$ | $K$ | 333 | – | – | – |
| $h_{sl}$ | $\frac{J}{kg}$ | 155881 | – | – | – |

## NUMERICAL RESULTS

The numerical calculations have been performed for the three cases of physical model. In order to speed up the simulations, axial symmetry of the observed cases has been used, i.e. only one radial cut of the domain have been analyzed. For example, the temperature distribution in PCM, in case of the heating surface geometry with 6 longitudinal fins, after 60 min of heat supply is shown in Fig.3, whilst Fig.4 shows temperature distribution for the same case after 120 min of heating.

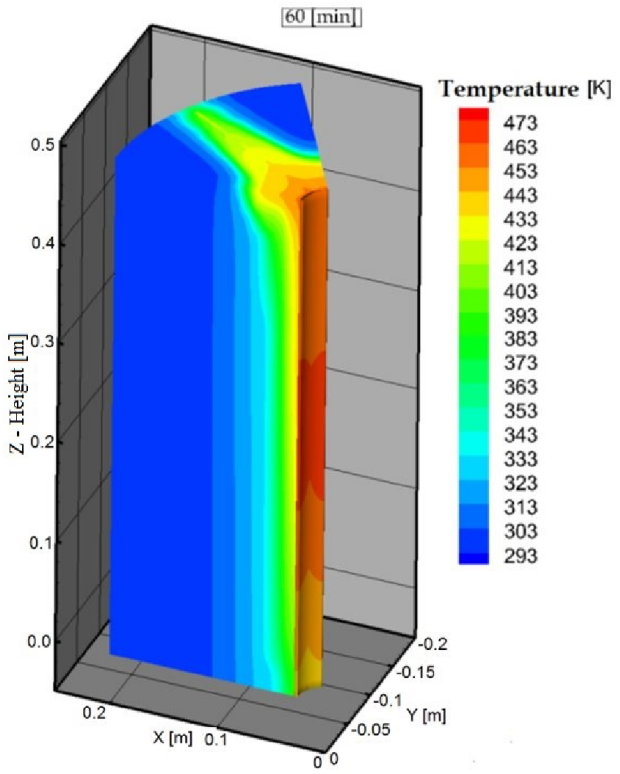


**Fig.3.** Temperature field inside TES with 6 fins after 60min of heating

The results of extensive numerical simulations, performed for the observed TES geometries, enabled derivation of functional dependences of heat transfer surface area (represented by dimensionless finned surface ratio) and time needed for full PCM melting by various initial and boundary conditions.

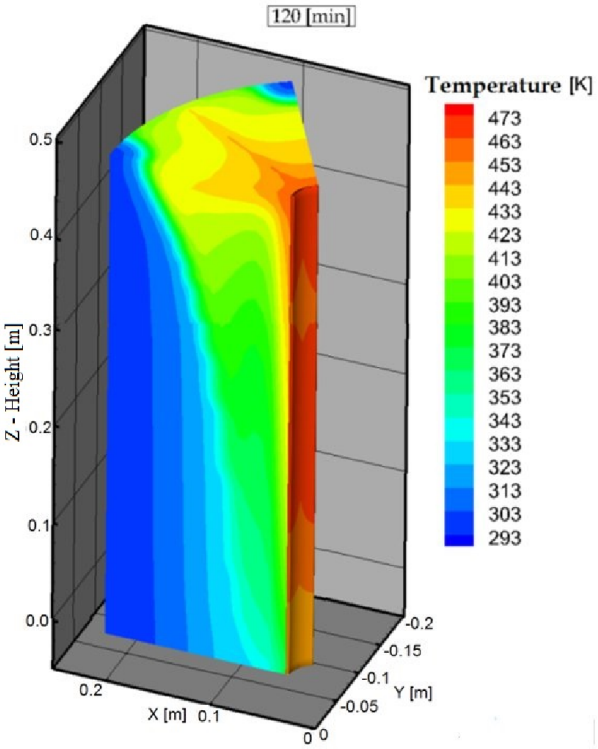


**Fig.4.** Temperature filled inside TES with 6 fins after 120min of heating

An example of such dependence, for copper fins, and initial and boundary conditions given in Table 1, is shown in Fig.5. It is noticeable that increasing the heat transfer surface, by adding the longitudinal rectangular fins to the heater, improves the heat transfer in TES and substantially decreases overall PCM melting time. Compared to the finless shell, adding of 6 fins, with the given geometry ($\gamma = 11.3$), accelerates the PCM melting approximately 4.4 times, i.e. the overall melting time amounts 22.7% of the melting time with finless heater (in the case of the same heat flux supplied to the PCM). In case of 12 fins ($\gamma = 21.5$) the heat transfer is expectedly further improved, and overall melting time amounts only 12% of the time needed in the case of finless heater.

In order to examine the influence of the applied fin material on the process of heating and melting of PCM, the simulations have been performed with three different fin materials: copper, steel and aluminum (Table 2). Increased fin material thermal conductivity contributes significantly to the heat

flow in radial direction, enabling higher temperatures of the fin towards the fin tips and thus supplying more heat to the further radial zones of the cylindrical PCM reservoir. For example, by the boundary and initial conditions given in Table 1, utilization of copper fins provides a relative decrease of overall melting time of 49.4% compared to steel fins, and of 8.6% compared to aluminum fins of the same shape, number and size (Fig.6).

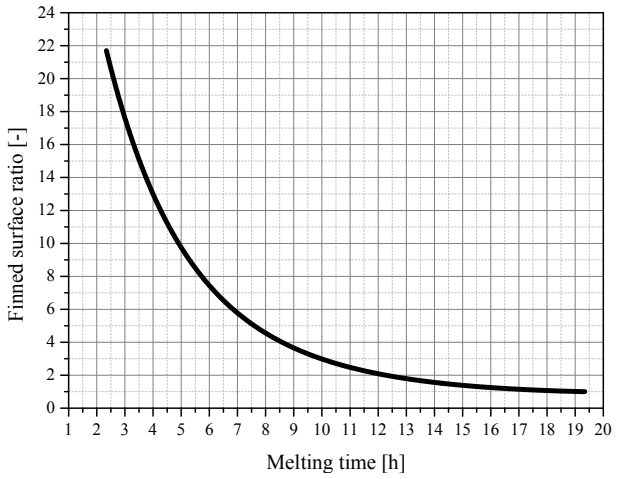


**Fig.5.** Dependence of PCM melting time upon heat transfer surface area (Finned surface ratio)

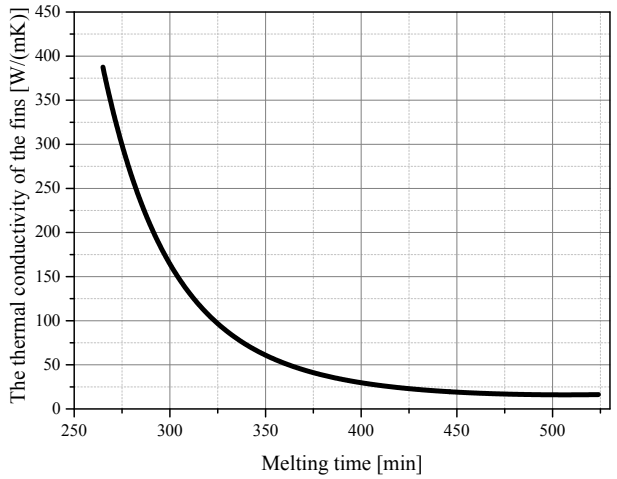


**Fig.6.** Dependence of PCM melting time upon thermal conductivity of fin (the 6 fins TES)

## EXPERIMENTAL VERIFICATION OF NUMERICAL RESULTS

In order to verify the results of numerical solving of the mathematical model, the comparison with the own experimental results is performed. The experimental investigations were performed at laboratory TES installation shown in Fig.7 and thoroughly described in [4].

**Fig.7.** Experimental installation

The experimental verification of the results is performed by observing and comparison of the PCM temperatures in several indicative locations of TES, during the melting process. For the illustration, the temperature readings of thermocouples, at locations $B_2$ *(r = 90 mm, z = 280 mm)* and $C_2$ *(r = 150 mm, z = 280 mm* are compared to the corresponding numerical results. The resemblance and conformity of the temperature curves derived experimentally and numerically is excellent (Fig.8 and Fig.9), both by their character overlapping and by the closeness of the absolute values during the process.

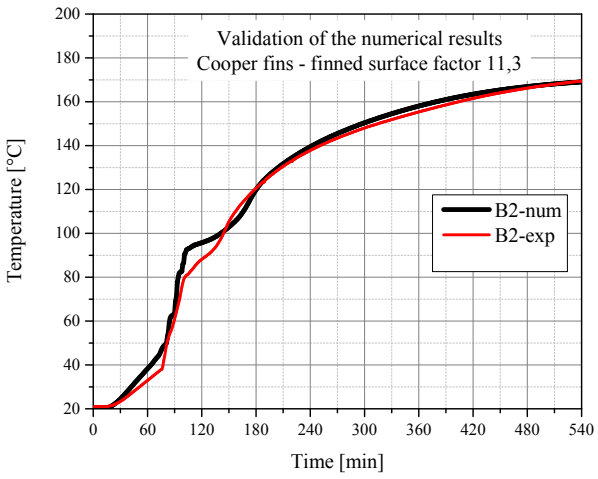


**Fig.8.** Temperature at location $B_2$ determined numerically and experimentally

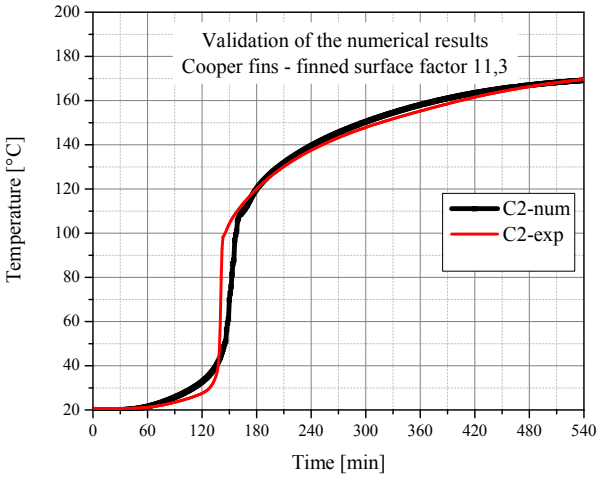


**Fig.9.** Temperature at location $C_2$ determined numerically and experimentally

## CONCLUSION

The longitudinal rectangular fins attached to the axially placed heater of the cylindrical TES with PCM, have been used for reduction of the prevailing thermal resistances caused by low thermal conductance of paraffin and for the stimulation of PCM heating and melting.

The proposed mathematical model of the processes inside TES has been solved numerically and the results compared to the characteristic results obtained experimentally. For a sharpened observation of the interrelations between enlarged heat transfer surfaces and achieved process improvements, the dimensionless finned surface ratio has been introduced. It has been concluded that the overall melting time of PCM inside the TES, by the observed initial and boundary conditions, decrease exponentially with the finned surface ratio increase.

An excellent agreement between the results of PCM temperature change in the control locations obtained numerically and experimentally has been demonstrated. The experimental and numerical temperature curves almost overlap in most TES locations. Thus, it has been concluded that the proposed mathematical model and the numerical procedure can be implemented for analysis and calculations of heating and melting processes of a PCM of known thermophysical characteristics utilized within a cylindrical TES, with longitudinal rectangular fins, of various size and design.

## ACKNOWLEDGMENT

The authors wish to thank the Ministry of Education, Science and Technological Development of Republic of Serbia, for financing projects III42011, TR 33042 and OI 176006.

## REFERENCES

1 A. Waqas, Z. Ud Din, *Renewable and Sustainable Energy Reviews,* 18, 607 (2013).
2 K.A. Ismail, C.L.. Alves, and M.S. Modesto, *Applied Thermal Engineering* , 21, 53 (2001).
3 A. Lázaro, E. Günther, H. Mehling, S. Hiebler, J.M. Marín, B. Zalba, *Measurement Science and Technology*, 17, 2168 (2006).
4 N. Rudonja, M. Komatina, G. Zivkovic, D. Antonijevic, *Thermal Science,* 136 (2015).
5 T. Rozenfeld, Y. Kozak, R. Hayat, G. Ziskind, *International Journal of Heat and Mass Transfer,* 86, 465 (2015).
6 H.H. S.A. Argyropoulos, *Modelling and Simulation in Materials Science and Engineering,* 4, 371 (1996).
7 A.H. Mosaffa, F. Talati, M.A. Rosen, H.B. Tabrizi, *International Communications in Heat and Mass Transfer,* 39, 318 (2012).
8 A. Castell, C. Solé, M. Medrano, J. Roca, L.F. Cabeza, D. García, *Applied Thermal Engineering,* 28, 1676 (2008).
9 S. Mat, A.A. Al-Abidi, K. Sopian, M.Y. Sulaiman, A.T. Mohammad, *Energy Conversion and Management*, 74, 223 (2013).
10 A.D. Brent, V.R. Voller, and K.J. Reid, *Numerical Heat Transfer,* 13, 297 (1988).
11 S. Patankar, Numerical heat transfer and fluid flow, McGraw-Hill Book Company, (1980).
12 A.R. Darzi, M. Farhadi, and K. Sedighi, *Applied Mathematical Modelling*, 36, 4080 (2012).

*Bulgarian Chemical Communications, Volume 48, Special Issue E (pp. 206 - 209) 2016*

# Synthesis and properties of microencapsulated phase change materials for thermal energy storage materials

Yeliz Konuklu[1,2*], Halime Ö. Paksoy[3]

[1]*Ömer Halisdemir University, Department of Chemistry, Nigde, Turkey*
[2]*Ömer Halisdemir University, Nanotechnology Application and Research Center, Nigde, Turkey*
[3] *Cukurova University, Department of Chemistry, Adana, Turkey*

This work presents and discusses the microencapsulation of pentadecane in polystyrene shell as thermal energy storage materials. The emulsion polymerisation method was used for the microencapsulation process. Styrene (S) was used as monomer to obtain polystyrene (PS) and ethylene glycol dimethacrylate was used as crosslinking agents. The influence of the core:shell mass ratio on the encapsulation process and the physical properties of the resulting microcapsules have been studied. The surface morphologies of the microencapsulated phase change materials (microPCMs) were studied by scanning electron microscopy (SEM) and the thermal properties of the MicroPCMs were investigated by differential scanning calorimetry (DSC). SEM photographs showed that these microPCMs have relatively spherical profiles with diameter ranging from 10 to 80 μm. It was determined that, the phase change enthalpies of melting and freezing were about 83.2 J/g and 81.8 J/g, respectively. The results show that pentadecane was microencapsulated successfully and its properties very suitable for thermal energy storage applications

**Keywords*:*** phase change material, thermal energy storage, latent heat, polystyrene

## INTRODUCTION

Heating and cooling are the main energy-consuming sectors in many countries [1]. Therefore it can be said that developing new energy storage devices are as important as developing new sources of energy [2]. Phase change materials (PCMs) which can be used as thermal energy storage material provides a high heat storage density and has the capability of storing a large amount of heat during the phase change process with a small variation of PCM volume and temperature [3]. Microencapsulated phase change materials have a wide range in thermal energy storage applications [4]. PCMs such as paraffin and fatty acids are microencapsulated with the purpose of make PCMs easier and safer to handle, increase the heat transfer area and protect material from environment [5].

Many studies use paraffin wax hydrocarbon mixtures as thermal energy storage materials [6]. Most of the researchers working on the microencapsulation of PCM have based their work on alkanes, waxes or paraffins [7]. Pentadecane which was used as core material in this study is known as saturated aliphatic hydrocarbon with the chemical formula C15H32. It has a suitable melting temperature (8.720C) and large latent heat storage capacity (176.15 J/g) especially for cooling applications.

* To whom all correspondence should be sent:
ykonuklu@nigde.edu.tr

Recently, styrene and styrene copolymers have been utilized in a wide range of experiments as shell materials for PCM microcapsules [8-13].

This work mainly focuses on microencapsulation of pentadecane in polystyrene shell as thermal energy storage materials. The properties of microPCMs have been characterized by scanning electron microscopy (SEM), differential scanning calorimetry (DSC) and Fourier transform infrared (FTIR) spectral analysis.

## EXPERIMENTAL

Pentadecane purchased from Sigma was used as a PCM. Styrene (>99%; Sigma Aldrich Company, USA) was used as a shell material; ethylene glycol dimethacrylate was used as a crosslinking agent and it was distilled before use. The initiator of ammonium peroxodisulfate (Merck, Germany) and other analytical reagents (tert-butylhydroperoxide (70%; Merck, Germany), Triton X-100 (Merck, Germany), iron (II) sulfate 7-hydrate ($FeSO_47H_2O$) (Panreac, Spain), and sodium thiosulfate ($Na_2O_3S_2$) (Merck, Germany)) were used without further purification. All experiments were conducted with distilled water.

A typical emulsion polymerization process was used in this study [8]. The chemicals and amounts that were used during the microenoencapsulation process are summarized in Table 1.

First solution (I) was prepared and then stirred for 30 minutes at 40˚C. Then second solution (II) was added slowly to solution I and stirring was

continued at 1000 rpm. Then, third solution (III) was added to the emulsion and heated to 95˚C. The solution was stirred for 3-4 hours and then was cooled to room temperature and washed with water five times. Finally, it was separated by filtration and dried at a room temperature for 72 hours. In this study two different core material:shell ratios 1: 1, 1.5:1, respectively, were chosen to prepare the microPCM1, and microPCM2.

**Table 1.** Emulsion copolymerization recipe

| | İngredients | Amount |
|---|---|---|
| I | Water | 30 ml |
| | Pentadecane | 10 g |
| | Triton X100 | 0,4 g |
| II | Styrene | 10 g |
| | EGDMA | 4 g |
| | $FeSO_4.7H_2O$ solution | 0,5 ml |
| | Amonyum persulfat | 0.25 g |
| III | $Na_2O_3S_2$ | 0.06 g |
| | tert-butylhydroperoxide | 0,25 ml |

The morphology of microPCMs was analyzed by SEM (JEOL JSM-600). The thermal properties of pentadecane and microPCMs were measured using a DSC and the (Perkin Elmer Diamond) with a heating/cooling rate of 5˚C/min in the range of -15–30˚C. During DSC analysis, about 5 mg of sample was used. DSC analyses were repeated three times for each sample. The thermal properties data were calculated from the average of three measurements. The determination of the phase change material content in the microPCMs followed from the formula:

$$PCM\% = \frac{\Delta \text{HmicroPCMs}}{\Delta \text{HPCMs}} \times 100\% \qquad (1)$$

where ΔHmicroPCMs is the melting enthalpy of the micro-PCMs; ΔHPCMs is the melting enthalpy of the PCMs.

FTIR spectra of pentadecane and microPCMs were obtained in the spectral wavelength range of 400–4000 $cm^{-1}$, using a Perkin Elmer FTIR spectrometer with Attenuated Total Reflectance (ATR) at room temperature.

## RESULTS AND DISCUSSION

In the microencapsulation of pentadecane emulsion polymerization method were used. The geometrical profile of the microcapsules was analyzed by SEM. As can be seen clearly, the microcapsules seen in Fig.1 were spherical without broken particles; the particle size distribution was approximately uniform with diameter ranging from 10 to 80 µm. SEM results confirm that pentadecane encapsulated successfully in this study.

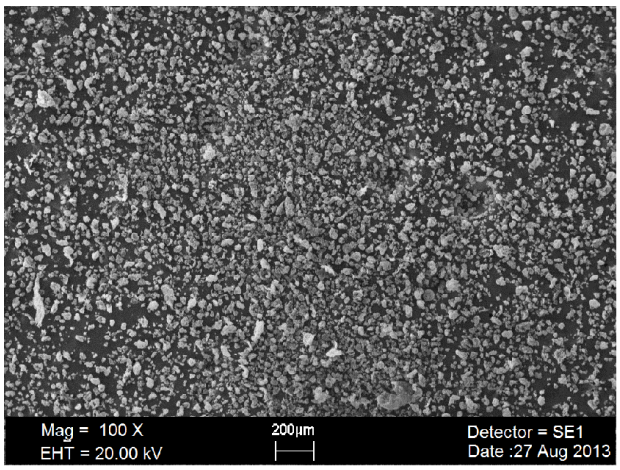


(a)

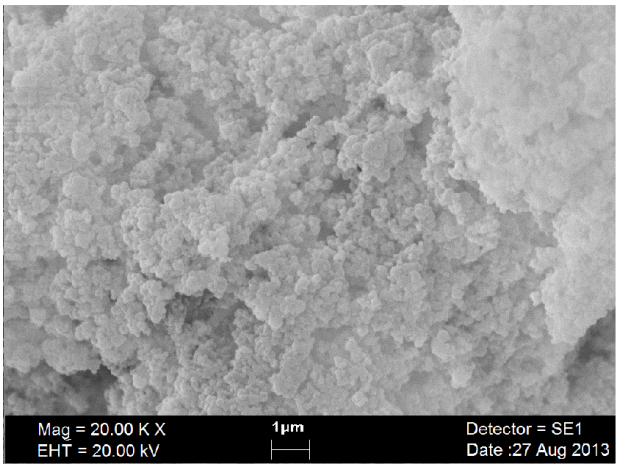


(b)

**Fig.1.** SEM micrographs of MicroPCM

DSC curves of pentadecane and microPCMs were shown in Fig.2 to Fig.4 and the results are summarized in Table 2. From the DSC, temperatures of melting and freezing were determined as 8.7 and 8.0°C for pentadecane; 8.1 and 8.0 °C for microPCM1 and 8.2 and 8.3 °C for microPCM2. The latent heats of melting and freezing were found to be 176.1 and −187,2 J/g for pentadecane; 68.7 and −66.5 J/g for microPCM1 and 83.2 and −81.8 J/g for microPCM2, respectively. The microencapsulation ratio of pentadecane was calculated as 39 wt % and 47 % respectively for microPCM1 and microPCM2 by using Equation 1.

As expected, increasing the amount of core material led to an increase in the encapsulation ability and latent heat storage capacity.

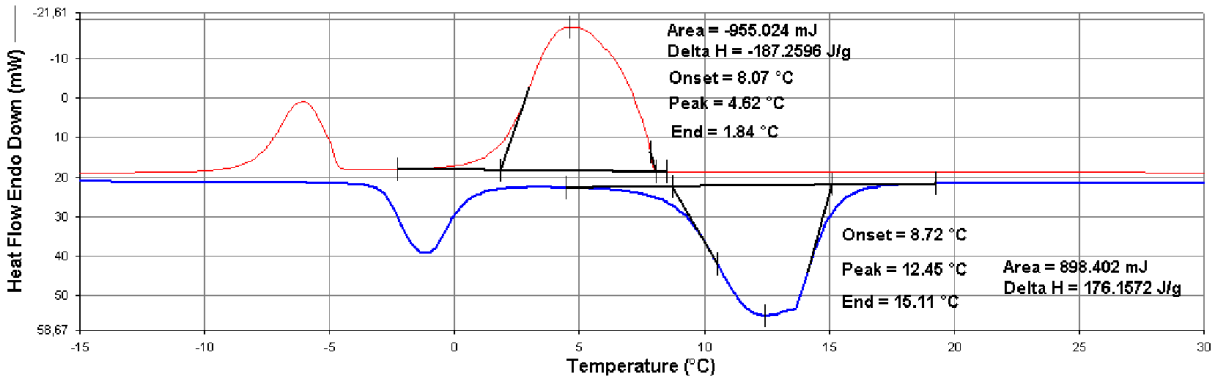


**Fig.2.** DSC Curves of Pentadecane

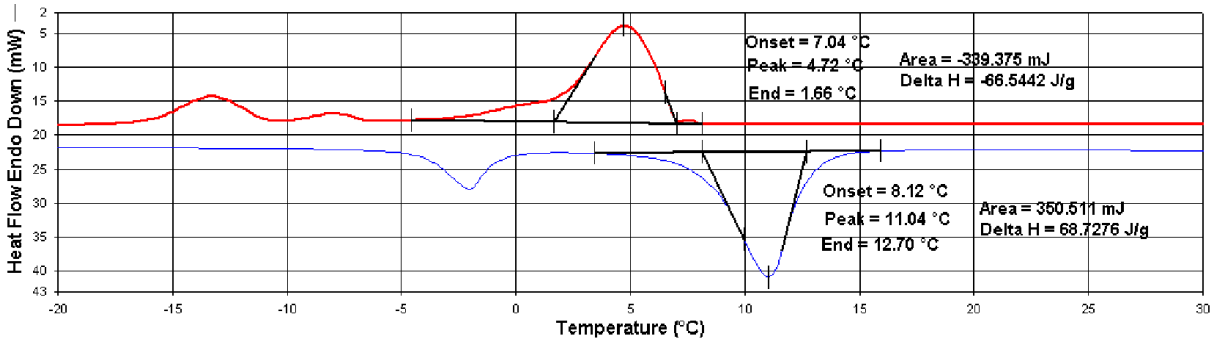


**Fig.3.** DSC Curves of MicroPCM1

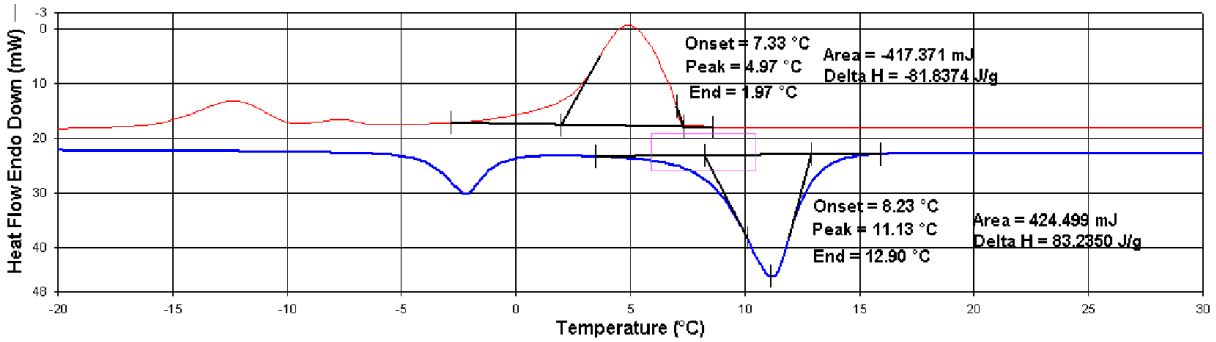


**Fig.4.** DSC Curves of MicroPCM2

**Table 2.** Thermal properties of pentadecane and MicroPCM

| Sample | Core:Shell | Tom(°C) | Tpm(°C) | Tem(°C) | Hm (J.g$^{-1}$) | Toc(°C) | Tpc(°C) | Tec(°C) | Hc (J.g$^{-1}$) | pentadecane content (wt%) |
|---|---|---|---|---|---|---|---|---|---|---|
| Pentadecane | - | 8.72 | 12.45 | 15.11 | 176.15 | 88.07 | 4.62 | 1.84 | 187.25 | 100 |
| microPCM1 | 1:1 | 8.12 | 11.04 | 12.70 | 68.72 | 78.04 | 4.72 | 1.66 | -66.54 | 39.01 |
| microPCM2 | 1.5:1 | 8.23 | 11.13 | 12.90 | 83.23 | 78.33 | 4.97 | 1.97 | -81.83 | 47.25 |

$T_{om}$: Onset melting temperature of DSC curve.
$T_{oc}$: Onset crystallizing temperature of DSC curve.
$T_{pc}$: Crystallizing peak temperature of DSC curve.
$T_{pm}$: Melting peak temperature of DSC curve.
$T_{ec}$: Endset crystallizing temperature of DSC curve.
$T_{em}$: Endset melting temperature of DSC curve.
$H_c$: Crystallization enthalpy of PCMs in DSC curve
$H_m$: Melting enthalpy of PCMs in DSC curve.

The chemical structure was investigated using Fourier transformed infrared spectrophotometer.

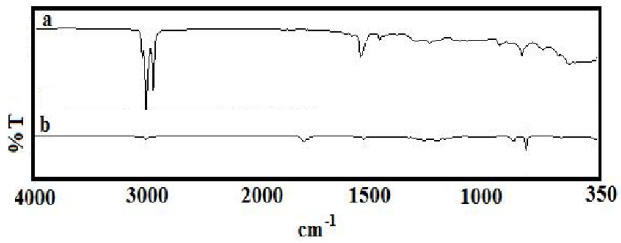


**Fig.5.** FTIR of (a) pentadecane and (b) microencapsulated pentadecane

The FTIR spectra of pentadecane and microencapsulated pentadecane are presented in Fig.5. Pentadecane which were used in this study are characterized with absorptions due to C–H stretching and bending. It is obvious that there is a double peak at a wave number of 3000–2850 $cm^{-1}$ caused by the C–H stretching vibration. Additionally, the C–H scissoring (1470–1450 cm−1), methyl rock (1370–1350 cm−1), and long-chain methyl rock (725–720 cm−1) are noted in this spectrum like as reported before [8]. It can be concluded that although the peaks corresponding to C-H stretching vibration and C–H scissoring are overlapped with PS shell material, some of the characteristic peaks belonging to the core material slightly preserve itself after microencapsulation.

## CONCLUSIONS

Alkanes, which were used as core materials in this study, are appropriate for many thermal energy storage applications due to their suitable melting temperatures ($8.72^0$C) and large latent heat storage capacity (176.15 J/g) and the fact that they do not have toxic properties. In this research, pentadecane was microencapsuled with a polystyrene shell via an emulsion polymerization technique. DSC results confirm that microencapsulated pentadecane could be considered to have good potential for energy storage. The DSC results revealed that the melting temperature and latent heat of microPCM1 and microPCM2 were 8.1 $^0$C ; 68.7 J/g and $8.2^0$C ; 83.2 J/g respectively. The microencapsulation ratio of pentadecane was calculated as 39 wt % and 47 % respectively for microPCM1 and microPCM2. As expected, increasing the amount of core material led to an increase in the encapsulation ability and latent heat storage capacity. SEM micrographs showed that the microencapsulated pentadecane had approximately spherical profiles. Based on all results; we recommend the prepared pentadecane/polystyrene microcapsules for thermal energy storage applications as novel microPCM with latent heat storage capacities and properties.

## ACKNOWLEDGEMENTS

The authors would like to thank The Scientific & Technical Research Council of Turkey (TUBITAK) (The Project Code: TUBITAK 111M614) for their financial support for this study.

## REFERENCES

1 Paksoy, H., Evliya, H., Bozdag, S., Mazman, M., Konuklu, Y., Turgut, B., ... & Beyhan, B., *International Journal of Global Warming*, 1(1-3), 253-269.
2 Sharma, A., Tyagi, V. V., Chen, C. R., & Buddhi, D. *Renewable and Sustainable energy reviews*, 13(2), 318-345, (2009).
3 Zhou, D., Zhao, C. Y., & Tian, Y., *Applied energy*, 92, 593-605, (2012).
4 Konuklu, Y., Ostry, M., Paksoy, H. O., & Charvat, P.. *Energy and Buildings*, 106, 134-155, (2015).
5 Özonur, Y., Mazman, M., Paksoy, H. Ö., & Evliya, H., *International Journal of Energy Research,* 30(10), 741-749, (2006).
6 Kumano, H., Saito, A., Okawa, S., Takeda, K., & Okuda, A., *International journal of heat and mass transfer*, 48(15), 3212-3220, (2005).
7 Zalba, B., Marín, J. M., Cabeza, L. F., & Mehling, H. *Applied thermal engineering*, 23(3), 251-283, (2003).
8 Konuklu, Y., Paksoy, H. O., & Unal, M., *Applied Energy*, 150, 335-340, (2015).
9 L. Sánchez, P. Sánchez, A. de Lucas, M. Carmona, J.F. Rodríguez, Colloid Polym Sci, 285 (12), 1377–1385, (2007).
10 L. Sánchez-Silva, J.F. Rodríguez, A. Romero, A.M. Borreguero, M. Carmona, P. Sánchez, *Chem Eng J*, 157 (1), 216–222, (2010).
11 G.H. Ma, Z.G. Su, S. Omi, D. Sundberg, J. Stubbs, *J Colloid Interface Sci*, 266 (2), 282–294, (2003).
12 D.P. Otto, H. Vosloo, W. Liebenberg, M.M. de Villiers, *Eur J Pharm Biopharm*, 69 (3), 1121–1134 (2008).
13 Sarı, A., Alkan, C., Döğüşcü, D. K., & Biçer, A. *Solar Energy Materials and Solar Cells*, 126, 42-50, (2014).

*Bulgarian Chemical Communications, Volume 48, Special Issue E (pp. 210 - 213) 2016*

# An ultrasonic-assisted direct impregnation method for preparation of diatomite-based phase change material nanocomposites

Yeliz Konuklu[1,2*], Orkun Ersoy[2,3]

[1]*Omer Halisdemir University, Department of Chemistry, Nigde, Turkey*
[2]*Omer Halisdemir University, Nanotechnology Application and Research Center, Nigde, Turkey*
[3]*Omer Halisdemir University, Faculty of Engineering, Geological Engineering, Nigde, Turkey*

Diatomite is an important natural raw material and the nanotube structures of diatomite are important in the preparation of composites. The nanotube structure of diatomite protects the phase change material from their environment. This work aims to develop leakage-free, thermally stable natural diatomite/phase change material nanocomposites (NanoCPCMs) by the ultrasonic-assisted direct impregnation method for thermal energy storage applications. This work uses diatomite and paraffin as the supporting and phase change materials, respectively. The diatomite-based form-stable nanoCPCMs were analyzed via scanning electron microscopy and differential scanning calorimetry. Paraffin leakage of nanoCPCMs was determined at 95˚ C by water bath for 45 minutes. At the end of test, thermal stability at 95˚ C evaluated with DSC analysis. The results show that the leakage-free NCPCMs were synthesized successfully for thermal energy storage applications.

**Keywords**: phase change material, diatomite, paraffin, thermal energy storage, latent heat

## INTRODUCTION

Diatomite is an important natural raw material with significant reserves in Turkey (44.2 million tons). Although we have large reserves of this raw material, our use of diatomite is insufficient. The responsible use and evaluation of natural minerals has the potential to significantly augment the national economy. For the evaluation of natural reserves such as diatomite in recent years, the preparation of diatomite/phase change material nanocomposites (NanoCPCMs) research has gained momentum [1, 2, 3, 4]. The nanotube structures of diatomite are important in the preparation of composites. PCMs are moved into nanotubes in the construction of composites; channels and phase changes occur in these tubes and surface area increases as in microencapsulation which may lead to better heat transfer characteristics. The nanotube structure of diatomite also protects the sensitive materials from their environment [1].

Tang et al. (2015) prepared shape-stabilized fatty acid eutectics and diatomite composites by absorbing liquid fatty acid eutectics into diatomite [2]. The lauric acid (LA)/diatomite composite phase change materials (PCMs) were prepared using a direct impregnation method by Fu et al. (2015). The melting and freezing temperatures of composite PCM were 40.9 °C and 38.7 °C, respectively.

In Li et al. (2011), a series of binary fatty acids were absorbed in diatomite by the fusion adsorption method to prepare shape-stabilized PCMs. The microstructure and thermal property of the prepared shape stabilized PCMs were tested.

Paraffins can be used as energy storage materials due to their availability in a large temperature range [5]. In our previous studies we developed an easy and industrially applicable impregnation process for preparation of diatomite-based phase change material nanocomposites for thermal energy storage applications [1]. For this purpose, a series of nanoCPCMs with different paraffin: diatomite mass ratios were prepared. Proposed method for preparation of diatomite-based phase change material nanocomposites can be used in large scale industrial fabrication for latent heat thermal energy storage systems applicable at high temperatures [1]. In this study we add two new steps including ultrasonic treatment before and during impregnation in order to increase efficiency. To the best of our knowledge, among all available phase change material/diatomite studies, no study has been reported on the preparation of NanoCPCMs with an ultrasonic treatment before and after impregnation. In this study, a thermally stable diatomite/phase change material nanocomposite (NanoCPCMs) was prepared for thermal energy storage applications.

The properties of composites have been characterized by scanning electron microscopy (SEM) and differential scanning calorimetry (DSC).

* To whom all correspondence should be sent:
ykonuklu@nigde.edu.tr

## EXPERIMENTAL

Paraffin 42–44 with purity above 98.0% (Merck, Germany; melting point; 42–44 °C) was used without further treatment as phase change material. Diatomite was used as supporting material for PCMs. Raw diatomite was in rock form including numerous consolidated individual shells. In order to separate each shell, raw diatomite was treated with ultrasonic probe in distilled water for 10 mins with 100% amplitude-1 cycle settings (UP400S, Hielscher, Germany).

The composite samples used in this work were manufactured by the direct impregnation method with ultrasonic bath. During the preparation of composites; firstly paraffin and diatomite were heated with a bain-marie method at 60 °C until the PCM was completely melted and mixed with hand. In the next step stirring and heating process were continued on a magnetic stirrer for 30 minutes. The final mixture was ultrasonically agitated for 30 minutes and at the end of process, composites were dried in an open air at 40°C for 48 h.

The morphological analysis of composites were analyzed using SEM (Zeiss EVO40). All samples were coated with a layer of gold prior to the observation. Thermal properties of core material and composites such as melting, crystallizing points and latent heats were measured by differential scanning calorimetry (DSC, Perkin Elmer Diamond) with a heating/cooling rate of 5˚C/min in the range of 10–60˚C. During DSC analysis, about 5 mg of sample was used.

In order to determine the leakage behavior and thermal properties of NanoCPCMs, PCMs and NanoCPCMs were heated to 95° C in a water bath for 45 minutes. At the end of 45 minutes, DSC analyses were performed.

## RESULTS AND DISCUSSION

In order to analyse the morphological properties of NCPCMs SEM analysis was carried out, as reported in the micrograph (Fig.1). It can be seen that the paraffin is completely dispersed into the pores of diatomite used as the supporting material. Treatment with ultrasonic probe had a destructive effect on diatom frustules. However, porous frustule walls protected paraffin from environmental factors as a supporting matrix and phase changes occurred in nanopores of diatomite frustule walls even though the whole frustule structure was damaged due to sonication.

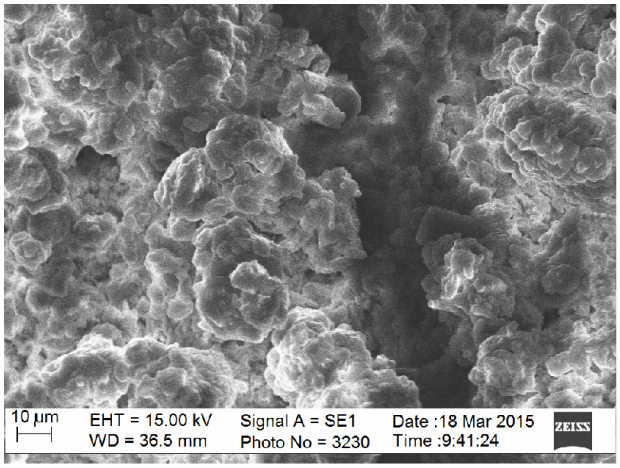


**Fig.1.** SEM images of CPCM

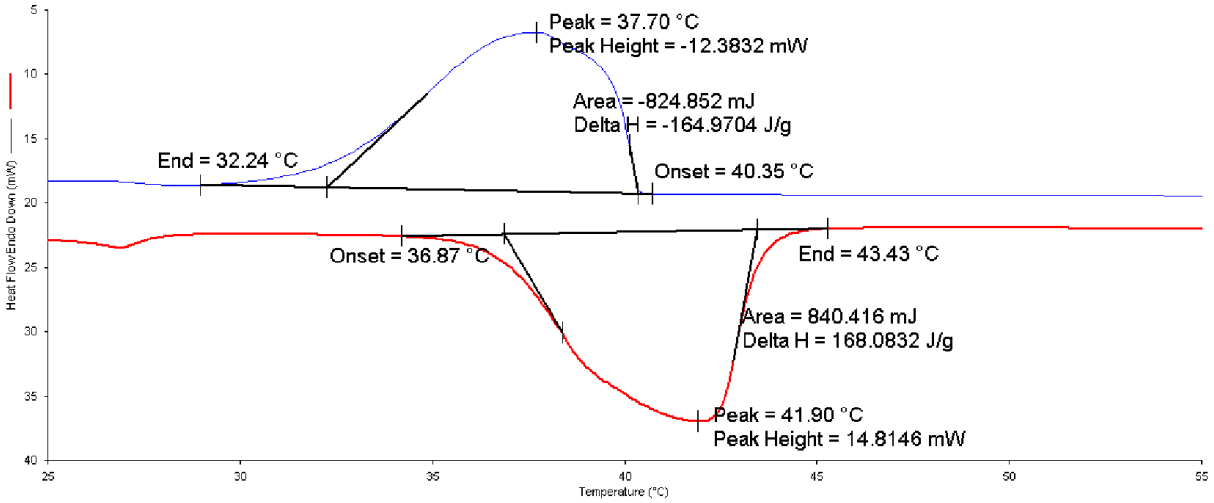


**Fig.2.** DSC Curves of paraffin

In order to investigate the presence of the PCM in the diatomite frustules, DSC analysis was carried out. The DSC curves of the paraffin and prepared NanoCPCMs are shown in Fig.2 to Fig.4. The

detailed melting and freezing temperatures and latent heat are presented in Table 1. The melting and freezing temperatures and latent heats of paraffin/diatomite nanocomposite were measured as 37,79 °C and 41,05 °C as well as 53,90 J/g and 57,67 J/g respectively. Based on obtained DSC results the prepared paraffin/diatomite composite could be a good alternative for solar thermal applications according to our previous studies for the studied temperature ranges [1].

In order to determine the leakage behavior and thermal stabilities of NanoCPCMs, PCMs and NanoCPCMs were heated to 95° C. Fig.4 shows DSC curve of NanoCPCMs treated at 95° C after 45 min. The DSC results are summarized in Table 1. We recommend prepared nanocomposites for thermally stable and leakage-free applications above 95 °C. The comparison of the energy storage capacity of NanoCPCMs prepared in this study and nanocomposites prepared in our previous study [1] are given in Table 2. Ultrasonic treatment didn't reduce paraffin content in diatomite mineral even though the whole frustule structure was damaged due to sonication. Pores on remaining walls of frustules from the whole structure were enough to protect the phase change material from environment. We recommend paraffin/diatomite composites prepared by an ultrasonic-assisted direct impregnation method as thermal energy storage materials.

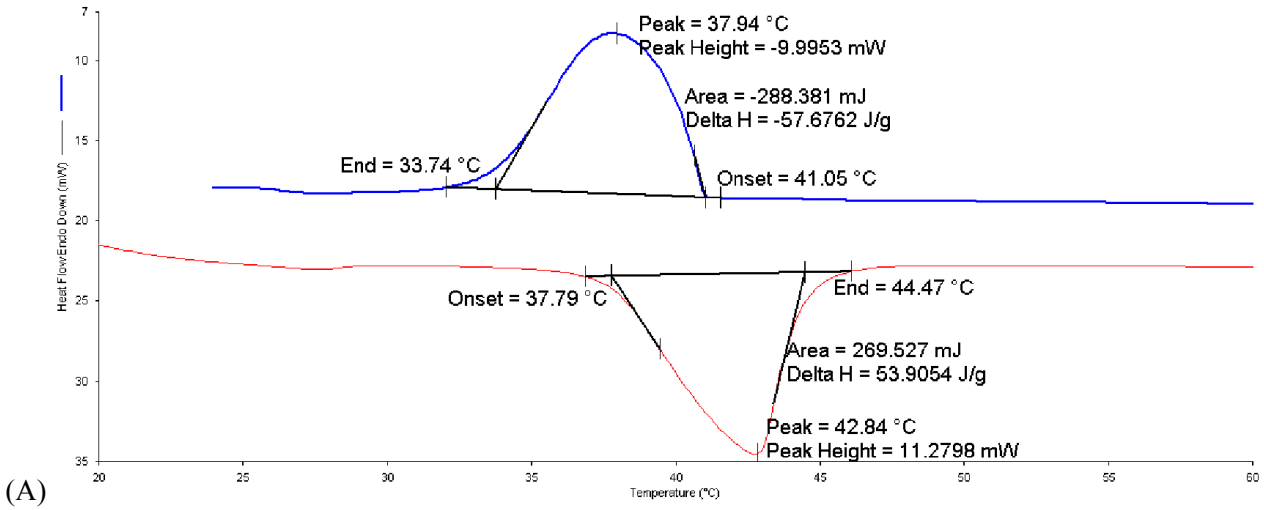


(A)

**Fig.3.** DSC Curves of nanoPCMs

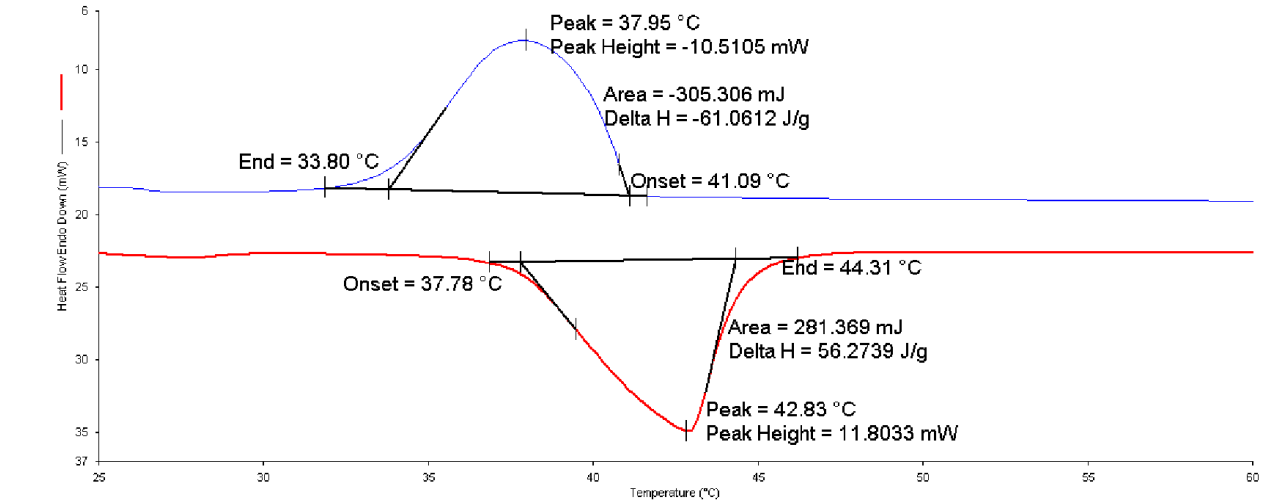


**Fig.4.** DSC Curves of nanoPCMs (95°C)

**Table 1.** Thermal properties of paraffin and microPCMs

| Sample | Tom($^o$C) | Tpm($^o$C) | Tem($^o$C) | Hm (J.g$^{-1}$) | Toc($^o$C) | Tpc($^o$C) | Tec($^o$C) | Hc (J.g$^{-1}$) |
|---|---|---|---|---|---|---|---|---|
| paraffin | 36,87 | 41,90 | 43,43 | 168,08 | 40,35 | 37,70 | 32,24 | -164,97 |
| NCPCM | 37,79 | 11,27 | 44,47 | 53,90 | 41,05 | 37,94 | 33,74 | -57,67 |
| NCPCM(95$^0$C) | 37,78 | 11,80 | 44,31 | 56,27 | 41,09 | 37,95 | 33,80 | -61,06 |

$T_{om}$: Onset melting temperature of DSC curve. $T_{oc}$: Onset crystallizing temperature of DSC curve.
$T_{pc}$: Crystallizing peak temperature of DSC curve. $T_{pm}$: Melting peak temperature of DSC curve.
$T_{ec}$: Endset crystallizing temperature of DSC curve. $T_{em}$: Endset melting temperature of DSC curve.
$H_c$: Crystallization enthalpy of PCMs in DSC curve $H_m$: Melting enthalpy of PCMs in DSC curve.

**Table 2.** Comparison of thermal properties prepared diatomite/ paraffin composite with our previous study

| Sample | Method | Tom ($^o$C) | Hm (J.g-1) | References |
|---|---|---|---|---|
| Diatomite/paraffin nanocomposite | Without ultrasonic treatment | 36.55 | 53.15 | Our previous study[1] |
| Diatomite/paraffin nanocomposite | With ultrasonic treatment | 37.79 | 53.90 | This study |

$T_{om}$: Onset melting temperature of DSC curve.
$H_m$: Melting enthalpy of PCMs in DSC curve.

## CONCLUSIONS

In this study paraffin/diatomite composite was prepared by an ultrasonic-assisted direct impregnation method as thermal energy storage materials. In the composites, the paraffin was used as PCMs for thermal energy storage, and the diatomite was used as supporting material. The structure and thermal properties of prepared nano composites have been characterized by SEM and DSC. The results indicate that treatment with ultrasonic probe had a destructive effect on diatom frustules. However, porous frustule walls protected paraffin from environmental factors as a supporting matrix and phase changes occurred in nanopores of diatomite frustule walls even though the whole frustule structure was damaged due to sonication. The ultrasonication treatment using different amplitude and cycle settings in order to protect the whole structure of frustules will be a subject of future research. Obtained from DSC results, the melting and freezing temperatures of paraffin/diatomite composite are 37,79 °C and 41,05 °C and the latent heats of paraffin/diatomite are 53,90 J/g and 57,67 J/g. We recommend paraffin/diatomite composites prepared by an ultrasonic-assisted direct impregnation method as thermal energy storage materials.

## ACKNOWLEDGEMENTS

We would like to thank The Scientific & Technical Research Council of Turkey (TUBITAK) (The Project Code: TUBITAK 115M525) for financial support for this study.

## REFERENCES

1 Konuklu, Y., Ersoy, O., & Gokce, O. *Applied Thermal Engineering,* 91, 759-76 (2015).
2 Tang, F., Su, D., Tang, Y., & Fang, G, *Solar Energy Materials and Solar Cells*, 141, 218-224.
3 Fu, X., Liu, Z., Xiao, Y., Wang, J., & Lei, J. *Energy and Buildings*, 104, 244-249(2015).
4 Li, M., Wu, Z., & Kao, H. (2011). *Solar Energy Materials and Solar Cells*, 95(8), 2412-2416.
5 Xu, S., Zou, L., Ling, X., Wei, Y., & Zhang, S. (2014). *Energy and Buildings*, 68, 372-375.

# BULGARIAN CHEMICAL COMMUNICATIONS

## Instructions about Preparation of Manuscripts

**General remarks:** Manuscripts are submitted in English by e-mail or by mail (in duplicate). The text must be typed double-spaced, on A4 format paper using Times New Roman font size 12, normal character spacing. The manuscript should not exceed 15 pages (about 3500 words), including photographs, tables, drawings, formulae, etc. Authors are requested to use margins of 3 cm on all sides. For mail submission hard copies, made by a clearly legible duplication process, are requested. Manuscripts should be subdivided into labelled sections, e.g. **Introduction, Experimental, Results and Discussion**, *etc*.

**The title page** comprises headline, author's names and affiliations, abstract and key words.

Attention is drawn to the following:

a) **The title** of the manuscript should reflect concisely the purpose and findings of the work. Abbreviations, symbols, chemical formulas, references and footnotes should be avoided. If indispensable, abbreviations and formulas should be given in parentheses immediately after the respective full form.

b) **The author**'s first and middle name initials, and family name in full should be given, followed by the address (or addresses) of the contributing laboratory (laboratories). **The affiliation** of the author(s) should be listed in detail (no abbreviations!). The author to whom correspondence and/or inquiries should be sent should be indicated by asterisk (*).

**The abstract** should be self-explanatory and intelligible without any references to the text and containing not more than 250 words. It should be followed by key words (not more than six).

**References** should be numbered sequentially in the order, in which they are cited in the text. The numbers in the text should be enclosed in brackets [2], [5, 6], [9–12], etc., set on the text line. References, typed with double spacing, are to be listed in numerical order on a separate sheet. All references are to be given in Latin letters. The names of the authors are given without inversion. Titles of journals must be abbreviated according to Chemical Abstracts and given in italics, the volume is typed in bold, the initial page is given and the year in parentheses. Attention is drawn to the following conventions:

a) The names of all authors of a certain publications should be given. The use of "*et al*." in the list of references is not acceptable.

b) Only the initials of the first and middle names should be given.

In the manuscripts, the reference to author(s) of cited works should be made without giving initials, e.g. "Bush and Smith [7] pioneered...". If the reference carries the names of three or more authors it should be quoted as "Bush *et al*. [7]", if Bush is the first author, or as "Bush and co-workers [7]", if Bush is the senior author.

**Footnotes** should be reduced to a minimum. Each footnote should be typed double-spaced at the bottom of the page, on which its subject is first mentioned.

**Tables** are numbered with Arabic numerals on the left-hand top. Each table should be referred to in the text. Column headings should be as short as possible but they must define units unambiguously. The units are to be separated from the preceding symbols by a comma or brackets.

Note: The following format should be used when figures, equations, *etc*. are referred to the text (followed by the respective numbers): Fig., Eqns., Table, Scheme.

**Schemes and figures**. Each manuscript (hard copy) should contain or be accompanied by the respective illustrative material as well as by the respective figure captions in a separate file (sheet). As far as presentation of units is concerned, SI units are to be used. However, some non-SI units are also acceptable, such as °C, ml, l, etc.

The author(s) name(s), the title of the manuscript, the number of drawings, photographs, diagrams, etc., should be written in black pencil on the back of the illustrative material (hard copies) in accordance with the list enclosed. Avoid using more than 6 (12 for reviews, respectively) figures in the manuscript. Since most of the illustrative materials are to be presented as 8-cm wide pictures, attention should be paid that all axis titles, numerals, legend(s) and texts are legible.

The authors are asked to submit **the final text** (after the manuscript has been accepted for publication) in electronic form either by e-mail or mail on a 3.5'' diskette (CD) using a PC Word-processor. The main text, list of references, tables and figure captions should be saved in separate files (as *.rtf or *.doc) with clearly identifiable file names. It is essential that the name and version of

the word-processing program and the format of the text files is clearly indicated. It is recommended that the pictures are presented in *.tif, *.jpg, *.cdr or *.bmp format, the equations are written using "Equation Editor" and chemical reaction schemes are written using ISIS Draw or ChemDraw programme.

The authors are required to submit the final text with a list of three individuals and their e-mail addresses that can be considered by the Editors as potential reviewers. Please, note that the reviewers should be outside the authors' own institution or organization. The Editorial Board of the journal is not obliged to accept these proposals.

## EXAMPLES FOR PRESENTATION OF REFERENCES

### REFERENCES


1. D. S. Newsome, *Catal. Rev.–Sci. Eng*., **21**, 275 (1980).
2. C.-H. Lin, C.-Y. Hsu, *J. Chem. Soc. Chem. Commun*., 1479 (1992).
3. R. G. Parr, W. Yang, Density Functional Theory of Atoms and Molecules, Oxford Univ. Press, New York, 1989.
4. V. Ponec, G. C. Bond, Catalysis by Metals and Alloys (Stud. Surf. Sci. Catal., vol. 95), Elsevier, Amsterdam, 1995.
5. G. Kadinov, S. Todorova, A. Palazov, in: New Frontiers in Catalysis (Proc. 10th Int. Congr. Catal., Budapest, 1992), L. Guczi, F. Solymosi, P. Tetenyi (eds.), Akademiai Kiado, Budapest, 1993, Part C, p. 2817.
6. G. L. C. Maire, F. Garin, in: Catalysis. Science and Technology, J. R. Anderson, M. Boudart (eds), vol. 6, Springer-Verlag, Berlin, 1984, p. 161.
7. D. Pocknell, *GB Patent* 2 207 355 (1949).
8. G. Angelov, PhD Thesis, UCTM, Sofia, 2001.
9. JCPDS International Center for Diffraction Data, Power Diffraction File, Swarthmore, PA, 1991.
10. CA **127**, 184 762q (1998).
11. P. Hou, H. Wise, *J. Catal.*, in press.
12. M. Sinev, private communication.
13. http://www.chemweb.com/alchem/articles/1051611477211.html.

*Bulgarian Chemical Communications, Volume 48, Special Issue E 2016*

# CONTENTS

## PART E1

SOLAR AND HYBRID THERMAL SYSTEMS

SOLAR PHOTOVOLTAIC SYSTEMS



STORAGES WITH PHASE CHANGE MATERIALS



**PART E2**

ENERGY EFFICIENCY

MATERIALS SCIENCE

FOOD ENGINEERING AND TECHNOLOGIES

BIOTECHNOLOGIES